

RUSSIAN ACADEMY OF SCIENCES
INSTITUTE FOR PROBLEMS IN MECHANICAL ENGINEERING
PETER THE GREAT ST. PETERSBURG POLYTECHNIC UNIVERSITY

Proceedings of the XLIV Summer School – Conference

ADVANCED PROBLEMS IN MECHANICS

A P M 2 0 1 6

St. Petersburg



POLYTECH

Peter the Great
St. Petersburg Polytechnic
University



IPME RAS

Institute for Problems in
Mechanical Engineering
Russian Academy of Sciences

<http://apm-conf.spb.ru>

St. Petersburg, 2016

SCIENTIFIC COMMITTEE AND EDITORIAL BOARD

- **D. A. Indeitsev** (*Co-Chairman*), IPME RAS, Peter the Great St. Petersburg Polytechnic University, Russia
- **A. M. Krivtsov** (*Co-Chairman*), Peter the Great St. Petersburg Polytechnic University, IPME RAS, Russia
- **P. A. Dyatlova** (*Scientific Secretary*), Peter the Great St. Petersburg Polytechnic University, IPME RAS, Russia
- **O. S. Loboda**, Peter the Great St. Petersburg Polytechnic University, IPME RAS, Russia
- **H. Altenbach**, Otto-von-Guericke University Magdeburg, Germany
- **V. A. Babeshko**, Southern Scientific Center RAS, Rostov-on-Don, Russia
- **A. K. Belyaev**, IPME RAS, St. Petersburg, Russia
- **I. E. Berinskii**, Tel Aviv University, Israel
- **I. I. Blekhman**, IPME RAS, Mekhanobr-tekhnika Corp., St. Petersburg, Russia
- **A. A. Burenin**, Institute of Metallurgy and Mechanical Engineering Far-Eastern Branch RAS, Komsomolsk-na-Amure, Russia
- **A. Castellanos**, University of Seville, Spain
- **A. V. Cherkaev**, University of Utah, Salt Lake City, USA
- **V. A. Eremeyev**, Rzeszow University of Technology, Poland
- **A. B. Freidin**, IPME RAS, Peter the Great St. Petersburg Polytechnic University, Russia
- **S. N. Gavrilov**, IPME RAS, St. Petersburg, Russia
- **R. V. Goldstein**, Institute for Problems in Mechanics RAS, Moscow, Russia
- **I. G. Goryacheva**, Institute for Problems in Mechanics RAS, Moscow, Russia
- **E. F. Grekova**, IPME RAS, St. Petersburg, Russia; University of Seville, Spain
- **N. Gupta**, Indian Institute of Technology, Delhi, India
- **H. Irschik**, Johannes Kepler University of Linz, Austria
- **M. L. Kachanov**, Tufts University, Medford, USA
- **B. L. Karihaloo**, Cardiff University, UK
- **V. A. Levin**, M. V. Lomonosov Moscow State University, Russia
- **A. M. Linkov**, IPME RAS, St. Petersburg, Russia; Rzeszow University of Technology, Poland
- **I. I. Lipatov**, Moscow Institute of Physics and Technology, Russia
- **E. V. Lomakin**, M. V. Lomonosov Moscow State University, Russia
- **A. V. Manzhurov**, Institute for Problems in Mechanics RAS, Moscow, Russia
- **G. A. Maugin**, Pierre and Marie Curie University, Paris, France
- **A. V. Metrikine**, Delft University of Technology, The Netherlands
- **G. Mishuris**, Aberystwyth University, UK
- **N. F. Morozov**, St. Petersburg State University, IPME RAS, Russia
- **W. H. Müller**, Technical University of Berlin, Germany
- **U. Nackenhorst**, Leibniz University of Hanover, Germany
- **V. A. Palmov**, Peter the Great St. Petersburg Polytechnic University, IPME RAS, Russia
- **E. Pavlovskaya**, University of Aberdeen, UK
- **Y. V. Petrov**, St. Petersburg State University, IPME RAS, Russia
- **M. B. Rubin**, Israel Institute of Technology, Haifa, Israel
- **A. I. Rudskoy**, Peter the Great St. Petersburg Polytechnic University, Russia
- **S. H. Sargsyan**, Gyumri State Pedagogical Institute, Armenia
- **E. N. Vilchevskaya**, Peter the Great St. Petersburg Polytechnic University, IPME RAS, Russia
- **M. Wiercigroch**, University of Aberdeen, UK
- **M. V. Zakrzhevsky**, Institute of Mechanics, Riga Technical University, Latvia

PREFACE

Dear Reader,

in this book you will find the Proceedings of the Summer School – Conference “Advanced Problems in Mechanics (APM) 2016”. The conference had been started in 1971. The first Summer School was organized by Prof. Ya.G. Panovko and his colleagues. In the early years the main focus of the School was on nonlinear oscillations of mechanical systems with a finite number of degrees of freedom. Since 1994 the Institute for Problems in Mechanical Engineering of the Russian Academy of Sciences organizes the Summer School. The traditional name of “Summer School” has been kept, but the topics covered by the School have been much widened, and the School has been transformed into an international conference. Now it is held under the patronage of the Russian Academy of Sciences. The topics of the conference cover now almost all fields of mechanics, being concentrated around the following main scientific directions:

- aerospace mechanics;
- computational mechanics;
- dynamics of rigid bodies and multibody dynamics;
- fluid and gas;
- mechanical and civil engineering applications;
- mechanics of media with microstructure;
- mechanics of granular media;
- nanomechanics;
- nonlinear dynamics, chaos and vibration;
- molecular and particle dynamics;
- phase transitions;
- solids and structures;
- wave motion.

The Summer School – Conference has two main purposes: to gather specialists from different branches of mechanics to provide a platform for cross-fertilization of ideas, and to give the young scientists a possibility to learn from their colleagues and to present their work. Thus the Scientific Committee encouraged the participation of young researchers, and did its best to gather at the conference leading scientists belonging to various scientific schools of the world.

We believe that the significance of Mechanics as of fundamental and applied science should much increase in the eyes of the world scientific community, and we hope that APM conference makes its contribution into this process.

We are happy to express our sincere gratitude for a partial financial support to Russian Foundation for Basic Research, Russian Academy of Sciences, St.Petersburg Scientific Center and Ministry of Education and Science of Russian Federation (project indentificator RFMEFI 60715X0120). This support has helped substantially to organize the conference and to increase the participation of young researchers.

We hope that you will find the materials of the conference interesting, and we cordially invite you to participate in the coming APM conferences. You may find the information on the future “Advanced Problems in Mechanics” Schools – Conferences at our website:

<http://apm-conf.spb.ru>

With kind regards,

Co-Chairmen of APM 2016

Dmitri A. Indeitsev, Anton M. Krivtsov

Contents

- B.E. Abali, W.H. Müller.* **Comparison of different methodologies leading to a generalized elasticity theory for modeling of the size effect** 9
- E.L. Aero, A.N. Bulygin, Yu.V. Pavlov.* **Functionally invariant solutions of the nonlinear nonautonomic Klein-Fock-Gordon equation** 19
- A.R. Arutyunyan, R.A. Arutyunyan.* **Mechanical model of damage and fracture of aging polymer materials** 27
- A.R. Arutyunyan, R.A. Arutyunyan, R.R. Saitova.* **The problem of damage and high-temperature creep fracture of metals** 33
- S.A. Atroshenko.* **Effect of electron beam processing on the characteristics of tool steels** 40
- V.A. Babeshko, O.V. Evdokimova, O.M. Babeshko, A.S. Muhin, I.B. Gladskoi, E.M. Gorshkova.* **Block element forms and factorization methods in cylindrical coordinate systems** 45
- N.V. Banichuk, S.Yu. Ivanova.* **Deformation and divergence of the moving beams made from thermoelastic materials** 53
- S.P. Bautin, I.Yu. Krutova, A.G. Obukhov.* **Mathematical and Experimental Simulation of the Ascending Twisting Flows** 58
- V.V. Eliseev, E.A. Oborin.* **Statics and harmonic oscillations of springs as rods of arbitrary spatial shape** 62
- A. Evgrafova, A. Sukhanovskii, E. Popova.* **The characteristics of steady-state convective cyclonic vortex** 68
- A.N. Fedorova, M.G. Zeitlin.* **Invariant calculations in beam physics: dynamics on semi-direct products and CWT** 75

- A.N. Fedorova, M.G. Zeitlin.* **Symplectic framework, discrete variational approach and Harten's multiresolution scheme in beam dynamics** 87
- S.I. Ezhenkova, S.A. Chivilikhin.* **Finding the distribution density of settling nanoparticles in a liquid with regard to their Brownian diffusion using the boundary layer theory** 102
- A.V. Fedotov.* **Biomorphic approach in application to vibration control of continuous systems** 106
- G.V. Filippenko.* **Energy aspects of axisymmetric wave propagation in an infinite cylindrical shell filled with the liquid.** 118
- K.P. Frolova, E.N. Vilchevskaya, W.H. Müller, W. Weiss.* **Comparison of numerical approaches for inverse Laplace transform by the example of intraocular pressure determination** 125
- M.P. Galanin, P.V. Gliznutsina, V.V. Lukin, A.S. Rodin.* **Lagrange multiplier method implementations for two-dimensional contact problems** 138
- G. Ganzosch, W.H. Müller.* **Experimental techniques applied to generalized continuum theories: A state-of-the-art report** 148
- O.K. Garishin, S.N. Lebedev.* **Determination of nanoscale mechanical properties of rubbers under uniaxial stretching by means atomic force microscopy** 161
- O.K. Garishin, V.V. Shadrin, V.A. Gerasin, M.A. Guseva.* **Experimental research and computer modeling of the mechanical behavior of polymer/clay nanocomposites under large deformations** 168
- I. Golovin, S. Palis, A. Timoschenko, V. Klepikov.* **Damping of friction-induced vibrations applying parallel compensator** 176
- M. Grehn, A. Fau, U. Nackenhorst.* **A Stochastic Finite Element**

Approach on Creep of Rock Salt	187
<i>R.V. Guchinsky, S.V. Petinov, V.G. Sidorenko.</i> Damage Accumulation-based and FEA-aided Fatigue Life Evaluation of Tubular Structures	198
<i>A. Hakem, A. Hakem, Y. Bouafia.</i> Influence of the treatments on the behavior and the damage in tensile and with the shock of the recovery alloy AlSi12: application to the recycling of waste	205
<i>A.V. Ivanov.</i> On homoclinics and heteroclinics of Lagrangian systems in a non-stationary force field	211
<i>V.M. Kolykhalin.</i> Investigation of the noise reduction effect of ventilating systems	223
<i>S.S. Kostyrko, G.M. Shuvalov.</i> Morphological stability of thin film materials during annealing	229
<i>N.A. Krylov, M.A. Skotnikova.</i> Phase transitions in titanium alloys at high-speed mechanical effect	237
<i>V.A. Levin, T.A. Zhuravskaya.</i> Detonation combustion in a supersonic gas flow in a plane channel	246
<i>C. Liebold, W.H. Müller, F.A. Reich.</i> Modified strain gradient theory and Timoshenko beam assumptions—A direct approach	255
<i>S.A. Lurie, Qi Chengzhi, P.A. Belov.</i> On correctness of gradient plasticity theory	265
<i>B. Markert, S.P. Patil.</i> Linking molecular and continuum mechanics with application to biomimetic nanomaterials and brittle fracture	279

<i>T.M. Michelitsch, B.A. Collet, A.P. Riascos, A.F. Nowakowski, F.C.G.A. Nicolleau.</i> Fractional Lattice Dynamics: Nonlocal constitutive behavior generated by power law matrix functions and their fractional continuum limit kernels	293
<i>I.A. Morozov.</i> Structural-mechanical AFM mapping of overstressed zones in stretched filled natural rubber	309
<i>E.A. Mosheva, A.I. Mizev, K.G. Kostarev.</i> Chemoconvective structures driven by a neutralization reaction	315
<i>W.H. Müller, W. Weiss, E.N. Vilchevskaya.</i> Assessing Deformation due to Self-Gravitation - Treacherous Pathways of Continuum Mechanics	323
<i>A.Yu. Nikonov, A.I. Dmitriev, W. Österle.</i> Molecular dynamics study of the relative sliding mechanisms in amorphous silica	336
<i>A.Yu. Nikonov, A.I. Dmitriev, Y.P. Sharkeev.</i> Molecular dynamics study of the influence of the parameters of the crystallization process during selective laser sintering of alloy Ti-Nb	344
<i>E.V. Prozorova.</i> Effects of dispersion and structure molecules on time relaxation	351
<i>A.V. Pyatkova, A.S. Semenova.</i> Acoustic streaming in a rectangular cavity	357
<i>S.H. Sargsyan, M.V. Khachatryan.</i> Mathematical model of static deformation of micropolar elastic circular thin bar	366
<i>M.V. Shamolin.</i> Cases of integrability corresponding to the motion of a pendulum in the three-dimensional space	374
<i>A.K. Sokolov, A.L. Svistkov, L.A. Komar, V.V. Shadrin, V.N. Terpugov.</i> Features of simulation of the tire under conditions of	

movement of the car with acceleration	387
<i>A.D. Stepanov, A.M. Linkov. On increasing efficiency of hydraulic fracture simulation by using dynamic approach of modified theory</i>	392
<i>A.K. Tiwari, N. Kumar. A Neural Network Model to Investigate the Effect of Frequency and Time on Loading Induced Osteogenesis</i>	403
<i>V.N. Zakcharov, O.N. Malinnikova, V.A. Trofimov. Formation and propagation of methane seepage wave in stressed coal</i>	412
<i>M.G. Zhuchkova. Scattering of flexural-gravitational waves by a periodic array of obstacles in an elastic plate floating on a thin fluid layer</i>	422

Comparison of different methodologies leading to a generalized elasticity theory for modeling of the size effect

B. Emek Abali, Wolfgang H. Müller
abali@tu-berlin.de

Abstract

Miniaturization in the production technology necessitates more accurate modeling of structures in the micrometer length scales. The well-known theory of elasticity shows inadequacies when trying to mimic experimental observations. Hence, it needs to be generalized. There are two different ways in continuum mechanics for the formulation of elasticity: Rational mechanics and classical analytical mechanics. Both methods can be used to study and generalize *traditional* elasticity theory. In this work we aim at a comparison of these methods in order to obtain more insight into their pros and cons as well as their limitations.

1 Introduction

Traditional elasticity theory of continuum mechanics fails to model structures on the micrometer length scale with sufficient accuracy. However, nowadays, for example in micro-electro-mechanical systems (MEMS), modeling and simulation of small scale designs are of paramount importance. Many experimental observations over the last decades—see for example [6], [7], [5]—indicate a size effect showing up at the micrometer length scale. By scaling down the dimensions of a structure, the deformation starts to deviate from the expected results calculated by traditional elasticity theory. This behavior is referred to as the size effect. As justified by many experimental observations we need a generalization of elasticity theory. There are, indeed, many propositions about possible generalizations in the literature. The different theories can be grouped into two methods.

Rational mechanics can be used to obtain a generalization of the elasticity theory. In addition to the balance of linear momentum, the balances of angular momentum and spin are used in order to capture the effects introduced by materials showing a size effect. In this work, we give a brief outline of the method based on rational mechanics, which has already been discussed in [3] and [2].

Classical analytical mechanics delivers a straightforward way for generalizing elasticity theory. Starting from the principle of least action, we can incorporate the effects

necessary for modeling the size effect. We will also outline the method stemming from classical analytical mechanics as done in [1].

The two different methodologies lead to weak forms that allow us to compute the size effect as observed in experiments. Both methods deliver the same deformation behavior as observed in experiments. However, the methods are inherently different. Hence, in this work, we want to compare the methods and find out their analogies as well as dissimilarities.

2 Rational mechanics

Throughout the paper we use the standard notation of continuum mechanics. Summation is implied if double indices appear in a product. In rational mechanics we start axiomatically with the balance equations. They are given at the current time for a material system, where the totality of particles compiling the continuum body remains the same. The continuum body, \mathcal{B} , consists of the same particles and the balances of mass, linear and angular momenta are:

$$\begin{aligned} \left(\int_{\mathcal{B}} \rho \, dv \right) &= 0 , \\ \left(\int_{\mathcal{B}} p_i^{\text{lin.}} \, dv \right) &= \int_{\partial\mathcal{B}} \sigma_{ji} \, da_j + \int_{\mathcal{B}} \rho f_i \, dv , \\ \left(\int_{\mathcal{B}} p_i^{\text{ang.}} \, dv \right) &= \int_{\partial\mathcal{B}} \alpha_{ji} \, da_j + \int_{\mathcal{B}} \rho z_i \, dv , \end{aligned} \tag{1}$$

respectively. The mass density, ρ , is the mass per unit volume. The linear and angular momenta densities read:

$$p_i^{\text{lin.}} = \rho v_i , \quad p_i^{\text{ang.}} = \rho a_i , \tag{2}$$

where the specific linear momentum (per mass) or velocity, v_i , and the specific angular momentum, a_i , are the sought variables. On the right-hand sides of the balance equations the fluxes and supplies of momenta appear. The flux of linear momentum, σ_{ji} , is called CAUCHY's stress. The flux term of angular momentum, α_{ji} , has no particular name. The supply of the linear momentum, f_i , is the specific body force, for example the gravitational force per mass (acceleration). The supply of the angular momentum, z_i , is also a volumetric effect, leading to a change in the angular momentum.

In solid mechanics we transform the balance equations onto the reference frame from where the particles can be tracked. For example, we can use the initial positions of particles, X_i , as the reference frame such that X_i denotes the particles. This configuration is called a LAGRANGEan frame and by employing tensor calculus we obtain the balance of mass and momenta in the LAGRANGEan frame, locally,

$$\begin{aligned} \rho_0 &= \rho J , \\ \rho J \frac{\partial v_i}{\partial t} &= \frac{\partial P_{ji}}{\partial X_j} + \rho J f_i , \\ \rho J \frac{\partial a_i}{\partial t} &= \frac{\partial A_{ji}}{\partial X_j} + \rho J z_i , \end{aligned} \tag{3}$$

with the fluxes of linear and angular momenta in the LAGRANGEan frame:

$$P_{ji} = (\mathbf{F}^{-1})_{jk} J \sigma_{ki} , \quad A_{ji} = (\mathbf{F}^{-1})_{jk} J \alpha_{ki} . \quad (4)$$

The deformation gradient, F_{ij} , is the mapping between the current and reference (here initial) frame and J is its determinant:

$$F_{ij} = \frac{\partial x_i}{\partial X_j} = \frac{\partial u_i}{\partial X_j} + \delta_{ij} , \quad J = \det(\mathbf{F}) . \quad (5)$$

The balance of mass is an equation instead of a differential equation, so we just use it instead of solving it. From the solution of the following differential equations:

$$\begin{aligned} \rho_0 \frac{\partial v_i}{\partial t} &= \frac{\partial P_{ji}}{\partial X_j} + \rho_0 f_i , \\ \rho_0 \frac{\partial a_i}{\partial t} &= \frac{\partial A_{ji}}{\partial X_j} + \rho_0 z_i , \end{aligned} \quad (6)$$

we obtain v_i and a_i as functions of (X_i, t) . We may introduce another quantity, called spin, s_i , as follows:

$$a_i = s_i + \epsilon_{ijk} X_j v_k . \quad (7)$$

In rigid body mechanics the second part of this relation is well-known. However, in continuum mechanics spin is an intrinsic property of a *polar* material, which we fail to observe directly, like internal energy. The best example is a nematic fluid (as in a liquid crystal display) where the change of spin varies the interaction of the matter with light. For non-polar materials spin vanishes, $s_i = 0$. The LEVI-CIVITA symbol, ϵ_{ijk} , allows to determine the cross product between the particle's position X_i and its velocity v_i . It is called the moment of linear momentum in the LAGRANGEan frame. Since we have to fulfill all balance equations simultaneously, we can multiply the balance of linear momentum with $\epsilon_{kli} X_l$ and then subtract from the balance of angular momentum to obtain the balance of spin exclusively:

$$\begin{aligned} \rho_0 \frac{\partial s_k}{\partial t} &= \frac{\partial}{\partial X_j} \left(A_{jk} - \epsilon_{kli} X_l P_{ji} \right) + P_{ji} \frac{\partial \epsilon_{kli} X_l}{\partial X_j} + \rho_0 (z_k - \epsilon_{kli} X_l f_i) , \\ \rho_0 \frac{\partial s_k}{\partial t} &= \frac{\partial \mu_{jk}}{\partial X_j} + \epsilon_{kji} P_{ji} + \rho_0 l_k , \end{aligned} \quad (8)$$

with the flux of spin and the specific supply of spin,

$$\mu_{jk} = A_{jk} - \epsilon_{kli} X_l P_{ji} , \quad l_k = z_k - \epsilon_{kli} X_l f_i , \quad (9)$$

respectively. In case of a non-polar material the spin vanishes, $s_i = 0$. Then we multiply the spin balance for a non-polar material by $\frac{1}{2} \epsilon_{mnk}$ and employ the identity $\epsilon_{mnk} \epsilon_{kji} = \delta_{mj} \delta_{ni} - \delta_{mi} \delta_{nj}$, such that we obtain

$$\begin{aligned} 0 &= \frac{1}{2} \epsilon_{mnk} \frac{\partial \mu_{jk}}{\partial X_j} + \frac{1}{2} \epsilon_{mnk} \epsilon_{kji} P_{ji} + \frac{1}{2} \epsilon_{mnk} \rho_0 l_k , \\ 0 &= \frac{\partial \mu_{jmn}}{\partial X_j} + \frac{1}{2} (P_{mn} - P_{nm}) + \rho_0 l_{mn} , \\ -\frac{\partial \mu_{jmn}}{\partial X_j} - \frac{1}{2} (P_{mn} - P_{nm}) - \rho_0 l_{mn} &= 0 \end{aligned} \quad (10)$$

with:

$$\mu_{jmn} = \frac{1}{2}\mu_{jk}\epsilon_{kmn} , \quad l_{mn} = \frac{1}{2}l_k\epsilon_{kmn} . \quad (11)$$

By using a shorthand notation with antisymmetric brackets we acquire:

$$-\frac{\partial\mu_{jmn}}{\partial X_j} - P_{[mn]} - \rho_0 l_{mn} = 0 . \quad (12)$$

The tensor of rank three, μ_{jmn} , is often called the couple stress. Since the spin vanishes for a non-polar material, the only unknown to be calculated that remains is the displacement. Its rate is velocity such that the balance of linear momentum reads:

$$\rho_0 \frac{\partial^2 u_i}{\partial t^2} - \frac{\partial P_{ji}}{\partial X_j} - \rho_0 f_i = 0 . \quad (13)$$

The nominal stress tensor, P_{ji} , as well as couple stress, μ_{jmn} , need to be defined by means of the displacement or its gradients in order to close Eqs. (12), (13). We refer to [4] for the detailed derivation of the following constitutive equations for an isotropic material:

$$S_{ij} = C_{ijkl}E_{kl} , \quad \mu_{ijk} = D_{ijklmn}E_{lm,n} , \quad (14)$$

where the second PIOLA-KIRCHHOFF, S_{ij} , and GREEN-LAGRANGE strains, E_{ij} , are given by

$$S_{ij} = (\mathbf{F}^{-1})_{jk}P_{ik} , \quad E_{ij} = \frac{1}{2}(F_{ki}F_{kj} - \delta_{ij}) . \quad (15)$$

We start using a simplified notation for the derivative in space:

$$(\cdot)_{,i} = \frac{\partial(\cdot)}{\partial X_i} . \quad (16)$$

For isotropic materials the stress depends only on strain and the couple stress depends only on strain gradients. The dependency is such that the stiffness tensor, C_{ijkl} , and the material tensor, D_{ijklmn} , is expanded as follows:

$$\begin{aligned} C_{ijkl} &= c_1\delta_{ij}\delta_{kl} + c_2(\delta_{ik}\delta_{jl} + \delta_{il}\delta_{jk}) , \\ D_{ijklmn} &= c_3(\delta_{ij}\delta_{kl}\delta_{mn} + \delta_{in}\delta_{jk}\delta_{lm} + \delta_{ij}\delta_{km}\delta_{ln} + \delta_{ik}\delta_{jn}\delta_{lm}) + c_4\delta_{ij}\delta_{kn}\delta_{ml} + \\ &+ c_5(\delta_{ik}\delta_{jl}\delta_{mn} + \delta_{im}\delta_{jk}\delta_{ln} + \delta_{ik}\delta_{jm}\delta_{ln} + \delta_{il}\delta_{jk}\delta_{mn}) + c_6(\delta_{il}\delta_{jm}\delta_{kn} + \delta_{im}\delta_{jl}\delta_{kn}) + \\ &+ c_7(\delta_{il}\delta_{jn}\delta_{mk} + \delta_{im}\delta_{jn}\delta_{lk} + \delta_{in}\delta_{jl}\delta_{km} + \delta_{in}\delta_{jm}\delta_{kl}) . \end{aligned} \quad (17)$$

For a linear, isotropic, homogeneous material, the seven material parameters, c_\times , are constant values. It is also beneficial to note the following relation for the so-called stored energy density:

$$w = \int S_{ij} dE_{ji} + \int \mu_{ijk} dE_{kj,i} = \frac{1}{2}C_{ijkl}E_{kl}E_{ji} + \frac{1}{2}D_{ijklmn}E_{lm,n}E_{kj,i} , \quad (18)$$

which holds, because C_{ijkl} and D_{ijklmn} are constants for a linear material. Obviously, the following relations result:

$$S_{ij} = \frac{\partial w}{\partial E_{ji}}, \quad \mu_{ijk} = \frac{\partial w}{\partial E_{kj,i}}. \quad (19)$$

For a numerical computation we need a so-called weak form. In order to obtain the weak form for the whole continuum body, \mathcal{B}_0 , we multiply the balance Eqs. (12), (13) written as a residuals by the so-called test functions, δu_i , $\delta u_{n,m}$, respectively,

$$\int_{\mathcal{B}_0} \left(\left(\rho_0 \frac{\partial^2 u_i}{\partial t^2} - P_{ji,j} - \rho_0 f_i \right) \delta u_i - \left(\mu_{jmn,j} + P_{[mn]} + \rho_0 l_{mn} \right) \delta u_{n,m} \right) dV = 0. \quad (20)$$

We discretize in time by using a EULER backwards finite difference scheme,

$$\int_{\mathcal{B}_0} \left(\rho_0 \frac{u_i - 2u_i^0 + u_i^{00}}{\Delta t^2} \delta u_i - P_{ji,j} \delta u_i - \rho_0 f_i \delta u_i - \mu_{jmn,j} \delta u_{n,m} - P_{[mn]} \delta u_{n,m} - \rho_0 l_{mn} \delta u_{n,m} \right) dV = 0, \quad (21)$$

where u_i^0 denotes the value from the last time step and u_i^{00} indicates the value from the two time steps before. According to the GALERKIN procedure in the finite element method, we choose the test functions, δu_i , from the same space as u_i . Stress and couple stress have already a derivative in u_i and $u_{i,j}$ such that another differentiation with respect to X_i increases the necessity of differentiability. We can weaken this fact by “shifting” the derivative to the test functions by employing integrations by parts as follows:

$$\int_{\mathcal{B}_0} \left(\rho_0 \frac{u_i - 2u_i^0 + u_i^{00}}{\Delta t^2} \delta u_i + P_{ji} \delta u_{i,j} - \rho_0 f_i \delta u_i + \mu_{jmn} \delta u_{n,mj} - P_{[mn]} \delta u_{n,m} - \rho_0 l_{mn} \delta u_{n,m} \right) dV - \int_{\partial \mathcal{B}_0} (P_{ji} \delta u_i + \mu_{jmn} \delta u_{n,m}) N_j dA = 0. \quad (22)$$

The boundary terms shall be known. The force per area, $\hat{t}_i = N_j P_{ji}$, is called the traction vector. Analogously, we can call the moment per area, $\hat{m}_{mn} = N_j \mu_{jmn}$, the torsion vector. Finally, the weak form for a non-polar, isotropic, linear elastic material reads:

$$\text{Form} = \int_{\mathcal{B}_0} \left(\rho_0 \frac{u_i - 2u_i^0 + u_i^{00}}{\Delta t^2} \delta u_i + P_{ji} \delta u_{i,j} - \rho_0 f_i \delta u_i + \mu_{jmn} \delta u_{n,mj} - P_{[mn]} \delta u_{n,m} - \rho_0 l_{mn} \delta u_{n,m} \right) dV - \int_{\partial \mathcal{B}_0} (\hat{t}_i \delta u_i + \hat{m}_{mn} \delta u_{n,m}) dA. \quad (23)$$

By using the finite element method we can compute the displacement, $u_i(X_j, t)$, satisfying the balance of momenta in the LAGRANGEan frame.

3 Classical analytical mechanics

In the case of classical analytical mechanics we start from a LAGRANGEan density, \mathcal{L} , and define an action:

$$\mathcal{S} = \int_{\Omega} \mathcal{L} d\Sigma, \quad d\Sigma = dx_1 dx_2 \dots dx_m, \quad (24)$$

in m -dimensional space. In mechanics the space, x_ν , is space-time, $x_\nu = \{X_1, X_2, X_3, t\}$, so that the infinitesimal volume element reads $d\Sigma = dV dt$. The axiom is the principle of least action stating the postulate that the action remains the same, if we transform the primitive variables. Primitive variables are displacements. In the application of the traditional elasticity theory, the LAGRANGEan density depends on the primitive variables and its derivatives:

$$\mathcal{L} = \mathcal{L}(x_\nu, u_i, u_{i,\nu}). \quad (25)$$

The comma notation means a partial derivative with respect to space-time:

$$u_{i,\nu} = \frac{\partial u_i}{\partial x_\nu} = \begin{pmatrix} \frac{\partial u_i}{\partial x_j} \\ \frac{\partial u_i}{\partial t} \end{pmatrix}. \quad (26)$$

For the next higher gradient theory, we incorporate the second derivatives, such that the LAGRANGEan density becomes:

$$\mathcal{L} = \mathcal{L}(x_\nu, u_i, u_{i,\nu}, u_{i,\nu\mu}). \quad (27)$$

The principle of least action states:

$$\delta\mathcal{S} = \int_{\Omega} \mathcal{L}' d\Sigma - \int_{\Omega} \mathcal{L} d\Sigma = 0, \quad (28)$$

where the transformed LAGRANGEan density is:

$$\mathcal{L}' = \mathcal{L}(x_\nu, u'_i, u'_{i,\nu}, u'_{i,\nu\mu}), \quad (29)$$

with arbitrary variations made linear by using a small constant number, ε , as follows:

$$u'_i = u_i + \varepsilon\delta u_i, \quad u'_{i,\nu} = u_{i,\nu} + \varepsilon\delta u_{i,\nu}, \quad u'_{i,\nu\mu} = u_{i,\nu\mu} + \varepsilon\delta u_{i,\nu\mu}. \quad (30)$$

Now by expanding \mathcal{L}' around \mathcal{L} we obtain:

$$\mathcal{L}' = \mathcal{L} + \frac{\partial \mathcal{L}}{\partial u_i} \varepsilon\delta u_i + \frac{\partial \mathcal{L}}{\partial u_{i,\nu}} \varepsilon\delta u_{i,\nu} + \frac{\partial \mathcal{L}}{\partial u_{i,\nu\mu}} \varepsilon\delta u_{i,\nu\mu}. \quad (31)$$

Hence, the principle of least action results in:

$$\delta\mathcal{S} = \int_{\Omega} \left(\frac{\partial \mathcal{L}}{\partial u_i} \delta u_i + \frac{\partial \mathcal{L}}{\partial u_{i,\nu}} \delta u_{i,\nu} + \frac{\partial \mathcal{L}}{\partial u_{i,\nu\mu}} \delta u_{i,\nu\mu} \right) d\Sigma = 0, \quad (32)$$

since ε is constant in space, x_ν . Moreover, the space, x_ν , is space-time in the LAGRANGEan frame, $\{X_i, t\}$, thus, the principle of least action asserts:

$$\int_\tau \int_{\mathcal{B}_0} \left(\frac{\partial \mathcal{L}}{\partial u_i} \delta u_i + \frac{\partial \mathcal{L}}{\partial \dot{u}_i} \delta \dot{u}_i + \frac{\partial \mathcal{L}}{\partial u_{i,j}} \delta u_{i,j} + \frac{\partial \mathcal{L}}{\partial \dot{u}_i} \delta \dot{u}_i + \frac{\partial \mathcal{L}}{\partial \dot{u}_{i,j}} \delta \dot{u}_{i,j} + \frac{\partial \mathcal{L}}{\partial u_{i,jk}} \delta u_{i,jk} \right) dV dt = 0 . \quad (33)$$

By using integration by parts on the terms with a time rate in test functions, we acquire:

$$\int_\tau \int_{\mathcal{B}_0} \left(\frac{\partial \mathcal{L}}{\partial u_i} \delta u_i - \left(\frac{\partial \mathcal{L}}{\partial \dot{u}_i} \right) \dot{\delta u}_i + \frac{\partial \mathcal{L}}{\partial u_{i,j}} \delta u_{i,j} + \left(\frac{\partial \mathcal{L}}{\partial \dot{u}_i} \right) \ddot{\delta u}_i + \left(\frac{\partial \mathcal{L}}{\partial \dot{u}_{i,j}} \right) \dot{\delta u}_{i,j} + \frac{\partial \mathcal{L}}{\partial u_{i,jk}} \delta u_{i,jk} \right) dV dt = 0 . \quad (34)$$

The boundary terms in time vanish by selecting the time domain in a specific way. The same arguments are used for a differential equation in time; instead of using an initial and an end value, we can use an initial value and a value for its rate. Furthermore, we may write the integral form locally in time:

$$\int_{\mathcal{B}_0} \left(\frac{\partial \mathcal{L}}{\partial u_i} \delta u_i - \left(\frac{\partial \mathcal{L}}{\partial \dot{u}_i} \right) \dot{\delta u}_i + \frac{\partial \mathcal{L}}{\partial u_{i,j}} \delta u_{i,j} + \left(\frac{\partial \mathcal{L}}{\partial \dot{u}_i} \right) \ddot{\delta u}_i - \left(\frac{\partial \mathcal{L}}{\partial \dot{u}_{i,j}} \right) \dot{\delta u}_{i,j} + \frac{\partial \mathcal{L}}{\partial u_{i,jk}} \delta u_{i,jk} \right) dV = 0 . \quad (35)$$

Moreover, for the boundary values we can select an appropriate action:

$$\mathcal{S} = \int_\tau \int_{\mathcal{B}_0} \mathcal{L} dV dt + \int_\tau \int_{\partial \mathcal{B}_0} W_s dA dt + \int_\tau \int_{\partial \partial \mathcal{B}_0} W_e d\ell dt , \quad (36)$$

where on the boundary surface a potential, W_s , and on the boundary edge another potential, W_e , have to be prescribed. After the analogous steps, the integral form becomes:

$$\int_{\mathcal{B}_0} \left(\frac{\partial \mathcal{L}}{\partial u_i} \delta u_i - \left(\frac{\partial \mathcal{L}}{\partial \dot{u}_i} \right) \dot{\delta u}_i + \frac{\partial \mathcal{L}}{\partial u_{i,j}} \delta u_{i,j} + \left(\frac{\partial \mathcal{L}}{\partial \dot{u}_i} \right) \ddot{\delta u}_i - \left(\frac{\partial \mathcal{L}}{\partial \dot{u}_{i,j}} \right) \dot{\delta u}_{i,j} + \frac{\partial \mathcal{L}}{\partial u_{i,jk}} \delta u_{i,jk} \right) dV + \int_{\partial \mathcal{B}_0} \frac{\partial W_s}{\partial u_i} \delta u_i dA + \int_{\partial \partial \mathcal{B}_0} \frac{\partial W_e}{\partial u_{i,j}} \delta u_{i,j} d\ell = 0 . \quad (37)$$

For elasticity we choose the following LAGRANGEan density and boundary potentials:

$$\mathcal{L} = \frac{1}{2} \rho_0 \dot{u}_i \dot{u}_i - \rho_0 \psi + \rho_0 (f_i u_i + l_{ij} u_{i,j}) , \quad W_s = \hat{t}_i u_i + \hat{m}_{ij} u_{j,i} , \quad W_e = 0 , \quad (38)$$

where the free energy density, $\rho_0 \psi$, is simply the stored energy density, w , in the case of isothermal systems. The stored energy density is a potential such that it depends on $u_{i,j}$ and $u_{i,jk}$, but not on their time rates. The first term is the kinetic energy

density and the last terms model the supply terms performed on the displacement and its gradient. The traction vector, \hat{t}_i , is given as a force per unit area and by the torsion vector, \hat{m}_{ij} , a moment per unit area is applied. Moreover, we neglect an edge boundary energy by setting $W_e = 0$ for easier comparison with the weak form attained from rational mechanics. Finally, by inserting the LAGRANGEan density and boundary potentials into the integral form we obtain:

$$\int_{\mathcal{B}_0} \left(\rho_0 f_i \delta u_i - \rho_0 u_i \ddot{\delta} u_i + \left(l_{ij} - \frac{\partial w}{\partial u_{i,j}} \right) \delta u_{i,j} - \frac{\partial w}{\partial u_{i,jk}} \delta u_{i,jk} \right) dV + \int_{\partial \mathcal{B}_0} \left(\hat{t}_i \delta u_i + \hat{m}_{ij} \delta u_{j,i} \right) dA = 0 . \quad (39)$$

Since it is zero we can multiply it by minus one. We discretize in time by using the same scheme as before and acquire the weak form:

$$\text{Form} = \int_{\mathcal{B}_0} \left(-\rho_0 f_i \delta u_i + \rho_0 \frac{u_i - 2u_i^0 + u_i^{00}}{\Delta t^2} \delta u_i - \left(\rho_0 l_{ij} - \frac{\partial w}{\partial u_{i,j}} \right) \delta u_{i,j} + \frac{\partial w}{\partial u_{i,jk}} \delta u_{i,jk} \right) dV - \int_{\partial \mathcal{B}_0} \left(\hat{t}_i \delta u_i + \hat{m}_{ij} \delta u_{j,i} \right) dA = 0 . \quad (40)$$

Out of that weak form we can compute the displacement, $u_i(X_j, t)$, by using the finite element method. We obtain the same displacement field if the weak forms obtained by the rational and classical analytical mechanics are identical.

4 Comparison and discussion

We have formulated one weak form of generalized elasticity by using rational mechanics in Eq. (23) and another weak form of generalized elasticity by using classical analytical mechanics in Eq. (40). A comparison shows an interesting result. We start with:

$$\frac{\partial w}{\partial u_{i,j}} = \frac{\partial w}{\partial E_{kl}} \frac{\partial E_{kl}}{\partial u_{i,j}} = S_{lk} F_{nk} \frac{\partial F_{nl}}{\partial u_{i,j}} = S_{lk} F_{nk} \frac{\partial u_{n,l}}{\partial u_{i,j}} = S_{lk} F_{nk} \delta_{ni} \delta_{lj} = S_{jk} F_{ik} , \quad (41)$$

and obtain after using the relation from Eq. (15)₁, $F_{kj} S_{ij} = P_{ik}$,

$$\frac{\partial w}{\partial u_{i,j}} = P_{ji} . \quad (42)$$

The latter shows that these two terms are equal in the weak forms. However, this is not the case for the following term:

$$\begin{aligned} \frac{\partial w}{\partial u_{i,jk}} &= \frac{\partial w}{\partial E_{lm,n}} \frac{\partial E_{lm,n}}{\partial u_{i,jk}} = \mu_{nml} \frac{\partial F_{ol} F_{om,n}}{\partial u_{i,jk}} = \mu_{nml} F_{ol} \frac{\partial u_{o,mn}}{\partial u_{i,jk}} = \\ &= \mu_{nml} F_{ol} \delta_{oi} \delta_{mj} \delta_{nk} = \mu_{kjl} F_{il} . \end{aligned} \quad (43)$$

This latter inconsistency may be amended by suggesting another formulation of the stored energy. Moreover, in Eq. (23) there is one term, $P_{[ij]}$, which does not vanish in

general. This term is introduced by first transforming into the LAGRANGEan frame and then defining the angular momentum with respect to X_i . This fact is another inconsistency between the formulations. These two ambiguities can be eliminated only for a special case, where $F_{ij} \approx \delta_{ij}$ is assumed. Then $P_{ij} \approx \sigma_{ij}$ and we know that for non-polar materials $\sigma_{ij} = \sigma_{ji}$ leading to $\sigma_{[ij]} = 0$. This case is known as neglecting the geometric nonlinearities so that the formulation is accurate only for small deformations.

By using two different methodologies we have realized that there are some ambiguities easily introduced to the formulation by both of the methodologies. Either we postulate a stored energy bringing an inconsistency, or transform from the current into the LAGRANGEan frame and define the physical variable in a specific way introducing another inconsistency. The correct formulation can be suggested by learning from both of methodologies. Unfortunately, many researchers get used to only one of the methodologies and, even further, they pretend that their used methodology is the *only true one*. We believe that human-beings' creativity is great enough to simply incorporate some ambiguities into one formulation. Hence, two different possibilities leading to the same formulation is an invaluable double-check for us. We have achieved a generalized elasticity only for small deformations and left a better theory including geometric nonlinearities to further research.

References

- [1] Abali, B. E. and Müller, W. H. 2016. Numerical solution of generalized mechanics based on a variational formulation. Oberwolfach reports - Mechanics of Materials, European Mathematical Society Publishing House, 17(1):9–12.
- [2] Abali, B. E., Müller, W. H., and Eremeyev, V. A. 2015a. Numerical investigation of thin films with strain gradient elasticity. In: Advanced Problems in Mechanics, International Summer School–Conference Proceedings. Institute for Problems in Mechanical Engineering, 22 June 2015 - 27 June 2015, St. Petersburg, Russia, pages 2–8.
- [3] Abali, B. E., Müller, W. H., and Eremeyev, V. A. 2015b. Strain gradient elasticity with geometric nonlinearities and its computational evaluation. Mechanics of Advanced Materials and Modern Processes, 1(1):1–11.
- [4] dell'Isola, F., Sciarra, G., and Vidoli, S. 2009. Generalized Hooke's law for isotropic second gradient materials. Proceedings of the Royal Society A: Mathematical, Physical and Engineering Science, 465:2177–2196.
- [5] Gruber, P. A., Böhm, J., Onuseit, F., Wanner, A., Spolenak, R., and Arzt, E. 2008. Size effects on yield strength and strain hardening for ultra-thin Cu films with and without passivation: A study by synchrotron and bulge test techniques. Acta Materialia, 56(10):2318–2335.

REFERENCES

- [6] Lam, D., Yang, F., Chong, A., Wang, J., and Tong, P. 2003. Experiments and theory in strain gradient elasticity. *Journal of the Mechanics and Physics of Solids*, 51(8):1477–1508.
- [7] McFarland, A. W. and Colton, J. S. 2005. Role of material microstructure in plate stiffness with relevance to microcantilever sensors. *Journal of Micromechanics and Microengineering*, 15(5):1060–1067.

B. Emek Abali, Technische Universität Berlin, Institute of Mechanics, Einsteinufer 5, D-10587 Berlin, Germany

Wolfgang H. Müller, Technische Universität Berlin, Institute of Mechanics, Einsteinufer 5, D-10587 Berlin, Germany

Functionally invariant solutions of the nonlinear nonautonomic Klein-Fock-Gordon equation

E. L. Aero, A. N. Bulygin, Yu. V. Pavlov
 bulygin_an@mail.ru

Abstract

We develop methods of finding of exact analytical solutions of the nonlinear nonautonomic Klein-Fock-Gordon equation. These methods are based on finding of functionally invariant solutions of the partial differential equations. Solutions are received in the form of some arbitrary function $f(W)$ with W depending on one $\tau(x, y, t)$ or two specially certain functions $\alpha(x, y, t)$, $\beta(x, y, t)$, which are called as ansatzes. Methods of construction of the ansatzes are developed.

1 Introduction

The nonlinear Klein-Fock-Gordon (NKFG) equation

$$U_{xx} + U_{yy} - \frac{U_{tt}}{v^2} = F(U) \quad (1)$$

appears in many field of modern natural sciences. Here $F(U)$ is arbitrary function, and the subscript means the derivative with respect to the corresponding variable. Eq. (1) is widely applied in fundamental and applied physics, mechanics, biology, chemistry and other field of science, when the right-hand side is a part of the exponential (e^{nU}) series, or hyperbolic function ($\sinh nU$, $\cosh nU$) series, or Fourier ($\sin nU$, $\cos nU$) series, or Taylor (U^n , $n = 1, 2, \dots$) series. These equations describe the different physical phenomena and are modeling various technological processes. In case of nonhomogeneous external media or external fields the corresponding equation is the nonlinear nonautonomic Klein-Fock-Gordon equation

$$U_{xx} + U_{yy} - \frac{U_{tt}}{v^2} = p(x, y, t) F(U). \quad (2)$$

Here $p(x, y, t)$ is some function.

In literature there are practically no methods of obtaining exact analytical solutions of the nonautonomic NKFG equation. The methods for finding of the solutions based on construction of the functionally invariant solutions of the partial differential equations are offered below.

2 Methods of construction of exact analytical solutions of nonautonomic nonlinear Klein-Fock-Gordon equation

The solution $U = W$ of the differential equation is called functionally invariant if for arbitrary function f the complex function of $U = f(W)$ is also the solution. The function W is called as ansatzes. For the first time the idea about existence of the functionally invariant solutions were stated by C. Jacobi [1]. A. Forsyth has found the functionally invariant solutions of the Laplace equation, the wave equation and the Helmholtz equation [2]. Idea of C. Jacobi has fundamentally developed H. Bateman in relation to the theory of propagation of electromagnetic waves [3]. S.L. Sobolev and V.I. Smirnov have successfully applied method of construction of the functionally invariant solutions to the problems of diffraction and distribution of a sound in homogeneous and layered media [4]– [6]. N.P. Erugin has made a big contribution to development of the theory [7]. Functionally invariant solutions of the autonomic NKFG equation and sine-Gordon equation are found by authors [8]– [12]. We will seek the solution of Eq. (2) in the form of complex function $U = f(W)$. Then Eq. (2) takes the form

$$f'' \left[W_x^2 + W_y^2 - \frac{W_t^2}{v^2} \right] + f' \left[W_{xx} + W_{yy} - \frac{W_{tt}}{v^2} \right] = p(x, y, t) F[f(W)]. \quad (3)$$

Here and further the prime designates an ordinary derivative with respect to argument. From (3) it is possible to make two obvious statements.

Proposition 1. If function W satisfies the equations

$$W_x^2 + W_y^2 - \frac{W_t^2}{v^2} = 0, \quad W_{xx} + W_{yy} - \frac{W_{tt}}{v^2} = p(x, y, t), \quad (4)$$

then the solution of Eq. (2) is given by the inversion of integral

$$\int \frac{df}{F(f)} = W(x, y, t). \quad (5)$$

Proposition 2. If function W satisfies the equations

$$W_x^2 + W_y^2 - \frac{W_t^2}{v^2} = p(x, y, t), \quad W_{xx} + W_{yy} - \frac{W_{tt}}{v^2} = 0, \quad (6)$$

then the solution of Eq. (2) is given by the inversion of integral

$$\int \frac{df}{\sqrt{E + V(f)}} = \pm \sqrt{2} W(x, y, t). \quad (7)$$

In integral (7) $F(U) = V'(U)$, and E is a constant of integration.

So, the problem of solution of the nonautonomic Eq. (2) is reduced to the finding of the function W , which satisfies Eqs. (4), (6). This problem can be solved by the methods of construction of functionally invariant solutions of the partial differential equations.

1-st way. The solution of Eqs. (4) we seek in the form

$$W = \varphi(\tau). \quad (8)$$

Here $\varphi(\tau)$ is arbitrary function, τ is a root of the algebraic equation

$$\begin{aligned} x\xi(\tau) + y\eta(\tau) - v^2t\tau &= \frac{s^2 + q^2}{2}, \\ s^2 = x^2 + y^2 - v^2t^2, \quad q^2 &= \xi^2(\tau) + \eta^2(\tau) - v^2\tau^2, \end{aligned} \quad (9)$$

$\xi(\tau)$, $\eta(\tau)$ are arbitrary functions of τ .

Eq. (9) defines implicit dependence τ on time and space coordinates. From (9), we find

$$\tau_x^2 + \tau_y^2 - \frac{\tau_t^2}{v^2} = 0, \quad \tau_{xx} + \tau_{yy} - \frac{\tau_{tt}}{v^2} = \frac{2}{\nu}, \quad (10)$$

$$\nu = \xi_\tau(x - \xi) + \eta_\tau(y - \eta) - v^2(t - \tau). \quad (11)$$

In Eq. (10) it was taking into account that

$$\xi_\tau\tau_x + \eta_\tau\tau_y + \tau_t = 1, \quad \nu_x\tau_x + \nu_y\tau_y - \frac{\nu_t\tau_t}{v^2} = 1. \quad (12)$$

On the basis of Proposition 1 and Eqs. (10) we come to a conclusion that (8) will be the solution of Eq. (2), if $f(W)$ is an inversion of the integral (5) and

$$p(x, y, t) = \frac{\varphi\tau}{\nu}. \quad (13)$$

For the purpose of obtaining new solutions of Eq. (2), we will introduce the function

$$\lambda = l(\tau)(x - \xi) + m(\tau)(y - \eta) - v^2w(\tau)(t - \tau). \quad (14)$$

here $l(\tau)$, $m(\tau)$, $w(\tau)$ are arbitrary functions. We will impose on them the following restrictions

$$l\xi_\tau + m\eta_\tau - v^2w = 0, \quad l^2 + m^2 = v^2w^2. \quad (15)$$

The function λ satisfies the equations

$$\lambda_x^2 + \lambda_y^2 - \frac{\lambda_t^2}{v^2} = 2\omega\frac{\lambda}{\nu}, \quad (16)$$

$$\lambda_{xx} + \lambda_{yy} - \frac{\lambda_{tt}}{v^2} = 3\frac{\omega}{\nu}, \quad (17)$$

$$\omega = l_\tau(x - \xi) + m_\tau(y - \eta) - v^2w_\tau(t - \tau). \quad (18)$$

Besides, it is possible to prove that function $\tau, l, m, w, \nu, \lambda$ are connected by the following relations

$$l\tau_x + m\tau_y + \omega\tau_t = \frac{\lambda}{\nu}, \quad (19)$$

$$l_\tau \tau_x + m \tau_y + \omega_\tau \tau_t = \frac{\omega}{\nu}, \quad (20)$$

$$\lambda_x \tau_x + \lambda_y \tau_y - \frac{\lambda_t \tau_t}{v^2} = \frac{\lambda}{\nu}, \quad (21)$$

$$\lambda_x \nu_x + \lambda_y \nu_y - \frac{\lambda_t \nu_t}{v^2} = \omega + (\sigma_0 - q_1^2) \frac{\lambda}{\nu}, \quad (22)$$

$$\sigma_0 = \xi_{\tau\tau}(x - \xi) + \eta_{\tau\tau}(y - \eta) - q_1^2, \quad q_1^2 = \xi_\tau^2 + \eta_\tau^2 - v^2. \quad (23)$$

We will seek the solution of Eqs. (6) in the form of arbitrary function depending from τ and λ

$$W = f(\tau, \lambda). \quad (24)$$

Then Eqs. (6) will take a form

$$W_x^2 + W_y^2 - \frac{W_t^2}{v^2} = 2 \frac{\lambda}{\nu} \left(\omega + \frac{f_\tau}{f_\lambda} \right) f_\lambda^2, \quad (25)$$

$$W_{xx} + W_{yy} - \frac{W_{tt}}{v^2} = \frac{1}{\nu} [2\lambda f_\lambda + f]_\tau + \frac{\omega}{\nu} [2\lambda f_\lambda + f]_\lambda. \quad (26)$$

From (25), (26) it follows that W will satisfy Eqs. (6) if

$$2\lambda f_\lambda + f = 0, \quad f = \frac{\varphi(\tau)}{\sqrt{\lambda}}, \quad (27)$$

$\varphi(\tau)$ are an arbitrary function.

On the basis of Proposition 2 we find that solution of Eq. (2) is an inversion of the integral (7) for

$$W = \frac{\varphi(\tau)}{\sqrt{\lambda}}, \quad p(x, y, t) = \frac{\varphi^2}{2\nu\lambda^2} \left[\omega - 2\lambda \frac{\varphi_\tau}{\varphi} \right]. \quad (28)$$

2-nd way. Ansatz τ , which is found from Eq. (9) depends on time and space coordinates. Set of analytical expressions for ansatz τ can be expanded assuming that τ , in addition to space coordinates and time, depends on some parameters (α, β) . Certainly the new equations are necessary for finding of parameters (α, β) . Let's find ansatz $\tau = \tau(x, y, t, \alpha, \beta)$ from the equations

$$x\xi(\alpha, \beta, \tau) + y\eta(\alpha, \beta, \tau) - v^2 t \theta(\alpha, \beta, \tau) = \frac{s^2 + q_2^2}{2}, \quad (29)$$

$$x\xi_\alpha + y\eta_\alpha - v^2 t \theta_\alpha = \frac{1}{2} (q_2^2)_\alpha, \quad (30)$$

$$x\xi_\beta + y\eta_\beta - v^2 t \theta_\beta = \frac{1}{2} (q_2^2)_\beta, \quad (31)$$

$$q_2^2 = \xi^2 + \eta^2 - v^2 \theta^2. \quad (32)$$

Eq. (29) is algebraic. This equation is linear to time and space coordinates like Eq. (9) but its coefficients are the functions of three arguments (τ, α, β) . Eqs. (30), (31) are partial differential equations of the first order. From Eqs. (29)–(31) one can

calculate partial derivatives τ of the first and second orders with respect to the time and space coordinates and to receive the following relations

$$\tau_x^2 + \tau_y^2 - \frac{\tau_t^2}{v^2} = 0, \quad (33)$$

$$\tau_{xx} + \tau_{yy} - \frac{\tau_{tt}}{v^2} = \frac{1}{\nu} [3 - (\xi_x + \eta_y + \theta_t)], \quad (34)$$

On the basis of Proposition 1 and Eqs. (33), (34) we find that solution of Eq. (2) is an inversion of the integral (5), W is arbitrary function of τ , $W = f(\tau)$, τ is defined by Eqs. (29)–(31), and the function $p(x, y, z, t)$ is defined by the equation

$$p(x, y, t) = \frac{1}{\nu} [3 - (\xi_x + \eta_y + \theta_t)] f_\tau. \quad (35)$$

3-d way. Let ansatz $\alpha(x, y, t)$ is a solution of the algebraic equation

$$xl(\alpha) + ym(\alpha) - v^2tw(\alpha) + q(\alpha) = 0. \quad (36)$$

Here $l(\alpha)$, $m(\alpha)$, $w(\alpha)$, $q(\alpha)$ are arbitrary functions coupled by the condition

$$l^2 + m^2 = v^2w^2. \quad (37)$$

Let's introduce the function β in according to the definition

$$\beta = xl_\alpha + ym_\alpha - v^2tw_\alpha + q_\alpha. \quad (38)$$

From Eqs. (36), (38) one can calculate the partial derivatives of the functions α, β and verify that they satisfy the equations

$$\alpha_x^2 + \alpha_y^2 - \frac{\alpha_t^2}{v^2} = 0, \quad \alpha_{xx} + \alpha_{yy} - \frac{\alpha_{tt}}{v^2} = 0, \quad (39)$$

$$\beta_x^2 + \beta_y^2 - \frac{\beta_t^2}{v^2} = l_\alpha^2 + m_\alpha^2 - v^2w_\alpha^2, \quad \beta_{xx} + \beta_{yy} - \frac{\beta_{tt}}{v^2} = \frac{2}{\beta}(l_\alpha^2 + m_\alpha^2 - v^2w_\alpha^2). \quad (40)$$

$$\alpha_x\beta_x + \alpha_y\beta_y - \frac{\alpha_t\beta_t}{v^2} = 0. \quad (41)$$

In Eqs. (40) the relation

$$ll_{\alpha,\alpha} + mm_{\alpha,\alpha} - v^2ww_{\alpha,\alpha} = -(l_\alpha^2 + m_\alpha^2 - v^2w_\alpha^2) \quad (42)$$

has been taken into account.

Let's that W is an arbitrary functions of the two variables (α, β)

$$W = f(\alpha, \beta) \quad (43)$$

Taking into account (39)–(41), we find

$$W_x^2 + W_y^2 - \frac{W_t^2}{v^2} = f_\beta^2 (l_\alpha^2 + m_\alpha^2 - v^2w_\alpha^2), \quad (44)$$

$$W_{xx} + W_{yy} - \frac{W_{tt}}{v^2} = \left(f_{\beta\beta} + \frac{2}{\beta} f_{\beta} \right) (l_{\alpha}^2 + m_{\alpha}^2 - v^2 w_{\alpha}^2). \quad (45)$$

Let's

$$f_{\beta\beta} + \frac{2}{\beta} f_{\beta} = 0, \quad f = A(\alpha) + \frac{B(\alpha)}{\beta}, \quad (46)$$

$A(\alpha)$, $B(\alpha)$ are arbitrary functions. Therefore, the function W , which is given by (43), (46), satisfies Eqs. (6) with

$$p(x, y, t) = (l_{\alpha}^2 + m_{\alpha}^2 - v^2 w_{\alpha}^2) \frac{B^2(\alpha)}{\beta^4}. \quad (47)$$

The obtained results allows to construct the solution of Eq. (2) on the basis of the Proposition 2.

Ansatz α is possible to use for construction of the function

$$W = xL + yM - v^2 tV + Q. \quad (48)$$

Here

$$L_{\alpha} = l, \quad M_{\alpha} = m, \quad V_{\alpha} = w, \quad Q_{\alpha} = q. \quad (49)$$

The function W , defining by (48), (49), satisfies the equations

$$W_x^2 + W_y^2 - \frac{W_t^2}{v^2} = L^2 + M^2 - v^2 V^2, \quad (50)$$

$$W_{xx} + W_{yy} - \frac{W_{tt}}{v^2} = -\frac{1}{\beta} (l^2 + m^2 - v^2 w^2). \quad (51)$$

From (50), (51) it follows that W will be the solution of Eqs. (4) if

$$L^2 + M^2 - v^2 V^2 = 0, \quad p = -\frac{1}{\beta} (l^2 + m^2 - v^2 w^2), \quad (52)$$

or the solution of (6), if

$$l^2 + m^2 - v^2 w^2 = 0, \quad p = L^2 + M^2 - v^2 V^2. \quad (53)$$

Thus, if the functions l, m, w, q satisfying to the conditions (52) or (53) are obtained, then one can find the function W and to construct the solution of Eq. (2).

So, if

$$L = \frac{1}{\cosh \alpha}, \quad M = \frac{\sinh \alpha}{\cosh \alpha}, \quad vV = 1, \quad Q = 0, \quad (54)$$

then

$$W = vt - \sqrt{x^2 + y^2}, \quad p = \frac{1}{\sqrt{x^2 + y^2}}. \quad (55)$$

Acknowledgements

This work was supported by RFBR, grant 16-01-00068-a.

References

- [1] C. G. J. Jacobi. Über eine particuläre Lösung der partiellen Differentialgleichung $\frac{\partial^2 V}{\partial x^2} + \frac{\partial^2 V}{\partial y^2} + \frac{\partial^2 V}{\partial z^2} = 0$. Crelle Journal für die reine und angewandte Mathematik **36**, 113–134 (1848) (*Reprinted in* C.G.J. Jacobi's Gesammelte Werke. Zweiter Band. Herausgegeben von K.Weierstrass. Verlag von G.Reimer, Berlin, 1882, pp. 191–216).
- [2] A. R. Forsyth. New solutions of some of the partial differential equations of mathematical physics. Messenger of Mathematics **27**, 99–118 (1898).
- [3] H. Bateman. The Mathematical Analysis of Electrical and Optical Wave-Motion on the Basis of Maxwell's Equations. Cambridge University Press, Cambridge, 1915.
- [4] V. Smirnoff, S. Soboleff. Sur une méthode nouvelle dans le problème plan des vibrations élastiques. Trudy Seismologicheskogo Inst. No. **20**, 1–37 (1932) [English transl.: S.L. Sobolev. On a new method in the plane problem on elastic vibrations. *In book: Selected Works of S.L. Sobolev, Vol. I, New York, 2006, pp. 45–80*].
- [5] V. Smirnoff, S. Soboleff. Sur le problème plan des vibrations élastiques. C. R. Acad. Sci. Paris. **194**, 1437–1439 (1932).
- [6] S.L. Sobolev. Functionally invariant solutions of wave equation. Trudy Fiz.-Mat. Inst. V.A. Steklov. Vol. **5**, 259–264 (1934) [English transl. in book: Selected Works of S.L. Sobolev, Vol. I, New York, 2006, pp. 195–199].
- [7] N. P. Erugin. On functionally invariant solutions. Uchenye Zap. Leningrad University. Vyp. **15**, No. 96. 101–134 (1948).
- [8] E. L. Aero, A. N. Bulygin, Yu. V. Pavlov. Solutions of the three-dimensional sine-Gordon equation. Teor. Matem. Fiz. **158**, 370–377 (2009) [English transl.: Theor. Math. Phys. **158**, 313–319 (2009)].
- [9] E. L. Aero, A. N. Bulygin, Yu. V. Pavlov. Solutions of generalized (3+1) sine-Gordon equation. Nelineinii Mir **7**, 513–517 (2009).
- [10] E. L. Aero, A. N. Bulygin, Yu. V. Pavlov. New approach to the solution of the classical sine-Gordon equation and its generalizations. Differentsial'nye Uravneniya **47**, 1428–1438 (2011) [English transl.: Differential Equations **47**, 1442–1452 (2011)].
- [11] E. L. Aero, A. N. Bulygin, Yu. V. Pavlov. Functionally invariant solutions of nonlinear Klein-Fock-Gordon equation. Applied Mathematics and Computation **223**, 160–166.

REFERENCES

- [12] E.L. Aero, A.N. Bulygin, Yu. V. Pavlov. Solutions of the sine-Gordon equation with a variable amplitude. *Teor. Matem. Fiz.* **184**, 79-91 (2015) [English transl.: *Theor. Math. Phys.* **184**, 961-972 (2015)].

*E. L. Aero, A. N. Bulygin, Yu. V. Pavlov,
Institute for Problems in Mechanical Engineering of Russian Academy of Sciences,
61 Bol'shoy, V.O., Saint Petersburg, 199178, Russia*

Mechanical model of damage and fracture of aging polymer materials

Alexander R. Arutyunyan, Robert A. Arutyunyan
r.arutyunyan@spbu.ru

Abstract

Polymers and polymer-based materials are used in many applications in medicine and industry. These applications frequently have a very high performance demand, which makes their long-term aging characteristics of paramount importance. At the same time they are subjected to degradation due to environmental factors, including light, temperature, stress, and others. During the aging the degradation of polymers lead to changes in the physical and mechanical properties. As a result of degradation the material may become less deformable and brittle. These effects are studied in long-term tests of specimens made of polyurethane in tension, compression, cyclic loading, climatic and strain aging, as well as in experiments carried out on the rubber samples in tension and climatic aging at room temperature. In all experiments a significant effect of hardening and embrittlement of materials during long-term aging is observed. The obtained results allow us to formulate the interconnected kinetic equations for the creep rate and damage parameter. These equations are written in the scale of real and effective time. The analytical relations for creep, damage parameter and the criteria of long-term strength are obtained. Corresponding theoretical curves are constructed and their qualitative agreement with the experimental curves is shown.

1 Introduction.

Polymers were introduced in many fields of modern industry as structural materials because they were relatively cheap and easy to manufacture compared with commonly known materials such as metals and wood. Today polymers and polymer-based materials are used in many applications in medicine and industry, including electronic and optical production. These applications frequently have a very high performance demand, which makes their long-term aging characteristics of paramount importance. At the same time they are subjected to degradation due to environmental factors, including light, temperature, stress, pollutants and others. During the aging the degradation of polymers lead to changes of their physical and mechanical properties. As a result of degradation the material may become less deformable and brittle. To predict these behaviors and useful lifetimes the aging of polymers to weathering is usually studied. However, the problem of deformation

aging is not considered sufficiently in literature. In this paper an effective time is introduced and a mechanical model (modified Maxwell model) for description of deformation aging behavior of polymer materials is presented. The relaxation time is considered as a measure of the aging process and the parameters of the model are defined to describe the experimental creep curves for aged and unaged polymer materials.

The most important results of polymer aging are obtained for the case of outdoor exposition [1-4], which often called weathering or UV-degradation. UV radiation can initiate chemical reactions, which may lead to breaking of the chemical bonds in the polymer chains. UV-radiation together with oxygen can lead to photo oxidation reactions. For example, in polyethylene products used outdoors, photo oxidation is a principal degradation process. Chain breaking and cross-linking will change the structure of polymers and finally may cause embrittlement (the strain decrease at failure). The increase in Young's modulus with exposure time is attributed to the uptake of oxygen, the change in the number of tie-molecules, the increase in crystallinity and the increase in density. The free volume concept can be applied to explain the aging phenomena. It states that the transport mobility of particles in a closely packed system primarily depends on the degree of packing, in other terms, on the free volume. With increasing degree of packing, this mobility decreases, at first slowly, but later on at an ever increasing rate. Since the relaxation time of polymers is directly related to the mobility and free volume, the mechanical parameters (elastic modulus and viscosity coefficient) also will be influenced by way of changing in the relaxation time. The other conclusion is that the viscosity coefficient changes essential relative to the elastic modulus. It happens because of the strong structural dependence of viscosity coefficient. In contrast the value of elastic modulus is in a very week dependence of the material structure.

As it was mentioned above, the deformation aging of polymers is not studied well. However it is known that, the processing methods (like injection molding or extrusion) can have an effect on the degradation and aging behavior. Some aspects of deformation aging were considered in [5]. It was determined that the deformation may promote the acceleration of aging process and, the additional increase in elastic modulus.

2 Modified Maxwell model for description of deformation aging of polymer materials.

To describe the process of deformation the aging parameter α is introduced [6]

$$d\alpha = f_1(\alpha, \varepsilon, T, t)dt + f_2(\alpha, \varepsilon, T, t)d\varepsilon, \quad (1)$$

where ε is the value of deformation, t is the real time, T is temperature. Parameter α will be considered as an effective time, which is capable to describe the aging (deformation and quench). According to relation (1) in the instantaneous active loading this parameter can be considered as 'deformation time' ε . In unloading state $d\varepsilon = 0$ and α reduces to the real time t . We may call it as the 'chemical time'. For the Maxwell equation we will receive the following modified relation

$$\frac{d\varepsilon}{d\alpha} = \frac{d}{d\alpha} \left[\frac{\sigma}{E(\alpha)} \right] + \frac{\sigma}{\eta(\alpha)}. \quad (2)$$

Further we will consider the simple version of elastic viscous model (2) expressed in scale of effective time (1)

$$\frac{d\varepsilon}{d\alpha} = \frac{1}{E} \frac{d\sigma}{d\alpha} + \frac{\sigma}{\eta}, \quad (3)$$

$$d\alpha = k(\alpha_\infty - \alpha)t^m dt, \quad (4)$$

where E , η , k , α_∞ , n are constants, α is a parameter of material degradation ($\alpha = N/N_0$, N_0 are the initial numbers of chemical bonds, N are the current numbers of fractured chemical bonds). So the equation (4) can be considered as an equation of chemical reaction and parameter α has a meaning of chemical time. With the initial conditions $t = 0$, $\alpha = \alpha_0$, $\varepsilon = \sigma_0/E_0$, the solution of the system (3)-(4) can be written in the form

$$\varepsilon = \frac{\sigma_0}{E_0} \left[1 + \frac{\alpha_\infty - \alpha_0}{\tau} \left(1 - \exp \left(-\frac{k}{m+1} t^{m+1} \right) \right) \right]. \quad (5)$$

The theoretical creep (compliance) curves (5) for the following coefficients: $\alpha_0 = 0$, $\alpha_\infty = 1$, $n = 0$, $k = 0,021 \text{ s}^{-1}$, relaxation times and modulus of elasticity $\tau_1 = 1 \text{ s}$, $E_0 = 25 \text{ MPa}$ (curve 1) and $\tau_2 = 1 \text{ s}$, $E_0 = 30 \text{ MPa}$ (curve 2) are shown on Fig. 1. The experimental results are marked by cross and circle points. The theoretical curves in this figure are in good agreement with the results of creep aging experiments [7] for the polyethylene films. Upper curve was received in experiments with unaged specimens; lower curve was received in experiments with aged specimens. The specimens were aged seven days at temperature 373°K .

3 The long-term strength criterion of polymer materials based on damage parameter.

For the formulation of long-term strength criterion in addition to the equations (3)-(4) we will consider the damage (continuity) parameter ψ [6, 8] which is determined by the following kinetic equation

$$\psi^a \frac{d\psi}{dt} = -A\sigma^n. \quad (6)$$

Taking into account the mass conservation law $\rho_0 l_0 F_0 = \rho l F$, from which follows the relation $\sigma = \sigma_0 \psi e^\varepsilon$, equation (6) can be written in the form

$$\psi^a \frac{d\psi}{dt} = -A\sigma_0^n \psi^n e^{n\varepsilon}. \quad (7)$$

where a , A , n are constants, $\psi = \rho/\rho_0$ ($1 \geq \psi \geq 0$, ρ_0 is initial, ρ is current density). We have considered several variants of the approximate solution of equation (7). The simplest solution, describing qualitatively the experimental curves of damage, can be obtained by taking the following approximations

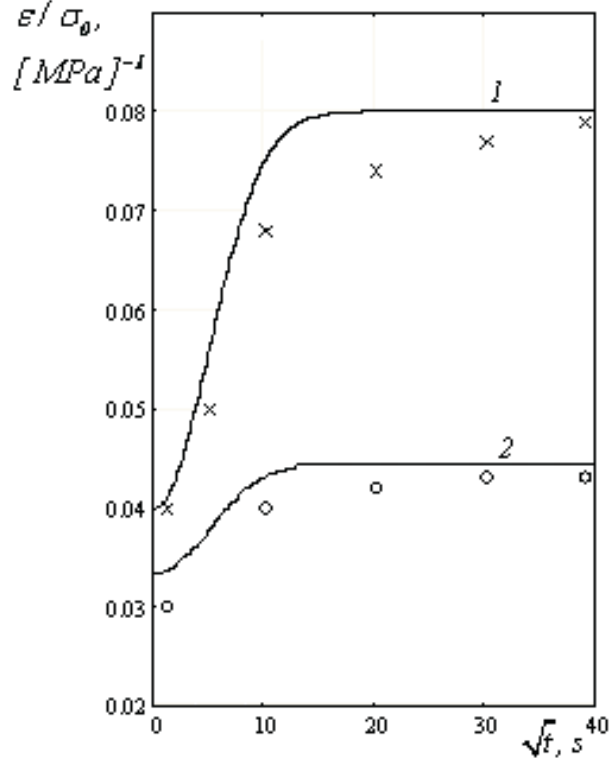


Figure 1: The theoretical creep curves according relation (5): $\tau_1 = 1$ s, $E_0 = 25$ MPa (curve 1) and $\tau_2 = 1$ s, $E_0 = 30$ MPa (curve 2).

$$\varepsilon = \frac{\sigma_0}{E_0} \left[1 + \frac{(\alpha_\infty - \alpha_0)k}{\tau(m+1)} t^{m+1} \right], \quad (8)$$

$$\psi^\alpha \frac{d\psi}{dt} = -A\sigma_0^n \psi^n (1 + n\varepsilon). \quad (9)$$

Introducing the relation (8) into equation (9) and solving it with the initial conditions $t = 0$, $\psi = 1$, we will receive the following relation

$$\psi = \left[1 - (a - n + 1)A\sigma_0^n \left(\frac{n\sigma_0(\alpha_\infty - \alpha_0)k}{E_0\tau(m+1)(m+2)} t^{m+2} + \left(\frac{n\sigma_0}{E_0} + 1 \right) t \right) \right]^{\frac{1}{a-n+1}}. \quad (10)$$

In Fig. 2 are shown the curves for the continuity parameter according to equation (10) for different values of constants ($\alpha = 6$ - curve 1, $\alpha = 4$ - curve 2 and $\alpha = 2$ - curve 3), which are in agreement with the corresponding experimental curves. In the calculations the following values of coefficients were used: $n = 0$, $A = 10^{-7}$ [MPa] $^{-2}$, $\sigma_0 = 60$ MPa, $\alpha_0 = 0$, $\alpha_\infty = 1$, $m = 0$, $k = 0,021$ s $^{-1}$, $\tau = 1$ s, $E_0 = 2000$ MPa.

Taking the fracture condition $t = t_f$, $\psi = 0$ and for $m = 0$ from (10) we obtain the creep fracture criterion

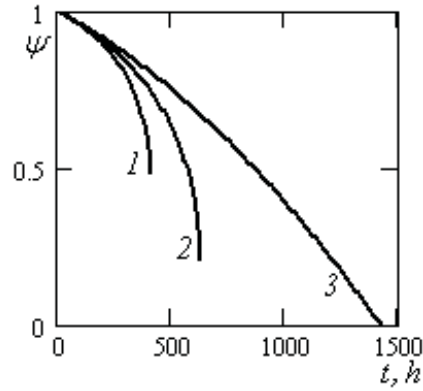


Figure 2: The curves for the parameter of continuity ψ according to the formula (10) for different values of constants: $\alpha = 6$ - curve 1, $\alpha = 4$ - curve 2 and $\alpha = 2$ - curve 3.

$$t_f = \frac{E_0 \tau}{n \sigma_0 (\alpha_\infty - \alpha_0) k} \left[- \left(\frac{n \sigma_0}{E_0} + 1 \right) + \left(\left(\frac{n \sigma_0}{E_0} + 1 \right)^2 + \frac{n (\alpha_\infty - \alpha_0) k}{E_0 \tau (a - n + 1) A \sigma_0^{n-1}} \right)^{\frac{1}{2}} \right]. \quad (11)$$

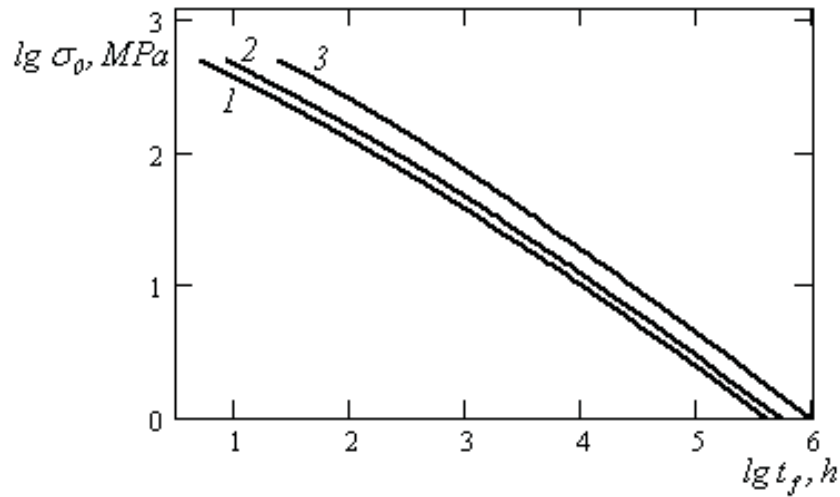


Figure 3: The long-term strength curves under criterion (11) for different values of constants: $\alpha = 6$ - curve 1, $\alpha = 4$ - curve 2 and $\alpha = 2$ - curve 3.

In Fig. 3 in the double logarithmic coordinates are shown the creep fracture curves according to the formula (11) for different values of the coefficients ($\alpha = 6$ - curve 1, $\alpha = 4$ - curve 2 and $\alpha = 2$ - curve 3). In the calculations the following values of coefficients were used: $n = 0$, $A = 10^{-7} [MPa]^{-2}$, $\alpha_0 = 0$, $\alpha_\infty = 1$, $m = 0$, $k = 0,021 s^{-1}$, $\tau = 1 s$, $E_0 = 2000 MPa$.

Acknowledgements

Financial support of the Russian Foundation for Basic Research (Grant N 14-01-00823) is gratefully acknowledged.

References

- [1] Climatic stability of polymer materials. M.: Nauka. 1983. 215p. (in Russian).
- [2] Aging of polyvinyl chloride based materials in the cold climate conditions. Novosibirsk: Nauka. Siberian branch. 1990. 118p. (in Russian).
- [3] The failure behavior of high density polyethylene with an embrittled surface layer due to weathering. Delft: Delft University press. 1992. 167p.
- [4] Physical aging in amorphous polymers and other materials. Amsterdam, Oxford, New York: Elsevier Sci. Publ.Comp. 1978. 229p.
- [5] Aging in fully annealed and subsequently strained polymethyl methacrylate // Polymer Journal. 2000. Vol. 32. N 1. P. 51-56.
- [6] The problem of strain aging and long-term fracture in mechanics of materials. SPb.: Publishing House of the St.-Petersburg State University. 2004. 252p. (in Russian).
- [7] On some deformation and fracture toughness laws of elastic viscous materials in aged condition // Izv. RAN. Mech. tvjord. tela. 1998. N 5. P. 137-145. (in Russian).
- [8] High-temperature embrittlement and long-term strength of metallic materials // Mechanics of solids. 2015. Vol. 50. I. 2. P. 191-197.

Alexander R. Arutyunyan, Robert A. Arutyunyan, Universitetskii pr., 28, Faculty of Mathematics and Mechanics Sankt-Petersburg State University, Sankt-Petersburg, Petrodvoretz, 198504, Russia.

The problem of damage and high-temperature creep fracture of metals

Alexander R. Arutyunyan, Robert A. Arutyunyan, Regina R. Saitova
 r.arutyunyan@spbu.ru, rigastr@yandex.ru

Abstract

Numerous experimental studies on changes of the porosity and density of various metals and alloys due to the formation and development of micropores and microcracks in the process of high-temperature creep are carried out. The results of these studies allow us to consider the density as an integral measure of the structural micro-defects accumulation, and the damage parameter is defined as the ratio of current density to initial density. Taking into account this parameter and the mass conservation law interconnected kinetic equations for creep deformation and damage parameter are formulated. In the case of pure brittle fracture the analytical solutions of these equations are received and the criterion of long-term strength is formulated. The ductile-brittle fracture is also considered. An analytical solution connecting the damage parameter to the value of deformation is obtained. In this case, the creep deformation is calculated approximately. The appropriate choice of the coefficients of the approximate solution allows describing the experimental creep curves.

1 Introduction.

Under the long action of high temperatures and relatively small stresses many metallic alloys and pure metals lose plasticity and fractured as brittle (the phenomenon of thermal brittleness). Because these effects are observed in elements of many important engineering objects, in particular, in power and nuclear, the problem of brittle fractures became a subject of numerous theoretical and experimental researches. In the Kachanov's brittle fracture model [1] the parameter of continuity ψ ($1 \geq \psi \geq 0$) is introduced formally without giving to it a certain physical meaning. In the model of Rabotnov brittle fracture [2, 3] the damage parameter ω ($0 \leq \omega \leq 1$) is introduced by the ratio $\omega = F_T/F_0$ (F_0 is initial, F_T is total area of pores) and characterize the degree of reduction of cross-section area of the specimen.

To materialize the damage parameter various definitions were offered: the relative size of pores or irreversible change of volume (loosening on Novozhilov's terminology [4]) or density (Arutyunyan [5, 6, 7]). In the paper the parameter of continuity is determined by the ratio $\psi = \rho/\rho_0$ (ρ_0 is initial, ρ is current density) and it is an integral measure of the structural microdefects accumulation during long-term high-temperature loading [8-14]. In the initial conditions $t = 0$, $\rho = \rho_0$, $\psi = 1$, at the fracture time $t = t_f$, $\rho = 0$, $\psi = 0$.

2 Interrelated Rabotnov's equations for the rate of creep and damage.

Robotnov's damage concept is based on the following system of equations for the creep ε and damage parameter ω [3]

$$\frac{d\varepsilon}{dt} = b\sigma^m(1 - \omega)^{-q}, \quad (1)$$

$$\frac{d\omega}{dt} = c\sigma^n(1 - \omega)^{-r}, \quad (2)$$

where b, c, m, n, q, r are constants, $\varepsilon = \ln(l/l_0)$ is deformation, l_0, l are initial and current length of the specimen.

In the case of pure brittle fracture and small strains can be considered that $F = F_0$, $\sigma = \sigma_0 = \text{const}$, and solving the system of equations (1)-(2) we will receive the relation for the creep strain

$$\varepsilon = \frac{k}{m} \frac{t_f^b}{t_f^v} \left[1 - \left(1 - \frac{t}{t_f^b} \right)^{1/k} \right], \quad (3)$$

where $k = \frac{r+1}{r+1-q}$, $t_f^b = \frac{1}{c(1+r)\sigma_0^n}$, $t_f^v = \frac{1}{bm\sigma_0^m}$.

Formula (3) is considered as a basic result of the Rabotnov's theory, because using it it is possible to describe the third region of the creep curve, which, in the region of brittle fractures, is completely determined by the damage of material. At the same time, the derivation of this formula is based on the condition $F = F_0$ from which follows $\omega = 0$, i.e. the conception of damage is lose the meaning itself. Further, when the criterion of ductile-brittle fracture is determined using equations (1)-(2), the condition of incompressibility, which is also contrary to the damage conception, is accepted.

3 The system of equations for the creep rate and the continuity parameter.

To overcome these contradictions in this paper a system of equations for the rate of creep and damage, based on the continuity parameter $\psi = \rho/\rho_0$, is proposed. Let's consider the following system of equations

$$\psi^\beta \frac{d\varepsilon}{dt} = B\sigma^m, \quad (4)$$

$$\psi^\alpha \frac{d\psi}{dt} = -A\sigma^n, \quad (5)$$

where B, A, α, β are constants.

Taking into account the mass conservation law $\rho_0 l_0 F_0 = \rho l F$, from which follows the relation $\sigma = \sigma_0 \psi e^\varepsilon$, these equations can be written in the form

$$\frac{d\varepsilon}{dt} = B\sigma_0^m \psi^{m-\beta} e^{m\varepsilon}, \quad (6)$$

$$\frac{d\psi}{dt} = -A\sigma_0^n \psi^{n-\alpha} e^{n\varepsilon}. \quad (7)$$

The system of equations (6)-(7) can be solved approximately, for example, for the case of purely brittle fracture and small deformations, when the approximations $e^{m\varepsilon} \approx 1$, $e^{n\varepsilon} \approx 1$ can be considered. In this case, taking into account the initial conditions $t = 0$, $\psi = 1$, $\varepsilon = 0$, we can receive the following analytical solutions

$$\psi = [1 - (\alpha - n + 1)A\sigma_0^n t]^{\frac{1}{\alpha-n+1}}, \quad (8)$$

$$\varepsilon = \frac{B\sigma_0^{m-n}}{A\gamma} \left\{ 1 - [1 - (\alpha - n + 1)A\sigma_0^n t]^{\frac{\gamma}{\alpha-n+1}} \right\}, \quad (9)$$

where $\gamma = m - \beta + \alpha - n + 1$.

On Fig. 1 the curves $\psi(t)$ according the formula (8) for different values of parameter α ($\alpha = 6$ - curve 1, $\alpha = 4$ - curve 2 and $\alpha = 2$ - curve 3) are shown. In the calculations the following values of coefficients were used: $A = 1 \cdot 10^{-9} [MPa]^{-2}$, $\sigma_0 = 100 MPa$, $n = 2$.

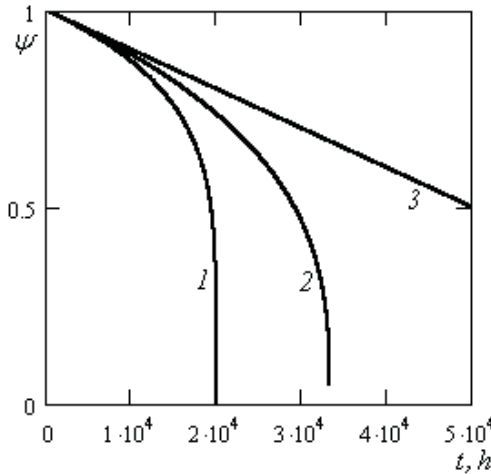


Figure 1: The curves $\psi(t)$ according (8) for different values of parameter α : $\alpha = 6$ - curve 1, $\alpha = 4$ - curve 2 and $\alpha = 2$ - curve 3.

From equations (6)-(7) the exact solution for function $\psi(\varepsilon)$ can be received. Dividing (7) to (6), we will obtain the following equation

$$\frac{d\psi}{d\varepsilon} = -\frac{A}{B}\sigma_0^{n-m}\psi^{n-\alpha-m+\beta}e^{(n-m)\varepsilon}. \quad (10)$$

Using the initial condition $\psi = 1$, $\varepsilon = 0$ and solving (10) we receive

$$\psi = \left[1 + \frac{A\sigma_0^{n-m}(1-n+\alpha+m-\beta)}{B(n-m)}(1-e^{(n-m)\varepsilon}) \right]^{\frac{1}{1-n+\alpha+m-\beta}}. \quad (11)$$

On Fig. 2 the curves $\psi(\varepsilon)$ according (11) for different values of parameter α ($\alpha = 6$ - curve 1, $\alpha = 4$ - curve 2 and $\alpha = 2$ - curve 3) are shown. In the calculations the following values of coefficients were used: $A = 1 \cdot 10^{-12} [MPa]^{-2}$, $B = 5 \cdot 10^{-17} [MPa]^{-4}$, $\sigma_0 = 100 MPa$, $n = 2$, $m = 4$, $\beta = 1$.

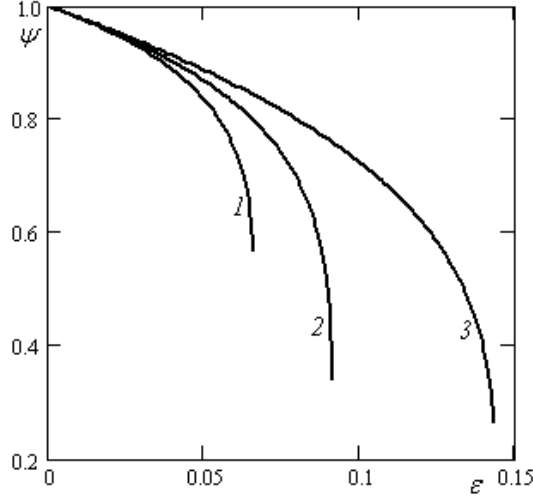


Figure 2: The curves $\psi(\varepsilon)$ according (11) for different values of parameter α : $\alpha = 6$ - curve 1, $\alpha = 4$ - curve 2 and $\alpha = 2$ - curve 3.

As can be seen from Fig. 1 and 2 the damage curves for formulas (8) and (11) are identical.

In scientific literature there are many experimental data on porosity changes (damage) of different metals and alloys on creep conditions. For comparison with the corresponding theoretical curves we chose the most characteristic experimental data for pure copper, aluminum and nickel [8, 9, 10, 12]. On Fig. 3 theoretical curves of density changes according (11) for $\alpha = 6$ and experimental points of density changes for pure copper in the process of high-temperature creep at $500^\circ C$ [8] are shown. From this figure it follows that the experimental points are described well by straight line and have the general character for different metals tested under various temperature and force conditions [9, 10, 12]. These results allow us to consider the damage parameter $\psi = \rho/\rho_0$ as universal characteristic of porosity accumulation in the creep process [14]. In the calculations the following values of coefficients were used: $A = 3 \cdot 10^{-9} [MPa]^{-2}$, $B = 7 \cdot 10^{-12} [MPa]^{-4}$, $\sigma_0 = 100 MPa$, $n = 2$, $m = 4$, $\beta = 1$.

Taking the fracture condition $t = t_f$, $\psi = 0$, from (8) we obtain the creep fracture criterion

$$t_f^b = \frac{1}{(\alpha - n + 1) \cdot A \sigma_0^n}. \quad (12)$$

When $\alpha = 2n$ the criterion (12) coincides with the Kachanov-Rabotnov criterion. In Fig. 4 in the double logarithmic coordinates are shown the creep fracture curves according to (12) for different values of the coefficient α ($\alpha = 6$ - curve 1, $\alpha = 4$ -

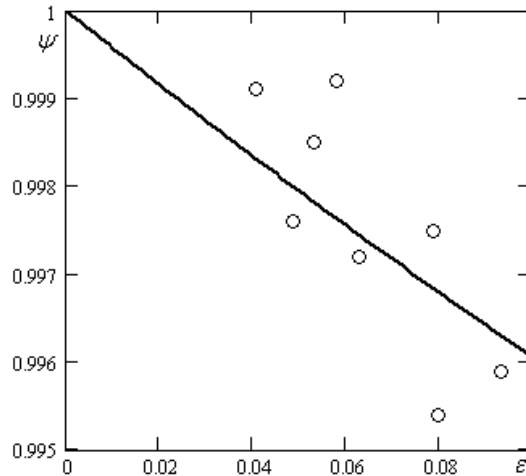


Figure 3: Theoretical curves of density changes (solid line) for $\alpha = 6$ and experimental points of density changes of pure copper during creep under $500^\circ C$ [8] (circle points).

curve 2 and $\alpha = 2$ - curve 3). In the calculations the following values of coefficients were used: $A = 1 \cdot 10^{-9} [MPa]^{-2}$, $n = 2$.

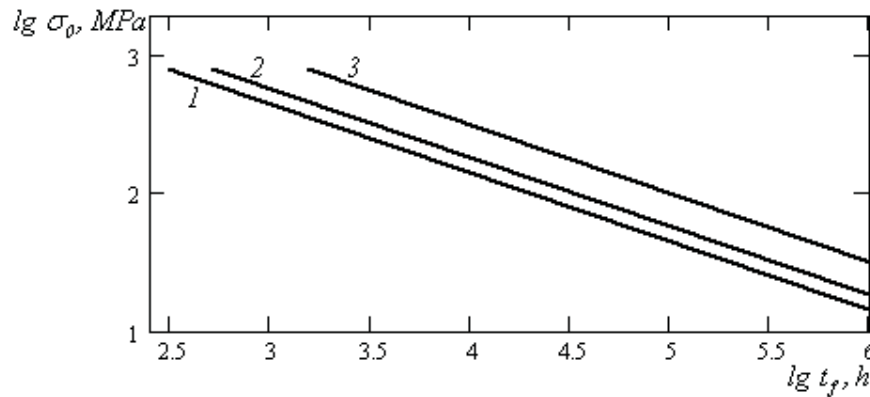


Figure 4: Curves of long-term strength under criterion (12): $\alpha = 6$ - curve 1, $\alpha = 4$ - curve 2 and $\alpha = 2$ - curve 3.

In Fig. 5 are shown the theoretical creep deformation curves according to the relation (9) for different values of the coefficient α ($\alpha = 6$ - curve 1, $\alpha = 4$ - curve 2 and $\alpha = 2$ - curve 3). As can be seen from this figure, the system of equations (6)-(7) is able to describe the third phase of creep curves, which is determined by the processes of damage accumulation. In the calculations the following values of coefficients were used: $A = 1 \cdot 10^{-12} [MPa]^{-2}$, $B = 5 \cdot 10^{-17} [MPa]^{-4}$, $\sigma_0 = 100 MPa$, $n = 2$, $m = 4$, $\beta = 1$.

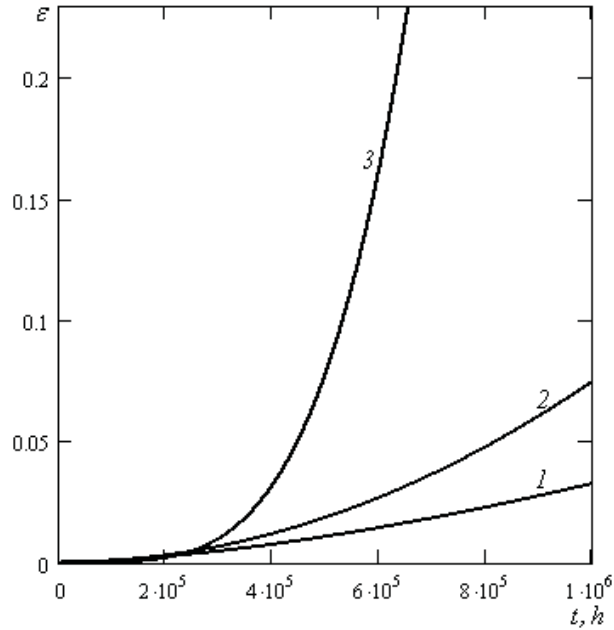


Figure 5: The theoretical creep deformation curves according to the relation (9) for different values of the coefficient α : $\alpha = 6$ - curve 1, $\alpha = 4$ - curve 2 and $\alpha = 2$ - curve 3.

Acknowledgements

Financial support of the Russian Foundation for Basic Research (Grants N 15-01-03159, N 14-01-00823) is gratefully acknowledged.

References

- [1] Kachanov L.M. Time of fracture under creep // Proceedings USSR Academy of Sciences. OTN. 1958. N 8. P. 26-31. (in Russian).
- [2] Rabotnov Y.N. On the mechanism of long-term fracture // Problems of strength of materials and structures. M.: Publishing House of the USSR Academy of Sciences. 1959. P. 5-7. (in Russian).
- [3] Rabotnov Y.N. Creep of elements of designs: M.: Nauka. 1966. 752p. (in Russian).
- [4] Novozhilov V.V. On plastic loosening // Applied Mathematics and Mechanics. 1965. N 4. P. 681-689. (in Russian).
- [5] Arutyunyan R.A. The problem of strain aging and long-term fracture in mechanics of materials. SPb.: Publishing House of the St. Petersburg State University. 2004. 252p. (in Russian).

REFERENCES

- [6] Arutyunyan R.A. High-temperature embrittlement and long-term strength of metallic materials // Mechanics of solids. 2015. vol. 50. Issue 2. P. 191-197.
- [7] Arutyunyan R.A. Embrittlement problem in mechanics of materials // Vestn. St. Petersburg. Univ. 2009. ser. 1. vol. 1. P. 54-57. (in Russian).
- [8] Boethner R.C., Robertson W.D. A study of the growth of voids in copper during the creep process by measurement of the accompanying change in density // Trans. of the Metallurg. Society of AIME. 1961. vol. 221. N 3. P. 613-622.
- [9] Beghi C., Geel C., Piatti G. Density measurements after tensile and creep tests on pure and slightly oxidised aluminium // J. Mat. Sci. 1970. vol. 5. N 4. P. 331-334.
- [10] Brathe L. Macroscopic measurements of creep damage in metals // Scand. J. Metal. 1978. vol. 7. N 5. P. 199-203.
- [11] Ratcliffe R.T., Greenwood G.W. Mechanism of cavitation in magnesium during creep // Phil. Mag. 1965. vol. 12. P. 59-69.
- [12] Woodford D.A. Density changes during creep in nickel // Metal science journal. 1969. vol. 3. N 11. P. 234-240.
- [13] Bowring P., Davies P.W., Wilshire B. The strain dependence of density changes during creep // Metal science journal. 1968. vol. 2. N 9. P. 168-171.
- [14] Kumanin V.I., Kovalev L.A., Alekseev S.V. The durability of the metal in the creep conditions. M.: Metallurgy. 1988. 223p. (in Russian).

Alexander R. Arutyunyan, Robert A. Arutyunyan, Regina R. Saitova, Universitetskii pr., 28, Faculty of Mathematics and Mechanics St.-Petersburg State University, St.-Petersburg, Petrodvoretz, 198504, Russia.

Effect of electron beam processing on the characteristics of tool steels

S.A. Atroshenko
satroshe@mail.ru

Abstract

One of the promising methods of energetic influences that have a significant impact on the structure, phase composition, physical and mechanical properties of metals and alloys is an electron beam processing (EBP). This method consists in treating the surface of the low-energy pulse high-current electron beams, providing adjustable over a wide range of energy density on the surface of the irradiated material. Ultrahigh heating speed to melting and subsequent cooling of a thin surface layer of material forms the limit temperature gradients. It is provides cooling of the surface layer due to heat transfer in the bulk material at a speed of 104..109 K/s, which can significantly improve the characteristics of the surface material. The electron beam treatment causes a change in the physicochemical properties of the metal surface layer that can be used to obtain protective and reinforcing coatings.

1 Materials and experimental technique

Investigation was carried out on 12Cr-V tool steel and speed steel R6M5 and R18. In this work it is used low-energy electron beam (20 KeV) [1], whereby hardened layer thickness of several tens of microns is heated by heat transfer. Using pulsed high-current electron beams with high-energy particles, it is possible to heat the surface layer of such thickness without heat transfer - as direct result of the energy of the electron beam. Experiments were conducted by electron-pulse treatment on the electron accelerator "Inus" (electron beam energy is $E \approx 230KeV$, the duration of the current pulse is $\leq 7mks$).

The phase state of metals was controlled by metallographic method using a microscope Axio-Observer-Z1-M after the appropriate chemical etching. The investigation of cross section structure was carried out on the optical microscope in the bright field. Quantitative phase relationship was determined by metallographic analysis with the help of random secant method.

Microhardness was determined using the Vickers method: measurements were carried out on a PMT-3 device with a load of 100g.

To determine the main parameters of the surface roughness pertometr M1 was used in the study. This device is designed to determine the most frequently used characteristics according to the ISO 4287. The average roughness Ra is arithmetic average

of all points of the roughness profile from the center line in the length of the assessment. The average height of roughness Rz is the arithmetic mean of the maximum protrusion height and the largest profile cavities. The greatest depth of roughness Rmax is the largest of the existing single roughness depths. The number of emissions per 1 cm R_{pc} is number of profile elements, which are sequentially intersect one upper and one lower section line.

Experimental conditions are shown in Table 1.

Table 1. Conditions of experiments

No	number of pulses	pulse energy	current density	pulse duration	tool steel
1		200 Mev			12Cr-V
2		200 Mev			12Cr-V
3	1	400 Mev			R18 quenched
4	1	400 Mev			R18 tempered
5	5	170 Kev	60 A/cm ²	2μs	R6M5
6	9	170 Kev	60 A/cm ²	2μs	R6M5
7	15	170 Kev	60 A/cm ²	2μs	R6M5

2 Results and discussion

The microstructure of the surface layer of steels after the EBP is shown in Figure 1.

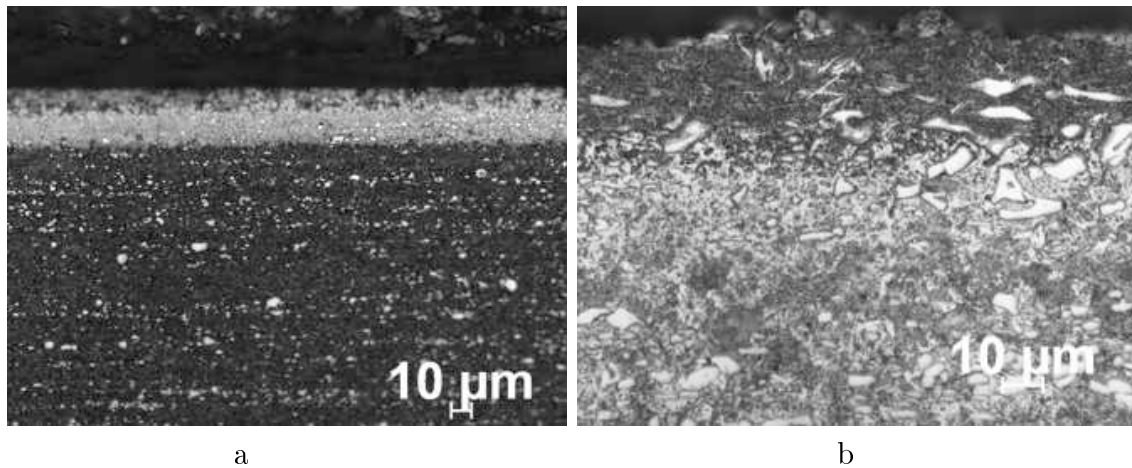


Figure 1: The structure of the surface layer of steel samples after the electron beam treatment: a - R18 steel, b - 12Cr-Vsteel

On the submitted micrographs in tool steels it can be seen weakly etching light or dark layer with uniform distribution of fine carbides. This area in the result of impact pulses was subjected to rapid heating up to the quenched temperature and rapid cooling, resulting in the formation of fine-grained, but in some cases of the amorphous structure in the layer.

The microstructure in the center of the sample of tool steels is shown in Figure 2. It is a dark matrix with bright carbides, among which there are also large, sometimes they form clusters.

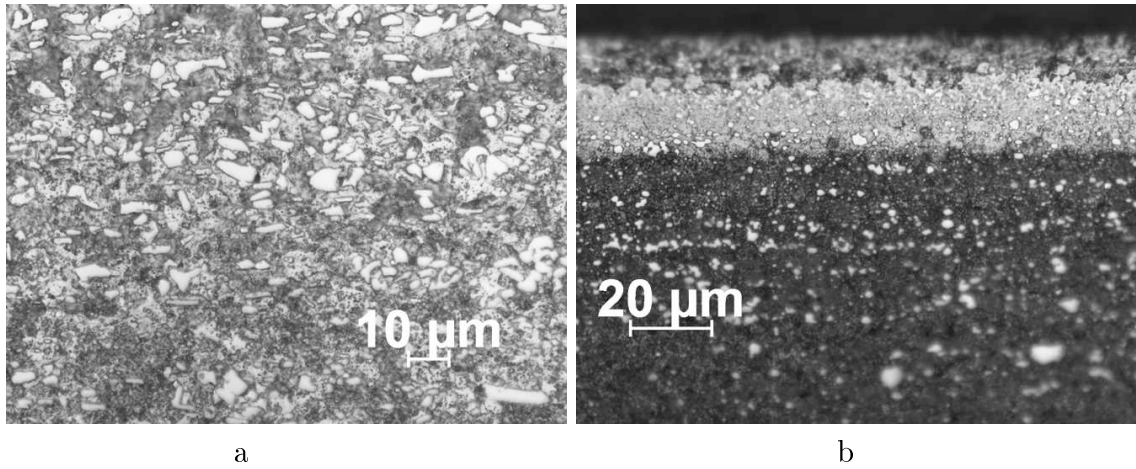


Figure 2: Structure of tool steel specimens in the center of the cross section: a - 12Cr-Vsteel, b - R18

Microhardness in the surface layer of the samples was higher microhardness values of the basic metal, which indicates an increase in the hardness of the material after electron beam processing, i.e. improved strength properties. Microhardness measurement results are shown in Table 2. The thickness of the strengthened layer was 18 – 86 microns (Table 3). The most significant hardening of the surface layer as compared to the steel base metal occurs in 12Cr-Vsteel - in 2.5 times. The surface layer of high-speed steels strengthened less - in 1 – 1,3 times since its initial strength is much higher. At the same time, the maximum hardening observed in R18 steel – up to 9235 MPa.

Table 2. Values of microhardness

No	material	microhardness, MPa	
		layer	Basic metal
1	12Cr-V steel	3360 ± 10	1255 ± 10
2	R18 quenched steel	9235 ± 10	7015 ± 10
3	R6M5 steel - BHII1	8390 ± 10	7016 ± 10
4	R6M5 steel - BHII2	8640 ± 10	7480 ± 10
5	R6M5 steel - BHII3	8005 ± 10	7702 ± 10

The results of the quantitative characteristics of the structure in the processed materials state (after EBP) are shown in Table 3. It can be seen that the maximum thickness layer is in steel R6M5 treated with the maximum number of pulses, and a minimum one is in steel R6M5 treated with a minimum number of pulses. The minimum grain size is in high speed steels - R18 and R6M5, so they have the maximum microhardness. Maximum carbide heterogeneity is observed in 12Cr-V steel (Figure 2 a) – 2 grade carbide heterogeneity according to standard.

Table 3 - Results of the quantitative characteristics of the steel structure.

Material	Layer thickness, μm	Grain size, μm	Carbide heterogeneity	
			Carbide size, μm	Carbide grade
R6M5 steel ВНД1	69.7 ± 0.2	7.1 ± 0.1	1.5 ± 0.1	1
R6M5 steel No 2	18.6 ± 0.2	3.2 ± 0.1	2.9 ± 0.1	1
R6M5 steel No 3	87.0 ± 0.2	3.6 ± 0.1	2.2 ± 0.1	1
R18 quenched steel	21.5 ± 0.2	2.0 ± 0.1	2.0 ± 0.1	1
R18 tempered steel	46.4 ± 0.2	1.6 ± 0.1	2.5 ± 0.1	1
12Cr-V steel No 4	31.3 ± 0.2	8.0 ± 0.1	2.0 ± 0.1	1
12Cr-V steel No 5	41.0 ± 0.2	8.6 ± 0.1	1.5 ± 0.1	2

Surface layer roughness of R6M5 steel after processing by EBP is higher than before the treatment (Table 4).

Table 4 - Results of the measurement of R6M5 steel surface roughness

N, pulses	condition	parameter			
		Ra, μm	Rz, μm	Rmax, μm	Rpc cm^{-1}
5	initial	0.1 ± 0.02	0.60 ± 0.02	0.85 ± 0.02	0.0 ± 1
	after EBP	2.9 ± 0.5	14.8 ± 1.8	18.5 ± 1.7	37 ± 4
9	initial	0.39 ± 0.02	3.79 ± 0.02	6.17 ± 0.02	48 ± 1
	after EBP	3.0 ± 0.5	14.2 ± 3.0	20.3 ± 3.1	27.7 ± 7
15	initial	0.12 ± 0.02	0.76 ± 0.02	0.90 ± 0.02	0.0 ± 1
	after EBP	3.9 ± 0.01	18.8 ± 0.9	26.1 ± 1.6	28 ± 6

After treatment by an electron beam regular relief of surface roughness is observed, which characterized by an increase of their number and height as compared with untreated surfaces. A more detailed analysis taking into account all characteristics shows that with increasing number of pulses the average roughness Ra and roughness depth Rmax increase. The average height roughness Rz is also maximum under the highest number of pulses. Regarding parameter Rpc – number of emissions per 1 cm, it is maximum with the minimum number of pulses.

3 Conclusion

1. The influence of electron beam processing on the quality of the surface layer of tool steels and the mechanical properties characteristics was carried out.
2. Changes of the structure of the material was revealed under EBP. There is a grain refinement and increase in microhardness. Electron beam processing of tool steels studied showed a significant improvement in the strength properties of the material.
3. The effect of the treatment of the electron beam on the geometry of the surface of the material was determined. The surface roughness of high-speed steel is strongly correlated with the number of pulses used in the processing, i.e. according to the selected treatment regime.

Acknowledgements

Work was financially supported by grants RFBR 16-01-00638, RFBR-NSFC 16-51-53006, and by St. Petersburg State University (Project no. 6.39.319.2014).

References

- [1] O.A. Gusev, Lazarenko A.B., Ivanov BA et al. The application of a pulsed electron beam for the heat treatment of metals // MiTOM, 9. -1984.- pp 95-100

Block element forms and factorization methods in cylindrical coordinate systems

V.A. Babeshko, O.V. Evdokimova, O.M. Babeshko, A.S. Muhin,
I.B. Gladskoi, E.M. Gorshkova
babeshko41@mail.ru, babeshko49@mail.ru, i.glad@list.ru,
gem@kubsu.ru, evdokimova.olga@mail.ru

Abstract

This work shows that being constructed, the block elements have several stages, where they may have different opportunities and functions. It was established that some stages are more opportune for the research aims and for the construction of new block structures. This stage is called packing up the block element and the element is called packed. At another stage, which is called unpacking, the block elements are more opportune for the performing calculations and clear research of solutions. It is shown that analyses of boundary-value problems by existed methods of variable separation, integral transformations and different insertions from the view of the developed theory are aimed at the analysis specifically in the form of the unblocked element. Exactly this restrained the use of these methods in the boundary problems in nonclassical fields, that didn't correspond to the framework of space transformation groups [1], [2]. The method of the block-level element, as it shown in [3], is convergent not only because it unites several approaches but also because it increases opportunities in research of boundary-value problems in nonclassical fields. Keywords: packed block element, factorization, topology, integral and differential factorization methods, exterior forms, block structures, boundary problems.

1 Introduction

For method's using it is necessary to make a few steps of transformations connected with engaging of external analysis device, factorization, topology and other branches of mathematics. In this work in collating of brick-element method with existing approaches and more complete revealing of ties with them and also with the view of convenience by its using in practical purposes three stages of transformations by building brick-element are represented which simplify its building and using. Algorithm of method's using on these stages by the example of boundary values in classical and non-classical areas is showed below.

2 The factorization method for block element

It is reasonable to call the first stage forming of block element. It comprises statement of boundary value for system of differential equations in partial derivatives with constant coefficients considered in space of slow-growing generalized functions \mathbf{H}_s . Boundary value for system P of differential equations with constant coefficients in partial derivatives of random order of differentiation in gibbous three-dimensional area Ω in speculation of resolvability without reference to type of boundary value of consideration can be written down in the form

$$\begin{aligned} \mathbf{K}(\partial x_1, \partial x_2, \partial x_3)\varphi &= \sum_{m=1}^M \sum_{n=1}^N \sum_{k=1}^K \sum_{p=1}^P A_{spmnk} \varphi_{p, x_1^{(m)} x_2^{(n)} x_3^{(k)}} = 0, \quad s = 1, 2, \dots, P, \\ A_{sqmnk} &= \text{const}, \quad \varphi = \{\varphi_1, \varphi_2, \dots, \varphi_P\}. \\ \varphi &= \{\varphi_s\}, \quad \varphi(\mathbf{x}) = \varphi(x_1, x_2, x_3), \quad \mathbf{x} = \{x_1, x_2, x_3\}, \end{aligned} \quad (1)$$

On the boundary $\partial\Omega$ following boundary conditions are assumed:

$$\begin{aligned} \mathbf{R}(\partial x_1, \partial x_2, \partial x_3)\varphi &= \sum_{m=1}^{M_1} \sum_{n=1}^{N_1} \sum_{k=1}^{K_1} \sum_{p=1}^P B_{spmnk} \varphi_{p, x_1^{(m)} x_2^{(n)} x_3^{(k)}} = f_s, \quad s = 1, 2, \dots, s_0 < P, \quad \mathbf{x} \in \partial\Omega \\ M_1 &< M, \quad N_1 < N, \quad K_1 < K. \end{aligned}$$

We can notice that in common with represented above integral method of factorization, boundary value in differential method of factorization is solved precisely if Ω is semispace. In case if area Ω is gibbous value reduces to solution of system of normally resolvable pseudodifferential equations. With the purpose of systemization of representation differential method of factorization let us a few stages. Reducing of differential equations by Fourier transformation or by other integral transformation to functional equation. Three-dimensional Fourier transformation of form $\Phi_n(\boldsymbol{\alpha}) = \iiint_{\Omega} \varphi_n(x) e^{i\langle \boldsymbol{\alpha}, \mathbf{x} \rangle} d\mathbf{x} \equiv F\varphi_n$, $\Phi_m = F\varphi_m$, $\langle \alpha^\nu \mathbf{x}^\nu \rangle = \alpha_1^\nu x_1^\nu + \alpha_2^\nu x_2^\nu + \alpha_3^\nu x_3^\nu$

It reduces to functional equation presentable in form

$$\mathbf{K}(\boldsymbol{\alpha})\Phi = \iint_{\partial\Omega} \boldsymbol{\omega} \equiv \sum_{n=1}^N \iint_{\partial\Omega_n} \boldsymbol{\omega}^n, \quad \mathbf{K}(\boldsymbol{\alpha}) \equiv -\mathbf{K}(-i\boldsymbol{\alpha}_1, -i\boldsymbol{\alpha}_2, -i\boldsymbol{\alpha}_3) = \|k_{nm}(\boldsymbol{\alpha})\|, \quad (3)$$

Here $\partial\Omega_n$ is orientable element of topological separation of boundary unity $\partial\Omega$, $\boldsymbol{\omega}^n$ is vector of exterior form built on this element. Here $\mathbf{K}(\boldsymbol{\alpha})$ is polynomial function matrix of order P . Vector of exterior forms $\boldsymbol{\omega}$ has in the function of component two-dimensional functions of the form

$$\boldsymbol{\omega} = \{\boldsymbol{\omega}_s\}, \quad s = 1, 2, \dots, P, \quad \boldsymbol{\omega}_s = P_{12s} dx_1 \wedge dx_2 + P_{13s} dx_1 \wedge dx_3 + P_{23s} dx_2 \wedge dx_3 \quad (4)$$

It relates also to exterior forms $\boldsymbol{\omega}^n$ on elements $\partial\Omega_n$. Operations of exterior forms have indications $dx_1 \wedge dx_2 = dx_1^1 dx_2^2 - dx_1^2 dx_2^1$, $dx_1 \wedge dx_3 = dx_1^1 dx_3^3 - dx_1^3 dx_3^1$, $dx_2 \wedge dx_3 = dx_2^2 dx_3^3 - dx_2^3 dx_3^2$. Here vectors of spontaneous coordinate system from the covers of tangent fibration of body surface are introduced. In rectangular coordinate system for tangent vectors of spontaneous element cover are assumed.

$x_1 = \{x_1^1, x_1^2, x_1^3\}$, $x_2 = \{x_2^1, x_2^2, x_2^3\}$. Coefficients of exterior forms are presented in [4]. Sufficing to stated boundary conditions (5) is reached by introducing in presentation of exterior forms of amounts of solution vector $\varphi(\partial\Omega)$ and its derivatives along the normal on $\partial\Omega$ taken from boundary conditions. Presence of derivatives on tangent line is left out of account. Exterior forms contain amounts of solution φ_n and its derivatives on boundary $\partial\Omega$. From boundary values (-) functions or derivatives along the normal on boundary are found by trial and error and conversion of nondegenerate matrix and are introduced in corresponding presentations of exterior forms ω . The rest of functions or derivatives along the normal must be found from pseudodifferential equations received by transformation of functional equations. Differential factorization of function matrix $\mathbf{K}(\alpha)$ of functional equation is occurred [4]. Consolidation of the functional equation to the system of pseudodifferential equation is achieved by calculation of residue form of Leray for functions of some complex variables. By such action the automorphism under the mapping of support towards itself is made. Waiving computations, which are in the noticed works were presented, we achieve correlations of the form

$$\sum_{\nu=1}^N \sum_{p=1}^P \iint_{\partial\Omega_\nu} \omega_p^\nu Z_{mp}(z_{s-}^\nu) = 0, \quad s- = 1, 2, \dots, G-, \quad (5)$$

Here $\alpha_{3s\pm}^\nu \equiv z_{s\pm}^\nu(\alpha_1^\nu, \alpha_2^\nu)$ laid above positive and under negative semiplanes nulls of determinant of function matrix $\mathbf{K}(\alpha)$. Built system is pseudodifferential equations. Admitted that demanded by problem to solve integral equations are derived from pseudodifferential equations and solved and the result is introduced to outer forms, the second stage of block element, named packing, is accomplished. Packed brick element has compact form. $\varphi(\mathbf{x}^\nu) = \frac{1}{8\pi^3} \iint_{-\infty}^{\infty} \mathbf{K}^{-1}(\alpha) \iint_{\partial\Omega} \omega e^{-i(\alpha^\nu \mathbf{x}^\nu)} d\alpha_1^\nu d\alpha_2^\nu d\alpha_3^\nu$, $\mathbf{x}^\nu \in \Omega$, $\mathbf{K}^{-1}(\alpha) = \mathbf{K}_r^{-1}(\alpha_3^\nu) \mathbf{K}^{-1}(\alpha_3^\nu, -)$. Here functions matrix $\mathbf{K}_r(\alpha_3^\nu)$, $\mathbf{K}(\alpha_3^\nu, -)$ are the results of differential factorization of functional matrix $\mathbf{K}(\alpha)$ by argument α_3^ν besides, determinant of the first contains nulls only on the upper semiplane, the second is on the lower one. In this pattern it represents topological manifold with the edge. In such form it is convenient for formation of brick structure for building non-homogeneity, hollows, and cracks, fixed and deformable inclusions couplings with deformable and fixed bricks in it. All of it is achieved by the formation of equality relations between given brick and similar adjoined one. For it on the basis of equivalence relations quotient topology of Cartesian product of brick elements \check{Y} supporter and topological space of vector-function built on them is building. An attribute of right built up brick element is the opportunity of calculation in model of solution of one integral by the method of theory of residues. It is called opening or unpacked of block element. Calculated this integral we achieve following presentation of opened brick element.

$$\varphi(\mathbf{x}^\nu) = \frac{1}{4\pi^2} \iint_{-\infty}^{\infty} \sum_s [\mathbf{A}_+(\alpha_1^v, \alpha_2^v, z_{s+}^v) e^{-i(z_{s+}^v x_3^v + \alpha_1^v x_1^v + \alpha_2^v x_2^v)} + \mathbf{B}_-(\alpha_1^v, \alpha_2^v, z_{s-}^v) e^{-i(z_{s-}^v x_3^v + \alpha_1^v x_1^v + \alpha_2^v x_2^v)}] d\alpha_1^v d\alpha_2^v \quad (6)$$

Here matrixes- functions $\mathbf{A}_+(\alpha_1^v, \alpha_2^v, z_{s+}^v)$, $\mathbf{B}_-(\alpha_1^v, \alpha_2^v, z_{s-}^v)$ depend on specified boundary conditions, form of Ω area and also on qualities of matrixes- function

K(α) . Considering the form of opened brick element (6) it is easy to notice in it the form of representation, in which solutions of common differential equations and also equations in partial differential quotient with constant coefficients with the method of exponential substitution or separation of variables are searched. [5], [6] on the base of it, it could be said that all practice of mentioned methods appliance is summarized to researches of opened or unpacked block elements. As a result scope of available for solution problems narrowed. It may be used only for classic areas denial of which excluded the opportunity to solve boundary problem with mentioned methods.

3 The packed block elements for cylindrical domain

For illustration of mentioned above let us look at examples. Example 1. In the layer Ω with parallel limits of thickness $b - a$ boundary problem for partial differential equation following form is placed:

$$\frac{\partial^2 \varphi}{\partial x_1^2} + \frac{\partial^2 \varphi}{\partial x_2^2} + \frac{\partial^2 \varphi}{\partial x_3^2} - r^2 \varphi = 0, \quad |x_1| \leq \infty, \quad |x_2| \leq \infty, \quad a \leq x_3 \leq b \quad (7)$$

. On the limits (-) boundary conditions are accepted

$$\begin{aligned} \varphi(x_1, x_2, x_3) &= f_1(x_1, x_2), \quad x_3 = a, \\ \frac{\partial \varphi(x_1, x_2, x_3)}{\partial x_3} &= f_2(x_1, x_2), \quad x_3 = b \end{aligned} \quad (8)$$

Applied to equations and boundary conditions double transformation in x_1, x_2 in form

$$\begin{aligned} \Phi(\alpha_1, \alpha_2, x_3) &= \iint_{-\infty}^{\infty} \varphi(x_1, x_2, x_3) e^{i(\alpha_1 x_1 + \alpha_2 x_2)} dx_1 dx_2, \\ \varphi(x_1, x_2, x_3) &= \frac{1}{4\pi^2} \iint_{-\infty}^{\infty} \Phi(\alpha_1, \alpha_2, x_3) e^{-i(\alpha_1 x_1 + \alpha_2 x_2)} d\alpha_1 d\alpha_2 \end{aligned}$$

Achieve one-dimensional boundary problem

$$\frac{\partial^2 \Phi}{\partial x_3^2} - k^2 \Phi = 0, \quad \Phi(\alpha_1, \alpha_2, a) = F_1, \quad \Phi'(\alpha_1, \alpha_2, b) = F_2, \quad k^2 = \alpha_1^2 + \alpha_2^2 + r^2, \quad (9)$$

Similar F_1, F_2 are obtained Fourier transformation of right parts of boundary conditions For building of boundary problem's solution use exponential substitution and receive solution in the form

$$\Phi(\alpha_1, \alpha_2, x_3) = c_1 e^{kx_3} + c_2 e^{-kx_3}, \quad (10)$$

Complying with the given solution of boundary problem receives constant describing solution as following:

$$c_1 = \frac{F_1 k e^{-kb} + F_2 e^{-ka}}{2kch k(b-a)}, \quad c_2 = \frac{F_1 k e^{kb} - F_2 e^{ka}}{2kch k(b-a)} \quad (11)$$

Inserted value (11) into (10) and made double Fourier inversion following parameters α_1, α_2 receive a solution of boundary problem. Let us apply method of block element in the Ω area for solution of this boundary problem. No complicated constructions lead to the functional equation with using of outer formula in form

$$\begin{aligned} (\alpha_3^2 + k^2) \Phi_0(\alpha_1, \alpha_2, \alpha_3) &= \int_a^b d\omega, \quad \omega(x_3, \alpha_3) = \left(\frac{\partial \Phi}{\partial x_3} - i\alpha_3 \Phi \right) e^{i\alpha_3 x_3}. \\ (\alpha_3^2 + k^2) \Phi_0(\alpha_1, \alpha_2, \alpha_3) &= \Phi'(\alpha_1, \alpha_2, b) e^{i\alpha_3 b} - \Phi'(\alpha_1, \alpha_2, a) e^{i\alpha_3 a} - \\ &\quad - i\alpha_3 \Phi(\alpha_1, \alpha_2, b) e^{i\alpha_3 b} + i\alpha_3 \Phi(\alpha_1, \alpha_2, a) e^{i\alpha_3 a} \end{aligned} \quad (12)$$

Inserted in right part (11) given boundary conditions (9) achieve equation as (-)

$$\Phi_0(\alpha_3) = (\alpha_3^2 + k^2)^{-1} [F_2 e^{i\alpha_3 b} - \Phi'(a) e^{i\alpha_3 a} - i\alpha_3 \Phi(b) e^{i\alpha_3 b} + i\alpha_3 F_1 e^{i\alpha_3 a}] \quad (13)$$

Here for formula simplification of function $\Phi(\alpha_1, \alpha_2, a), \Phi(\alpha_1, \alpha_2, b), \Phi(\alpha_1, \alpha_2, x_3)$, two first arguments are omitted and all actions are accomplished towards the third one i.e. their notations $\Phi(a), \Phi(b), \Phi(x_3)$, are accepted. Considering correlation in local coordinate system and requested accomplishment of automorphism - reflection of segment on yourself, we reach such pseudodifferential equation.

$$\begin{cases} kF_1 e^{-k(b-a)} + F_2 - \Phi'(a) e^{-k(b-a)} - k\Phi(b) = 0, \\ -kF_1 + F_2 e^{-k(b-a)} - \Phi'(a) + k\Phi(b) e^{-k(b-a)} = 0, \end{cases} \quad (14)$$

Their decision gives the follow meanings of sought expressions.

$$\Phi'(a) = \frac{-kF_1 \operatorname{sh}k(b-a) + F_2}{\operatorname{ch}k(b-a)}, \quad \Phi(b) = \frac{kF_1 + F_2 \operatorname{sh}k(b-a)}{k \operatorname{ch}k(b-a)}$$

Inserting these meanings in formula and applied triple access Fourier, we reach presence of decision- block element boundary problem in layer in the form of

$$\begin{aligned} \varphi(x_1, x_2, x_3) &= \frac{1}{8\pi^3} \iiint_{R^3} e^{-i(\alpha \mathbf{x})} (\alpha_3^2 + k^2)^{-1} [\{ k^2 F_1 e^{i\alpha_3 a} \operatorname{sh}k(b-a) + i\alpha k F_1 \operatorname{ch}k(b-a) e^{i\alpha_3 a} - \\ &\quad - k F_2 e^{i\alpha_3 a} \} + \{ -i\alpha e^{i\alpha_3 b} F_2 \operatorname{sh}k(b-a) + F_2 k \operatorname{ch}k(b-a) e^{i\alpha_3 b} - k F_1 i\alpha e^{i\alpha_3 b} \}] \\ &\quad [k \operatorname{ch}k(b-a)]^{-1} d\alpha_1 d\alpha_2 d\alpha_3, \quad (\alpha \mathbf{x}) = \alpha_1 x_1 + \alpha_2 x_2 + \alpha_3 x_3, \quad a \leq x_3 \leq b \end{aligned} \quad (15)$$

Received expression, representing topological object - manifold with boundary, is called packed block element. Similar packed block elements for other layers can conjugate with each other very simply, if they are in such form. According to topology, it is necessary to make factor - topology and determined functions on them, taking into account equivalence relation of boundary condition. In this simplest case, transit of boundary condition in arears of pasting together of layers is enough. In packed block element, if operations of building are carried out rightly, integral of parameter is always calculated according to theory of residues. Accomplished this act, we get uncovered or unpacked block element, which has form

$$\begin{aligned} \varphi(x_1 x_2 x_3) &= \frac{1}{4\pi^2} \iint_{R^2} e^{-i(\alpha_1 x_1 + \alpha_2 x_2)} \times \\ &\quad \{ (f_1 k e^{-kb} + f_2 e^{-ka}) e^{kx_3} + (f_1 e^{kb} k - f_2 e^{ka}) e^{-kx_3} \} 2k \operatorname{ch}k(b-a) \end{aligned}$$

Decision coincides with decision, built by means of exponential substitutions. As mentioned above, precisely these unpacked block elements were built by means of separation of variables, integral transformations, difference substitutions. They are slightly simpler, than packed block element, containing in it, but, as the follow example show, have more restricted set of boundary tasks, which can be researched by these methods. Below here is comparatively simple example of boundary task, which is accessibly for research by means of block element, and not solvable by listed approaches. Example 2. Learn considering above boundary task for differential equation (1) in domain Ω , occupying cylinder in direction of axis $0x_3$ with triangular section in plane x_10x_2 , having tops in point $(0, 0)$, $(x_{01}, 0)$, $(0, x_{02})$, $x_{01} > 0$, $x_{02} > 0$. Outer normal line to side $x_{01}x_{02}$ makes up ν with axis $0x_1$, but distance of this side from beginning of coordinate is p . In this case in accepted coordinate system, which we will call absolute, coordinate of top of triangle have expressions

$$x_{10} = \frac{p}{\cos \nu}, x_{20} = \frac{p}{\sin \nu}$$

. Applied to boundary task transformation Fourier on parameter x_3 we get two-dimension boundary task in section x_10x_2 . We will consider, that on reference bounders, sides of triangle $x_{01}0$, $0x_{02}$, $x_{02}x_{01}$, right local coordinate system of cordinates $x_1^\pi 0^\pi x_2^\pi$, $x_1^{0,5\pi} 0^{0,5\pi} x_2^{0,5\pi}$, $x_1^{0,5\pi-\nu} 0^{0,5\pi-\nu} x_2^{0,5\pi-\nu}$, are built, at that coordinate axis with index 1 have direction along the sides, but with index 2 - on outer normal line. The upper indexes in accepted indication characterized degree of rotation of local coordinate system concerning to absolute. On mentioned above sides of triangle, in such consistency, boundary conditions are assigned in form of functions $g_1(x_1^\pi)$, $g_2(x_1^{0,5\pi})$, $g_3(x_1^{0,5\pi-\nu})$ which are considered sufficiently smooth. Inserting boundary task in topology structure, described above, and accomplished acts, connected with method of block element, as in the first items and example by analogy, we reach to packed element, having form

$$\begin{aligned} \varphi(x_1, x_2, x_3) = \frac{1}{8\pi^3} \iiint_{R^3} e^{-i(\alpha x)} \frac{i}{(\alpha_1^2 + \alpha_2^2 + k^2)} [F_1(\alpha_1^\pi)(\alpha_{2-}^\pi - \alpha_2^\pi) + F_2(\alpha_1^{0,5\pi})(\alpha_{2-}^{0,5\pi} - \alpha_2^{0,5\pi}) \\ + F_3(\alpha_1^{0,5\pi-\nu})e^{i\alpha_2^{0,5\pi-\nu}p}(\alpha_{2-}^{0,5\pi-\nu} - i\alpha_2^{0,5\pi-\nu})] d\alpha_1 d\alpha_2 d\alpha_3 \end{aligned} \quad (16)$$

$$\begin{aligned} \alpha_{2\pm}^\pi &= \pm i \sqrt{(\alpha_1^\pi)^2 + k^2}, \quad \alpha_{2\pm}^{0,5\pi} = \pm i \sqrt{(\alpha_1^{0,5\pi})^2 + k^2}, \quad \alpha_{2\pm}^{0,5\pi-\nu} = \pm i \sqrt{(\alpha_1^{0,5\pi-\nu})^2 + k^2} \\ x_1 &= x_1^{0,5\pi-\nu} \sin \nu + x_2^{0,5\pi-\nu} \cos \nu, \quad x_2 = -x_1^{0,5\pi-\nu} \cos \nu + x_2^{0,5\pi-\nu} \sin \nu \\ \alpha_1 &= \alpha_1^{0,5\pi-\nu} \sin \nu + \alpha_2^{0,5\pi-\nu} \cos \nu, \quad \alpha_2 = -\alpha_1^{0,5\pi-\nu} \cos \nu + \alpha_2^{0,5\pi-\nu} \sin \nu, \\ \alpha_1^{0,5\pi-\nu} &= \alpha_1 \sin \nu - \alpha_2 \cos \nu, \quad \alpha_2^{0,5\pi-\nu} = \alpha_1 \cos \nu + \alpha_2 \sin \nu \\ x_1^{0,5\pi} &= x_2, \quad x_2^{0,5\pi} = -x_1, \quad x_1^\pi = -x_1, \quad x_2^\pi = -x_2 \\ \alpha_1^{0,5\pi} &= \alpha_2, \quad \alpha_2^{0,5\pi} = -\alpha_1, \quad \alpha_1^\pi = -\alpha_1, \quad \alpha_2^\pi = -\alpha_2 \end{aligned}$$

Here vector $\{ F_1(\alpha_1^\pi), F_2(\alpha_1^{0,5\pi}), F_3(\alpha_1^{0,5\pi-\nu}) \}$ is result of some linear continuous reflection of vector $\{ g_1(x_1^\pi), g_2(x_1^{0,5\pi}), g_3(x_1^{0,5\pi-\nu}) \}$ in space of transformation Fourier on basis vector. Unpacked block element by means of calculation one integral, it is possible in rightly packed block element, we reach to uncovered block

element, which is presented in form

$$\begin{aligned} \varphi(x_1, x_2, x_3) = \frac{1}{4\pi^2} \iint_{R^2} \langle [F_2(\alpha_1^{0,5\pi}) \exp [-i(\alpha_1^{0,5\pi} x_1^{0,5\pi} + \alpha_{2+}^{0,5\pi} x_2^{0,5\pi} + \alpha_3 x_3)] d\alpha_1^{0,5\pi} - \\ - F_1(\alpha_1^\pi) \exp [-i(\alpha_1^\pi x_1^\pi + \alpha_{2+}^\pi x_2^\pi + \alpha_3 x_3)] d\alpha_1^\pi - \\ - F_3(\alpha_1^{0,5\pi-\nu}) \exp [-i(\alpha_1^{0,5\pi-\nu} x_1^{0,5\pi-\nu} + \alpha_{2+}^{0,5\pi-\nu} x_2^{0,5\pi-\nu} + \alpha_3 x_3)] d\alpha_1^{0,5\pi-\nu} \rangle d\alpha_3 \end{aligned} \quad (17)$$

By calculating of integrals, it is necessary to claim the same point (x_1, x_2, x_3) , which situates in inside of triangle, to examine and Jacobean determinants by substitution of variable in integrals to take into account. The authors don't know works, in which decision of mentioned boundary task was accomplished by means of separation of variables or other analytical approach.

4 Conclusion

The difference between packed and uncovered block element consists, of that in packed form block element, which is capable boundary tasks, not yielding to other methods, can uniformly conjugate with other block elements of such or other dimensions and build packed block family, keeping singly topology structure. In his turn unpacked block element gives pictorial presentation about decision's character and allow learning its properties, to pick out features of localization's zone. In particular because of enumerated above, it was succeed in building of model of starting earthquake, revealed dangerous zones of stress concentration [7], [8].

Acknowledgements

Separate fragment of work are realized by support of grants of RFBR (14-08-00404), (15-08-01377), (15-01-01379), the Program of presidium of the RAS e 33.

References

- [1] Gelfand I.M., Graev M.I., Pyatetskiy- Shapiro I.I. "Representation theory and automorphic functions". M. Nauka. 1698. 512 p.
- [2] Vilenkin N. Ya. YSpecial functions and representation theory of groupsY. M. Nauka, 1991. 576p.
- [3] Babeshko V.A., Evdokimova O.V, Babeshko O.M., Gorshkova E.M., Zaret-skaya A.V., Muhin A.S., Pavlova A.V. "Convergent Properties of Block Elements"/// Doklady Physics. - 2015. - V. 60. - No.11 . - P. 515-518. DOI: 10.1134S1028335815110099
- [4] Babeshko V.A., Evdokimova O.V., Babeshko O.M. YAbout block element in applicationsY.// Physical mesomechanics. 2012. T.15.€1. C. 95-103.
- [5] Kurant R. YControl with partial derivativeY M.Mir, 1964.832p.

REFERENCES

- [6] Tihonov A.N., Samarskiy A.A. *Equations of mathematical physics*. M. Nauka, 1996. 724p.
- [7] Babeshko V.A., Evdokimova O.V., Babeshko O.M. *The Problem of Physical and Mechanical Precursors of an Earthquake: Place, Time, Intensity* // *Doklady Physics*. - 2016. - V. 61. - No.2 . - P. 92-97. DOI: 10.1134/S1028335816020099
- [8] Babeshko B.A., Evdokimova O.V., Babeshko O.M. *Topological methods in the problem of earthquake forecast* // *Ecological Bulletin of Scientific centers BSEC Cooperation*. 2015, ϵ 2, C. 8-13.

V.A. Babeshko, O.M. Babeshko, A.S. Muhin, I.B. Gladskoi, E.M. Gorshkova, Kuban State University, Krasnodar, 350040, Stavropolckia st. 149, Russia

V.A. Babeshko, O.V. Evdokimova, Southern Scientific Center RAS, Rostov-on-Don, 344006, Chehov st, 41, Russia

Deformation and divergence of the moving beams made from thermoelastic materials

Nikolay V. Banichuk, Svetlana Yu. Ivanova
banichuk@gmail.com

Abstract

The problem of stability and out-of-plane deformation analysis is considered for an axially moving elastic web modelled as a beam (undergoing cylindrical deformation). The beam is under homogeneous pure mechanical in-plane tension and thermal strains corresponding to the thermal tension and bending. In accordance with the static approach of stability analysis the problem of out-of-plane thermomechanical divergence (buckling) is reduced to an eigenvalue problem which is analytically solved. This problem corresponds to the case of in-plane thermomechanical tension and zero thermal bending. The general case of deformations induced by combined thermomechanical bending and tension is reduced to nonhomogeneous boundary-value problem and analyzed with the help of Fourier series.

1 Introduction

The study of the mechanical behavior of axially moving elastic systems has attracted the attention of researchers for a long time beginning with Skutch [1]. Studies in this direction written in the English language began to appear half a century later starting with those by Sack [2], Archibald and Emslie [3], Miranker [4]. Other classic studies of moving elastic systems include those by Mote [5] - [8], Thurman and Mote [9], Simpson [10], Mujumdar and Douglas [11], Pramila [12], [13], Wickert and Mote [14]. Recent studies include Wang et al. [15], Banichuk et al. [16] - [18]. Wide exposition of obtained results in domain of mechanics of moving materials is presented in the books by Marynowski [19] and Banichuk et al. [20]. An extensive literature review can also be found in these books.

2 Basic relations

Let us consider a beam which occupies the domain ($0 \leq x \leq l$, $-h/2 \leq z \leq h/2$, $0 \leq y \leq b = 1 \ll l$) in the rectangular coordinate system xyz and moves axially at a constant transport velocity V_0 in the x -direction. The transverse (out-of-plane) displacement is described by the function $w = w(x, t)$. By considering the wave equation in the co-moving coordinate and using transformations from the

Lagrange derivatives to the Euler derivatives of transverse displacements we can write the equation for small transverse vibrations in the following form [20]:

$$m \frac{d^2 w}{dt^2} = \mathcal{L}^M(w) - \mathcal{L}^B(w), \quad (1)$$

where m is the mass per unit length of the beam and

$$\mathcal{L}^M(w) = T \frac{\partial^2 w}{\partial x^2} = \left(T_0 - \frac{Eh}{1-\nu} \varepsilon_\theta \right) \frac{\partial^2 w}{\partial x^2}, \quad (2)$$

$$\mathcal{L}^B(w) = -\frac{\partial^2 M}{\partial x^2} = D \left[\frac{\partial^4 w}{\partial x^4} + (1+\nu) \frac{\partial^2 \kappa_\theta}{\partial x^2} \right]. \quad (3)$$

Here \mathcal{L}^M , \mathcal{L}^B are operators on w , $T_x = T$ is the in-plane tension, E is the Young modulus, ν is the Poisson ratio, M is the bending moment, D is the bending rigidity, h is the thickness of the beam. The quantities ε_θ and κ_θ are the generalized thermal strains corresponding to the thermal tension and bending of the beam defined as

$$\varepsilon_\theta = \frac{1}{h} \int_{-h/2}^{h/2} \alpha_\theta \theta dz, \quad \kappa_\theta = \frac{12}{h^3} \int_{-h/2}^{h/2} \alpha_\theta \theta z dz, \quad (4)$$

where α_θ is the coefficient of linear thermal expansion.

In the stationary case the behavior equation takes the form

$$\left(mV_0^2 + \frac{Eh}{1-\nu} \varepsilon_\theta - T_0 \right) \frac{d^2 w}{dx^2} + D \left[\frac{d^4 w}{dx^4} + (1+\nu) \frac{d^2 \kappa_\theta}{dx^2} \right] = 0 \quad (5)$$

with simply supported boundary conditions

$$w = 0, \quad \frac{d^2 w}{dx^2} + (1+\nu) \kappa_\theta = 0, \quad x = 0, l. \quad (6)$$

3 Divergence problem

Suppose that

$$T = T_0 - \frac{Eh}{1-\nu} \varepsilon_\theta \quad (7)$$

and $\kappa_\theta = 0$. Then, using (5) with dimensionless variables $\tilde{x} = x/l$ (the tilde will be omitted) and introducing the auxiliary function

$$\psi(x) = \frac{d^2 w}{dx^2}, \quad 0 \leq x \leq l \quad (8)$$

and the quantity

$$\lambda = \frac{l^2}{D} \left(mV_0^2 + \frac{Eh}{1-\nu} \varepsilon_\theta - T_0 \right) \quad (9)$$

we formulate the eigenvalue problem

$$\frac{d^2\psi}{dx^2} + \lambda\psi = 0, \quad \psi(0) = 0, \quad \psi(1) = 0. \quad (10)$$

Integrating the behavior equations and taking into account the formulated boundary conditions we find the unknown shape function $w = C \sin(j\pi x)$, $j = 1, 2, 3, \dots$ (C - arbitrary constant) and the correspondent critical velocity

$$(V_0^{div})_j^2 = \frac{j^2\pi^2 D}{ml^2} + \frac{T_0}{m} - \frac{Eh}{m(1-\nu)}\varepsilon_\theta. \quad (11)$$

Thus, we observe that the shape of the eigenmode coincides with the membrane (with $D = 0$ and $\kappa_\theta = 0$) eigenmode regardless of the value of the bending rigidity D and the thermal strain ε_θ , but the bending rigidity and thermal strain contribute additional terms to the divergence speed.

4 Deformations under combined thermomechanical bending and tension

Using dimensionless coordinate x ($0 \leq x \leq 1$) and assuming that $\kappa_\theta = const \neq 0$, $\varepsilon_\theta = const$ we consider an axially moving beam subjected to tension and bending and represent the behavior equation in the form

$$\frac{d^2}{dx^2} \left[\frac{d^2 w}{dx^2} + \lambda w + (1 + \nu) \kappa_\theta \right] = 0, \quad 0 \leq x \leq 1, \quad (12)$$

where λ is given by (9). Integrating (12) with boundary conditions (6) we obtain the second order differential equation for the displacement function:

$$\frac{d^2 w}{dx^2} + \lambda w + (1 + \nu) \kappa_\theta = 0, \quad 0 \leq x \leq 1. \quad (13)$$

To solve this equation we represent the desired solution $w(x)$ and the quantity $(1 + \nu)\kappa_\theta$ as the Fourier series

$$w = \sum_{n=1,3,\dots}^{\infty} a_n \sin n\pi x, \quad (14)$$

$$(1 + \nu)\kappa_\theta = \frac{4(1 + \nu)\kappa_\theta}{\pi} \sum_{n=1,3,\dots}^{\infty} \frac{1}{n} \sin n\pi x. \quad (15)$$

Substituting (14), (15) into (13) and performing elementary operations we obtain the equation

$$\sum_{n=1,3,\dots}^{\infty} \sin n\pi x \left\{ a_n [\lambda - (n\pi)^2] + \frac{4(1 + \nu)\kappa_\theta}{n\pi} \right\} = 0 \quad (16)$$

leading to the expressions for unknown coefficients

$$a_n = \frac{4(1 + \nu)\kappa_\theta}{n\pi [(n\pi)^2 - \lambda]}, \quad n = 1, 3, \dots \quad (17)$$

5 Conclusions

In this paper the deformation and stability of an axially moving elastic panel were considered. The panel was travelling at a constant velocity between the rollers modelled by the corresponding boundary conditions. Small transverse elastic displacements of the panel were described by a fourth-order differential equation that includes the terms expressing the action of in-plane tension and out-of-plane centrifugal forces and the terms taking into account a thermomechanical action. We investigated separately two important cases: the divergence of the panel loaded by in-plane thermomechanical tension and the deformation of the beam subjected to combined thermomechanical bending and tension. In both cases the considered problems have been studied analytically and the solutions have been found in an explicit form.

Acknowledgements

The research was performed under financial support of RFBR (grant 14-08-00016-a).

References

- [1] Skutch R. Über die Bewegung eines gespannten Fadens, welcher gezwungen ist durch zwei feste Punkte, mit einer constanten Geschwindigkeit zu gehen, und zwischen denselben in Transversalschwingungen von gerlanger Amplitude verzetzt wird. *Annalen der Physik und Chemie*. 1897, 61: 190-195.
- [2] Sack R.A. Transvers oscillations in travelling strings. *British Journal of Applied Physics*. 1954, 5: 224-226.
- [3] Archibald F.R., Emslie A.G. The vibration of a string having a uniform motion along its length. *ASME Journal of Applied Mechanics*. 1958, 25: 347-348.
- [4] Miranker W.L. The wave equation in a medium in motion. *IBM Journal of Research and Development*. 1960, 4: 36-42.
- [5] Mote C.D. Divergence buckling of an edge-loaded axially moving band. *International Journal of Mechanical Sciences*. 1968, 10: 281-295.
- [6] Mote C.D. Dynamic stability of an axially moving band. *Journal of the Franklin Institute*. 285(5): 329-346.
- [7] Mote C.D. Dynamic stability of axially moving materials. *Shock and Vibration Digest*. 4(4): 2-11.
- [8] Mote C.D. Stability of systems transporting accelerating axially moving materials. *ASME Journal of Dynamic Systems, Measurement, and Control*. 97: 96-98.
- [9] Thurman A.L., Mote C.D.Jr. Free, periodic, nonlinear oscillation of an axially moving strip. *ASME Journal of Applied Mechanics*. 1969, 36(1): 83-91.

-
- [10] Simpson A. Transvers modes and frequencies of beams translating between fixed end supports. *Journal of Mechanical Engineering Science*. 1973, 15: 159-164.
- [11] Mujumdar A.S., Douglas W.J.M. Analytical modelling of sheet flutter. *Svensk Papperstidning*. 1976, 79: 187-192.
- [12] Pramila A. Sheet flutter and the interaction between sheet and air. *TAPPI Journal*. 1986, 69: 70-74.
- [13] Pramila A. Natural frequencies of a submerged axially moving band. *Journal of Sound and Vibration*. 1987, 112(1): 198-203.
- [14] Wickert J.A. Mote, C.D. Classical vibration analysis of axially moving continua. *ASME Journal of Applied Mechanics*. 1990, 57: 738-744.
- [15] Wang J., Huang L., Liu X. Eigenvalue and stability analysis for transverse vibrations of axially moving strings based on Hamiltonian dynamics. *Acta Mechanica Sinica*. 2005, 21: 485-494.
- [16] Banichuk N., Jeronen J., Neittaamaki P., Tuovinen T. On the instability of an axially moving elastic plate. *International Journal of Solids and Structures*. 2010, 47(1): 91-99.
- [17] Banichuk N., Jeronen J., Kurki M., Neittaamaki P., Saksa T., Tuovinen T. On the limit velocity and buckling phenomena of axially moving orthotropic membranes and plates. *International Journal of Solids and Structures*. 2011, 48(13): 2015-2025.
- [18] Banichuk N., Kurki M., Neittaamaki P., Saksa T., Tirronen M., Tuovinen T. Optimization and Analysis of Processes with Moving Materials Subjected to Fatigue Fracture and Instability. *Mechanics Based Design of Structures and Machines*. 2013, 41(2): 146-167.
- [19] Marynowski K. Dynamics of the Axially Moving Orthotropic Web, Lecture notes in Applied and Computational Mechanics. Vol. 38. Berlin: Heidelberg: Springer-Verlag, 2008.
- [20] Banichuk N., Jeronen J., Neittaamaki P., Saksa T., Tuovinen T. *Mechanics of Moving Materials*. Switzerland: Springer International Publishing, 2014.

Nikolay V. Banichuk, Prospekt Vernadskogo, 101, bld.1, Moscow, Russia
Svetlana Yu. Ivanova, Prospekt Vernadskogo, 101, bld.1, Moscow, Russia

Mathematical and Experimental Simulation of the Ascending Twisting Flows

S.P. Bautin, I.Yu. Krutova, A.G. Obukhov
IYKrutova@mephi.ru

Abstract

The results of theoretical and experimental studies of the ascending twisting flows encountered in nature in the form of tornadoes and tropical cyclones [1-3] are represented.

Theorems on the existence and the uniqueness of the solutions to specific initial-boundary value problems that, in particular, set the rotation direction of tornadoes, tropical cyclones and fire vortices are proved for the system of gas dynamics equations and the complete system of Navier-Stokes equations.

There are the constructed numerically the solutions of indicated systems of partial differential equations that model the gas flow from the simple planar spiral currents to the three-dimensional nonstationary flows in general. The calculation results are consistent with both the data of natural observations and the results of laboratory experiments.

Results of laboratory experiments on the vertical upwards motion of air along the pipe, which confirmed the occurrence of the twisting in the near-bottom and the vertical parts of the flow in the appropriate direction are given in this investigations.

The results of theoretical and experimental studies of the ascending twisting flows encountered in nature in the form of tornadoes and tropical cyclones [1-3] are proven in this research.

We consider the complete system of Navier-Stokes equations in dimensionless variables under the action of gravity and Coriolis forces [3, 4]:

$$\left\{ \begin{array}{l} \rho_t + \mathbf{V} \cdot \nabla \rho + \rho \operatorname{div} \mathbf{V} = 0, \\ \mathbf{V}_t + (\mathbf{V} \cdot \nabla) \mathbf{V} + \frac{T}{\gamma \rho} \nabla \rho + \frac{1}{\gamma} \nabla T = \mathbf{g} - 2\boldsymbol{\Omega} \times \mathbf{V} + \\ + \frac{\mu_0}{\rho} \left[\frac{1}{4} \nabla (\operatorname{div} \mathbf{V}) + \frac{3}{4} \Delta \mathbf{V} \right], \\ T_t + \mathbf{V} \cdot \nabla T + (\gamma - 1) T \operatorname{div} \mathbf{V} = \frac{\varkappa_0}{\rho} \Delta T + \\ + \frac{\mu_0 \gamma (\gamma - 1)}{2\rho} \{ [(u_x - v_y)^2 + (u_x - w_z)^2 + (v_y - w_z)^2] + \\ + \frac{3}{2} [(u_y + v_x)^2 + (u_z + w_x)^2 + (v_z + w_y)^2] \}, \end{array} \right. \quad (1)$$

Which for the case of zero viscosity and vanishing thermal conductivity: $\mu_0 = \varkappa_0 = 0$ – the system (1) is the system of gas dynamics equations.

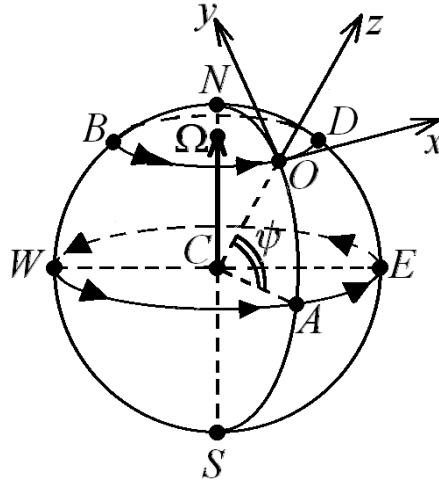


Fig. 1.

The symbols in system (1) are the following: ρ – is the density; u, v, w – are the projections of the velocity vector \mathbf{V} on the axis of Cartesian coordinate system $Oxyz$ (see Fig.1) rotating together with the Earth and the beginning of which lies on the surface of the Earth at the point O on the parallels with the latitude ψ ; T – is the temperature; \mathbf{g} – is the acceleration vector of gravity; $a = 2\Omega \sin \psi$; $b = 2\Omega \cos \psi$; Ω – is the modulus of the angular velocity vector $\mathbf{\Omega}$ of the Earth's rotation.

The theorem on the smooth flow into the vertical cylinder. For the system of gas dynamics equations there are the specified conditions describing the initial time of the uniform, resting outside the cylinder $\sqrt{x^2 + y^2} = r_0, r_0 > 0$ gas. Also the smooth radial flow into the cylinder are given. Then this problem has a unique solution in the neighbourhood of the given point ($t = 0, r = r_0, \varphi = \varphi_0, z = 0$). Here r, φ – are the polar coordinates in the plane xOy .

The properties of the solution of this problem that since the time $t = 0$ in the gas flow occurs the twisting directed in the positive direction in the case of the Northern Hemisphere and the negative direction in the case of the Southern Hemisphere. This direction of rotation corresponds to the direction of air like tornadoes and tropical cyclones. If for the problem $\Omega = 0$, so the twisting does not arise.

The theorem on the smooth heating of the vertical cylinder. For the system of gas dynamics equations there are the specified conditions describing the initial time of the uniform, resting outside the cylinder $\sqrt{x^2 + y^2} = r_0, r_0 > 0$ gas. Also the smooth heating of this cylinder are given. Then this problem has a unique solution in the neighbourhood of the given point ($t = 0, r = r_0, \varphi = \varphi_0, z = 0$).

The properties of the solution of this problem that since the time $t = 0$ the twisting directed in the negative direction in the case of the Northern Hemisphere and the positive one in the case of the Southern Hemisphere appears in the gas flow. The air around the fire vortices has such direction of twisting. If for the problem $\Omega = 0$, the twisting in the flow is absent.

The paper provides examples of numerical construction of flows under the action of gravity and Coriolis forces for the system (1) as in the case $\mu_0 = \varkappa_0 = 0$, as well, in the case $\mu_0 \neq 0, \varkappa_0 \neq 0$. They are constructed from the simple planar spiral flows in

the bottom parts of the being investigated flows to the three-dimensional stationary and notstationary flows in general. In numerical simulation time is set from the beginning of a natural atmospheric vortex before its release to stationary state. The calculation results are consistent with both the data of natural observations of tornadoes and tropical cyclones of varying intensity, and the results of laboratory experiments.

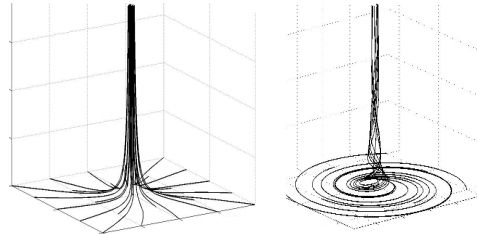


Fig. 2.

The results of laboratory experiments on the vertical upwards motion of air along the pipe, which confirmed the occurrence of twisting in the near-bottom and the vertical parts of the flow in the appropriate direction are represented. Fig. 2 shows the photograph of the room in which the experiment was conducted.



Fig. 3.

Fig. 3 shows the instantaneous streamlines constructed at different times in the simulation flow of the experiment with blowing.

References

- [1] Bautin S.P. Tornado i sila Koriolisa (Tornado and the Coriolis Force), Novosibirsk: Nauka, 2008.
- [2] Bautin S.P. and Obukhov A.G. Matematicheskoe modelirovanie razrushitel'nykh atmosferykh vikhrei (Mathematical Modeling of Destructive Atmospheric Vortices), Novosibirsk: Nauka, 2012.
- [3] Bautin S.P., Krutova I.Yu., Obukhov A.G., Bautin K.V. Razrushitel'nye atmosferyevikhri: Teoremy, raschety eksperimenty (Destructive Atmospheric Vortices: Theorems, Calculations, and Experiments), Novosibirsk: Nauka, 2013.

REFERENCES

- [4] Bautin S.P. *Kharakteristicheskaya zadacha Koshi i ee prilozheniya v gasovoi dinamike* (Characteristic Cauchy Problem and Its Applications to Gas Dynamics), Novosibirsk: Nauka, 2009.

S. P. Bautin, Ural State University of Railway Transport, Yekaterinburg, Russia

I. Yu. Krutova, National Research Nuclear University MEPhI, Moscow, Russia

A.G. Obukhov, Tyumen State University of Oil and Gas, Tyumen, Russia

Statics and harmonic oscillations of springs as rods of arbitrary spatial shape

Vladimir V. Eliseev, Evgenii A. Oborin
 oborin1@yandex.ru

Abstract

The springs are considered as linearly elastic rods of arbitrary spatial shape with taking into account tension and shear. The equations of rod dynamics are written in direct tensor form. The system of equations in components is derived using the assumption of cross-section symmetry. These equations admit the solution in quadratures. Also they can be solved by the shooting method implemented in the built-in function of computer mathematics packages. As an example, we present the static and dynamic analysis of a conical helical spring. The algorithm of calculation is presented for the forced and free harmonic oscillations.

1 Introduction

The springs applied in mechanical engineering have often forms of rods [1]. The progress in mechanics of deformable solid bodies [2] resolves the previous problems [3]. The calculation of rods is simplified especially by wide-spreading of computer mathematics [4, 5]. The transition to the case of harmonic oscillations has no difficulties.

From the recent studies into the spring dynamics, we note [6]–[9]. In [6] the effect of axial compression on the natural frequencies is studied. The comparison between different dynamic models of helical springs is discussed using dispersion curves in [7]. The barrel and hyperboloidal springs are investigated in the paper [8] using Laplace transform. The effects of rotational inertia, axial, shear and torsional deformation for helical springs of different cross sections are studied in [9].

2 Linear theory of rods

The equations of linear theory of rods are reliably established [2]. For harmonic oscillations with the frequency ω , they have the form:

$$\begin{aligned}
 \mathbf{Q}' &= -\mathbf{q} - \omega^2 \rho (\mathbf{u} + \boldsymbol{\theta} \times \boldsymbol{\varepsilon}), \\
 \mathbf{M}' &= -\mathbf{r}' \times \mathbf{Q} - \mathbf{m} - \omega^2 (\mathbf{I} \cdot \boldsymbol{\theta} + \rho \boldsymbol{\varepsilon} \times \mathbf{u}), \\
 \boldsymbol{\theta}' &= \mathbf{A} \cdot \mathbf{M} + \mathbf{C} \cdot \mathbf{Q}, \\
 \mathbf{u}' &= \boldsymbol{\theta} \times \mathbf{r}' + \mathbf{B} \cdot \mathbf{Q} + \mathbf{M} \cdot \mathbf{C}.
 \end{aligned} \tag{1}$$

The rods are considered as material lines whose particles are the elementary bodies with the vectors of displacement \mathbf{u} and rotation $\boldsymbol{\theta}$. The loads are external distributed per unit length forces and moments \mathbf{q} , \mathbf{m} and internal (in the cross sections) ones \mathbf{Q} , \mathbf{M} . Prime indicates derivative with respect to material coordinate s (not necessarily arc coordinate). The tensors of the second rank \mathbf{A} , \mathbf{B} , \mathbf{C} characterize the elastic compliances of rod including the bending, twisting, tension and shear compliance. Three-dimensional models have to be used to calculate them; for example, the Saint-Venant problem. The inertial rod parameters are the density ρ , the eccentricity vector $\boldsymbol{\varepsilon}$ and the tensor of inertia \mathbf{I} . The initial form of rod is given by the position vector dependence $\mathbf{r}(s)$ on the material coordinate.

The first two equations in (1) are the balance of momentum and the balance of moment of momentum. The third and the fourth are the relations of elasticity. These relations connect the strain vectors $\boldsymbol{\kappa} \equiv \boldsymbol{\theta}'$, $\boldsymbol{\gamma} \equiv \mathbf{u}' - \boldsymbol{\theta} \times \mathbf{r}'$ with the force factors \mathbf{Q} , \mathbf{M} . The entire system (1) can be derived from the principle of virtual work [2].

3 Integration of static equations in quadratures

In statics ($\omega = 0$) the equations (1) are integrated in quadratures [3] as follows:

$$\begin{aligned} \mathbf{Q} &= - \int_0^s \mathbf{q} ds + \mathbf{Q}_0, \quad \mathbf{M} = \int_0^s (\mathbf{Q} \times \mathbf{r}' - \mathbf{m}) ds + \mathbf{M}_0, \\ \boldsymbol{\theta} &= \int_0^s (\mathbf{A} \cdot \mathbf{M} + \mathbf{C} \cdot \mathbf{Q}) ds + \boldsymbol{\theta}_0, \quad \mathbf{u} = \int_0^s (\boldsymbol{\theta} \times \mathbf{r}' + \mathbf{B} \cdot \mathbf{Q} + \mathbf{M} \cdot \mathbf{C}) ds + \mathbf{u}_0. \end{aligned} \quad (2)$$

Here four vector constants arise, and they are determined by using the boundary conditions. If the rod is fixed at the tip $s = 0$ and loaded at the other tip $s = L$, then from the first two equations we determine \mathbf{Q}_0 , \mathbf{M}_0 right away, and in another equations we have $\boldsymbol{\theta}_0 = 0$, $\mathbf{u}_0 = 0$ - it is the statically determined problem. With the arbitrary given initial form $\mathbf{r}(s)$, the integrals (2) are calculated in components easily by means of computer mathematics. We can use the integration by parts:

$$\int \mathbf{Q} \times \mathbf{r}' ds = \mathbf{Q} \times \mathbf{r} + \int \mathbf{q} \times \mathbf{r} ds, \quad \int \boldsymbol{\theta} \times \mathbf{r}' ds = \boldsymbol{\theta} \times \mathbf{r} - \int (\mathbf{A} \cdot \mathbf{M} + \mathbf{C} \cdot \mathbf{Q}) \times \mathbf{r} ds$$

In the case of statically indetermined problem, we need to construct and solve the linear algebraic system following from the boundary condition in order to determine the vector constants \mathbf{Q}_0 , \mathbf{M}_0 , $\boldsymbol{\theta}_0$, \mathbf{u}_0 .

The case of a closed rod requires a special consideration. Instead of boundary conditions we have the conditions of periodicity: $\mathbf{Q}(0) = \mathbf{Q}(L)$ etc. For the first two equalities in (1), we obtain the identities, namely the balances of forces and moments. The constants \mathbf{Q}_0 , \mathbf{M}_0 are indeterminate herewith. The least equalities give the following conditions of the uniqueness of rotations and displacements:

$$\begin{aligned} \oint (\mathbf{A} \cdot \mathbf{M} + \mathbf{C} \cdot \mathbf{Q}) ds &= 0, \\ \oint [\mathbf{r} \times (\mathbf{A} \cdot \mathbf{M} + \mathbf{C} \cdot \mathbf{Q}) + \mathbf{B} \cdot \mathbf{Q} + \mathbf{M} \cdot \mathbf{C}] ds &= 0. \end{aligned} \quad (3)$$

This is the linear algebraic system for the unknowns $\mathbf{Q}_0, \mathbf{M}_0$.

Let us clarify the form of compliances. If the section has two axes of symmetry, then they are

$$\begin{aligned}\mathbf{A} &= (A_{\perp} \mathbf{E} + (A_{\tau} - A_{\perp}) \boldsymbol{\tau} \boldsymbol{\tau}) |\mathbf{r}'|, \quad \boldsymbol{\tau} = \mathbf{r}'/|\mathbf{r}'|, \\ \mathbf{B} &= (B_{\perp} \mathbf{E} + (B_{\tau} - B_{\perp}) \boldsymbol{\tau} \boldsymbol{\tau}) |\mathbf{r}'|, \quad \mathbf{C} = 0\end{aligned}\quad (4)$$

We denote: A_{\perp}, A_{τ} are the bending and twisting compliances, B_{τ}, B_{\perp} are the tension and shear compliances. \mathbf{E} is the identity tensor, $\boldsymbol{\tau}$ is the tangent vector. The factor $|\mathbf{r}'|$ is here because the length of the element is $|\mathbf{r}'| ds$. For the thin rods one usually assumes the absence of tension and shear $\mathbf{B} = 0$ (hence $\mathbf{C} = 0$).

4 Use of computer mathematics

We think about another approach to be more efficient. We use the numerical integration of the system of ordinary differential equations (ODE) of 12th order by means of the computer mathematics [5]. This requires to write the equations (1) in components. Projecting (1) into the Cartesian axes x, y, z , we have:

$$\begin{aligned}Q_x' &= -q_x, \quad Q_y' \dots, \quad M_x' = Q_y z' - Q_z y' - m_x, \quad M_y' \dots, \\ \theta_x' &= A_{\perp} |\mathbf{r}'| M_x + (A_{\tau} - A_{\perp}) x' |\mathbf{r}'|^{-1} (x' M_x + y' M_y + z' M_z), \quad \theta_y' \dots, \\ u_x' &= \theta_y z' - \theta_z y' + B_{\perp} |\mathbf{r}'| Q_x + (B_{\tau} - B_{\perp}) x' |\mathbf{r}'|^{-1} (x' Q_x + y' Q_y + z' Q_z), \quad u_y' \dots\end{aligned}\quad (5)$$

Then we rewrite it to the matrix form:

$$\begin{aligned}Y' &= F(s, Y); \quad Y = (Q_x \ Q_y \ \dots \ u_z)^T, \quad F_0 = -q_x(s), \ \dots, \\ F_{11} &= Y_6 y' - Y_7 x' + B_{\perp} m(s) Y_2 + \frac{B_{\tau} - B_{\perp}}{m(s)} z' (x' Y_0 + y' Y_1 + z' Y_2); \\ m(s) &\equiv \sqrt{x'^2 + y'^2 + z'^2}.\end{aligned}\quad (6)$$

With the given boundary conditions (six at both the ends), the system is solved in Mathcad by the shooting method with the built-in functions `sbval`–`Rkadapt` [4]. The same results are obtained by the finite difference method and the standard solver of algebraic systems in Wolfram Mathematica.

As a benchmark example we consider the steel conical spring with the following equations:

$$x(s) = \rho(s) \cos s, \quad y(s) = \rho(s) \sin s, \quad z(s) = z_1 s; \quad \rho(s) = \rho_0 + \rho_1 s \quad (7)$$

Here we have three constants; with $\rho_1 = 0$ the curve is the helix. The end $s = 0$ is fixed, hence displacement and rotation are zero: $\mathbf{u} = 0, \boldsymbol{\theta} = 0$. The free end $s = 10\pi$ (5 coils) is loaded by the force \mathbf{Q} (the moment is absent). We show the initial state of the spring and two deformed states: with $\mathbf{Q} = -P_1 \mathbf{k}$ (along z -axis) (Fig. 1a) and $\mathbf{Q} = P_2 \mathbf{i}$ (along x -axis) (Fig. 1b). The geometric parameters are: the section radius is $r = 1$ cm, the parameters of the curve are $\rho_0 = 10$ cm, $\rho_1 = -1.5$ cm, $z_1 = 2$ cm. The rod compliances are $A_{\perp} = 4/E\pi r^4$, $A_{\tau} = 2/\mu\pi r^4$, $B_{\tau} = 1/E\pi r^2$, $B_{\perp} = 7/6\mu\pi r^2$ (E is the Young's modulus, μ is the shear modulus and $6/7$ is the

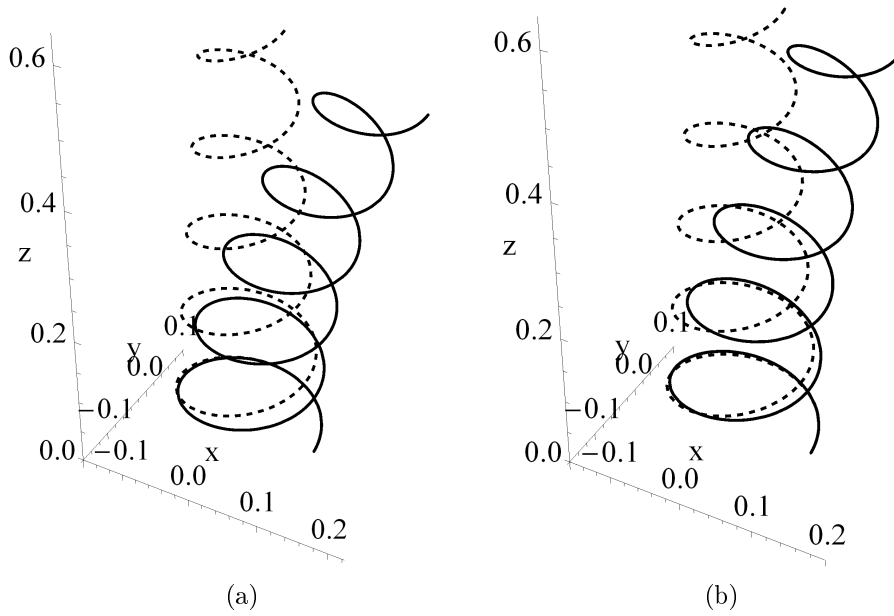


Figure 1: Configurations of spring

shear coefficient). In Fig. 1a the load is $P_1 = 5000$ N, in Fig. 1b $P_2 = 500$ N. Cartesian coordinates in the initial state correspond to the formulas (7), and in the actual state they correspond to $x + u_x$, $y + u_y$, $z + u_z$.

In Fig. 1 the deformations are large, because the loads are so. But the problem is linear, and hence the displacements are proportional to the loading parameters. In numerical integrating we can restrict ourselves with the small loads, avoiding the problems with convergence of the shooting method.

We can use the set of points instead of the analytic dependences as in (7) to define the initial shape. Using the set of points we apply the built-in functions for the regression (regress—interp in Mathcad). This approach is realized in [5] for the plane nonlinearly elastic springs.

5 Harmonic oscillations

The numerical algorithm discussed above can be extended easy to the case of forced harmonic oscillations. For this purpose we need to add the inertial loads (proportional to ω^2) [10]. In the case of the free oscillations we have the eigenvalue problem, for obtaining the solution of which we include in the system one more equation: $(\omega^2)' = 0$. We can prescribe an additional boundary condition because the modes of oscillations are determined to within a constant factor.

As a benchmark example we analyse the free oscillations of the spring considered above in Sect. 4. Eccentricity and inertia of rotation are not taken into account. The resulting eigenmodes are in Fig. 2.

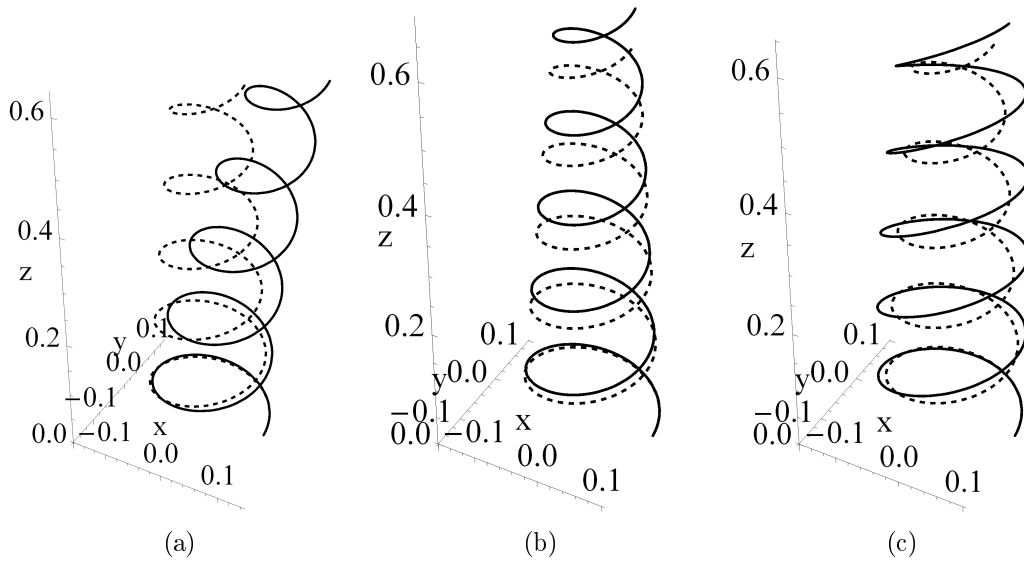


Figure 2: Eigenmodes of spring

6 Conclusion

One-dimensional rod model was applied to statical and dynamical analysis of springs of arbitrary spatial shape. The linear equations in the direct tensor form and in components were presented. The solution in quadratures and the solution by means of computer mathematics were proposed. The first approach is helpful in statically determined problems. The second approach uses the numerical integration methods such as the shooting method and the finite difference method. A benchmark example of conical spring was considered. Configuration of spring under the static loading and the first three eigenmodes were shown.

Acknowledgements

This work is carried out in the framework of the state task of the Ministry of Education and Science of the Russian Federation (Project No. 933-2014, 1972-2014).

References

- [1] Ponomarev, S.D., Andreeva, L.E. The calculation of the elastic elements of machines and instruments. Mashinostroyenie, Moscow, 1980. (in Russian)
- [2] Eliseev, V.V. Mechanics of elastic bodies. St. Petersburg State Polytechn. Univ. Publishing House, St. Petersburg, 2003 (in Russian)
- [3] Lurie, A.I. About small deformations of curved rods. Treatises of Leningrad Polytechn. Institute. No. 3, 1941. P. 143–157. (in Russian)

-
- [4] Kiryanov, D., Kiryanova, E. Computational science. Infinity Science Press, Hingham, 2007. 400 p.
- [5] Eliseev, V.V., Oborin, E.A. Theory and calculation of large elastic deformations of plane rods with tension and shear. Trans. Seminar Computer Methods in Continuum Mechanics 2013–2014. St. Petersburg Univ. Press, St. Petersburg. 2014. P. 107–119 (in Russian)
- [6] Becker, L.E., Chassie, G.G., Cleghorn, W.L. On the natural frequencies of helical compression springs. Int. J Mech. Sciences. No. 44, 2002. P. 825–841. DOI 10.1016/S0020-7403(01)00096-0
- [7] Sorokin, S.V. Linear dynamics of elastic helical springs: asymptotic analysis of wave propagation. Proc. Royal Soc. A. Vol. 465, No. 2105, 2009. P. 1513–1537. DOI 10.1098/rspa.2008.0468
- [8] Calim, F.F. Dynamic analysis of composite coil springs of arbitrary shape. Composites: Part B. No. 40, 2009. P. 741–757. DOI 10.1016/j.compositesb.2009.04.017
- [9] Yu, A.M., Hao, Y. Free vibrations analysis of cylindrical helical springs with noncircular cross-sections. J Sound and Vib. Vol. 330, 2011. P. 2628–2639. DOI 10.1016/j.jsv.2010.12.015
- [10] Eliseev, V.V., Moskalets, A.A., Oborin, E.A. Deformation analysis of turbine blades on complete one-dimensional model. Russian J Heavy Machinery. No. 5, 2015. P. 35–39. (in Russian)

Vladimir V. Eliseev, Department of Mechanical Engineering and Design, Peter the Great St. Petersburg Polytechnical University, 195251 Polytechnicheskaya str. 29, St. Petersburg, Russia

Evgenii A. Oborin, Department of Mechanical Engineering and Design, St. Petersburg, Russia

The characteristics of steady-state convective cyclonic vortex

Anna Evgrafova, Andrey Sukhanovskii, Elena Popova
eav@icmm.ru

Abstract

Experimental study of the steady-state cyclonic vortex from isolated heat source in a rotating fluid layer is described. The structure of laboratory cyclonic vortex is similar to the typical structure of tropical cyclones from observational data and numerical modelling including secondary flows in the boundary layer. Different constraints of the steady-state hurricane-like vortex were studied. The three main dimensional parameters that define the vortex structure for a fixed geometry - heating flux, rotation rate and viscosity were varied independently. It was shown that viscosity is one of the main parameters that define steady-state vortex structure. Along with the experiment a numerical simulation in a similar geometry was performed. For numerical simulation we used CFD package FlowVision. Numerical results showed good agreement with experimental data and proved efficiency of the use of numerical modeling.

1 Introduction

The phenomenon of vortex generation is found in a wide range of flows of different nature and scales. Synoptic vortices, such as cyclones and anticyclones, play a major role in the formation of weather conditions over the large areas. And secondary flows in the hurricane boundary layers may have a considerable effect on the heat and mass transfer between the water and the air [1]. Despite decades of research the problem of the intense large-scale atmospheric vortices generation is unsolved and attracts close attention from many scientific groups. The complexity of the problem forces researchers to study cyclones formation step by step using laboratory experiments as well as numerical modeling.

The main reason of the vortices formation in the atmosphere and ocean is interaction between Coriolis force and mass forces caused by the local temperature inhomogeneity. In this way laboratory model of hurricane-like vortex was proposed and studied in [2, 3, 4]. They considered rotating layer of fluid with the localized heater in the bottom. Local velocity measurements showed that the general structure of mean radial and azimuthal flows in a proposed model is similar to the typical structure of a hurricane and proved that chosen configuration is very promising for a studying of hurricane-like vortices. The studies were done with the use of the buoyant probe

for measurement of cyclonic rotation in a central part and many questions were left open for further studies.

In the current study, like [2, 3, 4], we consider steady-state hurricane-like vortex using a modern experimental technique and numerical simulation. For a fixed geometry there are only three main dimensional parameters that define the vortex structure - heating flux, rotation rate and viscosity. Independent controlled variation of these parameters gives possibility to analyse the influence of each dimensional parameter on the cyclonic vortex structure and to define government nondimensional parameters.

In addition to laboratory modeling the numerical calculations using CFD package Flow Vision were conducted. Despite of experiment numerical modeling provides an opportunity to get information about instantaneous velocity and temperature distribution throughout the volume. The geometrical dimensions of the computational domain and the values of the control parameters selected in accordance with the experimental regimes. Numerical results showed good agreement with experimental data. Using numerical modeling instant velocity and temperature distribution were obtained.

2 Experimental Setup

The formation of cyclonic vortex was studied in a cylindrical vessel of diameter 300 mm, and height 40 mm (Fig. 1, a). The sides and bottom were made of Plexiglas with a thickness 3 mm and 20 mm respectively. There was no cover or additional heat insulation at the sidewalls. The heater is a brass cylindrical plate mounted flush with the bottom. The diameter of the plate is 104 mm, and its thickness is 10 mm. The brass plate is heated by an electrical coil placed on the lower side of the disc. For studying the influence of the heating on the flow structure the series of experiments was carried out. For different experimental realizations the heating power was varied from 17 Wt to 78 Wt. For each realization the heating power was constant and controlled by Termodat system. Cylindrical vessel was placed on a rotating horizontal table (Fig. 1, b). The table provides uniform rotation in the angular velocity range $0.04 \leq \Omega \leq 0.30 \text{ s}^{-1}$. In the present study the angular velocity was varied from $\Omega = 0.07 \text{ s}^{-1}$ to $\Omega = 0.17 \text{ s}^{-1}$. Silicon oils with different values of kinematic viscosity, PMS-20, PMS-10, PMS-5 and PMS-3 (25, 10, 5 and 3 cSt at $T = 25 \text{ }^{\circ}\text{C}$) were used as working fluids. In all experiments, the depth of the fluid layer was 30 mm and the surface of the fluid was always open. The room temperature is kept constant by air-conditioning system, and cooling of the fluid is provided mainly by the heat exchange with surrounding air on the free surface and some heat losses through sidewalls. For low values of kinematic viscosity it takes about 2 hours to obtain a steady-state regime. Temperature inside the fluid layer was measured by copper-constantan thermocouples.

The velocity field measurements were made with a 2D particle image velocimetry (PIV) system Polis (Fig.1, b). The system included a dual pulsed Nd-YaG laser (1), a control unit, a digital CCD camera (3), placed in a rotating frame, and a computer. The synchronization of the operation of the laser and the CCD camera, the measurement, and the processing of the results were performed using the software

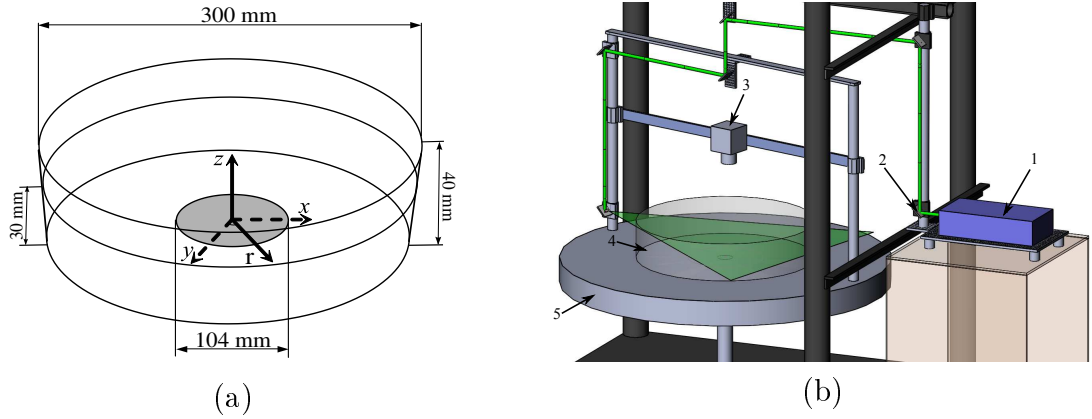


Figure 1: Experimental setup: (a) Dimensions and location of the coordinate system, (b) - Measurement system

package Actual Flow. All data were obtained in rotating coordinate system using optical mirrors (2). Optical mirrors route laser beam (4) from fixed laser to rotating vessel. Cylindrical vessel works as a lens and narrow horizontal light sheet (5) from the periphery to the center but all area of our interest in the central part of the vessel was illuminated. Also we need to note that due to strong optical distortions we did not make PIV measurements in a close proximity to the heater at height less than 2 mm. All PIV measurements were done for horizontal crosssections at different heights. Even variation of the three main dimensional parameters (heating, viscosity, rotation) leads to the many experimental realizations (62 in our case). So for the most of regimes the measurements were done only at three heights, near the bottom ($z = 3$ mm), in the central horizontal crosssection ($z = 15$ mm), and near the upper surface ($z = 27$ mm). It allowed us to study the flow structure in the boundary layers and in the bulk of the flow. Iteration algorithms and decreasing of the size of the interrogation windows from 32×32 to 16×16 pixels provided a dynamic range of approximately 500. The main subject of this study is cyclonic vortex over the heating area, so for keeping high spatial resolution the most of the PIV measurements were made only in a central part of the layer at different horizontal cross-sections.

3 Dependence of the cyclonic vortex structure on the main parameters

In this chapter we describe the general structure of large-scale radial flow and formation of the cyclonic motion in the central part of the vessel. The heat flux in the central part of the bottom initiates the intensive upward motion above the heater. Warm fluid cools at the free surface and moves toward the periphery where the cooled fluid moves downward along the side wall. After some time, large-scale advective flow occupies the whole vessel (Fig. 2, vertical cross-section). Structure and specifics of flows in the case of non-rotating cylindrical layer are described in details in [5].

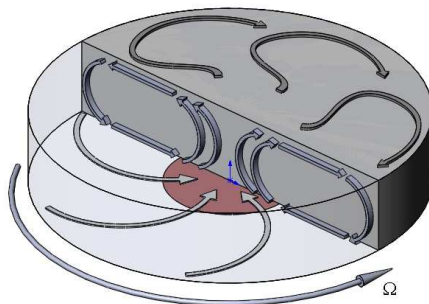


Figure 2: The structure of main flow in a rotating frame

In rotating case large-scale radial circulation leads to the angular momentum transport and angular momentum exchange on the solid boundaries. Convergent flow in the lower layer brings fluid parcels with large values of angular momentum from periphery to the center and produces cyclonic motion (Fig.2, lower horizontal cross-section). In the upper layer situation is the opposite - divergent flow takes fluid with low values of angular momentum to the periphery resulting in anticyclonic motion (Fig.2, upper horizontal cross-section).

The main motivation of investigation is to separate the role of the three main parameters of the problem - heating, rotation and viscosity, and analyze the influence of each dimensional parameter on the cyclonic vortex structure. In details research was described in [6]. Here the main results of this work are presented.

Relative motion in our system is driven by localized heating so the clear understanding how the increase of the heating changes the flow structure is very important. As is expected the increase of the heating produce more intensive meridional circulation. Meridional circulation provides angular momentum transport in the lower layer and magnitude of azimuthal velocity also increases with the heating. Structure of the cyclonic vortex changes with the heating, it becomes more uniform over depth. The shape of the vortex is conical for the weak heating and becomes cylindrical (in the central part) in the developed state.

Another important parameter is the rotation rate. In our case the rotation is the source of angular momentum so the faster we rotate the layer the more intensive vortex we potentially may produce. From the other side rotation suppresses convection which is the main source of the meridional circulation that brings extra angular momentum to the center and produces cyclonic vortex. It means that for the fixed rotation rate increasing of the heating leads to increasing of cyclonic vortex intensity but for the fixed heating there is the optimal rotation rate that provides the most intensive cyclonic vortex. Spatially and time averaged azimuthal velocity profiles for the fixed heating and different rotation rates in the middle of the layer ($z = 15\text{mm}$) for the two working fluid (PMS-5 and PMS-10) are presented in Fig. 3 . There is remarkable change of the flow structure with a relatively small variation of the rotation rate. Maximum of azimuthal flow moves to the periphery and decrease with the rotation rate growth, it means that convective cell moves from the center and its intensity is declined.

One more parameter that has crucial importance on the cyclonic vortex formation is viscosity. In order to separate effects of viscosity we have made three series of

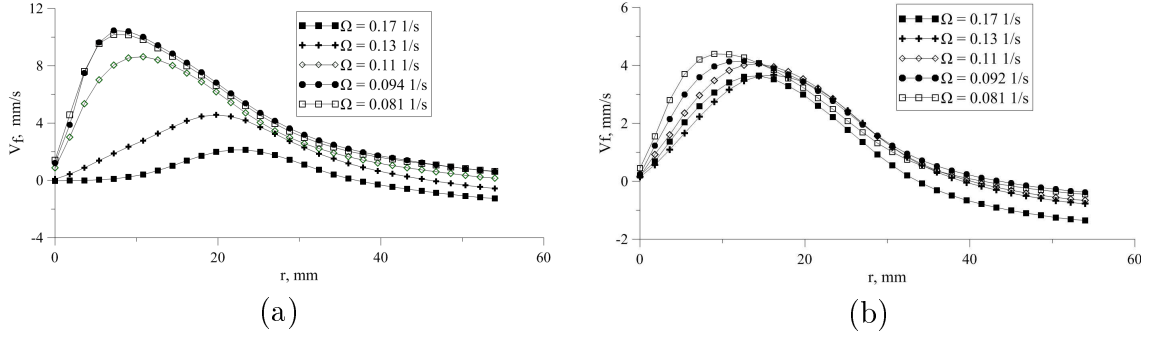


Figure 3: Mean azimuthal velocity profiles for height $z = 15\text{mm}$ for regimes with different rotation rates and fixed heat power $P = 17\text{wt}$: a - PMS-5, b - PMS-10

measurements for fluids with substantially different values of kinematic viscosity for fixed values of heat flux and rotation rate. It means that we consider the rotating layer of fluid with constant energy source and study what would happen with the cyclonic vortex with variation of the physical properties of the fluid.

In (Fig. 4) mean vector fields at $z = 15\text{ mm}$ for the fixed value of heating and rotating rate and for fluid with different viscosity are presented. Decrease of kinematic viscosity leads to the remarkable increase of cyclonic vortex intensity. The structure of vortex is also changed. We believe that this result might be very important because spatial or time dependence of turbulent viscosity in the atmospheric flows may lead to the strong variation of the magnitude of the wind velocity and spatial inhomogeneity of temperature and velocity fields.

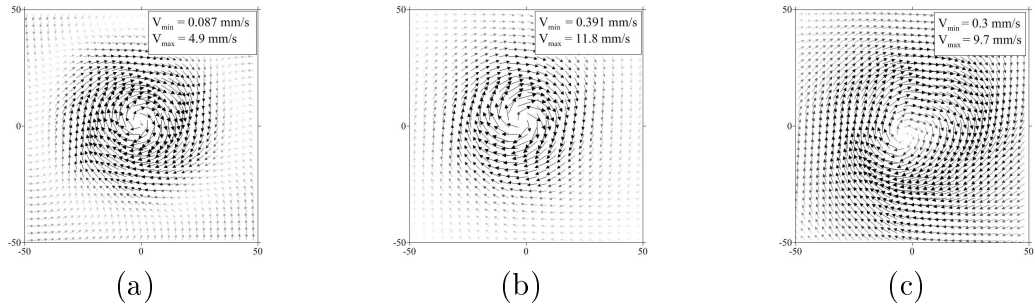


Figure 4: Mean vector velocity fields at $z = 15\text{ mm}$, heat power $P = 17\text{ Wt}$, $\Omega = 0.081\text{s}^{-1}$: a - PMS-10, b - PMS-5, c - PMS-3

Along with the experiment a numerical simulation in a similar geometry was performed. For the numerical simulation we used the CFD package Flow Vision. The fluid is assumed to be Newtonian and the flow is considered to be incompressible and laminar. The numerical finite volume code is used to solve the Boussinesq equations for thermal convection. Impermeable and no-slip velocity conditions are applied at the side wall and bottom. The upper boundary was stress-free. The bottom has a localized heat source in the central part defined through a heat flux and the diameter of the heating area was fixed at 100 mm . All numerical runs were done in 3D and the integration domain was a cylindrical cavity, equivalent to the one in the laboratory experiments. Silicon oil PMS-3 was used as a working fluid. The depth of the layer was 3 cm . The spatial resolution was 0.5 mm over the heat area in all

directions. At the periphery, the spatial resolution was decreased up to 1 mm in order to save computational costs. 1 mm in all directions.

The structure of the steady-state radial and azimuthal flows (in a rotating frame) for different values of heat flux and rotating rate are shown in Fig. 5. Positive (negative) values of velocity describe convergent and cyclonic (divergent and anticyclonic) motion respectively. To verify the numerical results, the vertical profiles of the mean radial velocity in the place of their maximum (Fig. 6) were compared. One can see that for regimes are shown below the mean velocity profiles have a very good quantitative agreement.

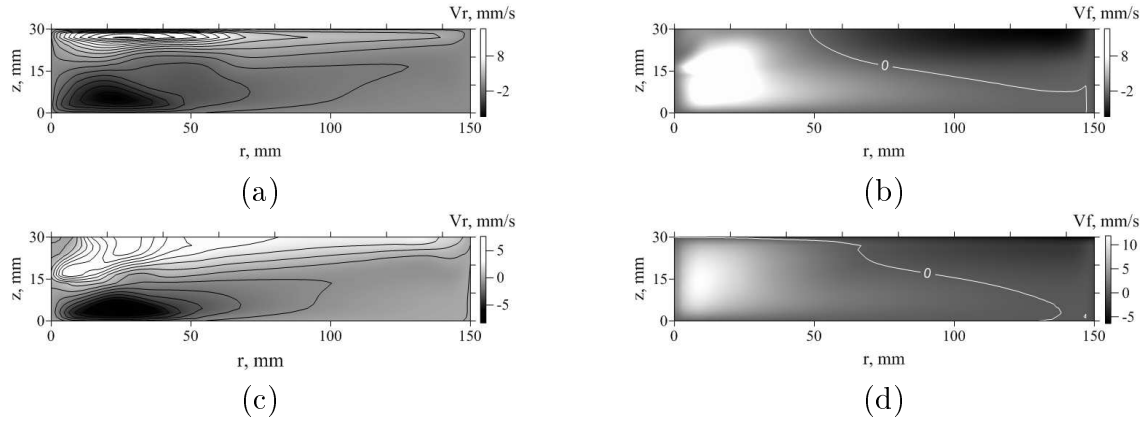


Figure 5: Mean radial (a, c) and azimuthal (b, d) velocity fields obtained from Flow Vision (PMS-3): a, b - $P = 26 \text{ Wt}$, $\Omega = 0.081 \text{ s}^{-1}$, c, d - $P = 38 \text{ Wt}$, $\Omega = 0.041 \text{ s}^{-1}$

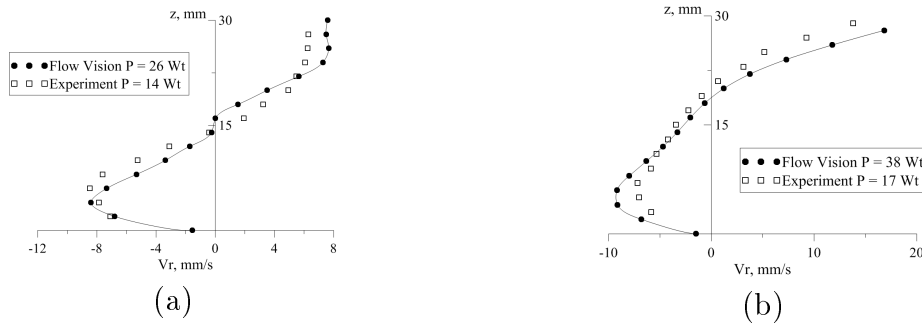


Figure 6: Mean radial velocity profiles (PMS-3): a - $P = 14 \text{ Wt}$, $\Omega = 0.081 \text{ s}^{-1}$, b - $P = 17 \text{ Wt}$, $\Omega = 0.041 \text{ s}^{-1}$

The significant advantage of the numerical simulation is that it gives full information about the 3D distribution of the different flow characteristics, which is hardly achievable experimentally. Instantaneous temperature and velocity fields give us a better understanding of the formation and evolution of the flow. Here instantaneous and mean vector velocity (Fig. 7) fields over a heat source at the height $z = 15 \text{ mm}$ are presented. One can see that instantaneous and mean velocity fields greatly differ. In this regime cyclonic vortex becomes unstable and start to precess around the center of the vessel. This precession leads to expansion of the vortex on the mean velocity field and to displacement of the azimuthal velocity maximum at the experimental profiles.

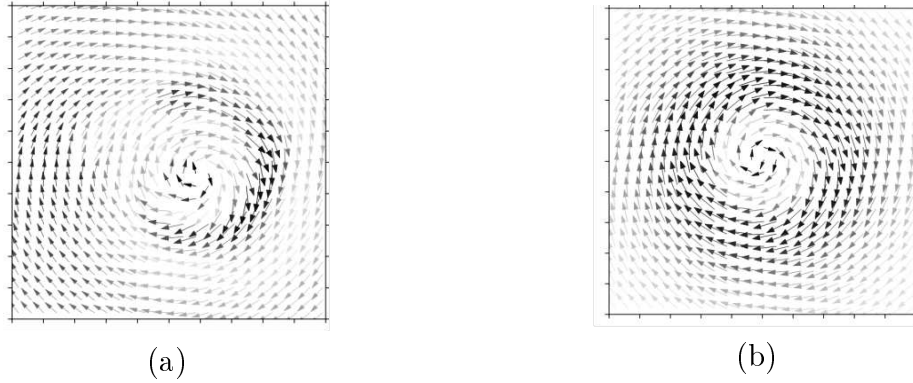


Figure 7: Instantaneous - a and mean - b vector velocity field at $z = 15$ mm, $P = 14$ Wt, $\Omega = 0.081s^{-1}$, PMS-3

Acknowledgements

The financial support of grant RFBR No.14-01-96011 and No.16-31-00150 is gratefully acknowledged.

References

- [1] I. Morrison, S. Businger, F. Marks et al. An Observational Case for the Prevalence of Roll Vortices in the Hurricane Boundary Layer. *Journal of Atmospheric Sciences*, 2005.
- [2] Bogatyrev G.P Excitation of a cyclonic vortex or a laboratory model for a tropical cyclone. *Pisma Zh.Eksp. Teor. Fiz.*, 1990
- [3] Bogatyrev G.P Physical model of the rotation of a tropical cyclone. *Pisma Zh.Eksp. Teor. Fiz.*, 1996
- [4] Bogatyrev G.P., Kolesnichenko I.V., Levina G.V. and Sukhanovsky A.N. Laboratory model of generation of a large-scale spiral vortex in a convectively unstable rotating fluid. *Izvestiya Atmospheric and Oceanic Physics*, 2006
- [5] Sukhanovskii A., Evgrafova A., and Popova, E. Horizontal rolls over localized heat source in a cylindrical layer. *J. Physica D*, 2015
- [6] Sukhanovskii A., Evgrafova A., and Popova, E. Laboratory study of a steady-state convective cyclonic vortex. *Q. J. R. Meteorol. Soc.*, 2016(submitted)

Anna Evgrafova, Perm, Russian Federation

Andrey Sukhanovskii, Perm, Russian Federation

Elena Popova, Perm, Russian Federation

Invariant calculations in beam physics: dynamics on semi-direct products and CWT

Antonina N. Fedorova, Michael G. Zeitlin
zeitlin@math.ipme.ru, anton@math.ipme.ru

Abstract

We outline, according to Marsden's approach, the semi-direct product structure that allows to consider, from the general point of view, all kinematics groups such as Euclidean, Galilei, Poincare. Then we consider the proper invariant Lie-Poisson equations and present the manifestation of the semi-product structure of (kinematic) symmetry group on the dynamical level. After that, we consider the Lagrangian theory related to the semi-product structure and the explicit form of the variation principle and the corresponding (semi-direct) Euler-Poincare equations. All that provides the needful invariant background for CWT and the corresponding analytical technique that allows to consider covariant wavelet analysis. The proper orbit technique allows to construct different types of invariant wavelet bases which are very useful in applications to a number of the beam dynamics problems.

1 Introduction

In this paper, we briefly consider the dynamical consequences of some set of general invariant approaches based on investigation of a structure of the underlying hidden symmetry, which is the key property of any reasonable complex dynamical problem. Our main examples are located in the areas of accelerator/beam/plasma/quantum physics [1].

First of all, we are interested in covariance properties [2] regarding to relativity (kinematical) groups and our main instrument here is the so-called Continuous Wavelet Transform (CWT) as a method for investigation of dynamical properties [3].

In Section 2.1, we explain, according to very productive Marsden's approach [2], the semi-direct product structure, which allows us to consider all kinematical groups such as Euclidean, Galilei or Poincare from the general point of view in unified framework.

Then, in Section 2.2 we move to the dynamical consequences of such an algebraic description: we consider proper (invariant) Lie-Poisson equations and obtain the manifestation of semi-product structure of (kinematic) symmetry group on the dynamical level. So, as usually, the correct description of dynamics is a consequence of the correct understanding of the underlying symmetry of a concrete problem under

investigation. Strictly speaking, we consider right equations on representations of proper orbits generated by actions of hidden symmetries we like to take into account. In Section 2.3, we consider the technique for simplifications of dynamics related to semi-product structure by using reduction to the corresponding orbit structure. As a result, we have the simplified Lie-Poisson equations in the momentum map approach.

In Section 2.4 we move from the Lie-Poisson side to the Lagrangian one: we present the Lagrangian theory based on semi-product structure, the explicit form of the variation principle and the corresponding dual (semi-direct) Euler-Poicare equations [2].

Section 3 is devoted to Continuous Wavelet Transform [3] as a natural and high-power analytical invariant instrument for analysis on orbits and the corresponding analytical technique allows to consider covariant wavelet analysis, very important part of Nolinear (non-abelian) Local Harmonic Analysis [4] which is a very useful non-commutative and localized generalization of orthodox (abelian) Fourier Analysis.

In concluding Section 4, we consider the corresponding orbit technique for constructing different types of invariant wavelet bases in the important for us affine (Galilei) group with the semi-product structure. Such a technique, considered here, together with the related ones presented in the companion paper in this Volume [5], based on analysis of the underlying symplectic structure, was applied by authors to a number of physical problems of beam physics, accelerator physics, plasma physics and quantum physics. In this short exposition we constrain ourselves by ideological paradigm only. All details, constructions, and results can be found in [6]-[28].

2 Semi-direct Product Structures and Momentum Maps: From Lie-Poisson to Euler-Poincare

2.1 Semi-direct Product

Relativity groups such as Euclidean, Galilei or Poincare groups are the particular cases of semi-direct product construction, which is very useful and simple general construction in the group theory [2]. We may consider as a basic example the Euclidean group $SE(3) = SO(3) \bowtie \mathbf{R}^3$, the semi-direct product of rotations and translations. In general case we have $S = G \bowtie V$, where group G (Lie group or automorphisms group) acts on a vector space V and on its dual V^* . Let V be a vector space and G is the Lie group, which acts on the left by linear maps on V (G also acts on the left on its dual space V^*). The semi-direct product $S = G \bowtie V$ is the Cartesian product $S = G \times V$ with group multiplication

$$(g_1, v_1)(g_2, v_2) = (g_1g_2, v_1 + g_1v_2), \tag{1}$$

where the action of $g \in G$ on $v \in V$ is denoted as gv . Of course, we can consider the corresponding definitions both in case of the right actions and in case, when G is a group of automorphisms of the vector space V . As we shall explain below both cases, Lie groups and automorphisms groups, are important for us.

So, the Lie algebra of S is the semi-direct product Lie algebra, $s = \mathcal{G} \bowtie V$ with brackets

$$[(\xi_1, v_1), (\xi_2, v_2)] = ([\xi_1, \xi_2], \xi_1 v_2 - \xi_2 v_1), \quad (2)$$

where the induced action of \mathcal{G} by concatenation is denoted as $\xi_1 v_2$. Also we need expressions for adjoint and coadjoint actions for semi-direct products. Let $(g, v) \in S = G \times V$, $(\xi, u) \in s = \mathcal{G} \times V$, $(\mu, a) \in s^* = \mathcal{G}^* \times V^*$, $g\xi = Ad_g \xi$, $g\mu = Ad_{g^{-1}}^* \mu$, ga denotes the induced left action of g on a (the left action of G on V induces a left action on V^* – the inverse of the transpose of the action on V), $\rho_v : \mathcal{G} \rightarrow V$ is a linear map given by $\rho_v(\xi) = \xi v$, $\rho_v^* : V^* \rightarrow \mathcal{G}^*$ is its dual. Then these actions are given by simple concatenation:

$$\begin{aligned} (g, v)(\xi, u) &= (g\xi, gu - (g\xi)v), \\ (g, v)(\mu, a) &= (g\mu + \rho_v^*(ga), ga) \end{aligned} \quad (3)$$

Below we use the following notation: $\rho_v^* a = v \diamond a \in \mathcal{G}^*$ for $a \in V^*$, which is a bilinear operation in v and a . So, we have the coadjoint action:

$$(g, v)(\mu, a) = (g\mu + v \diamond (ga), ga). \quad (4)$$

Using concatenation notation for Lie algebra actions we have alternative definition of $v \diamond a \in \mathcal{G}^*$. For all $v \in V$, $a \in V^*$, $\eta \in \mathcal{G}$ we have

$$\langle \eta a, v \rangle = - \langle v \diamond a, \eta \rangle \quad (5)$$

2.2 The Lie-Poisson Equations and Semi-product Structure

Below we consider the manifestation of semi-product structure of symmetry group on dynamical level [2]. Let F, G be real valued functions on the dual space \mathcal{G}^* , $\mu \in \mathcal{G}^*$. Functional derivative of F at μ is the unique element $\delta F / \delta \mu \in \mathcal{G}$:

$$\lim_{\epsilon \rightarrow 0} \frac{1}{\epsilon} [F(\mu + \epsilon \delta \mu) - F(\mu)] = \langle \delta \mu, \frac{\delta F}{\delta \mu} \rangle \quad (6)$$

for all $\delta \mu \in \mathcal{G}^*$, \langle, \rangle is pairing between \mathcal{G}^* and \mathcal{G} . Define the (\pm) Lie-Poisson brackets by [2]

$$\{F, G\}_{\pm}(\mu) = \pm \langle \mu, [\frac{\delta F}{\delta \mu}, \frac{\delta G}{\delta \mu}] \rangle \quad (7)$$

The Lie-Poisson equations, determined by

$$\dot{F} = \{F, H\} \quad (8)$$

read intrinsically

$$\dot{\mu} = \mp ad_{\partial H / \partial \mu}^* \mu. \quad (9)$$

For the left representation of G on $V \pm$ Lie-Poisson bracket of two functions $f, k : s^* \rightarrow \mathbf{R}$ is given by

$$\{f, k\}_{\pm}(\mu, a) = \pm \langle \mu, [\frac{\delta f}{\delta \mu}, \frac{\delta k}{\delta \mu}] \rangle \pm \langle a, \frac{\delta f}{\delta \mu} \frac{\delta k}{\delta a} - \frac{\delta k}{\delta \mu} \frac{\delta f}{\delta a} \rangle, \quad (10)$$

where $\delta f / \delta \mu \in \mathcal{G}$, $\delta f / \delta a \in V$ are the functional derivatives of f (6). The Hamiltonian vector field of $h : s^* \in \mathbf{R}$ has the expression

$$X_h(\mu, a) = \mp(ad_{\delta h / \delta \mu}^* \mu - \frac{\delta h}{\delta a} \diamond a, -\frac{\delta h}{\delta \mu} a). \quad (11)$$

Thus, Hamiltonian equations on the dual of a semi-direct product are [2]:

$$\begin{aligned} \dot{\mu} &= \mp ad_{\delta h / \delta \mu}^* \mu \pm \frac{\delta h}{\delta a} \diamond a \\ \dot{a} &= \pm \frac{\delta h}{\delta \mu} a \end{aligned} \quad (12)$$

So, we can see the explicit difference between Poisson brackets (7) and (10) and the equations of motion (9) and (12), which come from the semi-product structure.

2.3 Reduction of Dynamics on Semi-product

There is a technique for reducing dynamics that is associated with the geometry of semi-direct product reduction theorem[2]. Let us have a Hamiltonian on T^*G that is invariant under the isotropy G_{a_0} for $a_0 \in V^*$. The semi-direct product reduction theorem states that reduction of T^*G by G_{a_0} gives reduced spaces that are symplectically diffeomorphic to coadjoint orbits in the dual of the Lie algebra of the semi-direct product $(\mathcal{G} \bowtie V)^*$. If one reduces the semi-direct group product $S = G \bowtie V$ in two stages, first by V and then by G one recovers this semi-direct product reduction theorem. Thus, let $S = G \bowtie V$, choose $\sigma = (\mu, a) \in \mathcal{G}^* \times V^*$ and reduce T^*S by the action of S at σ giving the coadjoint orbit \mathcal{O}_σ through $\sigma \in S^*$. There is a symplectic diffeomorphism between \mathcal{O}_σ and the reduced space obtained by reducing T^*G by the subgroup G_a (the isotropy of G for its action on V^* at the point $a \in V^*$) at the point $\mu|_{\mathcal{G}_a}$, where \mathcal{G}_a is the Lie algebra of G_a .

Then we have the following procedure.

1. We start with a Hamiltonian H_{a_0} on T^*G that depends parametrically on a variable $a_0 \in V^*$.
2. The Hamiltonian regarded as a map: $T^*G \times V^* \rightarrow \mathbf{R}$ is assumed to be invariant on T^*G under the action of G on $T^*G \times V^*$.
3. The condition 2 is equivalent to the invariance of the function H defined on $T^*S = T^*G \times V \times V^*$ extended to be constant in the variable V under the action of the semi-direct product.
4. By the semi-direct product reduction theorem, the dynamics of H_{a_0} reduced by G_{a_0} , the isotropy group of a_0 , is symplectically equivalent to Lie-Poisson dynamics on $s^* = \mathcal{G}^* \times V^*$.

5. This Lie-Poisson dynamics is given by equations (12) for the function $h(\mu, a) = H(\alpha_g, g^{-1}a)$, where $\mu = g^{-1}\alpha_g$.

2.4 Lagrangian Theory, the Euler-Poincare Equations, Variational Approach on Semi-product

Now we consider according to [2] Lagrangian side of a theory. This approach is based on variational principles with symmetry and is not dependent on Hamiltonian formulation, although it is well-known that this purely Lagrangian formulation is equivalent to the Hamiltonian formulation on duals of semi-direct product (the corresponding Legendre transformation is a diffeomorphism).

We consider the case of the left representation and the left invariant Lagrangians (ℓ and L), which depend in addition on another parameter $a \in V^*$ (dynamical parameter), where V is representation space for the Lie group G and L has an invariance property related to both arguments. It should be noted that the resulting equations of motion, the Euler-Poincare equations, are not the Euler-Poincare equations for the semi-direct product Lie algebra $\mathcal{G} \bowtie V^*$ or $\mathcal{G} \bowtie V$.

So, we have the following:

1. There is a left presentation of Lie group G on the vector space V and G acts in the natural way on the left on $TG \times V^* : h(v_g, a) = (hv_g, ha)$.
2. The function $L : TG \times V^* \in \mathbf{R}$ is the left G -invariant.
3. Let $a_0 \in V^*$, Lagrangian $L_{a_0} : TG \rightarrow \mathbf{R}$, $L_{a_0}(v_g) = L(v_g, a_0)$. L_{a_0} is left invariant under the lift to TG of the left action of G_{a_0} on G , where G_{a_0} is the isotropy group of a_0 .
4. Left G -invariance of L permits us to define

$$\ell : \mathcal{G} \times V^* \rightarrow \mathbf{R} \tag{13}$$

by

$$\ell(g^{-1}v_g, g^{-1}a_0) = L(v_g, a_0). \tag{14}$$

This relation defines for any $\ell : \mathcal{G} \times V^* \rightarrow \mathbf{R}$ the left G -invariant function $L : TG \times V^* \rightarrow \mathbf{R}$.

5. For a curve $g(t) \in G$ let be

$$\xi(t) := g(t)^{-1}\dot{g}(t) \tag{15}$$

and define the curve $a(t)$ as the unique solution of the following linear differential equation with time dependent coefficients

$$\dot{a}(t) = -\xi(t)a(t), \tag{16}$$

with initial condition $a(0) = a_0$. The solution can be written as $a(t) = g(t)^{-1}a_0$.

Then we have four equivalent descriptions of the corresponding dynamics:

1. If a_0 is fixed then Hamilton's variational principle

$$\delta \int_{t_1}^{t_2} L_{a_0}(g(t), \dot{g}(t)) dt = 0 \quad (17)$$

holds for variations $\delta g(t)$ of $g(t)$ vanishing at the endpoints.

2. $g(t)$ satisfies the Euler-Lagrange equations for L_{a_0} on G .
3. The constrained variational principle

$$\delta \int_{t_1}^{t_2} \ell(\xi(t), a(t)) dt = 0 \quad (18)$$

holds on $\mathcal{G} \times V^*$, using variations of ξ and a of the form $\delta \xi = \dot{\eta} + [\xi, \eta]$, $\delta a = -\eta a$, where $\eta(t) \in \mathcal{G}$ vanishes at the endpoints.

4. The Euler-Poincare equations hold on $\mathcal{G} \times V^*$

$$\frac{d}{dt} \frac{\delta \ell}{\delta \xi} = a d_{\xi}^* \frac{\delta \ell}{\delta \xi} + \frac{\delta \ell}{\delta a} \diamond a \quad (19)$$

So, we may apply our wavelet methods either on the level of variational formulation (17) or on the level of Euler-Poincare equations (19).

3 Continuous Wavelet Transform

At this point, we need to take into account all features of the Hamiltonian or Lagrangian structures related with systems covered by (12) or (19). Therefore, we need to consider generalized (covariant) wavelets. It allows us to consider the corresponding invariant representations instead of standard and non-covariant ones, e.g., compactly supported wavelet decompositions [3].

In Nonlinear Local Harmonic Analysis the following three concepts are used now: 1). a square integrable representation U of a group G , 2). coherent states (CS) over G , 3). the wavelet transform associated to U . We consider now their unification [3], [4], [29], [30].

Let G be a locally compact group and U_a strongly continuous, irreducible, unitary representation of G on Hilbert space \mathcal{H} . Let H be a closed subgroup of G , $X = G/H$ with (quasi) invariant measure ν and $\sigma : X = G/H \rightarrow G$ is a Borel section in a principal bundle $G \rightarrow G/H$. Then we say that U is square integrable *mod*(H, σ) if there exists a non-zero vector $\eta \in \mathcal{H}$ such that

$$0 < \int_X | \langle U(\sigma(x))\eta | \Phi \rangle |^2 d\nu(x) = \langle \Phi | A_{\sigma} \Phi \rangle < \infty, \quad \forall \Phi \in \mathcal{H} \quad (20)$$

Given such a vector $\eta \in \mathcal{H}$ called admissible for (U, σ) we define the family of (covariant) coherent states or wavelets, indexed by points $x \in X$, as the orbit of η under G , though the representation U and the section σ [29], [30]:

$$S_{\sigma} = \eta_{\sigma(x)} = U(\sigma(x))\eta | x \in X \quad (21)$$

So, coherent states or wavelets are simply the elements of the orbit under U of a fixed vector η in representation space. We have the following fundamental properties:

1. Overcompleteness:

The set S_σ is total in $\mathcal{H} : (S_\sigma)^\perp = 0$

2. Resolution property:

the square integrability condition (20) may be represented as a resolution relation:

$$\int_X |\eta_\sigma(x)\rangle\langle\eta_\sigma(x)|d\nu(x) = A_\sigma, \quad (22)$$

where A_σ is a bounded, positive operator with a densely defined inverse. Define the linear map

$$W_\eta : \mathcal{H} \rightarrow L^2(X, d\nu), (W_\eta\Phi)(x) = \langle\eta_\sigma(x)|\Phi\rangle \quad (23)$$

Then the range H_η of W_η is complete with respect to the scalar product $\langle\Phi|\Psi\rangle_\eta = \langle\Phi|W_\eta A_\sigma^{-1} W_\eta^{-1}\Psi\rangle$ and W_η is unitary operator from \mathcal{H} onto \mathcal{H}_η . W_η is Continuous Wavelet Transform (CWT).

3. Reproducing kernel

The orthogonal projection from $L^2(X, d\nu)$ onto \mathcal{H}_η is an integral operator K_σ and H_η is a reproducing kernel Hilbert space of functions:

$$\Phi(x) = \int_X K_\sigma(x, y)\Phi(y)d\nu(y), \quad \forall\Phi \in \mathcal{H}_\eta. \quad (24)$$

The kernel is given explicitly by $K_\sigma(x, y) = \langle\eta_\sigma(x)|A_\sigma^{-1}\eta_\sigma(y)\rangle$, if $\eta_\sigma(y) \in D(A_\sigma^{-1})$, $\forall y \in X$. So, the function $\Phi \in L^2(X, d\nu)$ is a wavelet transform (WT) iff it satisfies this reproducing relation.

4. Reconstruction formula.

The WT W_η may be inverted on its range by the adjoint operator, $W_\eta^{-1} = W_\eta^*$ on \mathcal{H}_η to obtain for $\eta_\sigma(x) \in D(A_\sigma^{-1})$, $\forall x \in X$

$$W_\eta^{-1}\Phi = \int_X \Phi(x)A_\sigma^{-1}\eta_\sigma(x)d\nu(x), \quad \Phi \in \mathcal{H}_\eta. \quad (25)$$

This is inverse WT.

If A_σ^{-1} is bounded then S_σ is called a frame, if $A_\sigma = \lambda I$ then S_σ is called a tight frame. This two cases are generalization of a simple case, when S_σ is an (ortho)basis. The most simple cases of this construction are:

1. $H = \{e\}$. This is the standard construction of WT over a locally compact group. It should be noted that the square integrability of U is equivalent to U belonging to the discrete series. The most simple example is related to the affine $(ax + b)$ group and yields the usual one-dimensional wavelet analysis

$$[\pi(b, a)f](x) = \frac{1}{\sqrt{a}}f\left(\frac{x-b}{a}\right). \quad (26)$$

For $G = SIM(2) = \mathbf{R}^2 \bowtie (\mathbf{R}_*^+ \times SO(2))$, the similitude group of the plane, we have the corresponding two-dimensional wavelets.

2. $H = H_\eta$, the isotropy (up to a phase) subgroup of η : this is the case of the Gilmore-Perelomov CS. Some cases of group G are:

- a). Semisimple groups, such as $SU(N)$, $SU(N|M)$, $SU(p,q)$, $Sp(N, \mathbf{R})$.
- b). the Weyl-Heisenberg group G_{WH} which leads to the Gabor functions, i.e. canonical (oscillator)coherent states associated with windowed Fourier transform or Gabor transform [4], [5]:

$$[\pi(q, p, \varphi)f](x) = \exp(i\mu(\varphi - p(x - q)))f(x - q) \quad (27)$$

In this case H is the center of G_{WH} . In both cases time-frequency plane corresponds to the phase space of group representation.

c). The similitude group $SIM(n)$ of $\mathbf{R}^n (n \geq 3)$: for $H = SO(n - 1)$ we have the axisymmetric n -dimensional wavelets.

d). Also we have the case of bigger group, containing both affine and Weyl-Heisenberg group, which interpolate between affine wavelet analysis and windowed Fourier analysis: affine Weyl-Heisenberg group [30].

e). Relativity groups. In a nonrelativistic setup, the natural kinematical group is the (extended) Galilei group. Also we may add independent space and time dilations and obtain affine Galilei group. If we restrict the dilations by the relation $a_0 = a^2$, where a_0, a are the time and space dilation we obtain the Galilei-Schrödinger group, invariance group of both Schrödinger and heat equations. We consider these examples in the next section. In the same way we may consider as kinematical group the Poincare group. When $a_0 = a$ we have affine Poincare or Weyl-Poincare group. Some useful generalization of that affinization construction we consider for the case of hidden metaplectic structure in companion paper [5].

But the usual representation is not square-integrable and must be modified: restriction of the representation to a suitable quotient space of the group (the associated phase space in our case) restores square - integrability: $G \longrightarrow$ homogeneous space. Also, we can consider much more general approach which allows to describe generalized wavelets corresponding to more general groups and representations [29], [30].

Our final goal is the application of these results to Hamiltonian/Lie-Poissonian background and as a consequence we need to take into account symplectic/Poissonian nature of our dynamical problems [5]. So, the symplectic and wavelet structures must be consistent (like we have in the symplectic or Lie-Poisson integrator theory). We hope to use the point of view of geometric quantization theory (orbit method) instead of orthodox harmonic analysis, so it seems that we can consider the points (a)-(e) above in the unified framework.

4 Invariant Bases for Solutions

We consider an important particular case of affine relativity group (relativity group combined with dilations) — affine Galilei group in n -dimensions. So, we have combination of Galilei group with independent space and time dilations: $G_{aff} = G_m \bowtie D_2$,

where $D_2 = (\mathbf{R}_*^+)^2 \simeq \mathbf{R}^2$, G_m is extended Galilei group corresponding to mass parameter $m > 0$ (G_{aff} is noncentral extension of $G \bowtie D_2$ by \mathbf{R} , where G is usual Galilei group). Generic element of G_{aff} is $g = (\Phi, b_0, b; v; R, a_0, a)$, where $\Phi \in \mathbf{R}$ is the extension parameter in G_m , $b_0 \in \mathbf{R}$, $b \in \mathbf{R}^n$ are the time and space translations, $v \in \mathbf{R}^n$ is the boost parameter, $R \in SO(n)$ is a rotation and $a_0, a \in \mathbf{R}_*^+$ are time and space dilations. The actions of g on space-time is then $x \mapsto aRx + a_0vt + b$, $t \mapsto a_0t + b_0$, where $x = (x_1, x_2, \dots, x_n)$. The group law is [4], [29], [30]:

$$gg' = \left(\Phi + \frac{a^2}{a_0}\Phi' + avRb' + \frac{1}{2}a_0v^2b'_0, b_0 + a_0b'_0, b + aRb' + a_0vb'_0; \right. \\ \left. v + \frac{a}{a_0}Rv', RR'; a_a a'_0, aa' \right) \quad (28)$$

It should be noted that D_2 acts nontrivially on G_m . Space-time wavelets associated to G_{aff} corresponds to unitary irreducible representation of spin zero. It may be obtained via orbit method. The Hilbert space is $\mathcal{H} = L^2(\mathbf{R}^n \times \mathbf{R}, dkd\omega)$, $k = (k_1, \dots, k_n)$, where $\mathbf{R}^n \times \mathbf{R}$ may be identified with usual Minkowski space and we have for representation:

$$(U(g)\Psi)(k, \omega) = \sqrt{a_0 a^n} \exp i(m\Phi + kb - \omega b_0) \Psi(k', \omega'), \quad (29)$$

with $k' = aR^{-1}(k + mv)$, $\omega' = a_0(\omega - kv - \frac{1}{2}mv^2)$, $m' = (a^2/a_0)m$. Mass m is a coordinate in the dual of the Lie algebra and these relations are a part of coadjoint action of G_{aff} . This representation is unitary and irreducible but not square integrable. So, we need to consider reduction to the corresponding quotients $X = G/H$. We consider the case in which $H = \{\text{phase changes } \Phi \text{ and space dilations } a\}$. Then the space $X = G/H$ is parametrized by points $\bar{x} = (b_0, b; v; R; a_0)$. There is a dense set of vectors $\eta \in \mathcal{H}$ admissible mod(H, σ_β), where σ_β is the corresponding section. We have a two-parameter family of functions β (dilations): $\beta(\bar{x}) = (\mu_0 + \lambda_0 a_0)^{1/2}$, $\lambda_0, \mu_0 \in \mathbf{R}$. Then any admissible vector η generates a tight frame of Galilean wavelets [4], [29]:

$$\eta_{\beta(\bar{x})}(k, \omega) = \sqrt{a_0(\mu_0 + \lambda_0 a_0)^{n/2}} e^{i(kb - \omega b_0)} \eta(k', \omega'), \quad (30)$$

with $k' = (\mu_0 + \lambda_0 a)^{1/2} R^{-1}(k + mv)$, $\omega' = a_0(\omega - kv - mv^2/2)$. The simplest examples of admissible vectors (corresponding to usual Galilei case) are Gaussian vector: $\eta(k) \sim \exp(-k^2/2mu)$ and binomial vector: $\eta(k) \sim (1 + k^2/2mu)^{-\alpha/2}$, $\alpha > 1/2$, where u is a kind of internal energy. When we impose the relation $a_0 = a^2$ then we have the restriction to the Galilei-Schrödinger group $G_s = G_m \bowtie D_s$, where D_s is the one-dimensional subgroup of D_2 . G_s is a natural invariance group of both the Schrödinger equation and the heat equation. The restriction to G_s of the representation (29) splits into the direct sum of two irreducible ones $U = U_+ \oplus U_-$ corresponding to the decomposition $L^2(\mathbf{R}^n \times \mathbf{R}, dkd\omega) = \mathcal{H}_+ \oplus \mathcal{H}_-$, where

$$\mathcal{H}_\pm = L^2(D_\pm, dkd\omega) \\ = \{\psi \in L^2(\mathbf{R}^n \times \mathbf{R}, dkd\omega), \quad \psi(k, \omega) = 0 \quad \text{for} \quad \omega + k^2/2m = 0\} \quad (31)$$

These two subspaces are the analogues of usual Hardy spaces on \mathbf{R} , i.e. the subspaces of (anti)progressive wavelets (see also [5]). The two representation U_\pm are square

integrable modulo the center. There is a dense set of admissible vectors η , and each of them generates a set of CS of Gilmore-Perelomov type. Typical wavelets of this kind are [4], [29]:

the Schrödinger-Marr wavelet:

$$\eta(x, t) = (i\partial_t + \frac{\Delta}{2m})e^{-(x^2+t^2)/2} \quad (32)$$

the Schrödinger-Cauchy wavelet:

$$\psi(x, t) = (i\partial_t + \frac{\Delta}{2m}) \frac{1}{(t+i) \prod_{j=1}^n (x_j + i)} \quad (33)$$

So, in the same way we can construct invariant bases with explicit manifestation of the underlying symmetry to solve Hamiltonian (12) or Lagrangian (19) type of background equations.

References

- [1] A. H. Boozer, Rev. Mod. Phys., 76, 1071 (2004); R. C. Davidson and H. Qin, Physics of Intense Charged Particle Beams in High Energy Accelerators (World Scientific, Singapore, 2001); R. Balescu, Equilibrium and Nonequilibrium Statistical Mechanics, (Wiley, New York, 1975); Dragt, A.J., Lectures on Nonlinear Dynamics, CTP, 1996.
- [2] J. E. Marsden, Park City Lectures on Mechanics, Dynamics and Symmetry, CALTECH, 1998.
- [3] Y. Meyer, Wavelets and Operators (Cambridge Univ. Press, 1990); G. Beylkin, R. Coifman, V. Rokhlin, Fast Wavelet transform and Numerical Algorithms, Comm. Pure Applid Math, 44, 141-183, 1991; F. Auger e.a., *Time-Frequency Toolbox* (CNRS, 1996); D. Donoho, *WaveLab* (Stanford, 2000).
- [4] G. B. Folland, 'Harmonic Analysis in Phase Space', Princeton, 1989.
- [5] A. N. Fedorova and M. G. Zeitlin, Symplectic framework, discrete variational approach and Harten's multiresolution approach in beam dynamics, This Volume.
- [6] A. N. Fedorova, M. G. Zeitlin, 'Wavelets in Optimization and Approximations', *Math. and Comp. in Simulation*, **46**, 527-534 (1998).
- [7] A. N. Fedorova, M. G. Zeitlin, 'Wavelet Approach to Polynomial Mechanical Problems', *New Applications of Nonlinear and Chaotic Dynamics in Mechanics*, Kluwer, 101-108, 1998.
- [8] A. N. Fedorova, M. G. Zeitlin, 'Wavelet Approach to Mechanical Problems. Symplectic Group, Symplectic Topology and Symplectic Scales', *New Applications of Nonlinear and Chaotic Dynamics in Mechanics*, Kluwer, 31-40, 1998.

-
- [9] A. N. Fedorova, M. G. Zeitlin, 'Nonlinear Dynamics of Accelerator via Wavelet Approach', AIP Conf. Proc., vol. 405, ed. Z. Parsa, 87-102, 1997, Los Alamos preprint, physics/9710035.
- [10] A. N. Fedorova and M. G. Zeitlin, Quasiclassical Calculations for Wigner Functions via Multiresolution, Localized Coherent Structures and Patterns Formation in Collective Models of Beam Motion, in *Quantum Aspects of Beam Physics*, Ed. P. Chen (World Scientific, Singapore, 2002) pp. 527-538, 539-550; arXiv: physics/0101006; physics/0101007.
- [11] A. N. Fedorova and M. G. Zeitlin, BBGKY Dynamics: from Localization to Pattern Formation, in *Progress in Nonequilibrium Green's Functions II*, Ed. M. Bonitz, (World Scientific, 2003) pp. 481-492; arXiv: physics/0212066.
- [12] A. N. Fedorova and M. G. Zeitlin, Pattern Formation in Wigner-like Equations via Multiresolution, in *Quantum Aspects of Beam Physics*, Eds. Pisin Chen, K. Reil (World Scientific, 2004) pp. 22-35; Preprint SLAC-R-630; arXiv: quant-ph/0306197.
- [13] A. N. Fedorova and M. G. Zeitlin, Localization and pattern formation in Wigner representation via multiresolution, *Nuclear Inst. and Methods in Physics Research, A*, **502A/2-3**, pp. 657 - 659, 2003; arXiv: quant-ph/0212166.
- [14] A. N. Fedorova and M. G. Zeitlin, Fast Calculations in Nonlinear Collective Models of Beam/Plasma Physics, *Nuclear Inst. and Methods in Physics Research, A*, **502/2-3**, pp. 660 - 662, 2003; arXiv: physics/0212115.
- [15] A. N. Fedorova and M. G. Zeitlin, Classical and quantum ensembles via multiresolution: I-BBGKY hierarchy; Classical and quantum ensembles via multiresolution. II. Wigner ensembles; *Nucl. Instr. Methods Physics Res.*, **534A** (2004)309-313; 314-318; arXiv: quant-ph/0406009; quant-ph/0406010.
- [16] A. N. Fedorova and M. G. Zeitlin, Localization and Pattern Formation in Quantum Physics. I. Phenomena of Localization, in *The Nature of Light: What is a Photon? SPIE*, vol.**5866**, pp. 245-256, 2005; arXiv: quant-ph/0505114;
- [17] A. N. Fedorova and M. G. Zeitlin, Localization and Pattern Formation in Quantum Physics. II. Waveletons in Quantum Ensembles, in *The Nature of Light: What is a Photon?SPIE*, vol. **5866**, pp. 257-268, 2005; arXiv: quant-ph/0505115.
- [18] A. N. Fedorova and M. G. Zeitlin, Pattern Formation in Quantum Ensembles, *Intl. J. Mod. Physics B***20**(2006)1570-1592; arXiv: 0711.0724.
- [19] A. N. Fedorova and M. G. Zeitlin, Patterns in Wigner-Weyl approach, Fusion modeling in plasma physics: Vlasov-like systems, *Proceedings in Applied Mathematics and Mechanics (PAMM)*, Volume **6**, Issue 1, p. 625, p. 627, Wiley InterScience, 2006; arXiv:1012.4971, arXiv:1012.4965.

-
- [20] A. N. Fedorova and M. G. Zeitlin, Localization and Fusion Modeling in Plasma Physics. Part I: Math Framework for Non-Equilibrium Hierarchies, pp.61-86, in *Current Trends in International Fusion Research*, Ed. E. Panarella, R. Raman, National Research Council (NRC) Research Press, Ottawa, Ontario, Canada, 2009; arXiv: physics/0603167.
- [21] A. N. Fedorova and M. G. Zeitlin, Localization and Fusion Modeling in Plasma Physics. Part II: Vlasov-like Systems. Important Reductions, pp.87-100, in *Current Trends in International Fusion Research*, Ed. E. Panarella, R. Raman, National Research Council (NRC) Research Press, Ottawa, Ontario, Canada, 2009; arXiv: physics/0603169.
- [22] A. N. Fedorova and M. G. Zeitlin, Fusion State in Plasma as a Waveleton (Localized (Meta)-Stable Pattern), p. 272, in *AIP Conference Proceedings*, Volume **1154**, Issue 1, *Current Trends in International Fusion Research*, Ed. E. Panarella, R. Raman, AIP, 2009, doi:10.1063/1.3204585.
- [23] A. N. Fedorova and M. G. Zeitlin, Exact Multiscale Representations for (Non)-Equilibrium Dynamics of Plasma, p.291, in *AIP Conference Proceedings*, Volume **1154**, Issue 1, *Current Trends in International Fusion Research*, Ed. E. Panarella, R. Raman, AIP, 2009, doi:10.1063/1.3204592.
- [24] A. N. Fedorova and M. G. Zeitlin, Fusion Modeling in Vlasov-Like Models, *Journal Plasma Fusion Res. Series*, Vol. **8**, pp. 126-131, 2009.
- [25] A. N. Fedorova and M. G. Zeitlin, Quantum points/patterns, Part 2: from quantum points to quantum patterns via multiresolution, SPIE, vol. 8121, 81210K (2011), doi:10.1117/12.893537; arXiv:1109.5042.
- [26] A. N. Fedorova and M. G. Zeitlin, Quantum points/patterns, Part 1. From geometrical points to quantum points in sheaf framework , SPIE, vol. 8121, 81210J (2011), doi:10.1117/12.893502; arXiv:1109.5035.
- [27] A. N. Fedorova and M. G. Zeitlin, En route to fusion: confinement state as a waveleton, *Journal of Physics CS*, vol. 490, 012202, 2014, doi:10.1088/1742-6596/490/1/012202.
- [28] A. N. Fedorova and M. G. Zeitlin, a list of papers/preprints (including links to arXiv) can be found on web sites below.
- [29] J. -P. Antoine, UCL, 96-08, 95-02; C. Kalisa, B. Torresani, CPT-92 P.2811 Marseille, 1992.
- [30] T. Kawazoe, *Proc. Japan Acad.* **71** Ser. A, 1995, p. 154; P. G. Lemarie, *Proc. Int. Math. Congr., Satellite Symp.*, 1991, p. 154.
- Antonina N. Fedorova, Michael G. Zeitlin*
Mathematical Methods in Mechanics Group, IPME RAS, V.O. Bolshoj pr., 61, 199178, St. Petersburg, Russia
<http://www.ipme.ru/zeitlin.html>, <http://mp.ipme.ru/zeitlin.html>

Symplectic framework, discrete variational approach and Harten's multiresolution scheme in beam dynamics

Antonina N. Fedorova, Michael G. Zeitlin
zeitlin@math.ipme.ru, anton@math.ipme.ru

Abstract

We consider general symplectic set-up which provides common framework for a class of problems related to the (quasi)classical description of nonlinear beam dynamics: metaplectic structure, Segal-Bargmann representation, orbital theory. All that allows to unify different important and needful accessories of any reasonable dynamical approach: (Melnikov) perturbations, quasiclassics, Floer loops, symplectic/wavelet scales. After that, we consider the applications of discrete wavelet analysis technique (Harten's multiresolution calculus for maps) to the maps which arise as the discretization of continuous invariant nonlinear polynomial problems (Veselov-Marsden's approach). Our main point is a generalization of wavelet analysis which can be applied for both discrete and continuous cases. It provides explicit multiresolution decomposition for solutions of discrete problems which are the correct discretizations of the corresponding continuous cases.

1 Introduction

In this paper, we consider hidden dynamical symmetry as a key generic feature instead of kinematical one presented in the companion paper in this Volume [1]. In Section 2, according to the orbit method in geometric quantization theory background, we construct the symplectic and Poisson structures [2] associated with generalized representations and orbital theory [3], [4] by using metaplectic structure. We apply such an approach to analysis of Melnikov functions in the theory of homoclinic chaos in perturbed Hamiltonian systems [5] in Section 3 and for calculation of the Arnold–Weinstein curves (closed loops) in the Floer variational approach [6] in Section 4. In Sections 5 and 6, we sketched out possible applications of very useful fast wavelet transform technique [4] for analysis of symplectic scale of spaces [7], [8] and for quasiclassical Wigner-Weyl evolution dynamics [2], [3]. This method gives maximally sparse representation of the (differential) operator that allows, at least in principle, to calculate very fast the contributions from each level of resolution of the whole tower of hidden scales. Section 7 is divided in two parts devoted to

very useful scheme(s) of discretization. In Subsection 7.1, according to the Marsden-Veselov approach, we consider symplectic and Lagrangian background for the case of discretization of flows by the corresponding maps [9] and in Subsection 7.2, we present the construction of the corresponding solutions by applications of the multi-scale approach of A. Harten [10] based on generalization of multiresolution analysis for the case of maps. "All that jazz" considered here, was applied by the authors to a number of physical problems of beam physics, accelerator physics, plasma physics, and quantum physics. In this short exposition, we constrain ourselves by ideological paradigms only. All details, constructions, and results can be found in [11]-[33].

2 Symplectic Structure, Metaplectic Group, Representations

Let $Sp(n)$ be symplectic group, $Mp(n)$ be its unique two-fold covering – metaplectic group [2], [3]. Let V be a symplectic vector space with symplectic form (\cdot, \cdot) , then $R \oplus V$ is nilpotent Lie algebra - Heisenberg algebra:

$$[R, V] = 0, \quad [v, w] = (v, w) \in R, \quad [V, V] = R.$$

$Sp(V)$ is a group of automorphisms of Heisenberg algebra.

Let N be a group with Lie algebra $R \oplus V$, i.e. Heisenberg group. By Stone–von Neumann theorem Heisenberg group has unique irreducible unitary representation in which $1 \mapsto i$. Let us also consider the projective representation of symplectic group $Sp(V)$: $U_{g_1}U_{g_2} = c(g_1, g_2) \cdot U_{g_1g_2}$, where c is a map: $Sp(V) \times Sp(V) \rightarrow S^1$, i.e. c is S^1 -cocycle.

This representation is unitary representation of universal covering, i.e. metaplectic group $Mp(V)$. We give this representation without Stone-von Neumann theorem. Consider a new group $F = N' \rtimes Mp(V)$, \rtimes is semidirect product (we consider instead of $N = R \oplus V$ the $N' = S^1 \times V$, $S^1 = (R/2\pi Z)$). Let V^* be dual to V , $G(V^*)$ be automorphism group of V^* . Then F is subgroup of $G(V^*)$, which consists of elements, which acts on V^* by affine transformations.

This is the key point!

Let $q_1, \dots, q_n; p_1, \dots, p_n$ be symplectic basis in V , $\alpha = pdq = \sum p_i dq_i$ and $d\alpha$ be symplectic form on V^* . Let M be fixed affine polarization, then for $a \in F$ the map $a \mapsto \Theta_a$ gives unitary representation of G : $\Theta_a : H(M) \rightarrow H(M)$.

Explicitly we have for representation of N on $H(M)$:

$$(\Theta_q f)^*(x) = e^{-iqx} f(x), \quad \Theta_p f(x) = f(x - p)$$

The representation of N on $H(M)$ is irreducible. Let A_q, A_p be infinitesimal operators of this representation

$$A_q = \lim_{t \rightarrow 0} \frac{1}{t} [\Theta_{-tq} - I], \quad A_p = \lim_{t \rightarrow 0} \frac{1}{t} [\Theta_{-tp} - I],$$

$$\text{then} \quad A_q f(x) = i(qx)f(x), \quad A_p f(x) = \sum p_j \frac{\partial f}{\partial x_j}(x)$$

Now we give the representation of infinitesimal basic elements. Lie algebra of the group F is the algebra of all (nonhomogeneous) quadratic polynomials of (p,q) relatively Poisson bracket (PB). The basis of this algebra consists of elements $1, q_1, \dots, q_n, p_1, \dots, p_n, q_i q_j, q_i p_j, p_i p_j, \quad i, j = 1, \dots, n, \quad i \leq j,$

$$PB \text{ is } \{f, g\} = \sum \frac{\partial f}{\partial p_j} \frac{\partial g}{\partial q_i} - \frac{\partial f}{\partial q_i} \frac{\partial g}{\partial p_i} \quad \text{and} \quad \{1, g\} = 0 \quad \text{for all } g,$$

$$\{p_i, q_j\} = \delta_{ij}, \quad \{p_i q_j, q_k\} = \delta_{ik} q_j, \quad \{p_i q_j, p_k\} = -\delta_{jk} p_i, \quad \{p_i p_j, p_k\} = 0,$$

$$\{p_i p_j, q_k\} = \delta_{ik} p_j + \delta_{jk} p_i, \quad \{q_i q_j, q_k\} = 0, \quad \{q_i q_j, p_k\} = -\delta_{ik} q_j - \delta_{jk} q_i$$

so, we have the representation of basic elements $f \mapsto A_f : 1 \mapsto i, q_k \mapsto ix_k,$

$$p_l \mapsto \frac{\delta}{\delta x^l}, p_i q_j \mapsto x^i \frac{\partial}{\partial x^j} + \frac{1}{2} \delta_{ij}, \quad p_k p_l \mapsto \frac{1}{i} \frac{\partial^k}{\partial x^k \partial x^l}, q_k q_l \mapsto ix^k x^l$$

All that provides the structure of the Poisson manifolds for representation of any (nilpotent) algebra or in other words to some sort of continuous wavelet transform.

The Segal-Bargman Representation. Let $z = 1/\sqrt{2} \cdot (p - iq), \quad \bar{z} = 1/\sqrt{2} \cdot (p + iq), \quad p = (p_1, \dots, p_n), \quad F_n$ is the space of holomorphic functions of n complex variables with $(f, f) < \infty,$ where

$$(f, g) = (2\pi)^{-n} \int f(z) \overline{g(z)} e^{-|z|^2} dpdq$$

Consider a map $U : H \rightarrow F_n,$ where H is with real polarization, F_n is with complex polarization, then we have

$$(U\Psi)(a) = \int A(a, q) \Psi(q) dq, \quad \text{where} \quad A(a, q) = \pi^{-n/4} e^{-1/2(a^2+q^2)+\sqrt{2}aq}$$

i.e. the Bargmann formula produce wavelets. We also have the representation of Heisenberg algebra on $F_n :$

$$U \frac{\partial}{\partial q_j} U^{-1} = \frac{1}{\sqrt{2}} \left(z_j - \frac{\partial}{\partial z_j} \right), \quad U q_j U^{-1} = -\frac{i}{\sqrt{2}} \left(z_j + \frac{\partial}{\partial z_j} \right)$$

and also : $\omega = d\beta = dp \wedge dq,$ where $\beta = i\bar{z}dz.$

Orbital Theory for Representations. Let coadjoint action be $\langle g \cdot f, Y \rangle = \langle f, Ad(g)^{-1}Y \rangle,$ where \langle, \rangle is pairing $g \in G, \quad f \in g^*, \quad Y \in \mathcal{G}.$ The orbit is $\mathcal{O}_f = G \cdot f \equiv G/G(f).$ Also, let $A=A(M)$ be algebra of functions, $V(M)$ is A-module of vector fields, A^p is A-module of p-forms. Vector fields on orbit is

$$\sigma(\mathcal{O}, X)_f(\phi) = \left. \frac{d}{dt} (\phi(\exp tXf)) \right|_{t=0}$$

where $\phi \in A(\mathcal{O}), \quad f \in \mathcal{O}.$ Then \mathcal{O}_f are homogeneous symplectic manifolds with 2-form $\Omega(\sigma(\mathcal{O}, X)_f, \sigma(\mathcal{O}, Y)_f) = \langle f, [X, Y] \rangle,$ and $d\Omega = 0.$ PB on \mathcal{O} have the next form $\{\Psi_1, \Psi_2\} = p(\Psi_1)\Psi_2$ where p is $A^1(\mathcal{O}) \rightarrow V(\mathcal{O})$ with definition $\Omega(p(\alpha), X) = i(X)\alpha.$ Here $\Psi_1, \Psi_2 \in A(\mathcal{O})$ and $A(\mathcal{O})$ is Lie algebra with bracket $\{, \}.$ Now let N be a Heisenberg group. Consider adjoint and coadjoint representations in some particular case. $N = (z, t) \in C \times R, z = p+iq;$ compositions in N are $(z, t) \cdot (z', t') =$

$(z + z', t + t' + B(z, z'))$, where $B(z, z') = pq' - qp'$. Inverse element is $(-t, -z)$. Lie algebra \mathfrak{n} of N is $(\zeta, \tau) \in C \times R$ with bracket $[(\zeta, \tau), (\zeta', \tau')] = (0, B(\zeta, \zeta'))$. Center is $\tilde{z} \in \mathfrak{n}$ and generated by $(0, 1)$; Z is a subgroup $\exp \tilde{z}$. Adjoint representation N on \mathfrak{n} is given by formula $Ad(z, t)(\zeta, \tau) = (\zeta, \tau + B(z, \zeta))$ Coadjoint: for $f \in \mathfrak{n}^*$, $g = (z, t)$, $(g \cdot f)(\zeta, \zeta) = f(\zeta, \tau) - B(z, \zeta)f(0, 1)$ then orbits for which $f|_{\tilde{z}} \neq 0$ are plane in \mathfrak{n}^* given by equation $f(0, 1) = \mu$. If $X = (\zeta, 0)$, $Y = (\zeta', 0)$, $X, Y \in \mathfrak{n}$ then symplectic structure is

$$\Omega(\sigma(\mathcal{O}, X)_f, \sigma(\mathcal{O}, Y)_f) = \langle f, [X, Y] \rangle = f(0, B(\zeta, \zeta'))\mu B(\zeta, \zeta')$$

Also we have for orbit $\mathcal{O}_\mu = N/Z$ and \mathcal{O}_μ is Hamiltonian G-space.

According to this approach, we can construct, in principle, many generalized "symplectic wavelet constructions" with corresponding symplectic or Poisson structure on it by using methods of geometric quantization theory Very useful particular spline-wavelet basis with uniform exponential control on stratified and nilpotent Lie groups was considered in [4].

3 Invariant Perturbations: Melnikov Functions

We give now some point of applications of wavelet methods [11]-[33] to Melnikov approach in the theory of homoclinic chaos in perturbed Hamiltonian systems [5]. In explicit Hamiltonian form we have:

$$\dot{x} = J \cdot \nabla H(x) + \varepsilon g(x, \Theta), \quad \dot{\Theta} = \omega, \quad (x, \Theta) \in R^n \times T^m,$$

for $\varepsilon = 0$ we have:

$$\dot{x} = J \cdot \nabla H(x), \quad \dot{\Theta} = \omega \tag{1}$$

For $\varepsilon = 0$ we have homoclinic orbit $\bar{x}_0(t)$ to the hyperbolic fixed point x_0 . For $\varepsilon \neq 0$ we have normally hyperbolic invariant torus T_ε and condition on transversally intersection of stable and unstable manifolds $W^s(T_\varepsilon)$ and $W^u(T_\varepsilon)$ in terms of Melnikov functions $M(\Theta)$ for $\bar{x}_0(t)$:

$$M(\Theta) = \int_{-\infty}^{\infty} \nabla H(\bar{x}_0(t)) \wedge g(\bar{x}_0(t), \omega t + \Theta) dt$$

This condition has the next form:

$$M(\Theta_0) = 0, \quad \sum_{j=1}^2 \omega_j \frac{\partial}{\partial \Theta_j} M(\Theta_0) \neq 0$$

According to the approach of Birkhoff-Smale-Wiggins we determine the region(s) in parameter space in which we can observe the chaotic-like behaviour [13].

If we cannot solve equations (1) explicitly in time, then we use our wavelet approach [11]-[33] for the computations of homoclinic (heteroclinic) loops as the solution of

system (1) in general multiscale basis. For analysis of quasiperiodic Melnikov functions

$$M^{m/n}(t_0) = \int_0^{mT} DH(x_\alpha(t)) \wedge g(x_\alpha(t), t + t_0) dt$$

we used periodization of our wavelet construction.

We also used symplectic Melnikov function approach in which we have:

$$M_i(z) = \lim_{j \rightarrow \infty} \int_{-T_j^*}^{T_j} \{h_i, \hat{h}\}_{\Psi(t,z)} dt$$

$$d_i(z, \varepsilon) = h_i(z_\varepsilon^u) - h_i(z_\varepsilon^s) = \varepsilon M_i(z) + O(\varepsilon^2)$$

where $\{, \}$ is the Poisson bracket, $d_i(z, \varepsilon)$ is the Melnikov distance. So, we need symplectic invariant expression for Poisson brackets. The computations can be done according to invariant calculation of Poisson brackets considered here.

4 Floer Approach for Closed Loops

Now we consider the generalization of wavelet variational approach to the symplectic invariant calculations of closed loops in Hamiltonian systems [6]. As we demonstrated in [13] we have the parametrization of our solution by some reduced algebraical problem, but in contrast to the standard cases, where the solution is parametrized by construction based on scalar refinement equation, in symplectic case we have parametrization of the solution by matrix problems – Quadratic Mirror Filters equations. Now we consider a different approach.

Let (M, ω) be a compact symplectic manifold of dimension $2n$, ω is a closed 2-form (nondegenerate) on M which induces an isomorphism $T^*M \rightarrow TM$. Thus every smooth time-dependent Hamiltonian $H : \mathbf{R} \times M \rightarrow \mathbf{R}$ corresponds to a time-dependent Hamiltonian vector field $X_H : \mathbf{R} \times M \rightarrow TM$ defined by

$$\omega(X_H(t, x), \xi) = -d_x H(t, x) \xi \tag{2}$$

for $\xi \in T_x M$. Let H (and X_H) is periodic in time: $H(t + T, x) = H(t, x)$ and consider corresponding Hamiltonian differential equation on M :

$$\dot{x}(t) = X_H(t, x(t)) \tag{3}$$

The solutions $x(t)$ of (3) determine a 1-parameter family of diffeomorphisms $\psi_t \in \text{Diff}(M)$ satisfying $\psi_t(x(0)) = x(t)$. These diffeomorphisms are symplectic: $\omega = \psi_t^* \omega$. Let $L = L_T M$ be the space of contractible loops in M which are represented by smooth curves $\gamma : \mathbf{R} \rightarrow M$ satisfying $\gamma(t + T) = \gamma(t)$. Then the contractible T -periodic solutions of (3) can be characterized as the critical points of the functional $S = S_T : L \rightarrow \mathbf{R}$:

$$S_T(\gamma) = - \int_D u^* \omega + \int_0^T H(t, \gamma(t)) dt, \tag{4}$$

where $D \subset \mathbf{C}$ be a closed unit disc and $u : D \rightarrow M$ is a smooth function, which on boundary agrees with γ , i.e. $u(\exp\{2\pi i\Theta\}) = \gamma(\Theta T)$. Because $[\omega]$, the cohomology class of ω , vanishes then $S_T(\gamma)$ is independent of choice of u . Tangent space $T_\gamma L$ is the space of vector fields $\xi \in C^\infty(\gamma^*TM)$ along γ satisfying $\xi(t+T) = \xi(t)$. Then we have for the 1-form $df : TL \rightarrow \mathbf{R}$

$$dS_T(\gamma)\xi = \int_0^T (\omega(\dot{\gamma}, \xi) + dH(t, \gamma)\xi) dt \quad (5)$$

and the critical points of S are contractible loops in L which satisfy the Hamiltonian equation (3). Thus the critical points are precisely the required T-periodic solution of (3).

To describe the gradient of S we choose a on almost complex structure on M which is compatible with ω . This is an endomorphism $J \in C^\infty(\text{End}(TM))$ satisfying $J^2 = -I$ such that

$$g(\xi, \eta) = \omega(\xi, J(x)\eta), \quad \xi, \eta \in T_x M \quad (6)$$

defines a Riemannian metric on M . The Hamiltonian vector field is then represented by $X_H(t, x) = J(x)\nabla H(t, x)$, where ∇ denotes the gradient w.r.t. the x -variable using the metric (6). Moreover the gradient of S w.r.t. the induced metric on L is given by

$$\text{grad}S(\gamma) = J(\gamma)\dot{\gamma} + \nabla H(t, \gamma), \quad \gamma \in L \quad (7)$$

Studying the critical points of S is confronted with the well-known difficulty that the variational integral is neither bounded from below nor from above. Moreover, at every possible critical point the Hessian of f has an infinite dimensional positive and an infinite dimensional negative subspaces, so the standard Morse theory is not applicable. The additional problem is that the gradient vector field on the loop space L

$$\frac{d}{ds}\gamma = -\text{grad}f(\gamma) \quad (8)$$

does not define a well posed Cauchy problem. Fortunately, Floer [6] found a way to analyse the space \mathcal{M} of bounded solutions consisting of the critical points together with their connecting orbits. He used a combination of variational approach and Gromov's elliptic technique. A gradient flow line of f is a smooth solution $u : \mathbf{R} \rightarrow M$ of the partial differential equation

$$\frac{\partial u}{\partial s} + J(u)\frac{\partial u}{\partial t} + \nabla H(t, u) = 0, \quad (9)$$

which satisfies $u(s, t+T) = u(s, t)$. The key point is to consider (9) not as the flow on the loop space but as an elliptic boundary value problem. It should be noted that (9) is a generalization of equation for Gromov's pseudoholomorphic curves (correspond to the case $\nabla H = 0$ in (9)). Let $\mathcal{M}_T = \mathcal{M}_T(H, J)$ the space of bounded solutions

of (9), i.e. the space of smooth functions $u : \mathbf{C}/iT\mathbf{Z} \rightarrow M$, which are contractible, solve equation (9) and have finite energy flow:

$$\Phi_T(u) = \frac{1}{2} \int_{-\infty}^{\infty} \int_0^T \left(\left| \frac{\partial u}{\partial s} \right|^2 + \left| \frac{\partial u}{\partial t} - X_H(t, u) \right|^2 \right) dt ds < \infty. \quad (10)$$

For every $u \in M_T$ there exists a pair x, y of contractible T-periodic solutions of (3), such that u is a connecting orbit from y to x :

$$\lim_{s \rightarrow -\infty} u(s, t) = y(t), \quad \lim_{s \rightarrow +\infty} u(s, t) = x(t) \quad (11)$$

So, our approach, which we may apply as on the level of standard boundary problem (9) as on the level of variational approach (10), together with FWT representation for all involved operators (in our case, J and ∇) can provide economically computable multiscale representation for Hamiltonian closed loops.

5 Quasiclassical Evolution

Let us consider classical and quantum dynamics in phase space $\Omega = R^{2m}$ with coordinates (x, ξ) and generated by Hamiltonian $\mathcal{H}(x, \xi) \in C^\infty(\Omega; R)$. If $\Phi_t^{\mathcal{H}} : \Omega \rightarrow \Omega$ is (classical) flow then time evolution of any bounded classical observable or symbol $b(x, \xi) \in C^\infty(\Omega, R)$ is given by $b_t(x, \xi) = b(\Phi_t^{\mathcal{H}}(x, \xi))$. Let $H = Op^W(\mathcal{H})$ and $B = Op^W(b)$ are the self-adjoint operators or quantum observables in $L^2(R^n)$, representing the Weyl quantization of the symbols \mathcal{H}, b [2], [3]:

$$(Bu)(x) = \frac{1}{(2\pi\hbar)^n} \int_{R^{2n}} b\left(\frac{x+y}{2}, \xi\right) \cdot e^{i\langle(x-y), \xi\rangle/\hbar} u(y) dy d\xi,$$

where $u \in S(R^n)$ and $B_t = e^{iHt/\hbar} B e^{-iHt/\hbar}$ be the Heisenberg observable or quantum evolution of the observable B under unitary group generated by H . B_t solves the Heisenberg equation of motion

$$\dot{B}_t = \frac{i}{\hbar} [H, B_t].$$

Let $b_t(x, \xi; \hbar)$ is a symbol of B_t then we have the following equation for it

$$\dot{b}_t = \{\mathcal{H}, b_t\}_M, \quad (12)$$

with initial condition $b_0(x, \xi, \hbar) = b(x, \xi)$. Here $\{f, g\}_M(x, \xi)$ is the Moyal brackets of the observables $f, g \in C^\infty(R^{2n})$, $\{f, g\}_M(x, \xi) = f\sharp g - g\sharp f$, where $f\sharp g$ is the symbol of the operator product and is presented by the composition of the symbols f, g

$$(f\sharp g)(x, \xi) = \frac{1}{(2\pi\hbar)^{n/2}} \int_{R^{4n}} e^{-i\langle r, \rho\rangle/\hbar + i\langle \omega, \tau\rangle/\hbar} \cdot f(x + \omega, \rho + \xi) \cdot g(x + r, \tau + \xi) d\rho d\tau dr d\omega.$$

For our problems it is useful that $\{f, g\}_M$ admits the formal expansion in powers of \hbar :

$$\{f, g\}_M(x, \xi) \sim \{f, g\} + 2^{-j} \sum_{|\alpha+\beta|=j \geq 1} (-1)^{|\beta|} \cdot (\partial_\xi^\alpha f D_x^\beta g) \cdot (\partial_\xi^\beta g D_x^\alpha f),$$

where $\alpha = (\alpha_1, \dots, \alpha_n)$ is a multi-index, $|\alpha| = \alpha_1 + \dots + \alpha_n$, $D_x = -i\hbar\partial_x$. So, evolution (12) for symbol $b_t(x, \xi; \hbar)$ is

$$\dot{b}_t = \{\mathcal{H}, b_t\} + \frac{1}{2^j} \sum_{|\alpha+\beta|=j \geq 1} (-1)^{|\beta|} \cdot \hbar^j (\partial_\xi^\alpha \mathcal{H} D_x^\beta b_t) \cdot (\partial_\xi^\beta b_t D_x^\alpha \mathcal{H}). \quad (13)$$

At $\hbar = 0$ this equation transforms to classical Liouville equation

$$\dot{b}_t = \{\mathcal{H}, b_t\}. \quad (14)$$

Equation (13) plays a key role in many quantum (semiclassical) problem. We note only the problem of relation between quantum and classical evolutions or how long the evolution of the quantum observables is determined by the corresponding classical one [3]. Our approach to solution of systems (13), (14) is based on our technique from [11]-[33] and very useful FWT [4] parametrization for general (pseudo)differential operators.

6 Symplectic Hilbert Scales via Wavelets

We can solve many important dynamical problems such that KAM perturbations, spread of energy to higher modes, weak turbulence, growths of solutions of Hamiltonian equations in case if we consider scales of underlying functional spaces instead of one functional space. For Hamiltonian system and their perturbations for which we need take into account underlying symplectic structure we need to consider symplectic scales of spaces. So, if $\dot{u}(t) = J\nabla K(u(t))$ is Hamiltonian equation we need wavelet description of symplectic or quasicomplex structure on the level of functional spaces. It is very important that according to [5] Hilbert basis is in the same time a Darboux basis to corresponding symplectic structure. We need to provide Hilbert scale $\{Z_s\}$ with symplectic structure [5], [7]. All what we need is the following. J is a linear operator, $J : Z_\infty \rightarrow Z_\infty$, $J(Z_\infty) = Z_\infty$, where $Z_\infty = \cap Z_s$. J determines an isomorphism of scale $\{Z_s\}$ of order $d_J \geq 0$. The operator J with domain of definition Z_∞ is antisymmetric in Z : $\langle Jz_1, z_2 \rangle_Z = -\langle z_1, Jz_2 \rangle_Z$, $z_1, z_2 \in Z_\infty$. Then the triple

$$\{Z, \{Z_s | s \in R\}, \alpha = \langle \bar{J}dz, dz \rangle\}$$

is symplectic Hilbert scale. So, we may consider any dynamical Hamiltonian problem on functional level. As an example, for KdV equation we have

$$Z_s = \{u(x) \in H^s(T^1) | \int_0^{2\pi} u(x)dx = 0\}, \quad s \in R, \quad J = \partial/\partial x,$$

J is isomorphism of the scale of order one, $\bar{J} = -(J)^{-1}$ is isomorphism of order -1 . According to [8] general functional spaces and scales of spaces such as Holder-Zygmund, Triebel-Lizorkin and Sobolev can be characterized through wavelet coefficients or wavelet transforms. As a rule, the faster the wavelet coefficients decay,

the more the analyzed function is regular [8]. Most important for us example is the scale of Sobolev spaces. Let $H_k(R^n)$ is the Hilbert space of all distributions with finite norm

$$\|s\|_{H_k(R^n)}^2 = \int d\xi (1 + |\xi|^2)^{k/2} |\hat{s}(\xi)|^2.$$

Let us consider wavelet transform

$$W_g f(b, a) = \int_{R^n} dx \frac{1}{a^n} \bar{g}\left(\frac{x-b}{a}\right) f(x),$$

$b \in R^n$, $a > 0$, w.r.t. analyzing wavelet g , which is strictly admissible, i.e.

$$C_{g,g} = \int_0^\infty \frac{da}{a} |\hat{g}(\bar{a}k\hat{g})|^2 < \infty.$$

Then there is a $c \geq 1$ such that

$$c^{-1} \|s\|_{H_k(R^n)}^2 \leq \int_{H^n} \frac{db da}{a} (1 + a^{-2\gamma}) |W_g s(b, a)|^2 \leq c \|s\|_{H_k(R^n)}^2.$$

This shows that localization of the wavelet coefficients at small scale is linked to local regularity.

So, we need representation for differential operator (J in our case) in localized multiscale wavelet basis. The problem can be solved by the same FWT approach, mentioned above.

7 Maps and Multiresolution

7.1 Veselov-Marsden Discretization

Discrete variational principles lead to evolution dynamics analogous to the Euler-Lagrange equations [9]. Let Q be a configuration space, then a discrete Lagrangian is a map $L : Q \times Q \rightarrow \mathbf{R}$. usually L is obtained by approximating the given Lagrangian. For $N \in N_+$ the action sum is the map $S : Q^{N+1} \rightarrow \mathbf{R}$ defined by

$$S = \sum_{k=0}^{N-1} L(q_{k+1}, q_k), \quad (15)$$

where $q_k \in Q$, $k \geq 0$. The action sum is the discrete analog of the action integral in continuous case. Extremizing S over q_1, \dots, q_{N-1} with fixing q_0, q_N we have the discrete Euler-Lagrange equations (DEL):

$$D_2 L(q_{k+1}, q_k) + D_1 L(q_k, q_{k-1}) = 0, \quad (16)$$

for $k = 1, \dots, N-1$.

Let

$$\Phi : Q \times Q \rightarrow Q \times Q \quad (17)$$

and

$$\Phi(q_k, q_{k-1}) = (q_{k+1}, q_k) \tag{18}$$

is a discrete function (map), then we have for DEL:

$$D_2L \circ \Phi + D_1L = 0 \tag{19}$$

or in coordinates q^i on Q we have DEL:

$$\frac{\partial L}{\partial q_k^i} \circ \Phi(q_{k+1}, q_k) + \frac{\partial L}{\partial q_{k+1}^i}(q_{k+1}, q_k) = 0. \tag{20}$$

It is very important that the map Φ exactly preserves the symplectic form ω :

$$\omega = \frac{\partial^2 L}{\partial q_k^i \partial q_{k+1}^j}(q_{k+1}, q_k) dq_k^i \wedge dq_{k+1}^j \tag{21}$$

7.2 Generalized Discrete (Data) Multiresolution

Our approach to solutions of equations (20) is based on applications of general and very efficient methods developed by A. Harten [10], who produced a "General Framework" for multiresolution representation of discrete data. It is based on consideration of basic operators, decimation and prediction, which connect adjacent resolution levels. These operators are constructed from two basic blocks: the discretization and reconstruction operators. The former obtains discrete information from a given continuous functions (flows), and the latter produces an approximation to those functions, from discrete values, in the same function space to which the original function belongs. A "new scale" is defined as the information on a given resolution level which cannot be predicted from discrete information at lower levels. If the discretization and reconstruction are local operators, the concept of "new scale" is also local. The scale coefficients are directly related to the prediction errors, and thus to the reconstruction procedure. If scale coefficients are small at a certain location on a given scale, it means that the reconstruction procedure on that scale gives a proper approximation of the original function at that particular location. This approach may be considered as some generalization of standard wavelet analysis approach. It allows to consider multiresolution decomposition when usual approach is impossible or not efficient (δ -functions case, e.g.).

Let F be a linear space of mappings

$$F \subset \{f | f : X \rightarrow Y\}, \tag{22}$$

where X, Y are linear spaces. Let also D_k be a linear operator

$$D_k : f \rightarrow \{v^k\}, \quad v^k = D_k f, \quad v^k = \{v_i^k\}, \quad v_i^k \in Y. \tag{23}$$

This sequence corresponds to k level discretization of X . Let

$$D_k(F) = V^k = \text{span}\{\eta_i^k\} \tag{24}$$

and the coordinates of $v^k \in V^k$ in this basis are $\hat{v}^k = \{\hat{v}_i^k\}$, $\hat{v}^k \in S^k$:

$$v^k = \sum_i \hat{v}_i^k \eta_i^k, \quad (25)$$

D_k is a discretization operator. Main goal is to design a multiresolution scheme (MR) [10] that applies to all sequences $s \in S^L$, but corresponds for those sequences $\hat{v}^L \in S^L$, which are obtained by the discretization (22).

Since D_k maps F onto V^k then for any $v^k \in V^k$ there is at least one f in F such that $D_k f = v^k$. Such correspondence from $f \in F$ to $v^k \in V^k$ is reconstruction and the corresponding operator is the reconstruction operator R_k :

$$R_k : V_k \rightarrow F, \quad D_k R_k = I_k, \quad (26)$$

where I_k is the identity operator in V^k (R^k is right inverse of D^k in V^k).

Given a sequence of discretization $\{D_k\}$ and sequence of the corresponding reconstruction operators $\{R_k\}$, we define the operators D_k^{k-1} and P_{k-1}^k

$$\begin{aligned} D_k^{k-1} &= D_{k-1} R_k : V_k \rightarrow V_{k-1} \\ P_{k-1}^k &= D_k R_{k-1} : V_{k-1} \rightarrow V_k \end{aligned} \quad (27)$$

If the set D_k in nested [10], then

$$D_k^{k-1} P_{k-1}^k = I_{k-1} \quad (28)$$

and we have for any $f \in F$ and any $p \in F$ for which the reconstruction R_{k-1} is exact:

$$\begin{aligned} D_k^{k-1}(D_k f) &= D_{k-1} f \\ P_{k-1}^k(D_{k-1} p) &= D_k p \end{aligned} \quad (29)$$

Let us consider any $v^L \in V^L$, Then there is $f \in F$ such that

$$v^L = D_L f, \quad (30)$$

and it follows from (29) that the process of successive decimation [10]

$$v^{k-1} = D_k^{k-1} v^k, \quad k = L, \dots, 1 \quad (31)$$

yields for all k

$$v^k = D_k f \quad (32)$$

Thus the problem of prediction, which is associated with the corresponding MR scheme, can be stated as a problem of approximation: knowing $D_{k-1} f$, $f \in F$, find a "good approximation" for $D_k f$. It is very important that each space V^L has a multiresolution basis

$$\bar{B}_M = \{\bar{\phi}_i^{0,L}\}_i, \{\{\bar{\psi}_j^{k,L}\}_j\}_{k=1}^L \quad (33)$$

and that any $v^L \in V^L$ can be written as

$$v^L = \sum_i \hat{v}_i^0 \bar{\phi}_i^{0,L} + \sum_{k=1}^L \sum_j d_j^k \bar{\psi}_j^{k,L}, \quad (34)$$

where $\{d_j^k\}$ are the k scale coefficients of the associated MR, $\{\hat{v}_i^0\}$ is defined by (25) with $k = 0$. If $\{D_k\}$ is a nested sequence of discretization [10] and $\{R_k\}$ is any corresponding sequence of linear reconstruction operators, then we have from (34) for $v^L = D_L f$ applying R_L :

$$R_L D_L f = \sum_i \hat{f}_i^0 \phi_i^{0,L} + \sum_{k=1}^L \sum_j d_j^k \psi_j^{k,L}, \quad (35)$$

where

$$\phi_i^{0,L} = R_L \bar{\phi}_i^{0,L} \in F, \quad \psi_j^{k,L} = R_L \bar{\psi}_j^{k,L} \in F, \quad D_0 f = \sum_i \hat{f}_i^0 \eta_i^0. \quad (36)$$

When $L \rightarrow \infty$ we have sufficient conditions which ensure that the limiting process $L \rightarrow \infty$ in (35, 36) yields a multiresolution basis for F . Then, according to (33), (34) we have very useful representation for solutions of equations (20) or for different maps construction in the form which are a counterparts for discrete (difference) cases of our constructions in [11]–[33].

References

- [1] A. N. Fedorova and M. G. Zeitlin, Invariant calculations in beam physics: dynamics on semi-direct products and CWT, this Volume.
- [2] V. Guillemin, Sh. Sternberg, Geometric Asymptotics, AMS, 1990.
- [3] G. B. Folland, Harmonic Analysis in Phase Space, Princeton, 1989.
- [4] Y. Meyer, Wavelets and Operators, Cambridge Univ. Press, 1990; G. Beylkin, R. Coifman, V. Rokhlin, Fast Wavelet transform and Numerical Algorithms, Comm. Pure Applid Math, 44, 141-183, 1991; P. G. Lemarie, Proc. Int. Math. Congr., Satellite Symp., 1991, p. 154.
- [5] S. Kuksin, Nearly integrable Hamiltonian systems, Springer, 1993.
- [6] E. Hofer, E. Zehnder, Symplectic Topology, Birkhauser, 1994.
- [7] J. Bourgain, IMRN, 6, 277-304, 1996.
- [8] M. Holschneider, CPT-96/P3344, Marseille.
- [9] J. E. Marsden, Park City Lectures on Mechanics, Dynamics and Symmetry, CALTECH, 1998.
- [10] A. Harten, SIAM J. Numer. Anal., 31, 1191-1218, 1994.

-
- [11] A. N. Fedorova, M. G. Zeitlin, 'Wavelets in Optimization and Approximations', *Math. and Comp. in Simulation*, **46**, 527-534 (1998).
- [12] A. N. Fedorova, M. G. Zeitlin, 'Wavelet Approach to Polynomial Mechanical Problems', *New Applications of Nonlinear and Chaotic Dynamics in Mechanics*, Kluwer, 101-108, 1998.
- [13] A. N. Fedorova, M. G. Zeitlin, 'Wavelet Approach to Mechanical Problems. Symplectic Group, Symplectic Topology and Symplectic Scales', *New Applications of Nonlinear and Chaotic Dynamics in Mechanics*, Kluwer, 31-40, 1998.
- [14] A. N. Fedorova, M. G. Zeitlin, 'Nonlinear Dynamics of Accelerator via Wavelet Approach', *AIP Conf. Proc.*, vol. 405, ed. Z. Parsa, 87-102, 1997, Los Alamos preprint, physics/9710035.
- [15] A. N. Fedorova and M. G. Zeitlin, Quasiclassical Calculations for Wigner Functions via Multiresolution, Localized Coherent Structures and Patterns Formation in Collective Models of Beam Motion, in *Quantum Aspects of Beam Physics*, Ed. P. Chen (World Scientific, Singapore, 2002) pp. 527-538, 539-550; arXiv: physics/0101006; physics/0101007.
- [16] A. N. Fedorova and M. G. Zeitlin, BBGKY Dynamics: from Localization to Pattern Formation, in *Progress in Nonequilibrium Green's Functions II*, Ed. M. Bonitz, (World Scientific, 2003) pp. 481-492; arXiv: physics/0212066.
- [17] A. N. Fedorova and M. G. Zeitlin, Pattern Formation in Wigner-like Equations via Multiresolution, in *Quantum Aspects of Beam Physics*, Eds. Pisin Chen, K. Reil (World Scientific, 2004) pp. 22-35; Preprint SLAC-R-630; arXiv: quant-ph/0306197.
- [18] A. N. Fedorova and M. G. Zeitlin, Localization and pattern formation in Wigner representation via multiresolution, *Nuclear Inst. and Methods in Physics Research, A*, **502A/2-3**, pp. 657 - 659, 2003; arXiv: quant-ph/0212166.
- [19] A. N. Fedorova and M. G. Zeitlin, Fast Calculations in Nonlinear Collective Models of Beam/Plasma Physics, *Nuclear Inst. and Methods in Physics Research, A*, **502/2-3**, pp. 660 - 662, 2003; arXiv: physics/0212115.
- [20] A. N. Fedorova and M. G. Zeitlin, Classical and quantum ensembles via multiresolution: I-BBGKY hierarchy; Classical and quantum ensembles via multiresolution. II. Wigner ensembles; *Nucl. Instr. Methods Physics Res.*, **534A** (2004)309-313; 314-318; arXiv: quant-ph/0406009; quant-ph/0406010.
- [21] A. N. Fedorova and M. G. Zeitlin, Localization and Pattern Formation in Quantum Physics. I. Phenomena of Localization, in *The Nature of Light: What is a Photon? SPIE*, vol.**5866**, pp. 245-256, 2005; arXiv: quant-ph/0505114;
- [22] A. N. Fedorova and M. G. Zeitlin, Localization and Pattern Formation in Quantum Physics. II. Waveletons in Quantum Ensembles, in *The Nature of Light: What is a Photon?SPIE*, vol. **5866**, pp. 257-268, 2005; arXiv: quant-ph/0505115.

-
- [23] A. N. Fedorova and M. G. Zeitlin, Pattern Formation in Quantum Ensembles, *Intl. J. Mod. Physics B* **20**(2006)1570-1592; arXiv: 0711.0724.
- [24] A. N. Fedorova and M. G. Zeitlin, Patterns in Wigner-Weyl approach, Fusion modeling in plasma physics: Vlasov-like systems, *Proceedings in Applied Mathematics and Mechanics (PAMM)*, Volume **6**, Issue 1, p. 625, p. 627, Wiley InterScience, 2006; arXiv:1012.4971, arXiv:1012.4965.
- [25] A. N. Fedorova and M. G. Zeitlin, Localization and Fusion Modeling in Plasma Physics. Part I: Math Framework for Non-Equilibrium Hierarchies, pp.61-86, in *Current Trends in International Fusion Research*, Ed. E. Panarella, R. Raman, National Research Council (NRC) Research Press, Ottawa, Ontario, Canada, 2009; arXiv: physics/0603167.
- [26] A. N. Fedorova and M. G. Zeitlin, Localization and Fusion Modeling in Plasma Physics. Part II: Vlasov-like Systems. Important Reductions, pp.87-100, in *Current Trends in International Fusion Research*, Ed. E. Panarella, R. Raman, National Research Council (NRC) Research Press, Ottawa, Ontario, Canada, 2009; arXiv: physics/0603169.
- [27] A. N. Fedorova and M. G. Zeitlin, Fusion State in Plasma as a Waveleton (Localized (Meta)-Stable Pattern), p. 272, in *AIP Conference Proceedings*, Volume **1154**, Issue 1, *Current Trends in International Fusion Research*, Ed. E. Panarella, R. Raman, AIP, 2009, doi:10.1063/1.3204585.
- [28] A. N. Fedorova and M. G. Zeitlin, Exact Multiscale Representations for (Non)-Equilibrium Dynamics of Plasma, p.291, in *AIP Conference Proceedings*, Volume **1154**, Issue 1, *Current Trends in International Fusion Research*, Ed. E. Panarella, R. Raman, AIP, 2009, doi:10.1063/1.3204592.
- [29] A. N. Fedorova and M. G. Zeitlin, Fusion Modeling in Vlasov-Like Models, *Journal Plasma Fusion Res. Series*, Vol. **8**, pp. 126-131, 2009.
- [30] A. N. Fedorova and M. G. Zeitlin, Quantum points/patterns, Part 2: from quantum points to quantum patterns via multiresolution, SPIE, vol. 8121, 81210K (2011), doi:10.1117/12.893537; arXiv:1109.5042.
- [31] A. N. Fedorova and M. G. Zeitlin, Quantum points/patterns, Part 1. From geometrical points to quantum points in sheaf framework , SPIE, vol. 8121, 81210J (2011), doi:10.1117/12.893502; arXiv:1109.5035.
- [32] A. N. Fedorova and M. G. Zeitlin, En route to fusion: confinement state as a waveleton, *Journal of Physics CS*, vol. 490, 012202, 2014, doi:10.1088/1742-6596/490/1/012202.
- [33] A. N. Fedorova and M. G. Zeitlin, a list of papers/preprints (including links to arXiv) can be found on web sites below.

Antonina N. Fedorova, Michael G. Zeitlin

Mathematical Methods in Mechanics Group, IPME RAS, V.O. Bolshoj pr., 61, 199178,

REFERENCES

St. Petersburg, Russia

<http://www.ipme.ru/zeitlin.html>, <http://mp.ipme.ru/zeitlin.html>

Finding the distribution density of settling nanoparticles in a liquid with regard to their Brownian diffusion using the boundary layer theory

Ezhenkova S.I., Chivilikhin S.A.
sveta.ejenkova@yandex.ru

Abstract

The sedimentation process of nanoparticles in a liquid considering their Brownian diffusion was investigated with the methods of mathematical modeling. We have received solution of the equation of convective diffusion of nanoparticles in the case of the boundary layer formed at the bottom of the glassful.

1 Introduction

The problem of the influence of Brownian diffusion occurring between the nanoparticles on their deposition is still remain relevant [1].

Since the times of the experiment about the movement of pollen particles in a liquid drop, which was open by Scottish physicist Robert Brown in 1827, many scientists have studied the behavior of particles in different types of environments. For example, in works [2]-[3] studied the theoretical aspects of the sedimentation of nanoparticles and their characteristics, and in the works [4]-[6] - Brownian motion of nanoparticles in specific environments.

The examples of the elementary colloidal systems (a mixture in which small particles of the substance are distributed in another substance) are "Indian ink" (coal particles in water), smoke (particulate matter in the air) and butterfat (tiny balls of fat in a water).

In this paper, we investigate the sedimentation of spherical nanoparticles in a liquid. As object of research we take glassful with liquid, which contains particles of different sizes. More heavy particles settle to the bottom, a lighter particles stay at the surface, and thus it is distributed over the depth and creating a gradient medium.

2 A mathematical model

In this work we deals with the sedimentation process of spherical nanoparticles occurring under the influence of gravity in a glassful with liquid taking into account

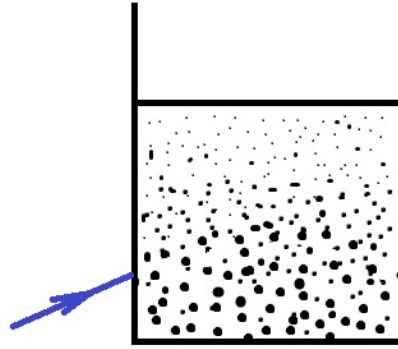


Figure 1: The object of research

the Brownian diffusion between them; where $f(x, t, R)$ - the density of function of particle size distribution in the time t at the depth x . The equation of convective diffusion:

$$\frac{\partial f}{\partial t} + v \frac{\partial f}{\partial x} = D(R) \frac{\partial^2 f}{\partial x^2} \quad (1)$$

where $v(R)$ - velocity of sedimentation, f - the particle distribution function, D - diffusion, x - coordinate, t - time of sedimentation.

The initial condition:

$$f|_{t=0} = f_0(R, x) \Theta(x) \quad (2)$$

where $\Theta(x)$ - the Heaviside step function.

The boundary conditions:

$$j|_{x=0} = 0 \quad (3)$$

$$f|_{x=L} = 0 \quad (4)$$

where $j = v(R)f - D \frac{\partial f}{\partial x}$ - the particles flux density, L - a boundary layer.

Let suppose formally $D = 0$ in the equation (1). Then we get a first order differential equation:

$$v(R) \frac{\partial f}{\partial x} + \frac{\partial f}{\partial t} = 0 \quad (5)$$

The solution of this equation (see [5]) The solution of this equation (which we describe in [5]) contain only one arbitrary constant, whereby it is impossible to satisfy two boundary conditions (3) and (4). The second boundary condition manifested in a rather small coordinate interval (a boundary layer) adjacent to the coordinate $x = L$.

To find the solution inside the boundary layer we are reduce (5) to a dimensionless form. For this we introduce the dimensionless parameters for variables x and t :

$$\begin{aligned} x &= L\bar{x} \\ t &= T\bar{t} \end{aligned} \tag{6}$$

$$\epsilon = \frac{L}{\gamma R^2} \frac{D(R)}{L^2} = \frac{D(R)}{\gamma R^2 L}, \tag{7}$$

where $T = \frac{L}{v(R)}$, L – height of liquid in the glass, $v(R) = \gamma R^2$ – velocity of sedimentation.

Rewrite the the equation in the new notation:

$$\epsilon^{1-2\lambda} \frac{\partial^2 f}{\partial \xi^2} + \epsilon^{-\lambda} \frac{\partial f}{\partial \xi} - \epsilon^0 \frac{\partial f}{\partial \bar{t}} = 0, \tag{8}$$

where $\xi = \epsilon^{-\lambda}(L - \bar{x}) = \epsilon^{-\lambda}\bar{z}$ – another dimensionless parameter.

For cross-linking the solution $\bar{f}^p(\xi)$ of the equation (8) inside the boundary layer, with the solution $f^0 = Ae^{-\alpha R}$ outside the boundary layer (see. [7]), the next asymptotic equality is must perform:

$$\lim_{\bar{x} \rightarrow 1} f^0(\bar{x}, \bar{t}) = \lim_{\xi \rightarrow \infty} f^p(\xi) \tag{9}$$

Let consider the behavior of individual members of the equation for $\epsilon \rightarrow 0$. Each term in (8) has form $\epsilon^{P(\lambda)}$, where $P(\lambda)$ – the linear function.

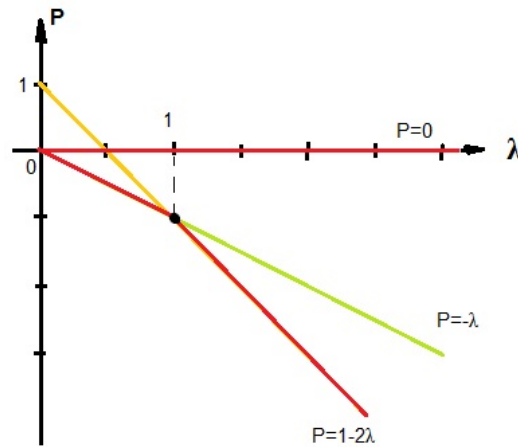


Figure 2: the Newton polygon

The asymptotic of (8) for $\epsilon \rightarrow 0$ is determined by the term with the lowest degree of ϵ , ie the bottom of the curve the family of lines. This curve which allocated a thick line is called the Newton polygon.

The solution of this equation outside the boundary layer:

$$f^0(\bar{x}, \bar{t}) = ARe^{-\lambda R^2} \Theta(\bar{x} - \bar{t}) \quad (10)$$

The solution of this equation inside the boundary layer:

$$f = A + Be^{-\xi} \quad (11)$$

Let substitute this solutions into (9) and then find the required coefficients.

Finally we find the final formula for the particle size distribution:

$$f = f_0(R) \Theta\left(1 - \frac{tv(R)}{L}\right) \left(1 + \frac{D(R)}{D(R) + v(R)L} e^{-\frac{v(R)}{D(R)}(L-x)}\right) \quad (12)$$

This equation is investigated analytically at the moment.

Acknowledgements

This work was financially supported by the Government of Russian Federation, Grant 074-U01.

References

- [1] H. Vahedi Tafreshi, P. Piseri, E. Barborini, G. Benedek and P. Milani Simulation on the effect of Brownian motion on nanoparticle trajectories in a pulsed microplasma cluster source *Journal of Nanoparticle Research* 4: 511-524, 2002
- [2] Suvankar Gangulya, Suman Chakraborty, Sedimentation of nanoparticles in nanoscale colloidal suspensions. *Physics Letters A* 375 (2011) 2394-2399
- [3] B. Demeler, Tich-Lam Nguyen, G. E. Gorbet, V. Schirf, E. H. Brookes, P. Mulvaney, A. O. El-Ballouli, J. Pan, O. M. Bakr, A. K. Demeler, B. I. Hernandez Uribe, N. Bhattarai, R. L. Whetten, Characterization of Size, Anisotropy, and Density Heterogeneity of Nanoparticles by Sedimentation Velocity. *Anal. Chem.* 2014, 86, 7688-7695
- [4] Eun Chul Cho, Qiang Zhang, Younan Xia The effect of sedimentation and diffusion on cellular uptake of gold nanoparticles. DOI: 10.1038/NNANO.2011.58
- [5] Ezhenkova S.I., Chivilikhin S.A. Mathematical modeling of sedimentation process of nanoparticles in gradient medium. *Journal of Physics: Conference Series* 643 (2015) 012111
- [6] Fisenko S.P., Shnip A.I. *Physics, Chemistry and Applications of Nanostructures*. Singapore, 2003. P. 291-293
- [7] Nayfeh A.H. *Perturbation Methods*. New York: J. Wiley, 1973

Ezhenkova S.I., ITMO University, Saint-Petersburg, Russia

Chivilikhin S. A., ITMO University, Saint-Petersburg, Russia

Biomorphic approach in application to vibration control of continuous systems

Aleksandr V. Fedotov
alvafed@yandex.ru

Abstract

One of important applications of the automatic control theory is suppression of vibrations of continuous systems, which have an infinite number of degrees of freedom. The study investigates the modal (or biomorphic) approach to this problem. The specified approach, unlike the local one, implies separate control of the eigenmodes of object, and requires appropriate setting of the control loops. The study analyses methods of identification of the object, which is necessary for correct mode separation in the control system.

The experimental part of the research is devoted to the comparison of local and biomorphic approaches to the problem of suppression of forced flexural vibrations of the metal beam. All control systems created use the same elements — piezoelectric sensors and actuators attached to certain locations on the beam. It is shown that the created modal control system is more efficient than the local ones in cases where it is necessary to suppress vibrations in the frequency range that include several resonance frequencies of the object.

1 Introduction

Vibrations occur in a great variety of mechanical systems during their exploitation. In certain cases, these vibrations can be undesirable or even dangerous for the system and cause failure, damage or unwanted noise. The problem of vibration control is especially complicated in the case of elastic systems with distributed parameters, such as antennas, cables, robot manipulators, different beam and shell structures etc.

The absence of controllability and observability for continuous mechanical systems is due to an infinite number of eigenmodes, each of them being a separate degree of freedom. Of course, the modal stiffness is growing rapidly with increasing mode number, which allows one to neglect the higher modes of the object. However, the presence of higher modes leads to reduced accuracy and stability of the feedback control system. Moreover, the resonance behavior of the elastic object causes phase shifts that limit gain values in the control loops.

Traditionally for controlling continuous systems the local method is used which implies that each sensor is connected to only one corresponding actuator located at the same region of the mechanical object. The phase shifts in this case are

to be compensated by means of a sophisticated design of the feedback controllers. The methods of optimal control are widely used for designing controllers [1–5] as well as for determining the optimal spatial configuration of the control system (the mechatronic approach).

Alternatively, there is a modal method [6,7] based on the idea of independent control of different vibration modes of the mechanical system. This method allows one to compensate the phase shift for each mode in the corresponding controller, and it can provide stability of the system for the case of different spatial locations of sensors and actuators. At the same time, the modal system requires sufficient number of sensors and actuators to provide independent control of the modes.

Today the mechatronic systems are developing rapidly, but in the control aspect they are still far from biological systems. Control process in the living organisms has been optimized during millions of years of evolution. The most natural types of motion are inertial motion and motion with eigenmodes, therefore muscles activate these two types of motion. For example, when walking, legs move with the first eigenmode; when running, they move faster with the second eigenmode. Thus, the separate control of eigenmodes of the object can be called biomorphic.

The present study investigates the modal or biomorphic approach to control of continuous systems. Firstly, it analyses methods of identification of the control object, which can be used for correct mode separation in the modal control system. Secondly, it contains experimental part, where the both methods described above are implemented and their efficiency in the problem of suppression of forced bending vibrations of a thin metal beam is analyzed.

2 Mode separation in the biomorphic control system

Consider a system designed to control forced flexural vibrations of a thin cantilevered beam. The control system contains sensors and actuators - piezoelectric patches mounted to both sides of the beam. The actuators cause the bending deformation of the beam at the places where they are located, while the sensors measure this deformation (or curvature) as the beam vibrates. Let there be n sensors and n actuators in the control system. Therefore, this system can control independently not more than n eigenmodes of the beam.

It is obvious that sensors and actuators should be located at special places of the beam, so that they could measure and activate the needed eigenmodes most efficiently. To ensure this efficiency, it is necessary to define the eigenmodes of the beam theoretically or experimentally as the first stage of the control system design.

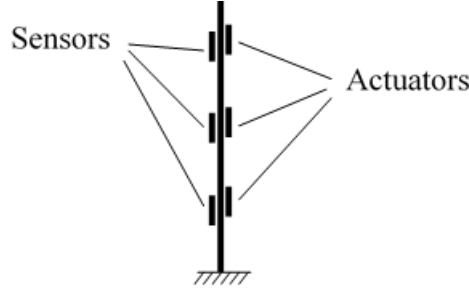


Fig.1. A beam with sensors and actuators

When the sensors and the actuators are mounted to the beam, it is necessary to set the control system, which links them together. We are going to analyze how this system should be organized in order to control the needed n eigenmodes of the beam separately. Consider that m eigenmodes are enough to describe the motion of the beam. The equation of motion of the beam in the form of mode decomposition has the following form:

$$\ddot{q} + \Omega^2 q = Q^c + Q^d, \quad (1)$$

where $q_{m \times 1}$ is a vector of generalized coordinates, corresponding to each of m eigenmodes; $\Omega_{m \times m}$ is a diagonal matrix of the eigenfrequencies; $Q_{m \times 1}^d$ is a vector of external disturbances; $Q_{m \times 1}^c$ is a vector of control influences.

The actuator influences on the modes depends on the control signals:

$$Q^c = \Theta_1 u, \quad (2)$$

where $u_{n \times 1}$ is a vector of control signals at the actuators, and $\Theta_{1m \times n}$ is an influence matrix, defining the influence of each actuator on each of the eigenmodes.

The sensor signals depend on the generalized coordinates q :

$$y = \Theta_2 q, \quad (3)$$

where $y_{n \times 1}$ is a vector of sensor signals, and $\Theta_{2n \times m}$ is a measurement matrix, defining the reaction of each sensor to activation of each eigenmode.

If the sensors and the actuators are located in pairs (at the same places of the beam), matrices Θ_1 and Θ_2 are related:

$$\Theta_1 = \Theta_2^T$$

In the simplest case of proportional control the control signal to the actuators depends on the measured signal as follows:

$$u = \mathcal{K} y \quad (4)$$

The work of the control system is specified by the matrix $\mathcal{K}_{n \times n}$. The system of equations looks as follows:

$$\ddot{q} + \Omega^2 q = \Theta_1 \mathcal{K} \Theta_2 q + Q^d \quad (5)$$

For the separate control of the first n modes of the beam the matrix $\Theta_1 \mathcal{K} \Theta_2$ should be diagonal. To separate the modes it is necessary to satisfy the following conditions:

$$\mathcal{K} = FKT, \quad \tilde{\Theta}_1 F = D_1, \quad T \tilde{\Theta}_2 = D_2, \quad (6)$$

where $\tilde{\Theta}_{1n \times n}$ and $\tilde{\Theta}_{2n \times n}$ are square parts of matrices Θ_1 and Θ_2 , corresponding to the first n eigenmodes; $K_{n \times n}$ is a diagonal matrix of gain values for each mode; $F_{n \times n}$ and $T_{n \times n}$ are modal matrices (mode synthesizer and mode analyzer), which are defined in such a manner that their multiplication by matrices $\tilde{\Theta}_1$ and $\tilde{\Theta}_2$ gives diagonal matrices $D_{1n \times n}$ and $D_{2n \times n}$.

Matrix T is a mode analyzer, it converts the vector of measured sensor signals y into a vector of estimations of the first n generalized coordinates $\hat{q}_{n \times 1}$:

$$\hat{q} = Ty = T\Theta_2 q \quad (7)$$

For the control system working correctly the following condition should be met:

$$T = \tilde{\Theta}_2^{-1} \quad (8)$$

Matrix K defines the gain values, which convert the vector of estimations of the modes \hat{q} into a vector of influences on each mode $\hat{Q}_{n \times 1}$:

$$\hat{Q} = K\hat{q} \quad (9)$$

Matrix F is a mode synthesizer, it converts the vector of influences to modes \hat{Q} into the vector of control signals to actuators u :

$$u = \mathcal{K}y = FKTy = FK\hat{q} = F\hat{Q}, \quad Q^c = \Theta_1 u = \Theta_1 F\hat{Q} \quad (10)$$

To provide the separate mode control it is necessary to satisfy the condition:

$$F = \tilde{\Theta}_1^{-1} \quad (11)$$

In this case the system of equations for the first n modes is the following:

$$\ddot{q} + \Omega^2 q = Kq + Q^d \quad (12)$$

The equations are separate since the matrix K is diagonal. Generally, it is possible to specify individual control laws for each of the eigenmodes. In this case the elements of the matrix K will be the functions of the complex variable s :

$$k_i = k_i(s)$$

3 Defining the modal matrices F and T

First, the modal matrices F and T can be calculated theoretically. To do this, it is necessary to know the eigenmodes of the beam and the locations of the sensors and the actuators on the beam. This allows one to calculate matrices $\tilde{\Theta}_1$ and $\tilde{\Theta}_2$. One needs to invert these matrices in order to obtain the desired matrices F and T . However, for most accurate determination of the desired matrices one needs to conduct certain experiments.

Each column of the measurement matrix $\tilde{\Theta}_2$ corresponds to one of the beam eigenmodes and shows, in what proportions sensors measure this eigenmode. In order to obtain this information experimentally it is necessary to induce resonant vibrations

of the beam at each of the n resonance frequencies. At each resonance one needs to measure the amplitude of signals of each sensor. Thus one obtains matrix $\tilde{\Theta}_2$.

Analogously, each row of the influence matrix $\tilde{\Theta}_1$ corresponds to one of the eigenmodes and shows, in what proportions actuators excite this mode. In order to obtain this information experimentally it is necessary to induce resonant vibrations of the beam by each actuator at each of the n resonance frequencies and measure the intensity of beam vibrations. This is the way to obtain matrix $\tilde{\Theta}_1$.

Modal matrices F and T are then calculated by inverting matrices $\tilde{\Theta}_1$ and $\tilde{\Theta}_2$. After that, one needs to perform verification of the obtained matrices F and T . For matrix T it means that at resonant modes vector of estimations of the generalized coordinates $\hat{q} = Ty$ should be zero except for only one component corresponding to the resonance frequency excited. In order to verify matrix F one needs to ensure that each control loop excites only one corresponding eigenmode and does not excite the others even if the excitation have resonance frequency. That means in fact that the vector of control influences on modes $Q^c = \Theta_1 F \hat{Q}$ matches the vector of desired influences on modes \hat{Q} .

However, sometimes it can be difficult to carry out all the experiments at each of the n resonance frequencies, especially if the number of sensors and actuators is redundant. Moreover, difficulties can occur with inverting of the experimentally obtained matrices. So let us assume that we want to limit ourselves to controlling independently only the first k eigenmodes of the object. Consider an algorithm of gradual increasing the number of eigenmodes used to control the system, or gradual optimization algorithm, for the mode synthesizer F . For the mode analyzer T this procedure is similar.

So, it is necessary that each column of the matrix F (denote them as F_i) is orthogonal to each row of the matrix $\tilde{\Theta}_1$ (denote them as θ_i) except for one row with the same number. Then the following condition will be met (6):

$$\tilde{\Theta}_1 F = D_1,$$

where D_1 is a diagonal matrix.

At the first step we want to control only the first eigenmode of the beam, and we are looking for only the first column of the mode synthesizer matrix F_1 . The other columns are zero. Experiments at the first resonance frequency give the first row of the influence matrix θ_1 . Vector F_1 is found from the condition of maximum correspondence to the vector θ_1 . This means that the first control loop have the maximum influence at the first eigenmode:

$$\max \theta_1^T F_1 \tag{13}$$

In addition, the normalization condition for the vector F_1 should be satisfied:

$$F_1^T F_1 = 1 \tag{14}$$

The method of Lagrange multipliers for this problem gives the following result:

$$J = \theta_1^T F_1 - \lambda(F_1^T F_1 - 1) \tag{15}$$

$$\frac{\partial J}{\partial F_1} = \theta_1 - \lambda F_1 = 0 \quad (16)$$

Then,

$$F_1 = \frac{1}{\lambda} \theta_1, \quad \lambda^2 = \theta_1^T \theta_1 \quad (17)$$

At the second step of the algorithm the first and the second columns of matrix F are calculated. In order to do this the first and the second rows of matrix $\tilde{\Theta}_1$ are obtained experimentally. Along with the conditions of maximum correspondence and normalization there are two orthogonality conditions: the first control loop should not excite the second eigenmode, while the second one should not excite the first mode. All this requirements have the following form:

$$\max \theta_1^T F_1, \max \theta_2^T F_2; \quad F_1^T F_1 = 1, F_2^T F_2 = 1; \quad \theta_2^T F_1 = 0, \theta_1^T F_2 = 0 \quad (18)$$

For the first column F_1 we obtain the following equations:

$$J = \theta_1^T F_1 - \lambda_1 (F_1^T F_1 - 1) - \lambda_2 \theta_2^T F_1; \quad \frac{\partial J}{\partial F_1} = \theta_1 - \lambda_1 F_1 - \lambda_2 \theta_2 = 0 \quad (19)$$

Then,

$$F_1 = \frac{1}{\lambda_1} \theta_1 - \frac{\lambda_2}{\lambda_1} \theta_2, \quad \lambda_2 = \frac{\theta_2^T \theta_1}{\theta_2^T \theta_2}, \quad \lambda_1^2 = \theta_1^T \theta_1 - \frac{(\theta_2^T \theta_1)^2}{\theta_2^T \theta_2} \quad (20)$$

For the second column F_2 the result is analogous:

$$F_2 = \frac{1}{\hat{\lambda}_1} \theta_2 - \frac{\hat{\lambda}_2}{\hat{\lambda}_1} \theta_1, \quad \hat{\lambda}_2 = \frac{\theta_1^T \theta_2}{\theta_1^T \theta_1}, \quad \hat{\lambda}_1^2 = \theta_2^T \theta_2 - \frac{(\theta_1^T \theta_2)^2}{\theta_1^T \theta_1} \quad (21)$$

Thus, the same procedure can be repeated for the next steps of the algorithm up to the n -th step. At k -th step for each vector F_i the conditions of maximum correspondence and normalization are formulated along with $k - 1$ conditions of orthogonality. This algorithm allows one to carry out the identification without any mathematical model of the object getting all necessary data from the certain limited number of experiments.

4 Experimental set-up

A control object is an aluminium beam 70 cm long with the cross-section 3×35 mm. It is disposed vertically and fixed at one point at the distance of 10 cm from the lower end. The external loading is a base excitation applied by means of a piezoelectric stack actuator which is a part of the fixation construction as it is shown in *figure 2*. The stack actuator **A** is connected to the beam through a flexible plate **B**. It allows the fixation point to move in single direction along the stack and prohibits to move in other directions. Through this plate two screws **C** and **D** at the top and the bottom of the stack actuator perceive the weight of the beam releasing the actuator itself from this weight. Longitudinal vibrations of the actuator cause bending vibration of the beam.

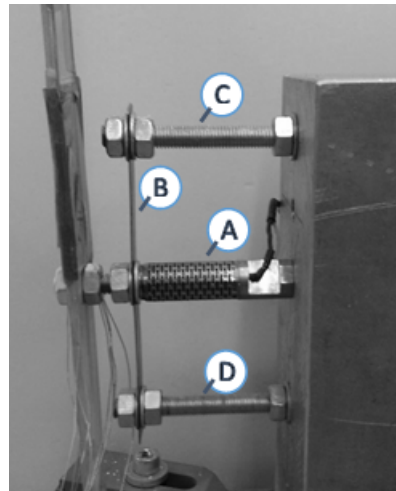


Fig.2. The fixation construction of the beam

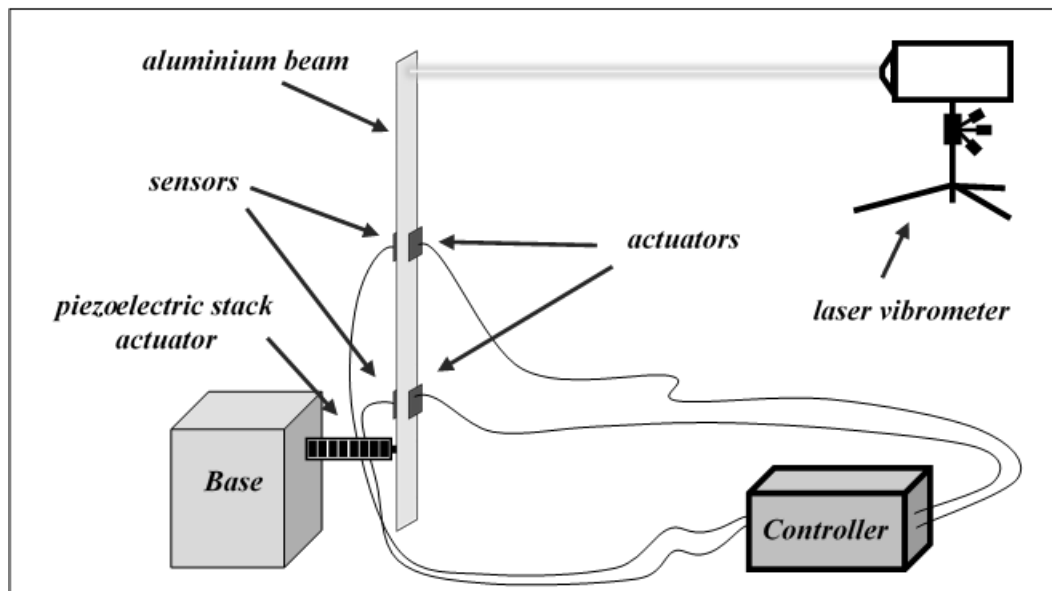


Fig.3. The scheme of the experiment

The control system includes two piezoelectric sensors and two actuators attached in pairs to the beam as it is shown in *figure 3*. Once attached, they keep the same positions for all the control systems created. The actuators change the curvature of the beam depending on the control signal applied, while the sensors measure this curvature as the beam vibrates [8,9]. Actuators and sensors are connected through a controller.

The purpose of the control system is to suppress forced resonance vibrations of the beam with the first and the second resonance frequencies. These frequencies correspond to the first and the second bending modes of the beam. Therefore, sensors and actuators are attached to special locations on the beam, so that they can most efficiently measure and influence these particular modes.

In order to design local and modal control systems with the best performance frequency methods of the Automatic Control Theory are used. To monitor the efficiency of the control systems obtained the vibration amplitude of the upper endpoint

of the beam is measured by the laser vibrometer. This choice is caused by the fact that the vibration amplitude of this point is the greatest one among all points of the beam for the vibration modes under consideration.

To work with the highest efficiency the piezoelectric sensors and actuators should be placed at the areas where the curvature of the modes to be controlled takes the maximum values. In order to satisfy this condition the first and the second bending modes of the beam are analyzed theoretically and experimentally (*figure 4*).

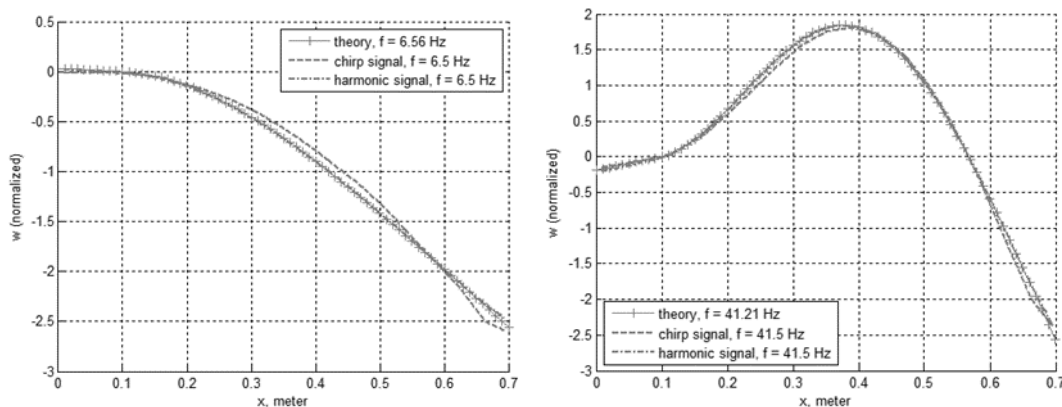


Fig.4. The first and the second bending modes of the beam

As a result, the location of the first pair of piezoelectric patches was defined to be near to the fixation point ($10.5\text{cm} \leq x \leq 16.5\text{cm}$), and the second pair was placed not far from the beam center ($37.5\text{cm} \leq x \leq 43.5\text{cm}$).

5 Local control system

The working scheme of the controller for the local control system is shown in *figure 5*. Here y_1 and y_2 mean the signals measured by the sensors, while u_1 and u_2 are the control signals being sent to the actuators. In order to design such a system one needs to determine transfer functions $R_1(s)$ and $R_2(s)$, which establish the relation between measured and control signals.

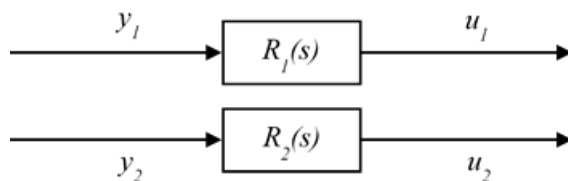


Fig.5. The scheme of the controller for the local control system

To design the transfer functions for the controller the logarithmic characteristics of the open-loop system are analyzed. The transfer function for each control loop is chosen in order to provide the most effective vibration suppression at the first and the second resonance frequencies of the beam. At the same time, special attention is paid to ensure stability of the systems obtained.

As a result two most effective local control systems were created. The first system shows the optimal performance at the first resonance frequency, while the second

one gives the best result at the second resonance. Frequency response functions in the vicinity of the first and the second resonance frequencies measured for the upper point of the beam are shown in *figure 6* for the first and the second local control systems, respectively. The black curve represents the uncontrolled system while the other curves correspond to the different gain values in control loops.

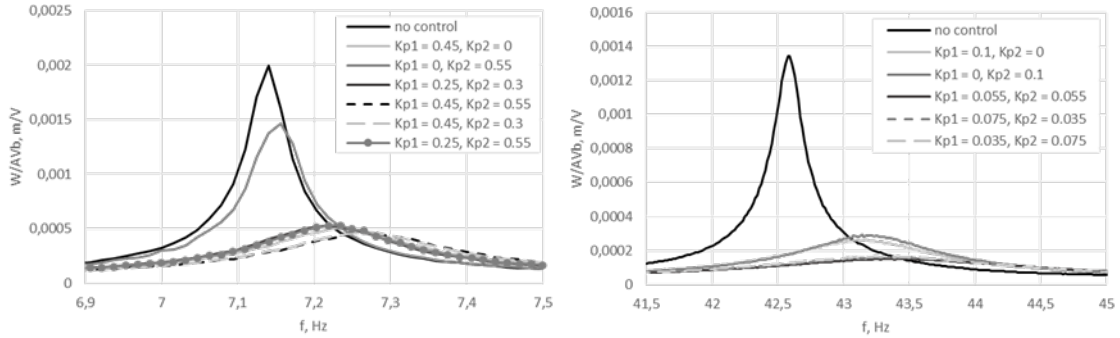


Fig.6. FRF of the local system #1 at the first resonance and the local system #2 at the second resonance

The first control system is effective at the first resonance, providing the decrease of the vibration amplitude by 77% (using gain values $K_p^{(1)} = 0.45$, $K_p^{(2)} = 0.55$), but it fails to suppress the second resonance. On the contrary, the second system has great performance at the second resonance (reduction of the amplitude is 88% with gain values $K_p^{(1)} = K_p^{(2)} = 0.055$), but at the first resonance it is not so good (only 45% reduction). The attempts to create a local system that could suppress both resonances with good efficiency were not successful.

6 Modal control system

The scheme of the controller for the modal or biomorphic control system is shown in *figure 7*. As before, y_1 and y_2 are the measured signals, while u_1 and u_2 are the control signals. In the control system all the sensors measure and all the actuators affect both first and second vibration modes of the beam, therefore the mode analyzer T and the mode synthesizer F are used to perform a linear transformation of signals in order to separate the modes. To design a modal system one needs to define these matrices and to determine the transfer functions $R_1(s)$ and $R_2(s)$.

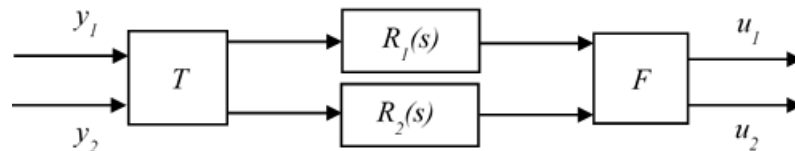


Fig.7. The scheme of the controller for the modal control system

At the first stage of creating a modal system mode analyzer T and synthesizer F are to be specified properly. As a result of this work, two requirements should be observed: the first control loop should not affect and react to the activation of the second bending mode of the beam, and the second one should not affect and

react to the activation of the first mode. The matrices T and F are first evaluated theoretically based on the known mode shapes and the measured frequency response functions of the control object. It is known that first and the second actuator excite the first mode in the ratio of approximately 3 to 1 with the same sign, and they excite the second mode in the ratio of 1 to 1 with the opposite sign. The same can be said about the sensors. Therefore, the influence matrix $\tilde{\Theta}_1$ and the measurement matrix $\tilde{\Theta}_2$ are estimated as follows:

$$\tilde{\Theta}_1^{(th)} = \left(\tilde{\Theta}_2^{(th)} \right)^T = \begin{pmatrix} 0.75 & 0.25 \\ -0.5 & 0.5 \end{pmatrix} \quad (22)$$

Consequently, an estimation for matrices T and F is calculated according to the formulas (8) and (11):

$$F^{(th)} = \left(\tilde{\Theta}_1^{(th)} \right)^{-1} = \begin{pmatrix} 1 & -0.5 \\ 1 & 1.5 \end{pmatrix}, \quad T^{(th)} = \left(\tilde{\Theta}_2^{(th)} \right)^{-1} = \begin{pmatrix} 1 & 1 \\ -0.5 & 1.5 \end{pmatrix} \quad (23)$$

Then, the matrices are to be specified more precisely by performing a set of additional experiments. Matrices $\tilde{\Theta}_1$ and $\tilde{\Theta}_2$ are defined experimentally:

$$\tilde{\Theta}_1^{(exp)} = \begin{pmatrix} 0.76 & 0.25 \\ -0.52 & 0.49 \end{pmatrix}, \quad \tilde{\Theta}_2^{(exp)} = \begin{pmatrix} 0.76 & -0.51 \\ 0.24 & 0.49 \end{pmatrix} \quad (24)$$

Thus, matrices T and F have the following form:

$$F = \left(\tilde{\Theta}_1^{(exp)} \right)^{-1} = \begin{pmatrix} 0.98 & -0.49 \\ 1.02 & 1.51 \end{pmatrix}, \quad T = \left(\tilde{\Theta}_2^{(exp)} \right)^{-1} = \begin{pmatrix} 0.99 & 1.03 \\ -0.49 & 1.53 \end{pmatrix} \quad (25)$$

Then the transfer functions are designed in order to provide the optimal performance of each modal control loop at the corresponding resonance frequency. The efficiency of the control systems obtained is limited by the requirement of their stability.

Frequency response functions in the vicinity of the first and the second resonance frequencies measured for the upper point of the beam for the created modal control system are shown in *figure 8*. The black curve represents the uncontrolled system while the other curves correspond to the different gain values in control loops.

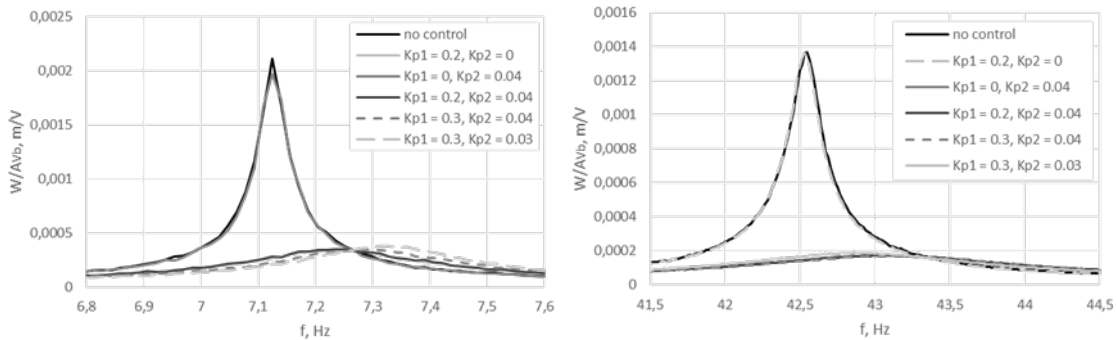


Fig.8. FRF of the modal system at the first and the second resonances

The graphs show that the modal system is very effective at both resonance frequencies, providing the reduction of the vibration amplitudes by 84% and 87%, respectively (the gain values in the control loops are $K_p^{(1)} = 0.2$ and $K_p^{(2)} = 0.04$).

7 Conclusions

The present research highlights application of the local and the modal or biomorphic approaches to active vibration control of continuous elastic systems. Firstly, it focuses on the problem of identification within the modal approach. This identification means the correct calculation of mode analyzer and mode synthesizer matrices. The algorithm of gradual optimization has been proposed, which allows one to control only the needed number of eigenmodes of the object.

Secondly, local and modal approaches were compared experimentally for the problem of suppression of bending vibrations of a thin metal beam. For both methods under consideration efficient control systems have been created. However, the local system failed to suppress efficiently vibrations at both resonances, showing the optimal performance either at the first or at the second resonance frequency. On the contrary, the modal system succeeded in reducing vibrations at both resonance frequencies efficiently. Thus, the advantage of the modal approach over the local one has been demonstrated for the cases where it is necessary to suppress vibrations in the frequency range containing multiple resonance frequencies of the control object. The result obtained can be explained by the fact that, in contrast to the local one, in the modal system each control loop corresponds to a particular vibration mode and can be designed to provide optimal performance at the corresponding resonance frequency.

Further investigation is devoted to development of the modal method and its generalization to a wider class of mechanical systems and different types of control elements. Further experimental study is aimed at implementing the modal approach and comparing it with the local one for systems with larger number of sensors and actuators. In addition, the problems of interest are to develop the methods of automatic identification and to modify the methods of biomorphic control in order to improve stability and robustness of modal control systems.

References

- [1] G.E. Stavroulakis, G. Foutsitzi, E. Hadjigeorgiou, D. Marinova, C.C. Baniotopoulos, Design and robust optimal control of smart beams with application on vibrations suppression // *Advances in Engineering Software* 36 (2005) 806—813
- [2] W. Shia, M. Alsarheed, E. Schuster, M.L. Walker, J. Leuer, D.A. Humphreys, D.A. Gates, Multivariable model-based shape control for the National Spherical Torus Experiment (NSTX) // *Fusion Engineering and Design* 86 (2011) 1107—1111
- [3] G.E. Stavroulakis, D.G. Marinova, E. Hadjigeorgiou, G. Foutsitzi, C.C. Baniotopoulos, Robust active control against wind-induced structural vibrations *J. Wind Eng. Ind. Aerodyn.* 94 (2006) 895—907
- [4] N.R. Fisco, H. Adeli, Smart structures: Part II — Hybrid control systems and control strategies // *Scientia Iranica, Transactions A: Civil Engineering* 18 (2011) 285—295

- [5] I. Kucuk, et al., Optimal control of a distributed parameter system with applications to beam vibrations using piezoelectric actuators, *Journal of the Franklin Institute*. (2012), <http://dx.doi.org/10.1016/j.jfranklin.2012.10.008>
- [6] L.A. Gould and M.A. Murray–Lasso. On the modal control of distributed parameter systems with distributed feedback. In *Transactions on Automatic Control*, volume 11, page 79. IEEE, 1966.
- [7] A.K. Belyaev, V.V. Kotov, V.A. Polyanskiy, N.A. Smirnova, Biomorphic control in problem on active suppression of vibrations (in russian), *Vestnik St. Petersburg University: Mathematics, Mechanics, Astronomy*, 1, 96–106 (2014)
- [8] H. Irschik, M. Krommer, A.K. Belyaev, K. Schlacher. Shaping of piezoelectric sensors/actuators for vibrations of slender beams: coupled theory and inappropriate shape functions // *Journal of intelligent materials, systems and structures*, Vol. 9 — July 1998.
- [9] M. Krommer, H. Irschik. An electromechanically coupled theory for piezoelectric beams taking into account the charge equation of electrostatics // *Acta Mechanica*. Springer-Verlag. 2002. P.141-158.

A.V. Fedotov, Tipanova str. 4, Saint-Petersburg, Russia
Institute of Problems of Mechanical Engineering, V.O., Bolshoj pr. 61, St. Petersburg, Russia

Energy aspects of axisymmetric wave propagation in an infinite cylindrical shell filled with the liquid.

George V. Filippenko
g.filippenko@gmail.com, g.filippenko@spbu.ru

Abstract

The problem of oscillations of the systems containing pipelines filled with the liquid is one of the actual problems of modern techniques. It is important to estimate the parameters of vibrations and acoustical fields of such objects in order to provide the construction from damaging, but calculation of these complicated systems demands major computing resources. Therefore the consideration of simple model problems which have exact analytical solution ([1] - [5]) is actual. On these models it is possible to analytically explore main effects and also to use them as the test problems for computing packages.

The problem of joint oscillations of infinite thin cylindrical shell with ideal acoustical fluid inside it is considered. The propagating waves and energy flux are analyzed in the system shell-liquid. The comparison of different mechanisms of energy transmission in the shell and input of the energy flux in the water is fulfilled.

1 Statement of the problem

Let us start considering an infinite cylindrical shell filled with an ideal compressible liquid, where the acoustic pressure $P(x, y, z)$ is described by the Helmholtz equation in the cylindrical system of coordinates where the axis Oz coincides with axis of the cylinder (see fig. 1). All processes are supposed to be harmonic with frequency ω and independent from angle φ .

$$(\Delta + k^2)P(r, z) = 0, \quad \text{where } k = \omega/c, \quad 0 < r < R. \quad (1)$$

The factor $e^{-i\omega t}$ describes the time-dependence and is omitted. The liquid is supposed to be ideal and compressible. The density is ρ_w , the velocity of sound is equal to c .

Two relations take place on the shell – fluid boundary: kinematic (the adhesion condition)

$$u_n(R, z) = \frac{1}{\rho_w \omega^2} \left. \frac{\partial P(r, z)}{\partial r} \right|_{r=R}; \quad (2)$$

and dynamic (balance of forces acting on the shell)

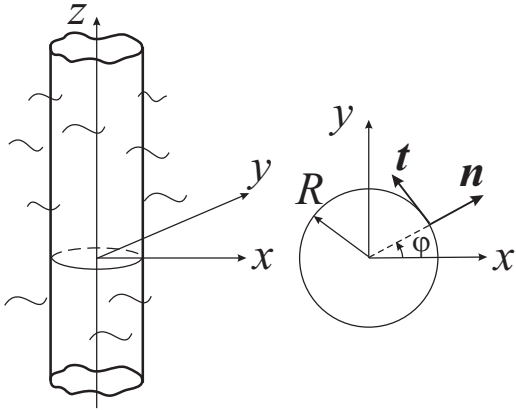


Figure 1: Physical Model

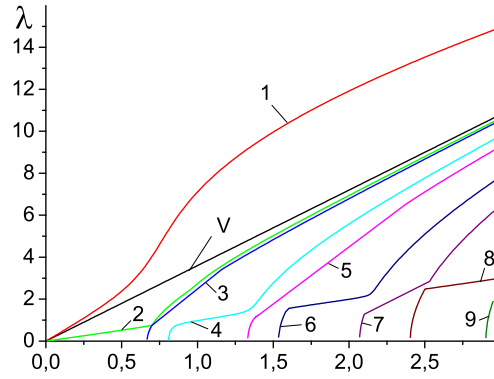


Figure 2: Dispersion curves 1-9

$$\frac{\rho c_s^2}{R^2} \mathbf{L} \vec{u} = (0, P)^t. \quad (3)$$

Here following notations are introduced: $\vec{u} = (u_z, u_n)^t$ (t is a badge of transposing) is the displacement vector of the shell, \mathbf{L} is matrix differential operator of the cylindrical shell of Kirchhoff–Love type

$$\mathbf{L} \equiv [L_{ij}] = w^2 \mathbf{I} + \tilde{\mathbf{L}}, \quad i, j = 1, 2.$$

The following notations are also used: \mathbf{I} is the unit matrix operator, \mathbf{L} and $\tilde{\mathbf{L}}$ are matrix differential operators. All these operators are represented by the matrixes 2×2 . In particular the elements of $\tilde{\mathbf{L}}$ are as follows:

$$\tilde{\mathbf{L}} = \begin{pmatrix} \tilde{\partial}_z^2 & \nu \tilde{\partial}_z \\ -\nu \tilde{\partial}_z & \alpha^2 (2\nu \tilde{\partial}_z^2 - \tilde{\partial}_z^4 - 1) - 1 \end{pmatrix}, \quad (4)$$

where $\tilde{\partial}_z = R \partial_z$. Here the following geometrical parameters of the shell are used: R is radius, h is thickness. Properties of a material of the cylinder are characterized by E , ν and ρ_s – Young’s module, Poisson coefficient and volumetric density accordingly.

The surface density of the shell ρ ($\rho = \rho_s h$) and the velocity of median surface deformation waves of the cylindrical shell c_s are introduced $c_s = \sqrt{E/(1-\nu^2)\rho_s}$.

The following dimensionless parameters are put in: $\alpha^2 = \frac{1}{12} \left(\frac{h}{R}\right)^2$ (the relative thickness of the cylindrical shell) and $w = \omega R / c_s$ (the dimensionless frequency).

The source of an acoustic field in a wave guide is the vibrations of the cylinder shell, caused by the incident wave propagating from infinite part of the shell. The frequency of this incident harmonic wave is equal to ω . All processes in the system shell – liquid are supposed to be harmonic with this frequency.

2 Determination of the general representation for acoustic and vibrational fields

The exact expression for displacements of the shell can be derived only after defining a field in the medium. So we come to the boundary problem with the Helmholtz equation. Further it is more convenient to involve the new vector $(u_z, P)^T$

$$\begin{pmatrix} u_z \\ u_n \\ P \end{pmatrix} = \mathbf{M} \begin{pmatrix} u_z \\ P \end{pmatrix}, \quad \text{where} \quad \mathbf{M} = \begin{pmatrix} 1 & 0 \\ 0 & \frac{1}{\rho_w \omega^2} \frac{\partial}{\partial r} \Big|_{r=R} \end{pmatrix}, \quad (5)$$

then the equation (3) can be rewritten in the form

$$\mathbf{S} \begin{pmatrix} u_z \\ P \end{pmatrix} = \begin{pmatrix} 0 \\ 0 \end{pmatrix} \equiv \mathbf{0}, \quad \text{where} \quad \mathbf{S} = \mathbf{L}\mathbf{M} - \mathbf{N}, \quad \mathbf{N} = \frac{w^2}{\rho \omega^2} \begin{pmatrix} 0 & 0 \\ 0 & 1 \end{pmatrix} \quad (6)$$

The solution of the equation (3) is searching in the form

$$\begin{pmatrix} u_z \\ P \end{pmatrix} = A e^{i\lambda z} \begin{pmatrix} \xi \\ \gamma J_0(r\sqrt{k^2 - \lambda^2}) \end{pmatrix}, \quad (7)$$

believing that $|\xi|^2 + |\gamma|^2 = 1$. Here following notations are introduced: J_0 is Bessel function with index 0, and A, ξ, γ are arbitrary constants, λ is the the wavenumber which we are looking for. It can be noted that if $k < \lambda$ then Bessel function J_0 is converted to I_0 function.

After substituting (7) into (3) the following algebraic system is obtained

$$\widehat{\mathbf{S}}\mathbf{x} = \mathbf{0}, \quad \text{where} \quad \mathbf{x} = (\xi, \gamma)^T \quad (8)$$

Operator $\widehat{\mathbf{S}}$ is the Fourier image of operator \mathbf{S} . The dispersion equation is obtained from the condition of existence of nontrivial solution of this system

$$\det \widehat{\mathbf{S}} = 0 \quad (9)$$

We are looking for real positive solutions of this equation. If the corresponding set of wavenumbers is founded one can solve the equation (8) and define the previously unknown constants ξ, γ . After defining constants, the complete solution of the problem in terms of displacements of the shell $\vec{u}(z)$ and pressure $P(r, z)$ in the liquid is determined.

3 Energy streams in the system shell-liquid

As it was mentioned above all processes in the liquid and shell are supposed to be harmonic with frequency ω . It is convenient to average the energy streams on period

of oscillations $T = 2\pi/\omega$. The integral energy stream Υ_{liq} in the liquid along axes z through the cross-section of the cylinder can be written in the form

$$\Upsilon_{\text{liq}} = \frac{\omega}{2} \frac{1}{2\rho\omega} \int_0^{2\pi} d\varphi \int_0^R \text{Im} \left(\bar{P} \frac{\partial P}{\partial z} \right) r dr. \quad (10)$$

The integral stream of the energy along axes z through the cross-section of the cylinder shell has a view

$$\Upsilon_{\text{cyl}} = \frac{\omega}{2} \int_0^{2\pi} \text{Im} \left(\vec{u}^3, \vec{f}^3 \right)_{\mathbf{C}^3} R d\varphi = \Upsilon_{\text{cyl}}^z + \Upsilon_{\text{cyl}}^n + \Upsilon_{\text{cyl}}^m, \quad \text{where} \quad (11)$$

$$\vec{f}^3 = \mathbf{F} \vec{u}^3 = \begin{pmatrix} f_z \\ f_n \\ f_p \end{pmatrix}, \quad \mathbf{F} = \frac{\rho c^2}{R} \begin{pmatrix} \tilde{\partial}_z & \nu & 0 \\ 0 & -\nu & -\tilde{\partial}_z \\ 0 & 0 & \nu - \tilde{\partial}_z^2 \end{pmatrix}$$

$$\vec{u}^3 = \begin{pmatrix} u_z \\ u_n \\ -\tilde{\partial}_z u_n \end{pmatrix}, \quad \left\{ \begin{array}{l} \Upsilon_{\text{cyl}}^z \\ \Upsilon_{\text{cyl}}^n \\ \Upsilon_{\text{cyl}}^m \end{array} \right\} = -\pi R \omega \text{Im} \left\{ \begin{array}{l} \bar{u}_z (\tilde{\partial}_z u_z + \nu \bar{u}_n) \\ -\nu \bar{u}_n u_n + \bar{u}_n \tilde{\partial}_z^2 u_n \\ \tilde{\partial}_z \bar{u}_n (\nu \tilde{\partial}_z u_n - \tilde{\partial}_z u_n) \end{array} \right\} \quad (12)$$

4 Numerical calculations

The formula (11) can be used for obtaining the normalized energy stream Π in the shell and its components $\Pi = \Upsilon_{\text{cyl}} / (\Upsilon_{\text{cyl}} + \Upsilon_{\text{liq}})$, $\Pi^{z,n,m} = \Upsilon_{\text{cyl}}^{z,n,m} / (\Upsilon_{\text{cyl}} + \Upsilon_{\text{liq}})$. On figures the curves corresponding Π, Π^z, Π^n, Π^m are marked by letters S, Z, N, M . The pressure P and vectors of generalized displacements \vec{u}^3 and forces \vec{f}^3 are also normalized: $P := P/|P|$, $\vec{u}^3 := \vec{u}^3/|\vec{u}^3|$, $\vec{f}^3 := \vec{f}^3/|\vec{f}^3|$. On figures the curves corresponding components vectors \vec{u}^3, \vec{f}^3 (12) are marked by letters Z, N, M .

The following values of parameters of the system are assumed for calculations $\nu=0.3$, $c_s/c=3.6$, $\rho_s/\rho_w=7.8$, $h/R=0.05$ that corresponds to interaction of water with shell made of steel.

On fig.2 the dependence of dimensionless wavenumber $\lambda := \lambda R$ with respect to nondimensional frequency w is shown for the first nine dispersion curves (these curves are marked by numbers 1-9). The multiple veering (quasiintersection) of these curves is well noted. It is caused by interaction of the two waveguides (liquid and cylindrical shell).

The behavior of the wave from the first dispersion branch differs from others significantly. On figure 3a and 3b is well seen that wave energy flux from the first dispersion branch is significant in more wide diapason of frequencies. The banding component in energy flux is dominated in it (fig. 4a,b).

The veering of the dispersion curves is well corresponds with the changing of the specific weight of different components of the energy flux (fig. 2 and fig.4).

Energy aspects of axisymmetric wave propagation in an infinite cylindrical shell filled with the liquid.

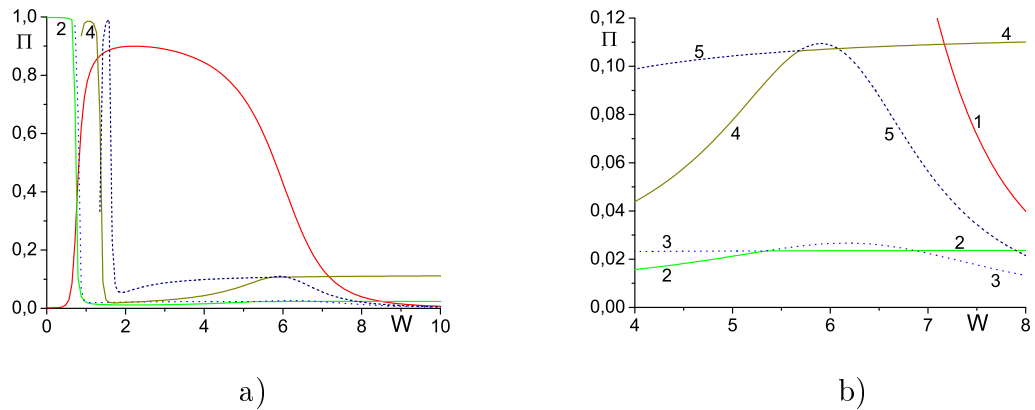


Figure 3: Normalized energy flux of the waves in the shell from first five dispersion branches (curves 1-5)(a); in greater scale (b)

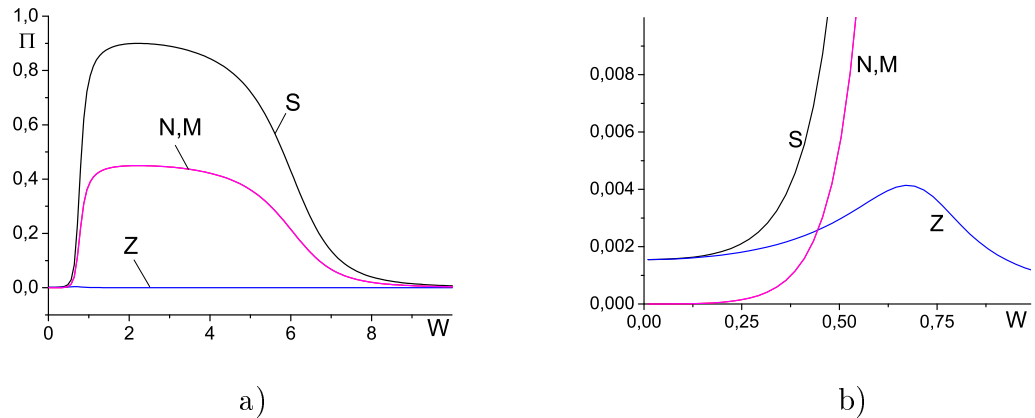


Figure 4: Energy fluxes in the shell for the wave from the first dispersion branch (a); in greater scale (b).

Pressure and energy flux in the wave from first dispersion curve are concentrated near the shell surface (curves 1a, 1b, 1c on fig. 5 and curve 1 on fig. 6). This dependence is most distinctive in the diapason of frequencies where the velocity of the waves in the shell is less than in the liquid infinite space. Unlike it the pressure and energy flux in the liquid in next dispersion branches are concentrated near the center of the cross section of the cylinder (curves 2a, 2b, 2c on fig. 5 and curves 2-7 on fig. 6). The general tendency is increasing of the role of the center part of the cross section for propagating of the energy in the system via increasing of the branch number or frequency increasing.

Even and odd branches (since second branch) have different behavior near the shell surface (fig. 6). While pressure and energy flux of even branches are near zero (dotted lines), the normal component of displacement vector is near zero for the odd branches (dashed lines). It corresponds to the wave guide with free and rigid surface correspondingly. But this dependence can be changed to opposite (fig.3b) due to the veering of the dispersion curves (fig.2).

Another speciality is that energy flux in even branches (corresponding to the "free surface") is stabilized on high frequencies (fig. 3b).

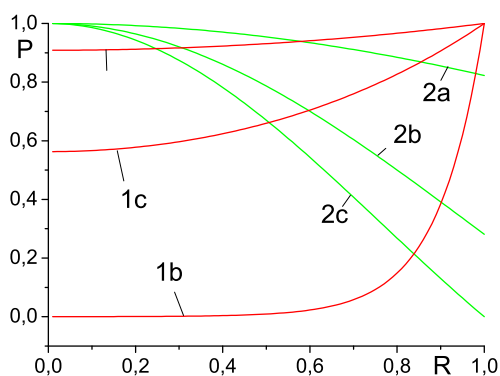


Figure 5: Pressure in the waves via radius from two first dispersion branches (1a,2a - $w=0.25$, 1b,2b - $w=2.5$, 1c,2c - $w=10.0$)

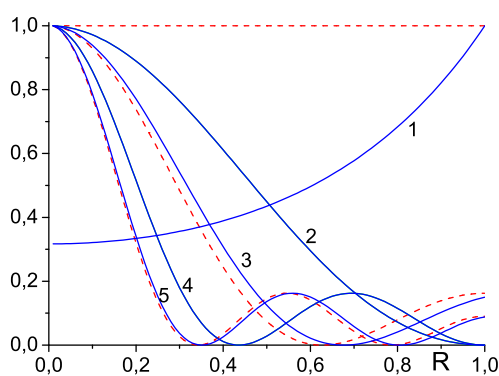


Figure 6: Energy flux of the waves from first seven dispersion branches via radius for $w=10.0$ (curves 1-5)

Acknowledgements

The author is deeply grateful to Prof. D.P.Kouzov for the inspiration.

References

- [1] Filippenko G.V., 2011, The energy analysis of shell-fluid interaction, *Proc. of the International Conference "Days on Diffraction 2011"*, May 30 – June 3, St.Petersburg, Russia., pp. 63–66.
- [2] Filippenko G.V., Energy aspects of axysymmetrical waves propogation in the infinite cylindrical shell fully submerged in to the liquid. *Vycisl. meh. splos. sred - Computational Continuum Mechanics*, 2013, vol. 6, no. 2, pp. 187-197.
- [3] Filippenko G.V. Energy aspects of wave propagation in an infinite cylindrical shell fully submerged in liquid. *Vycisl. meh. splos. sred - Computational Continuum Mechanics*, 2014, vol. 7, no. 3, pp. 295-305
- [4] Filippenko G.V. Analyzing of energy fluxes in the infinite cylindrical shell contacting with compressible liquid. *Proc. of the Conference "XXVII session of Russian Acoustical Society"*, 16-18 April 2014, St.-Petersburg, Russia, <http://rao.akin.ru/Rao/sess27/proceedings27.htm>
- [5] Ter-Akopyants G.L. Axisymmetrical wave processes in cylindrical shells filled with fluid. *Estestvennye-i-tehnicheskie-nauki (Natural and engineering science)*, 2015, e7 (85), pp.10-14, ISSN: 1684-2626.

Institute of Mechanical Engineering of RAS, Vasilievsky Ostrov, Bolshoy Prospect 61, St.Petersburg, 199178, Russia, g.filippenko@gmail.com

REFERENCES

Saint Petersburg State University, 7-9, Universitetskaya nab., St.Petersburg, 199034, Russia, g.filippenko@spbu.ru

Comparison of numerical approaches for inverse Laplace transform by the example of intraocular pressure determination

Kseniia P. Frolova, Elena N. Vilchevskaya, Wolfgang H. Müller, Wolf Weiss

kspfrolova@gmail.com

Abstract

The modification of existing human eye models and the creation of new ones, which take into account an increasing number of sclera parameters, allow ophthalmologists to correct disorders of the eye created by trauma, disease, or aging more rationally and qualitatively. The viscosity of the sclera is ignored in most existing models. The reason is that direct measurements of the sclera viscosity cause technical problems. However, the sclera has viscoelastic properties [1]. This paper investigates a method for determining the shear viscosity of the sclera based on a comparison of results from mathematical modeling with experimental data from discrete measurements of the IntraOcular Pressure (IOP) during several minutes after intravitreal injection (injection into the eyeball aqueous humor) [2]. We propose to find the time-dependent IOP by applying Laplace transforms. In the present case a numerical inverse Laplace transform is required. Several approximation criteria can be applied based on the numerical approach [3], [4], [5]. The main idea of this paper is to present a comparison of numerical approaches based on three different sets of nodes and weights for a quadrature formula for the inverse Laplace transform by the example of IOP determination.

1 Introduction

Healthy human eyes are roughly spherical, filled with a transparent gel-like substance called the aqueous or vitreous humor. The eyeball consists of three concentric layers: A fibrous tunic, including the opaque part called sclera behind and the transparent part called cornea in front; a vascular pigmented tunic called choroid and a nervous tunic called retina [6] (see Fig. ??). The fibrous tunic performs a protection function and determines the eyeball shape. The sclera occupies 93% of the eyeball layers [7].

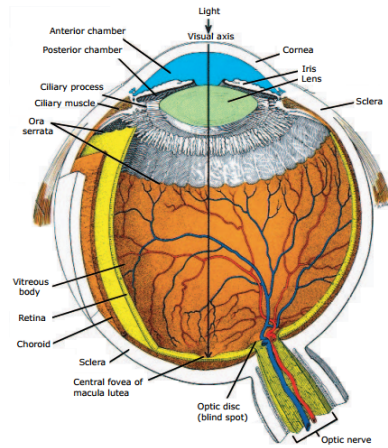


Figure 1: Schematic diagram of the human eye.

The biomechanical properties of the sclera play the leading role when determining the eyeball shape or the volume under IntraOcular Pressure (IOP). Therefore we will consider only the sclera during modeling of the eye behavior after intravitreal injection (injection into the eye, namely into the vitreous humor, near the retina at the back of the eye).

Experimental curves based on IOP measurements for several minutes after intravitreal injection show an increase of the IOP in form of a jump immediately after injection followed by steady decrease. Intraocular fluid outflow can be a reason for the reducing IOP. However, experience indicates that the sclera is a viscoelastic material [1]. Therefore one can explain a time-dependent IOP behavior also by an existing viscosity of the sclera. Direct measurements of sclera viscosity cause technical problems and so the viscosity of the sclera is ignored in most existing models. This paper presents a method for determining the shear viscosity of the sclera based on a comparison between results from mathematical modeling and experimental data of discrete IOP measurements during several minutes after intravitreal injection [2]. Moreover, this work investigates the underlying system of equations with two types of boundary conditions. In the first case we suppose that the eyeball volume does not change during the time of experiment. Therefore we explain the IOP reduction only by the viscous properties of the sclera. In the second case we take intraocular fluid outflow into account. Thus we explain the reducing IOP by both facts, the existing sclera viscosity and the existing intraocular fluid outflow.

The considered solution is based on the Laplace transform approach. We have to apply an inverse Laplace transform in order to determine the sclera displacement and the IOP. Because the mathematical expressions are complicated we apply a numerical approach. Several approximation criteria can be applied as a basis of the numerical inverse Laplace transform. Of particular interest is a comparison of results based on the well-known Zakian's technique [3], [4] and on a numerical approach offered by Jeffreson and Chow [5].

2 Problem statement and governing equations

The experiment we are going to describe is based on discrete measurements of the IOP for several minutes after an intravitreal injection equal to 0.05 ml. The IOP is defined as the difference between the pressure inside the eye and the atmospheric pressure. The experimental curve showing the IOP dependence on time is shown in Fig. 2 (obtained by Kotlyar, Bauer, and Plange [2]). Points on the graph correspond

to average IOP values ($n = 34$ patients took part in the experiment). The red line shows the average IOP of vaccinated eyes, the green line corresponds to an IOP control based on measurements of IOP of the second eye in a pair, which was not vaccinated. So far as we are going to use the Pascal (Pa) unit to express the IOP in the framework of this paper we would like to note that $1 \text{ mm Hg} = 133.322 \text{ Pa}$.

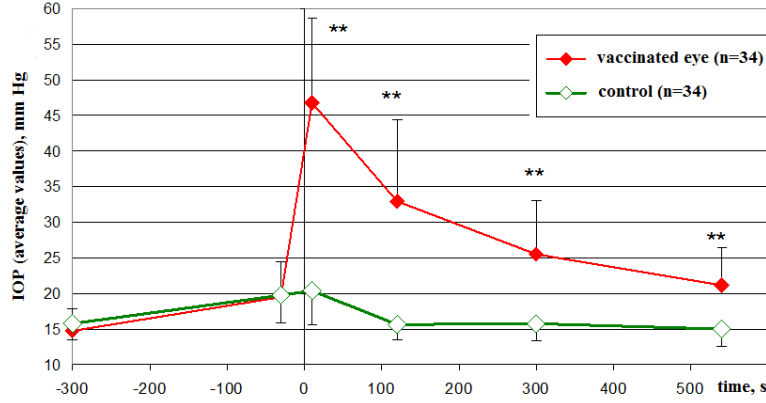


Figure 2: Time dependence of IOP: experimental curve.

In order to model the observed IOP reduction we consider a viscoelastic spherical layer of inner radius R_i and outer radius R_o under a centrally symmetric load: an external pressure is absent, the displacement of the inner boundary is specified and takes the intravitreal injection volume into account. We suppose the material of human sclera to be linear transversally isotropic (the axis of symmetry coincides with the radial direction). The problem will be considered within the framework of 3D-dimensional linear viscoelastic theory. The equation of motion reduces to the following equilibrium equation in so far as we consider a quasi-static problem:

$$\nabla \cdot \boldsymbol{\sigma} = 0, \quad (1)$$

where $\boldsymbol{\sigma}$ is the stress tensor.

Linear viscoelastic theory allows us to consider the elastic and the viscous behavior of the sclera separately. We use a Kelvin-Voigt rheological model, which means that we add elastic and viscous stresses. Moreover, in order to find the solution, we restrict ourselves to only one unknown viscous parameter, the shear viscosity of the sclera, η , and ignore volume viscosity. The constitutive equations in this case read:

$$\boldsymbol{\sigma} = {}^4\mathbf{C} : \boldsymbol{\varepsilon} + 2\eta\dot{\boldsymbol{\varepsilon}}, \quad (2)$$

where \mathbf{C} is the fourth-order stiffness tensor [8], $\boldsymbol{\varepsilon}$ is the linear strain tensor, and \boldsymbol{e} is the strain tensor deviator. To rewrite the stiffness tensor by using elastic modules we use the ratios between coefficients of the stiffness tensor and technical constants named elastic modules which are shown in [9], p.79.

Due to the inherent radial symmetry only the radial component of displacement in spherical coordinates is different from zero. Shear strains and stresses are absent. All components of vectors and tensors depend only on the radial coordinate. In this

case we have only one equilibrium equation in coordinate form:

$$\frac{\partial \sigma_{rr}}{\partial r} + 2 \frac{\sigma_{rr} - \sigma_{\varphi\varphi}}{r} = 0. \quad (3)$$

The nonzero components of the strain tensor read:

$$\varepsilon_{rr} = \frac{du_r}{dr}, \quad \varepsilon_{\varphi\varphi} = \varepsilon_{\theta\theta} = \frac{u_r}{r}. \quad (4)$$

We define dimensionless quantities for (radial) position, $\beta = R_i/R_o \leq x = r/R_o \leq 1$, displacement, $u = u_r/R_o$, stress components, $\sigma_{ij \text{ dim}} = \sigma_{ij}/E_{\theta\theta}$ (where $\sigma_{ij}, E_{\theta\theta}$ are given in Pa unit), time, $\tau = E_{\theta\theta}t/\eta$ and Young's modulus, $\xi = E_{rr}/E_{\theta\theta}$, where E_{rr} is Young's modulus in radial direction, and $E_{\theta\theta}$ is Young's modulus for the isotropic plane. The equilibrium equation (3) can be rewritten by applying Eqns. (2), (4). In this case we obtain the following differential equation for the radial displacement:

$$\frac{\xi^2(1 - \nu_{\theta\varphi})}{\xi(1 - \nu_{\theta\varphi}) - 2\nu_{r\theta}^2} \left[\frac{\partial^2 u}{\partial x^2} + \frac{2}{x} \frac{\partial u}{\partial x} - \frac{2(1 - \nu_{r\theta})}{\xi(1 - \nu_{\theta\varphi})} \frac{u}{x^2} \right] + \frac{4}{3} \left[\frac{\partial^2 \dot{u}}{\partial x^2} + \frac{2}{x} \frac{\partial \dot{u}}{\partial x} - 2 \frac{\dot{u}}{x^2} \right] = 0, \quad (5)$$

where ν_{ij} refers to Poisson's ratios. Here the indices i and j represent the longitudinal and the transverse direction, respectively.

The IOP is the negative radial stress at the inside of the sclera: The outward normal of the inner boundary of a spherical layer is directed inside the body. The IOP tends to inflate the body. Therefore the dimensionless IOP reads: $IOP_{\text{dim}}(\tau) = -\sigma_{xx}(\tau)|_{x=\beta}$. By applying Eqns. (2), (4) we determine the dimensionless radial stress $\sigma_{xx}(\tau) = \sigma_{rr \text{ dim}}(\tau)$ as a function of displacement (6):

$$\sigma_{xx}(\tau) = \frac{2\nu_{r\theta}\xi}{\xi(1 - \nu_{\theta\varphi}) - 2\nu_{r\theta}^2} \frac{u}{x} + \frac{(1 - \nu_{\theta\varphi})\xi^2}{\xi(1 - \nu_{\theta\varphi}) - 2\nu_{r\theta}^2} \frac{\partial u}{\partial x} + \frac{4}{3} \left[\frac{\partial \dot{u}}{\partial x} - \frac{\dot{u}}{x} \right]. \quad (6)$$

Two types of boundary condition for the inner radius displacement are considered. In the first case we suppose that the eye volume, which consists of the intravitreal injection volume, ΔV , which is added inside the eye ($r < R_i$), and of the eyeball volume before loading, V_0^{eye} , is constant during the time of the experiment. Hence, the displacement of the inner boundary depends on the intravitreal injection volume as follows:

$$\sigma_{xx}(\tau)|_{x=1} = 0, \quad u(\tau)|_{x=\beta} = u_0 H(\tau), \quad (7)$$

where $u_0 \approx \Delta V/(4\pi R_o R_i^2)$, $H(\tau)$ is the Heaviside unit step function.

In the second case the displacement of the inner boundary is caused by the intraocular fluid hydrodynamics. In order to estimate the eyeball volume change based on intraocular fluid in- and outflow we apply the tonography method [10], [11] which uses the velocity associated with the volume change of the eyeball. The current eyeball volume is:

$$V(t) = V(0) + \int_{\tilde{t}=0}^{\tilde{t}=t} \dot{V}(\tilde{t}) d\tilde{t} = V_0^{eye} + \Delta V + \int_{\tilde{t}=0}^{\tilde{t}=t} \dot{V}(\tilde{t}) d\tilde{t}. \quad (8)$$

The change of the eyeball volume due to the intraocular fluid hydrodynamics is: $V(t) - V(0) = V(t) - V_0^{eye} - \Delta V = 4\pi R_{inj}^2 u_r(t)$, where $R_{inj} \approx \sqrt[3]{R_i^3 + 3\Delta V/(4\pi)}$. The boundary conditions in this case are:

$$\sigma_{xx}|_{x=1} = 0, u(t)|_{x=\beta} = u_0 + \frac{\int_{\tilde{t}=0}^{\tilde{t}=t} \dot{V}(\tilde{t}) d\tilde{t}}{4\pi R_2 R_{inj}^2}. \quad (9)$$

Further use of the dimensionless time in the equation system in combination with the second type of BC becomes difficult because of the time occurs in the integral as well.

In order to estimate $\int_{\tilde{t}=0}^{\tilde{t}=t} \dot{V}(\tilde{t}) d\tilde{t}$ we turn to the tonography method consisting in IOP measurement during the time when the cornea is loaded by a known weight [10], [11]. In the framework of this method it is assumed that the velocity of the eyeball volume change depends on the intraocular fluid hydrodynamics (intraocular fluid in- and outflow). Based on the method proposed by Lyubimov and colleagues [11] we estimate the integral in the BC for the inner radius by the following expression:

$$\int_{\tilde{t}=0}^{\tilde{t}=t} \dot{V}(\tilde{t}) d\tilde{t} = \int_{\tilde{t}=0}^{\tilde{t}=t} C(P_0 - P_{e0} - P(\tilde{t}) + P_e) d\tilde{t}, \quad (10)$$

where C is a parameter characterizing the ease of intraocular fluid outflow, P_e is an intraepislcleral veins pressure, the index "0" corresponds to the values characterizing the eye condition before the weight is applied. To obtain the function $P(t)$ authors of [11] took the entire time dependence of the IOP into account and applied an exponential approximation. They obtained that $P(t) = P_{st} + (P(0) - P_{st}) \exp(-t/\hat{\tau})$, where P_{st} is an intraocular pressure which would take place if the cornea is loaded during the infinite time, $P(0)$ is an initial intraocular pressure, $\hat{\tau}$ is a characteristic time of an intraocular pressure change. We use the following average values for the corresponding values for 10 patients given in [11]: $P_0 = 13.8$ mm Hg, $P_{e0} = 8$ mm Hg, $P_e = 9.25$ mm Hg, $P_{st} = 15.0$ mm Hg, $P(0) = 27.0$ mm Hg, $\hat{\tau} = 2.8$ min. We also calculated that $C = 0.0087$ mm³/(mm Hg · s) due to the value of $\hat{\tau}$ obtained by Ljubimov and colleagues and formulas describing the dependence between C and $\hat{\tau}$, which are given in [10].

3 Laplace transform approach and numerical approaches for inverse Laplace transform

We obtain expressions for the time-dependent displacement and the radial stress by applying its Laplace transform, which, in general, is defined by:

$$\bar{f}(x, s) = \int_0^{\infty} \exp(-s\tau) f(x, \tau) d\tau, \quad (11)$$

where s is a complex variable, $s = c + i\omega$, $c > s_0$

The advantage of this method is that differentiation is replaced by multiplication by the operator variable s : $\dot{f}(x, \tau) \rightarrow \int_0^\infty e^{-s\tau} \dot{f}(x, \tau) d\tau = s\bar{f}(x, s) - f(x, 0)$. The partial differential equation in space-time turns into an ordinary differential equation in space-Laplace-time. As initial condition for displacement we cannot use corresponding experimental data because they are not known (due to measurement problems). Therefore, we assume that at the initial moment the displacement depends linearly on the radial coordinate. Consequently, the partial differential equations (5), (6) become ordinary differential equations with derivatives with respect to the coordinate:

$$\left[\frac{\xi^2(1 - \nu_{\theta\varphi})}{\xi(1 - \nu_{\theta\varphi}) - 2\nu_{r\theta}^2} + \frac{4}{3}s \right] \left(\frac{\partial^2 \bar{u}}{\partial x^2} + \frac{2}{x} \frac{\partial \bar{u}}{\partial x} - 2 \frac{\bar{u}}{x^2} \right) - \frac{2\xi[1 - \nu_{r\theta} - \xi(1 - \nu_{\theta\varphi})]}{\xi(1 - \nu_{\theta\varphi}) - 2\nu_{r\theta}^2} \frac{\bar{u}}{x^2} = 0.$$

$$\bar{\sigma}_{xx} = \left[\frac{2\nu_{r\theta}\xi}{\xi(1 - \nu_{\theta\varphi}) - 2\nu_{r\theta}^2} - \frac{4}{3}s \right] \frac{\bar{u}}{x} + \left[\frac{(1 - \nu_{\theta\varphi})\xi^2}{\xi(1 - \nu_{\theta\varphi}) - 2\nu_{r\theta}^2} + \frac{4}{3}s \right] \frac{d\bar{u}}{dx}. \quad (12)$$

In order to solve these equations we use BCs that are converted according to the Laplace transform. The solution technique is based on applying of **DSolve** and **Solve** commands from the computer algebra system **WolframMathematica**. As a result we obtain the displacement and the stress in Laplace time space.

The inverse Laplace transform is given by the following complex integral, which is known as the Bromwich inversion integral:

$$f(x, \tau) = \frac{1}{2\pi i} \int_C \bar{f}(x, s) \exp(s\tau) ds, \tau > 0, \quad (13)$$

where C is a contour extending from $c - i\infty$ to $c + i\infty$, falling to the right of all singularities of \bar{f} [12].

In order to find the true time-dependent displacement and radial stress we apply the inverse Laplace transform to $\bar{\sigma}_{xx}(s)$ and $\bar{u}(s)$. Due to the complex structures of these functions we use a numerical solution method instead of an analytical solution based on Eqn. (13), which is likely not to exist. We solve the numerical problem by applying a quadrature formula which approximates an unknown function by a finite linear combination of transform values [13]:

$$f(x, \tau) \approx f_n(x, \tau) \equiv f_{n,a,K}(x, \tau) = \frac{1}{\tau} \sum_{j=1}^n K_j \bar{f}\left(x, \frac{a_j}{\tau}\right), \quad (14)$$

where \mathbf{a} , \mathbf{K} are vectors, called nodes and weights, respectively. Eqn. (13) turns into Eqn. (14) after using a MacLaurin series for the exponential function $\exp(z)$, where $z = s\tau$, and an additional Padé approximation [14].

We would like to note that Zakian obtained Eqn. (14) alternatively by approximating a delta function by a finite linear combination of exponential functions. He showed [3] that the coefficients a_j, K_j have to be determined such that they provide a good approximation to the scaled Dirac delta function $\delta(\tilde{\tau} - 1), \tilde{\tau} \in [0, \infty)$:

$$\delta(\tilde{\tau} - 1) \approx \delta_n(\tilde{\tau} - 1) = \sum_{j=1}^n K_j \exp(-a_j \tilde{\tau}), \quad (15)$$

where a_j, K_j are complex numbers of vectors \mathbf{a}, \mathbf{K} respectively. As Zakian observed [4], the possibility of good approximations is evident if we take the Laplace transform of the scaled delta function: $\delta(\tilde{\tau}-1) \rightarrow \tilde{\tau} \exp(-\tilde{\tau}s)$. The nodes and weights obtained by Zakian are shown in Table 1. He also showed that if one uses these nodes and weights it is necessary to write $f_{n,a,K}^{Zakian}(x, \tilde{\tau}) = 2f_{n,a,K}(x, \tilde{\tau})$ instead of Eqn. (14).

Table 1: Nodes and weights obtained by Zakian

\mathbf{a}_j	\mathbf{K}_j
$1.283767675E + 01 + 1.666063445iE + 00$	$-3.690208210E + 04 + 1.969904257E + 05i$
$1.222613209E + 01 + 5.012718792iE + 00$	$6.127702524E + 04 - 9.540862551E + 04i$
$1.093430308E + 01 + 8.409673116iE + 00$	$-2.891656288E + 04 + 1.816918531E + 01i$
$8.776434715E + 00 + 1.192185389iE + 01$	$4.655361138E + 03 - 1.901528642E + 00i$
$5.225453361E + 00 + 1.572952905iE + 01$	$-1.187414011E + 02 - 1.413036911E + 02i$

Jeffreson and Chow offer different least-square (LS) sets of nodes and weights [5]. Their solution is based on the method of LS approximation by exponential functions as proposed by Miller [15]. They apply the LS approximation to match the function $\delta(\tilde{\tau}-1)$ by $\delta_n(\tilde{\tau}-1)$. In order to derive a set of LS coefficients Jeffreson and Chow minimize the following function:

$$E(a, A) = \int_0^{\infty} \left\{ f(\tilde{\tau}) - \sum_{j=1}^n A_j \exp(-a_j \tilde{\tau}) \right\}^2 d\tilde{\tau}, \quad (16)$$

where $A_j = K_j/a_j$. They consider the square pulse function:

$$f(\tilde{\tau}) = m(\tilde{\tau}-1) = 1 - \int_0^{\tilde{\tau}} \delta(\theta-1) d\theta = \begin{cases} 1, & \tilde{\tau} \in [0, 1] \\ 0, & \tilde{\tau} \in (1, \infty) \end{cases}, \quad (17)$$

which gives a finite integral in Eqn. (16). The values of the LS coefficients for $n = 10$ and $n = 15$ obtained by Jeffreson and Chow are shown in Table 2.

Stress and displacement are real-valued functions, so we approximate them by the real part of Eqn. (14). Then we obtain true time-dependent displacement and radial stress.

4 Results and conclusions

We obtained expressions for the displacement and radial stress in real time by applying the numerical approaches for the inverse Laplace transform. Consequently, we obtained different functions by using the sets of notes and weights for a quadrature formula for the inverse Laplace transform (Eqn. 14) obtained by Zakian, Jeffreson and Chow for $n = 10$ and $n = 15$. The shear viscosity of the sclera has been determined for two types of BC for the inner radius. During the numerical calculations

Table 2: Nodes and weights obtained by Jeffreson and Chow

\mathbf{a}_j	\mathbf{K}_j	*
$n = 10$		
$1.1230093058E + 01 - 2.352672861E + 01i$	$4.860502512E - 01 + 2.422640698E + 00i$	(2)
$1.948441344E + 00 - 1.838606040E + 01i$	$5.552772067E + 00 + 2.015535066E + 00i$	(2)
$2.486321472E + 00 - 1.294069981E + 01i$	$9.328911705E + 00 - 4.782670037E + 00i$	(2)
$3.049851019E + 00 - 7.477695691E + 00i$	$4.688193150E + 00 - 1.756397771E + 01i$	(2)
$3.662673996E + 00 - 2.340402588E + 00i$	$-2.290775011E + 01 - 1.934430556E + 01i$	(2)
$n = 15$		
$1.20190013E + 001 - 3.839128154E + 01i$	$+1.454512148E + 00 - 1.896165496E + 00i$	(2)
$1.862570769E + 00 - 3.320749609E + 01i$	$-1.715333565E + 00 - 5.172539073E + 00i$	(2)
$2.292993575E + 00 - 2.766209815E + 01i$	$-7.541523912E + 00 - 4.523961971E + 00i$	(2)
$2.661840425E + 00 - 2.198372929E + 01i$	$-1.295649648E + 01 + 7.506458220E - 01i$	(2)
$3.035577722E + 00 - 1.625582381E + 01i$	$-1.547416249E + 01 + 1.099375660E + 01i$	(2)
$3.470465540E + 00 - 1.055035834E + 01i$	$-1.018991823E + 01 + 2.717989379E + 01i$	(2)
$4.014204990E + 00 - 5.028754130E + 00i$	$+1.938392606E + 01 + 4.294784889E + 01i$	(2)
$4.382910986E + 00$	$6.166590165E + 01$	(1)

(*) means that the complex conjugate pair is also available.

we used the following values: $R_i = 11.75$ mm, $R_o = 12.25$ mm, $E_{22} = 14.3$ MPa, $E_{11} = 0.01E_{22}$, $\nu_{12} = 0.01$, $\nu_{23} = 0.45$ [16].

We start with a discussion of results obtained under the assumption that the eye-ball volume does not change during the time of the experiment. In this case we describe everything in dimensionless coordinates as listed in the second chapter of this paper, including dimensionless time. As it has already been discussed, $IOP_{\text{dim}}(\tau) = -\sigma_{xx}(\tau)|_{x=\beta}$. Note that the dimensionless radial stress is explicitly independent on the shear viscosity of the sclera. It depends on dimensionless time, which depends on the shear viscosity of sclera. This coefficient is not used in the equation system and is not specified as a known parameter. In order to estimate the value of the shear viscosity of the sclera we use the expression linking dimensionless and dimensional time. Consequently we write:

$$\eta = E_{\theta\theta}t/\tau. \tag{18}$$

Let us consider four experimental values of the IOP for fixed values of time measured by K. Kotlyar [2] (see Fig. 2): $IOP = 6266$ Pa ($IOP_{\text{dim}} \cdot 10^{-6} = 438.2$), $t = 10$ s; $IOP = 4533$ Pa ($IOP_{\text{dim}} \cdot 10^{-6} = 317.0$), $t = 120$ s; $IOP = 3466$ Pa ($IOP_{\text{dim}} \cdot 10^{-6} = 242.4$), $t = 300$ s; $IOP = 2800$ Pa ($IOP_{\text{dim}} \cdot 10^{-6} = 195.8$), $t = 500$ s. We use the theoretical function $\sigma_{xx}(\tau)$ which we have already obtained in order to determine τ , when the module of $\sigma_{xx}(\tau)$ is equal to the experimental data. The range of numerical IOP values obtained by simulation is less than the range of experimental values of IOP measured by Kotlyar. Indeed, $IOP_{\text{dim}} \cdot 10^{-6} \in 195.8 - 438.2$ for experimental data and $IOP_{\text{dim}} \cdot 10^{-6} \in 285 - 430$ for numerical simulation. Therefore we are able to use only the experimental value of IOP measured when the time is 120 s. Then

we estimate the value of dimensionless time corresponding to this value of IOP and obtain the shear viscosity of the sclera by applying Eqn. (18). When using Zakian's set of nodes and weights and Jeffreson's and Chow's set of nodes and weights for $n = 10$ we obtain $\eta = 12.8 \text{ MPa} \cdot \text{s}$. By using Jeffreson's and Chow's set of nodes and weights for $n = 15$ we arrive at $\eta = 12.9 \text{ MPa} \cdot \text{s}$. The time dependence of the IOP is shown in Fig. 3a. The graph is based on three different numerical approaches for the inverse Laplace transform considered in this paper coinciding for such an IOP scale.

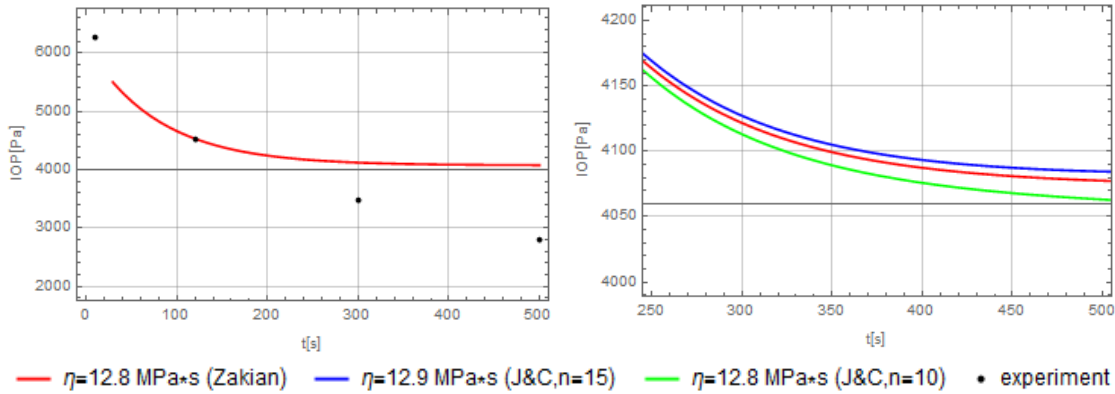


Figure 3: Time dependence of IOP.

A noticeable difference between the three considered approaches is observed only for the second half of the experimental time (see Fig. 3b). As we can use only the second point of the experimental curve corresponding to $IOP = 4533 \text{ Pa}$ we cannot really determine which numerical approach is the most acceptable on the whole, but we may say that all of these three approaches are good enough for application in the framework of the problem of IOP determination. However, Jeffreson's and Chow's approaches are more complicated due to a higher number of coefficients in Eqn. (14). As we can see from Fig. 3a stress relaxation cannot be explained only by an existing sclera viscosity. The match between the theoretical results and experimental data is not good enough since theoretical curves have another character of the decline. We now discuss the results obtained under the assumption that an intraocular fluid outflow exists. In this case we used a dimensional time (in seconds). The shear viscosity of the sclera is explicitly included in the system of equations. Since we use a numerical solution a starting value must be specified before simulation. The shear viscosity determination was based on the bisection-root-finding method which repeatedly bisects an interval and then selects a subinterval in which the root must be located for further processing. This method is based on Bolzano's Theorem: $\Phi(\eta) \in C[\eta_a, \eta_b], \Phi(\eta_a) \cdot \Phi(\eta_b) < 0 \Rightarrow \exists \eta_c \in [\eta_a, \eta_b] : \Phi(\eta_c) = 0$ [17]. As function $\Phi(\eta)$ we use the function $\Phi(\eta) = (IOP_{experiment(dim)} - (-\sigma_{xx}|_{x=\beta}))|_{t=t_{experiment}}$. This method allows us to find roots for all experimental values of IOP from Fig. 2 apart from the first value characterizing the IOP jump immediately after the intravitreal injection. As an initial range we used $\eta \in 0 - 200 \text{ MPa}$. The reason of this choice is that it is a really wide range. We obtained values of the function $\Phi(\eta)$ when $\eta = 0 \text{ MPa}$ and $\eta = 200 \text{ MPa}$ and made sure that they have different signs. The shear viscosity obtained by applying Zakian's, Jeffreson's and Chow's ($n = 10$), ($n = 15$)

vectors of nodes and weights are shown in Table 3. Coefficients are presented with one decimal of accuracy. The time dependence of the IOP is shown in Fig. 4.

Table 3: Values of shear viscosity obtained by applying different numerical approaches

Experimental point	Zakian, MPa · s	J&C, n=10, MPa · s	J&C, n=15, MPa · s
IOP = 4533 Pa, time = 120 s	57.1	57.1	57.1
IOP = 3466 Pa, time = 300 s	58.6	59.1	58.3
IOP = 2800 Pa, time = 500 s	33.8	35.3	33.0

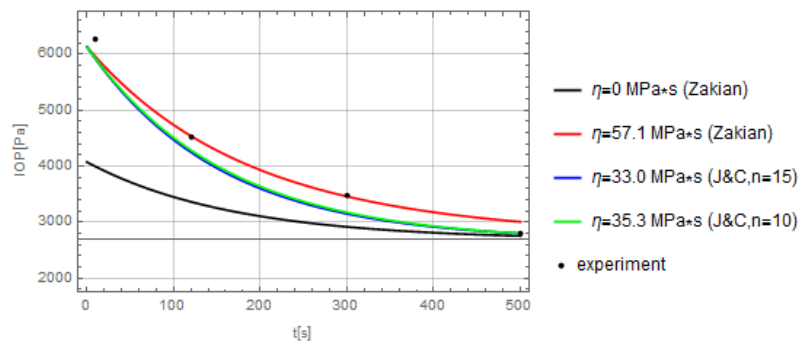


Figure 4: Time dependence of IOP.

The graphs based on three different numerical approaches for inverse Laplace transform considering in this paper coincide on the IOP scale. We also observe coinciding graphs for η obtained for the two middle points from the experimental curve (see Fig. 2). A minor difference can be observed for the last point. The decrease of the curve depends on the shear viscosity coefficient. The more the value of this coefficient the longer the relaxation time and the less abrupt the IOP will reduce. If $\eta = 0$ (this means that the sclera shows no viscosity) the match between the theoretical results and experimental data is not good enough. Hence, stress relaxation cannot be explained only by the existing intraocular fluid outflow. As we can see by comparison of Fig. 3a and Fig. 4 it is necessary to take both into account, the existing sclera viscosity and the existing intraocular fluid outflow, leading to the best agreement between theoretical results and experimental data.

In order to compare the time dependence of the IOP based on the different numerical approaches discussed in this paper we use average values of the IOP for the two middle points and for the three last points of the experimental curve (see Fig. 2). From the average values for the two middle points we find for the viscosity by applying Zakian's and Jeffreson's and Chow's approach for $n = 10$ and for $n = 15$, respectively: $\eta = 57.8 \text{ MPa} \cdot \text{s}$, $\eta = 58.1 \text{ MPa} \cdot \text{s}$, $\eta = 57.7 \text{ MPa} \cdot \text{s}$. The average values for three last points lead to $\eta = 49.8 \text{ MPa} \cdot \text{s}$, $\eta = 50.5 \text{ MPa} \cdot \text{s}$, $\eta = 49.5 \text{ MPa} \cdot \text{s}$, respectively for the listed approaches. A comparison of these approaches by using the average values for two middle points for the second point, the third point, and for the last point is shown in Fig. 5a, Fig. 5b, Fig. 5c respectively.

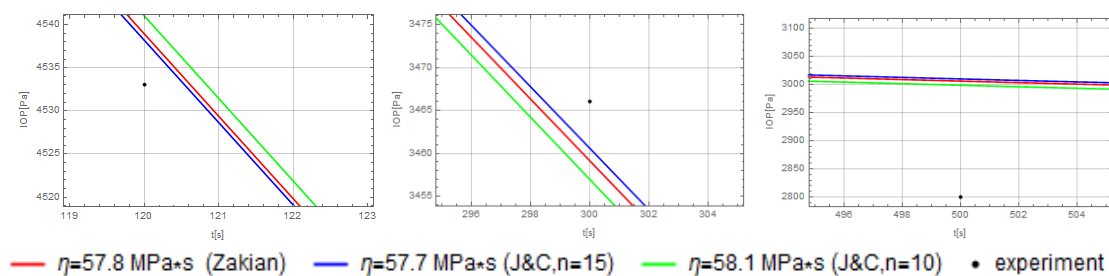


Figure 5: Time dependence of IOP: comparison of numerical approaches.

A comparison of these approaches by using the average values for three last points for the second point, the third point, and for the last point is shown in Fig. 6a, Fig. 6b, Fig. 6c, respectively.

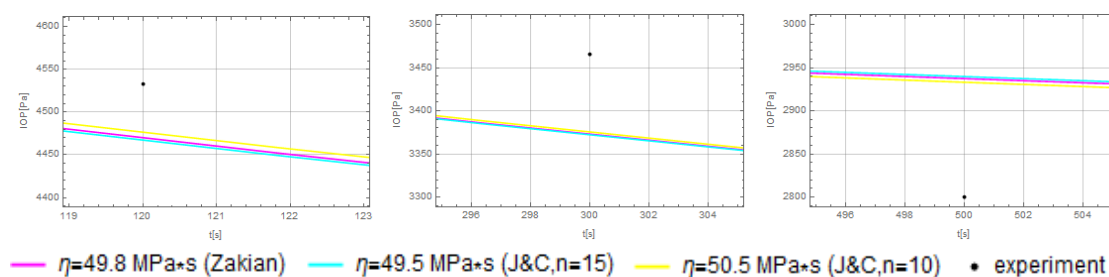


Figure 6: Time dependence of IOP: comparison of numerical approaches.

By comparing the results based on two different types of boundary condition for the inner radius displacement considering in this paper we can conclude that the value of the shear viscosity of the sclera is less if we suppose that the eye volume is constant during the time of the experiment. The possible reason of such a result is that by applying this type of BC we don't have a possibility to take into account all points from the experimental curve (see Fig. 3). We also can see by comparing Fig. 3 and Fig. 4 that we should take into account both facts: the existing sclera viscosity and the existing intraocular fluid outflow, - to have the best coincidence between the experimental data and theoretical results. We conclude that all approaches discussed in this paper are good enough for application in the framework of the problem of IOP determination. Hence, applying any of these approaches is reasonable. We should also note that Zakian's approach is the least complicated due to the least number of coefficients in Eqn. (14).

Consequently, a method for determination the shear viscosity of the sclera based on a comparison of results of mathematical modeling in the framework of 3D-dimensional linear viscoelastic theory and experimental data of IOP discrete measurements during several minutes after the intravitreal injection has been established. A comparison of numerical approaches based on three different sets of nodes and weights for a quadrature formula for the inverse Laplace transform has been performed.

Acknowledgements

The authors wish to acknowledge Prof. S.M. Bauer for her contribution to the scientific research of this article.

References

- [1] S.A. Regirer. *Lektsii po biologicheskoy mekhanike* (Lectures on biological mechanics). Moscow: Moscow university Publ., 1980, 144 p.
- [2] K. Kotlyar, S. Bauer, N. Plange. *Klinicheskie i biomekhanicheskie aspekty izmeneniya vnutriglaznogo davleniya posle intravitrealnykh inyeksyy* (Clinical and biomechanical aspects of the intraocular pressure changes after intravitreal injections). Russian National Ophthalmic Forum, 2013.
- [3] V. Zakian. Numerical inversion of Laplace transform. *Elec. Lett.*, 1969, No.5, pp. 120-121.
- [4] V. Zakian. Optimisation of numerical inversion of Laplace transforms. *Elec. Lett.*, 1970, No.6, pp. 677-679.
- [5] C.P. Jeffreson, E.-P. Chow. Least squares coefficients for a quadrature formula for Laplace transform inversion. *Journal of Computational and Applied Mathematics*, 1978, Vol.4, No.1, pp. 53-58.
- [6] D. Ljubimova. Biomechanics of the Human Eye and Intraocular Pressure Measurements. Ph.D. thesis, Royal Institute of Technology, 2009.
- [7] L.A. Karamshina. *Modeli mnogosloynnykh obolochek v zadachakh oftalmologii* (Models of multilayer shells in the problems of ophthalmology). Ph.D. thesis, St. Petersburg State University, 2011.
- [8] V. Novatski. *Teoriya uprugosti* (Theory of elasticity). M.: Mir, 1975, 863 p.
- [9] R. Kristensen. *Vvedeniye v makhaniku kompozitov* (Mechanics of composite materials). M.: Mir, 1982, 336 p.
- [10] E.N. Iomdina, S.M. Bauer, K.E. Kotlyar. *Biomekhanika glaza: teoreticheskie aspekty i klinicheskie prolozheniya* (Eye Biomechanics: Theoretical Aspects and Clinical Applications). Moscow: Real Time, 2015, 208 p.
- [11] G.A. Lyubimov, I.N. Moiseeva, A.A. Stein, E.N. Iomdina, L.A. Nazarenko Estimation of fluid outflow from the eye on the basis of a modified tonography method. *Russian journal of biomechanics*, 2012, Vol.16, No.2 , pp.8-20.
- [12] G. Doetsch. *Introduction to the Theory and Application of the Laplace Transformation*. Springer, 1974, 327 p.
- [13] J. Abate, W. Whitt. A Unified Framework for Numerically Inverting Laplace Transforms. *INFORMS Journal on Computing*, 2006, V.18, No.4, pp. 408-421.

- [14] G. A. Baker, P. Graves-Morris. Padé Approximants, 2nd ed. Cambridge University Press, Encyclopedia of Mathematics and Its Applications, Vol.59., 1996.
- [15] G. Miller. Least squares approximation of functions using exponentials. Ph.D. thesis, John Hopkins Univ., 1969.
- [16] S.M. Bauer, L.A. Zamuraev, K.E. Kotliar. Model of the transversely isotropic spherical layer for estimation of intraocular pressure changes after intravitreal injections. Russian journal of biomechanics, 2006, Vol.10, No.2, pp. 43-49.
- [17] C.H. Morales. A Bolzano's theorem in the new millennium. Nonlinear Analysis, 2002, No. 51, pp. 679-691.

Kseniia P. Frolova and Elena N. Vilchevskaya, Peter the Great St. Petersburg Polytechnic University, Department of Theoretical Mechanics, 29, Polytechnicheskaya st., 195251, St.Petersburg, Russia.

Elena N. Vilchevskaya, Institute of Problems of Mechanical Engineering, V.O., Bolshoj pr., 61, 199178, St. Petersburg, Russia.

Wolfgang H. Müller and Wolf Weiss, Technische Universität Berlin, Institute of Mechanics, Einsteinufer 5, D-10587 Berlin, Germany.

Lagrange multiplier method implementations for two-dimensional contact problems

M.P. Galanin, P.V. Gliznutsina, V.V. Lukin, A.S. Rodin
gliznutsinapv@gmail.com

Abstract

Two-dimensional elastic contact problem is considered. Finite element method with bilinear shape functions is used. The Lagrange multiplier method for contact conditions implementation is used in three ways: node-to-surface method, mortar method and advanced mortar method. In the first method integration is performed with one point from master body and one point from slave body (for each finite element), in the second method integral over a segment of master body is evaluated. The third method is more like the second, except dividing each segment of master body on subsegments according to segments of slave body. Tests showed that the mortar method and the advanced mortar method are more accurate than the node-to-surface method. The advanced mortar method is able to smooth the stress field fluctuations, but only in limited number of problems. A plane problem of contact interaction of the metal rail and composite orthotropic shell in cross-cut section of the electromagnetic accelerator barrel (railgun) is considered. Parallel software package for sparse linear systems of equations solving with MPI technology is designed.

1 Introduction

The contact of one deformable body with another has affect on in almost every mechanical structure behavior. Because of the contact problems importance, a considerable effort has been made in the modeling and numerical simulations.

The problem of elastic contact has been treated numerically by many authors [1, 2, 3, 4].

Contact problems are difficult for simulation since the most surfaces of solid bodies are rough. In addition, contact problems are often beeing simulated with mismatches meshes. Also, implementation of the stress contact conditions isn't a trivial problem. There are a few methods used for implementation of contact conditions: Lagrange multiplier method[5, 6], penalty method[6], Schwarz method [7] and others.

In this paper we consider Lagrange multiplier method for contact conditions with three variants of numerical integration: node-to-surface contact method, standart mortar method and advanced mortar method[8]. Methods efficiency are compared, numerical results are shown.

2 2d contact problem

2.1 Contact theory

Description of the problem is given in [10, 6].

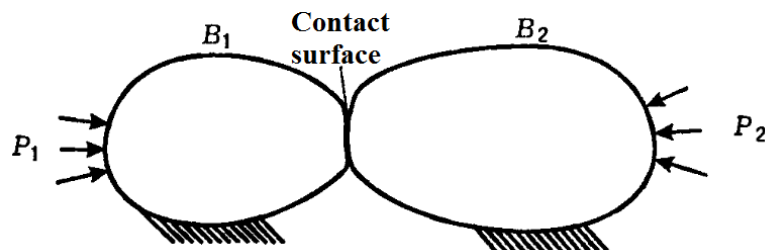


Figure 1: Contact between two bodies

Consider a 2-dimensional contact between two bodies B_1 and B_2 . A contact law is characterized by a geometric condition of non-penetration:

$$g^\alpha = \min_{\mathbf{x}^\beta \in \Gamma^\beta} (\mathbf{x}^\alpha - \mathbf{x}^\beta) \cdot \mathbf{n}^\alpha \geq 0, \quad \mathbf{x}^\alpha \in \Gamma^\alpha, \quad (1)$$

where α, β are indexes of contact bodies, Γ^α is surface of body B_α , turn to B_β , Γ^β is surface of body B_β , turn to B_α , \mathbf{n}^α is outer normal line in point x^α to contact surface for body B_α , g^α is a gap between x^α and body B_β . There is a contact between bodies if at least for one point of body B_α gap is null.

During the contact process distributed contact forces \mathbf{t} are appeared. There are normal and tangent components of the contact force:

$$t_n = \mathbf{t} \cdot \mathbf{n} \leq 0, \quad (2)$$

$$t_t = \mathbf{t} \cdot \boldsymbol{\tau}, \quad (3)$$

where \mathbf{n} is outer normal line to contact surface, $\boldsymbol{\tau}$ is tangent vector to contact surface.

We consider the case without friction and sticking. In this case tangent component of contact force is equal to zero.

$$t_t = 0. \quad (4)$$

2.1.1 Basic equations

In this paper we use Cartesian coordinate system and consider a plane stress case. There are a few basic equations:

1) Cauchy tensor:

$$\{\varepsilon\} = \{\varepsilon_x, \varepsilon_y, \gamma_{xy}\}^T = [B]\{u\}, \quad (5)$$

where $\{\varepsilon\}$ – strain tensor, $\{u\}(M) = \{u(M), v(M)\}^T$ – displacement of point M .

$$B = \begin{bmatrix} \frac{\partial}{\partial x} & 0 \\ 0 & \frac{\partial}{\partial y} \\ \frac{\partial}{\partial y} & \frac{\partial}{\partial x} \end{bmatrix}.$$

2) Hooke's law:

$$\{\sigma\} = \{\sigma_x, \sigma_y, \tau_{xy}\}^T = [H]\{\varepsilon - \varepsilon_0\}, \quad (6)$$

where $\{\sigma\}$ is a stress tensor, $\{\varepsilon\}$ is a strain tensor, $\{\varepsilon_0\}$ is a start strain tensor, (consider as zero-vector), $[H]$ is a elasticity tensor. For the case of plane strain, elasticity tensor for isotropic material becomes:

$$H = \frac{E(1-\nu)}{(1+\nu)(1-2\nu)} \begin{bmatrix} 1 & \frac{\nu}{1-\nu} & 0 \\ \frac{\nu}{1-\nu} & 1 & 0 \\ 0 & 0 & \frac{(1-2\nu)}{2(1-\nu)} \end{bmatrix},$$

where E and ν — Young's modulus and Poisson's ratio.

3) Equilibrium equations (without outer forces):

$$[B]^T\{\sigma\} = \{f\}, \quad (7)$$

4) Boundary conditions:

$$\begin{aligned} u(M) &= \tilde{u}(M), M \in \Gamma, \\ v(M) &= \tilde{v}(M), M \in \Gamma, \\ \sigma_x(N)n_x(N) &= \tilde{p}_x(N), N \in \Gamma, \\ \sigma_y(N)n_y(N) &= \tilde{p}_y(N), N \in \Gamma, \\ \tau_{xy}(N)n_y(N) &= \tilde{p}_{xy}(N), N \in \Gamma, \end{aligned}$$

where Γ is a surface of the body.

5) Contact conditions:

$$u_n^{(1)}|_{\Gamma_C} = u_n^{(2)}|_{\Gamma_C}, \quad (8)$$

$$\sigma_n^{(1)}|_{\Gamma_C} = \sigma_n^{(2)}|_{\Gamma_C}, \quad (9)$$

where $u_n^{(i)}$ and $\sigma_n^{(i)}$ are normal component of displacement and bf stress for body i , $i = 1, 2$, Γ_C is a contact surface.

2.2 Numerical method

The popular displacement finite element method is largely used for scientific computing in engineering. Without going into all the details, we present here just the algorithm for contact modeling. After finite element discretization in the context of small displacements, the global set of equilibrium equations of two contacting elastic bodies can be written as

$$[K]\{u\} = \{f\} + R, \quad (10)$$

where

$$[K] = \sum_e [k]^e, \{f\} = \sum_e \{f\}^e + G,$$

$$[k]^e = \int_{S^e} [B_N]^T [H] [B_N] dS, \{f\}^e = \int_{\Gamma^e} [N^e]^T \{p\} d\Gamma,$$

$[K]$ – global stiffness matrix, $[k]^e$ – local stiffness matrix, $\{f\}$ – global right-side vector, $\{f\}^e$ – local right-side vector, G – vector of node forces, $[B_N] = [B][N]^T$ – derivative matrix for shape functions, S^e – square of element, Γ^e – load bound of body, R – contact reaction vector.

2.2.1 Contact conditions

In this paper we use a Lagrange multiplier method for contact conditions [10]. According to the Lagrange multiplier method, we add a potential of contact forces to the potential energy of the whole system. Adding element can be written as:

$$W_C = - \int_{\Gamma_C} \Lambda \cdot (x^{(1)} - x^{(2)}) d\Gamma, \quad (11)$$

where Γ_C is a contact surface between B_1 and B_2 , Λ is a Lagrange multiplier function, $x^{(i)} = X^{(i)} + u^{(i)}$ are deformed positions of the congruent points for bodies B_1 and B_2 , $X^{(i)}$ and $u^{(i)}$ are start positions of the congruent points for bodies B_1 and B_2 . Consider energy minimization method:

$$\delta\Pi = \int_B \delta\{\varepsilon\}^T [H] \{\varepsilon\} dS - \int_{\Gamma} \delta\{u\}^T \{t\} d\Gamma - \int_{\Gamma_C} \delta\Lambda \cdot (u^{(1)} - u^{(2)}) d\Gamma - \int_{\Gamma_C} \Lambda \cdot (\delta u^{(1)} - \delta u^{(2)}) d\Gamma = 0. \quad (12)$$

Components u and Λ are independent, so we can write system of equations as:

$$\begin{cases} \int_S \delta\{\varepsilon\}^T [H] \{\varepsilon\} dS - \int_{\Gamma} \delta\{u\}^T \{t\} d\Gamma - \int_{\Gamma_C} \Lambda \cdot (\delta u^{(1)} - \delta u^{(2)}) d\Gamma = 0, \\ \int_{\Gamma_C} \delta\Lambda \cdot ((X^{(1)} + u^{(1)}) - (X^{(2)} + u^{(2)})) d\Gamma = 0. \end{cases} \quad (13)$$

Calculation of integral (11) consist of next steps. Let one discretize the integral (11). One of two bodies is called «master», another one - «slave» [8]. The main points are chosen from master body, after that we find congruent points from slave body. Then (11) can be written as:

$$W_C = - \int_{\Gamma_C} \lambda^T \cdot (x^{(m)} - x^{(s)}) d\Gamma, \quad (14)$$

where $x^{(m)}$ and $x^{(s)}$ are deformed positions for congruent points from master body and slave body, λ is a vector of Lagrange multipliers, Γ_C is contact surface on master body.

Common case for interpolation is:

$$x^{(m)} = N_\alpha(\xi)\tilde{x}_\alpha^{(m)}(t); \quad x^{(s)} = N_\beta(\xi)\tilde{x}_\beta^{(s)}(t); \quad \lambda = N_c(\xi)\tilde{\lambda}_c(t), \quad (15)$$

where N_α, N_β are shape functions for system (10), N_c is shape functions for Lagrange multiplier. There are three methods for interpolation in this paper – Node-to-surface contact, Standart mortar method, Advanced mortar method.

According to Node-to-surface contact method

$$N_c = \delta(\xi - \xi_c), \quad (16)$$

where ξ_c – conqurent point on slave.

Only one point from master and one point from slave are used for each element.

According to mortar method, integral carried out by quadrature on subsegments. Master shape function $N_c = \delta_{c\beta}N_\beta(\xi)$ gives standart mortar method. Partitioning subsegments in accordance with slave finite elements gives advanced mortart method. In this case (14) can be written as

$$W_C = - \sum_m \tilde{\lambda}_c^T \left[G_{c\alpha}^m \tilde{x}_\alpha^{(m)} - G_{c\beta}^s \tilde{x}_\beta^{(s)} \right] d\Gamma, \quad (17)$$

where

$$G_{c\alpha}^m = \int_{\Gamma_C} N_c(\xi)N_\alpha(\xi)d\Gamma I,$$

$$G_{c\beta}^s = \int_{\Gamma_C} N_c(\xi)N_\beta(\xi_s)d\Gamma I,$$

I – identity matrix.

There is vector $\lambda = \{\lambda_n, \lambda_\tau\}$ in each node of master.

2.3 Numerical results

Two numerical examples are solved for comparison by the previously describe node-to-surface, standart mortar and advanced mortar methods.

2.3.1 Two solid bars contact

One solid bar lies on another one. The first one lies on the smooth surface. The second bar is loaded with pressure p .

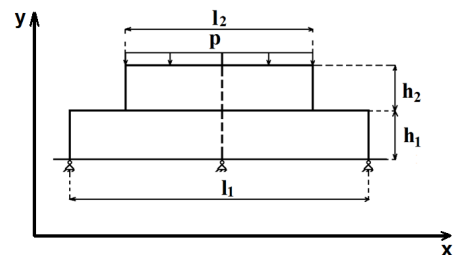


Figure 2: System of bars

Problem is symmetrical, so we consider only a half of the area. This way, x component of displacement in the left side of both bars and y component of displacement in the bottom of first bar are equal to zero.

In Fig. 3 - 4, we present the distribution of contact stresses σ_y over the contact surface for Node-to-surface contact and standart mortar methods. Advanced mortar method gives almost the same results as standart. Displacements scaling factor is equal to 100.

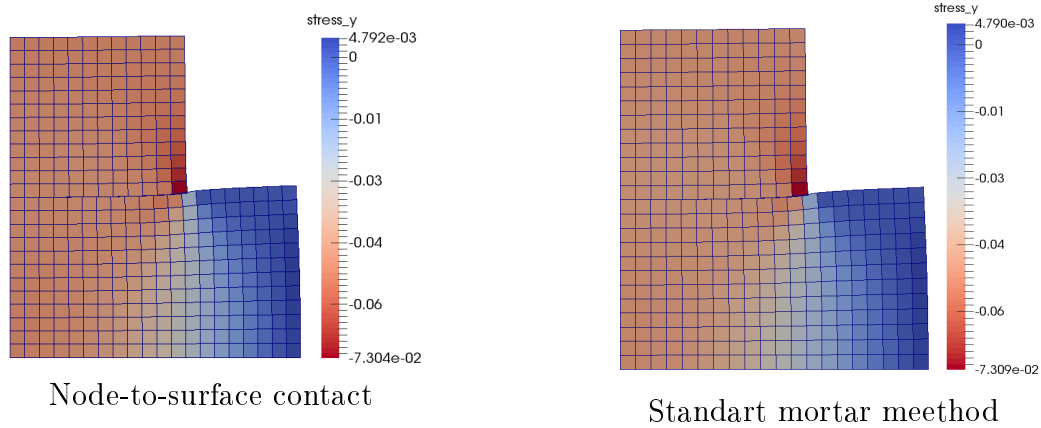


Figure 3: Step $h = 0.25$

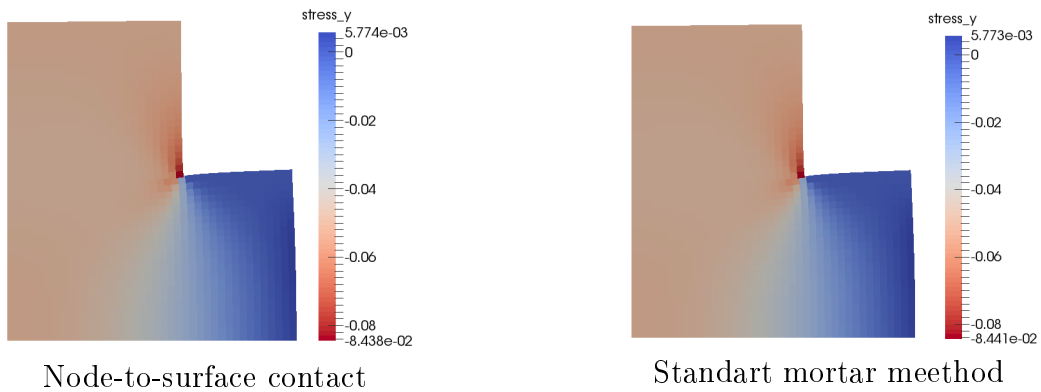


Figure 4: Step $h = 0.125$

Table 4: Input parametres

l_1	l_2	h_1	h_2	ν_1	ν_2	E_1	E_2	p
10 cm	6 cm	3 cm	3 cm	0.3	0.3	70 GPa	70 GPa	50 MPa

Due to geometry of the problem vertical components of displacements and stresses at the contact surface are close to the corresponding normal components. There are infinite normal stress in the corner point according to the analitical solution. Numerically obtained values of normal stresses are growing in absolute value when the step is decreasing.

Difference between results for both methods are small (0.1 percent). But the second method is more fit the physic parametres of the problem.

In Fig. 5 - 6 we present the distribution on the contact surface. Black line is used for distribution of contact stress for the first body, red line - for distribution of contact stress for the second body.

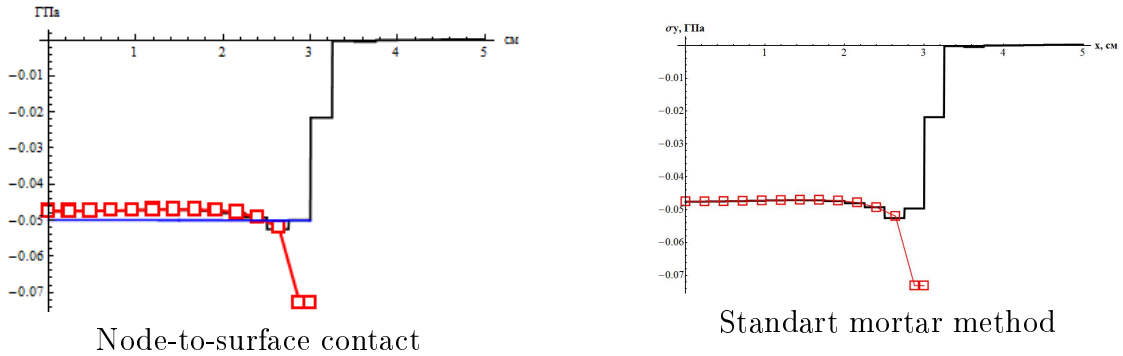


Figure 5: Distribution of contact stress, step $h = 0.25$

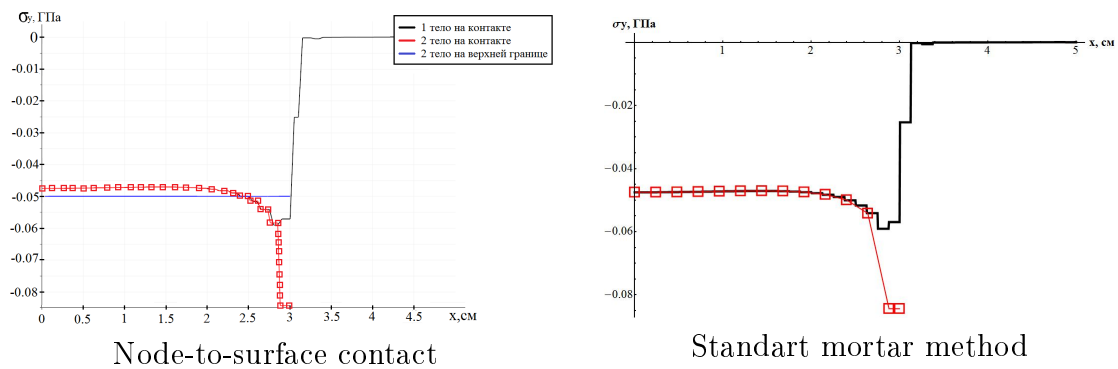


Figure 6: Distribution of contact stress, step $h = 0.125$

Consider the problem with mismatching meshes. Step is 0.08 cm for bottom body and 0.1 cm for top body.

In graphics 8 we present the distribution of contact stresses σ_y over the contact surface for Node-to-surface cotact and standart mortar methods. Black line is used for distribution of contact stress for the first body, red line - for distribution of contact stress for the second body.

As seen in the graphics, node-to-surface contact method gives difference of stress to the entire contact surface. Standart mortar method gives accurate contact stresses in the center of the system of bars, however, corner point, than bigger oscillations are and its amplitude is greater than in the node-to-surface contact method.

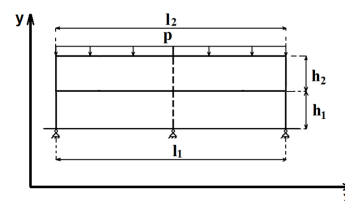


Figure 7: System of thwo bars

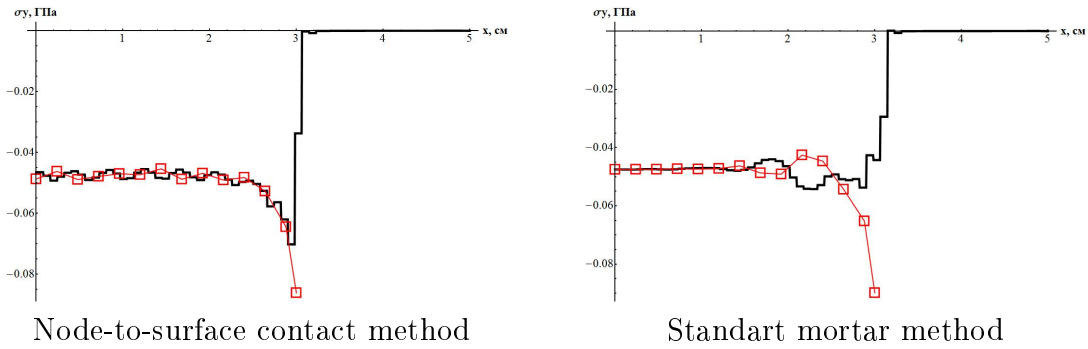


Figure 8: Distribution of contact stress, step $h = 0.08$ and $h = 0.1$

2.3.2 Two same-sized solid bars contact with mismatching meshes

Consider a contact problem with the same-sized bars to show the difference between standart mortar and advanced mortar methods (pic.7).

One solid bar lies on another one. The first one lies on the smooth surface. The second bar is loaded with a force p .

Problem is symmetrical, so we consider only a half of the area. This way, component x of displacement in the left side of both bars and component y of displacement in the bottom of first bar equals to zero.

Table 5: Input parameters

l_1	l_2	h_1	h_2	ν_1	ν_2	E_1	E_2	p
10 cm	10 cm	3 cm	3 cm	0.3	0.3	700 GPa	70 GPa	50 MPa

Consider the problem with mismatching meshes. Step is 0.12 sm for bottom body and 0.15 sm for top body.

In graphics 9 we present the distribution of contact stresses σ_y over the contact surface for Node-to-surface contact and standart mortar methods. Black line is used for distribution of contact stress for the first body, red line - for distribution of contact stress for the second body.

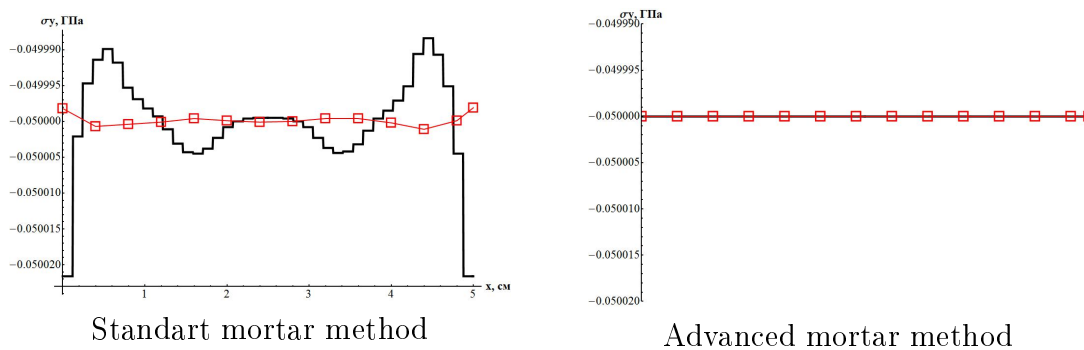


Figure 9: Distribution of contact stress, step $h = 0.12$ and $h = 0.15$

There is an analytic solution for this problem: $\sigma_y = p$. Standard mortar method gives oscillations in the contact surface. Advanced mortar method gives practically exact solution.

3 Conclusion

Methods for solving elastic frictionless contact problems are considered. Finite element method for numerical modeling and Lagrange multiplier method with different variants of presenting is used. Node-to-surface contact method, standard and advanced mortar method are described.

Mortar methods are more fit the physical parameters of the problem than node-to-surface contact method. But there are oscillations of stress during the contact surface. Node-to-surface contact method has difference between numerical and theoretical stress to the entire contact surface. Standard mortar method gives accurate contact stresses in the center of the system of bars, however, oscillations appear closer to the corner point and its amplitude is greater than in the node-to-surface contact method. Advanced mortar method gives smoother results, but in some class of problems.

References

- [1] Shtaerman A.Ia. Contact Problems of the Theory of Elasticity. M.-L.: Gostekhizdat. 1949. 270 p.
- [2] Johnson.K.L. Contact Mechanics. M.: Mir, 1989. 510 p.
- [3] Babeshko V.A. Static and dynamic contact problems with clutch // PMM. 1975. T. 39, N. 3. Pp. 505–512.
- [4] Burago N.G., Kukudzhanov V.N. A review of contact algorithms // Izv. RAS, Mechanics of Solids. 2005. No. 1. pp. 44-85.
- [5] Papadopoulos P., Solberg J.M. A Lagrange Multiplier Method for the Finite Element Solution of Frictionless Contact Problems // Math. Comp. Modelling, 1998, v. 28, p. 373–84.
- [6] Wriggers P. Computational Contact Mechanics. Springer, 2006. 521 p.
- [7] I.V. Stankevich, M.E. Yakovlev, Si Tu Htet, ?Development of algorithm of contact interaction on the basis of alternating Schwarz method?, Vestnik BMSTU, Ser. Natural Sciences, Spec. Vol. ?Applied mathematics?, 134-141 (2011).
- [8] Robert L. Taylor. Finite element solution of contact problems from: 1974 to 2004 URL: <http://www.ce.berkeley.edu/~rlt/presentations/hughes.pdf>
- [9] Feodosev V.I. Strength of materials. M.: MSTU im. N.E. Bauman, 1999. 592 p.

REFERENCES

- [10] Korobeynikov S.N. Nonlinear deformation of solid bodies. Novosibirsk: Publishing house of SB. 2000. 262 p.

P.V. Gliznutsina, Moscow, Russia

Experimental techniques applied to generalized continuum theories: A state-of-the-art report

Gregor Ganzosch, Wolfgang H. Müller
ganzosch@tu-berlin.de

Abstract

It is well known that the miniaturizing of modern mechanical systems toward micrometer or even nanometer length scale requires new equations for describing the mechanical and material behavior. The need for became evident from several experiments [7, 2]. Classical/traditional elasticity theory of continuum mechanics can not explain material behavior in this length scales (size effect). This is why generalized continuum theories are used to overcome these limits [2, 3, 4]. Also, lower computing time can be achieved by using generalized continuum theories for simulation models.

There are different reasons why experiments have to be performed for generalized continua. On the one hand new parameters show up in generalized continuum material equations. If one wants to use these equations, for example in a simulation study, these parameters have to be measured and determined in experiments before [7, 2, 3, 8]. On the other hand, simulations using generalized continuum models can be validated by experiments, provided that all parameters are known [5]. Unfortunately experimental data in the literature covering the size effect in elasticity is very rare. Some basic research on an Euler beam made out of epoxy is presented in [7, 8]. Other fundamental work was performed by [2] using atomic-force-microscopy and micro-Raman-microscopy on silicon nitride in a loading test.

In the recent past new experimental techniques have been developed to use generalized continuum theories [3, 5, 6]. Different experimental setups, different materials, and different structures were used [7, 3, 5, 6, 7, 8]. This state-of-the-art-report gives an overview on the different experimental techniques that have been applied to different generalized continuum theories. An outlook into future investigations will also be given.

1 Introduction

Modern mechanical and electrical systems are rapidly becoming smaller. Micrometer or nanometer length scaled systems require new mathematical theories and material equations. Liebold, for example, proved in [2] that YOUNG's Modulus of epoxy is increasing if the size of the target is in or below the micrometer scale. The reason of this behavior lies in the substructure of the target. These intrinsic characteristics,

which lead to this kind of mechanical behavior, are summarized by the term *size effect*. Classical/traditional elasticity theory of continuum mechanics can not explain material behavior in this length scales. That is why generalized continuum theories are used to overcome these limits.

An convincing example to illustrate the problem is a finite element simulation of materials showing small scale phenomena: Models of technical structures classically use equations based on the traditional CAUCHY-BOLTZMANN continuum and require a very detailed mesh if details in small structures need to be analyzed. This leads to higher computing time and associated higher costs. Alternatively, by using equations developed out of generalized continuum theories, a low-detail mesh can be used to get the same results. The computing costs are much less.

In the literature, some experiments applied to generalized continuum theories can be found [7, 2, 3, 5, 7, 8, 10, 14, 15]. Examples for generalized continuum theories are the strain-gradient-theory [17, 18], the micromorphic theory [4, 16, 17], and the surface-theory [19, 20], just to mention the most popular ones. When studying these theories more intensively, two main families of generalized continua representing extensions to the CAUCHY continuum can be identified - the micromorphic theory and the strain gradient theory. In micromorphic theory the intrinsic deformation is described by so-called directors. These vectors represent the deformation and the orientation of the material particles. The micromorphic continuum can be simplified to the micro-stretch continuum when the directors become orthogonal. The micro-stretch continuum can be simplified further to the popular micropolar continuum when the directors do not change their value in length (so that just the rotation is described by the directors). If desired, micropolar theory can be also transferred to couple-stress-theory. Then the constitutive equations for an isotropic solid read [13, 16, 4, 6]:

$$\sigma_{ij} = 2G\epsilon_{ij} + \lambda\epsilon_{kk}\delta_{ij} + \kappa e_{ijk}(r_k - \phi_k), \quad \mu_{ij} = \alpha\phi_{k,k}\delta_{ij} + \beta\phi_{i,j} + \gamma\phi_{j,i}. \quad (1)$$

σ_{ij} is the force-stress tensor (here antisymmetric in contrast to classical theory), μ_{ij} is the couple stress tensor (in general antisymmetric), G is the shear modulus, $\epsilon_{ij} = \frac{1}{2}(u_{i,j} + u_{j,i})$ is the small strain tensor, u_j is the displacement vector, and ϕ_i and r_i are the micro- and the macrorotation vector, respectively. ϕ_i refers to the rotation of points themselves, while r_i refers to the rotation associated with movement of nearby points [6]. e_{ijk} is the permutation symbol, δ_{ij} is the KRONECKER symbol. The EINSTEIN summation convention is valid for repeated indices and a comma denotes differentiation. α, β, γ and κ are the so-called independent COSSERAT constants (in classical theory these constants and the couple stress tensor become zero, just the LAMÉ constants stay). The couple-stress-theory represents the mostly used extension to the CAUCHY continuum in literature. By the use of special restrictions, the strain gradient theory can be simplified to the modified strain gradient theory and transferred into the couple stress theory as well as the micromorphic theory mentioned before. Also, surface theories, such as the core-shell-theory, gain in importance in the field of generalized continua. Based on the idea that the elastic behavior of a solid's surface is independent of its volume, these theories are even able to describe a negative *size effect* (meaning, a softer elastic response to external forces or deformations during the reduction of the dimensions of the specimen). This

behavior is shown in [15] for example.

Finally, two well-known and actively developed generalized continuum theories are the higher gradient [2, 15] and the micropolar theories [4, 13]. During the derivation of these theories additional constitutive equations are formulated, which include new and unknown specific parameters (*e.g.*, the couple stress tensor). Two possibilities in order to identify these new parameters are given by performing miniature experiments as well as macroscopic experiments. By choosing a special adjusted experimental setup applied on the explicit generalized continuum theory it is possible to localize and to determine the unknown parameters. Experiments on solids are mostly performed in static or dynamic beam loading tests. However, not just solids [16, 4] but also liquids or gases [24, 21, 23, 22] can be investigated. Hence there are a lot of different reasons why experiments have to be performed for generalized continua. On the one hand side newly identified parameters have to be measured and determined in experiments [7, 2, 3, 8], and on the other hand parameters obtained from theory or numerical analysis have to be validated by experiments [15, 5].

2 State of the Art

This section should give an overview of examples of the most important publications over the last years in the field of experiments applied on generalized continuum theories. Because of limited space not every publication related to this topic will be discussed.

2.1 Lam *et al.* 2003: Miniature beams

To find experimental data on the size effect in the literature is difficult. Some basic research on a miniaturized EULER beam made of epoxy is presented in “*Experiments and theory in strain gradient elasticity*” by Lam *et al.* (2003) in [7].

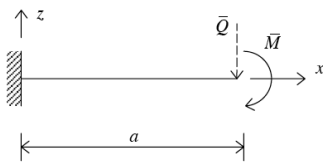


Figure 1: A beam with an applied force or moment at the free end from [7]

A simple thin cantilever beam bending test on epoxy was developed by using nano-indentation (see Figure 1). The load-deflection dependence of the beam can be classically described by:

$$w_0 = \frac{\bar{Q}a^3}{3D'_0h^3}. \quad (2)$$

When strain gradients effects are considered, the load-deflection dependence becomes according to [7]:

$$w_0 \approx \frac{\bar{Q}a^3}{3D'h^3}. \quad (3)$$

In classical bending theory, the bending rigidity D'_0 is independent of the length and thickness of the beam. But here a new strain gradient theory was developed: The higher-order bending rigidity D' becomes dependent of the thickness h and of the

material length scale parameters l_i of the beam:

$$D' = D'_0 \left[1 + \left(\frac{b_h}{h} \right)^2 \right], \quad D'_0 = \frac{E}{12\varphi}, \quad b_h^2 = 6(1 - 2\nu)l_0^2 + \frac{2}{5}(4 - \nu)l_1^2 + 3(1 - \nu)l_2^2. \quad (4)$$

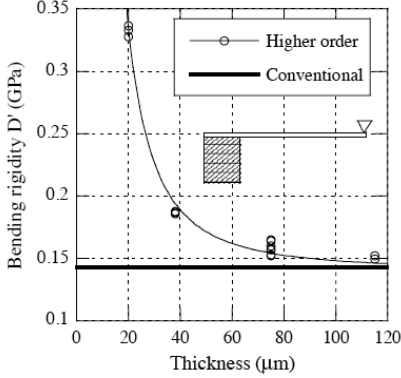


Figure 2: Plot of bending rigidity over thickness from [7]

this work shows that strain gradients can be a very powerful and important tool in order to determine parameters that describe the size effect in small-scale structures.

2.2 Wei *et al.* 2001: Strain-gradient plasticity applied to indentation tests

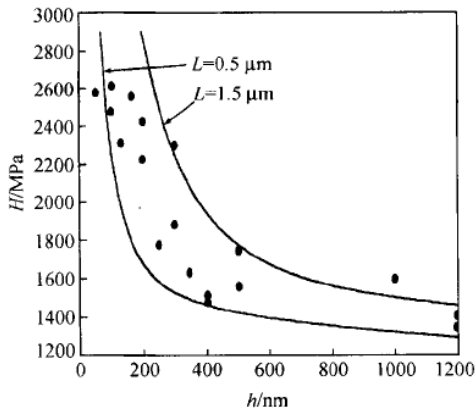


Figure 3: Experimental results (dots) and predicted results (line) for different lengths L : plot of hardness over depth for single crystal copper from [10]

The higher-order bending parameter is b_h , which includes the dependent length scale parameters l_i . D'_0 is a bending stiffness parameter, which is independent of the geometry of the beam with $\varphi = 1 - \nu^2$ for plain strain and $\varphi = 1$ for plane stress. ν is POISSON'S ratio, a is the distance between the load and the mounting and h is the thickness of the beam.

The bending rigidity D' is plotted over the thickness h in Figure 2. Obviously, the bending stiffness is enlarged by a factor 2.4 if the height of the beam is reduced from $115 \mu\text{m}$ to $20 \mu\text{m}$. The measured size effect fits to the developed higher-order bending solutions and cannot be described by classical elasticity. Consequently,

Another experiment used in context with strain gradient plasticity theory, which uses micro-indentation (instead of nano-indentation as mentioned above), was performed in [10] on single crystal copper plates (and also with aluminum, which is not considered further in this article): Based on strain gradient plasticity theory, the *size effect* was predicted by means of the finite element method for evaluation of experimental micro-indentation tests. Results for the hardness/depth relation are shown in Figure 3. It can be seen that the *size effect* is very pronounced, if the indentation depth is smaller than the micro-scale of the material (particularly, if the indentation depth is smaller than $1/3$ of the micro-scale). Finally it was shown that the size effect, which occurred in the experiments, can be described sufficiently by strain gradient plasticity theory.

2.3 Dell'Isola *et al.* 2015: Pantographic beam structures

In the recent past new experimental techniques have been developed with the objective of working toward making generalized continuum theories useful for technology [3, 5, 6, 12]. Different experimental setups, different materials, and different structures were used [7, 3, 5, 6, 7, 8, 10, 14].

A particularly promising experiment was performed by [5] last year in *"Designing a light fabric meta-material being highly macroscopically tough under directional extension: First experimental evidence,"* influenced by and based on the thoughts of Placidi *et al.* [12]. So-called pantographic structures have been designed and afterwards manufactured by 3D-prototyping, using the material PA 2200 (polyamide powder). Two families of inextensible "fibers," which can also be treated as beams, are printed in two arrays orthogonal to other other in parallel planes, which are then superimposed. The parallel planes are interconnected by cylinders (elastic pivots) of small height. A model of this pantographic lattice is shown in Figure 4.

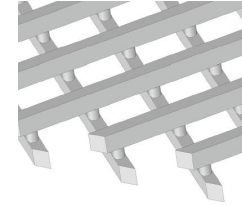


Figure 4: 3D-Model of the lattice structure from [5]

The Pipkin continuum model (for further information of the Rivlin-Pipkin decomposition of plane displacement of continua see [25, 26, 27]) is used to estimate the behavior of the samples during a biaxial extension test in numerical simulations. Here, the elastic pivots are described by the first-gradient (in displacement) dependence of the deformation energy density. The bending stiffness of the fibers is described by a second-gradient dependence (in displacement). Finally, four deformation energy densities were used for the numerical simulation. The force-displacement plot for the considered energy models of the elastic simulation is shown in Figure 5 for a specimen, one side of which is three times longer than the other. It can be recognized, that the resultant force increases when the limit of maximum elongation is reached because of the inextensibility constraint. Finally, based on the results of the simulation, the experimental measurements of the aforementioned pantographic structures have been designed. Three samples with different pivot heights and different pivot diameters were investigated. We concentrate on sample 2 (0.5 mm height and 0.9 mm diameter). Real macroscopic tensile tests were performed, resulting in an elongation along the direction of the shorter sides of the pantographic samples (an example of sample 2 is given in Figure 6). The beams at the lower right corner experience a large elongation between the pivots marked with two black points. In this region, the bending energy of fibers is concentrated (traction stress of approximately 200 MPa). This could not be shown in the numerical simulations.

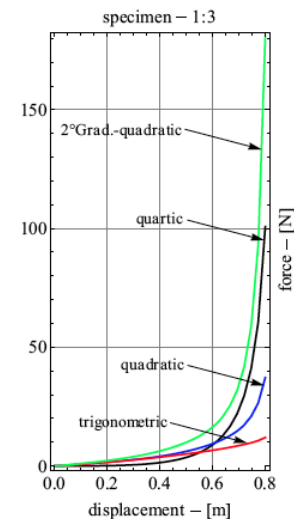


Figure 5: Force-displacement plot of different energy models in numerical simulation from [5]

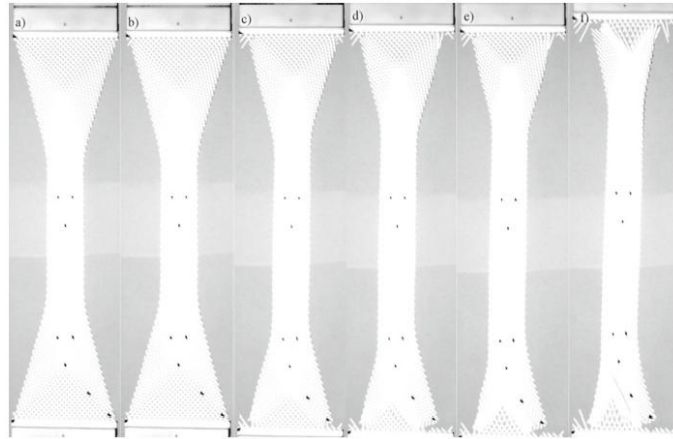


Figure 6: Tensile test of sample 2 from [5]: (a) before first beam failure, (b) after breakage of the fiber in the upper left corner, (c)–(f) damage of further fibers

The three points, which are arranged in a triangle, visualize the shear angle (one in the middle and another one on the bottom in Figure 6). These angles are obviously not constant during the deformation. Furthermore, in Figure 6 the moment of first beam failure can be recognized when sample 2 is subjected to increasing stretch. Figure 6b shows a rupture of a beam in the upper left corner. From Figure 6c through Figure 6f more and more beams and pivots fail. In Figure 7 force over displacement is plotted with its characteristic points corresponding to the loading steps from Figure 6a through 6f.

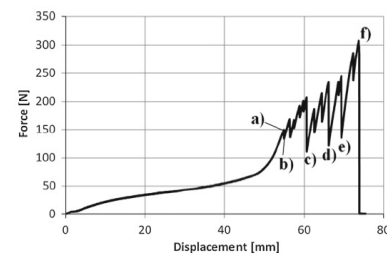


Figure 7: Force over displacement plot of sample 2 from [5]

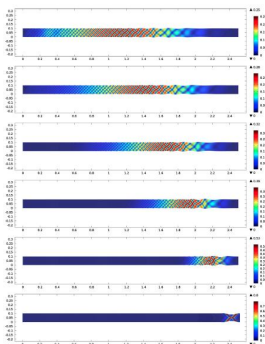


Figure 8: Numerical analysis of wave propagation from [11]

In general, toughness can be defined as the amount of energy needed to lead it to failure. By looking at Figure 7, the failure of the pantographic lattice is visualized by the local minima in the plot. Surprisingly after one failure within the structure, which was subjected to external loading, the specimen “recovers” and is able to carry even higher loads than before. Because of the complex geometry the beams reorganize themselves, resulting in an increasing resistance to elongation. Hence, the maximum energy before reaching final failure is greater than the maximum of elastic energy that can be stored in the developed specimen [5]. Consequently, it is likely that this newly developed structure will serve as an extremely tough metamaterial [5]. Other conceivable applications for pantographic 2D sheets are discussed in [11]. There a dynamic analysis of pantographic sheets (where the beams are connected via hinges) is presented.

Figure 8 shows an example of wave propagation as a consequence of an imposed time-dependent longitudinal displacement at the right side of the sheet [11]. It is shown that the homogenized limit of this structure is best modeled by a second gra-

dent theory instead of a classic continuum. Three other dynamic analyses have been performed, which will not be discussed in this article. Summarizing one may say that the combination of high mechanical strength, lightness, and flexibility makes these structures extremely attractive for technical solutions in lightweight constructions, for space/aircraft technology, or for the medical industry.

2.4 Kong *et al.* 2009: Static and dynamic analysis of microbeams

Another static and dynamic simulation-analysis was conducted by Kong *et al.* (2009) in [14]. Based on strain gradient theory from Lam *et al.* [7] microbeams were investigated. The newly developed model contained three additional material length-scale-parameters. A static and a dynamic analysis was performed based on the assumption that all length-scale-parameters are the same and that the thickness of the beam is approximately equal to the material length-scale-parameter ($h = 20 \mu\text{m}$, $l = 17.6 \mu\text{m}$). The numerical analyses are shown in Figure 9 for a static simulation (deflection *vs.* ratio of length to thickness) and in Figure 10 for a dynamic simulation (natural frequency *vs.* the ratio of length to thickness). The static analysis shows that the deflection of the beam predicted by classical beam theory is about 12 times higher than the one predicted by strain gradient elastic beam theory for the smallest thickness (see Figure 9a). Classical beam theory can only predict the deflection of the beam with the biggest thickness with sufficient accuracy (see Figure 9d). The dynamic analysis showed that the natural frequencies of the beam predicted by strain gradient elastic beam theory are about 3.5 times higher than the ones predicted by classical beam theory (see Figure 10). If the thickness of the beam is of the size of the material length-scale-parameter, the beam deflections decrease and the natural frequen-

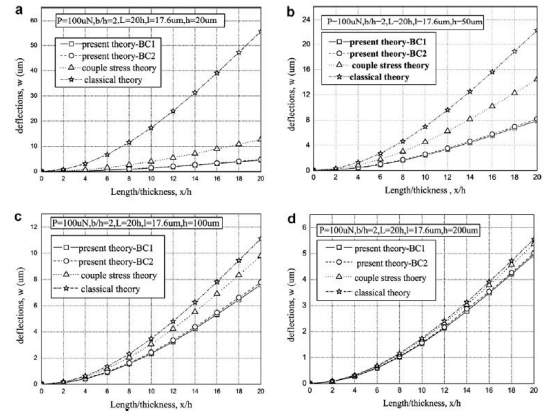


Figure 9: Static plot of deflections over the ratio of length to thickness for different thickness values and different theories from [14]

the ratio of length to thickness).

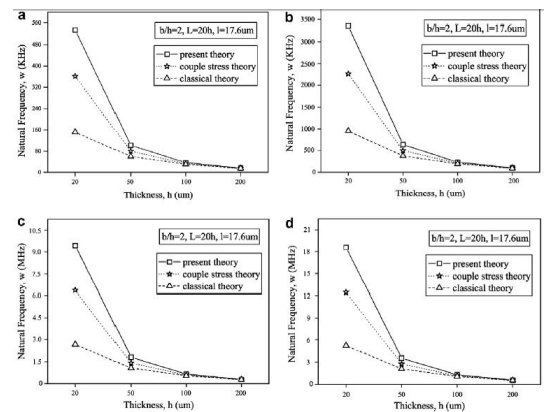
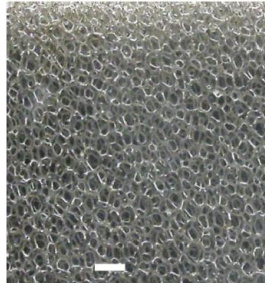


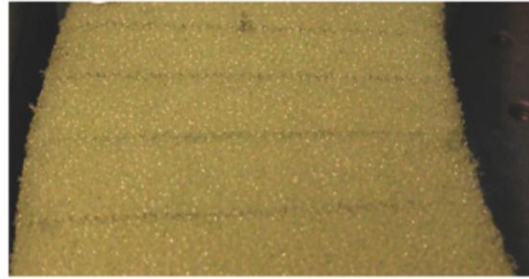
Figure 10: Dynamic plot of natural frequencies over the ratio of length to thickness for different thickness values and different theories from [14]: a) first natural frequencies, b) second, c) third, d) fourth

cies increase [14]. If the thickness is much higher than the length-scale-parameter, the size effects almost vanish.

2.5 Lakes *et al.* 2015: Foams



(a) Inner structure of first investigated foam from [6], scale bar is 5 mm.



(b) Structure of second investigated foam during bending of the beam from [6].

Figure 11: The structures of the investigated foams are shown: a) Open cell polyurethane foam with a cell size of about 1.2 mm, b) Bent test beam of foam with a cell size of about 0.4 mm

Fundamental work on experiments in context with generalized continuum theories was presented in 1995 and 2015 in [7, 6]. Experimental methods for determining the six COSSERAT elastic constants of isotropic solids with *size effects* were considered. *Inter alia* COSSERAT elasticity [13], micromorphic elasticity and nonlocal elasticity was used. It has been shown, for example, that polycrystalline and particulate type

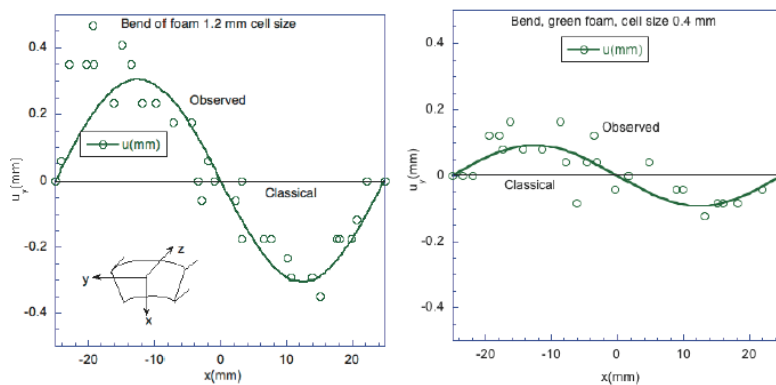


Figure 12: Experimental data and its fit is shown as a plot of deformation over position from [6], the plot of larger cell-sized foam is demonstrated on the left side and the one of the smaller cell-sized foam is demonstrated on the right side

material microstructures behave nearly classically (like a metal or an amorphous polymer) and that the behavior of several cellular solids can be characterized by COSSERAT elasticity. A bending test was conducted in [6], where bars of open cell reticulated polyurethane foams were examined. Two foams, distinguishable by

cell size, were investigated: One foam with an average cell size of 1.2mm is shown in Figure 11a, while the other foam with 0.4mm cell size is shown in Figure 11b. Bending was achieved by bringing the ends of cemented stalks into contact. The displacement of the surface was measured via digital photography. Figure 12 shows the experimental results for both foams where deformation is plotted *vs.* position (without deformation due to tilting because of lack of sufficient image processing). A sinusoidal bulge deformation in both specimen can be recognized from the lateral side. The magnitude of deformation for the larger cell foam is bigger than the one for the foam with the smaller cells. This suggests a local length scale effect. The foam with the 1.2mm-sized cells has a ratio for the moduli in the different directions of 1.6 and is therefore anisotropic, the foam with the 0.4mm-sized cells has a POISSON'S ratio of approximately 0.3 and is considered as isotropic. An approximated three-dimensional COSSERAT bending solution was developed for the isotropic material and compared to experimental measurements of the isotropic foam (with 0.4mm-sized cells). The analytical COSSERAT solution is shown in Figure 13. By comparing Figure 13 with the right plot of Figure 12 it can be recognized that the observed behavior in the experiments fits very well to the analytical solution (qualitatively as well as quantitatively). This reveals the presence of COSSERAT elastic effects. Hence, macroscopical experiments can lead to the determination of unknown parameters, which show up in generalized continuum theories.

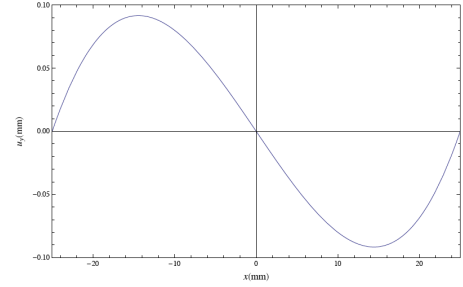


Figure 13: Analytical solution based on the COSSERAT model developed by [6]

2.6 Liebold *et al.* 2015 and 2016: AFM and Micro-Raman-spectroscopy

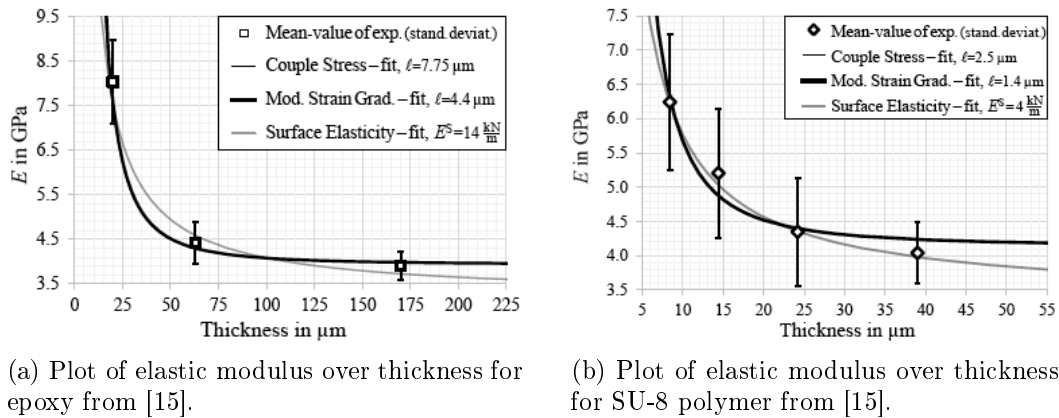


Figure 14: Evaluated fits of the used generalized continuum theories and averaged results of the measured elastic modulus of: a) epoxy b) SU-8 polymer

Further experimental work in the fields of generalized continua was performed by Liebold in 2015 [2] and in 2016 [15] by using atomic-force-microscopy and micro-Raman-microscopy on epoxy as well as on the polymer SU-8 during bending tests with the help of the EULER-BERNOULLI beam model.

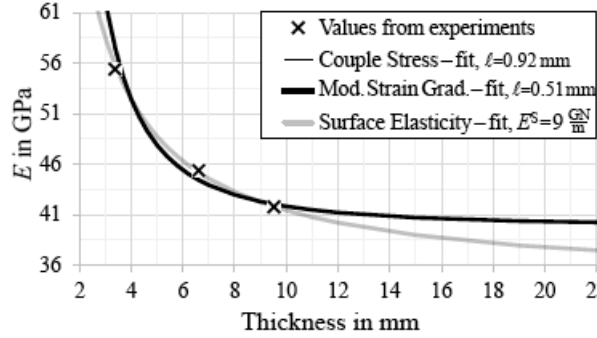


Figure 15: Plot of elastic modulus over thickness of drilled aluminium sample obtained from frequency measurements from [15]

Also, a vibration analysis for measuring eigenfrequencies of macroscopically sized pieces of aluminum foams as well as an aluminum bar with artificial heterogeneities was obtained. Modified strain gradient theory, micropolar theory, and couple stress theory, as well as the core-surface model (surface elasticity) and the core-shell model (surface layer) have been developed. The last model was developed because it is even able to characterize *negative* size effects in contrast to higher-order theories. The averaged results from measurements of the elastic modulus of epoxy and evaluated fit functions for parameters of the generalized continuum theories are plotted in Figure 14a. The ones for the SU-8 polymer are plotted in Figure 14b.

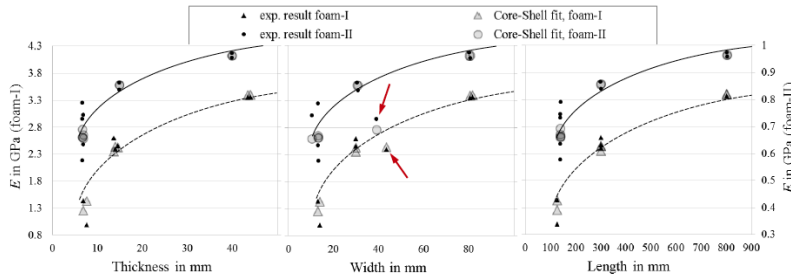


Figure 16: Plot of elastic modulus over thickness (on the left side), width (in the middle) and length (on the right side) of two aluminium foams, which were investigated in vibration analysis from [15]

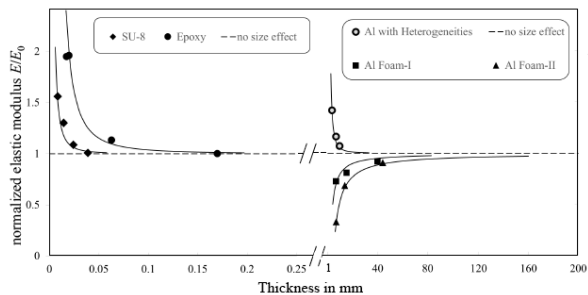


Figure 17: A multiscale-graph: Normalized elastic modulus is plotted over the thickness for all materials from [15]

It can be recognized that experimentally measured values match the values of the numerical functions of the generalized continuum models very well. The results of the frequency measurements of the elastic modulus of the aluminum with artificial heterogeneities and the evaluation of the fit functions from the generalized continuum theories are plotted

ted in Figure 15. Experimental values fit particularly well when using the surface elasticity model.

The fit functions of the core-shell model of the aluminum foams are plotted in Figure 16. The results from the frequency analysis point up a *negative* size effect. It is reflected in a softer elastic response when outer dimensions of a body are reduced [15]. The arrows in Figure 16 highlight the values which differ from the ratio of $\text{length}/\text{width} = 10$. Consequently, a dependence of the width can be established.

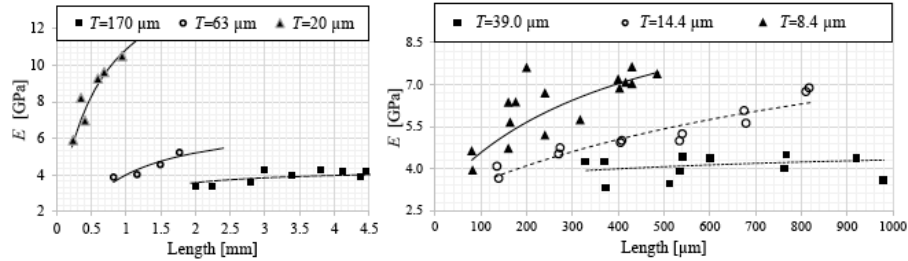


Figure 18: Elastic modulus is plotted over the length for epoxy (on the left side) and for SU-8 polymer (on the right side) for different thicknesses from [15]

To visualize the size effect of all materials used in this work in a better way, the normalized elastic modulus is plotted for all different materials over the thickness in Figure 17. The dependence of measured elastic moduli to the length of the beam for epoxy and SU-8 polymer is made obvious in Figure 18: The shorter the length of the beam, the smaller the elastic modulus. But no model is able to describe the dependence of the elastic modulus from both, the length and the thickness of a beam.

With the macroscopic samples of drilled aluminum, it could be shown, that the parameter l is of the order of the physical dimension of the internal structure, *i.e.*, the diameter of the holes. No size effect was observed during tensile testing of epoxy samples of the same thickness. This was also reported by [7].

3 Conclusion and Outlook

An overview of the developments of different experimental techniques applied on generalized continuum theories in the recent past was given. Noticeably, micropolar theory and higher-strain-gradient theory are one of the most used theories for characterizing size effects [15]. There are different experimental techniques, macroscopic as well as small scale experiments, which are capable of determining the specific higher material parameters pertinent to generalized continuum theories. New type of structures, such as the pantographic ones developed in [5], lead to new technical opportunities for strong lightweight materials. This is important in the space and aircraft as well as automobile or medicine industries, where inexpensive and light materials are of high importance and great urgency. Moreover, it should be mentioned that numerical analyses, which use generalized continuum models, should be improved to get more knowledge of how to develop and construct new experiments

to investigate, for example, new lightweight materials or the size effects in nano- and microstructures. In the recent past, mostly models for isotropic solids were developed, but also anisotropic solids or even fluids and gases should be investigated more intensively in the future [4, 22].

References

- [1] Lam, D. C. C., Yang, F., Chong A. C. M., Wang, J., Tong, P. (2003): Experiments and theory in strain gradient elasticity. *Journal of the Mechanics and Physics of Solids*. 51(8), pp. 1477-1508
- [2] Liebold, C. (2015): Größeneffekt in der Elastizität, Dissertation, TU Berlin.
- [3] Liebold, C., Müller, W.H. (2013): Measuring material coefficients of higher gradient elasticity by using AFM techniques and Raman-spectroscopy. In: *Generalized continua as models for materials*, Altenbach, H., Forest, S., Krivtsov, A. (editors). Springer Berlin Heidelberg, pp. 255-271.
- [4] Eremeyev V.A., Lebedev L.P., Altenbach H. (2013): *Foundations of micropolar mechanics*. Springer.
- [5] Dell'Isola, F., Lekszycki, T., Pawlikowski, M., Grygoruk, R., Greco, L. (2015): Designing a light fabric metamaterial being highly macroscopically tough under directional extension: first experimental evidence. *Zeitschrift für angewandte Mathematik und Physik, ZAMP*, 66(6), pp. 3473-3498.
- [6] Lakes, R., Drugan, W.J. (2015): Bending of a Cosserat elastic bar of square cross section: Theory and experiment. *Journal of Applied Mechanics*, 82(9), 091002.
- [7] Lakes, R. (1995): Experimental methods for study of Cosserat elastic solids and other generalized elastic continua. Ed. H. Mühlhaus, J. Wiley, N.Y., Ch. 1, pp. 1-25.
- [8] Chong, C.M. (2002): Experimental investigation and modeling of size effect in elasticity, Dissertation, Hong Kong University of Science and Technology.
- [9] Fleck N.A., Muller G.M., Ashby M.F., Hutchinson J.W. (1994): Strain gradient plasticity: Theory and experiment. *Acta metall. mater.*, 42(2), pp. 475-487.
- [10] Wei Y., Wang X., Wu X., Bai Y. (2001): Theoretical and experimental researches of size effect in micro-indentation test, *Science in China Series A: Mathematics*, 44(1), pp. 74-82.
- [11] Dell'Isola, F., Della Corte, A., Giorgio, I., Scerrato, D. (2016): Pantographic 2D sheets: Discussion of some numerical investigations and potential applications. *International Journal of Non-Linear Mechanics*, Elsevier, 80, pp. 200-208.
- [12] Placidi, L., Andreaus, U., Della Corte, A., Lekszycki, T. (2015): Gedanken experiments for the determination of two-dimensional linear second gradient elasticity coefficients. *ZAMP*, 66(6), pp. 3699-3725.
- [13] Cosserat, E. and F. (1909): *Theorie des Corps Deformables*. Hermann et Fils, Paris

-
- [14] Kong, S., Zhou, S., Nie, Z., Wang, K. (2009): Static and dynamic analysis of micro beams based on strain gradient elasticity theory. *International Journal of Engineering Science*, 47(4), pp. 487-498.
- [15] Liebold, C., Müller, W.H. (2016): Applications of Higher-Order Continua to Size Effects in Bending: Theory and Recent Experimental Results. In: *Generalized Continua as Models for Classical and Advanced Materials* (pp. 237-260). Springer International Publishing.
- [16] Eringen, A.C. (2010): *Nonlocal Continuum field theories*. Springer-Verlag, 2010, New York.
- [17] Toupin, R.A. (1962): Elastic materials with couple-stresses. *ARMA*, 1962, 11(1), pp. 385-414.
- [18] Bertram, A. (2013): *The Mechanics and Thermodynamics of Finite Gradient Elasticity and Plasticity*. Preprint, Institut fuer Mechanik, Otto-von-Guericke Universität Magdeburg.
- [19] Javili, A., McBride, A., Steinmann, P. (2013): Thermomechanics of Solids With Lower-Dimensional Energetics: On the Importance of Surface, Interface, and Curve Structures at the Nanoscale. *A Unifying Review, Applied Mechanics Reviews*, 65, pp. 010802-1-010802-31.
- [20] Gurtin, M.E., Murdoch, A.I. (1975): A Continuum Theory of Elastic Material Surfaces. *ARMA*, 57(4), pp. 291-323.
- [21] Atkin, R.J., Leslie, F.M. (1970): Couette flow of nematic liquid crystals. *The Quarterly Journal of Mechanics and Applied Mathematics*, 23(2), 3-24.
- [22] Sengupta, A. (2013): *Topological Microfluids: Nematic Liquid Crystals and Nematic Colloids in Microfluidic Environment*. Springer Science & Business Media.
- [23] Müller, I. (1985): *Thermodynamics*. Pitman Advanced Publishing Program, Boston, London, Melbourne.
- [24] Leslie, F.M. (1968): Some Constitutive Equations for Liquid Crystals. *Archive for Rational Mechanics and Analysis*, 28(4), pp. 265-283.
- [25] Pipkin, A.C. (1981): Plane Traction Problems for inextensible Networks. *Q.J. Mech. Appl. Math.*, 34(4), pp. 415-429.
- [26] Rivlin, R.S. (1997): *Plane Strain of a Net formed by inextensible Cords*. *Collected Papers of RS Rivlin*, Springer, Berlin, pp. 511-534.
- [27] Dell'Isola, F., d'Agostino, M. V., Madeo, A., Boisse, P., Steigmann, D. (2016): Minimization of shear energy in two dimensional continua with two orthogonal families of inextensible fibers: the case of standard bias extension test. *Journal of Elasticity*, 122(2), pp. 131-155.

Wolfgang H. Müller, Berlin University of Technology, Department of Mechanics, Chair of Continuum Mechanics and Materials Theory, Einsteinufer 5, 10587 Berlin, Germany
Gregor Ganzosch, Berlin University of Technology, Department of Mechanics, Chair of Continuum Mechanics and Materials Theory, Einsteinufer 5, 10587 Berlin, Germany

Determination of nanoscale mechanical properties of rubbers under uniaxial stretching by means atomic force microscopy

Oleg K. Garishin and Sergey N. Lebedev
gar@icmm.ru

Abstract

Polymers and various composites on their basis have long and successfully used in a variety of industries. Currently one of the most promising directions for further improvement of their mechanical and operational characteristics associated with different types of nanoparticles as a filler, i.e. the creation of nanostructured materials. Atomic force microscopy (AFM) is one of the most promising tools for the study of such materials internal structure. Its principal advantage is that the AFM allows to obtain information not only on the morphology of the matter structure at the nanoscale level, but also on its local physical and mechanical properties (which, as experience shows, may differ significantly from what we see at the macro level). The successful development of modern nanotechnologies in materials science is not possible without this knowledge.

Atomic force microscopy also allows to explore local strength properties of nanostructured materials. Appropriate experimental studies of the nanostructure of elastomers and elastomeric nanocomposites, pre-stretched at the macro level until pre-scission states were held in ICMM UB RAS. Experiments have shown that the interaction of the AFM probe with previously deformed surface differs substantially from that observed in samples unloaded. Most of the standard models used for interpretation of the results of AFM scanning, are based on the solution of the classical problem of Hertz contact between a rigid sphere and a flat linearly elastic half-space, which does not take into account the given factor.

Model studies of contact interaction between the AFM probe and the surface of uniaxially stretched polymer sample were carried out to assess emerging errors. Two types of materials have been considered: 1) neo-Hookean material; 2) real natural rubber NR0-799A (its mechanical properties were approximated by Ogden potential). Contact boundary problem on pressing of hard cone probe with a rounded tip (probe) in a nonlinearly elastic surface has been solved for this purpose. At calculations the sample was subjected to uniaxial tension before the probe indentation. Pre-stretching elongation ratio varied from 1 to 7. The problem was solved in a three-dimensional formulation, finite element method was used. As a result the dependencies between elastic

reaction force on the indenter F , the indentation depth of the AFM probe into the material u and pre-stretching elongation ratio of the sample λ_s were built.

Calculations showed that the indentation force essentially depends on the pre-stretching of the sample, with the relationship between F and λ_s is nonlinear. The more deformed polymer is the more it manifests itself. These results are planned further to use in the study of the destruction of nanostructured polymer materials with the help of atomic force microscopy.

Using advanced nanostructured materials in modern industry we need more profound knowledge of their internal structure and physical properties at micro, meso and nanolevels. Atomic force microscope (AFM) is one of the most promising tools to solve this problem [1, 2]. The force interaction between investigated surface and the cantilever beam (cantilever) with a sharp silicon probe at the free end underlies of its work. Typically, this probe (indenter) has a conical shape with rounded apex. The length of the beam is around 100–200 microns, the height of the cone is equal to 1–3 microns, tip radius (defining measurement accuracy) varies from 10 to 100 nm. Three operating modes of an atomic force microscopy are determined depending on the interaction between cantilever and sample surface: contact, non-contact and semi-contact. The greatest interest for the materials science is the contact mode (power or indentation mode) when the top of the probe is in direct contact with the surface and pressed monotonically into a specimen surface [3]. This mode allows to obtain information not only about the surface topography but also local mechanical properties at micro and nanoscale [4, 5, 6, 7], which can be very much different from the macroscopic characteristics [8].

AFM probe scans the surface of the test sample in an experiment. Obtained thereby data are the relationship between the coordinates of scanning points, the reaction force acting on the probe and the depth of indentation. These results of themselves are not sufficiently informative. Therefore the further theoretical decoding involving various physical and mechanical models is required (taking into account the various factors that affect the interaction of the probe and the surface, as well as additional knowledge about the research subject) [9, 10].

Atomic force microscopy allows you also to investigate the local strength properties of nanostructured materials. Experimental studies of the nanostructure of elastomers and elastomeric nanocomposites, pre-stretched at the macro level until pre-scission state, were carried out in ICMM UB RAS [11]. It was established that nanofibers (nanostrands) with mechanical properties different on characteristics of the base material can be formed in the top of the microcrack and the interaction of the AFM probe and the pre-deformed surface differs substantially from that observed in samples unloaded.

Standard software supplied to decrypt the atomic force scanning (AFM), based mainly on the models using Hertz classical solution of the contact between rigid sphere and a linearly elastic flat halfspace [12, 13]. In case of pre-loaded specimens these methods should be used with great caution for the following reasons: At first, the Hertz solution takes no account of that halfspace can be deformed previously. Secondly, the studied polymers are "soft" non-linear elastic materials, that is, an AFM probe can be pressed into the surface under study to a considerable depth (thereby the theory of finite deformations must be used).

The computer modeling of the AFM probe indentation in pre-stretched non linear elastic specimen was carried out to evaluate arising due to this errors in decoding results of AFM scanning. Mechanical response of the interaction was determined from the solution of the contact boundary value problem of pressing a hard cone with rounded apex in a soft elastic surface. Calculated scheme is shown in Fig. 1. The sample was subjected to a uniaxial pre-deformation (λ_s is the extension ratio of pre-stretching). Solution was sought by finite element method (in 3D formulation). Mechanical properties of elastomer were described by using various elastic potentials. As a result, dependences of the elastic reaction force F on mechanical properties of the sample material and geometric characteristics of the probe (tip radius R and cone angle α) were calculated. Typical values of $R=10$ nm and $\alpha = 40^\circ$ for modern probes were taken in the calculations.

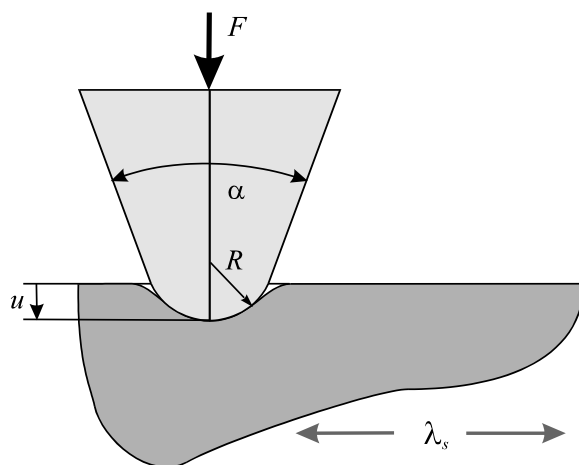


Figure 1: Calculated scheme of the model study of AFM probe indentation in pre-loaded specimen

Fig. 2 shows the dependence of $F(u, \lambda_s)$ when the mechanical properties of the polymer sample are described by neo-Hookean potential (E_s is the Young's initial modulus). Extension ratio λ_s was varied from 1 to 7 (tension) and from 1 to 0.45 (compression). The finite element mesh was composed of linear tetrahedral elements (polymer – about 250,000 elements, the probe – 25000). It was found that pre-deformation of the surface significantly affects the reaction force of the probe F for sufficiently large stretchings and not so much at small. For example, at the depth of probe indentation $u = 0.5R$ force F for $\lambda_s = 5$ increases 2.67 times compared with the case $\lambda_s = 1$, but for sample extension $\lambda_s = 2$ the increase was only 16%. Clear from the graph that the reaction force F on indentation the probe into a pre-compressed polymer with decreasing values of λ_s weakens. This can be explained by the fact that uniaxial compression of the body (e.g., a cube) with free lateral boundaries is equivalent to biaxially stretched on other faces. That is, pressing at $\lambda_s < 1$ is equivalent to the case of indentation into material, stretched along mutually perpendicular directions.

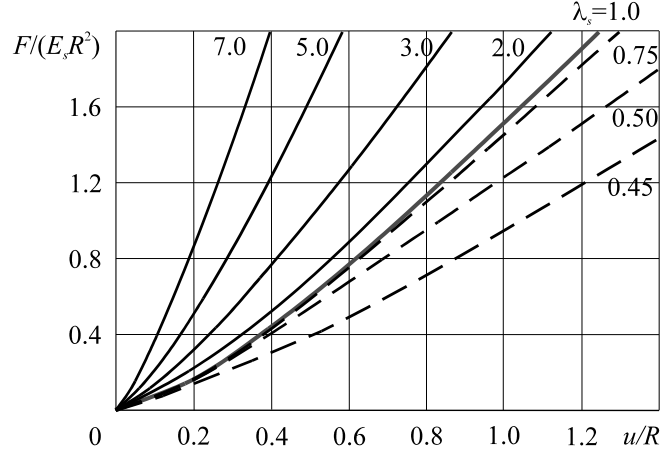


Figure 2: The interaction of the AFM probe with uniaxially deformed polymer sample (neo-Hooke). Solid lines — stretching, dashed lines — compression

Similar model studies were also carried out for the real elastomer (natural rubber NR0-799). As before, the contact boundary value problem of the AFM probe indentation in the polymer was solved using finite element method (in 3D setting). The finite element mesh composed of the same linear tetrahedral elements was similar to the previous neo-Hookean version.

Mechanical macro uniaxial tensile test (sevenfold elongation of the sample) was carried out to determine the elastic properties of this rubber. The resulting strain curves were approximated by Ogden potential of the 2nd order ($N = 2$) [14, 15]. Approximation error was less than 2%.

$$w_{Ogden} = \sum_{i=1}^N \frac{2\mu_i}{\alpha_i^2} (\bar{\lambda}_1^{\alpha_i} + \bar{\lambda}_2^{\alpha_i} + \bar{\lambda}_3^{\alpha_i} - 3) + \sum_{i=1}^N \frac{1}{D_i} (J^{el} - 1)^{2i},$$

where $J^{el} = \lambda_1 \lambda_2 \lambda_3$, $\bar{\lambda}_n = J^{-1/3} \lambda_n$ are deviators of principal extensions λ_n . D_i are material parameters responsible for the thermal expansion. The initial shear modulus μ_0 , bulk modulus K_0 , as well as the initial Young's modulus E_0 and Poisson's ratio ν_0 (for the sample $\mu_s = \mu_0$, $K_s = K_0$, $E_s = E_0$, $\nu_s = \nu_0$) are expressed through the parameters of Ogden potential as

$$\mu_s = \sum_{i=1}^N \mu_i, \quad K_s = \frac{2}{D_1}, \quad E_s = \frac{9K_s \mu_s}{3K_s + \mu_s}, \quad \nu_s = \frac{3K_s - 2\mu_s}{6K_s + 2\mu_s}.$$

The dependence of nominal stress σ^0 on the sample extension ratio λ in uniaxial tension is shown in Fig. 3. The values of Ogden potential parameters were determined from this curve. They are given in Table 1.

Table 1. Parameters of Ogden elastic potential for natural rubber NR0-799A

$i = 1, N$	μ_i , MPa	α_i	D_i , MPa ⁻¹
1	+7.269567E-17	+7.28334893	5.3885E-1
2	+7.473002E-2	-3.19357443	0.0

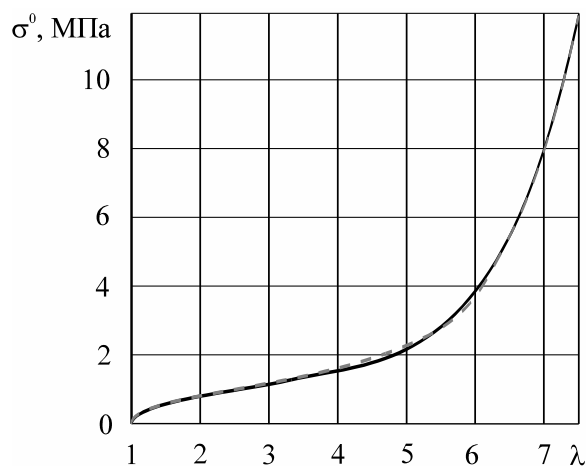


Figure 3: Approximation of the real stress–strain dependence (dashed line) for natural rubber NR0-799A by means Ogden potential (solid line)

Fig. 4 shows dependences of the reaction force on the probe F on the indentation depth u in the pre-stretched samples of natural rubber NR0-799A. The pre-stretched extension ratio λ_s has ranged from 1 to 7.

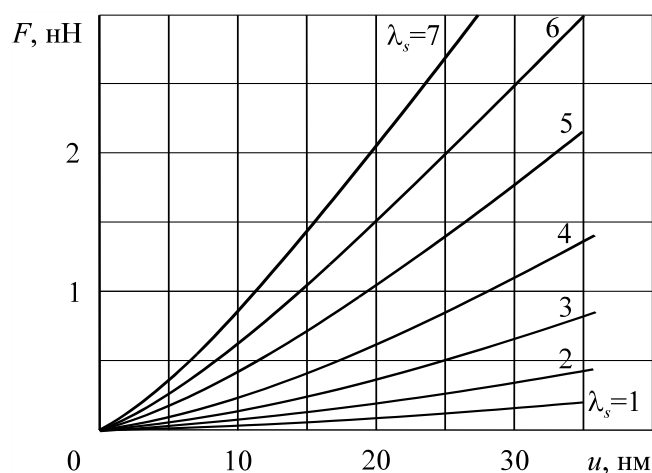


Figure 4: Model dependences of the force pressing an AFM probe into a sample of the natural NR0-799A rubber on the indentation depth u and pre-stretched extension ratio λ_s

Comparing these results with the neo-Hookean material showed that in natural rubber the pre-stretching of material considerably stronger effect on the process of probe indentation. For example, in case of $\lambda_s=7$, and $u=20$ nm in the reaction force F for natural rubber increases almost by 30 times as compared to not pre-stretched sample, whereas for neo-Hookean material the increase is about 6 times. That is to say this factor affects the process of AFM probe indentation and consequently the determination of material nanoscale elastic characteristics very essentially.

Obtained dependences are planned to be used in 2016 for the correct interpretation of the results of AFM scanning pre-stretched real natural rubber, i.e. in studying the processes of its destruction at nano and micro levels.

Acknowledgements

This work is executed at a financial support of RFBR (Grant 14-01-96002-r_urals_a) and Complex program UB RAS 15-10-1-18.

References

- [1] Binnig G., Rohrer H., Gerber C., Weibel E. Surface studies by scanning tunneling microscopy. *Phys. Rev. Lett.*, 1982, V. 49, N 1, P. 57–61.
- [2] Mironov V.L. Fundamentals of the scanning probe microscopy. Nizhnij Novgorod, 2004. 115 p. (In Russian)
- [3] Schuh C.A. Nanoindentation studies of materials. *Materials Today*, 2007, V. 9, N 5, P. 32–40.
- [4] Fischer-Cripps A.C. Nanoindentation. Springer, 2002, 217 p.
- [5] Bhushan B. Nanotribology and nanomechanics. Springer, 2005, 1148 p.
- [6] Giessib F.J. AFM's path to atomic resolution. *Materials Today*, 2005, V. 8, N 5, P. 32–41.
- [7] Butt H.-J., Capella B., Kappl V. Force measurements with atomic force microscope: Technique, interpretation and applications. *Surface Science reports*, 2005, V. 59, P. 1–150.
- [8] Chvalun S.N. Polymeric nanocomposites. *Priroda*, 2000, N 7, P. 22–30. (in Russian)
- [9] Dao M., Chollacoop N., Van Vliet K.J., Venkatesh T.A., Suresh S. Computational modeling of the forward and reverse problems in instrumented indentation // *Acta Mater.*, 2001, V. 49, B. 19. P. 3899–3918.
- [10] Garishin O.K. Simulation of atomic-force microscope contact mode operating taking into account nonmechanical forces of interaction with a specimen surface // *Computational continuum mechanics*, 2012, V. 5, N 1, P. 61–69.
- [11] Morozov I.A., Lauke B., Heinrich G. AFM investigation of structure and mechanical properties of crack zones in CB filled/unfilled vulcanizates. *Kautschuk Gummi Kunststoffe*, 2013, N. 10. P. 71–76.
- [12] Timoshenko S.P. *Theory of elasticity*, Moscow, 1975, 576 p.
- [13] Deryagin B.V., Churaev N.V., Muller V.M. *The surface forces*. Moscow, 1985, 398 p. (in Russian)
- [14] Ogden R.W. Large Deformation Isotropic Elasticity – On the Correlation of Theory and Experiment for Incompressible Rubberlike Solids, *Proceedings of the Royal Society of London. Series A, Mathematical and Physical Sciences*, 1972, V. 326, No. 1567, P. 565–584.

REFERENCES

- [15] Ogden R.W. Non-Linear Elastic Deformations. Dover Publications, 1997, 544 p.
endthebibliography

Oleg K. Garishin, Institute of Continuous Media Mechanics, Perm, Russia
Sergey N. Lebedev, Institute of Continuous Media Mechanics, Perm, Russia

Experimental research and computer modeling of the mechanical behavior of polymer/clay nanocomposites under large deformations

Oleg K. Garishin, Vladimir V. Shadrin, Victor A. Gerasin,
Maria A. Guseva
shadrin@icmm.ru

Abstract

The results of experimental and theoretical studies of the mechanical properties of nanocomposites based on polyethylene filled with ultrathin flakes of modified clay (montmorillonite) are presented. Experimental studies were carried out using a special technique, based on the cyclic deformation of the sample in the mode: stretching — stress relaxation — reducing the strain to some predetermined constant value of tensile strength — again relaxation — the next cycle of deformation. Each subsequent cycle is made with increasing amplitude in the deformations. The calculations were executed using structural-phenomenological model describing elastic- viscous-plastic behavior of finite-deformable medium. The model is based on a differential approach to the construction of constitutive equations of material mechanical behavior with the help of symbolic schemes. The model symbolic schema consists of two parallel branches containing two serially connected elements: a) the elastic and plastic, b) the elastic and viscous. As a result, theoretical deformation and relaxation dependences of model parameters that characterize the change in the elastic, viscous and plastic properties of the composite during deformation were obtained. Comparison of calculated and experimental dependences showed that they are practically identical.

Polymer clay nanocomposites is a promising class of industrial materials. At present time they are the subject of intense basic and applied research [1, 2]. The main advantages of filled polyolefins compared to metal products are light weight (low mass density), high corrosion resistance, good heat and electrical insulation properties. These materials are easy to various kinds of mechanical machining and well molded. They are thermoplastic, that is, they are easy to recycle, and then re-used to make new products, which is important from an environmental point of view. Disadvantages include a lower strength, so the plastic parts are usually used as elements of designs, and mechanisms where the load is relatively small.

The object of these studies were nanocomposites based on polyethylene (semicrystalline polymer) filled with nanoparticles of a modified clay (montmorillonite). The filler particles have a shape of ultrathin flakes: thickness about 1 nm, characteristic

transverse size — from 30 nm to several microns. These materials are characterized by a complex mechanical behavior, showing well-defined elastic-plastic and visco-elastic properties during deformation. The experimental and theoretical study of these properties is the subject of this work.

Experimental studies were carried out using a special technique based on cyclic uniaxial loading of the sample with increased amplitude of strain at each step. This type of test is used for the study of polymers, when you want to get in one experiment data not only on the elastic, but also the viscous or plastic material properties [3, 4, 5, 6]. Novelty of the proposed test method consists in entering relaxation stops into the loading cycle when the direction of the motion of gripping clamps changes [7]. This mode allowed to clearly separate the visco-elastic and elastic-plastic behavior of the sample and to obtain all necessary input data for further theoretical studies.

The calculations were carried out using structural-phenomenological model describing elastic- viscous-plastic behavior of finite-deformable structural-heterogeneous medium. The model is based on a differential approach to the construction of constitutive equations of material mechanical behavior with the help of symbolic schemes. The mathematical apparatus of mechanics of nonlinear finite deformations involving Runge–Kutta computing method and Nelder–Mead simplex method [8] are used. Additive decomposition of the strain rate tensors (elastic, viscous and plastic) by analogy with the decomposition proposed by Palmov for elastoplastic medium [9] is used at construction of constitutive equations. One major advantage of the additive decomposition is that in this case the dissipation inequality is satisfied automatically [10], so these math expressions are always correct from the point of view of thermodynamics. Algorithm for automated selection of the model parameters from experimental curves of cyclic loading and relaxation dependences is realized in the software suite MatLab.

1 Experiment and computer modeling

The widespread industrial polyethylene PE 107-02K filled by clay ultrathin nanoflakes (modified montmorillonite brand Cloucite 20A) was taken as a main research object. The filler concentration φ was varied from 0 to 15%-mas. Mechanical tests were carried out using a tensile testing machine Testometric FS100kN CT and a mechanical sensor LC100.

Each cycle of the loading program includes the following operations:

- 1) stretching to some value exceeding the maximum strain obtained in the previous cycle;
- 2) stop of the gripping clamps for a given time for stress relaxation;
- 3) unloading up to the given (but not zero) stress;
- 4) again stop of the gripping clamps for relaxation (the same time period);
- 5) termination of the cycle and beginning of the next cycle (with increasing strain amplitude).

The speed of motion of the gripping clamps under loading–unloading was set 100% per minute. The relaxation time was equal to 10 minutes. The test program consisted of 8 cycles at maximum strain 10%, 20%, 30%, 40%, 60%, 80%, 100%, and

120%. The tensile force during unloading was reduced to 0.6 MPa at each cycle. The possibility of transverse bending of the sample during the return stroke of grips due to error of the force sensor was excluded by this — sample remained stretched all the test time. As a result, the dependencies of experimental stresses on strain and time (relaxation curves) were obtained for nanocomposites with filler concentration 0, 5, 10 and 15%-mas.

The proposed phenomenological model of the elastic-viscous-plastic medium is a further development of the differential approach to the construction of constitutive equations based on the interpretation of the mechanical behavior of the material with the help of symbolic schemes. Previously, this approach has been used to describe the elastic-plastic behavior of polymers. The results of modeling the elastic-plastic properties of nanocomposites based on the polyolefin matrix and ultrafine filler of layered clay minerals (smectites) are presented in [11]. Further, this model has been modernized, which allows us to take into account the changes in the volume of the polymer due to the accumulation of internal damage (micro debondings) [12].

This approach was extended to the modeling of not only plastic, but viscous polymer properties of the medium in 2014–2015. Detailed description of this variant of the model is given in [7, 13]. The symbolic model scheme (Fig. 1) consists of two parallel branches containing two serially connected elements: a) elastic (1) and plastic (3), b) elastic (2) and viscous (4). Tensor equations that specify the properties of the medium correspond to each element. Stresses in the elements in each branch are the same, and strain rates are summed to such combination of elements. The overall stress in the material is the sum of stresses in the branches, and strain rates in the branches are equal to the total rate of deformation of the material. That is, the additive decomposition of the strain rate tensor (elastic, viscous and plastic) was used in the model.

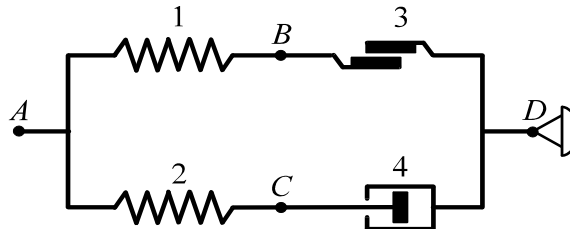


Figure 1: Symbolic scheme of elastic-viscous-plastic model

It was assumed that the elastic-plastic branch simulates displacements, destruction or rearrangement of agglomerates of crystallites (more rigid than the amorphous phase) and filler particles (i.e. irreversible changes in the material structure). The visco-elastic one describes the flow of the amorphous polymer between the lamellae inside crystallites and in the space around the crystallites and particles [14, 15].

The equations of the nonlinear elasticity theory are used to calculate stress tensors in elastic elements 1 and 2. It is assumed that the body volume and temperature in the deformation process do not change, and the elastic properties of the material are described by the neo-Hookean potential. The mechanical properties of the plastic element are determined by analogy with the basic Prandtl-Reuss equations of plastic flow. To close the system of equations defining the plastic features of the

material, proportional relation between the deviators of strain rate tensors of the plastic element \mathbf{D}_3 and the entire medium \mathbf{D} was used:

$$\sqrt{\mathbf{D}_3 \cdot \mathbf{D}_3} = \kappa \sqrt{\text{dev} \mathbf{D} \cdot \text{dev} \mathbf{D}},$$

where κ is the nonnegative parameter (hereinafter the plasticity parameter) indicating the portion of plastic deformation rate in the total deformation rate of the medium. So, if $\kappa = 0$ the material behaves as an elastic, at $0 < \kappa < 1$ — as the elastic-plastic with hardening, the case when $\kappa = 1$ corresponds to perfect plasticity, and finally, when $\kappa > 1$, the load curve becomes a falling, that is the softening of material occurs.

For the yield function Φ , the medium intensity of the medium left stretch tensor \mathbf{V} is used:

$$\Phi = \sqrt{\text{dev} \mathbf{V} \cdot \text{dev} \mathbf{V}}.$$

In the case of the incompressible uniaxially loaded material, $\lambda_1 = \lambda$, $\lambda_2 = \lambda_3 = \lambda^{-1/2}$, it can be written as

$$\Phi = \sqrt{2/3} \left(\lambda - \sqrt{1/\lambda} \right).$$

For the viscous element, the stress tensor \mathbf{T}_4 and its deviator are determined by formula

$$\mathbf{T}_4 = 2\eta \mathbf{D}_4 - \sigma_0 \mathbf{I}, \quad \text{dev} \mathbf{T}_4 = 2\eta \text{dev} \mathbf{D}_4 = 2\eta \mathbf{D}_4,$$

Where η is the shear viscosity, $\sigma_0 = 1/3 \text{tr} \mathbf{T}_4$ is the mean normal stress or negative pressure.

Thus, to describe the nonlinear elastic-viscous-plastic behavior of the polymer using this model, we need to know the following four dependencies: $C_1(q)$, $C_2(q)$, $\kappa(q)$ and $\eta(q)$, where $q = \max \Phi(\mathbf{V})$ — invariant measure of deformation (the analog of the Odkvist hardening parameter [16] of the classical theory of plasticity that characterizes the accumulated plastic strain). Choosing q as a deformation measure was caused by the fact that in the process of loading its value can only increase or remain constant (in contrast to the elongation ratio λ). Thus the condition of irreversibility of the changes of the above model parameters is defined in the model. These four dependencies were determined from the analysis of relevant experimental data.

$C_1(q)$ is an elastic parameter (the neo-Hookean stiffness of the first element), which depends on the irreversible structural rearrangements during deformation (processes that lead to the appearance of residual plastic deformations). Stiffness of the second elastic element $C_2(q)$, defining the elastic properties of amorphous polymer phase, that relied unchanged during deformation, was considered constant and taken equal to 10 MPa.

2 Results discussion

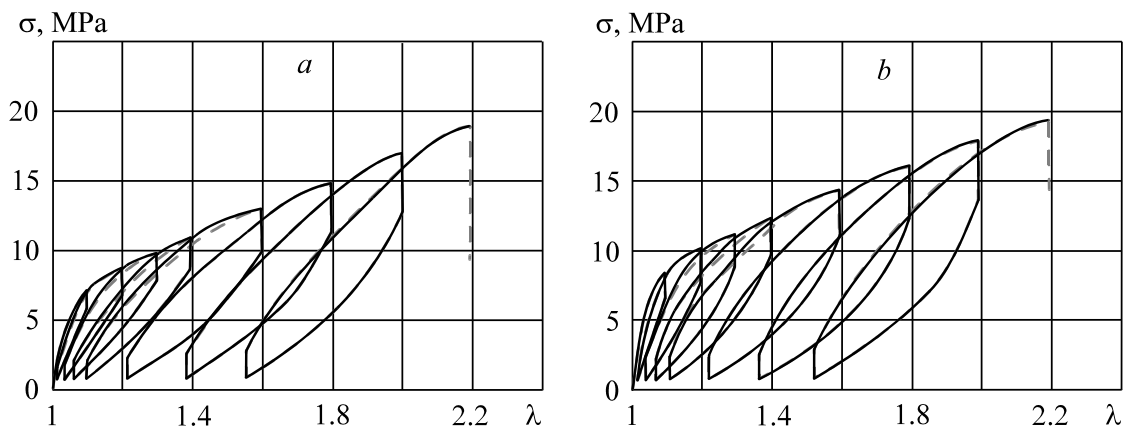
The experimental data obtained in the above described experiments were theoretically treated using this elastic-viscous-plastic model. This allowed to make quantitative estimates of the processes of development of plastic and viscous flows in

these polymeric/clay composites depending on the nanofiller concentration. A comparison of the calculated and experimental results shows that they are practically identical. This is indicative of the fact that the conclusions from the analysis of the findings of model parameters are close to reality. Depending of the true stress σ on the sample elongation ratio λ for filler concentrations 0, 5, 10 and 15%-mas. are shown in Fig. 2. Calculated dependences of the model parameters C_1 , κ and η of q are shown in Figures 3, 4 and 5 relatively.

As for elastic properties, in all cases, the stiffness C_1 initially drop sharply, and then again begin to grow (but with much less intensity). The calculations showed that increasing the filler concentration in the polymer increases the natural stiffness of the composite. It is interesting that there is a significant convergence of dependency $C_1(q)$, corresponding to different values of φ with the increase of plastic deformation in the sample. Most likely, this is due to the development of the structural orientation processes: translation and rotation of crystallite agglomerates and filler particles.

For unfilled and filled systems the plasticity parameter κ at the elastic stage of deformation (elastic zone corresponds to $q < 0.24$ that is similar to $\lambda < 1.2$) are close to zero, then its monotonic increase occurs. For pure polymer the values of κ approach 1 for q equal to about 0.85 ($\lambda = 1.8$), i.e. deformation becomes completely plastic. As for the filled systems κ values even exceed 1 (in physical sense, this corresponds to the material softening). The greater the value of φ , the curves $\kappa(q)$ are higher. All curves go up sharply with a further increase in q ($\lambda > 2$) when the plastic neck formation begins. The plastic neck causes the mechanical inhomogeneity along the sample, but the model does not take it into account. This stage is beyond the scope of this model, and this effect, and we did not studied it.

As for dependencies between viscosity and deformation in all cases η increases monotonically throughout the load range, and the filler input enhances viscosity of the system (as should be expected).



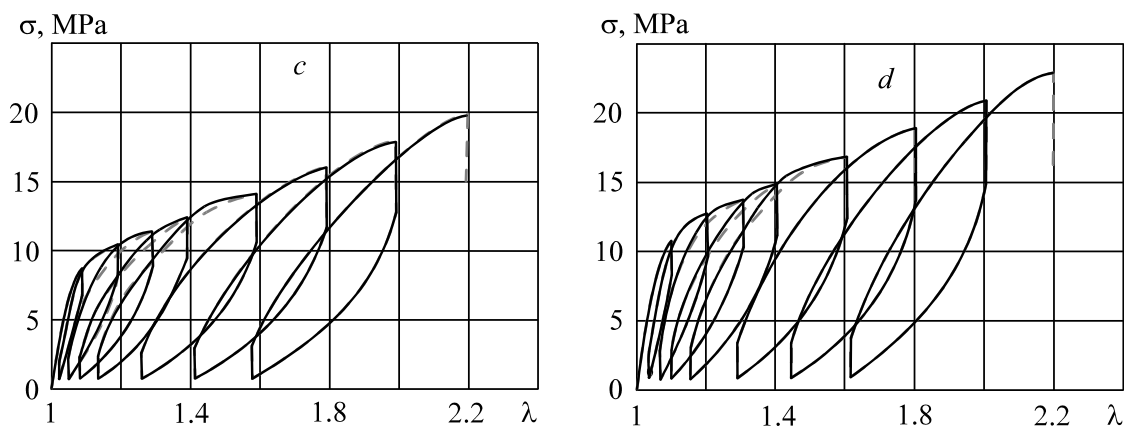


Figure 2: Strain cyclic loading curves for PE 107-02K filled by clay nanoparticles: a) $\varphi=0\%$ -mas.; b) 5%-mas.; c) 10%-mas.; d) 15%-mas. Black lines — calculation, gray lines — experiment.

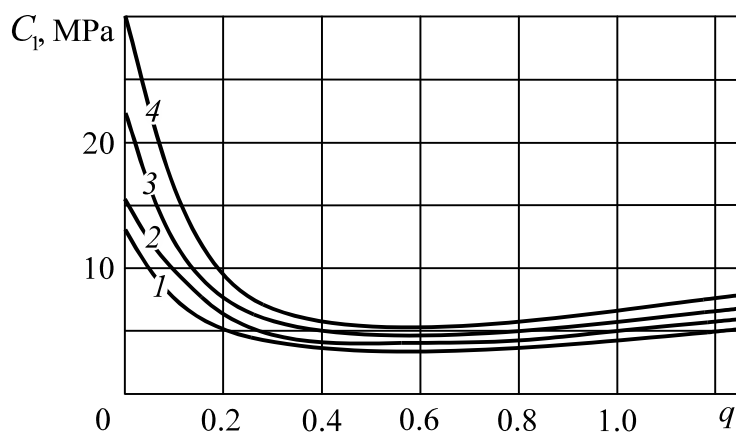


Figure 3: Calculated dependences of elastic parameter C_1 on q for PE 107-02K filled by clay nanoparticles: 1) $\varphi=0\%$ -mas.; 2) 5%-mas.; 3) 10%-mas.; 4) 15%-mas.

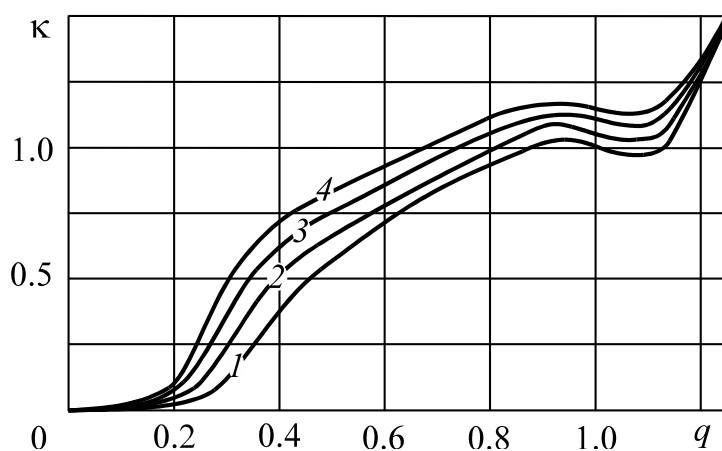


Figure 4: Calculated dependences of plasticity parameter κ on q for PE 107-02K filled by clay nanoparticles: 1) $\varphi=0\%$ -mas.; 2) 5%-mas.; 3) 10%-mas.; 4) 15%-mas.

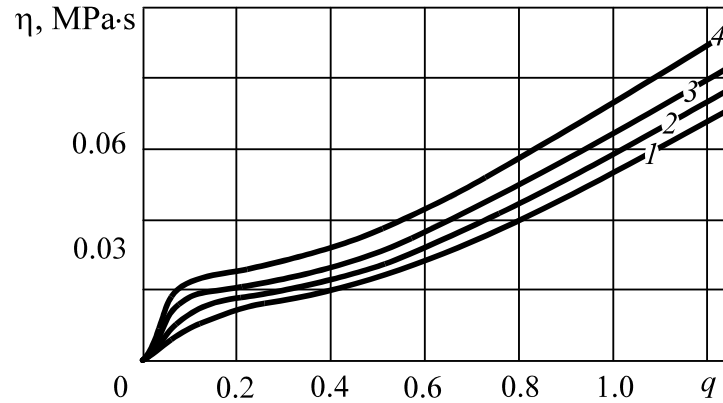


Figure 5: Calculated dependences of viscosity η on q for PE 107-02K filled by clay nanoparticles: 1) $\varphi=0\%$ -mas.; 2) 5%-mas.; 3) 10%-mas.; 4) 15%-mas.

The studies carried out in this work demonstrated the adequacy and validity of the proposed model for investigation of the elastic-viscous-plastic properties nanoclay filled polymers. Combining experimental and theoretical modeling allowed evaluating the development of plasticity and viscosity during the deformation of these materials not only qualitatively but also quantitatively.

Acknowledgements

This work is executed at a financial support of RFBR Grants: 16-08-00756 (computer modeling), 14-08-96013 p_ural_a) (experiment), 15-03-08483(samples production).

References

- [1] Utracki L.A. Clay-Containing Nanocomposites. RAPRA Technology Limited, UK, 2004, 434 p.
- [2] Fengge G. Clay/polymer composites: the story // Materials Today, 2004, No 11, P. 50–55.
- [3] Meyer R.W., Pruitt L.A. The effect of cyclic true strain on the morphology, structure, and relaxation behavior of ultra high molecular weight polyethylene // Polymer, 2001, V. 42, P. 5293–5306.
- [4] Bergstrom J.S., Rimnac C.M., Kurtz S.M. An augmented hybrid constitutive model for simulation of unloading and cyclic loading behavior of conventional and highly crosslinked UHMWPE. // Biomaterials, 2004, V. 25, P. 2171–2178.
- [5] Ayoub G., Zairi F., Nait-Abdelaziz M., Gloaguen J.M. Modelling large deformation behaviour under loading-unloading of semicrystalline polymers: application to a high density polyethylene // Int. J. Plasticity, 2010, V. 6, P. 329–347.

-
- [6] Drozdov A.D., Klitkou R., Christiansen J.C. Cyclic viscoplasticity of semicrystalline polymers with finite deformations // *Mechanics of Materials*, 2013, V. 56, P. 53–64.
- [7] Garishin O.K., Korlyakov A.S., Shadrin V.V. Study of visco-elastic-plastic properties of thermoplastic polymers. Experimental-theoretical integrated approach // *Computational Continuum Mechanics*, 2014, V. 7, P. 208–218. (in Russian)
- [8] Lagarias J.C., Reeds J.A., Wright M.H., Wright P.E. Convergence Properties of the Nelder-Mead Simplex Method in Low Dimensions // *SIAM Journal of Optimization*, 1998, V. 9, No. 1, P. 112–147.
- [9] Palmov V.A. Comparison of different approaches in viscoelastoplasticity for large strain // *ZAMM*, 2000, V. 80, P. 801–806.
- [10] Svistkov A.L., Lauke B. Differential constitutive equations of incompressible media at finite strains // *Applied Mechanics and Technical Physics*, 2009. V. 50, No 3, P. 158–170.
- [11] Garishin O.K., Svistkov A.L., Gerasin V.A., Guseva M.A. Simulation of the elastic-plastic behavior of polyolefin-based nanocomposites with a different structure of layered filler // *Polymer Science, Ser. A*, 2009, V. 51, No 4, P. 407–415.
- [12] Garishin O.K., Gerasin V.A., Guseva M.A. A study of the elastoplastic properties of polymer-silicate nanocomposites with allowance for the change in their volumes during deformation. // *Polymer Science, Ser. A*, 2011, V. 53, No 12, P. 1187–1197.
- [13] Garishin O.K., Korlyakov A.S., Shadrin V.V. Investigation of the elastic-viscous-plastic behavior of thermoplastic materials. Experiment and simulation // *XLII Summer School-Conference "Advanced problems in mechanics": Proceedings*. St.-Petersburg, 2014, P. 547–553.
- [14] White J.L., Choi D. *Polyolefins: Processing, Structure Development and Properties*. Hanser Publishers, 2005. 271 p.
- [15] Oleinik E.F. Plasticity of semicrystalline flexible-chain polymers at the microscopic and mesoscopic levels // *Polym. Sci., Ser. C*, 2003, V. 45, No 1. P. 17–117.
- [16] Odkvist F.K.G. *Mathematical Theory of Creep and Creep Rupture*. Stockholm: Darendon Press, 1966. 170 p.

Oleg K. Garishin, Institute of Continuous Media Mechanics, Perm, Russia

Vladimir V. Shadrin, Institute of Continuous Media Mechanics UB RAS, Perm, Russia, Perm State National Research University, Perm, Russia

Victor A. Gerasin, Institute of Petrochemical Synthesis RAS, Moscow, Russia

Maria A. Guseva, Institute of Petrochemical Synthesis RAS, Moscow, Russia

Damping of friction-induced vibrations applying parallel compensator

Golovin I., Palis S., Timoschenko A., Klepikov V.
ievgen.golovin@ovgu.de

Abstract

In this contribution a new damping approach of friction-induced self-excited vibrations is presented. The idea is to extend the conventional drive control system with an additional parallel compensator. For this purpose a mathematical model of a generic two degree-of-freedom electromechanical system with a nonlinear friction curve and a classical cascade drive control is investigated. It has been shown that the classical cascade approach can not solve the problem of self-excited vibrations without an additional sensors or redesign of feedback control law. However, utilizing the parallel compensation as an extension for conventional control scheme gives promising results.

1 Introduction

In many electromechanical systems a number of different frictional effects has to be taken into account. In some cases, when the friction curve has a negative slope [1, 2], self-excited oscillations may occur [3, 4, 5]. In most cases these oscillations decrease the operational performance and can lead to mechanical breakdowns. Their occurrence has been reported in different areas, e.g. rail transport, metal-working machinery, bridge cranes, rolling mills, industrial robots, drilling systems etc. [3, 6, 7]. In order to solve the described problem several approaches have been proposed [6, 8, 9]. All of them are based on designing a complex control law. However the majority of electric drive systems are equipped with power converters which have their own software and conventional drive control system. Implementing a new control law in this case becomes difficult and thus increases costs considerably.

In this contribution a different approach will be presented allowing the application of standard drive control systems. The closed loop stability can be preserved applying an additional compensator acting in parallel with the drive control system. For this purpose, a generic two degree-of-freedom electromechanical system with a nonlinear friction curve and conventional cascade drive control is studied. The parallel compensator augmenting the conventional feedback control system is derived by straightforward root locus design.

The contribution is structured as follows: in section 2 the mathematical model of a generic electromechanical two degree-of-freedom (DoF) system with nonlinear friction curve is introduced and analyzed. In section 3 the main problems applying

standard control approaches are presented. In section 4 the design procedure for an appropriate parallel compensator is proposed.

2 Mathematical modelling and stability

As a simple simulation model a prototypic electromechanical system with two DoF and nonlinear friction curve is studied (Fig. 1). Here, the first mass is actuated by the DC motor with separately excited field winding whereas friction loads are acting on the second mass. The equations of motion can be represented as follows:

$$J_1 \frac{d\omega_1(t)}{dt} = \tau_1(t) - \tau_y(t), \quad (1)$$

$$\tau_y(t) = c_{12} \int_0^t (\omega_1(\tau) - \omega_2(\tau)) d\tau + b_{12}(\omega_1(t) - \omega_2(t)), \quad (2)$$

$$J_2 \frac{d\omega_2(t)}{dt} = \tau_y(t) - \omega_2(t)\tau_f(\omega_2), \quad (3)$$

where J_1 and J_2 are inertial masses of the drive system and the actuator, $\omega_1(t)$ and $\omega_2(t)$ are angular velocities of two masses, c_{12} and b_{12} are torsional stiffness and damping of linear spring connection between masses, $\tau_1(t)$ is the drive torque, $\tau_y(t)$ is the elastic torque and $\tau_f(\omega_2)$ is the friction load torque function depending on the second mass angular velocity.

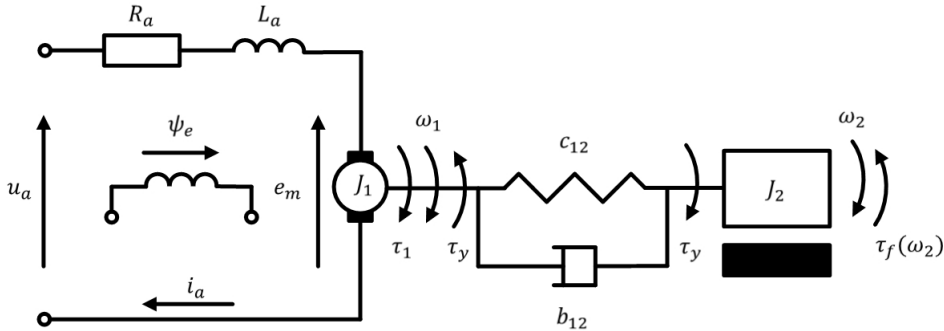


Figure 1: Two DoF electromechanical system with nonlinear friction load

The governing equation of DC motor armature circuit can be derived based on Kirchhoff's voltage law:

$$u_a(t) = e_m(t) + R_a i_a(t) + L_a \frac{di_a(t)}{dt}, \quad (4)$$

where $u_a(t)$ and $i_a(t)$ are armature voltage and current, R_a and L_a are armature resistance and inductance and $e_m(t)$ is electromotive force.

Assuming that the magnetic field is fixed, electrical and mechanical system variables

can be coupled as:

$$\omega_1(t) = \frac{1}{k_m \psi_e} e_m(t), \quad (5)$$

$$\omega_0(t) = \frac{1}{k_m \psi_e} u_a(t), \quad (6)$$

$$\tau_1(t) = k_m \psi_e i_a(t), \quad (7)$$

where k_m is DC motor ratio, ψ_e is constant magnetic field flow and $\omega_0(t)$ is non-loaded angular velocity.

As in equations 1, 2, 3 the motor torque $\tau_1(t)$ is defined as acting variable, a relation between the motor velocity and the motor torque should be derived. Taking into account relations 5, 6, 7 the equation 4 can be reformulated as:

$$\tau_1(t) = \beta \omega_0(t) - \beta \omega_1(t) - T_e \frac{d\tau_1(t)}{dt}, \quad (8)$$

where $\beta = (k_m \psi_e)^2 / R_a$ is the slope of the motor mechanical curve and $T_e = L_a / R_a$ is the electromagnetic time constant of the armature circuit.

Modeling of friction loads for a specific system is typically a non-trivial task, due to the limited understanding of the friction phenomenon at hand. This often results in high uncertainties and time variance of model quality. However, for this study the presence of a negative slope region in the friction curve is sufficient to result in the occurrence of instabilities and limit cycles. That is why for a qualitative analysis a simple piecewise linear approximation of a humped friction model with the Stribeck effect can be used (Fig. 2) [3, 9]. Nominal numerical values for this piecewise approximation are given in equation 9. This kind of approximation allows to divide the curve into specific regions and to deal with the linear system in certain region preserving a nonlinear behavior globally. For each curve region the slope parameter for linear model can be expressed as $b_{sn} = \Delta\tau_f / \Delta\omega_s$.

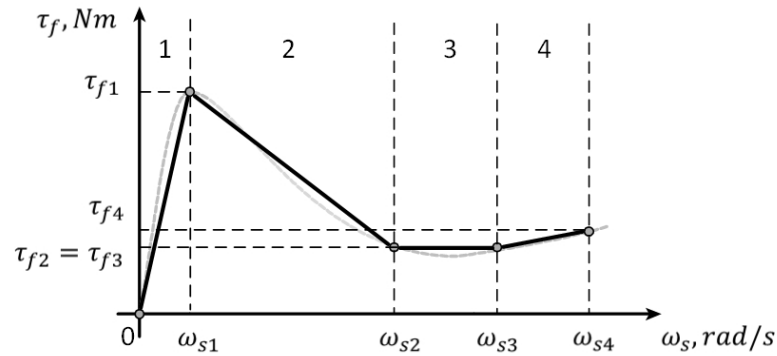


Figure 2: Friction curve

$$\tau_f(\omega_s) = \begin{cases} 50\omega_s, & 0 < \omega_s < 5 \text{ rad/s} \\ -1.2\omega_s + 255, & 5 < \omega_s < 155 \text{ rad/s} \\ 100, & 155 < \omega_s < 165 \text{ rad/s} \\ 1.43\omega_s - 135.7, & 165 < \omega_s < 200 \text{ rad/s} \end{cases} \quad (9)$$

Applying the Laplace transformation, the above modeling equations 1, 2, 3 and 8 can be represented for a certain region of operating points in terms of the Laplace variable s .

$$\omega_1(s) = \frac{1}{J_1 s}(\tau_1(s) - \tau_y(s)), \quad (10)$$

$$\tau_y(s) = \frac{c_{12}}{s}(\omega_1(s) - \omega_2(s)) + b_{12}(\omega_1(s) - \omega_2(s)), \quad (11)$$

$$\omega_2(s) = \frac{1}{J_2 s}(\tau_y(s) - \omega_2(s)b_{sn}), \quad (12)$$

$$\tau_1(s) = \frac{\beta}{T_e s + 1}(\omega_0(s) - \omega_1(s)). \quad (13)$$

The equivalent block diagram is illustrated in Fig. 3.

As has been mentioned above, the source of instability in the model is, from a mathematical point of view, the occurrence of the negative slope ratio b_{sn} for specific regions of the friction velocity curve. For the linear piecewise curve (Fig. 2) the unstable dynamics can occur for the region of operating points between angular velocities ω_{s1} and ω_{s2} . This phenomenon, i.e. the decrease of the friction torque for an increased velocity, results in a further acceleration assuming a constant motor torque. In practical applications negative slope of the friction curve occurs only in a limited region and would therefore prevent the system from speeding up infinitely. Nevertheless, this mechanism of instability may result in limit cycles, i.e. nonlinear oscillations with high amplitudes, which is a frequently observed phenomenon leading to decreased system performance and damages.

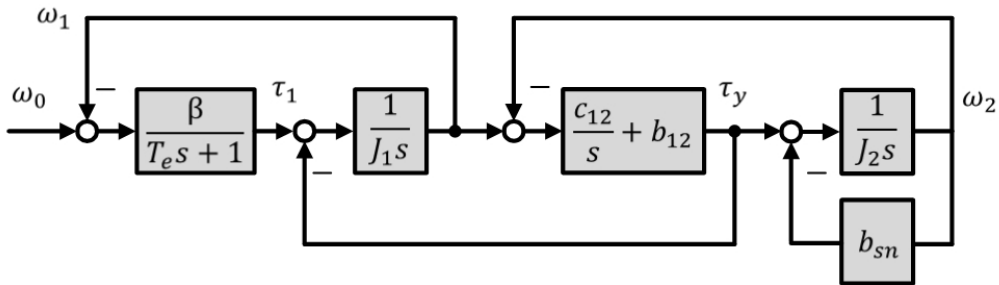
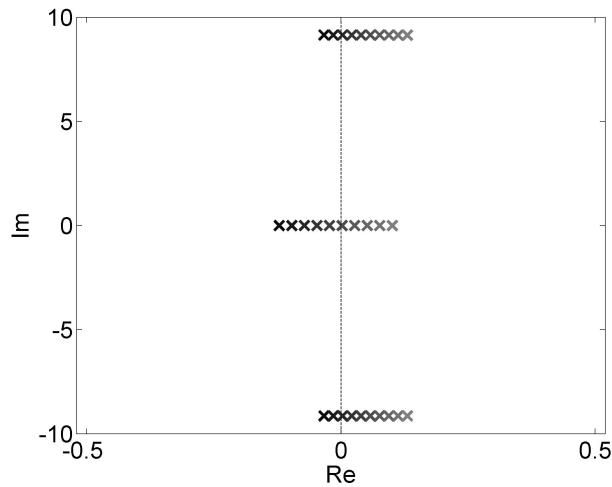


Figure 3: Block diagram of two DoF's electromechanical system

In order to analyze the stability properties of linearized system (Fig. 3), poles location of the transfer function $G(s) = \omega_2(s)/\omega_0(s)$ for a set of nominal parameter values (Tab. 6) and for varying uncertain slope ratio $-1 < b_{sn} < 0.1$ has been obtained. As can be seen from Fig. 4, the transfer function has one real and one complex pole pair. It should be also stressed, that the fast pole at $s = -10$ is not depicted in figure and its location does not depend on the ratio b_{sn} . From Fig. 4 it also becomes apparent that for small negative friction coefficients, i.e. $b_{sn} < -0.1$, the complex pole pair moves into the right-half plane (RHP) which results in an unstable system dynamics. It should be emphasized that this instability is a local effect for the described linear system resulting globally in nonlinear oscillations.

T_e	0.1	[s]
β	0.5	$[(V/(rad\ s))^2/\Omega]$
J_1	3	$[kg\ m^2]$
J_2	2	$[kg\ m^2]$
c_{12}	100	$[Nm/rad]$
b_{12}	0	$[Nm\ s/rad]$
ω_0	100	$[rad/s]$

Table 6: System model parameters


 Figure 4: Root locus for slope variations ($b_{sn} = 0.1$ (black) and $b_{sn} = -1$ (gray))

3 Problem of standard control approaches and zero dynamics

3.1 Conventional electric drive control system

In the modern machines and mechanisms design controlled electric drives have become a quasi-standard. In order to control the electric energy flow, these drive systems are equipped with power converters based on thyristor or transistor schemes. In most cases manufacturers provide a complex product augmenting their converters by a fully-parameterizable standard control system and a manufacture-specific software solution. Although, such a design allows fast engineering solutions in many application cases, whereas implementation of non-standard control laws by the user is at least difficult if not impossible.

Velocity control of the electric drive is one of the classical tasks for different electromechanical systems. In this case the cascade control with PI controllers is the most widely used control structure (Fig. 5). It includes an inner current (or sometimes torque) control loop $G_i(s)$ and an outer velocity control loop $G_\omega(s)$. The inner controller $C_{i,PI}(s)$ for the motor current plant $P_i(s)$ is designed first, after which the outer controller $C_{\omega,PI}(s)$ for the whole plant $G_i(s)$ and $P_\omega(s)$ is designed.

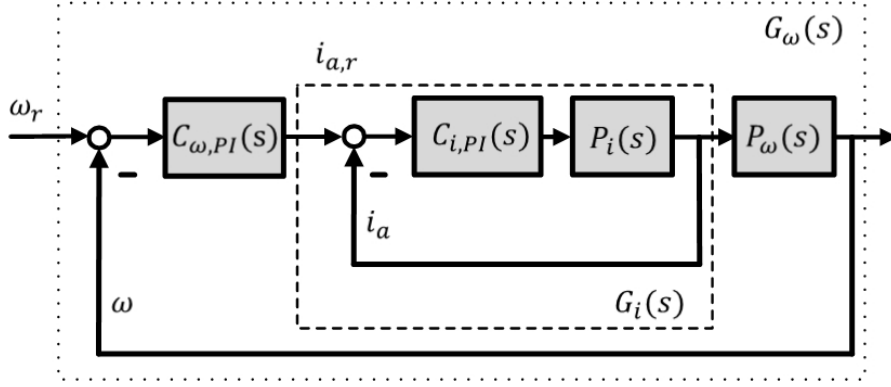


Figure 5: Standard cascade control

The electrical subsystem $P_i(s)$ is classically represented by two first order systems, the rectifier associated with the time constant T_μ and the electrical part of the motor (eq. 13) with the time constant T_e , where $T_\mu \ll T_e$. As the motor torque $\tau_1(t)$ has been defined as acting variable, the open loop plant $P_i(s)$ should also consider relations 6 and 7. For the current controller a standard PI control structure is chosen.

$$P_i(s) = \frac{i_a(s)}{u_c(s)} = \frac{1}{T_\mu s + 1} \frac{\beta}{T_e s + 1} \frac{1}{(k_m \psi_e)^2}, \quad (14)$$

$$C_{i,PI}(s) = \frac{u_c(s)}{e_i(s)} = k_i \frac{T_i s + 1}{T_i s}. \quad (15)$$

Here, $u_c(s)$ is the controller voltage, $e_i(s)$ is the measured inner loop error, k_i and T_i are the PI-controller parameters.

Applying the modulus (magnitude) optimum tuning procedure [10] as a standard controller design procedure for electric drive systems PI-controller parameters are given by $k_i = T_e(k_m \psi_e)^2 / (2T_\mu \beta)$ and $T_i = T_e$. Here, the main idea is to compensate the largest time constant T_e in order to achieve fast reference tracking.

In a second step the outer controller is designed for the closed inner loop $G_i(s)$ and the mechanical motor subsystem $P_\omega(s) = (k_m \psi_e) / (J_1 s)$. In order to achieve both good reference tracking and disturbance rejection the parameters of the velocity PI-controller can be adjusted according to the symmetrical optimum so that $k_\omega = J_1 / (4T_\mu k_m \psi_e)$ and $T_\omega = 8T_\mu$.

$$C_{\omega,PI}(s) = \frac{i_{a,r}(s)}{e_\omega(s)} = k_\omega \frac{T_\omega s + 1}{T_\omega s} \quad (16)$$

Using these tunings for both loops with a reference prefilter $G_r(s) = 1 / (8T_\mu s + 1)$ gives an overshoot of approximately 8% and a settling time of approximately $26 T_\mu$ [10, 11].

$k_m \psi_e$	1	[-]
T_μ	0.01	[s]
k_i	10	[-]
T_i	0.1	[s]
k_v	75	[-]
T_v	0.08	[s]
T_r	0.08	[s]

Table 7: Control system parameters

3.2 Problem of unstable zero dynamics

The above described conventional control scheme and tuning procedures are widely used by engineering companies in practice. The velocity measurements in electromechanical systems are often provided with incremental or optical sensors on the motor shaft. A direct velocity measurements on the working element of the mechanisms increase costs and are often complicated or even impossible. From the theoretical point of view this means that the first mass velocity can be measured for electromechanical systems with more than one DoF only.

In order to investigate the behavior of the cascade control scheme for the two DoF electromechanical system with friction, the transfer function for the overall system, i.e. including the inner current loop $G_i(s)$, the two DoF system with frictional load and the inner counter electromotive force feedback, has to be obtained. Taking into account the models from Fig. 3 and Fig. 5, the open loop velocity transfer function can be expressed as:

$$P_{\omega,m}(s) = \frac{\omega_1(s)}{i_{a,r}(s)} = \frac{k_i \beta (T_e s + 1) (J_2 s^2 + b_{sn} s + c_{12})}{Q(s)}, \quad (17)$$

where $Q(s)$ is the polynomial of the open loop plant denominator.

In order to study the overall dynamic behavior the above presented velocity controller $C_{\omega,PI}(s)$ with the prefilter $G_r(s)$ is applied to the transfer function 17. Taking into account model parameters from Tab. 6, Tab. 7 and the nominal value of slope coefficient $b_{sn} = -1.2$ for a falling region of curve (eq. 9) the resulting pole-zero plot is depicted in Fig. 6. As can be seen the closed loop system has two RHP poles and is hence unstable. It should be stressed that this problem exists due to the presence of RHP zeros in the numerator term $J_2 s^2 + b_{sn} s + c_{12}$ of the equation 17 which occur for slope ratio $b_{sn} < 0$. Systems with unstable zero dynamics, i.e. possessing RHP zeros, are challenging from a control point of view as they are well-known to be unstable under high controller gains and the locations of system zeros are invariant with respect to feedback.

A conventional solution approach would involve a full controller redesign increasing the overall control system complexity significantly. However, as has been mentioned above implementation of new control structures in electric drive system is in most cases expensive and time-consuming. In this contribution a different approach will be presented allowing the application of a standard drive control system augmented by an additional parallel compensator as illustrated in Fig. 7. Here, the first step

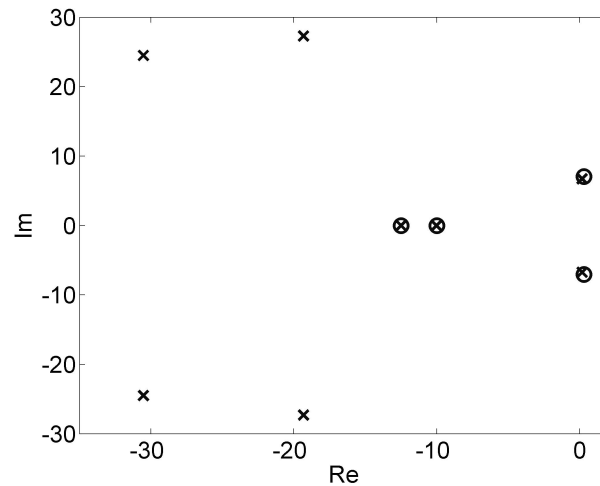


Figure 6: Pole-zero plot of the closed loop system applying a conventional velocity control

is to design an appropriate parallel compensator stabilizing the friction-induced unstable zero dynamics. Secondly, the standard feedback controller may be retuned in order to stabilize RHP poles.

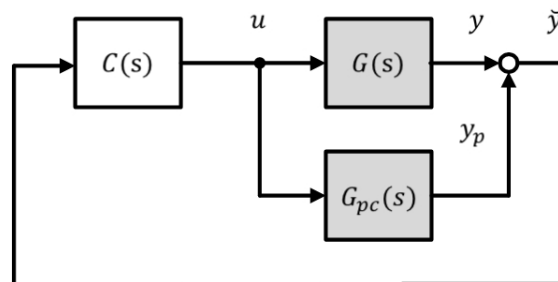


Figure 7: Overall control structure

4 Parallel compensator design

In order to influence the stability behavior of the zero dynamics an appropriate parallel compensator as depicted in Fig. 8 has to be designed [12].

In case of a single-input single-output system the associated transfer function $G(s)$ can be separated into four fractions

$$G(s) = \frac{N^+(s)N^-(s)}{D^+(s)D^-(s)}, \quad (18)$$

where $N^+(s)$ and $D^+(s)$ contain the left-half plane (LHP) zeros and poles and $N^-(s)$ and $D^-(s)$ the RHP zeros and poles. It is assumed that the parallel compensator

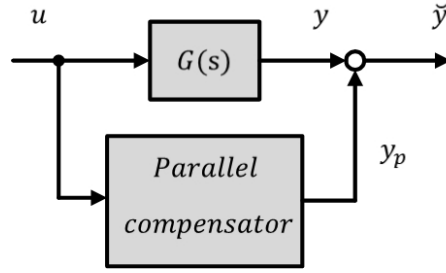


Figure 8: Parallel compensator

consists of the fractions containing all plant poles and zeros in the left half plane, i.e. $N^+(s)$ and $D^+(s)$, plus two additional fractions $N_c(s)$ and $D_c(s)$.

$$G_{pc}(s) = \frac{N^+(s)N_c(s)}{D^+(s)D_c(s)}. \quad (19)$$

The parallel connection of the plant $G(s)$ and the parallel compensator $G_{pc}(s)$ results in

$$G_s(s) = G(s) + G_{pc}(s) = \frac{N^+(s) [N^-(s)D_c(s) + N_c(s)D^-(s)]}{D^+(s)D^-(s)D_c(s)}. \quad (20)$$

It can be shown that the design of a parallel compensator stabilizing the unstable zero dynamics is equivalent to designing a controller $G_c = N_c(s)/D_c(s)$ which stabilizes the virtual plant $G_{vir}(s) = D^-(s)/N^-(s)$.

Taking into account the aforementioned nominal parameters the plant transfer function (17) can be calculated as:

$$G(s) = \frac{1666.7(s^2 - 0.6s + 50)}{(s - 0.24)(s^2 - 0.35s + 83.19)(s^2 + 99.96s + 4998)}. \quad (21)$$

Here, the system can be separated into the following stable and unstable fractions

$$N^-(s) = s^2 - 0.6s + 50, \quad (22)$$

$$D^-(s) = (s - 0.24)(s^2 - 0.35s + 83.19), \quad (23)$$

$$N^+(s) = 1666.7, \quad (24)$$

$$D^+(s) = (s^2 + 99.96s + 4998). \quad (25)$$

In order to achieve stable zero dynamics the following polynomial should have no RHP zeros:

$$1 + G_c(s)G_{vir}(s) = 1 + G_c(s) \frac{(s - 0.24)(s^2 - 0.35s + 83.19)}{s^2 - 0.6s + 50}. \quad (26)$$

Applying the root locus feedback design procedure for the virtual plant G_{vir} an appropriate controller as a simple gain $G_c = 0.11$ can be designed which results in the following parallel compensator considering equation 19

$$G_{pc}(s) = \frac{183.34}{(s^2 + 99.96s + 4998)}. \quad (27)$$

Applying the designed compensator hence yields a new system with locally stable zero dynamics. In this specific example no additional controller retuning is needed and hence the above presented PI-controller can be used. Simulation results with and without the designed parallel compensator are depicted in Fig. 9 (right) and (left), respectively. As can be seen in Fig. 9 (left), assuming piecewise linear approximation of friction curve (eq. 9) the aforementioned unstable zero dynamics leads to system instability and the occurrence of nonlinear oscillations.

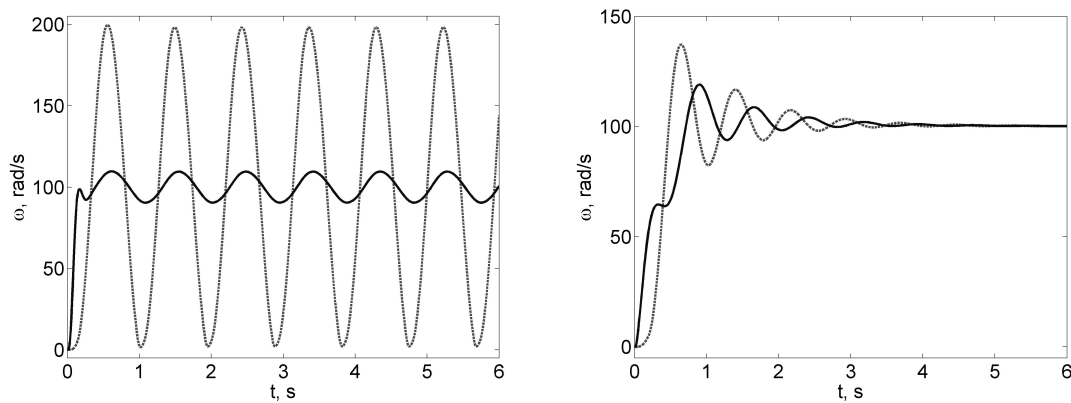


Figure 9: Angular velocities of the first (solid black) and second (dotted gray) masses without (left) and with (right) parallel compensator

Conclusion and future work

A new damping approach of friction-induced self-excited vibrations has been proposed. The mathematical model of two degree-of-freedom electromechanical system with the nonlinear friction curve and the classical cascade velocity PI-control for electric drive system has been investigated. It has been shown that conventional control approaches may result in the occurrence of self-excited vibrations requiring a controller redesign and often a time-consuming reimplementation. In order to overcome this problem the design of a parallel compensator stabilizing the unstable zero dynamics has been proposed in this contribution.

As has been mentioned, exact friction behavior is often unknown or time-varying. Hence, application of robust or adaptive methods for compensator design is an interesting field for future research.

References

- [1] K. Farhang, A. L. Lim, A Non-Phenomenological Account of Friction/Vibration Interaction in Rotary Systems, *Journal of Tribology* Vol. 128, 2006, pp. 103 - 112.
- [2] M. Rahmani, S. Krall, F. Bleicher, Experimental Investigations on Stick-Slip Phenomenon and Friction Characteristics of Linear Guides, *Procedia Engineering* 100, 2015, pp. 1023 - 1031.

-
- [3] V. Klepikov, Dynamics of Electromechanical Systems with Nonlinear Friction, NTU "KhPI", 2014.
- [4] A. Fidlin, Nonlinear Oscillations in Mechanical Engineering, Springer-Verlag Berlin Heidelberg, 2006.
- [5] D. P. Hess, Interaction of vibration and friction at dry sliding contacts, Dynamics with Friction: Modeling, Analysis and Experiment, 2001, pp. 1 - 27.
- [6] Y.F. Wang, D.H. Wang, T.Y. Chai, Active control of friction self-excited vibration using neuro-fuzzy and data mining techniques, Expert Systems with Applications 40, 2013, pp. 975 - 983.
- [7] M.A. Kiseleva, N.V. Kondratyeva, N.V. Kuznetsov, G.A. Leonov, Hidden oscillations in drilling systems with salient pole synchronous motor, IFAC-Papers, 2015, pp. 700 - 705
- [8] M. B. Saldivar Marquez, I. Boussaada, H. Mounier, S. I. Niculescu, Analysis and control of oilwell drilling vibrations: a time-delay systems approach, Springer, 2015.
- [9] N. Mihajlović, Torsional and Lateral Vibrations in Flexible Rotor Systems with Friction, Technische Universiteit Eindhoven, 2005.
- [10] C. Bajracharya, M. Molinas, J. A. Suul, T. M. Undeland, Understanding of tuning techniques of converter controllers for VSC-HVDC, Nordic Workshop on Power and Industrial Electronics, 2008.
- [11] D. Schröder, Elektrische Antriebe - Grundlagen, Springer, 2013.
- [12] S. Palis, A. Kienle, Discrepancy based control of particulate processes, Journal of Process Control 24, 2014, pp. 33 - 45.

Ievgen Golovin, Otto-von-Guericke University Magdeburg, Universitätsplatz 2, 39106 Magdeburg, Germany

Stefan Palis, Otto-von-Guericke University Magdeburg, Universitätsplatz 2, 39106 Magdeburg, Germany

Andrii Timoschenko, NTU "Kharkiv Polytechnic Institute", Frunse 21, 61002 Charkov, Ukraine

Vladimir Klepikov, NTU "Kharkiv Polytechnic Institute", Frunse 21, 61002 Charkov, Ukraine

A Stochastic Finite Element Approach on Creep of Rock Salt

M. Grehn, A. Fau, U. Nackenhorst
mathias.grehn@ibnm.uni-hannover.de

Abstract

A robust computational material model for rock salt with a stochastic approach for Young's modulus is developed to predict rock salt behavior during a creep test. The uncertain input data as well as the unknown displacement fields are described by Hermite polynomial chaos. The numerical problem is solved using Stochastic Finite Element Procedure. The material model is able to reproduce the experimental results during the two first creep periods including the scattering of experimental creep curves.

Keywords: Stochastic Finite Element Method, Polynomial Chaos, Creep Test, Viscoelastic, Rock Salt

1 Introduction

Old salt domes are used as reservoirs for toxic and nuclear waste in Germany. Nuclear waste has a long half-life time, so the mechanical stability of salt domes has to be guaranteed for a long period. In the last decades, a large expertise in the mechanical behavior of rock salt was gained. This led to a variety of material models, which may be based on a macroscopic phenomenological approach [1], derived from Burger's modified model [2], or from micromechanics using the composite dilatancy model [3, 4, 5, 6] for examples.

However, from experimental results obtained during creep tests for rock salt from Asse mine in Germany [7] reproduced in Figure 1 it can be seen that the material properties are subject to large variation as also observed by [4, 8]. The goal of this paper is to reproduce this creep test including the scattering of experimental data by introducing a stochastic material model for rock salt.

2 Origin of uncertainties

To analyze numerically the behaviour of rock salt, we refer to a material model based on different established works from the literature [7, 9, 5, 6].

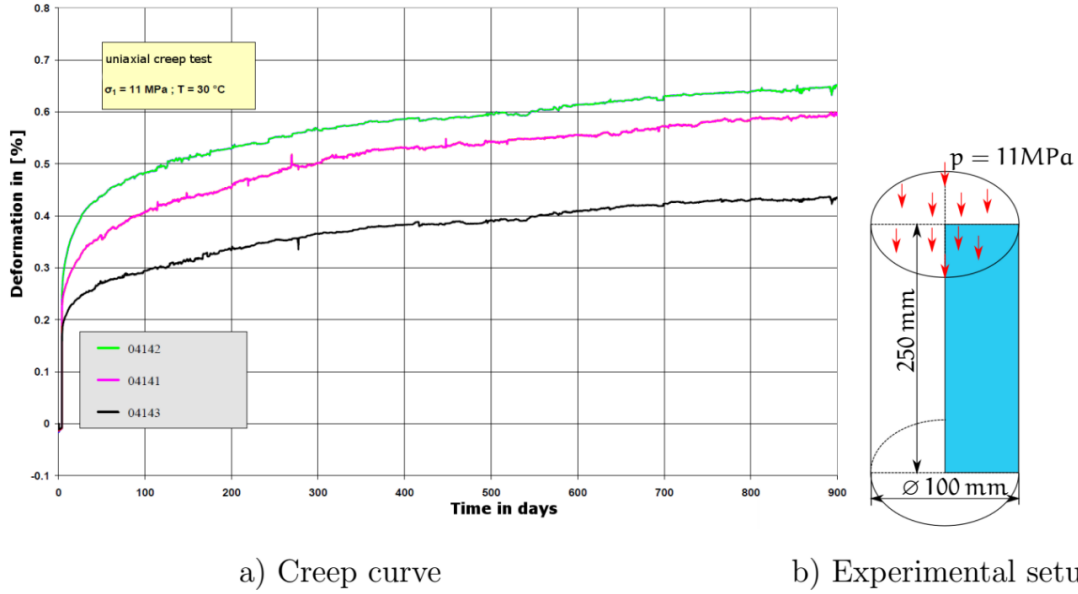


Figure 1: Experimental uniaxial creep test for three samples of Asse rock salt reproduced after [7]

2.1 Material model

The analysis of the creep test can be split into three parts as illustrated in Figure 2 [10]. During the primary creep period (I), the dislocations move in the lattice structure of the crystal salt. The strain rate is relatively high, but it slows down by increasing time. In the secondary or steady-state creep period (II) the dislocation density increases leading to an increasing resistance. The strain rate is nearly constant. The tertiary creep period (III) is characterized by an exponentially increasing of the strain rate. We focus here only on the two first creep periods to reproduce the experimental results previously presented.

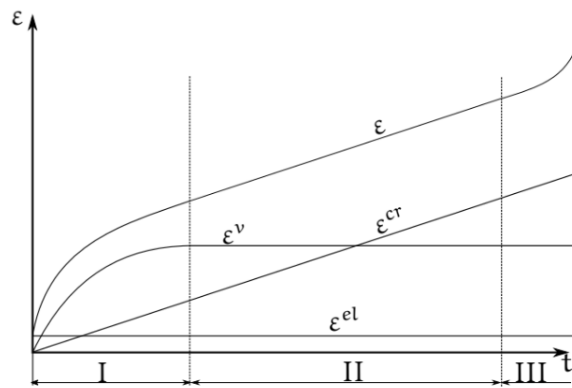


Figure 2: Analysis of the creep behavior of rock salt

The material model is based on an additive split of the strain tensor $\boldsymbol{\varepsilon}$:

$$\boldsymbol{\varepsilon} = \boldsymbol{\varepsilon}^{el} + \boldsymbol{\varepsilon}^v + \boldsymbol{\varepsilon}^{cr}. \quad (1)$$

The elastic strain tensor $\boldsymbol{\varepsilon}^{el}$ and the viscous strain tensor $\boldsymbol{\varepsilon}^v$ describe the primary creep period. The steady-state creep period is described by the creep strain tensor $\boldsymbol{\varepsilon}^{cr}$. We can reproduce the viscoelastic part for one-dimensional systems by springs of stiffnesses E_i and dampers of coefficients η_i using a generalized Maxwell model and the following free energy function [9]:

$$\psi(\boldsymbol{\varepsilon}, \mathbf{q}_i) = W^\circ(\boldsymbol{\varepsilon}) + \sum_{i=1}^{N_{MW}} \mathbf{q}_i \cdot \tilde{\boldsymbol{\varepsilon}} + \Xi \left(\sum_{i=1}^{N_{MW}} \mathbf{q}_i \right). \quad (2)$$

The function W° is the initial stored energy function. The internal variables \mathbf{q}_i characterize the viscoelastic response and $\tilde{\boldsymbol{\varepsilon}} = \boldsymbol{\varepsilon} - \frac{1}{3}tr(\boldsymbol{\varepsilon})\mathbf{1}$ is the deviatoric strain. N_{MW} is the number of Maxwell elements. We consider one spring of stiffness E_∞ connected in parallel with two Maxwell elements whose stiffnesses are respectively E_1 and E_2 . The total Young modulus E is computed as a summation of all single Young's modulus:

$$E = E_\infty + \sum_{i=0}^2 E_i. \quad (3)$$

The creep behavior of rock salt for the deviatoric part of the creep strain tensor is described by Norton's law:

$$\dot{\tilde{\boldsymbol{\varepsilon}}}^{cr} = A \exp\left(\frac{-Q}{RT}\right) \cdot (\sigma^{vM})^N, \quad (4)$$

where N is a material parameter and σ^{vM} denotes the von Mises stress. The temperature dependency of the creep curve is described by Arrhenius equation, which is linked multiplicative with the creep rates. The pre-exponential factor A is determined by experiments. R denotes the universal gas constant and T the absolute temperature. The macroscopic activation energy Q is provided by [5].

Experiments [7, 6] show that for rock salt, the volumetric deformation depends on the state of stress in comparison with the dilatancy boundary. This material behavior is described by the functional r_v introduced in [7]:

$$r_v = \begin{cases} 3 \left[\frac{\tau_{okt} - \tau_D}{\sigma_{okt}} \right]^2 & \text{for } \tau_{okt} > \tau_D \\ 0 & \text{otherwise.} \end{cases} \quad (5)$$

The function τ_D represents the dilatancy boundary equation [7]. τ_{okt} is the octahedral shear stress and σ_{okt} is the octahedral normal stress. When the state of stress is below the dilatancy boundary, the deformation is at constant volume, otherwise arises the volumetric part of the creep strain tensor defined as:

$$\dot{\boldsymbol{\varepsilon}}^{cr,vol} = r_v \dot{\tilde{\boldsymbol{\varepsilon}}}^{cr}. \quad (6)$$

In loosened rock salt the moisture has a big influence on the creep rate. This behavior is modeled by the following equations [7]:

$$\begin{aligned}
f_{\Phi} &= c_{\Phi 1} \sinh(c_{\Phi 2} \Phi), \\
f_c &= \begin{cases} \left[1 + \left(\frac{\sigma_3}{\sigma_u} \right)^{c_{fc1}} \tau_{okt} \right]^{-\left(\frac{c_{fc2}}{1 + \left(\frac{\tau_{okt}}{\sigma_u} \right)} \right)^2} & \text{for } \sigma_3 \geq 0 \\ 1 & \text{otherwise,} \end{cases} \\
F_h &= 1 + f_{\Phi} f_c.
\end{aligned} \tag{7}$$

The factor F_h , which is linked multiplicative with the creep rates, sets together two effects. The first part f_{Φ} describes the influence of relative humidity Φ on the creep rate. The second one f_c takes into account the influence of minimum principal stress σ_3 and the octahedral shear stress τ_{okt} . The other components in this equation are material parameters defined by [6].

To predict the primary and the secondary creep behavior of rock salt over long time the evolution equations must be solved efficiently by numerical techniques. We apply finite element technique to an axisymmetric geometrical model to reduce the computational efforts. We use for the primary creep periode the algorithm introduced in [9] and for the secondary creep periode the one proposed in [11].

2.2 Identifying the random parameters

The three uniaxial creep tests performed by [7] have the same set up with an axial stress equal to 11 MPa, see Figure 1. We investigate which material parameters have to be considered different for the three rock salt samples to reproduce consistently the scattering of the experimental curves.

Based on Equation 4 we can see that a scattering of the material parameters A or N or of the relative humidity Φ changes the slope of the secondary creep period, which is contradictory with the experimental results. The stiffness of the first spring E_{∞} in the generalized Maxwell model characterizes the asymptotic solution $\varepsilon^v(t = \infty)$ for the second creep period. For this reason the free energy function in Equation 2 will be stochastically distributed assuming an uncertain Young's modulus E_{∞} . The stochastic approaches chosen to describe E_{∞} as a random field and to solve the stochastic finite element problem are introduced in the following section.

3 Stochastic Finite Element Approach

For solving the boundary value problem, we use the stochastic finite element method [12] with the aid of polynomial chaos expansions to describe the input random field $E_{\infty}(\theta)$ as well as the displacement random field $u(\theta)$. Each random quantity is characterized by θ .

3.1 Representation of the random input

The Young modulus $E_\infty(\theta)$ is approximated as a Hermite polynomial chaos (PC) series expansion:

$$E_\infty(\theta) \approx \sum_{i=0}^p a_i H_i(\xi(\theta)), \quad (8)$$

where p is the order of Hermite polynomials H_i defined as in [13]:

$$H_i(x) = (-1)^i \frac{1}{\varphi(E_\infty)} \frac{d^i \varphi(x)}{dx^i}, \quad (9)$$

$\varphi(x) = \frac{1}{\sqrt{2\pi}} e^{-\frac{x^2}{2}}$ is the standard normal probability density function (PDF). To compute the coefficients a_i in Equation 8, we use the projection method [13]. The Hermite polynomials are orthogonal with respect to the Gaussian measure. For a probability space with dimension M equals to 1 one obtains

$$\mathbb{E}[E_\infty H_i(\xi(\theta))] = a_i \mathbb{E}[H_i^2(\xi(\theta))], \quad (10)$$

where \mathbb{E} is the mean operator and $\mathbb{E}[H_i^2(\xi(\theta))] = i!$. With help of the transformation to the standard normal space $E_\infty \rightarrow \xi : F_x(E_\infty) = \Phi(\xi(\theta))$, we can write the random variable as following:

$$E_\infty(\xi(\theta)) = F_x^{-1}(\Phi(\xi(\theta))). \quad (11)$$

The coefficients $\{a_i, i = 0, \dots, \infty\}$ are computed as:

$$a_i = \frac{1}{i!} \mathbb{E}[[E_\infty(\xi(\theta)) H_i(\xi(\theta))] = \frac{1}{i!} \int_{\mathbb{R}} F_x^{-1}(\Phi(t)) H_i(t) \varphi(t) dt. \quad (12)$$

Therefore, for the specific cases of normal or log-normal distributions, we get:

$$\begin{aligned} \text{if } E_\infty(\theta) &\equiv N(\mu_{E_\infty}, \sigma_{E_\infty}), & a_0 &= \mu_{E_\infty}, a_1 = \sigma_{E_\infty}, a_i = 0 \text{ for } i \geq 0 \\ \text{if } E_\infty(\theta) &\equiv LN(\lambda_{E_\infty}, \zeta_{E_\infty}), & a_i &= \frac{\zeta_{E_\infty}^i}{i!} \exp\left[\lambda_{E_\infty} + \frac{1}{2} \zeta_{E_\infty}^2\right] \text{ for } i \geq 0, \end{aligned} \quad (13)$$

where the index i goes from 0 to P the dimension of PC basis. The parameters $\lambda_{E_\infty}, \zeta_{E_\infty}$ for log-normal distributions depend on the mean and the standard deviation see [13]. The size P of the polynomial chaos basis is given by:

$$P = \frac{(M+p)!}{M!p!}. \quad (14)$$

Based on the independence of the random variable $\xi(\theta)$ inside the PC expansion, we can compute the multi-dimensional basis:

$$\psi_\alpha = \prod_{i=1}^M H_{\alpha_i}, \quad (15)$$

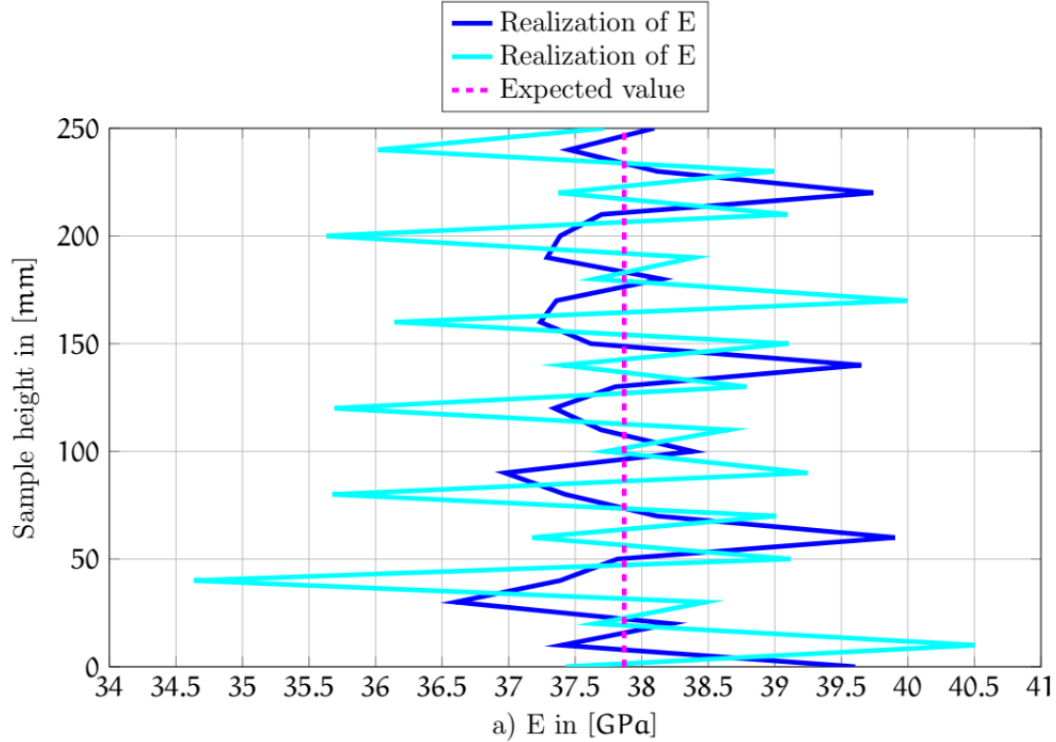


Figure 3: Two realizations of Young's modulus [GPa] field for a rock salt sample.

with $\alpha_i \geq 0$ and $\sum_{i=1}^M \alpha_i \leq p$ as a product of one-dimensional basis. An illustrative transmission of an urn problem is introduced in [13]. Thus the PC can be written as:

$$E_\infty = \sum_{i=0}^{P-1} \hat{E}_{\infty_i} \psi_i(\xi(\theta)), \quad (16)$$

where \hat{E}_∞ is the deterministic PC-coefficient.

The considered creep test results are not statistically representative to have a trustable representation of material uncertainties, a large number of experimental data would be required. We assume for E_∞ a normal (N) or a lognormal (LN) distribution. The mean of the Young modulus μ_{E_∞} is estimated as the parameter reproducing the mean of the three experimental results, i.e. $\mu_{E_\infty} = 2,140$ GPa. The standard deviation σ_{E_∞} is computed such that at least about 60% of the probabilistic creep test results are between the two extreme experimental curves i.e. $\sigma_{E_\infty} = 0,535$ GPa.

In Figure 3 two realizations of the Young modulus random field ($\mu_E = 37,8$ GPa and $\sigma_E = 0,535$ GPa) are shown over the cross section $x = 30$ mm for a polynomial chaos basis up to order 2. For all the Gauss points, Young's modulus values are scattered around the mean value, which is represented by a dashed line.

3.2 Estimation of the random displacement field

The linearization of the deterministic discrete FEM for static problems yields a linear system of size $N_d \times N_d$ where N_d is the number of degrees of freedom in the

FEM geometry:

$$\mathbf{K}\Delta\mathbf{u} = \mathbf{r} - \mathbf{r}^{int}, \quad (17)$$

\mathbf{K} is the total stiffness matrix, \mathbf{u} is the displacement field, \mathbf{r} and \mathbf{r}^{int} are respectively the vectors of external and internal forces.

In the stochastic finite element model we assume the loading and the geometry as certain. We introduce input random variables for material properties as a PC expansion:

$$\mathbf{K}(\theta)\Delta u(\theta) = \mathbf{r} - \mathbf{r}^{int}(\theta), \quad (18)$$

where $\mathbf{K}(\theta)$ is the stochastic stiffness matrix. Details to compute the total stiffness matrix can be found in [12, 13, 14]. By expanding each component of the unknown displacement field as:

$$u(\theta) \approx \sum_{i=0}^{P-1} u_i \psi_i(\xi(\theta)), \quad (19)$$

we get the following discretized problem:

$$\sum_{i=0}^{P-1} \hat{\mathbf{K}}_i \psi_i(\xi) \sum_{j=0}^{P-1} \Delta \hat{\mathbf{u}}_j \psi_j(\xi) = \sum_{j=0}^{P-1} \hat{\mathbf{r}}_j \psi_j(\xi) - \sum_{j=0}^{P-1} \hat{\mathbf{r}}_j^{int} \psi_j(\xi) \quad (20)$$

where $\hat{\cdot}$ represents the nodal discretization. The resulting linear system:

$$\begin{bmatrix} \mathbf{K}_{0,0} & \cdots & \mathbf{K}_{0,P-1} \\ \vdots & \ddots & \vdots \\ \mathbf{K}_{0-1,0} & \cdots & \mathbf{K}_{P-1,P-1} \end{bmatrix} \cdot \begin{bmatrix} \Delta \mathbf{u}_0 \\ \vdots \\ \Delta \mathbf{u}_{P-1} \end{bmatrix} = \begin{bmatrix} \mathbf{r}_1 \\ \vdots \\ \mathbf{r}_{P-1} \end{bmatrix} - \begin{bmatrix} \mathbf{r}_1^{int} \\ \vdots \\ \mathbf{r}_{P-1}^{int} \end{bmatrix} \quad (21)$$

has a size $(N_d * P) \times (N_d * P)$. The mean value contribution is contained in the main diagonal elements [13]. Considering a probability space of dimension 1, the size of the linear system is $(N_d * \frac{(p+1)!}{p!}) \times (N_d * \frac{(p+1)!}{p!})$. The size of the linear system is largely increased considering random input data. For a case using 156 nodes, the size of the deterministic stiffness matrix is 312×312 , whereas for a polynomial chaos of order 1, the size of the stochastic stiffness matrix is 624×624 . But, these matrices are symmetric and sparse matrices.

To solve the large system of equation, we can choose to use a direct solver or an iterative scheme as for example the Gauss-Seidel PC solver introduced in [15, 16]. The advantage of the direct solver is that the equation system must be solved only one time but it may face memory problems for very large stiffness matrix. Here, as we tackle an axisymmetric case with a unique random field, we can use a direct solver for this calculation.

4 Numerical results for the creep test

We reproduce the creep test using the parameters listed in Table 8:

Parameter	Value	Unit
μ_E	2.140	<i>GPa</i>
σ_E	0.535	<i>GPa</i>
P	3	-
Distribution	log-normal	-
Realizations	300	-

Table 8: Stochastic parameters

The results of the stochastic finite element calculation of the creep test are illustrated in Figure 4. The robust stochastic numerical model for rock salt allows to reproduce the test for a time period of 900 days. The dashed line represents the mean of the deformation of the rock salt sample. With the assumed distribution (see Section 3.1), 64,2% of the stochastic deformation lies between the two extreme experimental curves reproduced by the black lines.

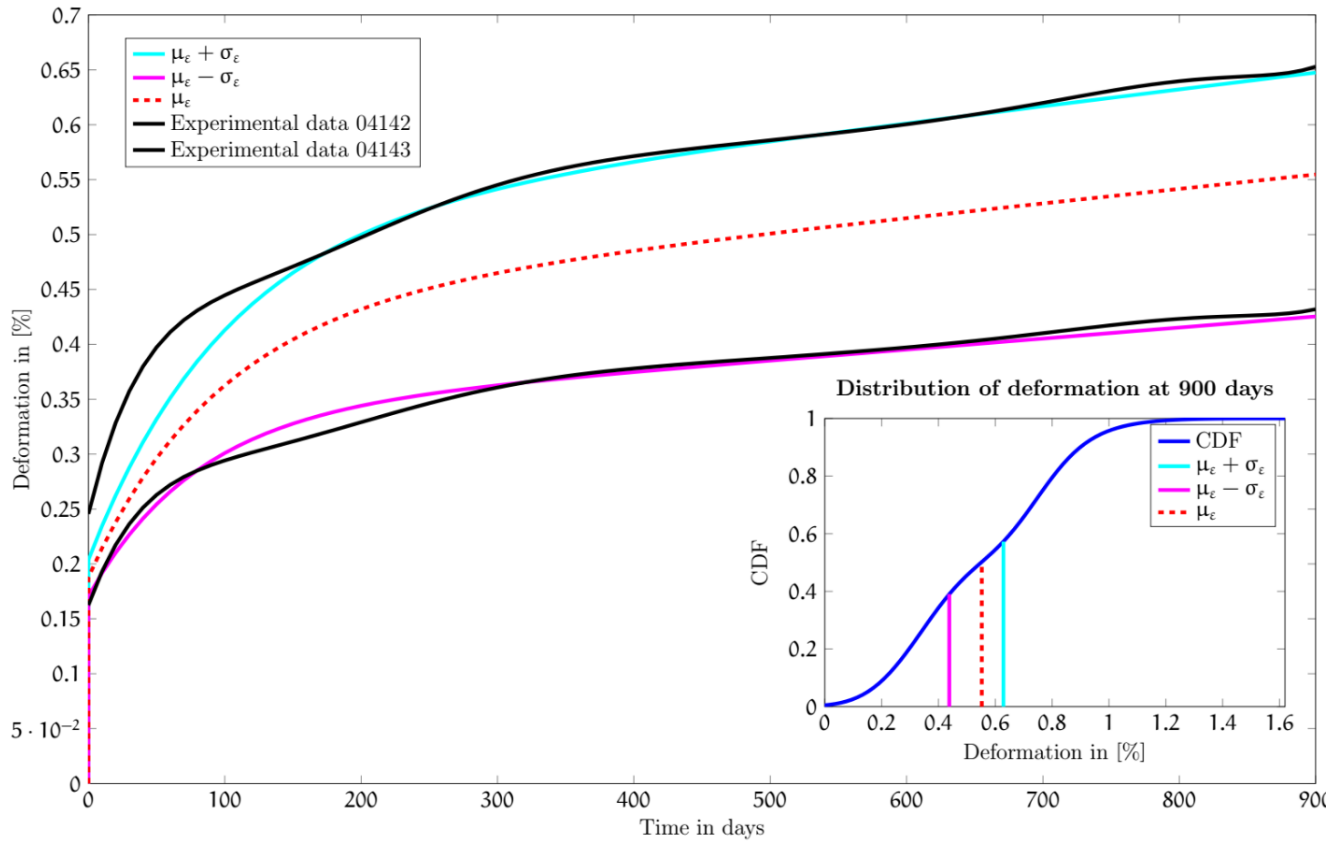


Figure 4: Distribution of strain field

4.1 Convergence of the expected value

We investigate the convergence of our computations with respect to the number of realizations. The calculation parameters are summarized in Table 9:

Parameter	Value	Unit
μ_{E_∞}	2.140	<i>GPa</i>
σ_{E_∞}	0.535	<i>GPa</i>
r	2	-
Realizations	[3,...,2187]	-

Table 9: Stochastic parameters

Figures 5a and 5b show the means of Young's modulus E_∞ in [*GPa*] and of the deformation in [%] at 900 days. The convergence behavior for the input and output random fields are quite similar. We consider they reach an acceptable error for 200 realizations. By increasing the number of realizations, the computational time becomes larger. From three to 2000 realizations, the computational times has been multiplied by nine. For further computations we consider a number of 300 realizations as a good compromise between accuracy and computing time. As we

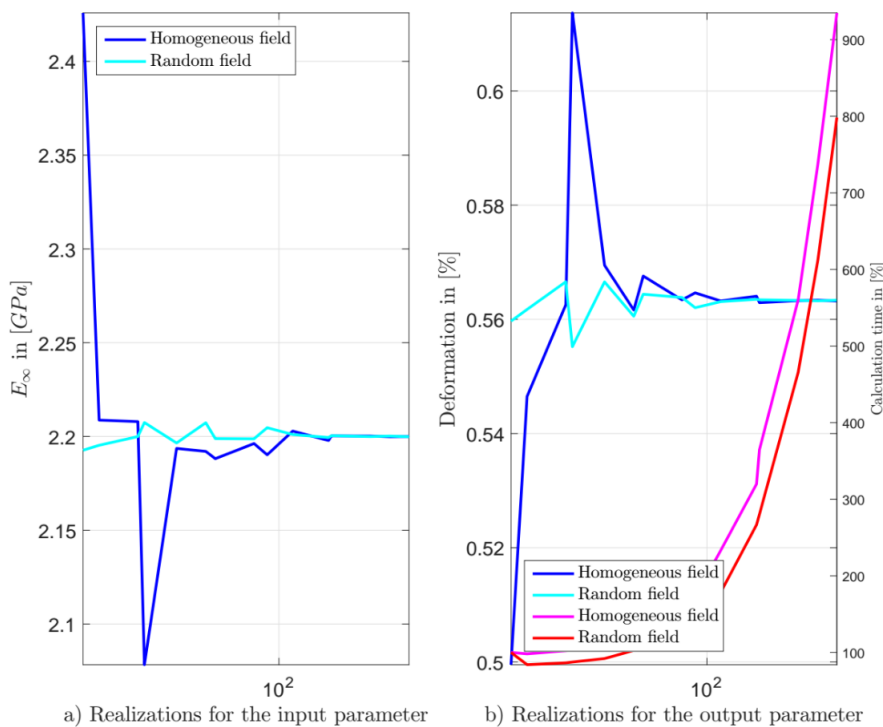


Figure 5: Convergence of the expected value for the input parameter and the deformation.

assume here an axisymmetric geometry, we impose a priori a specific structure for the random field. So, we also investigate the results considering the Young modulus

as a random variable and a homogeneous field. We see that this assumption does not influence the results largely. Homogeneous field using a unique random variable convergences by around 500 realizations whereas the computations for random field converge by around 200 realizations to the expected value. For this simple creep test, a homogeneous field allows to describe correctly the behavior. The development of the random field has been done as a preparation to compute damage for the third creep period.

5 Conclusions

In this paper, we have presented a numerically robust stochastic material model to predict the creep behavior for rock salt. We can reproduce the creep tests shown in [7] and [6].

Here, we have considered homogeneous random fields. We could extend our computations to heterogeneous random fields to include for example some localized impurities. Further work is to simulate the third creep period of the experimental tests and to predict the damage in real salt domes within a stochastic framework.

References

- [1] Z. Hou, R. Wolters, and U. Düsterloh. Die Modellierung des mechanischen Verhaltens von Steinsalz: Vergleich aktueller Stoffgesetze und Vorgehensweisen. BMBF-Verbundvorhaben, Ergebnisbericht zu Teilvorhaben 1, Förderkennzeichen 02 C 1004, 2007.
- [2] R. Günther, W. Minkley, and K. Salzer. Die Modellierung des mechanischen Verhaltens von Steinsalz: Vergleich aktueller Stoffgesetze und Vorgehensweisen. BMBF-Verbundvorhaben, Ergebnisbericht zu Teilvorhaben 1, Förderkennzeichen 02 C 1004, 2007.
- [3] A. Hampel, U. Hunsche, P. Weidinger, and W. Blum. Description of the Creep of Rock Salt with the Composite Model - II. Steady-State Creep. Series on soil and rock mechanics, 1996.
- [4] U. Hunsche. Visco-Plastic Behaviour of Geomaterials, chapter Uniaxial and Triaxial Creep and Failure Tests on Rock: Experimental Technique and Interpretation, pages 1-53. Springer Vienna, Vienna, 1994.
- [5] P. Weidinger, A. Hampel, W. Blum, and U. Hunsche. Creep behaviour of natural rock salt and its description with the composite model. Materials Science and Engineering: A, 234236:646 - 648, 1997.
- [6] A. Hampel. Die Modellierung des mechanischen Verhaltens von Steinsalz: Vergleich aktueller Stoffgesetze und Vorgehensweisen. BMBF-Verbundvorhaben, Ergebnisbericht zu Teilvorhaben 1, Förderkennzeichen 02 C 1004, 2006.

-
- [7] U. Heemann and O. Schulze. Die Modellierung des mechanischen Verhaltens von Steinsalz: Vergleich aktueller Stoffgesetze und Vorgehensweisen. BMBFVerbundvorhaben, Ergebnisbericht zu Teilvorhaben 1, Förderkennzeichen 02 C 1004, 2007.
- [8] G. Wang, L. Zhang, Y. Zhang, and G. Ding. Experimental investigations of the creepdamagerupture behaviour of rock salt. *International Journal of Rock Mechanics and Mining Sciences*, 66:181 - 187, 2014.
- [9] J. C. Simo and T. J. R. Hughes. *Computational Inelasticity*. Springer, Berlin, 1998.
- [10] M.L. Jeremic. *Rock Mechanics in Salt Mining*. Taylor and Francis, 1994.
- [11] H. L. Schreyer. On time integration of viscoplastic constitutive models suitable for creep. *Int. J. Numer. Meth. Engng.*, 2001.
- [12] O.C. Zienkiewicz and R.L. Taylor. *Finite Element Method (5th Edition) Volume 1 - The Basis*. Elsevier, 2000.
- [13] B. Sudret, M. Berveiller, and M. Lemaire. A stochastic finite element procedure for moment and reliability analysis. *European Journal of Computational Mechanics*, 2012.
- [14] B. Sudret and A. Kiureghian. *Stochastic Finite Element Methods and Reliability A State-of-the-Art Report*. Department of civil and environmental engineering university of california, 2000.
- [15] Y. Saad. *Iterative Methods for Sparse Linear Systems: Second Edition*. EngineeringPro collection. Society for Industrial and Applied Mathematics (SIAM, 3600 Market Street, Floor 6, Philadelphia, PA 19104), 2003.
- [16] D.M. Young and W. Rheinboldt. *Iterative Solution of Large Linear Systems*. Computer science and applied mathematics. Elsevier Science, 2014.
- M. Grehn, Leibniz Universität Hannover, Institute of Mechanics and Computational Mechanics, Appelstr. 9a, 30167 Hannover*
- A. Fau, Leibniz Universität Hannover, Institute of Mechanics and Computational Mechanics, Appelstr. 9a, 30167 Hannover*
- U. Nackenhorst, Leibniz Universität Hannover, Institute of Mechanics and Computational Mechanics, Appelstr. 9a, 30167 Hannover*

Damage Accumulation-based and FEA-aided Fatigue Life Evaluation of Tubular Structures

Ruslan V. Guchinsky, Sergei V. Petinov, Valentina G. Sidorenko
ruslan239@mail.ru, spetinov@mail.ru, Valentina.sidorenko@list.ru

Abstract

Fatigue assessment of tubular structures in various applications according current design codes is based on S-N criteria with uncertain characterization of the damage. In case the crack is detected residual service life may be estimated by applying the Linear fracture mechanics techniques, again, with incomplete defining the exhaustion of life. An approximate procedure based on application of the Strain-life criterion for fatigue failure and of the finite element modeling of successive damage accumulation is implemented for evaluation of fatigue life of tubular components under the cyclic loading. The procedure allows assessment of fatigue life from the moment structure is put into service up to the through crack development in the shell, or alternatively, up to the onset of fast fracture conditions. Efficiency of the approach is illustrated in example of fatigue life evaluation of the pipeline component subjected to internal pulsating pressure.

1 Introduction

The current rules for fatigue design of structures are based on application of the S-N (Stress-Life) approaches which presume assumption that material of a structure deforms elastically in service loading conditions. The mechanics of fatigue damage of a material is implied (not definitely specified) as built into the design S-N curves based on analysis of results of fatigue testing of the base material and typified welded joints (e.g., [1]). Specific of the testing procedure is the termination of test when initiated and growing fatigue crack notably affects the specimen compliance preceding complete fracture. Respectively, when the test data are applied to assessment of fatigue resistance of a structural detail, the state of damage, corresponding crack size occurs uncertain.

When in the service conditions fatigue crack is detected the residual fatigue life of a structure is recommended to estimate by using the Linear fracture mechanics approach, i.e. by evaluation of the stress intensity factor values through the anticipated crack progress in affected component and further by integrating the Paris equation. However, the stress intensities may be calculated only if the stress field at the crack tip (or the crack front) is characterized by singularity. When the crack initiated, e.g., in a tubular component or in a pipe shell, would approach the back face of

the shell, the stress field in ligament becomes non-singular, at relative depth of the crack, approximately, 0.7-0.8 of the shell thickness [2]. Consequently, the through crack regarded as indicator of the limit state of a component can not be assessed.

An attempt was made to apply the strain energy approach in conjunction with the Hutchinson-Rosengren stress-strain field solution for the near crack tip area to predict crack growth considering for the material plasticity [3]; again, the problem of incorporating the crack initiation stage into the continuous fatigue process was not solved.

Summing up, it may be stated that the fatigue life evaluation presently is composed of application of the two approaches, but the link between these is missing and the limit state may be estimated in the course of the fatigue crack extensions only when the conditions for fast fracture are attained.

A reasonable solution of the fatigue life problem may be application of the approach based on implementation of the Strain-life criterion and the damage accumulation in material elements supported by the means of the finite-element modeling of the crack initiation and growth.

2 Description of the approach

The Strain-Life approach considered in the present rules as optional may be a reasonable method for fatigue analysis and design of structures by the mentioned reasons. The approach includes an appropriate Strain-Life criterion for fatigue failure of material together with the experimentally obtained lumped stress-strain cyclic diagram. The damage accumulation procedure developed for fatigue assessment under irregular loading in crack analysis is necessarily supported by the finite-element modeling of the affected structure.

According to the approach the expected crack path is considered in design of the finite element mesh, the finite elements assumed the grain clusters with approximately close (or, alternatively, random) slip resistance. The damage is supposed to be uniformly distributed within these elements. Each element is provided with a scalar damage variable, estimated by the selected damage accumulation theory for irregular loading. The number of cycles prior to failure of each element is evaluated using the Strain-life Manson's criterion.

When the damage in the element reaches a critical unity, its compliance is artificially increased, and nodal forces are redistributed in the surrounding elements. The damage calculation is repeated considering for the renewing stress-strain state ahead the crack tip; "killed" elements form the crack front progress.

This idea was first suggested in pioneering studies of G. Glinka and F. Ellyin focused on analysis of cracks in thin plates at the plane stress [4, 5]; further analysis had shown that the procedure may be applied to assessment of fatigue process including crack initiation and growth of plane cracks in arbitrary bodies [6, 7].

3 Fatigue life assessment of a pipeline loaded by the inside pulsating pressure

The briefly explained in above approach is applied for fatigue life evaluation of a pipeline subjected to pulsating pressure from inside. The fatigue life is estimated as initiated in undamaged structure from the very first load application until development of the through crack.

Fig.1 shows failure of a pipeline along the generating line caused by hoop stress. Respectively and accordingly the principles of modeling fatigue process the finite element model of the cylindrical shell is designed where the fatigue crack initiation and growth may be expected. The size of elements is assumed encircling a number of grains characterized by approximately equal resistance to the cyclic loading. The finite-element model of a fragment of the pipeline is presented in Fig.2. The arrow shows the fine mesh at the expected fatigue crack origination and propagation through the shell thickness.



Figure 1: Example of the through crack in a fractured pipeline

Material of the pipeline - higher strength steel 09G2 grade, the yield stress of which $\sigma_y = 300$ MPa, ultimate strength $\sigma_u = 450$ MPa. Resistance of the material (finite elements) to cyclic loading is characterized by the strain-life (Manson's) criterion [8], parameters of which are given in [9]:

$$\Delta\varepsilon = \Delta\varepsilon_p + \Delta\varepsilon_e = CN^{-\alpha} + BN^{-\beta}, \quad (1)$$

where $\Delta\varepsilon_p$ is the plastic strain range component, $\Delta\varepsilon_e$ is the elastic strain, $C = 0.34$ (the crack is expected in rolling direction of the plate steel, Bklamellar-tearingBН effect considered), $B = 0.011$, $\alpha = 0.654$, $\beta = 0.170$.

The stabilized lumped cyclic curve of the steel obtained based on the principle of equivalent strain energy also taken from [9] is given in Table 1.

To initiate the fatigue process in selected area (fine mesh area) several elements at the inner surface of the shell are provided with reduced cyclic proportionality stress with respect to that for elements of the model.

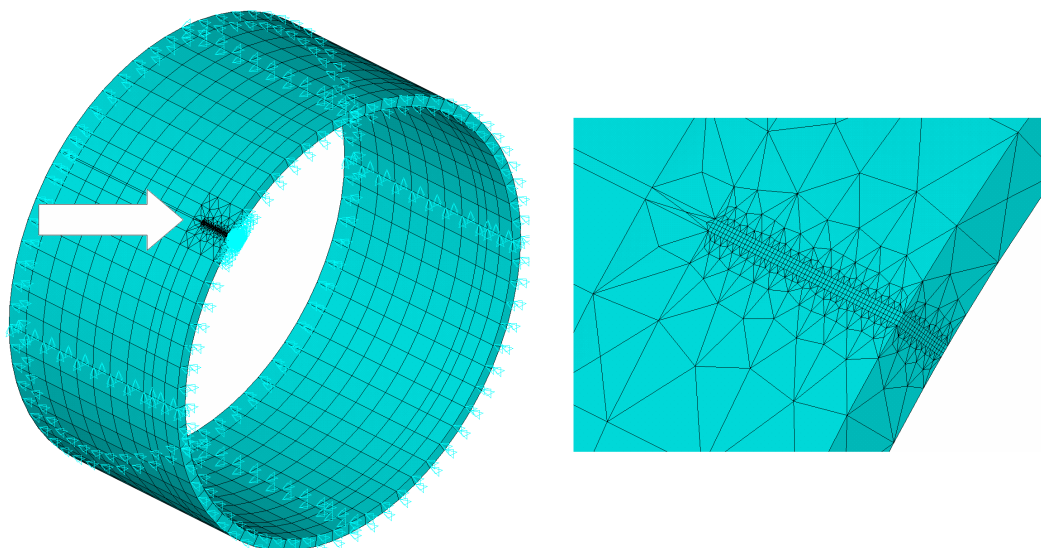


Figure 2: FE model of the pipeline and fragment of the shell (right-hand) with fine mesh where the crack is expected

Table 10: Stabilized lumped cyclic curve of the 09G2 grade steel

$\Delta\sigma, MPa$	105.0	210.0	303.2	363.2	435.0	482.1
$\Delta\varepsilon$	0.0005	0.0010	0.0015	0.0020	0.0025	0.0030
$\Delta\varepsilon\Delta\sigma$	0.0525	0.2100	0.4548	0.7264	1.0875	1.4463

With initiation of cyclic loading the damage accumulation in elements is estimated by applying the Palmgren-Miner linear damage summation rule. In initial step of the procedure, $j = 1$, the strain field in " i " elements located in the area of expected crack extensions is calculated. The number of cycles to failure of the above mentioned "weak", the most affected, elements is estimated by the criterion (1). The damage in initial step is calculated also for the elements of surrounding volume; the damage for failing elements is equal to unity. Failure of elements is modeled by decreasing the stiffness of those by several decimal orders with respect to the stiffness of surrounding volume of material. Through the following step the new stress-strain field (changed in the course of failure of elements forming the crack extensions) in elements is calculated and failure of sequential elements is assessed considering the damage accumulated at the previous steps.

So far, the damage accumulated in i -th element through " j " steps can be presented in the form of the recurrence:

$$d_i^j = \sum_j \min\{n_i^j\}/N_i^j = \sum_j \min\{N_i^j(1 - d_i^{j-1})\}/N_i^j, \quad (2)$$

where n_i^j is the number of cycles prior to failure of i -th element at the j -th step. The total accumulated damage at every sequential step of the procedure depends on

the previous damage magnitude and on failure of elements in the affected area. For every element the number of step, j_{cr} , when it fails, may be indicated; the minimum number of cycles prior to failure at this step is related to this particular i -th element:

$$\min\{N_i^{j_{cr}}(1 - d_i^{j_{cr}-1})\} = N_i^{j_{cr}}(1 - d_i^{j_{cr}-1}). \quad (3)$$

Respectively, the damage in i -th element corresponding to failure may be presented as:

$$d_i^{j_{cr}} = d_i^{j_{cr}-1} + \min\{n_i^{j_{cr}}\}/N_i^{j_{cr}} = d_i^{j_{cr}-1} + N_i^{j_{cr}}(1 - d_i^{j_{cr}-1})/N_i^{j_{cr}} = 1. \quad (4)$$

When the crack initiates the problem of effective part of the load cycle arises which concerns the phase when the crack opens and up the maximum load. The crack opening effect can be taken into account within this approach by introducing an effective strain range in the failure criterion via total strain range multiplied by the crack opening parameter identical to that suggested by Elber [10]:

$$\Delta\varepsilon_{eff} = U\Delta\varepsilon. \quad (5)$$

It was shown [6] that crack opening parameter, U , can be estimated by changing the stress sign in elements at the crack tip in direction perpendicular to the crack front.

The procedure was applied to calculate both the crack expansion and number of cycles in several steps. Fig. 3 illustrates the crack progress initiated at the inner surface of the shell until it reaches the outer surface and becomes the through-crack. The crack front seems a relatively short along the cylindrical shell generating line. This may be explained by relatively short model of the affected area where the mesh is essentially fine (with respect to the shell thickness), Fig.2.

The fatigue life of the pipeline assessed from the initiation of cyclic loading up to the through crack is illustrated in Fig.4 as the dependence of the number of cycles on the hoop stress range.

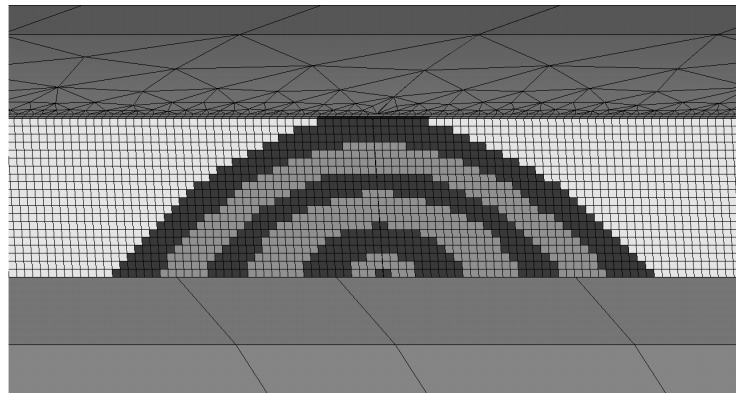


Figure 3: Crack progress towards the outer surface of the pipeline

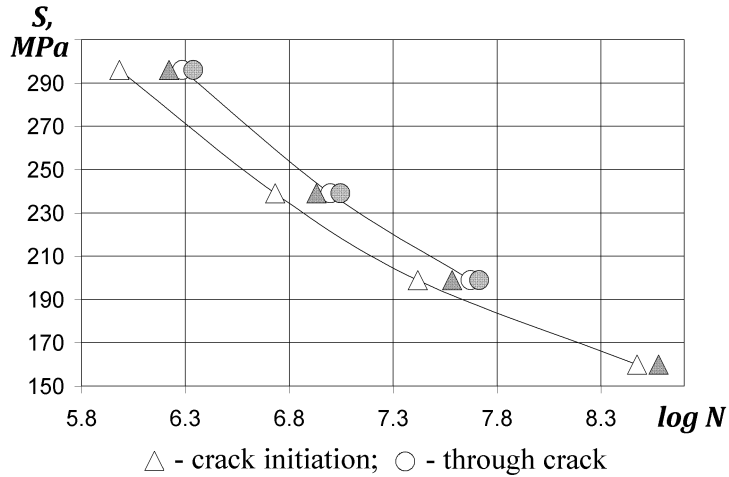


Figure 4: Fatigue life of the pipeline

4 Conclusions

The approach based on application of the Strain-life criterion for fatigue, characterization of the cyclic elastic-plastic properties of material (cyclic stress-strain curve), damage summation procedure and finite-element modeling of structure with the due attention to FE-modeling of the critical area provides evaluation of fatigue life of a structural component including both, the crack initiation and the crack propagation phases. In considered example of the pipeline, it is shown that the fatigue can be assessed from the initiation of cyclic loading (pulsating pressure of the transported media in pipeline) up to formation of the through crack.

References

- [1] Det Norske Veritas. Fatigue Assessment of Offshore Steel Structures. Recommended Practice (DNV-RP-C203). (2010), Hovik, Norway.
- [2] Murakami, Y. et al. Stress intensity factor handbook (1989). The Society of Materials Science Japan: Pergamon Press, Oxford, 448 p.
- [3] Panovko, O.Ja., Petinov, S.V. Crack Growth Analysis by the Inelastic Strain Energy Criterion for Fatigue / Pre-print IPME RAS, (1990). No.39, 20 p.
- [4] Ellyin, F. Fatigue Damage, Crack Growth and Life Prediction. (1997). Chapman & Hall, London.
- [5] Glinka, G. A Cumulative Model of Fatigue Crack Growth. Int. Journal of Fatigue, (1982), April, pp.59-67
- [6] Guchinsky, R.V., Petinov, S.V. Two-Dimensional Surface Fatigue Crack Propagation and its Finite Element Simulation. Applied Mechanics and Materials, vol. 725-726, Ch.5, pp.654-661.

REFERENCES

- [7] Guchinsky, R.V., Petinov, S.V. Fatigue of fillet-welded joint assessment by the FEA simulation of damage accumulation. Magazine of Civil Engineering, (2011). 4(22), pp. 5-9.
- [8] Manson S.S. Fatigue: A Complex Subject - Some Simple Approximations. Experimental Mechanics (1965). Vol.7, No.5, pp.193-226
- [9] Petinov, S.V. Fatigue Analysis of Ship Structures. Backbone Publishing Co., Fair Lawn, NJ, USA, 2003, 262 p.
- [10] Elber W. Fatigue crack closure under cyclic tension. Engineering Fracture Mechanics. (1970). V.2, pp. 37-44.

Ruslan V. Guchinsky, Institute for problems of mechanical engineering, Bolshoy pr., 61, V.O., St. Petersburg, 199178, Russia

Sergei V. Petinov, Valentina G.Sidorenko, Peter the Great St.Petersburg Polytechnic University, Polytechnicheskaya str. 29, St.Petersburg, 195251, Russia

Influence of the treatments on the behavior and the damage in tensile and with the shock of the recovery alloy AlSi12: application to the recycling of waste

Ahmed Hakem, Amayas Hakem, Youcef Bouafia
a_hakem1951@yahoo.fr

Abstract

This study aims to determine the influence of the chemical composition of industrial sand casting and metal shell cast by gravity at room temperature or under pressure both mechanical and manual metal parts for the various achievements SNVI (Aluminum Foundry Unit Rouiba) and ENEL (Unit engine Freha in Tizi-Ouzou) Algeria and heat treatments on mechanical behavior of fracture, quasi-static axial tensile united, Brinell hardness, almost dynamic resilience and microstructure of the alloy foundry chemical designation AlSi12 and digital 44000, The addition of 12% silicon and magnesium percentage (0,1% Mg) in aluminum are the principal agents of the improvement of mechanical properties in addition to specific heat treatments which show different types of precipitates that hinder the movement of dislocations.

Keywords: Al-Si, sand, shell, maturation, income, mechanical properties

1 Introduction

The physical characterization, chemical and general engineering in particular is crucial for the design of various metal parts subject to external forces varied constituents various mechanisms in motion a mechanical component. The designer can neither calculate nor resize these parts without identifying and quantifying their characteristics. To determine them, we reproduce these solicitations using static and dynamic tests, usually conducted on standard specimens.

The alloy AlSi12, which governs our study, is a shade containing some magnesium added in small amounts (0,05 to 0,10) % Mg alloy to allow hardening and efficient use in applications with high mechanical properties in T46 condition. This alloy contains 12low volumetric contraction during solidification, reduction of withdrawal to the solid state and the expansion coefficient.). It is used for complex shapes, to requirements of mechanical strength and maximum thicknesses which are very low ($\sim 3mm$).

2 Problematic

The unalloyed aluminum with mechanical properties very reduced, leading to add two items of very low density with 13% silicon and traces of magnesium less than 1% ($\leq 0,1\%$ Mg) which is the lightest of all metals capable of stable industrial employment to improve their properties and obtain an alloy AlSi12 super lightweight. The alloy foundry ultimate AlSi12 governing our study is an alloy with a set of properties that in many circumstances make it an irreplaceable material. Among these include the addition of a high percentage of silicon and a low percentage of magnesium to aluminum as the main potential agents of improvement largely mechanical properties, low density (~ 26) results in equal volumes of documents about three times less severe than if they were made of steel or copper, combined with very good corrosion resistance and low melting temperature (660 C) facilitating its development in all casting processes. These alloying elements come into solution and may also be present as intermetallic phases. The composition of these phases, but above all their delicacy, their distribution, their consistency vis-à-vis the aluminum matrix, their frailties, their stability as a function of heat treatments are also decisive for the properties of the alloy.

3 Elaboration of alloy studied

3.1 Casting

The melting of the metal takes place in a gas oven production, to tilting of the front to back, comprising a graphite crucible with a load capacity 350Kg is composed of approximately $\approx 50\%$ in ingots new AlSi12 of standard dimensions, composition and specified characteristics., delivered by the French company Pechiney and a mixture of jet casting $\approx 50\%$ return (appendages supply, drainage, control, defective parts and scrap).

To seek to increase over the characteristics of resistance to state F and obtain substantially large elastic stresses, the stiffness of large modules with small deformations, the material of 44000 numerical designation is subject to specific treatments T46.

3.2 Molding

- a Sand: This mold has two halves by the footprints in the sand packed model.
- b Shell: In this mode of molding, the mold consists of two steel yokes (5% chromium), which is responsible for maintaining the tracks. These caps, separated by a parting line, possibly to be prepared and heated to a temperature $(200\text{div } 300)^\circ \text{C}$. After analysis, the samples cast in sand and metal shell by gravitation have the following chemical composition:

Chemical elements	Fe	Fe	Mg	Mn
% according to analysis	0.64	12	0.08	0.31

Table.1. Results of chemical analysis after control samples cast in sand and shell. This alloy is prepared by two different methods: sand casting and shell casting, considering 05 states, F, T, M0h, M6h and M12h.

4 Experimental procedure

To determine the behavior of the material deal with various stresses it may encounter during use, these solicitations are reproduced using static or dynamic tests, usually conducted on standard specimens in order to know the characteristics Figures of the material. Four techniques are used, namely traction to identify the various constraints, the Brinell hardness HB for the stress field, resilience Kcv us about the mode of fracture, fragility and resistance to shock and metallographic to identify structures.

The specimens are divided into 05 identical batches each consisting of 05 tensile specimens, 05 specimens of resilience and 02 samples for each mode and casting (sand noted: S and shell noted: K). The 1st batch noted: F - crude of casting, - the 2nd lot is designated: T - hardened condition, - the 3rd, 4rd and 5rd batch are rated: M0h, M6h and M12h - maturation time. We will describe in more detail and present in the main mechanical characteristics obtained from the chemical composition of material being AlSi12 purpose of this study.

5 Results obtained and discussion

The mean values of tensile mechanical properties, toughness and hardness of the alloy AlSi12 are those given by averaging five identical specimens for each of the respective cases and are represented in Figures 1 to 3 below.

Influence of molding processes in the sand and in the shell for alloy AlSi12 on the characteristics in

5.1 Resistances

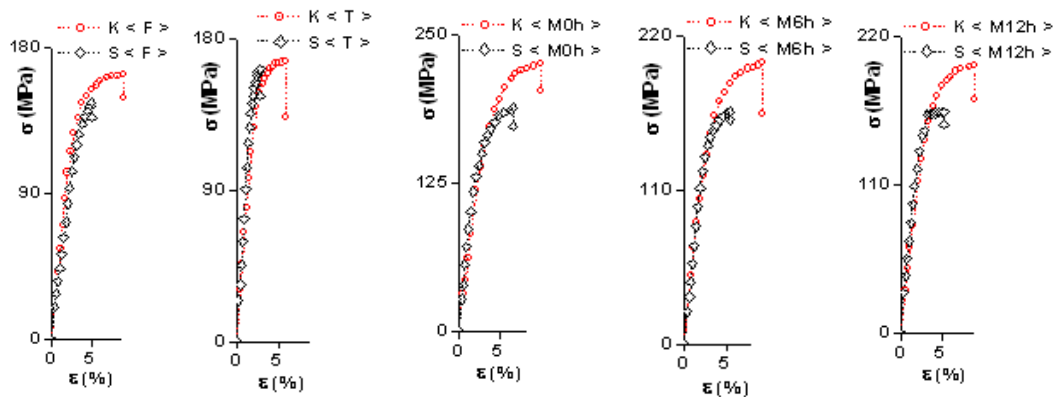


Fig-

ure1. Grouping of the mean curves of comparison (mean stress - deformation) of the AlSi12 alloy casted in sand and in shell: a - $K < F > / S < F >$, b - $K < T > / S < T >$, c - $K < M0h > / S < M0h >$, d - $K < M6h > / S < M6h >$ and e - $K < M12h > / S < M12h >$.

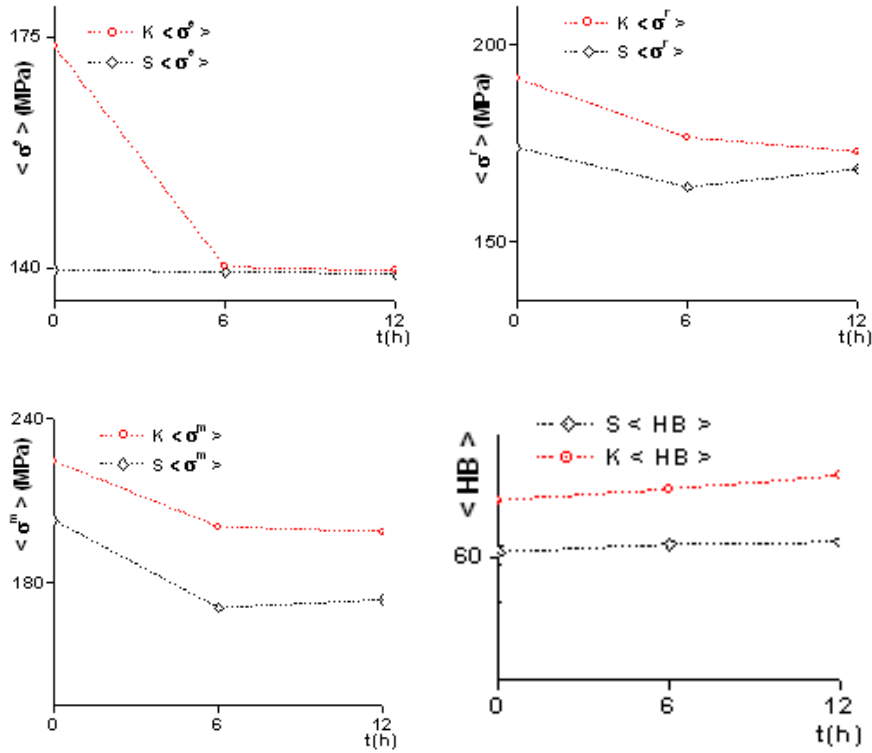
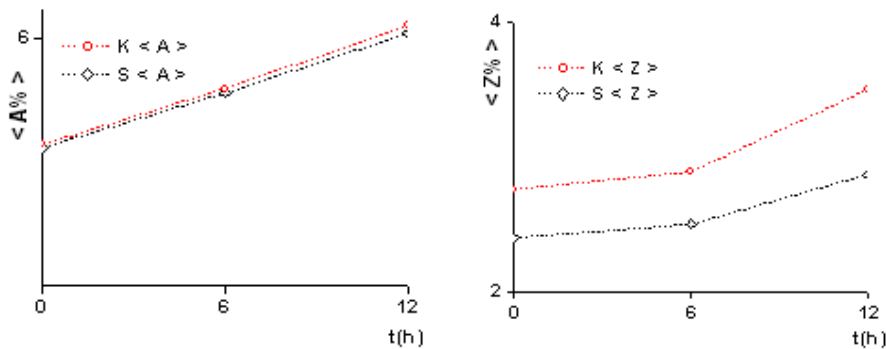


Figure2. Grouping of the mean Graphs of comparison (mean stress and mean hardness - states) of the AlSi12 alloy casted in sand and in shell: $a - K \langle e \rangle / S \langle e \rangle$, $b - K \langle r \rangle / S \langle r \rangle$, $c - K \langle m \rangle / S \langle m \rangle$ and $d - K \langle HB \rangle / S \langle HB \rangle$.

Discussion The results of these comparative studies show that all curves and all graphs of the shell casting are above those of the sand casting, whatever of the states considered. In addition to the increase in mean values of the characteristics of resistance is the state F to the T state, reaching its maximum value to the state M0h, then decrease to the states and M6H M12h whatever the two modes of elaboration at the expense of ductility, and this is probably due on the one hand, the mode for cooling the molds, on the other hand the addition of alloying elements combined with structural hardening treatment by precipitation.

5.2 Ductility



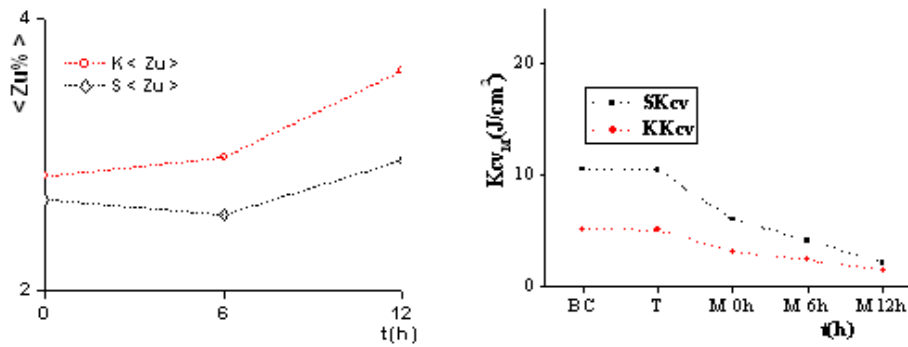


Figure3. Grouping of the mean Graphs of comparison (mean elongation, mean Coefficient and elongation of necking and mean resilience - states) of the AlSi12 alloy casted in sand and in shell $a - K \langle A \rangle / S \langle A \rangle$, $b - K \langle Z \rangle / S \langle Z \rangle$, $c - K \langle Zu \rangle / S \langle Zu \rangle$ and $d - K \langle Kcv \rangle / S \langle Kcv \rangle$.

Discussion: we see that all curves of sand casting are above those of the shell casting whatever of the states considered. In addition to the increase in mean values of ductility characteristics is the state M0h that of M6h to reach its maximum value at state M12h regardless of the two modes of elaboration to the detriment of the characteristics of resistance.

Notation: $\langle m \rangle$ (MPa) - mean maximum stress (Mega Pascal), $\langle e \rangle$ (MPa) - mean elastic stress (Mega Pascal), $\langle r \rangle$ (MPa) - mean breaking stress (Mega Pascal), Ox (%) - deformation (%), $\langle HB \rangle$ - mean hardness Brinell HB, $\langle A\% \rangle$ - mean elongation (%), $\langle Z\% \rangle$ - mean Coefficient of necking (%) and $\langle Zu\% \rangle$ - mean elongation of necking (%), F - crude of casting, T - Brhardened, M0h, M6h and M12h - maturation 0h, 6h and 12h, S - Sand and K - shell.

6 Conclusion

The analysis of experimental results show that the best compromise is the method of shell casting followed by maturation of 0 hours (M0h) regardless of the states considered. To meet manufacturers' requirements for a rational use of this material in various mechanisms subjected to mechanical stresses, it is best to develop the different parts for the use of different natures in metallic shells followed by maturation of 0h for spare resistance and inversely.

References bibliographiques

- [1] Ahmed Hakem, doctoral thesis, Effects of elaboration mode and maturation on mechanical properties and microstructure of casting alloys Al-Si, 2014, Department of Engineering - Mechanical, Faculty of Engineering Construction, University Mouloud Mammeri Tizi - Ouzou, Algeria
- [2] *** PECHINEY ALUMINUM - Casting alloys: Catalog datasheets 1998, Catalogue Technical Publishing Foundry 1998, Brochures Technical Centre for the Foundry Industry, Internal Documentation Aluminium Pechiney.

- [3] Sylvain Jacob, properties of aluminum alloys foundry, M 442-10, Engineering Techniques, treated metallic materials
- [4] Ahmed Hakem and al. Influence of User Development and Aging on Mechanical Characteristics and microstructure of the alloy foundry AlSi10Mg, ACMA, 2010, 12-14 May 2010, Marrakech, Marocco.
- [5] M. Colombia and Coll, Industrial Materials: Metal Materials, p.867, Dunod, Paris (2000).
- [6] Jean-Paul Baillon, Jean-Marie Dorlot, Materials, p.729, 3rd edition, Ecole Polytechnique de Montreal, Montreal (2000).
- [7] Ahmed Hakem and al. Development of industrial aluminum alloys foundry AlSi7Mg, AlSi10Mg and AlSi13, International Symposium - Characterization and Modeling of Materials and Structures 16, 17 and 18 November, 2008 - University Mouloud Mammeri Tizi-Ouzou, Algeria.
- [8] Asserin-Lebert Experimental study and prediction of failure mechanisms of plates and joints butt welded aluminum alloy 6056, and presented publicly defended February 18, 2005, Ecole des Mines de Paris, p190.
- [9] PORTALIER (R.). - Foundry and casting of aluminum alloys. M 810 M 813 (1990). Technical Engineer, treated metallic materials
- [10] Ahmed Hakem, memory magister, Microstructure and Mechanical Properties of Alloy hypoeutectic AlSi7Mg, 2005, Department of Engineering - Mechanical Engineering, Faculty of Engineering Building, University Mouloud Mammeri Tizi - Ouzou . Algeria.
- [11] Jean Baralis Gerard Maeder, Handbook of Metallurgy: (Preparation, structure, properties, normalization), p.232, 1ere Edition, AFNOR-Nathan, Paris (1997).
- [12] Bruno Barlas, study of behavior and fatigue damage in aluminum alloy casting, thesis submitted and publicly defended the 5th in February 2004, Ecole des Mines de Paris, p228.

Ahmed Hakem, Laboratory LaMoMS, Mouloud MAMMERI university of Tizi-Ouzou, 15000 Algeria, Corresponding Author E-mail: a_hakem1951@yahoo.fr

Amayas Hakem, Department of Mechanical Engineering, Faculty of Engineering of Construction, Mouloud Mammeri University of Tizi-Ouzou, 15000 Algeria

Youcef Bouafia, Laboratory LaMoMS, Mouloud MAMMERI university of Tizi-Ouzou, 15000 Algeria

On homoclinics and heteroclinics of Lagrangian systems in a non-stationary force field

Alexey V. Ivanov
a.v.ivanov@spbu.ru

Abstract

We study homoclinic and heteroclinic orbits of a natural Lagrangian systems defined on a complete Riemannian manifold being subjected to action of a non-stationary potential force field. It is assumed that Lagrangian of such a system can be written in the following form $L(q, \dot{q}, t) = K(q, \dot{q}) - U(q, t)$, where the kinetic energy K is a positive definite quadratic form in velocity \dot{q} and the potential $U(q, t)$ has special representation $U(q, t) = f(t)V(q)$. We also assume that there exists $t_0 \in \mathbb{R}$ such that $f(t_0) = 0$, i.e. at the moment t_0 the system becomes free and $|f(t)|$ is monotonic on both intervals $t > t_0$ and $t < t_0$. Let X_+ , X_- denote the set of isolated critical points of $V(x)$ at which $U(x, t)$ distinguishes its maximum for $t > t_0$ and $t < t_0$, respectively. Under nondegeneracy conditions on points of X_{\pm} we prove the existence of infinitely many doubly asymptotic trajectories connecting X_- and X_+ .

1 Introduction

During the last two decades many authors studied connecting (i.e. homoclinic and heteroclinic) orbits of Lagrangian systems by use of variational methods and critical points theory [1]-[4]. Being a part of intersection of invariant manifolds associated with some hyperbolic objects such trajectories usually lead to chaotic dynamics of a system. In the present work we study a natural Lagrangian system on a complete Riemannian manifold. Namely, we consider a compact Riemannian manifold \mathcal{M} to be configuration space of a Lagrangian system with Lagrangian $L \in C^2(T\mathcal{M} \times \mathbb{R}, \mathbb{R})$ such that

$$L(q, \dot{q}, t) = K(q, \dot{q}) - U(q, t), \quad (1)$$

where the kinetic energy $K \in C^2(T\mathcal{M}, \mathbb{R})$ is a positive definite quadratic form in velocity \dot{q} , while the potential energy $U(q, t) \in C^2(\mathcal{M} \times \mathbb{R}, \mathbb{R})$ has the following special form

$$U(q, t) = f(t)V(q). \quad (2)$$

The equations of motion take the form

$$\frac{d}{dt} \frac{\partial T}{\partial \dot{q}} - \frac{\partial T}{\partial q} = -f(t) \frac{\partial V}{\partial q}. \quad (3)$$

In addition we suppose that f satisfies the following assumptions:

(A₁) there exists $t_0 \in \mathbb{R}$ such that $f(t_0) = 0$,

(A₂) the function $|f|$ is strictly monotone for $t > t_0$ and $t < t_0$,

(A₃) $|f(t)| \rightarrow +\infty$ as $t \rightarrow \pm\infty$,

(A₄) there exist constants $\mu, T > 0$ such that $|f(t)| > \mu|f'(t)|$ for all $|t| > T$.

Making a time shift and changing, if necessary, the time sign we may always suppose that $t_0 = 0$ and the function f is increasing on the interval $\mathbb{R}_+ = (0, +\infty)$ and, hence, $f(+\infty) = +\infty$. We also denote $\mathbb{R}_- = (-\infty, 0)$. The simplest examples of functions f satisfying A₁ – A₄ may be given by t^m , $\sinh(\alpha t)$ and $\log(1 + \alpha t^2)$ for some $m \in \mathbb{N}$, $\alpha > 0$.

Since \mathcal{M} is a compact manifold, the function V has minimum and maximum on \mathcal{M} . Denote by X_+ , X_- the subsets of \mathcal{M} on which $U(x, t)$ distinguishes global maximum for $t > 0$ and $t < 0$, respectively. We suppose that X_\pm consist of isolated critical points of V and that they are nondegenerate.

We will say that a solution $q : \mathbb{R} \rightarrow \mathcal{M}$ is a *homoclinic (heteroclinic)* solution if there exist $z_1, z_2 \in \mathcal{M}$ (for homoclinic solution $z_2 = z_1$) such that q joins z_1 to z_2 , i.e. $\lim_{t \rightarrow -\infty} q(t) = z_1$, $\lim_{t \rightarrow +\infty} q(t) = z_2$ and $\lim_{t \rightarrow \pm\infty} \dot{q}(t) = 0$.

Theorem 1. *Under assumptions A₁ – A₄ for any $z_1 \in X_-$ and $z_2 \in X_+$ there exist infinitely many heteroclinic (homoclinic) trajectories emanating from z_1 and terminating at z_2 .*

Remarks. - 1. One may note that the sets X_+ , X_- do not coincide in the case $f(-\infty) = -\infty$ what lead to connection between different regions of the configuration space.

2. If we denote by Y_+ , Y_- the subsets of \mathcal{M} consisting of minima of $U(x, t)$ for positive and negative t , then under weak additional assumptions almost each trajectory $q(t)$ tends to a point from Y_\pm as $t \rightarrow \pm\infty$ [6]. However, $\limsup_{t \rightarrow \pm\infty} |\dot{q}(t)| = \infty$ and these solutions cannot be called asymptotic.

Systems of type (3) often arise in mechanical applications. In particular, this work was inspired by [1], where the authors applied Routh's reduction to a Lagrangian system with symmetry which led to a system (3) with $f(t) = t^2$. In particular, they studied the Kirchhoff problem. We also refer to [5], [6], [9], [3] where the systems of type (3) are discussed.

2 Variational settings

We use variational arguments to prove Theorem 1. Consider a smooth embedding of the manifold \mathcal{M} into \mathbb{R}^N for $N = 2n + 1$ with $n = \dim \mathcal{M}$ and denote by $\langle \cdot, \cdot \rangle$ the Euclidean structure in \mathbb{R}^N together with its restriction to \mathcal{M} . Let ∇ stands for the gradient operator with respect to the variable x . First we study the case when each of the subsets X_\pm consists of one point, i.e. $X_\pm = x_\pm$.

Denote

$$\mathcal{E}_f = \left\{ v \in AC(\mathbb{R}, \mathbb{R}^N) : \|v\|_f^2 = \int_{-\infty}^{+\infty} (|\dot{v}(t)|^2 + |f(t)| \cdot |v(t)|^2) dt < \infty \right\}, \quad (4)$$

where $AC(\mathbb{R}, \mathbb{R}^N)$ is the set of absolutely continuous curves from \mathbb{R} to \mathbb{R}^N .

Let $\mathcal{E}_1 = W^{1,2}(\mathbb{R}, \mathbb{R}^N)$ be the Sobolev space with the norm $\|\cdot\|_1$ such that $\|v\|_1^2 = \int_{-\infty}^{+\infty} (|\dot{v}(t)|^2 + |v(t)|^2) dt$.

One may prove the following lemma.

Lemma 1. $\mathcal{E}_f \subset \mathcal{E}_1$ and $\|v\|_1 \leq C_f \|v\|_f$ with $C_f^2 = \max\{(b-a)^2 + 1, 2\}$, where $a, b \in \mathbb{R}$ such that $a < 0$, $b > 0$ and $|f(a)| = |f(b)| = 1$.

Since \mathcal{E}_1 is continuously embedded into $C^0(\mathbb{R}, \mathbb{R}^N)$ with $\|v\|_\infty = \sup_{t \in \mathbb{R}} |v(t)| \leq \|v\|_1$ we arrive at the following lemma.

Lemma 2. \mathcal{E}_f is a Hilbert space.

PROOF: - Let $\{v_n\}, v_n \in \mathcal{E}_f$ be a Cauchy sequence. Then due to Lemma 1 $\{v_n\}$ is a Cauchy sequence in \mathcal{E}_1 . Since \mathcal{E}_1 is complete there exists $v = \lim_{n \rightarrow \infty} v_n \in \mathcal{E}_1$. One may extract a subsequence $\{v_{n_k}\}$ such that $\|v_{n_k} - v\|_\infty \rightarrow 0$ and $\dot{v}_{n_k} \rightarrow \dot{v}$ almost everywhere. Fix $\varepsilon > 0$ and take $k(\varepsilon)$ such that for any $l, m > k(\varepsilon)$ $\|v_{n_l} - v_{n_m}\|_f < \varepsilon$. Then by the Fatou lemma we have

$$\begin{aligned} \|v_{n_l} - v_{n_m}\|_f^2 &= \int_{-\infty}^{\infty} \lim_{m \rightarrow \infty} (|\dot{v}_{n_l}(t) - \dot{v}_{n_m}(t)|^2 + |f(t)| \cdot |v_{n_l}(t) - v_{n_m}(t)|^2) dt \leq \\ &\leq \liminf_{m \rightarrow \infty} \|v_{n_l} - v_{n_m}\|_f^2 \leq \varepsilon^2. \end{aligned}$$

Due to arbitrary choice of ε one concludes that $\|v_{n_l} - v\|_f \rightarrow 0$ as $l \rightarrow \infty$. \square

The next lemma gives an estimate on the absolute value of an element of the space \mathcal{E}_f .

Lemma 3. If $v \in \mathcal{E}_f$ then

$$|v(t)| \leq \frac{\sqrt{2}}{|f(t)|^{1/4}} \|v\|_f.$$

PROOF: - Define $g(t) = |f(t)|^{1/2}$. For any $v \in \mathcal{E}_f$ consider

$$g(t)|v(t)|^2 = \int_{-\infty}^t \dot{g}(s)|v(s)|^2 ds + 2 \int_{-\infty}^t g(s)\langle v(s), \dot{v}(s) \rangle ds. \quad (5)$$

Note that (5) is valid if $-\infty$ is replaced by $+\infty$. Then substituting $t = 0$ into (5) and using monotonicity of g on \mathbb{R}_\pm together with the Schwartz inequality one gets

$$\left| \int_{\mathbb{R}_\pm} \dot{g}(s)|v(s)|^2 ds \right| = 2 \left| \int_{\mathbb{R}_\pm} g(s)\langle v(s), \dot{v}(s) \rangle ds \right| \leq \int_{\mathbb{R}_\pm} (|\dot{v}(s)|^2 + g^2(s)|v(s)|^2) ds. \quad (6)$$

Finally, (5) and (6) give $g(t)|v(t)|^2 \leq 2 \int_{-\infty}^{+\infty} (|\dot{v}(s)|^2 + g^2(t)|v(s)|^2) ds = 2\|v\|_f^2$. \square

Denote

$$\mathfrak{M} = \left\{ q \in AC(\mathbb{R}, \mathbb{R}^N) : q(t) \in \mathcal{M} \text{ for each } t \in \mathbb{R} \text{ and } \int_{-\infty}^{+\infty} \left(|\dot{q}(t)|^2 + |f(t)| \cdot |q(t) - \chi(t)|^2 \right) dt < \infty \right\},$$

where the function $\chi(t) = x_-$ for $t < 0$ and $\chi(t) = x_+$ for $t \geq 0$.

Proposition 1. *The set \mathfrak{M} is a Hilbert manifold of class C^2 with tangent space at q given by*

$$T_q \mathfrak{M} = \left\{ v \in \mathcal{E}_f : v(t) \in T_{q(t)} \mathcal{M} \text{ for all } t \in \mathbb{R} \right\}.$$

PROOF: - It follows from lemmae 1 and 3 that if a sequence $\{q_k\}$ converges to q in \mathfrak{M} with respect to (4) then it also converges to q uniformly on \mathbb{R} . Since $q(t) \rightarrow x_{\pm}$ as $t \rightarrow \pm\infty$ for any $q \in \mathfrak{M}$ we may use local coordinates in \mathbb{R}^N and apply the classical arguments [7] as in the case of the space

$$\Omega(\mathcal{M}, x_-, x_+) = \{q \in C^0([0, 1], \mathcal{M}) : q(0) = x_-, q(1) = x_+\}.$$

Further there will be given an alternative description of the Hilbert structure through the representation (10). \square

Define $\hat{L}(q, \dot{q}, t) = L(q, \dot{q}, t) + f(t)V(\chi(t))$ and consider the Hamilton action I defined on \mathfrak{M} :

$$I(q) = \int_{-\infty}^{+\infty} \hat{L}(q, \dot{q}, t) dt. \tag{7}$$

Since $K(q, \dot{q})$ is a homogeneous quadratic form in \dot{q} and $U(q, t)$ has unique maximum at x_{\pm} for all $t \in \mathbb{R}_{\pm}$ there exist constants $\alpha, \beta > 0$ such that

$$\alpha(|\dot{q}|^2 + |f(t)||q - \chi(t)|^2) \leq |L_{\pm}(q, \dot{q}, t)| \leq \beta(|\dot{q}|^2 + |f(t)||q - \chi(t)|^2) \tag{8}$$

for all $(q, \dot{q}) \in T\mathcal{M}$ and consequently the integral (7) converges for any $q \in \mathfrak{M}$.

The following lemma plays an important role in further analysis.

Lemma 4. *For any constants $r, c > 0$ there exists $T(r, c)$ such that $q(t) \in B_r(x_{\pm})$ for all $q \in \mathfrak{M}_c$ and $|t| > T(r, c)$, where $\mathfrak{M}_c = \{q \in \mathfrak{M} : I(q) < c\}$, $B_r(x) = \{x \in \mathbb{R}^N : |x| < r\}$.*

PROOF: - First we observe that if $I(q) < c$ then $\int_{-\infty}^{+\infty} (|\dot{q}(s)|^2 + |f(s)||q(s) - \chi(s)|^2) ds < \alpha^{-1}c$. Applying to the function $q(t) - \chi(t)$ the same arguments as in lemma 3 we get

$$|q(t) - \chi(t)|^2 < \frac{\alpha^{-1}c}{|f(t)|^{1/2}}. \tag{9}$$

Since $|f|$ is increasing and unbounded (9) proves the lemma. \square

Now we represent the functional I in a way suggested in [1]. Namely, one may construct an embedding of \mathcal{M} into \mathbb{R}^N such that small neighborhoods of x_{\pm} lie in linear subspaces $\mathbb{R}^{n,\pm} \subset \mathbb{R}^N$. Taking $r > 0$ to be sufficiently small we may always assume that these neighborhoods coincide with the balls $B_r(x_{\pm}) = \{x \in \mathbb{R}^{n,\pm} : |x - x_{\pm}| < r\}$.

Then for any $c > 0$ set

$$\begin{aligned} \Lambda &= W^{1,2}([-T, T], \mathcal{M}), \\ \Lambda_- &= \{q \in AC((-\infty, -T], B_r(x_-)) : \|q - x_-\|_{f,-} < \infty\}, \\ \Lambda_+ &= \{q \in AC([T, +\infty), B_r(x_+)) : \|q - x_+\|_{f,+} < \infty\}, \end{aligned}$$

where $T = T(r, c)$ from lemma 4 and $\|v\|_{f,-}^2 = \int_{-\infty}^{-T} (|\dot{v}(s)|^2 + |f(s)||v(s)|^2) ds$,

$$\|v\|_{f,+}^2 = \int_T^{+\infty} (|\dot{v}(s)|^2 + |f(s)||v(s)|^2) ds.$$

Define mappings $g_{\pm} : \mathfrak{M} \rightarrow \Lambda_{\pm}$ and $g : \mathfrak{M} \rightarrow \Lambda$ as

$$g_-(q) = q|_{(-\infty, -T]}, \quad g(q) = q|_{[-T, T]}, \quad g_+(q) = q|_{[T, +\infty)}.$$

Lemma 5. *The mappings g, g_{\pm} are of class C^{∞} .*

PROOF: - Note that the map $g_- \times g \times g_+ : \mathfrak{M} \rightarrow \Lambda_- \times \Lambda \times \Lambda_+$ identifies \mathfrak{M}_c with an open set in the Hilbert submanifold $\{(z_-, z_0, z_+) \in \Lambda_- \times \Lambda \times \Lambda_+ : z_{\pm}(\pm T) = z_0(\pm T)\}$ of codimension $2n$ in $\Lambda_- \times \Lambda \times \Lambda_+$. Hence the lemma immediately follows from the equality $\|q\|_f^2 = \|g_-(q)\|_{f,-}^2 + \|g(q)\|_{f,0}^2 + \|g_+(q)\|_{f,+}^2$ for all $q \in \mathfrak{M}_c$, where

$$\|v\|_{f,0}^2 = \int_{-T}^{-T} (|\dot{v}(s)|^2 + |f(s)||v(s)|^2) ds. \quad \square$$

Now we may represent the restriction $I|_{\mathfrak{M}_c}$ in the following way [1]:

$$I|_{\mathfrak{M}_c} = J_- \circ g_- + J \circ g + J_+ \circ g_+, \tag{10}$$

where the functionals $J : \Lambda \rightarrow \mathbb{R}$, $J_{\pm} : \Lambda_{\pm} \rightarrow \mathbb{R}$ are

$$J_-(q) = \int_{-\infty}^{-T} \hat{L}(q, \dot{q}, t) dt, \quad J(q) = \int_{-T}^T \hat{L}(q, \dot{q}, t) dt, \quad J_+(q) = \int_T^{\infty} \hat{L}(q, \dot{q}, t) dt.$$

Proposition 2. *The functional $I \in C^1(\mathfrak{M})$ with locally Lipschitz derivative.*

PROOF: - The proof of this proposition is rather straightforward. First we observe that the functional J is of class C^2 on \mathfrak{M} (see e.g. [2]). Hence it remains to consider the functionals J_{\pm} . They can be studied in analogous ways, so we consider only J_+ . To prove smoothness of J_+ , take sufficiently small $r, q \in \Lambda_+(r, c)$ and $v \in T_x \Lambda_+$ such that $\|v\|_f < r/C_f$. Then due to lemma 3 we see that $\|v\|_{\infty} < r$ and $q(t) + v(t) \in B_{2r}(x_+)$ for all $t > T(r, c)$. Due to smallness of r we may assume to be on \mathbb{R}^n and use Taylor's formula:

$$\begin{aligned} L(q(t) + v(t), \dot{q}(t) + \dot{v}(t), t) - L(q(t), \dot{q}(t), t) &= \\ &= \langle K_q(q(t), \dot{q}(t)), v(t) \rangle + \langle K_{\dot{q}}(q(t), \dot{q}(t)), \dot{v}(t) \rangle - \langle U_q(q(t), t), v(t) \rangle + \\ &+ \frac{1}{2} \langle K_{qq}v(t), v(t) \rangle + \langle K_{q\dot{q}}\dot{v}(t), v(t) \rangle + \frac{1}{2} \langle K_{\dot{q}\dot{q}}\dot{v}(t), \dot{v}(t) \rangle - \frac{1}{2} \langle U_{qq}v(t), v(t) \rangle, \end{aligned}$$

where the second derivatives of K and U are evaluated at a point $(q(t) + \theta(t)v(t), \dot{q}(t) + \theta(t)\dot{v}(t), t)$ with measurable function $\theta(t) \in [0, 1]$. By assumptions on K and U , for any $(q, \dot{q}, t) \in B_{2r}(x_+) \times \mathbb{R}^n \times \mathbb{R}$ one has

$$\|K_{qq}\| \leq c_1|\dot{q}|^2, \|K_{q\dot{q}}\| \leq c_2|\dot{q}|, \|K_{\dot{q}\dot{q}}\| \leq c_3, \|U_{qq}\| \leq c_4|f(t)| \cdot |q|^2,$$

for some positive constants c_i and $\|\cdot\|$ standing for the operator norm. Using these estimates, lemma 3 and the Schwartz inequality we get

$$\begin{aligned} \left| \int_T^{+\infty} \langle K_{qq}v(t), v(t) \rangle dt \right| &\leq c_1 \int_T^{+\infty} |\dot{q}(t) + \theta(t)\dot{v}(t)|^2 |v(t)|^2 dt \leq \\ &\leq c_1 \|v\|_{f,+}^2 (\|q - x_+\|_{f,+}^2 + \|v\|_{f,+}^2) \leq c_5 \|v\|_{f,+}^2 \\ \left| \int_T^{+\infty} \langle K_{q\dot{q}}v(t), v(t) \rangle dt \right| &\leq c_2 \int_T^{+\infty} |\dot{q}(t) + \theta(t)\dot{v}(t)| |\dot{v}(t)| |v(t)| dt \leq \\ &\leq c_2 \|v\|_{f,+} (\|q - x_+\|_{f,+} + \|v\|_{f,+} + \|v\|_{f,+}^2) \leq c_6 \|v\|_{f,+}^2 \\ \left| \int_T^{+\infty} \langle K_{\dot{q}\dot{q}}v(t), v(t) \rangle dt \right| &\leq c_3 \int_T^{+\infty} |\dot{v}(t)|^2 dt \leq c_7 \|v\|_{f,+}^2 \\ \left| \int_T^{+\infty} \langle U_{qq}v(t), v(t) \rangle dt \right| &\leq c_4 \int_T^{+\infty} |f(t)| |q(t) + \theta(t)v(t)|^2 |v(t)|^2 dt \leq \\ &\leq c_4 \|q - x_+\|_{f,+}^2 \|v\|_{f,+}^2 \leq c_8 \|v\|_{f,+}^2 \end{aligned} \quad (11)$$

Estimates (11) prove differentiability of J_+ on \mathfrak{M} and provide an expression for J'_+ :

$$J'_+(q)v = \int_T^{+\infty} \left(\langle K_q(q(t), \dot{q}(t)), v(t) \rangle + \langle K_{\dot{q}}(q(t), \dot{q}(t)), \dot{v}(t) \rangle - |f(t)| \langle V_q(q(t)), v(t) \rangle \right) dt.$$

Now take $q_1, q_2 \in \Lambda_+(2r)$, $v \in T\Lambda_+$ and consider the difference

$$\begin{aligned} J'_+(q_2)v - J'_+(q_1)v &= \int_T^{+\infty} \left(\langle K_{qq}\Delta q(t), v(t) \rangle + \langle K_{q\dot{q}}v(t), \Delta\dot{q}(t) \rangle + \right. \\ &\left. \langle K_{\dot{q}\dot{q}}\Delta q(t), \dot{v}(t) \rangle + \langle K_{\dot{q}\dot{q}}\Delta\dot{q}(t), \dot{v}(t) \rangle - |f(t)| \langle V_{qq}\Delta q(t), v(t) \rangle \right) dt, \end{aligned}$$

where $\Delta q(t) = q_2(t) - q_1(t)$ and the second derivatives of K and V are evaluated at a point $(q(t) + \theta(t)v(t), \dot{q}(t) + \theta(t)\dot{v}(t), t)$. Using (11) one may get

$$\left| J'_+(q_2)v - J'_+(q_1)v \right| \leq c_9 \|q_2 - q_1\|_{f,+} \|v\|_{f,+}$$

with some positive constant c_9 , what proves that J'_+ is locally Lipschitz. \square

Proposition 3. *Critical points of I correspond to doubly asymptotic trajectories of (3) such that $q(t) \rightarrow x_{\pm}$ and $\dot{q}(t) \rightarrow 0$ as $t \rightarrow \pm\infty$.*

PROOF:- Assume $q \in \mathfrak{M}$ is a critical point of I . Then $I'(q)v = 0$ for any $v \in T_q\mathfrak{M}$. Using classical arguments (see e.g. [7]) one may show that q is of class $C^2(\mathbb{R})$ and satisfies the Lagrange equations (3). By lemma 3 $q(t) \rightarrow x_{\pm}$ as $t \rightarrow \pm\infty$. Hence it remains to prove that $\dot{q}(t) \rightarrow 0$ as $t \rightarrow \pm\infty$. The following lemma admits this statement:

Lemma 6. *If $q(t)$ satisfies the Lagrange equations (3) and $\lim_{t \rightarrow \pm\infty} |q(t) - x_{\pm}| = 0$ then $\lim_{t \rightarrow \pm\infty} |\dot{q}(t)| = 0$.*

PROOF: - Introduce a symmetric positive definite operator $A(x) : T\mathcal{M} \rightarrow T^*\mathcal{M}$ by the formula $K(x, \dot{x}) = \frac{1}{2}\langle A(x)\dot{x}, \dot{x} \rangle$ and rewrite the Lagrange equations as

$$A(q)\ddot{q} + \frac{1}{2}\langle B(q)\dot{q}, \dot{q} \rangle + f(t)\nabla V(q) = 0, \quad (12)$$

where $B(x) = A'(x)$.

We consider the case $t \rightarrow +\infty$ (the case $t \rightarrow -\infty$ can be treated similarly). Let $\mathcal{A} = A(x_+)$ and $h(t) = \langle \mathcal{A}(q(t) - x_+), q(t) - x_+ \rangle$. Then $\dot{h}(t) = \langle \mathcal{A}\dot{q}(t), q(t) - x_+ \rangle$ and

$$\ddot{h}(t) = \langle \mathcal{A}\ddot{q}(t), q(t) - x_+ \rangle + \langle \mathcal{A}\dot{q}(t), \dot{q}(t) \rangle. \quad (13)$$

Taking sufficiently small $r > 0$ we define T such that $q(t) \in B_r(x_+)$ for all $t > T$. We note that there exist positive constants $C_A^{(1)}, C_A^{(2)}, C_B$ such that for all $x \in B_r(x_+)$

$$C_A^{(1)} \leq \|A(x)\| \leq C_A^{(2)}, \quad \|B(x)\| \leq C_B. \quad (14)$$

. Using (12), (13) we conclude

$$\ddot{h}(t) \geq \delta(|\dot{q}(t)|^2 + f(t)|q(t) - x_+|^2) \quad (15)$$

with some positive constant δ . Integrating (15) we get for any $t_2 > t_1 > T$

$$\left| \dot{h}(t_2) - \dot{h}(t_1) \right| \geq \delta \int_{t_1}^{t_2} (|\dot{q}(s)|^2 + f(s)|q(s) - x_+|^2) ds. \quad (16)$$

Since $h(t) \rightarrow 0$ as $t \rightarrow +\infty$ we have $\liminf_{t \rightarrow \infty} |\dot{h}(t)| = 0$ and by (16) $\|q - x_+\|_{f,+} < \infty$.

We now prove that $f(t)|q(t) - x_+|^2 \rightarrow 0$ as $t \rightarrow +\infty$. Note that (15) also implies

$$\ddot{h}(t) \geq \frac{\delta f(t)}{C_A^{(2)}} h(t).$$

Then fix $\varepsilon > 0$ and assume that there exists a sequence $t_k \rightarrow +\infty$ such that $f(t_k)h(t_k) > \varepsilon$. Without loss of generality we may suppose that $\dot{h}(t_k) < 0$ (or $\dot{h}(t_k) > 0$) for all k . Since $\ddot{h}(t) > 0$ and

$$\dot{h}(s) = \dot{h}(t_k) - \int_s^{t_k} \ddot{h}(p) dp$$

we obtain that $\dot{h}(t) < 0$ for all $t \in [T, t_k]$. Hence $h(t)$ is monotonically decreasing for $t > T$ and $h(s) > h(t_k) > \varepsilon/f(t_k)$. By (A_4) one may also assume that

$$\int_{t_{k-1}}^{t_k} f(s)ds > \mu f(t_k).$$

Then

$$\int_{t_{k-1}}^{t_k} f(s)|q(s) - x_+|^2 ds \geq \frac{2}{C_A^{(2)}} \int_{t_{k-1}}^{t_k} f(s)h(s)ds \geq \frac{2\varepsilon}{f(t_k)} \int_{t_{k-1}}^{t_k} f(s) \geq \frac{2\varepsilon\mu}{C_A^{(2)}}.$$

Summarizing over k we get a contradiction with $\|q - x_+\|_{f,+} < \infty$.

To prove that $|\dot{q}(t)| \rightarrow 0$ as $t \rightarrow +\infty$ introduce the Hamiltonian $H(q, \dot{q}, t) = K(q, \dot{q}) + f(t)(V(q) - V(x_+))$. If q satisfies the Lagrange equations then $\dot{H} = -f'(t)(V(q) - V(x_+))$ and by (A_4) we have for any $t_2 > t_1 > T$ that

$$\left| H(q(t_2), \dot{q}(t_2), t_2) - H(q(t_1), \dot{q}(t_1), t_1) \right| \leq \beta\mu \int_{t_1}^{t_2} f(s)|q(s) - x_+|^2 ds$$

or equivalently

$$\begin{aligned} \left| \langle A(q(t_2))\dot{q}(t_2), \dot{q}(t_2) \rangle - \langle A(q(t_1))\dot{q}(t_1), \dot{q}(t_1) \rangle \right| &\leq \\ &\leq \beta \int_{t_1}^{t_2} f(s)|q(s) - x_+|^2 ds + \beta \left(f(t_2)|q(t_2) - x_+|^2 - f(t_1)|q(t_1) - x_+|^2 \right). \end{aligned} \tag{17}$$

Since $q \in \Lambda_+$ then $\liminf_{t \rightarrow \pm\infty} |\dot{q}(t)|^2 = 0$, $\int_T^\infty |f(s)||q(s) - x_+|^2 ds < +\infty$ and $\lim_{t \rightarrow +\infty} f(t)|q(t) - x_+|^2 = 0$. Then by (17) for any $\varepsilon > 0$ there exists $\tau(\varepsilon)$ such that for any $t_2 > t_1 > \tau(\varepsilon)$

$$\left| \langle A(q(t_2))\dot{q}(t_2), \dot{q}(t_2) \rangle - \langle A(q(t_1))\dot{q}(t_1), \dot{q}(t_1) \rangle \right| \leq \varepsilon.$$

$A(x)$ is bounded from below and we conclude that $\dot{q}(t) \rightarrow 0$ as $t \rightarrow \pm\infty$. \square

3 The Palais-Smale conditions

Proposition 4. *The functional I satisfies the Palais-Smale conditions.*

PROOF: - Let $q_n \in \mathfrak{M}$ be a PS sequence, i.e. a sequence for which $I(q_n)$ is bounded and $I'(q_n) \rightarrow 0$ as $n \rightarrow \infty$. Then there exists $c > 0$ such that $q_n \in \mathfrak{M}_c$ and due to lemma 4 $\{q_n\}$ is uniformly bounded. Hence, up to a subsequence, q_n converges uniformly to a function $q_\infty \in L_\infty(\mathbb{R}, \mathcal{M})$. For the constant c and some small $\varepsilon > 0$

we define $T = T(\varepsilon, c)$ as in lemma 4 and introduce the sets Λ, Λ_{\pm} to represent the functional I in the form (10).

Denote

$$z_n = g(q_n), \quad z_n^{\pm} = g^{\pm}(q_n).$$

Since $I'(q_n) \rightarrow 0$ as $n \rightarrow \infty$ we have $|I'(q_n)v| \leq \varepsilon_n \|v\|_f$ for all $v \in T_{x_n} \mathfrak{M}$, where $\varepsilon_n \rightarrow 0$ as $n \rightarrow \infty$. If we consider $v \in T_{q_n} \mathfrak{M}$ such that $v|_{\mathbb{R} \setminus [-T, T]} \equiv 0$ then

$$I'(q_n)v = J'(z_n)v|_{[-T, T]}.$$

and we conclude that

$$|J'(z_n)v| \leq \varepsilon_n \|v\|_{f, T} \quad \text{for all } v \in T_{z_n} \Lambda \text{ such that } v(\pm T) = 0, \quad (18)$$

where $\|v\|_{f, T}$ stands for the norm in $T_{z_n} \Lambda$. Taking $v \in T_{q_n} \mathfrak{M}$ such that $v(t) \equiv 0$ for all $t \leq T$ (respectively $t \geq -T$) we get

$$I'(q_n)v = J'_+(z_n^+)v|_{[T, \infty)}, \quad I'(q_n)v = J'_-(z_n^-)v|_{(-\infty, T]}$$

and

$$|J'_{\pm}(z_n^{\pm})v| \leq \varepsilon_n \|v\|_{f, \pm} \quad \text{for all } v \in T_{z_n^{\pm}} \Lambda_{\pm} \text{ such that } v(\pm T) = 0. \quad (19)$$

Denote by z_{∞}, z_{∞}^- and z_{∞}^+ the restriction of x_{∞} to $[-T, T], (-\infty, -T]$ and $[T, \infty)$, respectively. Since $q_n \rightarrow x_{\infty}$ in L_{∞} , $z_n \rightarrow z_{\infty}$ and $z_n^{\pm} \rightarrow z_{\infty}^{\pm}$ uniformly.

Lemma 7. *If $J(z_n)$ is uniformly bounded, $z_n \rightarrow z_{\infty}$ uniformly and satisfies (18) then $\{z_n\}$ has a subsequence converging in Λ to z_{∞} .*

PROOF: - The proof repeats the proof of Lemma 5.1 from [1].

Lemma 8. *If $J_{\pm}(z_n^{\pm})$ is uniformly bounded, $z_n^{\pm} \rightarrow z_{\infty}^{\pm}$ uniformly and satisfies (19) then $\{z_n^{\pm}\}$ has a subsequence converging in Λ_{\pm} to z_{∞}^{\pm} .*

PROOF: - We outline the proof for the sequence $\{z_n^+\}$ whereas the case $\{z_n^-\}$ can be studied in a similar way. Using notations from [1] we set

$$\xi_{nm}(t) = z_m^+(t) - z_n^+(t), \quad \zeta_{nm}(t) = \frac{T f^{1/2}(T)}{t f^{1/2}(t)} \xi_{nm}(T). \quad (20)$$

Since $\|\zeta_{nm}\|_{f, +} \rightarrow 0$ as $n, m \rightarrow \infty$ and $\zeta_{nm}(T) = \xi_{nm}(T)$ one may apply (19) and get $J'_+(z_n^+)(\xi_{nm} - \zeta_{nm}) \rightarrow 0$ as $n, m \rightarrow \infty$. Now using boundness of J'_+ we see that $J'_+(z_n^+)\xi_{nm} \rightarrow 0$ as $n, m \rightarrow \infty$. Extract a subsequence, denoting also by z_n^+ , such that the sequence $J_+(z_n^+)$ is converging. Then we obtain

$$\Psi_{nm} = J_+(z_m^+) - J_+(z_n^+) + J'_+(z_n^+)\xi_{nm} \rightarrow 0 \text{ as } n, m \rightarrow \infty. \quad (21)$$

We estimate separately the terms in the integral Ψ_{nm} involving the kinetic and potential energy. Assume the radius r is so small that the estimates (14) are fulfilled. One may observe that

$$\begin{aligned} K(z_m^+, \dot{z}_m^+) - K(z_n^+, \dot{z}_n^+) &= \langle K_x(z_n^+, \dot{z}_n^+), \xi_{nm} \rangle - \langle K_{\dot{x}}(z_n^+, \dot{z}_n^+), \dot{\xi}_{nm} \rangle = \\ &= K(z_n^+, \dot{\xi}_{nm}) + \langle K_x(\tau_{nm}, \dot{z}_m^+), \xi_{nm} \rangle - \langle K_x(z_n^+, \dot{z}_n^+), \xi_{nm} \rangle \geq \\ &\geq C_A^{(1)} |\xi_{nm}|^2 - C_B (|\dot{z}_m^+|^2 + |\dot{z}_n^+|^2) |\xi_{nm}|, \end{aligned} \quad (22)$$

where τ_{nm} is some intermediate point between z_n^+ and z_m^+ . For the potential energy terms we get

$$V(z_m^+) - V(z_n^+) - \langle \nabla V(z_n^+), \xi_{nm} \rangle = \frac{1}{2} \langle \nabla^2 V(\tau_{nm}) \xi_{nm}, \xi_{nm} \rangle \geq \alpha |\xi_{nm}|^2. \quad (23)$$

Substituting (22) and (23) into (21) one obtains

$$\begin{aligned} \Psi_{nm} &\geq \int_T^\infty (C_A^{(1)} |\xi_{nm}(s)|^2 + \alpha |\xi_{nm}(s)|^2 - C_B (|\dot{z}_m^+(s)|^2 + |\dot{z}_n^+(s)|^2) |\xi_{nm}(s)|) ds \geq \\ &\geq c_{10} \|\xi_{nm}\|^2 - \Theta_{nm}, \end{aligned}$$

where $c_{10} = \min\{C_A^{(1)}, \alpha\}$ and

$$\Theta_{nm} = C_B (\|z_m\|_{f,+}^2 + \|z_n\|_{f,+}^2) \|\xi_{nm}\|_\infty.$$

Since $\{z_n^+\}$ is bounded and $\|\xi_{nm}\|_\infty \rightarrow 0$ as $n, m \rightarrow \infty$ we have $\Theta_{nm} \rightarrow 0$. Hence

$$\|\xi_{nm}\|_{f,+}^2 \leq c_{10}^{-1} (\Psi_{nm} - \Theta_{nm}) \rightarrow 0, \text{ as } n, m \rightarrow \infty.$$

Thus we showed that $\{z_n^+\}$ is a Cauchy sequence what finishes the proof. \square

Combining lemmata 6 and 7 we prove proposition 4. \square

To prove Theorem 1 we notice that \mathfrak{M} is homotopically equivalent to the space of paths

$$\Omega(\mathcal{M}, x_-, x_+) = \{q \in C^0([0, 1]) : q(0) = x_-, q(1) = x_+\}.$$

Since \mathcal{M} is compact, the Lusternik-Schnirelmann category $cat(\mathcal{M}) = \infty$ [8]. This implies the existence of infinitely many critical points for the functional I and due to propositions 4,5 the existence of infinitely many doubly asymptotic trajectories of (3) such that $q(t) \rightarrow x_\pm, \dot{q}(t) \rightarrow 0$ as $t \rightarrow \pm\infty$. \square

To prove Theorem 1 for the case when subsets X_\pm consist of more than one point we note that one may proceed in the same way except the estimate (8), which is not valid. Following [4], [3] define for $\varepsilon > 0$ a subset $\Gamma_\varepsilon(x_-, x_+) \subset \mathfrak{M}$:

$$\Gamma_\varepsilon(x_-, x_+) = \left\{ q \in \mathfrak{M} : \text{for all } t \in \mathbb{R}_\pm \quad q(t) \notin B_\varepsilon(X_\pm \setminus \{x_\pm\}) \right\}.$$

We also consider the restriction of the action functional $I_\varepsilon = I|_{\Gamma_\varepsilon(x_-, x_+)}$. For $\Gamma_\varepsilon(x_-, x_+)$ the estimate (8) is valid and using the same arguments one may prove that for any $\varepsilon > 0$ the functional I_ε achieves its minimum on some function $q_\varepsilon \in \Gamma_\varepsilon(x_-, x_+)$. Moreover, $q_\varepsilon(t)$ is a classical solution of (3) whenever $q_\varepsilon(t) \notin \partial B_\varepsilon(X_\pm \setminus \{x_\pm\})$, where $\partial B_\varepsilon(A)$ stands for the ε -neighbourhood of a set A . Let us take a sequence $\varepsilon_j \rightarrow 0$ as $j \rightarrow \infty$.

Lemma 9. *For sufficiently large $j \in \mathbb{N}$ $q_{\varepsilon_j}(t) \notin B_{\varepsilon_j}(X_\pm \setminus \{x_\pm\})$ for all $t \in \mathbb{R}$.*

PROOF: - The proof of this lemma is similar to lemma 2.10 from [3].

This lemma guarantees that q_{ε_j} is a heteroclinic solution of (3) joining x_- to x_+ and satisfying $\dot{q}_{\varepsilon_j}(t) \rightarrow 0$ as $t \rightarrow \pm\infty$.

To illustrate the result consider a pendulum-like system with Lagrangian

$$L(\varphi, \dot{\varphi}, t) = \frac{1}{2}|\dot{\varphi}|^2 - t \left(1 - \cos(\varphi) - \frac{1}{2} \cos(2\varphi) \right). \quad (24)$$

The configuration space of this example is a circle and the system possesses four equilibria $\varphi = 0, \pi, \pm\pi/3$. Since the factor $f(t) = t$, the subset X_+ consists of one point $X_+ = \{\pi\}$ whereas the subset X_- consists of two points $X_- = \{-\pi/3, \pi/3\}$. Application of Theorem 1 to this system yields the following

Proposition 5. *For any $m \in \mathbb{Z}$ there exists a doubly asymptotic trajectory $\varphi_m^\pm(t)$ of the system (24) such that $\lim_{t \rightarrow -\infty} \varphi_m^\pm(t) = \pm\pi/3$ and $\lim_{t \rightarrow +\infty} \varphi_m^\pm(t) = (2m + 1)\pi$, i.e. the trajectories $\varphi_m^\pm(t)$ join the points $\pm\pi/3$ with π via m full rotations.*

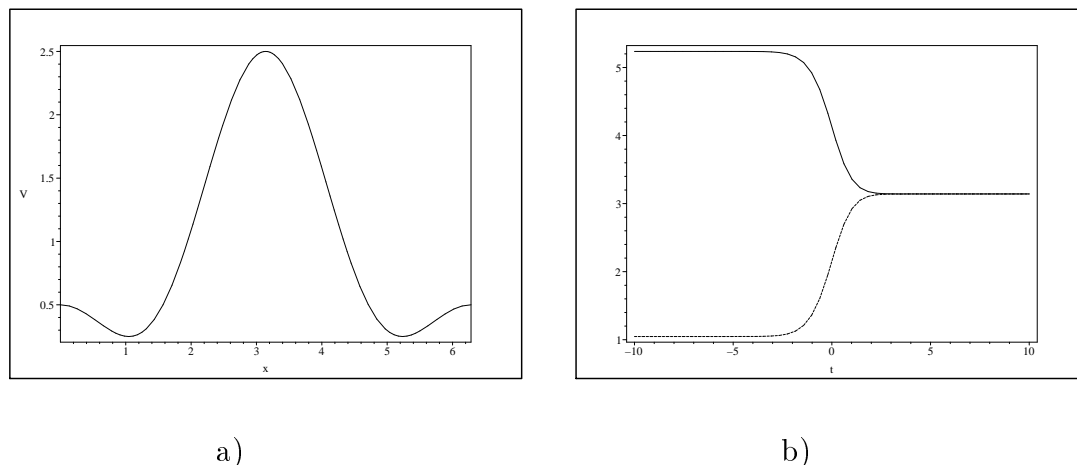


Figure 1: a. The profile of potential $V(x) = 1 - \cos(\varphi) - \frac{1}{2} \cos(2\varphi)$; b. heteroclinic trajectories $\varphi_0^\pm(t)$, connecting $\pm\pi/3$ with π without rotations (the solid curve corresponds to $\varphi_0^-(t)$ and the dashed curve - to $\varphi_0^+(t)$)

References

- [1] M.L. Bertotti, S.V. Bolotin, Doubly asymptotic trajectories of Lagrangian systems in homogeneous force fields, Ann. Mat. Pura Appl. (4), 1998, vol. 174, pp. 253 - 275.
- [2] V. Coti Zelati, P.H. Rabinowitz, Heteroclinic solutions between stationary points at a different energy levels, Topol. Methods Nonlinear Anal. 17 (1) (2001) pp. 1 - 21.
- [3] M. Izydorek, J. Janczewska, Heteroclinic solutions for a class of the second order Hamiltonian systems, J. Differential Equations 238 (2007) pp. 381 - 393.

REFERENCES

- [4] P.H. Rabinowitz, Periodic and heteroclinic orbits for a periodic hamiltonian system, Ann. Inst. H. Poincaré 6 (5) (1989) pp. 331 - 346.
- [5] V.V. Kozlov, On the fall of an heavy rigid body in a ideal fluid, Meck. Tverd. Tela, 5 (1989), pp. 10 - 17 (Russian).
- [6] V.V. Kozlov, On the stability of equilibrium positions in nonstationary force fields, J. Appl. Math. Mech., 55 (1991), pp. 8-13.
- [7] R.S. Palais, S. Smale, A generalized Morse theory, Bull. Amer. Math. Soc., 70 (1964), pp. 165-171.
- [8] J.P. Serre, Homologie singuliere des espaces fibres. Applications, Ann. Math., 54 (1951), pp. 425-505.
- [9] A.V. Borisov, V.V. Kozlov, I.S. Mamaev, Asymptotic stability and associated problems of dynamics of falling rigid body, Regul. Chaotic Dyn., 2007, vol. 12, No. 5, pp. 531-565.

Alexey V. Ivanov, Saint-Petersburg State University, 199034, Russian Federation, Saint-Petersburg, Universitetskaya nab. 7/9

Investigation of the noise reduction effect of ventilating systems

Vitaly M. Kolykhalin
cap-007@mail.ru

Abstract

The well known magnetostrictive effect of electric motors results the non-linear dependence of magnetic noise components in the wide sound range from infrasonic frequencies. In the open ventilating pipe the electric motor with the fan impeller and the fan impeller without the electric motor on a quarter length wave distance of electric network frequency are installed. On the same distance the same series identical a pair of elements is set up but two electric motors on half length wave distance of electric network frequency are fixed and through the phase-shift device are switched on. The compensatory effect of the basic component of magnetic electric motor noise is considered. The theoretical and experimental data of the ventilating systems noise reduction are commented on.

1 Formulation of the problem of the reducing magnetic fan noise component

Increasing application of power electronics on transport, manufactures, home equipments and as a matter of fact growing up low-frequency and infrasonic fluctuations were taken care of by investigation methods and techniques for human audition protection. It is common observation that monaural personal threshold of audibility for sound fluctuations with 1 Hz frequency is coincident with listening pain barrier for acoustic pressure 140 dB. Such low person acoustic sensitivity in infrasonic range is masked by greater person sensitivity in the average frequencies. The infrasonic makes an attacking on the human health by emotional and biological influences. A person surface by infrasonic fluctuations through air, body and bone conductivity is affected [1].

Not expensive asynchronous electric motors with such basic noise components as magnetic, mechanical and aerodynamic in the conditioning and typical ventilation systems are used.

The aerodynamic noise components such as air interaction cores of a rotating rotor with a stationery stator, motor construction and a number of its ventilation blades are consist on. The intensity of such noise is growing up with increasing motor size and speed of rotation. Strong ventilation noise in low-frequency and infrasonic

range has the tendency of decrease 5 dB on an octave with frequency increase and a centrifugal force is made by.

Without taking into account executive mechanisms a mechanical component of motor noise also is depended on out-of-balance rotor, deformation of winding and rotor elements which really inertia, friction and heating are caused by. As well transitive effects of a rotor with a rotation stator asynchronous electromagnetic field and transformation its fluctuation into stator windings as infrasonic modulations is taken notice of.

As a whole the mechanical component of fan noise is less effective then other because of the smaller radiation areas, difference wave resistances in air and vibrating elements are turned out.

Noted noise components are brought about electrodynamic, electromagnetic and magnetostrictive forces a power electromagnetic field formed. Radial ring plates of stator electrotechnical steel are deform by a magnetostrictive Fms force taking place under working alternative magnetic field. Force lines of alternative magnetic field on circles with the centers on an axis of rings are settled down.

Peak value of these forces as time depended functions B_{mi} is proportional to a square of stator voltage U_{mi} and is founded from the ratio [2]

$$F_{mc} = \pi a_i S_{st} B_{mi}^2 = \pi a_i S_{st} \left(\frac{U_{mi}}{n\omega_i} \right)^2 \quad (1)$$

where $S_{st} = (R_{ex} - R_{in})h$ is the sectional area of magnetic core R_{ex} and R_{in} is accordingly external and internal radiuses, h is the length of magnetic core); i - the magnetostrictive constant of steel; ω_i is the angular frequency of fluctuations.

The aerodynamic noise is known to prevail in the average and high frequency ranges when an impeller with typical asynchronous electric motor is a basic source. The aerodynamic and mechanical motor noise components are carried on by magnetic noise component on frequency 50 Hz.

For the magnetic component carried on to reduce there must be method including the effect called as standing wave barrier. The standing wave barrier is formed into pipe on frequency 50 Hz of the basic tone and its harmonics.

The fan sound energy is reduced by dissipative losses, outflow of energy through walls and by reflection from obstacles into ventilation pipe.

The first part of source sound energy is radiated from the waveguide aperture in the form of running sound waves. Having been reflected from passive impeller by reason of jumping of acoustic resistance the other part of source sound energy was spent on formation reverberation sound field into pipe.

Then the sound energy outside radiated from the waveguide aperture is summarized two components: the running sound waves and the component of reverberation sound field. In order to reduce the last one a pair of identical impellers (with motor and without one) should be installed on the distance of half-wavelength due to frequency electric network 50 Hz between them. This procedure is necessary to formation standing sound waves in a pipe.

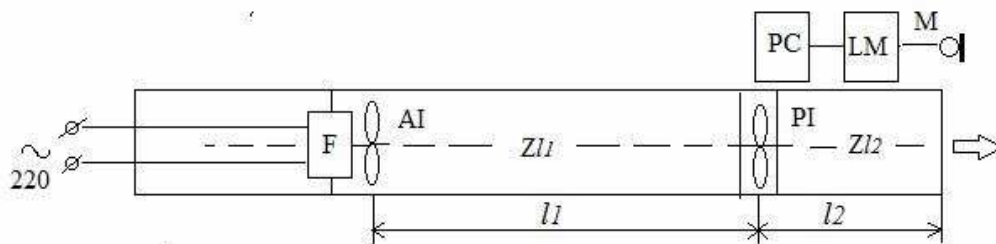


Figure 1: Installation diagram of elementary standing wave barrier

2 Elementary standing wave barrier

The special acoustic room in St. Petersburg State Cinema and Television University enables measurements to be carried out without external noise sources. The measuring installation consisting of the round metal pipe with length 4 m, diameter 0,1 m, thickness 0,004 m, the single-phase electric motor F (100 Wt) with the impeller AI and the passive impeller PI on the support isolated from the pipe wall by rubber are given in Fig.1. This apparatus for estimation of the standing wave barrier effect by microphone M102 and sound level meter RFT0024 are applied.

The distance l_1 between impellers AI and PI on half-wavelength due to frequency electric network 50 Hz is installed. It is impotent that PI from the waveguide aperture on distance l_2 quarters-wavelength due to frequency 50 Hz is settled down. Impellers AI and PI for blowing out of a gas stream are used and at the same time like big resistances for sound waves are happened.

The expression for entrance mechanical resistance is

$$Z_m = Z_s + Z_{l_1} + Z_{l_2} \quad (2)$$

where Z_s is the entrance mechanical resistance of the fan source; Z_{l_1} is the air resistance in the pipe interval l_1 ; Z_{l_2} is the air resistance in the pipe interval l_2 .

Provided $f_s = (2n + 1)c_0/2l_1$, $n = 0$ the entrance mechanical resistance for two pipe sides closed on the interval l_1 will be in the form:

$$Z_{l_1} = -j\rho_0c_0S \cot kl_1 = -j\rho_0c_0S \cot \pi \quad (3)$$

where ρ_0 is a specific density of air; c_0 is a sound speed; S is an area of cross-section of a pipe; $k = 2\pi f/c_0$ is a wave number.

Provided $f_s = (2n + 1)c_0/2l_1$, $n = 0$ the entrance mechanical resistance for the waveguide aperture on the interval l_2 will be in the form:

$$Z_{l_2} = j\rho_0c_0S \tan kl_2 = j\rho_0c_0S \tan \frac{\pi}{2} \quad (4)$$

If the l_1 and l_2 have absolutely rigid boundary conditions the values Z_{l_1} and Z_{l_2} will tend to infinity. However fan impellers are represented the impedance boundary conditions that make it difficult enough to analyze analytically the effect of standing

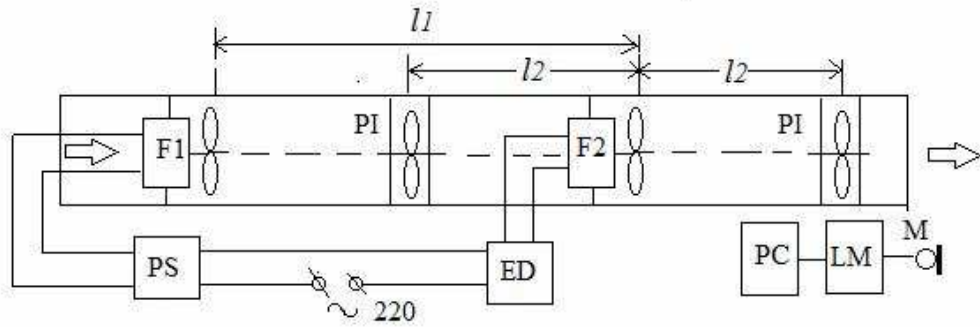


Figure 2: Installation diagram with standing wave barriers and the negative correlation effect

waves barrier but might be it possible in next paper. If the AI is moved from the PI along pipe on the distance up to 3,44 m between impellers then the sound pressure at waveguide aperture will be changed. So the standing wave barrier using half-wavelength due to frequency electric network 50 Hz effect is illustrated in Fig.1 to reduce the noise pressure at the pipe outlet on 6 dB in the broadband range from 16Hz to 10000Hz.

3 Joint action the standing wave barriers with the negative correlation effect

In the pipe two acoustic effects for reducing electric motor noise on the basic frequency 50 Hz and coincidence harmonics was realized: the effect of standing waves barrier and the negative correlation effect between antiphase amplitudes of acoustic noise pressure a pair of fan electro motors. The first effect in this paper is illustrated. The second effect in the previous paper was investigated [3].

It is impotent to make a few remarks concerning last one. In solving the decreasing electric motor noise problem in a short pipe closed it was necessary to install a pair of identical single-phase electric motors F1 and F2 at opposites into a pipe. The system of standing and pseudo-standing waves on frequencies of the basic tone 50 Hz and other components was excited by the motors. F1 and F2 influence the flat sound wave excitations as pulsing cylinders and as an interference result of the negative correlation effect on the basic frequency 50 Hz and coincidence harmonics was registered.

The same installation of the electric motors F1 and F2 but for ventilation system with the long pipe both sides opened was used. A pair of identical single-phase electric motors installed on half-wavelength distance due to frequency 50 Hz with the passive impeller PI between them are shown in Fig.2. As F1 as F2 with the passive impeller PI on a quarters-wavelength distance due to frequency 50 Hz are turned out.

For a correlation effect on the basic frequency 50 Hz to exist there must be two objects involved in the motor electric supply: phase shifter PS and electric delay ED.

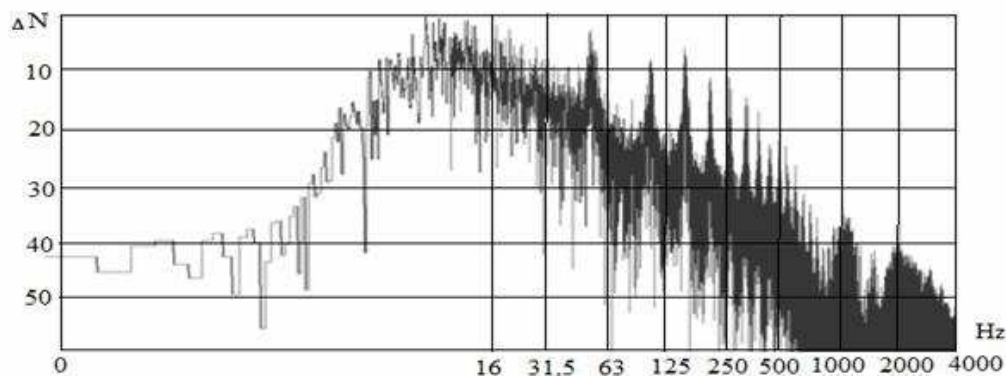


Figure 3: Noise spectrogram with two identical motors and identical impellers excluding the standing wave barriers and the negative correlation effect

In operation mode the network signal goes to the electric delay line ED (Fig.2) and the phase shifter PS. Electricity for the motor F1 through phase shifter with lagging 90 degrees against the motor F2 is supplied. After interval $\tau = l/c$ (l is the distance between motors) the acoustic process into the pipe arrives at the motor F2. But on the same time the electricity for supplying F2 through the electric delay is delayed. For estimation of the pressure by microphone M and sound level meter LM are applied.

In order to find out affectivity of the fan noise reducing methods the experiment data due to scheme in Fig.2 and the same scheme but apart from the electric delay line ED, the phase shifter PS, installation motors and impellers in position were standing wave barrier effects working should be compared.

The noise spectrogram using two identical motors and two identical impellers excluding any standing wave barriers and the negative correlation effect into the ventilation pipe is illustrated in Fig.3.

The frequency on abscissa (Hz) and the relative acoustic pressure on ordinate axis are constructed.

The noise spectrogram using two identical motors and two identical impellers including the some standing wave barriers and the negative correlation effect into the ventilation pipe is illustrated in Fig.4. The noise spectrogram commenced on affectivity of the reducing the basic frequency 50 Hz and coincidence harmonics are shown.

The frequency on abscissa (Hz) and the relative acoustic pressure on ordinate axis are constructed. The reducing fan noise pressure on 13 dB in broadband range by the negative correlation effect and the standing waves barriers effect are obtained.

4 Results

It follows that the standing waves barriers effect help us to reduce fan noise pressure at the pipe outlet on 6 dB in broadband range from 16 Hz to 10000 Hz when this data is fixed by the sound level meter. The negative correlation effect makes it possible to obtain reducing fan noise pressure on 7 dB not only reducing sound fluctuations with frequency electric network 50 Hz but also in low-frequency and infrasonic

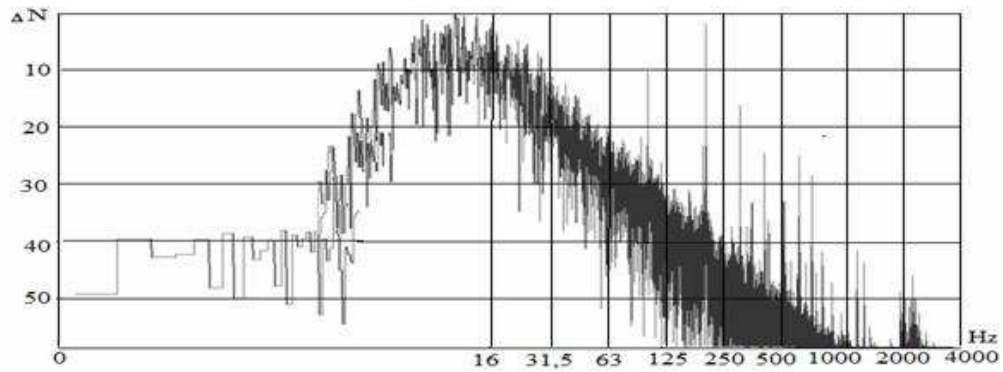


Figure 4: Noise spectrogram with two identical motors and identical impellers including the standing wave barriers and the negative correlation effect

range. Such low-frequency and infrasonic fluctuations are excited by transformation asynchronous electromagnetic fluctuations into stator windings as infrasonic modulations and modulation electromagnetic distortions. One must expect that reducing fan noise on transport, manufactures and home equipments will be taken care of by using the standing waves barriers with the negative correlation effect for human audition protection.

References

- [1] GOST P 51401-99. Acoustics. Definition of sound power levels of noise sources with sound pressure. - M.: Gosstandart of the Russian Federation, 1998.
- [2] Kolykhalin V.M., Davydov V.V. Device of the electric motor noise compensation. Patent of the Russian Federation ϵ 2528552, M. Federal serv., RU RU 2528552 C1, published 20.09.2014 Bul. 26.
- [3] Davydov V. V., Kolykhalin V. M. About compensation method of the electric motor noise.- B.: Vestnik BGTU named after V.G. Shukhov (2), 2014.

Lenynskiy pr., 95, korp.2, 403, 198330, St.Petersburg, Russia, cap-007@mail.ru

Morphological stability of thin film materials during annealing

Sergey S. Kostyrko, Gleb M. Shuvalov
s.kostyrko@spbu.ru

Abstract

Multilayer thin film materials are extensively used in engineering systems to accomplish a wide range of specific functions. The layered structure could be used for improving mechanical, optical, electrical, magnetic and thermal properties of microelectronic devices. However, multilayer thin film structures are inherently stressed owing to lattice mismatch between different layers. Similar to other stressed solids, such materials can self-organize a surface shape with mass redistribution to minimize a total energy. But the morphological stability is very important in fabrication of defect-free microelectronic devices. In this paper, we present a model of surface pattern formation in multilayer thin film structure with an arbitrary number of layers by considering combined effect of volume and surface diffusion. Based on Gibbs thermodynamics and linear theory of elasticity, we design a procedure for constructing a governing equation that gives the amplitude change of surface perturbation. A parametric study of this equation leads to the definition of a critical undulation wavelength which stabilizes the surface. As an application of presented solution, we analyze the surface stability of two-layered film under different conditions.

1 Introduction

Nowadays it's a well-established phenomena that during film deposition and subsequent thermal processing the film surface evolves into an undulating profile. Surface roughness affects on many important aspects in the engineering application of thin film materials such as wetting, heat transfer, mechanical, electromagnetic and optical properties. Numerous experimental results demonstrate that surface effects become important in mechanical behavior of nanosized structural elements. Analyzing a regular surface patterns in mono- and multilayer film coatings, it was found that even a slight undulation in surface morphology can lead to nucleation of microcracks and film delamination. It should be noted, that there are some positive aspects of surface roughening. For instance, control annealing of thin film causes to break up it to nanosized islands, which exhibit unusual electrical and optical properties. So, to accurately control the morphological surface modifications at the micro- and nanoscale and improve manufacturing techniques, we need to model this process to gain a better theoretical understanding.

2 Problem formulation

Consider an isotropic multilayer film coating of a total thickness $h_f = \sum_{r=1}^N h_r$, which consists of N dissimilar layers and is deposited on a substrate with Poisson's ratio ν_{N+1} and shear modulus μ_{N+1} under plane strain conditions (see Fig. 1). The layer of thickness h_j has Poisson's ratio ν_r and shear modulus μ_r .

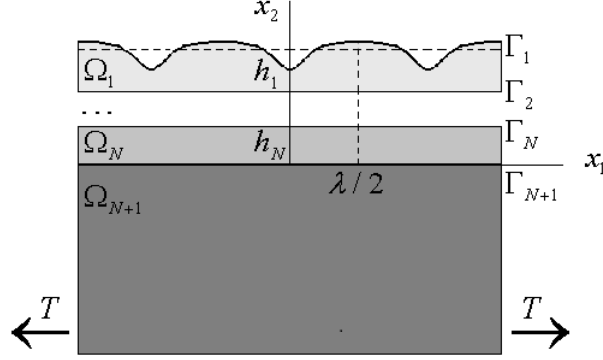


Figure 1: Multilayer film coating with curved surface.

The substrate is modeled as an elastic half-plane of complex variable $z = x_1 + ix_2$

$$\Omega_{N+1} = \{z : x_2 < 0, x_1 \in \mathbb{R}^1\}. \quad (1)$$

The coating is modeled as coherently bonded strips Ω_r

$$\Omega_r = \{z : H_{r+1} < x_2 < H_r, x_1 \in \mathbb{R}^1\}, \quad (2)$$

$$H_N = h_N, H_{N+1} = 0, H_r = H_{r+1} + h_r, r = \overline{2, N}$$

with rectilinear boundaries

$$\Gamma_r = \{z : z \equiv z_r = x_1 + iH_r\}, r = \overline{2, N+1}. \quad (3)$$

Taking into account the results of experimental studies, we assume that the film surface has an arbitrary small perturbation which changes with time τ through the mass transport

$$\Gamma_1 = \{z : z \equiv z_1 = x_1 + i[H_1 + g(x_1, \tau)]\},$$

$$g(x_1, \tau) = \sum_{n=1}^{+\infty} A_n(\tau) \cos kx_1, A_n(0) = a_n, \quad (4)$$

$$\max_n |A_n(\tau)| / \lambda = \varepsilon(\tau) \ll 1 \quad \forall \tau, k = 2\pi n / \lambda.$$

The conditions at free surface, interfaces and infinity are, respectively

$$\sigma(z_1) = 0, z_1 \in \Gamma_1, \quad (5)$$

$$\Delta u(z_r) = u^+ - u^- = 0, \quad \Delta \sigma(z_r) = \sigma^+ - \sigma^- = 0, \quad (6)$$

$$\sigma_{22}^\infty = \sigma_{12}^\infty = 0, \quad \sigma_{11}^\infty = T, \quad \omega^\infty = 0. \quad (7)$$

In Eqs. (5)–(7), $u = u_1 + iu_2$, $\sigma = \sigma_{nn} + i\sigma_{nt}$; u_1, u_2 are displacements along corresponding axes of Cartesian coordinates x_1, x_2 ; σ_{nn}, σ_{nt} are components of the stress vector σ at the area with unit normal \mathbf{n} in the local Cartesian coordinate system n, t (vector \mathbf{n} is perpendicular to the boundary Γ_1 in Eq. (5) and the interface Γ_r in Eq. (6)); $u^\pm = \lim_{z \rightarrow z_r \pm i0} u(z)$, $\sigma^\pm = \lim_{z \rightarrow z_r \pm i0} \sigma(z)$, $z_r \in \Gamma_r$, $r = \overline{2, N+1}$; $\sigma_{\alpha\beta}^\infty = \lim_{x_2 \rightarrow -\infty} \sigma_{\alpha\beta}$, $\omega^\infty = \lim_{x_2 \rightarrow -\infty} \omega$; $\sigma_{\alpha\beta}$ ($\alpha, \beta = 1, 2$) are the components of the stress tensor in the axes x_1, x_2 ; ω is the rotation angle of a material particle.

As it was mentioned above, the analysis of morphological instability is based on combined effect of surface and volume diffusion that are assumed to take place in the region close to the free surface Γ_1 . Following Panat et al.[1], the normal velocity of the surface can be computed as

$$\begin{aligned} \frac{\partial g(x_1, \tau)}{\partial \tau} = & K_s \frac{\partial^2}{\partial x_1^2} \left[U(x_1, \tau) - \gamma \frac{\partial^2 h(x_1, \tau)}{\partial x_1^2} \right] + \\ & + K_v k \left[\gamma \frac{\partial^2 h(x_1, \tau)}{\partial x_1^2} + \Delta P(x_1, \tau) \right], \end{aligned} \quad (8)$$

where $K_s = D_s C_s \Omega^2 / k_b T_a$, $K_v = D_v C_v \Omega / k_b T_a$; Ω is the atomic volume, D_s is the surface self-diffusivity, C_s is the number of diffusing atoms per unit area, k_b is the Boltzmann constant, T_a is the absolute temperature, D_v is the vacancy self-diffusivity in bulk of top layer, C_v is the concentration of vacancies in the bulk of top layer in equilibrium with a flat film surface under a remote stress, γ is the surface energy, U is the elastic strain energy at the perturbed film surface, ΔP is the variation of the hydrostatic pressure at rough and flat free surface.

Here, the elastic deformation caused by surface perturbation is treated as a quasi-static state. Thus, in order to integrate the surface evolution equation (8), we solve the corresponding boundary-value problem of plane elasticity for multiply connected domain $\Omega = \bigcup_{r=1}^{N+1} \Omega_r$ under boundary conditions (5)–(6) and conditions at infinity (7).

3 Perturbation Solution

In accordance with the superposition technique [2, 3], the solution of formulated problem of linear elasticity (1)–(7) is represented as

$$G(z) = \begin{cases} G_k^k(z, \eta_k) + G_k^{k+1}(z, \eta_k), & z \in \Omega_k, \\ G_{N+1}^{N+1}(z, \eta_{N+1}), & z \in \Omega_{N+1}, \end{cases} \quad (9)$$

where $k = \overline{1, N}$.

In Eq. (9), the following notations are introduced

$$G(z, \eta_j) = \begin{cases} \sigma(z), \quad \eta_j = 1, \\ -2\mu_j v(z), \quad \eta_j = -\kappa_j, \end{cases} \quad z \in \Omega_j, \quad (10)$$

$$G_j^r(z, \eta_j) = \begin{cases} \sigma^r(z), & \eta_j = 1, \\ -2\mu_j v^r(z), & \eta_j = -\kappa_j, \end{cases} \quad z \in \Omega_j. \quad (11)$$

Here, $\kappa_j = 3 - 4\nu_j$; $v = \frac{du}{dz}$; $v^r = \frac{du^r}{dz}$; σ^r and u^r are the stress and displacement vectors in the problem with number r , similar to σ and u ; $r, j = \overline{1, N+1}$. The derivative is taken along the area with normal \mathbf{n} , i.e. in the direction of the axis t . In the first problem, it is supposed that unknown self-balanced periodic load p is applied to the periodic curvilinear boundary Γ_1 of the homogeneous half-plane with the same period λ . The longitudinal load at infinity is equal to T_1^1 .

In the problem r ($r = \overline{2, N+1}$), the coupled deformation of two dissimilar half-planes Θ_{r-1} and Θ_r with elastic properties of the corresponding phases Ω_{r-1} and Ω_r is caused by the unknown jumps of tractions $\Delta\sigma^r$ and displacements Δu^r at the rectilinear interface Γ_r under longitudinal remote load T_j^r in Θ_j ($j = r-1, r$).

Quantities T_1^1, T_{r-1}^r, T_r^r ($r = \overline{2, N+1}$) are found from recurrence relations which follow from conditions (6) and equations $\Delta\sigma^r = \Delta u^r = 0$ corresponding to the case of the coating with the flat surface.

Boundary conditions (5) and (6) at Γ_i lead to the system of boundary equations for unknown functions $p, \Delta\sigma^r$ and Δu^r .

According to papers [2, 3], the stresses σ^r and displacements u^r are related to Goursat-Kolosov complex potentials Φ_j^r and Υ_j^r by the equality

$$G_j^r(z, \eta_j) = \eta_j \Phi_j^r(w_k) + \overline{\Phi_j^r(w_k)} - (\Upsilon_j^r(\overline{w_k}) + \overline{\Phi_j^r(w_k)} - (w_k - \overline{w_k}) \overline{\Phi_j^{r'}(w_k)}) e^{-2i\alpha}, \quad z \in \Omega_j, \quad (12)$$

where α is the angle between axis t of the local coordinates n, t and axis x_1 , the prime denotes differentiation with respect to the argument; $r, j = \overline{1, N+1}$; $w_1 = z + i(g(x_1) - H_1)$, $w_k = z + iH_k$, $k = \overline{r-1, r}$, $k \neq j$.

Following boundary perturbation technique, we expand functions Φ_j^r, Υ_j^r and p in power series of small parameter ε

$$p(z_1) = \sum_{n=0}^{\infty} \frac{\varepsilon^n}{n!} p_n(z_1), \quad \Phi_j^r(w_k) = \sum_{n=0}^{\infty} \frac{\varepsilon^n}{n!} \Phi_{jn}^r(w_k), \quad \Upsilon_j^r(\overline{w_k}) = \sum_{n=0}^{\infty} \frac{\varepsilon^n}{n!} \Upsilon_{jn}^r(\overline{w_k}). \quad (13)$$

And boundary values of functions $\Phi_{1n}^1, \Upsilon_{1n}^1$ and p_n at Γ_1 into Taylor series in the vicinity of the line $\text{Im } w_1 = 0$, i.e. $z = iH_1$, considering x_1 as parameter

$$\Phi_{1n}^1(w_1) = \sum_{m=0}^{\infty} \frac{[i\varepsilon f(x_1)]^m}{m!} \Phi_{1n}^{1(m)}(x_1), \quad \Upsilon_{1n}^1(\overline{w_1}) = \sum_{m=0}^{\infty} \frac{[-i\varepsilon f(x_1)]^m}{m!} \Upsilon_{1n}^{1(m)}(x_1), \quad (14)$$

$$p_n(z_1) = \sum_{m=0}^{\infty} \frac{[i\varepsilon f(x_1)]^m}{m!} p_n^{(m)}(x_1).$$

In view of relation $\varepsilon f'(x_1) = \text{tg}(\alpha_1)$ and condition $|\varepsilon f'(x_1)| < 1$, one can write

$$e^{-2i\alpha_1} = 1 + 2 \sum_{m=0}^{\infty} (-i\varepsilon f'(x_1))^{m+1}. \quad (15)$$

Based on the solution of Riemann-Hilbert problem for holomorphic functions $\Phi_{1n}^r(w_1)$, $\Upsilon_{1n}^r(\bar{w}_1)$ ($r = \overline{1, N+1}$), representations (12)-(15) allows us to transform the system of boundary equations for unknown functions p , $\Delta\sigma^r$ and Δu^r into Fredholm integral equations of the second kind in expansion coefficients σ_n^r and v_n^r ($r = \overline{2, N}$) and their conjugates

$$\begin{aligned} \Delta\sigma_n^r(x_1) + \int_{-\infty}^{+\infty} K_{r1}(x_1, \xi)\Delta\sigma_n^r(\xi)d\xi + \int_{-\infty}^{+\infty} K_{r2}(x_1, \xi)\overline{\Delta\sigma_n^r(\xi)}d\xi + \\ + \int_{-\infty}^{+\infty} K_{r3}(x_1, \xi)\Delta v_n^r(\xi)d\xi + \int_{-\infty}^{+\infty} K_{r4}(x_1, t)\overline{\Delta v_n^r(t)}dt = H_{1n}^r(x_1), \\ \Delta v_n^r(x_1) + \int_{-\infty}^{+\infty} K_{r5}(x_1, \xi)\Delta\sigma_n^r(\xi)d\xi + \int_{-\infty}^{+\infty} K_{r6}(x_1, \xi)\overline{\Delta\sigma_n^r(\xi)}d\xi + \\ + \int_{-\infty}^{+\infty} K_{r7}(x_1, \xi)\Delta v_n^r(\xi)d\xi + \int_{-\infty}^{+\infty} K_{r8}(x_1, \xi)\overline{\Delta v_n^r(\xi)}d\xi = H_{2n}^r(x_1). \end{aligned} \quad (16)$$

Here the kernels $K_{rj}(x_1, \xi)$, $j = \overline{1, 8}$ are the same for every order of approximation and belong to the class of continuous functions. The right hand sides $H_{1n}^r(x_1)$, $H_{2n}^r(x_1)$ are known continuous functions which depend on solutions of all previous approximations.

Periodicity of a surface perturbation (4) makes it possible to solve the problem in a form of Fourier series as in the case of the single layer coating [2, 3, 4]

$$\Delta\sigma_n^r(x_1) = \sum_{k=-\infty}^{+\infty} A_{kn}^r E_k(x_1), \quad \Delta v_n^r(x_1) = \sum_{k=-\infty}^{+\infty} B_{kn}^r E_k(x_1) \quad (17)$$

where $A_{kn}^r, B_{kn}^r \in C$, $E_k(x_1) = \exp(b_k x_1)$, $b_k = \frac{2\pi ik}{\lambda}$.

Functions $H_{1n}^r(x_1)$ and $H_{2n}^r(x_1)$ are periodic as well and can be represented by Fourier series with known coefficients

$$\begin{aligned} H_{1n}^r(x_1) = \sum_{k=-\infty}^{+\infty} C_{kn}^r E_k(x_1), \quad C_{kn}^r = \frac{1}{\lambda} \int_{-\lambda/2}^{\lambda/2} H_{1n}^r(t) E_{-k}(x_1) dt, \\ H_{2n}^r(x_1) = \sum_{k=-\infty}^{+\infty} D_{kn}^r E_k(x_1), \quad D_{kn}^r = \frac{1}{\lambda} \int_{-\lambda/2}^{\lambda/2} H_{2n}^r(t) E_{-k}(x_1) dt \end{aligned} \quad (18)$$

Using expansions (17) and (18), the system of $2N - 2$ integral equations (16) is reduced to the linear system of algebraic equations in the unknown coefficients A_{kn}^r, B_{kn}^r .

4 Stability conditions

Using the method described above, a stress and strain distribution modified by surface perturbation (4) is obtained in the first-order approximation

$$\begin{aligned}\sigma_{ij}(x_1, \tau) &\approx \sigma_{ij(0)}(x_1, \tau) + \varepsilon(\tau)\sigma_{ij(1)}(x_1, \tau), \\ \varepsilon_{ij}(x_1, \tau) &\approx \varepsilon_{ij(0)}(x_1, \tau) + \varepsilon(\tau)\varepsilon_{ij(1)}(x_1, \tau).\end{aligned}\quad (19)$$

Substituting obtained equations for the elastic strain energy U at the wavy surface and the hydrostatic pressure variation ΔP into Eq. (8), equating coefficients of $\cos(kx_1)$ and then integrating over the time we derive the governing equations which give the exponential growth of each Fourier wavemodes A_n with time [5]

$$\ln\left(\frac{A_n(t)}{a_n}\right) = P_n(\lambda, h_1, \dots, h_N, \mu_1, \dots, \mu_{N+1}, \nu_1, \dots, \nu_{N+1}, \gamma, D, T)\tau, \quad (20)$$

while $\lambda > \lambda_{cr}$, where critical wavelength λ_{cr} is determined from equations

$$P_n(\lambda, h_1, \dots, h_N, \mu_1, \dots, \mu_{N+1}, \nu_1, \dots, \nu_{N+1}, \gamma, D, T) = 0, \quad D = \frac{D_v C_v}{D_s C_s}. \quad (21)$$

As an example, we consider two-layered film structure where the surface undulation is specified by the periodic function [4]

$$f(x_1) = \frac{\lambda}{d} \left[\text{Imctg}\left(\frac{\pi x_1}{\lambda} - iy\right) - 1 \right], \quad d = \text{Imctg}(iy) + 1, \quad (22)$$

here the real quantity $y \in (0, +\infty)$ plays the role of the parameter determining the surface shape. Fig. 2 presents the film surface relief for $y = 0.5$ and 5 .

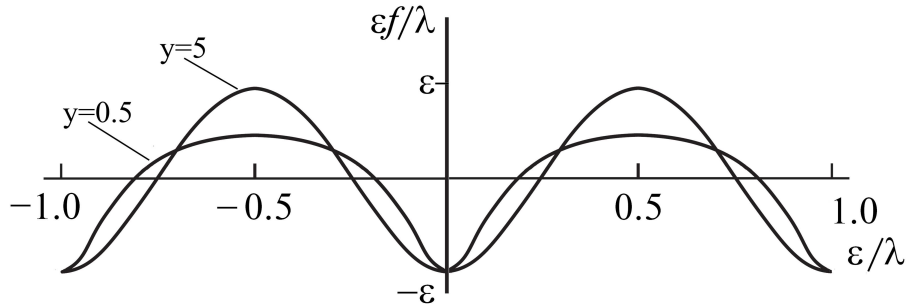


Figure 2: The surface shape with different values of parameter y .

Table 1 shows the critical values of surface perturbation wavelength where shear modulus is $\mu_1 = 100\text{GPa}$, Poisson ratios are $\nu_1 = \nu_2 = \nu_3 = 0.3$, surface energy is $\gamma = 1\text{J/m}^2$, volume to surface diffusion ratio is $D = 10^{-25}\text{m}^2$ and atomic volume is $\Omega = 4.29 \times 10^{-29}\text{m}^3$. Young modulus ratios E_1/E_2 , E_2/E_3 ; thicknesses of layers h_1 , h_2 and parameter y are varying in Eq. (22).

As one can see from the table, the surface shape has most significant effect on critical wavelength. The relative difference of critical values in the case of $y = 0.5$ and $y = 5$

Table 11: The critical perturbation wavelength for various system parameters.

E_1/E_2			0.3	0.3	3	3
E_2/E_3			0.3	3	0.3	3
$h_1, \mu m$	$h_2, \mu m$	y	$\lambda_{cr}, \mu m$			
0.6	0.6	0.5	1.287	1.287	1.248	1.248
		5	2.887	2.625	1.926	1.911
1.2	0.6	0.5	1.264	1.264	1.263	1.263
		5	2.190	2.186	2.100	2.098
0.6	1.2	0.5	1.287	1.287	1.247	1.247
		5	2.728	2.694	1.917	1.916

 Table 12: The effect of different longitudinal load T signs.

E_1/E_2			0.3	0.3	3	3
E_2/E_3			0.3	3	0.3	3
$h_1, \mu m$	$h_2, \mu m$	y	$(\lambda_{cr}^+ - \lambda_{cr}^-)/\lambda_{cr}^+$			
0.6	0.6	0.5	0.153	0.152	0.138	0.138
		5	0.365	0.306	0.185	0.180
1.2	0.6	0.5	0.144	0.144	0.143	0.143
		5	0.242	0.240	0.215	0.214
0.6	1.2	0.5	0.153	0.153	0.138	0.138
		5	0.330	0.322	0.182	0.181

ranges from 53% to 125% for different parameters. In the case of a sinusoidal surface ($y = 5$), effect of Young modulus ratios E_1/E_2 and E_2/E_3 and thicknesses of layers h_1 and h_2 are also considerably (33%, 10%, 25%, respectively). However, in the case of $y = 0.5$ variation of these parameters has insignificant effect on the result.

The contribution of volume diffusion depends on the sign of the stress T [1]. The relative differences of critical wavelengths λ_{cr}^- and λ_{cr}^+ for compressive and tensile stresses, consequently, are presented in the Table 2. According to the results, the load sign has greater influence in the case of the soft film coating.

5 Conclusion

In the present study, we designed the theoretical model of multilayer thin film coating in order to analyze the stability of free surface against diffusional perturbations. Using the complex variable representations, superposition method and boundary perturbation technique, the original boundary value problem is reduced to the successive solution of the set of Fredholm integral equations, which is given in the terms of Fourier series. As a result, governing equation is derived and gives the amplitude of morphological evolution as a function of time.

Acknowledgements

This research was supported by the Russian Foundation for Basic Research under Grant 14-01-00260.

References

- [1] Panat R., Hsia K.J., Cahill D.G. Evolution of surface waviness in thin films via volume and surface diffusion // *J. Appl. Phys.* Vol. 97(1). P. 013521. 2005.
- [2] Grekov M. A., Kostyrko S. A. A film coating on a rough surface of an elastic body // *J. Appl. Math. Mech.* Vol. 77. P. 79–90. 2013.
- [3] Grekov M. A., Kostyrko S. A. A multilayer film coating with slightly curved boundary // *Int. J. Eng. Sc.* Vol. 89. P. 61–74. 2015.
- [4] Grekov M. A., Kostyrko S. A. Surface defect formation in nanosized film coatings due to diffusion // *International Conference on Mechanics Seventh Polyakhov's Reading.* P. 1–4. 2015.
- [5] Kostyrko S. A., Shuvalov G. M. Morphological stability of multilayer film surface during diffusion processes // *2015 International Conference "Stability and Control Processes" in Memory of V.I. Zubov (SCP).* P. 392–395. 2015.

Sergey S. Kostyrko, St.Petersburg State University, 7/9 Universitetskaya nab., St. Petersburg, 199034 Russia

Gleb M. Shuvalov, St.Petersburg State University, 7/9 Universitetskaya nab., St. Petersburg, 199034 Russia

Phase transitions in titanium alloys at high-speed mechanical effect

Nikolay A. Krylov, Margarita A. Skotnikova
skotnikova@mail.ru

Abstract

TEM, SEM-technique and X-ray diffraction analysis are used to investigate the structural and phase changes occurring in a material of chip after turning treatment of blanks from titanium alloys PT-3V, VT-23, VT-6 in speed range of cutting 2...275 m/mines and plane targets-samples from VT-6 ($\alpha + \beta$) titanium alloy, processed by a shock wave with the help of a pneumatic gun, within impact velocity range of 400...600 m/s (at speeds of deformation $10^5 - 10^6 s^{-1}$) were investigated. It is shown, that the compressing shock wave modulates a material structure, breaking it on mezo-volumes by the size 100...400 microns, under which boundaries the unloading wave, connecting rotational (rotary) modes, makes located adiabatic shears. Is shown, that on an input the loading wave resulting in decomposition β -phases and enrichment by a vanadium of α -phase up to formation soft orthorhombic of α'' -phase, braking a shock wave was formed. The shock wave was reflected in an output from the back party and the unloading wave was formed. Here there was a change of the mechanism of plastic deformation, from shift to rotational.

1 Introduction

The high-speed deformation is a modern high-efficiency way of metal materials treatment. In various fields of the industry with success energy of explosion and other methods of reception of shock waves for are ductile, press forming, welding and cutting treatment of materials is used. In practice most difficultly treated the titanium alloys, especially, two-phase of martensite class. It is possible to believe, what is it occurs because of localization of plastic deformation in blank metal in a zone of contact to the instrument, that is caused by their low heat conduction, high contact temperatures, high propensity to structural and phase transformations at deformation are considered.

2 Experiment

2.1 Cutting Treatment of Titanium Alloys

The treatment of titanium alloys PT-3V and VT-23 was carried out by a hard-alloy cutter VK8 without lubrication with a feed speed $S = 0,26$ mm/revolutions and cutting depth $t = 3$ mm, in a range of cutting speeds 2...120 m/mines. The geometrical parameters of a cutter made corners: $\varphi = 45^\circ$; $\varphi_1 = 15^\circ$; $\alpha = 6^\circ$; $\gamma = 12^\circ$.

2.2 Morphology of Chip

As it is visible from Fig. 1a, at increase of speed of cutting treatment blank from titanium alloy VT-23, the linear wear of the tool was much higher, in comparison with treatment of steel HVG or aluminium alloy AMz. Thus it was formed chip local (adiabatic) shear with traces of localization of plastic deformation (ε_{local}), Fig. 1b. The period of localization (width of chip segments) on the average 300...400 microns.

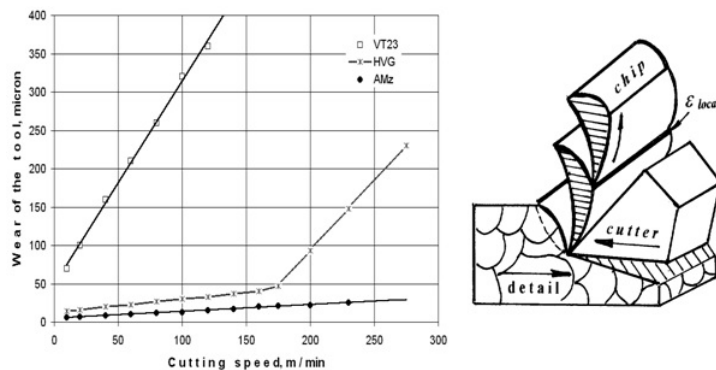


Figure 1: Wear of tool with increase of speed cutting treatment of alloys VT-23 (1), HVG (2), AMz (3), (a). The scheme of Вкадиабatic shiftВН chip formation (strong localization of plastic deformation) (b).

2.3 Structure of Chip Metal

The structure of blank from titanium alloy VT-23 in an initial state represented colonies of parallel plates of α -phase, disjointed interlayers of β -phase, Fig. 2c. At cutting treatment, beginning already from speed 2 m / mines, the inhomogeneous plastic deformation, its strong localization in narrow iterating with a period 300...400 microns volumes of metal on the mechanism of formation of a superfine structure, Fig. 2d, took place.

As have shown results of scanning electronic microscopy, free surfaces of chips from alloys VT-23 (Fig. 2b) and PT-3V (Fig. 2a) were formed on the rotational mechanism with attributes of destruction in conditions local adiabatic shear.

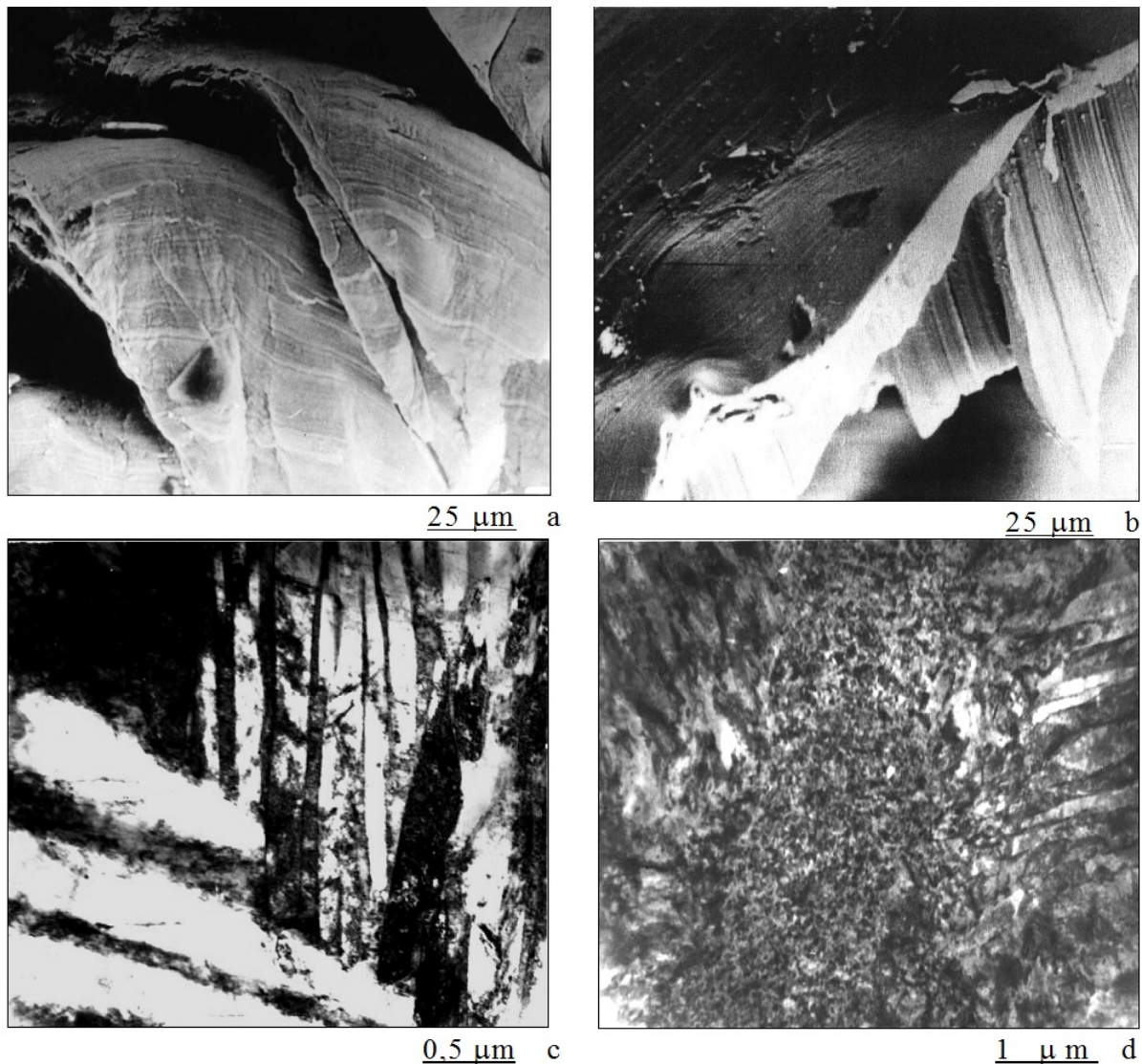


Figure 2: Reference photos of chips surface from alloy VT-23 (b) and PT-3V (a). Structure of chip from alloy VT-23 before (c) and after (d) cutting treatment with speed 120 m/min.

2.4 Estimate of Chip Microhardness

The microhardness testings were made in chip metal from alloy VT23 along a direction of movement of cutter in with speed 120 m/min, with an interval 20 microns at loading of 20 grams. Results of microhardness testing of chips had wavy character, is especial close their free edge, Fig. 3.

The maximal values of microhardness had on places of an articulation of segments of chips, in which with the help of transmission electronic microscopy the localization of plastic deformation on the mechanism of formation of narrow zones has been earlier found out by a superfine structure. Here absolute values of microhardness for alloys VT-23 reached 4381 MPa at average hardness of chips and metal in an initial condition, accordingly 3761 and 3903 MPa. It is necessary to note, that the specified

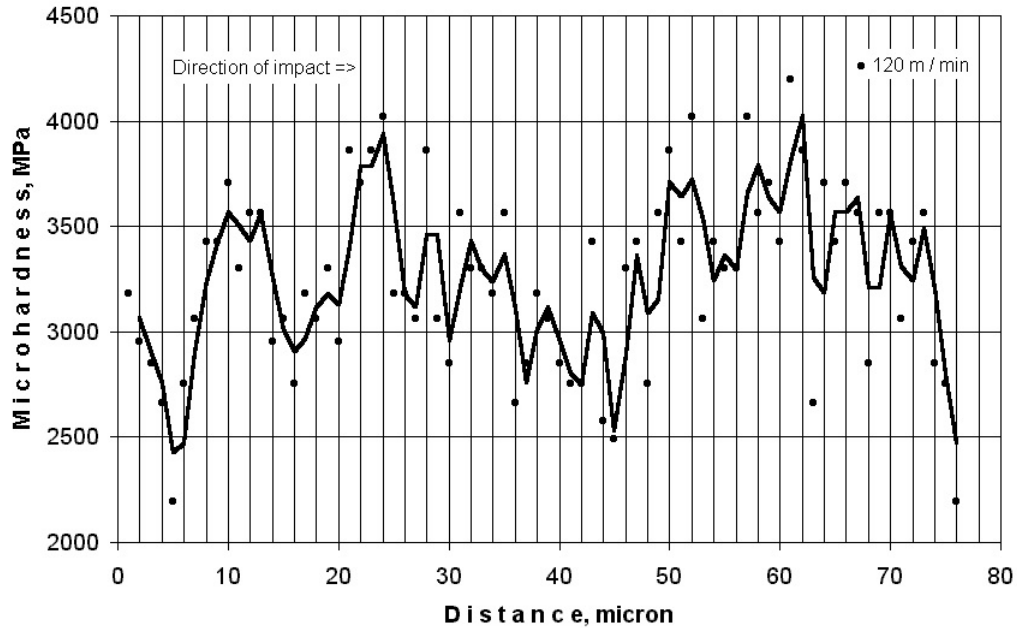


Figure 3: Distribution of microhardness in chip metal from alloy VT23 along a direction of movement of cutter in with speed 120 m/minutes.

changes of structure, Fig. 2d and modulation of microhardness, Fig. 3, near to free edge of chip were more essential, than in at cutter zone that testified to passage there more intensive relaxation processes. Thus, the cutter at the movement along treated blank material forms a wave of compression which modulates material structure, dissecting it on mezo-volumes by the size 300...400 microns. Having reflected from a surface of blank material, the unloading wave of the plastic deformation providing connection of rotational (rotary) modes of plastic deformation and making located adiabatic shears along the boundaries educated mezo- volumes is formed. Dissipative modulation of structure and microhardness in titanium alloys could be the reason of decrease of tool wearproofity.

3 Shock Stressing of titanium alloys

The treatment by a shock wave was carried out in a material of plane blanks - samples from two-phase ($\alpha + \beta$) titanium alloys OT4, VT6 and VT-23, tested by anvil block, or blast wave [1]. Thus blanks have been finished with full destruction with education of two free surfaces or cavities.

3.1 Morphology of destruction of targets- blanks after shock loading

In Fig. 4, the photos and the scheme of destruction of target- blank №2 from the VT6 alloy tested over impact velocity of 568 m/s are submitted. It is visible, that formed turnpike the crack was parallel to a free surface of a target and had the step form.

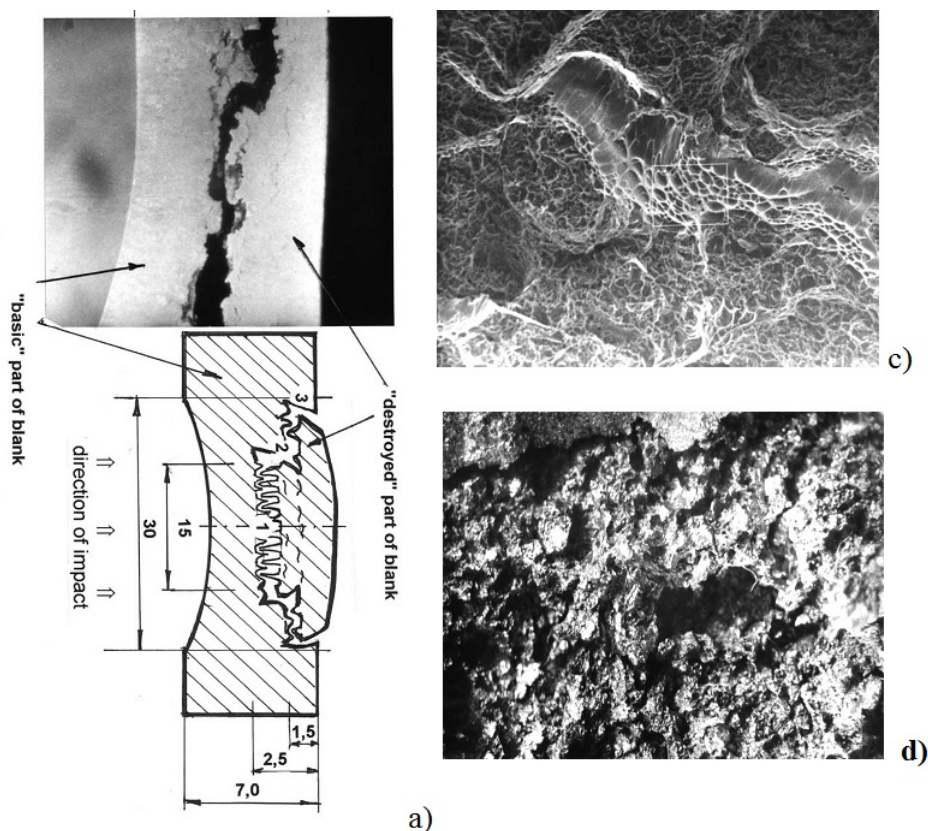


Figure 4: The scheme of destruction of planar target- blank №2, tested over impact velocity of 568 m/s, (b). Sizes are specified in mm. The surface cross-micro-section (a) and free surface of breaking-offs "destroyed" (c) and "basic" (d) parts of target-blank in a zone 1. x 3 (a), x 220 (c), x 14 (d).

It is possible to allocate three stages (3 zones) destructions. Zone 1 - "epicentre" of shock wave in diameter no more than 15 mm, in which characteristic viscous "tunnels" (\varnothing 100...400 microns) focused along a direction of impact were formed. Zone 2 - "periphery" of shock wave as a ring. Zone 3 - "final destruction". There were, that the surfaces of breaks having at a macro-level antisymmetric character, at micro- level did not coincide. Took place disposal of material, it is especial in a zone 2, Fig. 4(a-b). On Fig. 4(a-d) electron microscope photos of cross-sections and fractures "destroyed" (a, c) and "basic" (a, d) of parts of the target- blank in zone 1 are submitted. It is visible, that fracture of the destroyed blank on mezo- level was formed components of round forms by the size 100...400 microns, Fig. 4(c-d). Such viscous of metal sites could be generated as a result of the rotational mechanism of plastic deformation along narrow micro channels, which direction coincided with a direction of operation of the maximal stress [2]. It is possible to believe, that at the high-speed treatment, the compressing shock wave modulates a structure of target- blank, breaking it on mezo-volumes by the size 100...400 microns, along which boundaries the unloading wave, connecting rotational (rotary) modes, makes located adiabatic shears [2] and destruction.

3.2 Estimation of microhardness of blank metal after shock stressing

On Fig. 5 results of microhardness testing with an interval 20 microns are submitted at loading of 20 grams, in blank metal from alloy VT6 after treatment by a shock wave with speed 568 m/s.

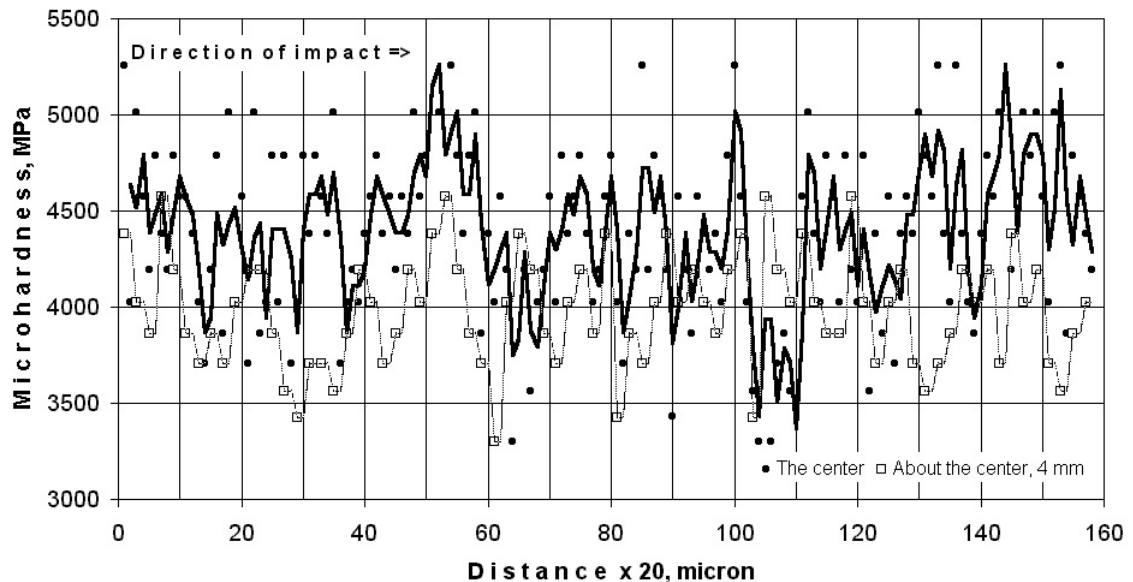


Figure 5: Distribution of microhardness in blank metal from alloy VT6 along a direction of movement of shock wave in a zone 1 with speed 568 m/s

Measurements have been executed starting from edge of "basic" blank part on a trace of movement of wave in the central and peripheral field on distance of 4 mm from the center, in both cases at level of zone 1. Absolute values of microhardness in the center and on periphery reached on the average 4413 and 3996 MPa, accordingly, at average hardness of sample metal in an initial condition 2416 MPa. Apparently from Fig. 5, results of measurement of microhardness after shock stressing had wavy character with the size of a half wave 100...200 microns. In comparison with central, the peripheral wave on distance of 4 mm from the center was in an antiphase and thus, they were self-consistent in mezo-volume 100...200 microns (zone 1). Similar comparative results have been received and at level of zone 2. Peripheral wave on distance of 11 mm from the center, was self-consistent with central less often, but the size of such volumes increased up to 300...600 microns.

3.3 A structure of targets-blanks after shock loading

Structure of blanks metal from alloy VT6, tested anvil block and a blast wave investigated with the help of microhardness measurements, transmission electronic microscopy [5] and X-ray diffraction analysis, Fig. 6.

Results have shown, that with increase of speed of shock wave, took place localization of plastic deformation, to which decomposition of enriched solid solutions

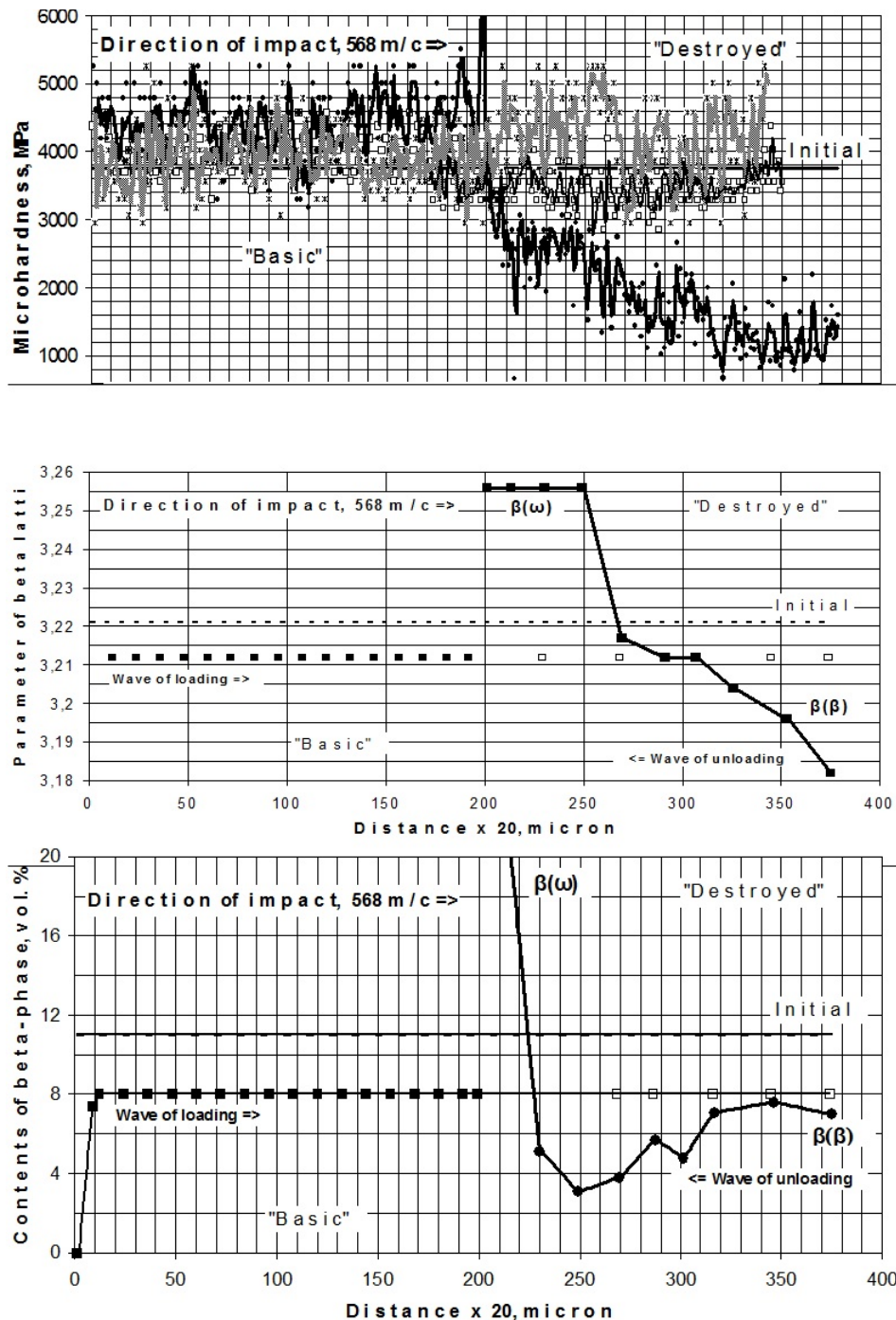


Figure 6: The results of microhardness measurements (a), of analysis parameter lattice (b) and contents (c) of β -phase along the shock wave propagation after shock loading for target-blank N^o2, tested with impact velocity 568 m/s.

always preceded. In all investigated materials in boundary layers generated mezo-volumes, interlayers of β -solid solution under operation of shock wave, were exposed to fractional or decomposition (dissolution) in result $\beta \rightarrow \alpha$ -transformation. In such places the structure from fine grains of different orientation which had the heightened microhardness was formed and yielded in condition of microdiffraction "ring"

electronograms,[5], origin of micro-cracks here was observed. Microhardness testing on targets blanks from the VT6 alloy after tested by a shock wave with velocity 568 m/s. On the target №1, remained the whole, results of microhardness measurement changed concerning of an initial level 3760 ± 470 MPa. On the destroyed target №2, along the central zone, microhardness in the "basic" part was above of an initial (4430 MPa), and in "destroyed" parts its sharp decrease up to level 1800 MPa was observed, figure 6 (a). In Fig. 6 (b, c) the results of analysis parameter lattice and contents of β -phase in a target- material №2 before and after shock loading along the shock wave propagation are submitted. As it is seen, in "destroyed" part of target- sample were observed significant changes. Results have shown, that on an input the "loading wave" resulting in decomposition $\beta(\alpha)$ - phases and enrichment by vanadium of α -phase up to formation soft orthorhombic of α' -phase, braking a shock wave was formed. As seen in Fig. 6 (c), on an input of target of β -phase was not. The shock wave was reflected in an output from the back party target and the "unloading wave" was formed. Here there was a change of the mechanism of plastic deformation, from shift to rotational [2], and there was an intensive heat-generating, increase of a temperature and opposite $\alpha \rightarrow \beta$ phase transformation. The soft enriched vanadium the $\beta(\beta)$ - phase, was inclined to decomposition up to formation of brittle ω -phase was formed [4]. As seen in Fig. 6 (b), on an output of target, a lattice parameter of β -phase sharply decreased up to level 3,183 Å. At movement of the reflected shock wave from the back surface of target- sample, and pauperization of β -phase by vanadium, its lattice parameter considerably was raised.

4 Conclusion

It is possible to believe, that at the high-speed deformation, compressing the "loading shock wave" modulates material structure, breaking it on mezo-volumes by the size 100...400 microns. Inside formed mezo-volumes the phases of waves are opposite on the sign, that results in a relative relaxation in them of stresses. In titanium alloys of martensite class in which, the "loading wave" resulting in decomposition β -phases with formation α' -phases. As a result of self-organizing of system, the "unloading wave" of plastic deformation and destruction, depending on relaxation ability of a material (structural and concentration [3-4], energies of defect of packing, ability of transformation of mechanical energy in thermal, realization of phase transformations) is formed. Here there was a change of the mechanism of plastic deformation, from shift to rotational. Thus there was an intensive heat-generating, increase of a temperature and opposite $\alpha \rightarrow \beta$ phase transformation. By the generated soft enriched vanadium the β -phase, was inclined to decomposition down to formation of brittle ω -phase. In this place the crack was formed.

Acknowledgements

The authors thank Dr. Yu.I. Mescheryakov and S.V. Shtelymakh for help in tests of samples. Work is performed with financial support of the Ministry of Education

and Science of the Russian Federation within the grants №933-2014; №1972-2014.

References

- [1] Yu.I. Mescheryakov, A.K. Divakov, Institute of Mechanical Engineering Problems, RAS, Russia, Saint-Petersburg, pre-print, 25, 1989.
- [2] M.A. Skotnikova, T.I. Strokina, N.A. Krylov, The American Physical Society, Maryland, 2004.
- [3] M.A. Skotnikova, M.A. Martynov, S.S. Ushkov, The Germany CCC-Congress Center, Hamburg, 2003.
- [4] M.A. Skotnikova, S.S. Ushkov, The Russia Central Research Institute of Structural Materials "Prometey", Saint Petersburg, 1999.
- [5] M.A. Skotnikova, N.A. Krylov, J.I. Mescheryakov, The China Beijing conference, Beijing, 2011.

Nikolai A. Krylov, Peter the Great St.Petersburg Polytechnic University, St.Petersburg, Russia

Margarita A. Skotnikova, Pyrotechnics str. 29, St.Petersburg, Russia

Detonation combustion in a supersonic gas flow in a plane channel

Vladimir A. Levin, Tatiana A. Zhuravskaya
levin@imec.msu.ru, zhuravskaya@imec.msu.ru

Abstract

Using a detailed chemical kinetics the possibility of a control of detonation propagation in a stoichiometrical hydrogen-air mixture flowing at a supersonic velocity into a plane channel was investigated. The conditions that provide detonation stabilization in the flow (without any energy input) were studied. The possibility of controlling a stabilized detonation wave location in the high-velocity gas mixture flow is examined.

1 Introduction

The study of detonation combustion in high-velocity gas flows is the one of the main branches of detonation investigation. In particular, detection of the technique of controlling detonation propagation in a supersonic gas flow and determination of conditions that provide detonation stabilization in a flow are of great interest. So, the method of detonation stabilization in a supersonic gas flow in a plane channel with parallel walls by means of weak discharges has been proposed in [1]. However, the detonation stabilization without any expenditure of energy is more preferable. So, the formation of stabilized detonation in supersonic flows of hydrogenous mixtures in an axisymmetric nozzle was investigated (see, for example, [2]). Stabilization of rotating detonation in an axisymmetric combustion chamber was studied in [3]. The formation of stationary detonation in plane channels with a wedge-shaped part for some combustible gas mixtures was examined in [4], [5]. In [1] the possibility of stabilization of formed detonation in a stoichiometrical hydrogen-air mixture flowing at a supersonic velocity into the symmetrical plane channel with narrowing cross-section was ascertained. However, the stability of the formed flow with a stabilized detonation wave was not studied.

In this work advancing the research [1] the stability of the flow with stabilized detonation in the channel with narrowing to strong disturbances was examined. In addition, the capability of a control of a stabilized detonation wave location in the high-velocity flow of a stoichiometrical hydrogen-air mixture in the channel with narrowing is investigated. The possibility of initiation and stabilization detonation combustion in the supersonic flow of the gas mixture due to using the special form plane channels (without any energy input) is studied.

2 Mathematical Model

Detonation propagation in a premixed stoichiometrical hydrogen-air mixture flowing into a plane channel (inflow cross-section and outflow one are perpendicular to the incoming flow direction) is studied. The combustible gas mixture under the normal conditions ($p_0=1\text{atm}$, $T_0=298\text{K}$) is incoming into the channel at a supersonic velocity that exceeds a velocity of self-sustaining detonation propagation in the quiescent mixture with incoming flow parameters: that is $M_0 > M_{J0}$ (here M_0 is the incoming flow Mach number, M_{J0} is the Mach number of self-sustaining detonation). A stoichiometrical hydrogen-air mixture flowing into the channel is considered as the mixture of the H_2 , O_2 , N_2 and Ar gases in the volumetric relation 42 : 21 : 78 : 1. The set of gas dynamics equations describing a plain two-dimensional nonstationary flow of the inviscid reactive multi-component gas mixture is:

$$\begin{aligned} \frac{\partial \rho}{\partial t} + \frac{\partial(\rho u)}{\partial x} + \frac{\partial(\rho v)}{\partial y} &= 0 \\ \frac{\partial(\rho u)}{\partial t} + \frac{\partial(\rho u^2 + p)}{\partial x} + \frac{\partial(\rho uv)}{\partial y} &= 0 \\ \frac{\partial(\rho v)}{\partial t} + \frac{\partial(\rho vu)}{\partial x} + \frac{\partial(\rho v^2 + p)}{\partial y} &= 0 \\ \frac{\partial(\rho(u^2 + v^2)/2 + \rho h - p)}{\partial t} + \frac{\partial(\rho u((u^2 + v^2)/2 + h))}{\partial x} + \\ &+ \frac{\partial(\rho v((u^2 + v^2)/2 + h))}{\partial y} = 0 \\ \frac{\partial(\rho n_i)}{\partial t} + \frac{\partial(\rho u n_i)}{\partial x} + \frac{\partial(\rho v n_i)}{\partial y} &= \rho \omega_i \end{aligned}$$

where x and y are the Cartesian coordinates; u and v are the corresponding velocity components; t is the time; ρ , p and h are the density, the pressure and the enthalpy, respectively; n_i is the molar concentration of the i th species in the mixture; and ω_i is the rate of formation/depletion of the i th component.

The equations of state for the mixture have the usual form

$$p = \rho R_0 T \sum_i n_i, \quad h = \sum_i n_i h_i(T).$$

Here T is the temperature, R_0 is the universal gas constant. The partial enthalpy $h_i(T)$ of the i th mixture component is determined by the Gibbs reduced energy of this component [6].

The inflow boundary conditions are the incoming flow parameters, the outflow boundary condition is necessary only in the boundary points with the subsonic velocity of gas outflow (in this case, the boundary condition is $p_{out} = p_0$). Slip condition is imposed at the channel surface.

A set of Euler gas dynamics equations coupled with detailed chemical kinetics equations [7] (in case of symmetrical channels with narrowing cross-section) or [8] (for channels of special shape) has been solved using a finite-difference method based on the Godunov's scheme [9]. The size of mesh was selected so that the flow behind the detonation front (in particular, the flow in the induction zone) was represented

correctly. Thus the computational mesh with cell size 0.03mm – 0.01mm was used in numerical calculations.

3 A gas flow with a stabilized detonation wave in a symmetrical plane channel with narrowing cross-section

The possibility of stabilization of formed detonation without any energy input in the combustible gas mixture flowing at a supersonic velocity into a symmetrical plane channel with narrowing cross-section has been investigated in [1]. The schematic of the upper part of the channel is shown in Fig. 1a: the inflow boundary is $x = x_4$, the outflow boundary is $x = 0$; the channel width is a continuously differentiable function of a longitudinal coordinate. The initial condition is the steady supersonic plane two-dimensional flow of the gas mixture in this channel obtained by the stabilization method. The initial instantaneous supercritical energy input E_0 in the narrow layer shaped domain located near the $x = x_1$ section (shaded region in Fig. 1a) was used for detonation initiation. Two detonation waves are formed as a result of the energy input: the first one propagates downstream (this wave is transferred by the flow) and the other propagates upstream. The influence of geometrical parameters of the channel on propagation of the latter detonation wave has been studied. In [1] numerical calculations were carried out with the fixed geometrical characteristics $l = 0.025\text{m}$, $x_1/l = 5$, $x_2/l = 10$, $x_3/l = 15$, $x_4/l = 20$ and with different values of M_0 , l_2 and l_3 . It has been established that for some values of the incoming flow Mach number M_0 the geometrical channel parameters may be selected so that the detonation wave is stabilized in the flow without any energy input. In particular, in case of $M_0 = 5.2$ the using of the channel with parameters $l_2/l = 0.7$ and $l_3/l = 1.4$ is the sufficient condition for stabilization of the detonation wave in the flow.

The numerical modeling of this research that performed with the use of a finer computational grid (the mesh size is reduced more than 6 times as compared with a modeling of [1]) has confirmed the formation of the flow with the stabilized detonation wave in the channel under consideration in case of $M_0 = 5.2$. The pressure field and the density contours for this gas flow with the stabilized detonation wave are presented in Fig. 1b. In the case under consideration the detonation wave initiated by energy input near the $x' = 5$ section moves upstream and is stabilized with time in the divergent (in the line of flow) part of the channel at a short distance from the $x' = 6$ section. The stabilized detonation wave and the oblique shock wave of the initial steady flow form a Mach configuration; the formed flow with stabilized detonation is unsteady due to instability of the contact surface.

The stability of this flow with the stabilized detonation wave in the channel to strong disturbances excited by energy input has been studied. The input of energy E_{test} ($E_{test} = E_0/3$ and $E_{test} = 5E_0/3$) with an exponential dependence of energy input density on transversal coordinate (or uniform energy input) in the narrow layer located in other parts of channel has been considered.

In case of the energy input in a domain placed in front of the stabilized detonation wave it has been established that in spite of a disturbance of stabilized detonation

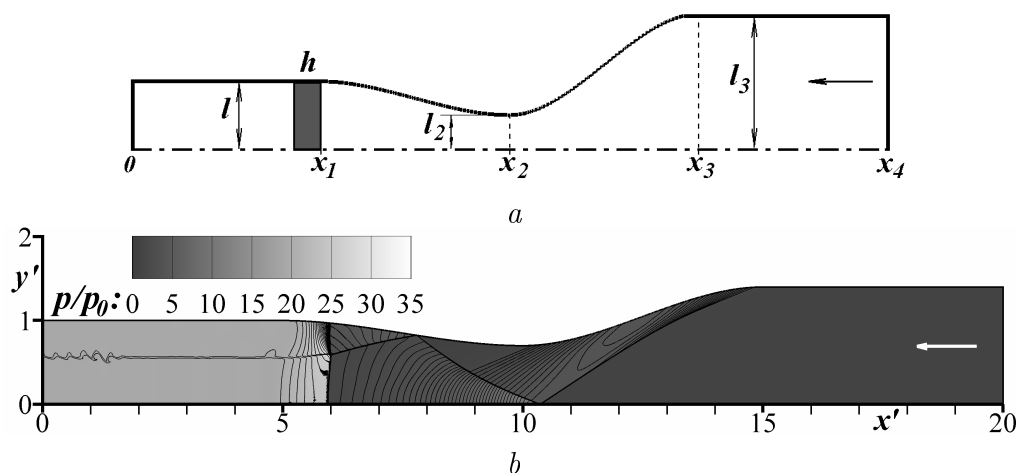


Figure 1: Detonation stabilization in the symmetrical plane channel with narrowing cross-section: *a* – the scheme of the plane channel; *b* – stabilization of the detonation wave in the divergent channel part in case of $M_0 = 5.2$. Here and further $y' = y/l$, $x' = x/l$, where l is the half of the outflow section width; the arrows show the flow direction.

after energy release, the energy input under consideration does not break the wave stabilization and does not change the location of the stabilized detonation wave (Fig. 2a). In case of the energy input in the domain located near the $x' = 7$ section, energy supply E_{test} leads to formation of a new detonation wave upstream (DW). The initial wave transforms to a shock wave (SW). However, new detonation wave is transferred by the flow and is stabilized with time in that particular place where the initial stabilized detonation wave was located (Fig. 2b).

In case of the disturbing energy input $E_{test} = 5E_0/3$ near the narrowest part of the channel (either in the convergent part or in the part of the constant width near the inflow section) a formed new detonation wave moves upstream from the channel. Thus, these disturbances destroy the detonation stabilization in the flow.

As a result of the detailed analysis it has been established that the flow under consideration with stabilized detonation in the channel with narrowing cross-section is stable to those disturbances (excited by energy input) that do not initiate a new detonation wave upstream some critical cross section of the channel. At such disturbances detonation wave remains in the divergent part of the channel and the flow with stabilized detonation restores with time. Otherwise, the detonation wave appears in the convergent channel part and wave moves upstream from the channel. The possibility of controlling a stabilized detonation wave location in the high-velocity gas mixture flow in the plane channel with narrowing was investigated. So, the influence of increase of the incoming flow Mach number and of dustiness of the incoming combustible gas mixture to detonation stabilization in the flow was studied. In particular, it has been obtained that in the channel the form of which provides detonation stabilization in case of incoming flow Mach number $M_0=5.2$ (Fig. 1b), dustiness of the incoming combustible gas mixture leads to transferring of a stabilized detonation wave location in the downstream direction (Fig. 3).

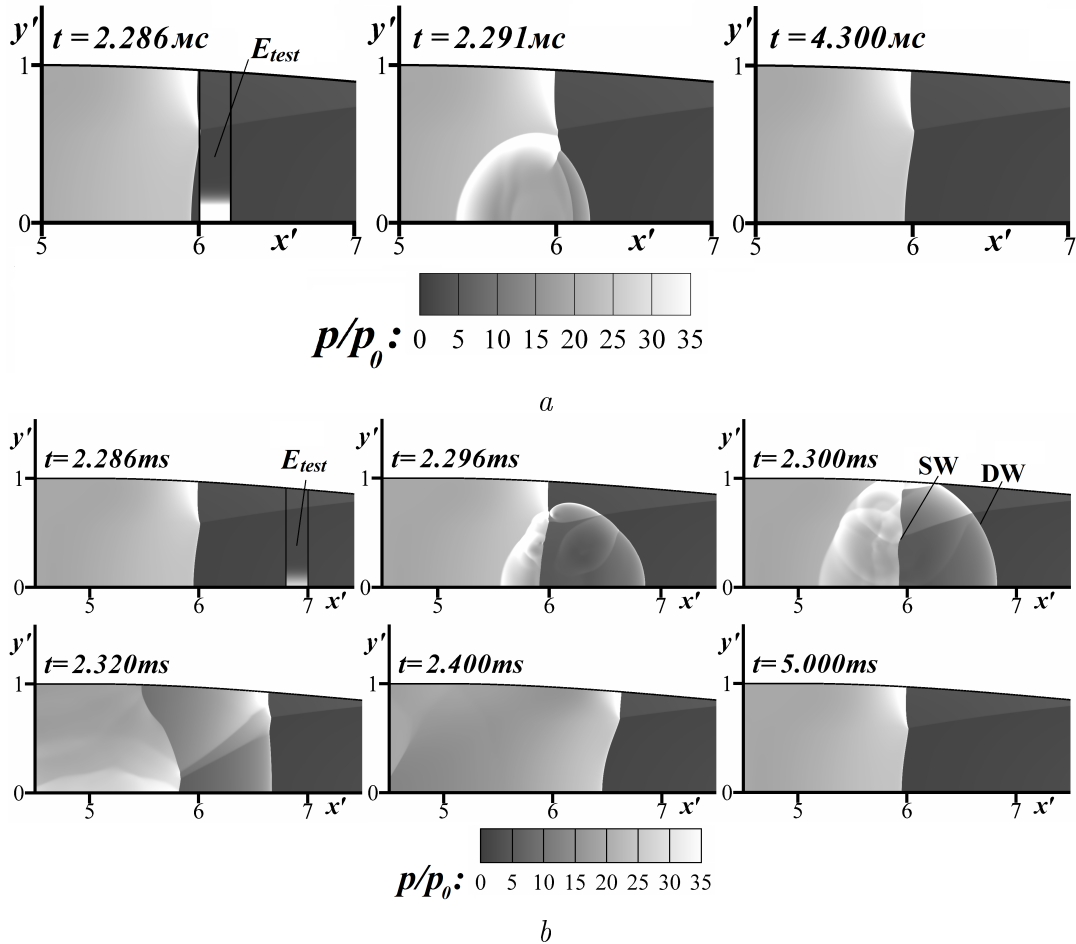


Figure 2: The conservation of stabilized detonation in case of energy input at the moment of time $t=2.286ms$ for $M_0=5.2$: *a* - the energy input domain is located in front of the detonation wave ($E_{test} = 5E_0/3$); *b* - the energy input domain is located near the $x' = 7$ section ($E_{test} = E_0/3$). The channel part containing the stabilized detonation wave and a domain of energy input E_{test} is depicted.

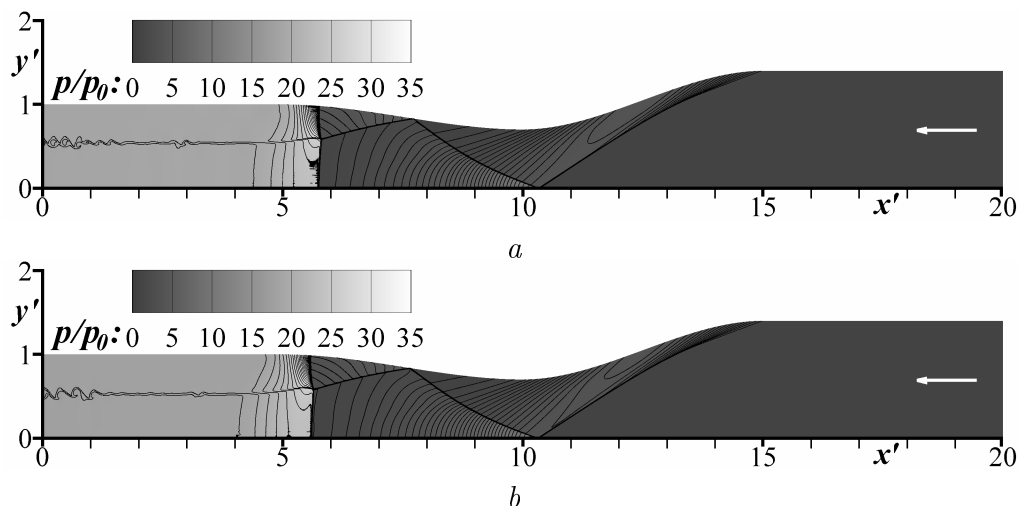


Figure 3: Stabilization of detonation combustion of the dusty gas mixture in the channel with narrowing cross-section for $M_0=5.2$: $a - \rho_{so}=0.1\text{kg/m}^3$, $b - \rho_{so}=0.2\text{kg/m}^3$. Here ρ_{so} is a dust density in the incoming flow.

4 Detonation wave stabilization in the supersonic flow in a plane channel of special shape

For determination of a channel shape which gives detonation initiation and its stabilization in the flow without any expenditure of energy, a plane two-dimensional supersonic flow of the combustible gas mixture with Mach number $M_0=5.5$ and $M_0=6$ about the symmetrical semi-infinite plane obstacle placed along the stream was considered. The obstacle configuration was chosen so that the flow with detonation was formed. There is formation of a detonation wave stabilized near the obstacle due to a flow velocity which is more than a detonation one ($M_0 > M_{J0}$). In cases under consideration the flow with stabilized detonation is unsteady due to transverse waves propagating along the detonation front (Fig. 4a).

The structure of the stabilized ahead of the obstacle detonation wave in case of $M_0=5.5$ was considered in [10]. It has been established that the detonation wave is divided into three sections with different structures. So, a part of the wave near the symmetry plane is overdriven detonation; with the increase of the distance from the plane of symmetry the left-running transverse waves (facing upstream) propagate along the detonation front; with the further distance increase the transverse waves of both sets (left-running and the right-running) are formed and define a cellular structure that is qualitatively similar to a plane detonation wave structure. The detected structure of the detonation wave stabilized ahead of the obstacle is conformed with a structure of a wedge-induced oblique detonation wave [11], [12].

Then detonation combustion of the gas mixture flowing at the same velocity into plane channels (the top walls of which are determined by streamlines of the flow under consideration, the bottom one is determined by the plane of symmetry and by the obstacle surface) was studied. The initial condition is the incoming gas flow. The flow in the channel was investigated under different values of width of the inflow

cross-section. It has been established that for a fixed value of M_0 there is the critical value of inflow cross-section width such that detonation is stabilized in the channel if width of the inflow cross-section is more than critical one. A configuration of the stabilized detonation wave is the Mach one and the flow in the channel is qualitative identical to represented in Fig. 4b. In case of subcritical width of the inflow cross-section the overdriven detonation wave moves upstream from the channel.

Acknowledgements

This research has been partly supported by the Russian Foundation for Basic Research (14-01-00742a), by the President Grant for Support of Leading Science Schools of Russian Federation (NSh-5436.2014.1), by the Presidium of the RAS (the program No. 31). The study of the stability of the flow with stabilized detonation in the channel with narrowing cross-section and the investigation of detonation stabilization in the dusty combustible gas mixture have been supported by the Russian Science Foundation (14-19-01759 and 14-11-00773, respectively). This research has been supported by the Supercomputing Center of Lomonosov Moscow State University [13].

References

- [1] Zhuravskaya T.A., Levin V.A. Investigation of certain techniques for stabilizing detonation waves in a supersonic flow. *Fluid Dynamics*. 2012. 47(6). P.793 – 801.
- [2] Tunik Yu.V. Numerical modeling of detonation combustion of hydrogen-air mixtures in a convergent-divergent nozzle. *Fluid Dynamics*. 2010. 45(2). P.264 – 270.
- [3] Fujiwara T, Hishida M, Kindracki J, Wolanski P. Stabilization of detonation for any incoming Mach numbers. *Combustion, Explosion, and Shock Waves*. 2009. 45(5). P.603 – 605.
- [4] Trotsyuk A.V., Kudryavtsev A.N., Ivanov M.S. Numerical investigations of detonation waves in supersonic steady flows. In: *Pulse and continuous detonation propulsion* / Eds. G. Roy et al. Moscow: TORUS PRESS, 2006. P.125 – 138.
- [5] Fan H.Y., Lu F.K. Numerical modelling of oblique shock and detonation wave induced in a wedged channel. *Proceedings of the Institution of Mechanical Engineers. Part G: Journal of Aerospace Engineering*. 2008. 222. P.687 – 703.
- [6] Glushko V.P. et al. (eds.) *Thermodynamic properties of individual substances*. Moscow: Nauka, 1978 [in Russia].
- [7] Warnatz J., Maas U., Dibble R.W. *Combustion. Physical and Chemical Fundamentals, Modeling and Simulation, Experiments, Pollutant Formation*. Berlin: Springer, 2001.

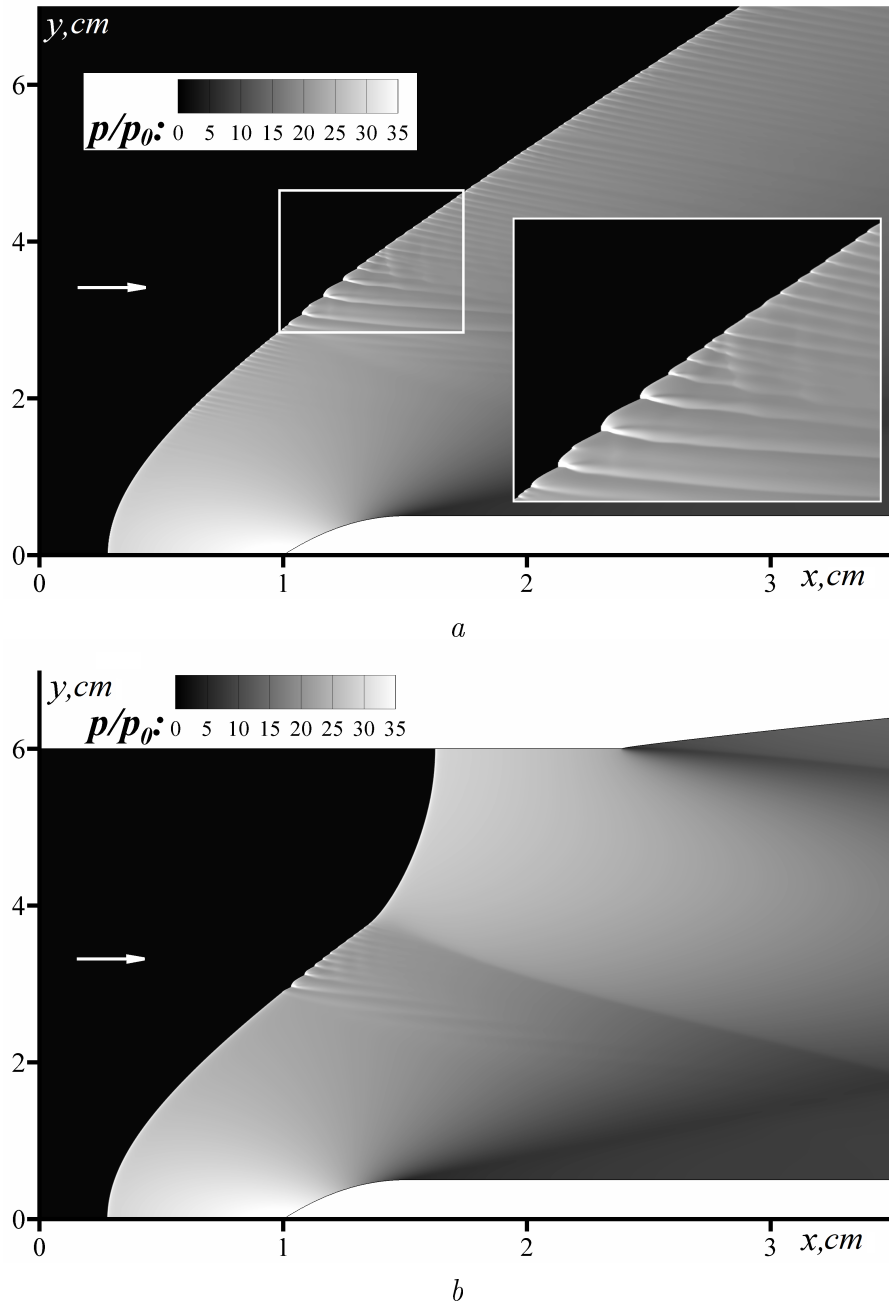


Figure 4: The flow in case of $M_0=5.5$: a – the detonation wave stabilized ahead of the obstacle; b – formation of stabilized detonation in the channel of the special shape with supercritical width of the inflow cross-section.

-
- [8] Starik A.M., Titova N.S., Sharipov A.S., Kozlov V.E. Syngas Oxidation Mechanism. *Combustion, Explosion, and Shock Waves*. 2010. 46(5). P.491 – 506.
- [9] Godunov S.K., Zabrodin A.V., Ivanov M.Ya., Kraiko A.N., Prokopov G.P. *Numerical Solution of Multidimensional Problems of Gasdynamics*. Moscow: Nauka, 1976 [in Russia].
- [10] Zhuravskaya T.A., Levin V.A. Stabilization of detonation combustion of a high-velocity combustible gas mixture flow in a plane channel. *Fluid Dynamics*. 2015. 50(2). P. 283 – 293.
- [11] Gui M.Y., Fan B.C., Dong G. Periodic oscillation fine structure of wedge-induced oblique detonation waves. *Acta Mach. Sin.* 2011. 27(6). P.922 – 928.
- [12] Verreault J., Higgins A., Stowe R. Formation of transverse wave in oblique detonations. *Proc. Comb. Inst.* 2013. 34. P.1913 – 1920.
- [13] Sadovnichy V., Tikhonravov A., Voevodin Vl., Opanasenko V. "Lomonosov": Supercomputing at Moscow State University. In *Contemporary High Performance Computing: From Petascale toward Exascale* (Chapman and Hall/CRC Computational Science). Boca Raton, USA: CRC Press, 2013. P.283 – 307.

Vladimir A. Levin, Michurinskiy av. 1, Institute of Mechanics M.V. Lomonosov Moscow State University, Moscow, Russia

Tatiana A. Zhuravskaya, Michurinskiy av. 1, Institute of Mechanics M.V. Lomonosov Moscow State University, Moscow, Russia

Modified strain gradient theory and Timoshenko beam assumptions—A direct approach

Christian Liebold, Wolfgang H. Müller, Felix A. Reich
christian.liebold@tu-berlin.de

Abstract

Materials with intrinsic micro- or nano-structure may show size-dependent material behavior, which is reflected by a stiffer elastic response to external forces when the size of the material body is reduced. In order to account for the so-called size effect strain gradient theories are applied. In this paper a modified strain gradient theory of elasticity for isotropic materials is investigated by discussing a higher order model for static beam bending. With the analytical solution for the EULER-BERNOULLI beam model being known, we apply the TIMOSHENKO beam assumptions in the present work. In contrast to the EULER-BERNOULLI beam model the TIMOSHENKO model takes independent rotations of the cross-sections of the beam into account. A system of coupled differential equations for the functions of beam deflections and rotations is derived. TIMOSHENKO's shear coefficient and the shear modulus are involved. A non-dimensional form of the functions and coefficients is provided and first numerical results are discussed. Deflections and rotations are calculated for a straight beam with a unified load distribution. The solution includes the size-effect and the refined results of a TIMOSHENKO beam.

1 Introduction

When modeling Micro- and Nanoelectromechanical Systems (MEMS/NEMS), a quantitative understanding of a possible size effect in micro- and submicrostructures is of great importance. A size effect is reflected in a varying elastic response to external loads if the size of the material body is reduced. Experimental validation is given in, *e.g.*, [16, 4, 7, 13, 1, 9]. It was shown by LAM *et al.* (2003) [7] that in the absence of strain gradients (in uniaxial tensile tests) the elastic behavior of epoxy is independent of the thickness of the sample. This is confirmed by the results of strain gradient models. Since conventional continuum theories based on the BOLTZMANN (a.k.a. CAUCHY) continuum are not able to predict size effects, the present work deals with the *Strain Gradient theory* (SG) developed by several authors, *e.g.*, [17, 14, 6, 15]. By employing second order derivatives of the displacement vector, the SG-theories are able to account for quantities like curvature or rotation. A generalization of strain gradient continua has been promoted by ERINGEN, who proposed “nonsimple materials of gradient type [2]” in order to derive the

corresponding higher-order material dependencies in a rational manner. One of the advantages of the TIMOSHENKO beam assumptions is the inclusion of an additional rotational freedom w.r.t. the cross-sections of the beam. The solution of this model yields two functions, describing deflection and rotation of the beam. For a modified couple stress continuum, the TIMOSHENKO beam assumptions have already been analyzed by [5]. The scope of this work is to combine these assumptions with the modified strain gradient theory.

2 Modified strain gradient theory

The present study starts with one of the three reduced forms of the strain energy densities for small deformations u^{SG} , postulated by MINDLIN (1962) [14]. EINSTEIN summation convention on repeated indices is used and spatial partial derivatives in the CARTESIAN coordinate system are denoted by comma-separated indices. MINDLIN's second form of the strain energy density reads:

$$u^{\text{SG}} = u(\varepsilon_{ij}, \eta_{ijk}), \quad \sigma_{ij} = \frac{\partial u^{\text{SG}}}{\partial \varepsilon_{ij}}, \quad \mu_{ijk} = \frac{\partial u^{\text{SG}}}{\partial \eta_{ijk}}, \quad (1)$$

where σ_{ij} denotes the CAUCHY stress tensor, $\varepsilon_{ij} = u_{(i,j)} = 1/2(u_{i,j} + u_{j,i})$ the small strain tensor, μ_{ijk} the higher-order stress tensor and $\eta_{ijk} = 1/2(u_{k,ij} + u_{j,ki}) = \varepsilon_{kj,i}$ the gradient of strain. As in isotropic strain gradient elasticity the decomposition of the strain gradient tensor η_{ijk} yields five irreducible parts [8]. The inclusion of the macroscopic rotation vector φ_i leads to a reduction of independent additional material parameters from five to three. FLECK & HUTCHINSON (1997) [3] introduced independent expressions of η_{ijk} and decomposed the second order displacement gradient into its symmetric and anti-symmetric part, $\bar{\eta}_{ijk}$ and η_{ijk}^{A} :

$$\bar{\eta}_{ijk} = \frac{1}{3}(u_{k,ij} + u_{i,jk} + u_{j,ki}), \quad \eta_{ijk}^{\text{A}} = \frac{2}{3}(\epsilon_{ikl}\bar{\eta}_{lj} + \epsilon_{jkl}\bar{\eta}_{li}), \quad (2)$$

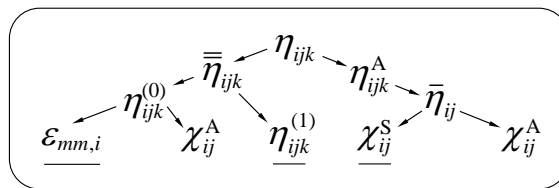


Figure 1: Scheme of decomposition of the second order gradient of displacement

where $\bar{\eta}_{ij} = \varphi_{i,j}$ is the gradient of rotation (decomposed into its symmetric and anti-symmetric part, χ_{ij}^{S} and χ_{ij}^{A} as well):

$$\varphi_i = \frac{1}{2}\epsilon_{ilk}u_{k,l}, \quad \bar{\eta}_{ij} = \frac{1}{2}\epsilon_{ilk}u_{k,lj}, \quad \chi_{ij}^{\text{A}} = \frac{1}{2}(\varphi_{i,j} - \varphi_{j,i}), \quad \chi_{ij}^{\text{S}} = \frac{1}{2}(\varphi_{i,j} + \varphi_{j,i}). \quad (3)$$

Here, ϵ_{ilk} is the LEVI-CIVITA symbol. The tensor $\bar{\eta}_{ijk}$ is further decomposed into its spherical and deviatoric part, $\eta_{ijk}^{(0)}$ and $\eta_{ijk}^{(1)}$, cf. Fig. 1. The quantity $\eta_{ijk}^{(0)}$ is related to χ_{ij}^{A} and the dilatation gradient $\varepsilon_{mm,i}$ in the following manner [3]:

$$\eta_{ijk}^{(0)} = \frac{1}{5}(\delta_{ij}\bar{\eta}_{mmk} + \delta_{jk}\bar{\eta}_{mmi} + \delta_{ki}\bar{\eta}_{mmj}) \quad \text{and} \quad \bar{\eta}_{mmi} = \varepsilon_{mm,i} + \frac{2}{3}\epsilon_{iln}\chi_{ln}^{\text{A}}. \quad (4)$$

As shown in [10, 18] the anti-symmetric part of the gradient of rotation does not influence the strain energy, if symmetry of the couple stress tensor μ_{ij} is assumed. Consequently, a linear strain energy density for non-simple isotropic materials of the modified gradient type reads:

$$u^{\text{MSG}} = \hat{u}(\varepsilon_{ij}, \varepsilon_{mm,i}, \eta_{ijk}^{(1)}, \chi_{ij}^S) = \frac{1}{2}\sigma_{ij}\varepsilon_{ij} + \frac{1}{2}p_i\varepsilon_{mm,i} + \frac{1}{2}\mu_{ijk}^{(1)}\eta_{ijk}^{(1)} + \frac{1}{2}\mu_{ij}\chi_{ij}^S . \quad (5)$$

The corresponding work-conjugated stress measures are:

$$\begin{aligned} \sigma_{ij} &= \frac{\partial u^{\text{MSG}}}{\partial \varepsilon_{ij}} = \lambda \varepsilon_{kk} \delta_{ij} + 2G \varepsilon_{ij} , & p_i &= \frac{\partial u^{\text{MSG}}}{\partial \varepsilon_{mm,i}} = 2G \ell_0^2 \varepsilon_{mm,i} , \\ \mu_{ijk}^{(1)} &= \frac{\partial u^{\text{MSG}}}{\partial \eta_{ijk}^{(1)}} = 2G \ell_1^2 \eta_{ijk}^{(1)} , & \mu_{ij} &= \frac{\partial u^{\text{MSG}}}{\partial \chi_{ij}^S} = 2G \ell_2^2 \chi_{ij}^S . \end{aligned} \quad (6)$$

Here, λ and G are LAMÉ's constants, whereas ℓ_0 , ℓ_1 and ℓ_2 denote additional material length scale parameters.

3 Differential equations of the problem

In this section, the TIMOSHENKO beam theory is analyzed in context of the modified strain gradient theory. Following this, the resulting differential equations of the beam are transformed to a non-dimensional form in order to analyze the results numerically.

3.1 TIMOSHENKO beam assumptions

The TIMOSHENKO beam model—in contrast to a the EULER-BERNOULLI model—distinguishes between the current angle of the cross-section $\phi(x)$ and the derivative of the bending line $w(x)$, see [11, 5]. The displacement field u_i of a straight TIMOSHENKO beam reads:

$$u_x = -z\phi(x) \quad , \quad u_y = 0 \quad , \quad u_z = w(x) , \quad (7)$$

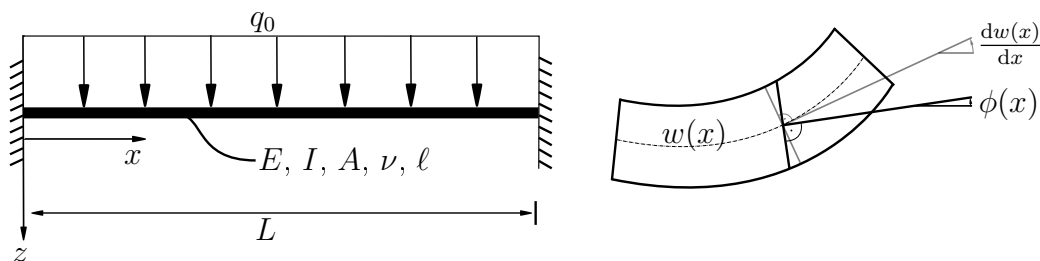


Figure 2: Loading of the TIMOSHENKO beam.

where E , I , A , L , ν and q_0 are YOUNG's modulus, second moment of inertia, area of cross-section, length of the beam, POISSON's ratio and load distribution,

respectively, *cf.*, Fig. 2. The non-zero components of the small strain tensor ε_{ij} read:

$$\varepsilon_{ij} = \frac{1}{2}(u_{i,j} + u_{j,i}) \quad \Rightarrow \quad \varepsilon_{xx} = -z\phi', \quad \varepsilon_{xz} = \frac{1}{2}(w' - \phi) = \varepsilon_{zx}, \quad (\cdot)' = \frac{d(\cdot)}{dx}, \quad (8)$$

where a prime denotes a derivative with respect to x . Using HOOKE's law for isotropic linear-elastic materials, the non-zero components of the CAUCHY stress tensor σ_{ij} read:

$$\sigma_{ij} = 2G\varepsilon_{ij} + \lambda\varepsilon_{kk}\delta_{ij} \quad \Rightarrow \quad \sigma_{xx} = -Ez\phi', \quad \sigma_{xz} = G(w' - \phi) = \sigma_{zx}. \quad (9)$$

In what follows, the displacement field of Eq. (7) is used to derive the non-zero components of the higher-order stress and strain measures. From

$$\varepsilon_{mm,i} = (-z\phi')_{,i}, \quad p_i = 2G\ell_0^2\varepsilon_{mm,i}, \quad \text{and} \quad \mu_{ij} = 2G\ell_2^2\chi_{ij}^S \quad (10)$$

it follows that:

$$\begin{aligned} \varepsilon_{mm,x} &= -z\phi'', & \varepsilon_{mm,z} &= -\phi', \\ p_x &= -2G\ell_0^2z\phi'', & p_z &= -2G\ell_0^2\phi', \\ \chi_{xy} &= -\frac{1}{4}(\phi' + w'') = \chi_{yx}, & \mu_{xy} &= -\frac{1}{2}G\ell_2^2(\phi' + w'') = \mu_{yx}. \end{aligned} \quad (11)$$

Further computations yield:

$$\begin{aligned} \eta_{xxx}^{(1)} &= -\frac{4}{5}z\phi'', & \eta_{zzz}^{(1)} &= \frac{1}{5}(\phi' - w''), \\ \eta_{xzz}^{(1)} &= \frac{2}{15}z\phi'', & \eta_{xxz}^{(1)} &= \left(\frac{4}{15}w'' - \frac{3}{5}\phi'\right), \\ \eta_{xzx}^{(1)} &= \left(\frac{4}{15}w'' - \frac{3}{5}\phi'\right), & \eta_{zxx}^{(1)} &= \left(\frac{4}{15}w'' - \frac{3}{5}\phi'\right), \\ \eta_{zzx}^{(1)} &= \frac{2}{15}z\phi'', & \eta_{zxx}^{(1)} &= \frac{2}{15}z\phi'', \end{aligned} \quad (12)$$

and from $\mu_{ijk}^{(1)} = 2G\ell_1^2\eta_{ijk}^{(1)}$ we have:

$$\begin{aligned} \mu_{xxx}^{(1)} &= -\frac{8}{5}Gz\ell_1^2\phi'', & \mu_{zzz}^{(1)} &= \frac{2}{5}G\ell_1^2(\phi' - w''), \\ \mu_{xzz}^{(1)} &= \frac{4}{15}G\ell_1^2z\phi'', & \mu_{xxz}^{(1)} &= G\ell_1^2\left(\frac{8}{15}w'' - \frac{6}{5}\phi'\right), \\ \mu_{xzx}^{(1)} &= G\ell_1^2\left(\frac{8}{15}w'' - \frac{6}{5}\phi'\right), & \mu_{zxx}^{(1)} &= G\ell_1^2\left(\frac{8}{15}w'' - \frac{6}{5}\phi'\right), \\ \mu_{zzx}^{(1)} &= \frac{4}{15}G\ell_1^2z\phi'', & \mu_{zxx}^{(1)} &= \frac{4}{15}Gz\ell_1^2\phi''. \end{aligned} \quad (13)$$

The higher-order strain energy density u^{MSG} in Eq. (5) of the present beam bending problem, incorporating the terms of Eqs. (8)–(13), reads:

$$\begin{aligned} u^{\text{MSG}} &= \frac{1}{2} \left[\sigma_{xx}\varepsilon_{xx} + \sigma_{xz}\varepsilon_{xz} + \sigma_{zx}\varepsilon_{zx} + p_x\varepsilon_{mm,x} + p_z\varepsilon_{mm,z} + \right. \\ &\quad \left. + \mu_{xy}\chi_{xy}^S + \mu_{yx}\chi_{yx}^S + \mu_{xzz}^{(1)}\eta_{xzz}^{(1)} + \mu_{xxz}^{(1)}\eta_{xxz}^{(1)} + \mu_{xzx}^{(1)}\eta_{xzx}^{(1)} + \right. \\ &\quad \left. + \mu_{xxz}^{(1)}\eta_{xxz}^{(1)} + \mu_{zzz}^{(1)}\eta_{zzz}^{(1)} + \mu_{zxx}^{(1)}\eta_{zxx}^{(1)} + \mu_{zxx}^{(1)}\eta_{zxx}^{(1)} + \mu_{zxx}^{(1)}\eta_{zxx}^{(1)} \right] \\ &= \frac{1}{2} \left[E(z\phi')^2 + G(w' - \phi)^2 + 2G\ell_0^2(z\phi'')^2 + 2G\ell_0^2\phi'^2 + \right. \\ &\quad \left. + \frac{1}{4}G\ell_2^2(\phi' + w'')^2 + \frac{8}{225}G\ell_1^2(z\phi'')^2 + \frac{32}{25}G\ell_1^2(z\phi'')^2 + \right. \\ &\quad \left. + 2G\ell_1^2\left(\frac{4}{15}w'' - \frac{3}{5}\phi'\right)^2 + 2G\ell_1^2\left(\frac{4}{15}w'' - \frac{3}{5}\phi'\right)^2 + \frac{2}{25}G\ell_1^2(\phi' - w'')^2 + \right. \\ &\quad \left. + 2G\ell_1^2\left(\frac{4}{15}w'' - \frac{3}{5}\phi'\right)^2 + \frac{8}{225}G\ell_1^2(z\phi'')^2 + \frac{8}{225}G\ell_1^2(z\phi'')^2 \right] \\ &= \frac{1}{2} \left[\phi^2G + w'^2G + \phi'^2(Ez^2 + 2G\ell_0^2 + \frac{1}{4}G\ell_2^2 + \frac{56}{25}G\ell_1^2) + \right. \\ &\quad \left. + w''^2\left(\frac{1}{4}G\ell_2^2 + \frac{114}{225}G\ell_1^2\right) + \phi''^2(2G\ell_0^2z^2 + \frac{312}{225}G\ell_1^2z^2) - \right. \\ &\quad \left. - \phi w'2G + \phi'w''\left(\frac{1}{2}G\ell_2^2 - \frac{156}{75}G\ell_1^2\right) \right]. \end{aligned} \quad (14)$$

We want to make use of the principle of virtual work and find the strain energy of the body and the work of the external loads that minimize $\delta U - \delta W \rightarrow 0$. The variation of the strain energy $\delta U = \int_V \delta u^{\text{MSG}} dV$ of the problem reads:

$$\begin{aligned} \delta U = \int_x \int_y \int_z & [\phi \delta \phi G + w' \delta w' G + \phi' \delta \phi' (Ez^2 + 2G\ell_0^2 + \frac{1}{4}G\ell_2^2 + \frac{56}{25}G\ell_1^2) + \\ & + w'' \delta w'' (\frac{1}{4}G\ell_2^2 + \frac{114}{225}G\ell_1^2) + \phi'' \delta \phi'' (2G\ell_0^2 z^2 + \frac{312}{225}G\ell_1^2 z^2) - \\ & - (\delta \phi w' + \phi \delta w') G + (\delta \phi' w'' + \phi' \delta w'') (\frac{1}{4}G\ell_2^2 - \frac{156}{150}G\ell_1^2)] dz dy dx . \end{aligned} \quad (15)$$

We take TIMOSHENKO's shear factor κ into account, where $\int_{A^*} dy dz = A\kappa$ and A^* denotes the current cross-section. Integration over the variables y and z leads to:

$$\begin{aligned} \delta U = \int_0^L & [\phi \delta \phi G A \kappa + w' \delta w' G A \kappa + \phi' \delta \phi' (EI + 2GA\kappa\ell_0^2 + \frac{1}{4}GA\kappa\ell_2^2 + \frac{56}{25}GA\kappa\ell_1^2) + \\ & + w'' \delta w'' (\frac{1}{4}GA\kappa\ell_2^2 + \frac{114}{225}GA\kappa\ell_1^2) + \phi'' \delta \phi'' (2GI\ell_0^2 + \frac{312}{225}GI\ell_1^2) - \\ & + (\delta \phi w' + \phi \delta w') GA \kappa + (\delta \phi' w'' + \phi' \delta w'') (\frac{1}{4}GA\kappa\ell_2^2 - \frac{156}{150}GA\kappa\ell_1^2)] dx \\ = \int_0^L & [\delta \phi (T\phi - Tw') + \delta w' (Tw' - T\phi) + \delta \phi' (K\phi' + Nw'') + \\ & + \delta w'' (Pw'' + N\phi')] dx , \end{aligned} \quad (16)$$

where the following substitutions are used:

$$\begin{aligned} T &= GA\kappa , \\ K &= EI + 2GA\kappa\ell_0^2 + \frac{1}{4}GA\kappa\ell_2^2 + \frac{56}{25}GA\kappa\ell_1^2 , \\ P &= \frac{1}{4}GA\kappa\ell_2^2 + \frac{114}{225}GA\kappa\ell_1^2 , \\ S &= 2GI\ell_0^2 + \frac{312}{225}GI\ell_1^2 , \\ N &= \frac{1}{4}GA\kappa\ell_2^2 - \frac{156}{150}GA\kappa\ell_1^2 . \end{aligned} \quad (17)$$

The virtual work of external loads and higher-order loads is assumed to be:

$$\delta W = \int_0^L (\delta \phi m(x) + \delta w q(x)) dx + V \delta w \Big|_0^L + M \delta \phi \Big|_0^L + M^i \delta w' \Big|_0^L + M^h \delta \phi' \Big|_0^L , \quad (18)$$

where V is the single force acting at a boundary, M the single moment acting at a boundary, M^i an internal moment acting at a boundary which influences $w'(\tilde{x})$ and M^h denotes a higher-order moment acting at a boundary that influences the gradient of the angle of the cross-sections, *cf.* Eq. (19). Double partial integration

of Eq. (16)₂ results in:

$$\begin{aligned}
 \delta U = & \int_0^L (\delta\phi \overbrace{[T(\phi - w') - K\phi'' - Nw'' + S\phi^{IV}]}^{m(x)} + \\
 & + \delta w \overbrace{[T(w'' - \phi') + Pw^{IV} + N\phi''']}^{q(x)}) dx + \underbrace{(T(w' - \phi) - Pw'' - N\phi'')}_{V} \delta w \Big|_0^L + \\
 & + \underbrace{(K\phi' + Nw'' - S\phi''')}_{M} \delta\phi \Big|_0^L + \underbrace{(Pw'' + N\phi')}_{M^i} \delta w' \Big|_0^L + \underbrace{S\phi''}_{M^h} \delta\phi' \Big|_0^L. \quad (19)
 \end{aligned}$$

By comparison, the governing differential equations are $\forall x \in (0, L)$:

$$\begin{aligned}
 [T(\phi - w') - K\phi'' - Nw'' + S\phi^{IV}] &= m(x), \\
 [T(w'' - \phi') + Pw^{IV} + N\phi'''] &= q(x). \quad (20)
 \end{aligned}$$

The boundary conditions at $x = 0$ and $x = L$ become:

$$\begin{aligned}
 (T(w' - \phi) - Pw''' - N\phi'') &= V(x), \\
 (K\phi' + Nw'' - S\phi''') &= M(x), \\
 (Pw'' + N\phi') &= M^i(x), \\
 S\phi'' &= M^h(x), \quad (21)
 \end{aligned}$$

where $m(x)$ denotes a distribution of moments and $q(x)$ the force distribution.

3.2 Non-dimensional forms

For the purpose of improving the condition of the numerical problem, a non-dimensional form of the deflection w and the beam coordinate x is chosen as follows:

$$w(x) = \frac{FL^3}{EI} \tilde{w}(\tilde{x}), \quad x = L\tilde{x} \quad \Rightarrow \quad \frac{\partial^n(\cdot)}{\partial x^n} = \frac{1}{L^n} \frac{\partial^n(\cdot)}{\partial \tilde{x}^n}, \quad n = 1, 2, 3, \dots, \quad (22)$$

where the reference force is chosen w.r.t. the analyzed loading as $F = q_0L$. Normalized with respect to the highest order of the derivatives Eqs. (20) read:

$$\begin{aligned}
 \underbrace{\frac{L^4 T}{S}}_{c_1} \phi - \underbrace{\frac{L^6 T F}{E I S}}_{c_2} \tilde{w}' - \underbrace{\frac{L^2 K}{S}}_{c_3} \phi'' - \underbrace{\frac{L^5 N F}{E I S}}_{c_4} \tilde{w}'' + \phi^{IV} &= \underbrace{\frac{L^4}{S} m(\tilde{x})}_{\tilde{m}}, \\
 \underbrace{\frac{T L^2}{P}}_{c_5} \tilde{w}'' - \underbrace{\frac{T E I}{P F}}_{c_6} \phi' + \tilde{w}^{IV} + \underbrace{\frac{N E I}{L^2 P F}}_{c_7} \phi''' &= \underbrace{q(\tilde{x}) \frac{L E I}{P F}}_{\tilde{q}}, \quad (23)
 \end{aligned}$$

We re-substitute T , K , P , S and N from Eq. (17) and choose $\ell_0 = \ell_1 = \ell_2 = \ell$, $\kappa = \frac{5}{6}$, and $G = \frac{E}{2}$ (which is equivalent to $\nu = 0$). Furthermore, we only consider

beams of rectangular cross-sections. The constants c_1, c_2, \dots, c_7 now read:

$$\begin{aligned} c_1(\ell) &= \frac{375}{127} \frac{L^4}{H^2 \ell^2}, & c_2(\ell) &= \frac{4500}{127} \frac{L^7 q_0}{EH^4 A \ell^2}, & c_3(\ell) &= \frac{75}{127} \left(\frac{L^2}{\ell^2} + 22.45 \frac{L^2}{H^2} \right), \\ c_4 &= -\frac{180}{127} \frac{L^6 q_0}{EAH^4}, & c_5(\ell) &= \frac{300}{227} \frac{L^2}{\ell^2}, \\ c_6(\ell) &= \frac{300}{2724} \frac{EAH^2}{q_0 L \ell^2}, & c_7 &= -\frac{12}{2724} \frac{EAH^2}{q_0 L^3}, \end{aligned} \quad (24)$$

where H is the thickness of the beam. The system of differential equations in the present nondimensionalized form reads:

$$\boxed{\begin{aligned} c_1 \phi - c_2 \tilde{w}' - c_3 \phi'' - c_4 \tilde{w}'' + \phi^{\text{IV}} &= \tilde{m} \\ c_5 \tilde{w}'' - c_6 \phi' + \tilde{w}^{\text{IV}} + c_7 \phi''' &= \tilde{q}. \end{aligned}} \quad (25)$$

These equations are implemented using Mathematica [12] for further numerical investigation.

4 Numerical solution

According to Fig. 2 the physical boundary conditions of the problem are identified as:

$$\tilde{m} = 0, \quad V = 0, \quad \tilde{q} = \frac{EI}{P}, \quad (26)$$

whereas the geometrical boundary conditions are:

$$\begin{aligned} \tilde{w}(\tilde{x} = 0) = 0, \quad \tilde{w}(\tilde{x} = 1) = 0, \quad \tilde{w}'(\tilde{x} = 0) = 0, \quad \tilde{w}'(\tilde{x} = 1) = 0, \\ \phi(\tilde{x} = 0) = 0, \quad \phi(\tilde{x} = 1) = 0, \quad \phi'(\tilde{x} = 0) = 0, \quad \phi'(\tilde{x} = 1) = 0. \end{aligned} \quad (27)$$

Table 13: Dimensions, loads and material parameters.

L	W	H	E	G	ℓ	q_0
80 μm	20 μm	20 μm	3.8 GPa	1.9 GPa	16 μm	10 $\frac{\text{kN}}{\text{m}}$

For a beam with the dimensions, loads and material parameters shown in Table 13, Mathematica numerically computes a solution to the ordinary differential equations (25) after incorporating the prescribed boundary conditions. It should be noted that the ratio of length to thickness is 4 : 1, which is no longer in the range of the classical EULER-BERNOULLI beam model. For a verification of the numerical method, the material length scale parameter ℓ is set equal to zero. The resulting differential equations are derived by modifying Eqs. (20)–(21). The analytical solution w_{T} for the classical TIMOSHENKO model,

$$w_{\text{T}}(x = \frac{L}{2}) = \frac{q_0 L^2}{48EI} \left(\frac{L^2}{4} + \frac{H^2}{\kappa} \right), \quad (28)$$

is then approximated by the numerical solution with a difference of about $10\ \mu\%$ for a wide range of dimensions. In Figure 3 the deflection line $w(\tilde{x})$ and the rotation angle $\phi(\tilde{x})$ are shown, both taking into account higher-order terms.

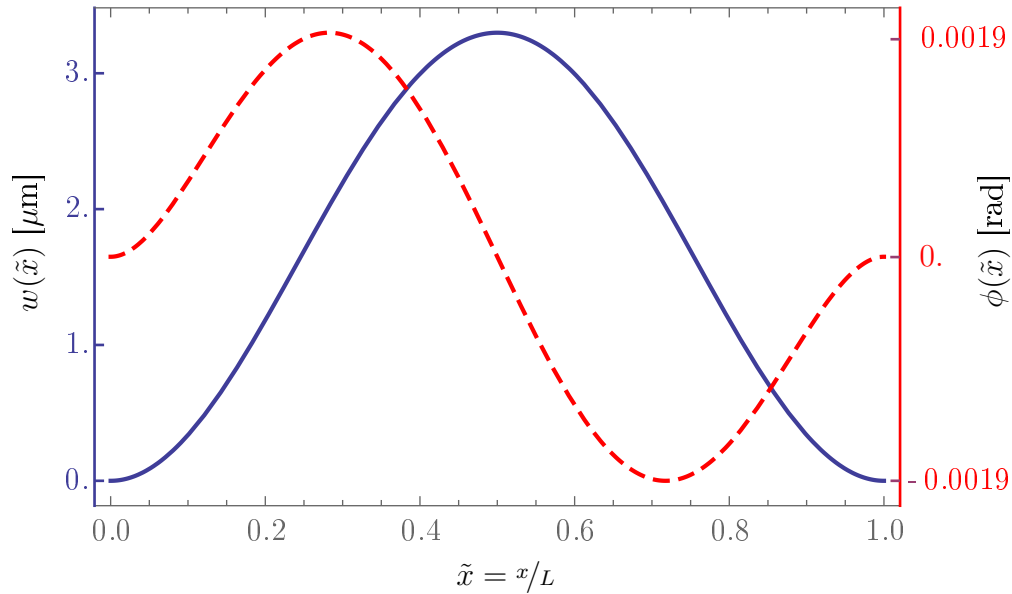


Figure 3: Plot of the deflection line (blue) and the rotation angles (dashed, red).

The solution is in good agreement to the boundary conditions stated in Eqs. (27). A size effect becomes evident when evaluating different beam thicknesses. Figure 4 shows the ratio of maximum deflection of (a) the classical analytical solution of TIMOSHENKO's beam equation w_T and (b) the numerically computed maximum deflection $w_{\text{num}}^{\text{MSG}}$ for the presented modification employing the strain gradient. We considered a short rectangular beam with a range of thicknesses between $10\text{--}60\ \mu\text{m}$.

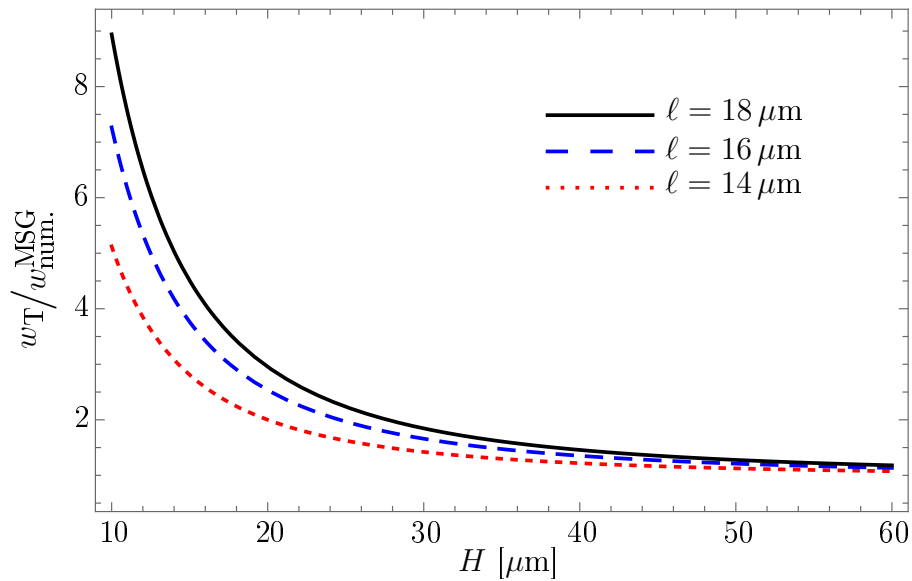


Figure 4: The ratio of maximum deflections from the classical to the higher-order model, plotted for different material length scale parameters.

The figure shows that the ratio w_T/w_{num}^{MSG} increases for decreasing thicknesses. Here, the modified model yields up to eight times higher bending rigidities in comparison to the classical analytical solution. For high thickness values, both models converge to the same values. This so-called size effect is increased for larger material length scale parameters, as demonstrated with the values: $\ell = 14, 16$ and $18 \mu\text{m}$.

References

- [1] Cuenot S., Fretigny C., Demoustier-Champagne S., Nysten B.: *Surface tension effect on the mechanical properties of nanomaterials measured by atomic force microscopy*. Physical Review B, **69**, pp. 01–05 (2004)
- [2] Eringen A.C.: *Nonlocal Continuum field theories*. Springer-Verlag, New York (2010)
- [3] Fleck N.A., Hutchinson J.W.: *Strain gradient plasticity*. In: Hutchinson J.W., Wu T.Y. (Eds.), *Advances in Applied Mechanics*, **33**, Academic Press, New York, pp. 295–361 (1997)
- [4] Guo X.H., Fang D.N., Li X.D.: *Measurement of deformation of pure Ni foils by speckle pattern interferometry*. Mechanical in Engineering, **27**(2), pp. 21–25 (2005)
- [5] Kahrobaiyan M.H., Asghari M., Rahaeifard M., Ahmadian M.T.: *Investigation of the size effect on the flexural characteristic of Timoshenko beams based on the couple stress theory*. International Journal of Engineering Science, **48**(12), pp. 1985–1994 (2010)
- [6] Koiter W.T.: *Couple-stresses in the theory of elasticity. Pt. I-II*. Proc. Koninkl. Nederland Akad. Wetensch., **67**, pp. 17–44 (1964)
- [7] Lam D.C.C., Yang F., Chong C.M., Wang J., Tong P.: *Experiments and theory in strain gradient elasticity*. J. Mech. Phys. Sol., **51**(8), pp. 1477–1508 (2003)
- [8] Lazar M.: *Irreducible decomposition of strain gradient tensor in isotropic strain gradient elasticity*. ZAMM Z. Angew. Math. Mech., doi: 10.1002/zamm.201500278 (2016)
- [9] Li X.-F., Wang B.-L., Lee K.Y.: *Size Effect in the Mechanical Response of Nanobeams*. J. of Adv. Research in Mech. Eng., **1**(1), pp. 4–16 (2010)
- [10] Liebold C., Müller W.H.: *Measuring material coefficients of higher gradient elasticity by using AFM techniques and Raman-spectroscopy*. In: Generalized continua as models for materials (Eds. Altenbach H., Forest S., Krivtsov A.), *Advanced Structured Materials* **22**, pp. 255–271 (2013)
- [11] Ma H.M., Gao X.-L., Reddy J.N.: *A microstructure-dependent Timoshenko beam model based on a modified couple stress theory* Journal of the Mechanics and Physics of Solids **56**(12), pp. 3379–3391 (2008)

- [12] Wolfram Research, Inc.: Mathematica, Version 10.1. Champaign, IL (2015)
- [13] McFarland A.W., Colton J.S.: *Role of material microstructure in plate stiffness with relevance to microcantilever sensors*. Journal of Micromechanics and Microengineering, **15**(5), pp. 1060–1067 (2005)
- [14] Mindlin R.D., Tiersten H.F.: *Effects of couple-stresses in linear elasticity*. ARMA, **11**, pp. 415–448 (1962)
- [15] Mindlin R.D., Eshel N.N.: *On first strain-gradient theories in linear elasticity*. International Journal of Solids and Structures, **4**, pp. 109–124 (1968)
- [16] Poole W.J., Ashby M.F., Fleck N.A.: *Micro-hardness of annealed and work-hardened copper polycrystals*. Scripta Materialia, **34**(4), pp. 559–564 (1996)
- [17] Toupin R.A.: *Elastic materials with couple-stresses*. ARMA, **11**, pp. 385–414 (1962)
- [18] Yang F., Chong C.M., Lam D.C.C., Tong P.: *Couple stress based strain gradient theory for elasticity*. International Journal of Solids and Structures, **39**(10), pp. 2731–2743 (2002)

Christian Liebold, Wolfgang H. Müller, Felix A. Reich, Einsteinufer 510587 Berlin, Germany

On correctness of gradient plasticity theory

Lurie S.A., Qi Chengzhi, Belov P.A.
 salurie@mail.ru

Abstract

In contrast to classical elasticity in which there are no scale parameters that characterize the internal structure of the material, in nonlocal theories of elasticity such parameters appear in a natural way. Therefore, gradient theories are suitable for modeling multi-scale effects and are used to solve numerous applications for inhomogeneous structures with an extended internal surface where the degree of influence of scale effects is related to the density of interfaces. Non-local models of continuous media are especially appealing in the simulation of properties of structured materials with submicron and nanoscale internal structures, where the effective properties are largely determined by the scale effects (the cohesion and adhesion interaction effects). There is no doubt that the non-local models are also promising with the study of elastic-plastic deformations. Generalized elasticity theories even for isotropic materials include many additional physical constants, experimental determination of which is difficult or even impossible. Therefore, applied theories with a small number of additional physical parameters are of considerable interest. However, the process of reduction of nonlocal theories, which has the goal to reduce the number of additional parameters, is not quite trivial and can lead to incorrect theories. In this paper we consider non-local theories of media with defects fields, gradient theories of elasticity and plasticity.

We give a construction of kinematic model of media with the fields of conserved defects, determine the free and constrained deformations, formulate the basic kinematic relations, and make up complete lists of arguments for the formulation of variational models of deformation of different options of media models. The variational equation for dissipative models and Lagrangian for reversible models also proposed.

It is noted that the kinematic models built on the basis of kinematics restrictions for the constrained and free distortions (consistent and inconsistent distortions/deformations), that may be considered as the criteria of the correctness of theories of defective media and gradient plasticity theories. We give a revision of versions of theories, of media with defects fields, where the properties of integrability and generalized Cauchy relations are unjustifiably attributed to the total strains.

1 Introduction

Generalized models of continuous medias, the development of which is related to the fundamental works [1]–[3], are promising for modeling the properties of various micro/nanostructures in which the effects of both interaction of cohesion and adhesion and other manifestations of scale effects may be of crucial importance [4]–[14]. The applications of applied gradient theories are associated not only with the problems of the theory of elasticity, but also with the objectives of thermo-elastic-plasticity [15], thermal conductivity and diffusion [16], multiphase materials [17]. In formulation of models, the variational approach is the most correct and complete, the variational model allows us to formulate a concerted equations of balance (movement) of the media and the boundary problem as a whole. At the same time, kinematic model of the media and the physical model are linked and coordinated. In this paper we formulate the kinematic model, identify free and constrained deformations and draw up the lists of items for the formulation of variational models of deformation of different options of media models. It is proposed to use the kinematic models constructed on the basis of definitions of consistent and inconsistent generalized deformations as criterias for the correctness of theories of defective medias and gradient plasticity theories. We formulate the variational equation for reversible models of medias. We write the conditions allowing to formulate formally the conditions of potentiality or its absence for density of energy. It is presented the general form of variational equations for the description of deformation processes of the dissipative medias, consistent in terms of the variational approach. It is shown that the proposed approach makes it possible to formulate correct physical models of dissipative processes of deformation and write down a complete system of equations and boundary conditions determining the mathematical model.

Generalized models of continuous medias, the development of which is related to the fundamental works [1]–[3], are promising for modeling the properties of various micro/nanostructures in which the effects of both interaction of cohesion and adhesion and other manifestations of scale effects may be of crucial importance [4]–[14]. The applications of applied gradient theories are associated not only with the problems of the theory of elasticity, but also with the objectives of thermo-elastic-plasticity [15], thermal conductivity and diffusion [16], multiphase materials [17].

In formulation of models, the variational approach is the most correct and complete, the variational model allows us to formulate a concerted equations of balance (movement) of the media and the boundary problem as a whole. At the same time, kinematic model of the media and the physical model are linked and coordinated. In this paper we formulate the kinematic model, identify free and constrained deformations and draw up the lists of items for the formulation of variational models of deformation of different options of media models. It is proposed to use the kinematic models constructed on the basis of definitions of consistent and inconsistent generalized deformations as criterias for the correctness of theories of defective medias and gradient plasticity theories. We formulate the variational equation for reversible models of medias. We write the conditions allowing to formulate formally the conditions of potentiality or its absence for density of energy. It is presented the general form of variational equations for the description of deformation processes of

the dissipative medias, consistent in terms of the variational approach. It is shown that the proposed approach makes it possible to formulate correct physical models of dissipative processes of deformation and write down a complete system of equations and boundary conditions determining the mathematical model.

2 Kinematics of defective media

We suppose that the defective mediums are considered. Kinematics of a defective medium is determined not only by the vector field of displacements R_i , but also by the second rank tensor field of inconsistent (free) distortions D_{ij} . The inconsistency D_{ij} is given by the equation: $\Xi_{ij} = D_{im,n}e_{mnj} \neq 0$, where Ξ_{ij} is the tensor of density of dislocations(tensor De Vita). The symmetric part of the field D_{ij}^2 is a field of inconsistent (free and non-integrable) strains $\varepsilon_{ij}^{\text{free}} = (D_{ij} + D_{ji})/2$. By definition, a tensor field of free distortions D_{ij} can not be represented in the form of a gradient of some vector field. Simultaneously with the free (inconsistent) distortions there are also integrable distortions. In contrast, the field of constrained (integrable) distortions is defined as the gradient of the displacements field. Such a field of distortions will be denoted by the superscript equal to unity: $d_{ij} = R_{i,j}$. Consequently, the total field of distortions (deformations) along with an inconsistent part must also contain the consistent part:

$$D_{ij}^{\text{full}} = d_{ij} + D_{ij} = R_{i,j} + D_{ij}, \quad d_{ij} = R_{i,j}. \quad (1)$$

The total field of distortions D_{ij} is not consistent:

$$D_{im,n}^{\text{full}}e_{mnj} = d_{im,n}e_{mnj} + D_{im,n}e_{mnj} = R_{i,mn}e_{mnj} + D_{im,n}e_{mnj} = 0 + D_{im,n}e_{mnj} \neq 0. \quad (2)$$

Quite often the physical sense of plastic deformations is prescribed to the tensor $\varepsilon_{ij}^{\text{free}}$, and the physical sense of the elastic deformations is prescribed to the tensor $\varepsilon_{ij}^e = (d_{ij} + d_{ji})/2 = (R_{i,j} + R_{j,i})/2$.

We will show that both of these statements should be used with extreme caution. Below we'll give the examples of theories with reversible deformation processes, containing non-integrable (free or, as they are interpreted, plastic) deformations / distortions. At the same time, it is quite justified to interpret the free distortions as plastic, for two reasons. Firstly, they are associated with the field of defects – dislocations, and therefore, they are free or not integrable and are not related to the displacements field (although, they are continuous). Secondly, in the classical theory of plasticity, dissipative processes are usually associated exactly with plastic deformations/distortions. Here we note that the Cauchy relation is valid only for constrained distortions, and not for the total ones, as it is often treated in many studies. This follows directly from the definition of constrained and free distortions. Therefore, equations (1), (2) may be a criterion for the correctness of the kinematic theory.

Now let's go back to the interpretation of free distortions as plastic in terms of dissipative processes. Using the feature of dissipativeness for such an interpretation is not entirely correct. Indeed, in this work, we will show that there are models of dissipative processes of deformations, where only constrain deformations/distortions

are used as the kinematic variables. Thus, dissipative processes can occur in completely defect-free environments where the traditional kinematic model of elasticity determined only by constrained, integrable distortions is used. The reversibility and irreversibility of the deformation process is determined only by the physical model (not by the kinematic model) which ultimately allows you to conclude whether or not there is the potential energy of deformation.

3 Physical models of defective media

We use a variational approach which by the selected kinematic model allows to construct the variational equation recorded in variations (Sedov's equation), to obtain Green's formulas and to use them to determine force model of the theory. Regardless of the choice of dissipative or reversible model of deformation, we establish from Sedov variational equation the equilibrium equations and the whole range of boundary value problems.

We present an algorithm for constructing physical models of medias with the fields of conserved [18], [19] dislocations, ie the medias, the kinematic model of which is determined by the vector of displacements R_i , by two kinds of distortions d_{ij} , D_{ij} and two kinds of curvatures $d_{ij,k}$, $D_{ij,k}$. For such a kinematic model, the principle of possible displacements allows to present uniquely the linear variational form of possible work of external and internal forced factors:

$$\bar{\delta}L = \delta A - \iiint [\sigma_{ij}^\alpha \delta D_{ij}^\alpha + m_{ijk}^\alpha \delta D_{ij,k}^\alpha] dV. \quad (3)$$

Here $\bar{\delta}L$ is generally non integrable linear variation form which in the case of integrability coincides with the Lagrangian variation. $A = \iiint P_i^V R_i dV + \iint P_i^F R_i dF$ is the work of the external volume P_i^V and external surface forces P_i^F , $D_{ij}^1 \equiv d_{ij}$, $D_{ij}^2 \equiv D_{ij}$, σ_{ij}^α are the stresses of two types, producing work respectively on constrained and free of distortions; m_{ijk}^α are moment stresses of two kinds; α is the grade index that takes values 1 and 2.

The condition for the existence of bulk density of the potential energy U_V in (3) are the generalized Green's formulas:

$$\sigma_{ij}^\alpha = \frac{\partial U_V}{\partial D_{ij}^\alpha}, \quad m_{ijk}^\alpha = \frac{\partial U_V}{\partial D_{ij,k}^\alpha}. \quad (4)$$

When the conditions (4) are satisfied, linear variation form is integrable and provides the definition of the Lagrangian L of corresponding reversible theory:

$$\begin{aligned} \delta L &= \delta \left(A - \iiint U_V dV \right) = \delta A - \iiint [\sigma_{ij}^\alpha \delta D_{ij}^\alpha + m_{ijk}^\alpha \delta D_{ij,k}^\alpha] dV = \\ &= \delta A - \iiint \left[\frac{\partial U_V}{\partial D_{ij}^\alpha} \delta D_{ij}^\alpha + \frac{\partial U_V}{\partial D_{ij,k}^\alpha} \delta D_{ij,k}^\alpha \right] dV. \end{aligned} \quad (5)$$

If the linear variation form in (5) is non integrable, the model defines the theory of some dissipative processes of deformation. Then, instead of (4), there are more

general relations:

$$\sigma_{ij}^\alpha = \frac{\partial U_V}{\partial D_{ij}^\alpha} + \bar{\sigma}_{ij}^\alpha, \quad m_{ijk}^\alpha = \frac{\partial U_V}{\partial D_{ij,k}^\alpha} + \bar{m}_{ijk}^\alpha. \quad (6)$$

Where $\bar{\sigma}_{ij}^\alpha$ and \bar{m}_{ijk}^α are components of tensors of the second and third rank, respectively, which can not be presented as partial derivatives of some function of distortions and their gradients. In this respect, there is some analogy with (1): the first term in it has the potential, and the second one has no potential. From (4) and (6) we have:

$$\begin{aligned} \frac{\partial \sigma_{ij}^\alpha}{\partial D_{mn}^\beta} - \frac{\partial \sigma_{mn}^\beta}{\partial D_{ij}^\alpha} &= 2\bar{C}_{ijmn}^{\alpha\beta} = -2\bar{C}_{mnij}^{\beta\alpha}, \\ \frac{\partial m_{ijk}^\alpha}{\partial D_{mn,l}^\beta} - \frac{\partial m_{mnl}^\beta}{\partial D_{ij,k}^\alpha} &= 2\bar{C}_{ijkmnl}^{\alpha\beta} = -2\bar{C}_{mnljik}^{\beta\alpha}. \end{aligned} \quad (7)$$

Upper Greek indices are grade indices (take the values 1 and 2).

It is easily seen that for reversible deformation processes $\bar{C}_{ijmn}^{\alpha\beta} = 0$ and $\bar{C}_{ijkmnl}^{\alpha\beta} = 0$, and for the irreversible (dissipative processes) $\bar{C}_{ijmn}^{\alpha\beta} \neq 0$ and $\bar{C}_{ijkmnl}^{\alpha\beta} \neq 0$.

We rewrite (7) for reversible processes in the following form:

$$\begin{aligned} \frac{\partial \sigma_{ij}^\alpha}{\partial D_{mn}^\beta} &= \frac{\partial \sigma_{mn}^\beta}{\partial D_{ij}^\alpha} = C_{ijmn}^{\alpha\beta} = C_{mnij}^{\beta\alpha}, \\ \frac{\partial m_{ijk}^\alpha}{\partial D_{mn,l}^\beta} &= \frac{\partial m_{mnl}^\beta}{\partial D_{ij,k}^\alpha} = C_{ijkmnl}^{\alpha\beta} = C_{mnljik}^{\beta\alpha}. \end{aligned} \quad (8)$$

From equations (8) it follow that tensors of the fourth $C_{ijmn}^{\alpha\beta}$ and sixth grade $C_{ijkmnl}^{\alpha\beta}$ have the physical meaning of tensors of elastic moduli. By analogy, it is possible to treat the tensors of the fourth $\bar{C}_{ijmn}^{\alpha\beta}$ and sixth grade $\bar{C}_{ijkmnl}^{\alpha\beta}$ as tensors that have a physical meaning of tensors of dissipative modules. Taking into account (7) and (8), we can obtain:

$$\begin{aligned} \frac{\partial \sigma_{ij}^\alpha}{\partial D_{mn}^\beta} &= C_{ijmn}^{\alpha\beta} + \bar{C}_{ijmn}^{\alpha\beta}, \\ \frac{\partial m_{ijk}^\alpha}{\partial D_{mn,l}^\beta} &= C_{ijkmnl}^{\alpha\beta} + \bar{C}_{ijkmnl}^{\alpha\beta}. \end{aligned} \quad (9)$$

The sort of distortions does not influence at all the fact whether the physical model describes the reversible or irreversible processes. It is determined only by the symmetry of the tensors $C_{ijmn}^{\alpha\beta}$, $\bar{C}_{ijmn}^{\alpha\beta}$, and also of the tensors $C_{ijkmnl}^{\alpha\beta}$ and $\bar{C}_{ijkmnl}^{\alpha\beta}$:

$$\begin{aligned} C_{ijmn}^{\alpha\beta} &= C_{mnij}^{\beta\alpha}, & \bar{C}_{ijmn}^{\alpha\beta} &= -\bar{C}_{mnij}^{\beta\alpha}, \\ C_{ijkmnl}^{\alpha\beta} &= C_{mnljik}^{\beta\alpha}, & \bar{C}_{ijkmnl}^{\alpha\beta} &= -\bar{C}_{mnljik}^{\beta\alpha}. \end{aligned}$$

Note that the reversible and irreversible models (9) in a particular case can be formulated in a physically linear statement. Indeed, if we hypothesize that in (9) tensors

of four and six rank are independent of distortions and curvatures components, the relations (9) can be integrated and we can obtain the corresponding special case of linear equations of Hooke's law:

$$\sigma_{ij}^\alpha = (C_{ijmn}^{\alpha\beta} + \bar{C}_{ijmn}^{\alpha\beta})D_{mn}^\beta, \quad m_{ijk}^\alpha = (C_{ijkmnl}^{\alpha\beta} + \bar{C}_{ijkmnl}^{\alpha\beta})D_{mn,l}^\beta. \quad (10)$$

For the physically linear medias (10), the expression of possible work (3) takes the form:

$$\begin{aligned} \bar{\delta}L &= \delta A - \iiint [\sigma_{ij}^\alpha \delta D_{ij}^\alpha + m_{ijk}^\alpha \delta D_{ij,k}^\alpha] dV = \\ &= \delta A - \iiint [(C_{ijmn}^{\alpha\beta} + \bar{C}_{ijmn}^{\alpha\beta})D_{mn}^\beta \delta D_{ij}^\alpha + \\ &\quad + (C_{ijkmnl}^{\alpha\beta} + \bar{C}_{ijkmnl}^{\alpha\beta})D_{mn,l}^\beta \delta D_{ij,k}^\alpha] dV = \\ &= \delta \left\{ A - \frac{1}{2} \iiint [C_{ijmn}^{\alpha\beta} D_{ij}^\alpha D_{mn}^\beta + C_{ijkmnl}^{\alpha\beta} D_{ij,k}^\alpha D_{mn,l}^\beta] dV \right\} - \\ &\quad - \iiint [\bar{C}_{ijmn}^{\alpha\beta} D_{mn}^\beta \delta D_{ij}^\alpha + \bar{C}_{ijkmnl}^{\alpha\beta} D_{mn,l}^\beta \delta D_{ij,k}^\alpha] dV = \\ &= \delta L - \frac{1}{2} \iiint [\bar{C}_{ijmn}^{\alpha\beta} (D_{mn}^\beta \delta D_{ij}^\alpha - D_{ij}^\alpha \delta D_{mn}^\beta) + \\ &\quad + \bar{C}_{ijkmnl}^{\alpha\beta} (D_{mn,l}^\beta \delta D_{ij,k}^\alpha - D_{ij,k}^\alpha \delta D_{mn,l}^\beta)] dV. \end{aligned} \quad (11)$$

Relation (11) can be formulated as a **theorem 1**:

"Any physical linear reversible model can be associated with dissipative model by the addition of possible work of all dissipation channels that are permissible within the selected kinematic model to the Lagrangian variation of the reversible model". Here, by the channel of dissipation we understand non integrable linear variational form (see also [20]):

$$\begin{aligned} &\frac{1}{2} \iiint e_{ijmn}^A (D_{mn}^\beta \delta D_{ij}^\alpha - D_{ij}^\alpha \delta D_{mn}^\beta) dV, \\ &\frac{1}{2} \iiint e_{ijkmnl}^B (D_{mn,l}^\beta \delta D_{ij,k}^\alpha - D_{ij,k}^\alpha \delta D_{mn,l}^\beta) dV. \end{aligned} \quad (12)$$

Here e_{ijmn}^A and e_{ijkmnl}^B are the components of the orthonormal bases in the space of tensors of fourth and sixth order. Each of $3(A + B)$ channels of dissipation is associated with its own dissipative module. Indeed, let's present the tensors of dissipative modules in the form of expansions on the basis tensors:

$$\bar{C}_{ijmn}^{\alpha\beta} = \bar{C}_A^{\alpha\beta} e_{ijmn}^A, \quad \bar{C}_{ijkmnl}^{\alpha\beta} = \bar{C}_B^{\alpha\beta} e_{ijkmnl}^B. \quad (13)$$

Substituting (13) into (11), (12) we obtain:

$$\begin{aligned} \bar{\delta}L &= \delta L - \\ &\quad - \bar{C}_A^{\alpha\beta} \frac{1}{2} \iiint [e_{ijmn}^A (D_{mn}^\beta \delta D_{ij}^\alpha - D_{ij}^\alpha \delta D_{mn}^\beta)] dV - \\ &\quad - \bar{C}_B^{\alpha\beta} \frac{1}{2} \iiint [e_{ijkmnl}^B (D_{mn,l}^\beta \delta D_{ij,k}^\alpha - D_{ij,k}^\alpha \delta D_{mn,l}^\beta)] dV \end{aligned} \quad (14)$$

From equation (14) it follows that the number of channels of dissipation is equal to the number of dissipative modules $\bar{C}_A^{\alpha\beta}$ and $\bar{C}_B^{\alpha\beta}$.

4 Variational formulation of physically linear reversible theories

For the formulation of physically linear reversible models of media with field of defects, we will Lagrange principle. From the requirement of the stationarity of Lagrangian (5) follow the Euler equations and the entire spectrum of the boundary value problems:

$$\begin{aligned}
 \delta L &= \delta A - \iiint [\sigma_{ij}^\alpha \delta D_{ij}^\alpha + m_{ijk}^\alpha \delta D_{ij,k}^\alpha] dV = \\
 &= \delta A - \iiint [\sigma_{ij}^\delta d_{ij} + s_{ij} \delta D_{ij} + m_{ijk}^\delta d_{ij,k} + \beta_{ijk}^\delta D_{ij,k}] dV = \\
 &= \delta A - \iiint [(\sigma_{ij} - m_{ijk,k}) \delta R_{i,j} + (s_{ij} - \beta_{ijk,k}) \delta D_{ij}] dV + \\
 &\quad + \iint \{-m_{ijk} n_k \delta R_{i,j} - \beta_{ijk} n_k \delta D_{ij}\} dF = \\
 &= \iiint [(\sigma_{ij,j} - m_{ijk,kj} + P_i^V) \delta R_i - (s_{ij} - \beta_{ijk,k}) \delta D_{ij}] dV + \\
 &\quad + \iint \{[P_i^F - (\sigma_{ij} - m_{ijk,k}) n_j + (m_{ijk} n_k)_{,p} \delta_{pj}^*] \delta R_i - \\
 &\quad - m_{ijk} n_j n_k \delta (R_{i,p} n_p) - \beta_{ijk} n_k \delta D_{ij}\} dF - \\
 &\quad - \sum \oint m_{ijk} v_j n_k \delta R_i ds = 0.
 \end{aligned} \tag{15}$$

Here $D_{ij}^1 \equiv d_{ij}$, $D_{ij}^2 \equiv D_{ij}$, $\sigma_{ij}^1 \equiv \sigma_{ij}$, $\sigma_{ij}^2 \equiv s_{ij}$, $m_{ijk}^1 \equiv m_{ijk}$, $m_{ijk}^2 \equiv \beta_{ijk}$.

The static model of physically linear reversible theories is determined by the particular case of the system (10):

$$\begin{cases} \sigma_{ij} = C_{ijmn}^{11} R_{m,n} + C_{ijmn}^{12} D_{mn}, \\ s_{ij} = C_{ijmn}^{21} R_{m,n} + C_{ijmn}^{22} D_{mn}, \end{cases} \quad \begin{cases} m_{ijk} = C_{ijkmnl}^{11} R_{m,nl} + C_{ijkmnl}^{12} D_{mn,l}, \\ \beta_{ijk} = C_{ijkmnl}^{21} R_{m,nl} + C_{ijkmnl}^{22} D_{mn,l}. \end{cases} \tag{16}$$

In this way, physically linear reversible theory of defective medias with the fields of conserved dislocations [18]–[20] is generally defined by twelve equilibrium equations:

$$\sigma_{ij,j} - m_{ijk,kj} + P_i^V = 0, \quad \sigma_{ij} - \beta_{ijk,k} = 0. \tag{17}$$

The spectrum of the boundary value problems is defined by fifteen pares of alternate the system of the boundary conditions in each non-singular point of the body surface:

$$\begin{cases} [P_i^F - (\sigma_{ij} - m_{ijk,k}) n_j + (m_{ijk} n_k)_{,p} \delta_{pj}^*] \delta R_i = 0, \\ m_{ijk} n_j n_k \delta (R_{i,p} n_p) = 0, \\ \beta_{ijk} n_k \delta D_{ij} = 0. \end{cases} \tag{18}$$

In the special points of the body surface (on surface edges) there are additional conditions for continuity of the vector of displacements R_i and the vector of meniscus forces $m_{ijk}^1 v_j n_k$ at the transition of the body surface through the rib.

In the result variational equation (15) define the mathematical statement of the common enough model of media with defects for the reversible processes including constitutive equations (16), equilibrium equations (17) and the boundary conditions (18).

4.1 Particular theories

Let's consider as the particular cases of the theory (15) the gradient theory of Mindlin –Toupin [1], [3]. Assume that the kinematic model of the media does not allow the existence of conserved dislocations or fields of free distortion. Then the Lagrangian (15) coincides with the Lagrangian of the theory of Mindlin-Toupin:

$$L = A - \frac{1}{2} \iiint (C_{ijmn} R_{i,j} R_{m,n} + C_{ijkml} R_{i,jk} R_{m,nl}) dV.$$

Static model (constitutive equations) of such gradient theory is determined by the particular case of the system (10), (16):

$$\sigma_{ij} = C_{ijmn} D_{mn}, \quad m_{ijk} = C_{ijkml} D_{mn,l}.$$

Accordingly, the Euler equations are defined by three equations of equilibrium of high order relatively to classical equations of the fourth order (in displacements):

$$\sigma_{ij,j} m_{ijk,kj} + P_i^V = 0.$$

The spectrum of the boundary value problems is defined by six pares of alternate boundary conditions in each non-singular point of the surface of the body:

$$\begin{cases} [P_i^F - (\sigma_{ij} - m_{ijk,k}) n_j + (m_{ijk} n_k)_{,p} \delta_{pj}^*] \delta R_i = 0, \\ m_{ijk}^1 n_j n_k \delta (R_{i,p} n_p) = 0. \end{cases}$$

As in general theory, in the singular points of the body surface (on surface edges) there are additional conditions for continuity of the vector of displacements R_i and the vector of meniscus forces $m_{ijk} v_j n_k$ at the transition of the body surface through the rib.

As the second particular case let us consider the theory of defective medium. Assume that the tensors of modules in (16) are such that ${}^{11}_{ijkml} = {}^{12}_{ijkml} = {}^{21}_{ijkml} = 0$. Then the Lagrangian (15) coincides with the Lagrangian of Mindlin theory cite2:

$$L = A - \frac{1}{2} \iiint (C_{ijmn}^{11} R_{i,j} R_{m,n} + 2C_{ijmn}^{12} R_{i,j} D_{mn} + C_{ijmn}^{22} D_{ij} D_{mn} + C_{ijkml} D_{ij,k} D_{mn,l}) dV.$$

The static model of Mindlin theory is determined by the particular case of the system (10), (16):

$$\begin{cases} \sigma_{ij} = C_{ijmn} R_{m,n} + C_{ijmn}^{12} D_{mn}, & \begin{cases} m_{ijk} = 0 \\ \beta_{ijk} = C_{ijkml} D_{mn,l}, \end{cases} \\ s_{ij} = C_{ijmn}^{21} R_{m,n} + C_{ijmn}^{22} D_{mn}, \end{cases}$$

Accordingly, the Euler equations (see (17)) are determined by twelve equations:

$$\sigma_{ij,j} + P_i^V = 0, \quad s_{ij} - \beta_{ijk,k} = 0.$$

The spectrum of the boundary value problems (see ((18)) is defined by twelve pares of alternate boundary conditions in each non-singular point of the surface body:

$$(P_i^F - \sigma_{ij} n_j) \delta R_i = 0, \quad \beta_{ijk} n_k \delta D_{ij} = 0.$$

In the Mindlin's type theory (22) there are no additional conditions on the surface edges.

Let's pay attention to the fact that, the formulated theory (15) has place for the reversible processes. However, there are free distortions and their gradients. This confirms the some incorrectness of the interpretation of the tensor of inconsistent deformities $\varepsilon_{ij}^{\text{free}} = (D_{ij} + D_{ji})/2$ as the tensor of plastic deformations, because plasticity is a dissipative property.

5 The variational formulation of physically linear irreversible theories

Using the definition of possible work of all static factors and equating it to zero, we can get instead (15) the following Sedov's variational equation for physically linear irreversible theories:

$$\begin{aligned} \bar{\delta}L = & \delta\left\{A - \frac{1}{2} \iiint [C_{ijmn}^{\alpha\beta} D_{ij}^{\alpha} D_{mn}^{\beta} + C_{ijkml}^{\alpha\beta} D_{ij,k}^{\alpha} D_{mn,l}^{\beta}] dV\right\} - \\ & - \frac{1}{2} \iiint [\bar{C}_{ijmn}^{\alpha\beta} (D_{mn}^{\beta} \delta D_{ij}^{\alpha} - D_{ij}^{\alpha} \delta D_{mn}^{\beta}) + \\ & + \bar{C}_{ijkml}^{\alpha\beta} (D_{mn,l}^{\beta} \delta D_{ij,k}^{\alpha} - D_{ij,k}^{\alpha} \delta D_{mn,l}^{\beta})] dV = 0, \end{aligned} \quad (19)$$

here $C_{ijmn}^{\alpha\beta} (D_{mn}^{\beta} \delta D_{ij}^{\alpha} + D_{ij}^{\alpha} \delta D_{mn}^{\beta})$ is the variation of the bilinear part of the potential energy, $\bar{C}_{ijmn}^{\alpha\beta} (D_{mn}^{\beta} \delta D_{ij}^{\alpha} - D_{ij}^{\alpha} \delta D_{mn}^{\beta})$ is the non integrable variational form, which define the channels of the dissipation

The static model for physically linear irreversible theories is determined from (19) and can be written as (see (10)):

$$\begin{cases} \sigma_{ij} = (C_{ijmn} + \bar{C}_{ijmn}) R_{m,n} + (C_{ijmn}^{12} + \bar{C}_{ijmn}^{12}) D_{mn}, \\ \sigma_{ij}^2 = (C_{ijmn}^{21} + \bar{C}_{ijmn}^{21}) R_{m,n} + (C_{ijmn}^{22} + \bar{C}_{ijmn}^{22}) D_{mn}, \\ m_{ijk} = (C_{ijkml}^{11} + \bar{C}_{ijkml}^{11}) R_{m,nl} + (C_{ijkml}^{12} + \bar{C}_{ijkml}^{12}) D_{mn,l}, \\ \beta_{ijk} = (C_{ijkml}^{21} + \bar{C}_{ijkml}^{21}) R_{m,nl} + (C_{ijkml}^{22} + \bar{C}_{ijkml}^{22}) D_{mn,l}, \end{cases} \quad (20)$$

By example we consider the stresses of first grade. They can be represented as a sum of reversible and irreversible parts (20):

$$\begin{aligned} \sigma_{ij} &= (C_{ijmn} + \bar{C}_{ijmn}) R_{m,n} + (C_{ijmn}^{12} + \bar{C}_{ijmn}^{12}) D_{mn} = \\ &= (C_{ijmn} R_{m,n} + C_{ijmn}^{12} D_{mn}) + (\bar{C}_{ijmn} R_{m,n} + \bar{C}_{ijmn}^{12} D_{mn}). \end{aligned}$$

The reversible part of the stresses depends on both constrain and free distortions with the tensors of reversible modules C_{ijmn}^{11} , C_{ijmn}^{12} . The irreversible part of the stresses also depends on both sorts of distortions, but with another set of tensors of modules – with the dashed modules \bar{C}_{ijmn}^{11} , \bar{C}_{ijmn}^{12} .

In expanded form, Sedov's equation becomes:

$$\begin{aligned}
 & \iiint [(\sigma_{ij,j} - m_{ijk,kj} + P_i^V)\delta R_i - (s_{ij} - \beta_{ijk,k})\delta D_{ij}] dV + \\
 & + \iint \{ [P_i^F - (\sigma_{ij} - m_{ijk,k})n_j + (m_{ijk}n_k)_{,p}\delta_{pj}^*] \delta R_i - \\
 & - m_{ijk}n_jn_k\delta(R_{i,p}n_p) - \beta_{ijk}n_k\delta D_{ij} \} dF - \\
 & - \sum \oint m_{ijk}v_jn_k\delta R_i ds = 0.
 \end{aligned} \tag{21}$$

It is easy to make sure that the dissipative (21) and reversible (15) models have the same form, being recorded in the static factors.

At the same time, the formulation of physically linear irreversible theories in kinematic variables will be different due to other equations of generalized law (20).

5.1 Model of Mindlin–Toupin gradient theory with dissipation

Let us consider Mindlin–Toupin gradient theory for the reversible processes. Then we must assume that $D_{ij} = 0$. Then (19) takes the form:

$$\begin{aligned}
 \bar{\delta}L = \delta \left\{ A - \frac{1}{2} \iiint C_{ijmn}^{11} R_{i,j} R_{m,n} + C_{ijkmnl} R_{i,jk} R_{m,nl} dV \right\} - \\
 - \frac{1}{2} \iiint [\bar{C}_{ijmn} (R_{m,n} \delta R_{i,j} - R_{i,j} \delta R_{m,n}) + \\
 + \bar{C}_{ijkmnl} (R_{m,nl} \delta R_{i,jk} - R_{i,jk} \delta R_{m,nl})] dV = 0.
 \end{aligned} \tag{22}$$

It is easy to see that there are non-zero dissipation channels in the variational equation (22).

Let's note that the formulated theory (22) is a dissipative gradient theory. However this theory is written using only constrain distortions and has not free distortions and their gradients.

This confirms the incorrectness of the interpretation of the tensor of constrain deformations $\varepsilon_{ij} = (d_{ij} + d_{ji})/2 = (R_{i,j} + R_{j,i})/2$ as the tensor of elastic deformations, since the joint deformations allows plasticity, a dissipative property, too.

5.2 Dissipative Landau theory

Taking into account theorem 1 (see (11) in section 3) we can introduce in the list of dissipation channels also the bilinear non-integrable variational forms, containing gradients of velocity fields and write Sedov's equation in the form:

$$\bar{\delta}L = \delta L - \iiint \int \bar{E}_{ijmn}^{(} \dot{R}_{m,n} \delta R_{i,j} - R_{i,j} \delta \dot{R}_{m,n}) dV dt = 0. \tag{23}$$

The qualitative feature of the Landau model (23) is that there are new kinematic variables in it – the distortions of rates. Accordingly, we define the new static factors – tensor of momentums p_{mn} :

$$p_{mn} = \frac{\partial L_V}{\partial \dot{R}_{m,n}} + \bar{E}_{mnij} R_{i,j}. \tag{24}$$

Along with this, the classical stresses get additional terms associated with dissipation:

$$\sigma_{ij} = \frac{\partial L_V}{\partial R_{i,j}} + \bar{E}_{ijmn} \dot{R}_{m,n}. \quad (25)$$

Sedov's equation in this case (24), (25) gives to the following variation equation:

$$\begin{aligned} \delta L = & \delta A - \iiint \int \left\{ \left(\frac{\partial L_V}{\partial R_{i,j}} + \bar{E}_{ijmn} \dot{R}_{m,n} \right) \delta R_{i,j} + \frac{\partial L_V}{\partial R_{i,jk}} \delta R_{i,jk} - \right. \\ & \left. - \rho \dot{R}_m \delta \dot{R}_m + \left(\frac{\partial L_V}{\partial \dot{R}_{m,n}} - \bar{E}_{ijmn} R_{i,j} \right) \delta \dot{R}_{m,n} \right\} dV dt = \\ = & \iiint \int \left\{ \left[\frac{\partial}{\partial x_j} \frac{\partial L_V}{\partial R_{i,j}} - \frac{\partial}{\partial x_j \partial x_k} \frac{\partial L_V}{\partial R_{i,jk}} + \bar{E}_{ijmn}^{11} \dot{R}_{m,nj} - \rho \ddot{R}_i + P_i^V + \right. \right. \\ & \left. \left. + \frac{\partial}{\partial t \partial x_j} \left(\frac{\partial L_V}{\partial \dot{R}_{i,j}} - \bar{E}_{pqij}^{11} R_{p,q} \right) \right] \delta R_i \right\} dV dt - \\ & + \oint \int \left\{ \left[P_i^F - \left(\frac{\partial L_V}{\partial R_{i,j}} - \frac{\partial}{\partial x_k} \frac{\partial L_V}{\partial R_{i,jk}} - \frac{\partial}{\partial t} \frac{\partial L_V}{\partial \dot{R}_{i,j}} \right) n_j + \left(\frac{\partial L_V}{\partial R_{i,jk}} n_k \right)_{,p} \delta_{pj}^* \right] \delta R_i + \right. \\ & \left. + \left(-\frac{\partial L_V}{\partial R_{i,jk}} n_j n_k \right) \delta (R_{i,p} n_p) \right\} dF dt - \sum \oint \int \left(\frac{\partial L_V}{\partial R_{i,jk}} v_j n_k \right) \delta R_i ds dt - \\ & - \left\{ \iiint \left[\rho \dot{R}_m - \frac{\partial}{\partial x_n} \left(\frac{\partial L_V}{\partial \dot{R}_{m,n}} - \bar{E}_{ijmn}^{11} R_{i,j} \right) \right] \delta R_m dV + \right. \\ & \left. + \oint \left(\frac{\partial L_V}{\partial \dot{R}_{m,n}} - \bar{E}_{ijmn}^{11} R_{i,j} \right) n_n \delta R_m dF \right\} \Big|_{t=t_0}^{t=t_k} = 0. \end{aligned} \quad (26)$$

As a result using (26) we can write the equations of motion of dissipative medias in the form:

$$\frac{\partial}{\partial x_j} \frac{\partial L_V}{\partial R_{i,j}} - \frac{\partial}{\partial x_j \partial x_k} \frac{\partial L_V}{\partial R_{i,jk}} - \rho \ddot{R}_i + P_i^V = -\frac{\partial}{\partial t \partial x_j} \frac{\partial L_V}{\partial \dot{R}_{i,j}} - 2\bar{E}_{ijmn}^{11} \dot{R}_{m,nj} \quad (27)$$

The left side of equations (27) is the operator of the reversible theory, and the right one describes the corrections defined by the dissipation.

Boundary problem in (26) still defines six pairs of alternative boundary conditions in each non-singular point of a surface:

$$\begin{cases} \left[P_i^F - \left(\frac{\partial L_V}{\partial R_{i,j}} - \frac{\partial}{\partial x_k} \frac{\partial L_V}{\partial R_{i,jk}} - \frac{\partial}{\partial t} \frac{\partial L_V}{\partial \dot{R}_{i,j}} \right) n_j + \left(\frac{\partial L_V}{\partial R_{i,jk}} n_k \right)_{,p} \delta_{pj}^* \right] \delta R_i = 0, \\ \left(-\frac{\partial L_V}{\partial R_{i,jk}} n_j n_k \right) \delta (R_{i,p} n_p) = 0. \end{cases} \quad (28)$$

As follows from conditions (28) Sedov's equation requires continuity of the vector of displacements R_i in the specific points on the surface (on the surface edges, if any one exist) and the vector of meniscus forces $\left(\frac{\partial L_V}{\partial R_{i,jk}} v_j n_k \right)$ at the transition of the body surface through the rib:

$$\sum \oint \int \left(\frac{\partial L_V}{\partial R_{i,jk}} v_j n_k \right) \delta R_i ds dt = 0.$$

It is important that the Landau theory leads to a boundary value problem on time instead of the Cauchy problem (initial value problem).

$$\left\{ \iiint \left[\rho \dot{R}_m - \frac{\partial}{\partial x_n} \left(\frac{\partial L_V}{\partial \dot{R}_{m,n}} - \bar{E}_{ijmn}^{11} R_{i,j} \right) \right] \delta R_m dV + \iint \left(\frac{\partial L_V}{\partial \dot{R}_{m,n}} - \bar{E}_{ijmn}^{11} R_{i,j} \right) n_n \delta R_m dF \right\} \Bigg|_{t=t_0}^{t=t_k} = 0.$$

6 Conclusion

We formulated the Lagrangian in the case of static problems and we proposed the applied version of the theory, which provides the reduction of the physical constants up to the maximum reduction when the physical properties are determined by the classical elastic moduli. We show that the kinematic model built on the basis of strict concepts for integrable and non-integrable generalized strains can be a criterion of correctness of theories of defective media and gradient theories of plasticity. It is proposed the revision of the variants of theories with defects fields where the integrable properties and generalized Cauchy relations are unreasonably attributed to the total strains. We consider the models of the dynamic dissipative media in which dissipative properties are associated with the strain rates. It is given the formulation of the variation of the dissipative part of energy which provides the dissipativeness properties (properties of the lack of potential). We establish the conditions under which the introduction of energy of dissipation, can be justified formally by comparing the motion equations and boundary conditions with equations obtained correctly using the variation of energy of dissipation.

References

- [1] Toupin, R.A., "Elastic materials with couple stresses," *Arch. Rational Mech. Anal.*, no. 11, pp. 385-414, 1962.
- [2] Mindlin, R.D., "Micro-structure in linear elasticity," *Arch. Rational Mech. Anal.* no.16, pp. 51-78, 1964.
- [3] Mindlin, R.D., Eshel, N.N., "On first strain-gradient theories in linear elasticity," *Int. J. Solids Struct.* no. 4, pp. 109-124, 1968.
- [4] Mindlin, R.D., "Elasticity, piezoelectricity and crystal lattice dynamics," *J. Elasticity.* vol. 2, no. 4, pp. 217-280, 1972.
- [5] Maugin, G.A., "Material forces: concepts and applications," *Appl. Mech. Rev.*, no. 48, pp. 213-245, 1995.
- [6] Maugin, G.A., Alshits, V.I., Kirchner, H.O.K., "Elasticity in multilayers: properties of the propagation matrix and some applications," *Math. Mech. Solids*, no. 6, pp. 481-502, 2001.

-
- [7] Aifantis, K.E., Willis J.R., "The role of interfaces in enhancing the yield strength of composites and polycrystals," *J. Mech. Phys. Solids.*, no 53, pp. 1047–1070, 2005.
- [8] Aifantis, E.C., Exploring the applicability of gradient elasticity to certain micro/nano reliability problems, *Microsystems Technol.* no. 15, pp. 109-115, 2009.
- [9] Guzev, M., Qi, C., Bai, J., and Li, K., Equilibrium equations and boundary conditions of strain gradient theory in arbitrary curvilinear coordinates, *J Mech Behav Mater* vol. 23, no. 5-6, pp. 169–176, 2014.
- [10] Evans, A.G., Hutchinson, J.W., "A critical assessment of theories of strain gradient plasticity," *Acta Mater.*, vol. 57, no. 5, pp.1675-1688, 2009.
- [11] Wang, M. Y., Qi, C.Z., Qian, Q.H., and Chen J.J., One plastic gradient model of zonal disintegration of rock mass near deep level tunnels, *J. of Mining Sci.*, vol. 47, no. 6, pp. 736–744, 2011.
- [12] Lurie, S.A., Belov, P.A., Volkov-Bogorodsky, D.B., Tuchkova, N.P., "Nanomechanical modeling of the nanostructures and dispersed composites," *Comp. Mater. Sci.*, vol. 28, no.3–4, pp.529-539, 2003.
- [13] Lurie, S.A., Belov, P.A., Tuchkova, N. P., "The application of the multiscale models for description of the dispersed composites," *Int. J. Comp. Mater. Sci.*, vol. 36, no. 2, pp.145-152, 2005.
- [14] Lurie, S.A., Belov, P.A., Volkov-Bogorodsky, D.B., Tuchkova, N.P., "Interphase layer theory and application in the mechanics of composite materials," *J. Mat. Sci.* vol. 41, no. 20, pp. 6693-6707, 2006.
- [15] Lurie S., Kalamkarov A., "General theory of continuous media with conserved dislocations," *Int. J. Solids Struct.*, no 44, pp. 7468-7485, 2007.
- [16] Forest S. and Aifantis, E.C., "Some links between recent gradient thermo-elasto-plasticity theories and the thermodynamics of generalized continua," *Int. J. Solids Struct.*, no. 47, pp. 3367-3376, 2010.
- [17] Askes H. and Aifantis, E.C., "Gradient elasticity in statics and dynamics an overview of formulations, length, scale identifications procedures, finite element implementation procedures and new results," *Int. J. Solids Struct.*, no. 48, pp. 1962–1990, 2011.
- [18] Lurie, S. A. and Belov, P. A., Theory of media with conserved dislocations. Particular cases: The Cosserat and Aero-Kuvshinskii continua, porous media, and media with "twinning", in: Proc. Contemporary Problems of Mechanics of Heterogeneous Media, vol. 1, Moscow: Institute of Applied Mechanics RAS, pp. 235–267, 2005.
- [19] Belov, P. and Lurie, S., A continuum model of microheterogeneous media, *J. Appl. Math. Mech.*, vol. 73, no. 5, pp. 599–608, 2009.

REFERENCES

- [20] Lurie, S.A., Belov, P.A., Theory of space-time dissipative elasticity and scale effects, *Nanoscale Systems: Mathematical Modeling, Theory and Applications*, vol. 2, pp. 166-178, 2013.

S. Lurie, Institute of Applied Mechanics of RAS, Moscow, Institute for Problems in Mechanics of RAS

Qi Chengzhi, Beijing University of Civil Engineering and Architecture

P. Belov, Scientific-innovation Center "Institute of Research, Development and Technology Transfer"

Linking molecular and continuum mechanics with application to biomimetic nanomaterials and brittle fracture

Bernd Markert, Sandeep P. Patil
markert@iam.rwth-aachen.de

Abstract

The mechanical properties of hierarchically structured materials relies on the characterization and understanding of their nanostructure. A classical example is the dragline silk. Experimental studies have shown that the extraordinary mechanical properties of silk are conferred largely to the nanostructure. In the first part, we propose a three dimensional (3D) finite element model of a silk fiber, which is based on the secondary (nano-scale) structure of the *Araneus diadematus* silk fiber, taking into account the plasticity of the β -sheet crystals as well as the viscous behavior of the amorphous matrix. Our bottom-up approach to dragline silk fiber predicted mechanical properties agree with the experimental ones within the limits of the experimental accuracy. In the second part, a novel combined method for highly brittle materials such as aragonite crystals is proposed, which provides an efficient and accurate in-sight understanding for multi-scale fracture modeling. In particular, physically-motivated molecular dynamics (MD) simulations are performed for crack modeling on the nano-scale, whereas a macroscopic modeling of fracture has proven successful using the diffusive phase-field modeling (PFM) approach. A link between the two modeling schemes is proposed by deriving PFM parameters from the MD atomistic simulations. Thus, in this combined approach, MD simulations provide a more realistic meaning and physical estimation of the PFM parameters.

The proposed computational approach, not requiring any empirical parameters, contributes towards an improved understanding of mechanics at all length-scale levels. Hence, it is an efficient model for the design of new materials as well as applicable to other semi-crystalline polymeric systems or composite materials.

1 Introduction

Molecular dynamics simulations are an efficient approach to study objects on the nanometer scale. They become impracticable when the investigated system has significantly larger dimensions, i. e., on the meso or macroscale. Large-scale simulations of protein materials are not feasible using MD simulations, neither macroscale

structural and mechanical properties can be straightforwardly inferred from MD simulations due to the complexity of biological systems. Typical MD simulations can nowadays be performed on systems containing hundred thousands, or, perhaps, millions of atoms, and for simulation times ranging from a few hundred nanoseconds to more than one millisecond. These numbers are certainly respectable but one may run into conditions where time and/or size limitations become important. On the other hand, continuum structural mechanics can significantly extend the length and time scale of the system.

Continuum structural mechanics is a classical method applicable at all scales. Here, as its name suggests, atomic details of the object are disregarded to focus on the effect of the discretized structure on mechanics. In certain cases, such as determining an elastic modulus of a rubber band, or understanding the stress bearing pattern of a building, the atomic details are normally not the determinant of the property under investigation. In such cases, the object or parts thereof are treated as a continuum sharing the same physical properties. This approach has invincible computational efficiency by greatly reducing the complexity, but is only applicable as long as the continuum approximation is adequate. The hierarchical nanoscale structure of silk renders FEM unfeasible on the small scale, since the atomistic structure crucially defines the material's mechanics. Figure 1 shows a hierarchical structure of spider dragline silk. Crystalline units, the amorphous phase (representative unit) and a combination of both are studied using MD simulations. However, molecular simulations of additional crystalline units and the amorphous matrix are computationally unfeasible. In conjunction to MD, FEM allows to carry out simulations of individual constituents, combinations of them, and full fiber of dragline silk, provided the appropriate parameters, obtained for instance by MD simulations.

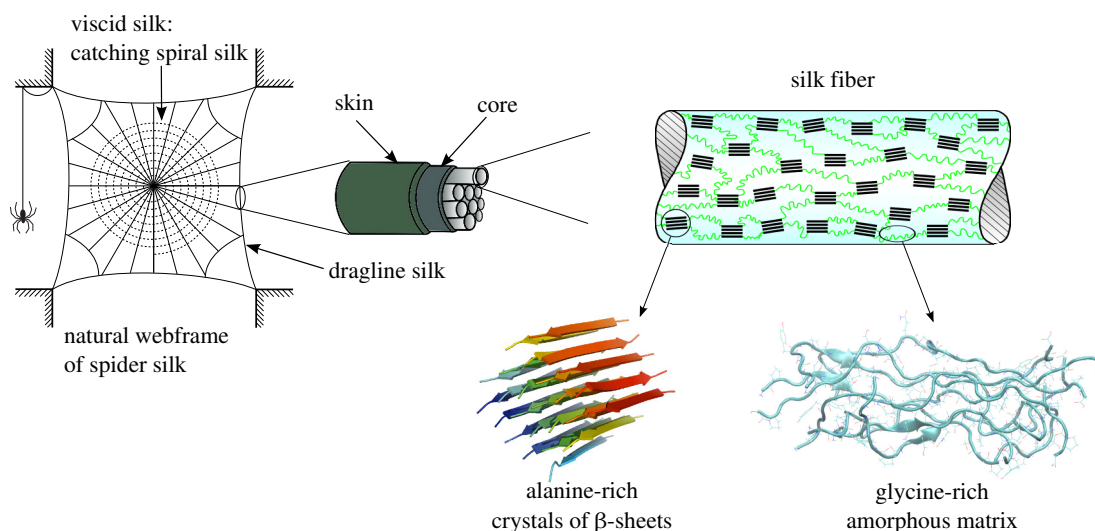


Figure 1: Schematic representation of the spider dragline silk fiber architecture, highlighting the more viscous catching spiral silk (dotted black line), and the much tougher web-frame and dragline silk. Dragline silk fibers are mainly composed of alanine-rich stiff nano-crystals of β -sheets in the glycine-rich disordered peptide chains, whose composition is shown schematically. Figure adopted from [37].

Using different levels of simplifications, continuum mechanics is able to tackle problems for structure sizes that cannot be reached by MD simulations. In spite of the conceptual differences between continuum mechanics and all-atom simulations, the combination of these two different methods is promising. Parameters for continuum mechanics can be obtained from all-atom simulations to ensure high accuracy. The efficiency of continuum mechanics allows to infer mechanical properties on the macroscopic scale from the molecular scale, which is the key to understand a material's interplay of the atomic structure and its overall performance. Here, continuum mechanics and all-atom MD simulations are employed for the silk fiber modeling. Thus, a bottom-up computational approach is used in this work with the aim to create a bridge between molecular level properties and macroscopic mechanical behavior. In this approach, first, all atom simulations are carried out to obtain key mechanical properties and structural parameters, which are then used to develop a macroscopic model using FEM. In this work, this approach is discussed with the brittle fracture of aragonite crystals.

2 Brittle Fracture of Aragonite Crystals

Molecular Dynamics (MD) simulations are considered new computational methods that are employed to describe the time evolution of a system of interacting particles. They require the numerical solution of Newton's equations for every particle governed by an interatomic potential, i. e., bonded and non-bonded potentials, keeping track of the evolution of the system in space. Due to their real time scales (pico seconds), MD methods are perfectly suited to study the high-speed crack propagation of brittle materials, as demonstrated in the work of Rountree et al. [30]. Additionally, there have also been some applications of the method for a variety of inorganic crystals, such as Si_3N_4 [16], SiO_2 [31], 3C-SiC [17], and GaAs [34]. Although these studies have provided valuable in-sights into crack dynamics, a systematic analysis of mechanical properties at an atomistic scale, as well as a link to the macroscopic continuum mechanical approaches are still not well established.

Nowadays, typical MD simulations can be performed on systems containing hundreds of thousands, or perhaps, a few millions of atoms for simulation times ranging from a few hundred nanoseconds up to a millisecond. These numbers are certainly respectable, but one may run into conditions, where size and/or time limitations become important. The challenges related to the limited dimensions or time scales can be tackled by upscaling MD parameters and frameworks through continuum models. In fact, as it has been shown in numerous other studies, i. e., [5, 26, 27, 28], the mechanical behavior of a given continuous material can be reproduced in a different scale by using mechanical parameters derived directly from atomistic MD simulations.

In what numerical modeling regards, phase-field modeling (PFM) has emerged as a powerful tool to model brittle fracture under a macroscopic continuum approach, offering a good accordance between numerical treatment, accuracy, and computational costs. The pioneering works related to an elastic energy-based approach to describe brittle fracture, namely the works of Griffith [9] and Irwin [15], as well as the variational formulations presented in [4, 8], can be considered as the pillars of

a well-established energy-based framework for brittle fracture. In the past decades, many PFMs, which approximate the sharp edges of the crack by a diffusive interface, have been developed. Due to their simple implementation, these models are able to predict quasi-static and dynamic cases of brittle and ductile fracture, considering different fracture modes and loadings, under several discretization schemes [4, 8, 3, 11, 22, 35, 19, 21].

Consequently, this research work pursues to establish a link between the understanding of brittle fracture of a material at an atomistic scale and its macroscopic mechanical features. To this end, an aragonite (CaCO_3) tablet undergoing fracture is studied, using both MD and PFM. Herein, the key mechanical properties (e. g., Young's modulus, Poisson's ratio), as well as the phase-field transition width (ϵ) and the mechanical energy release rate (G) of an aragonite crystal are obtained *ab initio*. These physical properties are subsequently employed to reproduce a nanoscale model under a continuous PFM approach.

Given that PFM and MD are relatively new topics in the realm of mechanics, the second and third sections of this work will briefly introduce the implementation of both methods. In the fourth section, a thorough description and brief evaluation of the numerical experiments in MD, as well as PFM are presented. The last section is dedicated to the conclusion and outlook of the present work.

2.1 Materials and MD Simulations

In the present work, MD and PFM simulations are employed to describe the behavior under fracture of Aragonite (CaCO_3), a highly brittle ceramic and major constituent of nacre (95 % vol.). Tablets of this material were modeled, as seen in Fig. 2, by using the software Visual Molecular Dynamics (VMD) [14]. One double-notched tablet model was built with length (l), width (w) and height (h) of $15.38 \times 11.12 \times 4.30 \text{ nm}^3$, respectively. The pulling layer thicknesses (pt) was considered to be three atomic layers wide. For the subsequent MD simulations, the molecular dynamics program GROMACS 5.0.4 package [33] was used. For aragonite interactions, newly-developed CaCO_3 forcefield [36], that describes angle, planar, dihedral, electrostatic and van der Waals interactions, was implemented.

The model in question was minimized and equilibrated in the NPT (isothermal-isobaric) ensemble for 10 ns at 300 K and 1.013 bar. The tablet did not show any significant changes neither in structural ordering nor in cell dimensions. The last frames were used to create notched systems as follows: The simulation boxes were extended 12 nm along l and h , leaving as much empty space as required to allow the tablet extension during pulling simulations. The periodic vector through the width w was not extended, resulting in tablets of infinite length along w -direction. Then, the v-shaped notches were introduced by removing atoms. The cut lines followed the (101) and ($\bar{1}01$) lattice planes, which resulted in an opening angle of 84.4° . Such cut lines impose the removal of one calcium atom per carbonate group, preserving the electroneutrality of the systems.

Whereas in the MD calculations, the simulation box, in which the aragonite tablets were pulled, was repeated periodically in all three dimensions using 2 fs time steps. Van der Waals interactions were calculated using a cutoff of 1.0 nm. The Particle

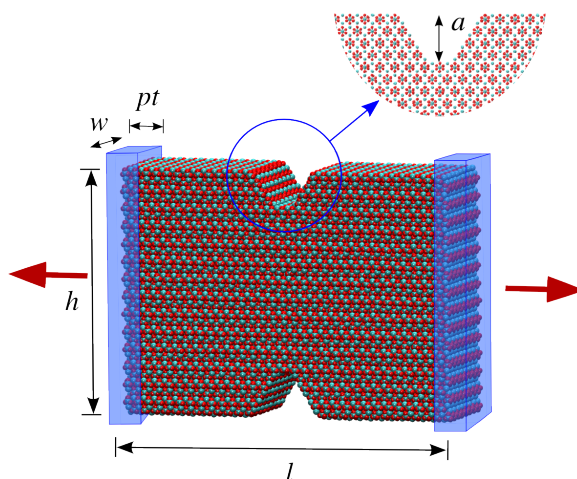


Figure 2: Double-notched all-atom model of an aragonite tablet. Oxygen and carbon atoms of carbonate groups are shown in cyan and red beads, respectively. Calcium atoms are shown with green beads. The dimension a (center) denotes the notch depth, while h , l , w and pt represent the height, length, width and pulling layer thickness, respectively. Pulling directions are perpendicular to the notch depth, which is marked by red arrows. Inset: enlargement of the front view of v-notch region.

Mesh Ewald (PME) method [6] was chosen to account for long-range electrostatic interactions. To increase the simulation time step, a linear constraint solver for molecular simulations (LINCS) [12] was used to constrain all bond vibrations. The Nosé-Hoover [24, 13] temperature coupling was applied with a coupling time constant of 0.1 ps.

Fig. 2 shows an aragonite notched model with loading conditions and representative dimensions. The aragonite tablet model was not constrained at any point (which allows for rigid body motions) to capture a natural behavior in the simulations. The system was further equilibrated in the NVT (canonical ensemble, amount of substance N , volume V and temperature T are conserved) for 10 ns at 300 K. To avoid tablet drifting, two cuboid volumes parallel to the (100) lattice plane were restrained, each cuboid volume containing the three outermost layers of CaCO_3 atoms. This resulted in a system of 66,720 atoms.

Once the equilibration of the system was achieved, a force-probe Molecular Dynamics (FPMD) simulation [10] was employed to enforce an external load. The restrained layers were released and pulled axially outwards with a spring-like force applied to the outer surfaces, with a constant velocity of 10 nm ns^{-1} and a spring constant of $1000 \text{ kJ mol}^{-1} \text{ nm}^{-2}$. FPMD simulations were performed until tablet rupture, which usually occurred within 13 ns. Altogether, five FPMD simulations were performed. The obtained results were later post-processed to obtain critical material parameters, as well as the phase-field transition width and crack resistance energy.

Postulated in 1920, though still in force, the Griffith's energy-based analysis of cracks [9] states that the fracture strength is always lower than theoretical cohesive strength and attributes this discrepancy to the inherent defects in brittle materials,

leading to stress concentration.

One of the underlying principles of fracture mechanics is that crack propagation occurs when the released elastic strain energy is at least equal to the energy required to generate new crack surface. The Griffith's energy criterion for fracture of brittle materials can then be written as

$$\sigma_f = \frac{1}{\alpha} \left[\frac{2E\gamma}{\pi a} \right]^{1/2}, \quad (1)$$

where σ_f is the rupture strength, a is the notch depth, γ is the surface energy, E is the Young's modulus, and α is a geometry correction factor. For double edge notched tension of a semi-infinite tablet with notch depth a and tablet height h , α reads [29]

$$\alpha = 1.12 + 0.43 \left[\frac{a}{h} \right] - 4.79 \left[\frac{a}{h} \right]^2 + 15.46 \left[\frac{a}{h} \right]^3. \quad (2)$$

It is now assumed that the available external and internal energy is transferred into surface energy. In what brittle fracture regards, dissipation and kinetic energy are neglected. This results in the so-called Griffith energy balance where the energy release rate G is equal to 2γ in J/m². The mechanical energy release rate in the CaCO₃ geometry is the amount of energy per unit area that is supplied by the elastic energy stored in the system.

The energy release rate can alternatively be calculated by integrating the stress-strain curve with respect to strain [20, 17]

$$G = l \int_0^\varepsilon \sigma(\varepsilon') d\varepsilon', \quad (3)$$

where l is the model width in the loading direction, see Fig. 2, and σ is the loading direction component of the stress well ahead of the crack tip. At a strain above ε_c , crack propagation at constant velocity is achieved after an initial transient [20].

2.2 Brittle Fracture Modeling using the PFM Approach

The macroscopic modeling of brittle fracture is based on the PFM approach, which has been widely discussed in several research works, see, e.g. [3, 22, 35] for an overview. In this, a phenomenological phase-field variable ϕ is introduced, which approximates the sharp interface of the crack by a diffusive transition zone. Thus, the global potential energy function \mathcal{F} can be written with the help of ϕ and its gradient as an integral over the whole body ([4, 8, 19, 21]) as

$$\mathcal{F}(\phi, \text{grad } \phi, \boldsymbol{\varepsilon}) = \int_V [\Psi_{elast}(\phi, \boldsymbol{\varepsilon}) + \Psi_{crack}(\phi, \text{grad } \phi)] dv \quad (4)$$

with $\boldsymbol{\varepsilon}$ being the linear strain tensor. The phase-field variable $\phi \in [0, 1]$, in the sense of an indicator function, represents the crack state, where $\phi = 0$ for a cracked state

and $\phi = 1$ for an undamaged state. The fracture energy Ψ_{crack} is defined as

$$\Psi_{crack}(\phi, \text{grad } \phi) = \frac{G}{4\epsilon}(1 - \phi)^2 + G\epsilon |\text{grad } \phi|^2, \quad (5)$$

where ϵ is an internal length related to the width of the diffusive crack transition zone. As the degradation of the material is assumed to occur only under tension or shear, one applies an additive splitting of the linear elastic energy into a positive part Ψ_{elast}^+ , that considers the tension and shear responses, and a negative part Ψ_{elast}^- , that considers the compression response. Moreover, the degradation function $g(\phi)$ can simply be defined in a quadratic form as $g(\phi) = [(1 - \eta)(\phi)^2 + \eta]$ to obtain

$$\Psi_{elast}(\phi, \boldsymbol{\varepsilon}) = g(\phi) \Psi_{elast}^+ + \Psi_{elast}^-. \quad (6)$$

Here, η is a residual stiffness added for numerical stability purpose. The linear elastic stress $\boldsymbol{\sigma}$ is obtained through the derivation of the phase-field potential with respect to the strain tensor, see [23].

$$\boldsymbol{\sigma}(\phi, \boldsymbol{\varepsilon}) = \frac{\partial \mathcal{F}}{\partial \boldsymbol{\varepsilon}} = g(\phi) \frac{\partial \Psi_{elast}^+}{\partial \boldsymbol{\varepsilon}} + \frac{\partial \Psi_{elast}^-}{\partial \boldsymbol{\varepsilon}}. \quad (7)$$

Furthermore, the momentum balance equation under the assumptions of a quasi-static state and neglecting the body forces can be expressed as

$$\text{div } \boldsymbol{\sigma} = \mathbf{0}, \quad (8)$$

allowing the computation of displacement field \mathbf{u} . To this end, the evolution of the phase field is derived using the Allen-Cahn model, which describes the process of crack evolution via a reaction-diffusion equation as

$$\begin{aligned} \dot{\phi} &= \frac{\partial \phi}{\partial t} = -M \frac{\partial \mathcal{F}}{\delta \phi} \\ &= -M \left[2(1 - \eta)\phi \Psi_{elast}^+ - \frac{G}{2\epsilon}(1 - \phi) - 2G\epsilon \text{div grad } \phi \right], \end{aligned} \quad (9)$$

where $M \geq 0$ represents a mobility constant.

For the numerical implementation of the PFM problem, an initial boundary-value problem of mode-I fracture, illustrated in Figure 3, is solved using the finite element package FlexPDE.

The numerical solution is computed considering quadratic shape functions for the displacement and the phase-field variable, and the time integration is applied using the 2nd-order backward difference formula (BDF2), where a time-step automatic adaptivity is also employed. Moreover, a fixed mesh, refined in the area between the notches, is implemented. A plane stress, linear elastic model is used to reproduce the MD simulation. Under this setup, the stress is applied until instantaneous rupture of the plate takes place.

The material parameters, E, ϵ and G , for the PFM of the aragonite plate were directly derived from the outcomes of the MD simulations as will be discussed in the next section. Therewith, the obtained values were $E = 126$ GPa for the Young's modulus. The crack resistance (or energy release rate) was found to be $G = 2.091$

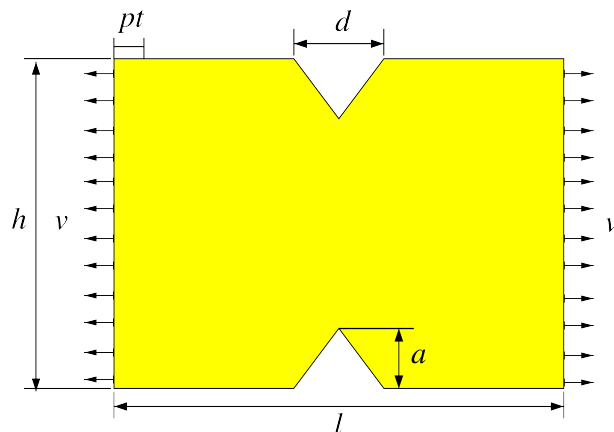


Figure 3: Boundary conditions of the IBVP (load-controlled). For the boundary layers with width pt , $\nu = 0$ and zero-stress in vertical direction. In the middle of the extreme edges (left and right), two points are fixed in the vertical direction to prevent a rigid body motion. The dimensions here are $h=11.2$ nm, $l=15.3$ nm, $d=3.08$ nm, and $a=1.84$ nm.

J/m² and the internal length scale $\epsilon = 0.05$ nm. The values of the mobility and the residual stiffness parameters were set to $M = 10 \times 10^9$ nm²/Ns and $\eta = 10^{-5}$, respectively, whereas the applied Poisson's ratio is $\nu = 0.44$. The material properties such as Poisson's ratio ν and the density ρ were benchmarked with the aragonite-related literature ([1, 2, 7, 25]), whereas the mobility parameter M and the residual stiffness parameter η are in good agreement with the ranges proposed in, e.g., [18, 23].

2.3 Results and Discussion

As stated previously, to examine the fracture behavior at atomistic scale of aragonite, monotonic tension tests were performed by means of FPMD. The molecular system was loaded by moving virtual springs applied to the outer surfaces of the tablets with constant velocity. The force is obtained directly from the resultant spring force at the boundaries. Accordingly, the stress is computed by dividing the spring force by the cross sectional area comprehended between two notches. Moreover, the relative displacement of atoms was measured between the center of mass of both pulling layers. Here, the engineering strain is obtained by dividing the total displacement of the center of mass of any pulling layer by the original distance between this layer and the center of specimen. The crystals deformed during the FPMD simulations until the externally applied stress reached the ultimate tensile strength σ_f , resulting in a sudden rupture. Due to the chemical structure of calcium carbonate $[\text{Ca}^{2+}][\text{CO}_3^{2-}]$, and its arrangement in compact crystal, it is not always possible to have symmetric notches on both edges as well as notches at the exact center of all tablets of CaCO_3 models. Therefore, the v-notches in the tablets are not sharp, and the notch tips can have, either, single or double CaCO_3 units (enlarged view in Fig. 2). Thus, different crack propagations were observed in the tablet models, e.g., the crack starts at the

top edge, bottom edge or at both edges simultaneously (shown in Fig. 4). For all simulations, the cracks propagated with an s-shape along the (101) and ($\bar{1}01$) lattice planes, as expected.

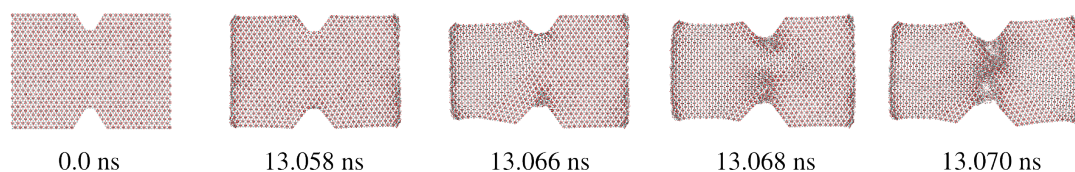


Figure 4: Rupture of the double-notched aragonite tablets. The snapshots show the fracture of the aragonite tablets under constant pulling velocity. As the two atom groups at the ends are pulled, the tablets slightly stretch and break abruptly around the notch. Here, the crack initiates at the bottom, though, is propagated from both sides and with an s-shape.

Fig. 4 shows snapshots of the rupture processes observed in the CaCO_3 tablet models. The model was loaded with a constant velocity for 12.88 to 13.056 ns, without observing crack initiation. However, the crack initiation took place during the following 0.012 ns, inducing an instantaneous total failure.

The results describe a good agreement with the expectations. First of, the energy release rate G can be calculated using the MD results together with either Griffith's criterion given in Eq. (1) or by use of Eq. (3). Both equations confirm that the fracture of the CaCO_3 tablet occurs at a value $G \approx 2.091 \text{ J/m}^2$. This value is slightly lower than the theoretical values of G for CaCO_3 ($2.10\text{--}3.74 \text{ J/m}^2$), which can be found in the literature [1, 2, 7], though this difference is merely negligible. Therefore, $G = 2.091 \text{ J/m}^2$ is adopted for the PFM.

To avoid model dependency in MD simulations, five different aragonite tablet models were considered, and the stress-strain curves were jointly analyzed. The recovered elasticity modulus E of aragonite ranges between 106 to 148 GPa, which is in the range of experimental and theoretical studies, see [1, 2, 7]. With regard to the ultimate tensile strength, the resulting MD simulations value of the aragonite notched samples is 4.6 GPa. This value is slightly lower than the theoretical strength of flawless minerals, which was estimated to lie in the range of 5 to 10 GPa [32].

Fig. 5 shows the force-displacement curves of the continuous PFM (considering a Young's modulus of $E = 126 \text{ GPa}$) and all-atom simulations. With regard to the force at failure, the resulting MD simulations value of the aragonite notched samples is $47 \mu\text{N}$ and the nonlinear behavior, which is due to the potential energy nonlinearities, is clearly observed. Although, a linear elastic model was considered for the PFM, an outstanding correlation of the results is observed.

Phenomenologically, the s-shaped crack propagation (along the (101) and ($\bar{1}01$) lattice planes) is obtained in both MD and PFM approaches. Moreover, the ultimate tensile strength obtained in the PFM simulations falls perfectly into the ranges described in the all-atom simulations. Nevertheless, a discrepancy between the two schemes can be seen which can be traced to two main reasons: On the one side, the boundary conditions in the MD simulation allow for rigid body rotations and translations, which are constrained in the continuum model by fixing the vertical displacement of two points. This fixation causes an artificial symmetry and si-

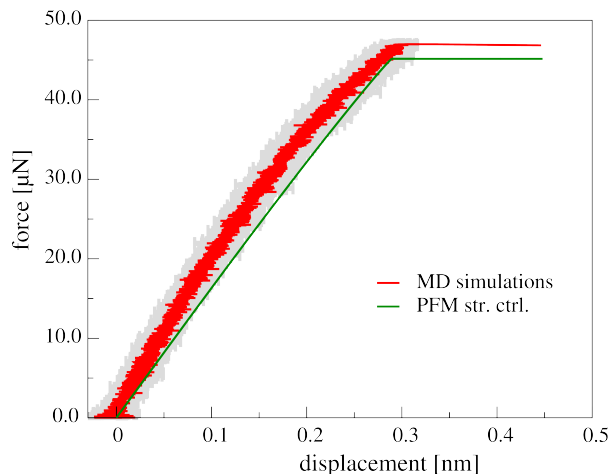


Figure 5: Force-displacement curves for the aragonite tablet models. The red line is the averaged force-displacement curve from the MD simulations, and the gray shaded area indicates the standard error deviation. The green line indicate the force-displacement curves obtained from the PFM stress-controlled simulation.

multaneously stiffens the material. On the other side, the PFM considers a linear elastic material response, which is not able to account for the inherent material non-linearities. As seen in Fig. 5, these non-linearities are naturally captured in the atomistic simulations.

An important outcome, particularly for the phase-field parameters, is the theoretical and numerical consistency of the critical energy release rate G , and a potential relationship between the molecular transition (distortion) zone and the phase-field transition width governed by the internal length parameter ϵ . The former can be estimated by means of the Griffith's theory or by integration of the stress-strain curve, yielding a value within the literature range (approximately 2.1 J/m^2). The latter can be obtained by measuring the cracked surfaces in a straightforward post-processing step. The results of the MD and PFM simulations are shown in Fig. 6. Taking into account the density plot of the MD and overlapping it with the resultant intact-to-cracked material transition of the PFM, as seen in Fig. 6, the phenomenological correlation is evident.

3 Conclusions

As shown in this work, the efficiency of continuum mechanics allows to infer mechanical properties from the molecular scale, which is the key to understand a material's interplay of the atomic structure and its overall performance. Through an atomistic obtention of the material parameters, the PFM presented in this work observes a fair convergence, and more important remains qualitatively and quantitatively within the outcomes of MD simulations and the benchmarked literature. Moreover, a correlation between the phase-field parameter ϵ (which is of extreme importance for convergence) and an MD transition zone was captured for the first time. Through further study, this could result in a physical meaning and obtention of the parameter value, which is up to date fitted according to each model. Moreover, the observed

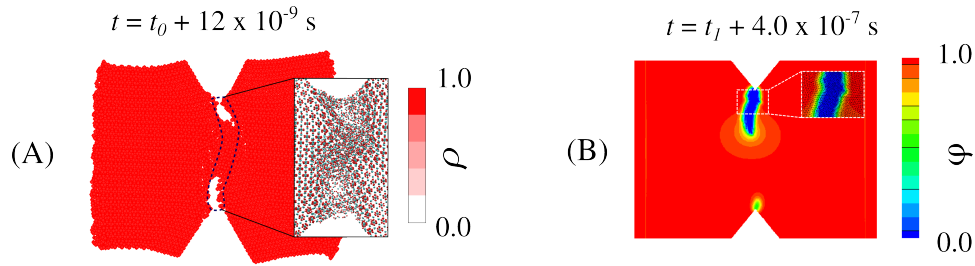


Figure 6: Crack initiation and propagation comparison: (A) Density plots of atoms in MD simulations (ρ stands for density). The s-shaped crack is illustrated with a dotted line, and the inset shows an all-atom simulation snapshot of the crack propagated area. (B) PFM results for stress-controlled simulations (ϕ stands for the damage phase-field, blue corresponds to cracked material, and red refers to undamaged material). The times t_0 and t_l are the total loading times before crack initiation in MD ($t_0 = 13056$ ps) and PFM stress-controlled ($t_l = 0.0403089$ s) respectively.

molecular dissipative zone between the undamaged and cracked material allows to think that in fact, brittle fracture observe a transition zone, under a purely atomistic standpoint.

The presented bottom-up approach thus represents, an important tool in the field of artificial material design. The approach proposed here can be extended to other bio-materials, and partially or highly ordered polymeric and composite materials, which are characterized by a similar interplay of structure and mechanics on different scales.

References

- [1] F. Barthelat and H. D. Espinosa. Elastic properties of nacre aragonite tablets. In SEM Annual Conference and Exposition on Experimental and Applied Mechanics, page 187, 2003.
- [2] F. Barthelat, C. M. Li, C. Comi, and H. D. Espinosa. Mechanical properties of nacre constituents and their impact on mechanical performance. *J. Mater. Res.*, 21:1977–1986, 2006.
- [3] M. J. Borden, C. V. Verhoosel, M. A. Scott, T. J. R. Hughes, and C. M. Landis. A phase-field description of dynamic brittle fracture. *Comput. Method. Appl. M.*, 217–220:77–95, 2012.
- [4] B. Bourdin, G.A. Francfort, and J.J. Marigo. The variational approach to fracture. *J. Elasticity*, 91:5–148, 2008.
- [5] Murat Cetinkaya, Senbo Xiao, Bernd Markert, Wolfram Stacklies, and Frauke Gräter. Silk fiber mechanics from multiscale force distribution analysis. *Biophys J*, 100(5):1298–1305, Mar 2011.

-
- [6] T. Darden, D. York, and L. Pedersen. Particle mesh ewald: An $n \log(n)$ method for ewald sums in large systems. *J. Chem. Phys.*, 98:10089–10092, 1993.
- [7] T. Z. Forbes, A. V. Radha, and A. Navrotsky. The energetics of nanophase calcite. *GeoChim. Cosmochim. Ac.*, 75:7893–7905, 2011.
- [8] G.A. Francfort and J.-J. Marigo. Revisiting brittle fracture as an energy minimization problem. *J. Mechan. and Phys. Solids.*, 46:1319–1342, 1998.
- [9] A. A. Griffith. The phenomena of rupture and flow in solids. *Phil. Trans. Roy. Soc. Lond. A*, 221:163–198, 1921.
- [10] H. Grubmüller, B. Heymann, and P. Tavan. Ligand binding: molecular mechanics calculation of the streptavidin-biotin rupture force. *Science*, 271(5251):997–999, Feb 1996.
- [11] C. A. Hernandez Padilla and B. Markert. A coupled ductile fracture phase-field model for crystal plasticity. *Continuum Mech. Thermodyn.* DOI:10.1007/s00161-015-0471-0, pages 1–10, 2015.
- [12] B. Hess, H. Bekker, H. J. C. Berendsen, and J. G. E. M. Fraaije. Lincs: a linear constraint solver for molecular simulations. *J. Comput. Chem.*, 18(12):1463–1472, 1997.
- [13] W. G. Hoover. Canonical dynamics: Equilibrium phase-space distributions. *Phys. Rev. A*, 31(3):1695–1697, 1985.
- [14] W. Humphrey, A. Dalke, and K. Schulten. Vmd: visual molecular dynamics. *J. Mol. Graph.*, 14(1):33–38, 1996.
- [15] G. R. Irwin. Analysis of stresses and strains near the end of a crack traversing a plate. *J Appl Mech*, 24:361–364, 1957.
- [16] R. K. Kalia, A. Nakano, A. Omeltchenko, K. Tsuruta, and P. Vashishta. Role of ultrafine microstructures in dynamic fracture in nanophase silicon nitride. *Phys. Rev. Lett.*, 78:2144, 1997.
- [17] H. Kikuchi, R. K. Kalia, A. Nakano, P. Vashishta, P. S. Branicio, and F. Shimajo. Brittle dynamic fracture of crystalline cubic silicon carbide (3c-sic) via molecular dynamics simulation. *J. Appl. Phys*, 98:103524, 2005.
- [18] C. Kuhn and R. Müller. A continuum phase field model for fracture. *Eng. Fract. Mech.*, 77:3625–3634, 2010.
- [19] C. Kuhn, A. Schlüter, and R. Müller. A phase field approach for dynamic fracture. *PAMM*, 13(1):87–88, 2013.
- [20] B. Lawn. *Fracture of Brittle Solids*. Cambridge University Press, Cambridge, 1993.

-
- [21] B. Markert and Y. Heider. Coupled multi-field continuum methods for porous media fracture. In Miriam Mehl, Manfred Bischoff, and Michael Schäfer, editors, *Recent Trends in Computational Engineering - CE2014*, volume 105 of *Lecture Notes in Computational Science and Engineering*, pages 167–180. Springer International Publishing, 2015.
- [22] C. Miehe, M. Hofacker, and F. Welschinger. A phase field model for rate-independent crack propagation: Robust algorithmic implementation based on operator splits. *Comput. Method. Appl. M.*, 199:2765–2778, 2010.
- [23] C. Miehe, F. Welschinger, and M. Hofacker. Thermodynamically consistent phase-field models of fracture: Variational principles and multi-field fe implementations. *Int. J. Numer. Meth. Eng.*, 83:1273–1311, 2010.
- [24] S. Nosé. A molecular dynamics method for simulations in the canonical ensemble. *Mol. Phys.*, 52(2):255–268, 1984.
- [25] S. P. Patil, Y. Heider, C.A. Hernandez-Padilla, E.R. Cruz-Chú, and B. Markert. A combined molecular dynamics-phase-field modeling approach to fracture. *Comput. Methods Appl. Mech. Engrg.*, DOI: 10.1016/j.cma.2016.04.005BTK, 2016.
- [26] S. P. Patil, B. Markert, and F. Gräter. Refining a bottom-up computational approach for spider silk fibre mechanics. *Proceedings of the 3rd GAMM Seminar on Continuum Biomechanics*, II-21:75–87, 2012.
- [27] Sandeep P. Patil, Bernd Markert, and Frauke Gräter. Rate-dependent behavior of the amorphous phase of spider dragline silk. *Biophys J*, 106(11):2511–2518, Jun 2014.
- [28] Sandeep P. Patil, Senbo Xiao, Konstantinos Gkagkas, Bernd Markert, and Frauke Gräter. Viscous friction between crystalline and amorphous phase of dragline silk. *PLoS One*, 9(8):DOI: 10.1371/journal.pone.0104832, 2014.
- [29] N. Perez. *Fracture Mechanics*. Kluwer Academic Publisher Group, 2004.
- [30] C. L. Rountree, R. K. Kalia, E. Lidorikis, A. Nakano, L. van Brutzel, and P. Vashishta. Atomistic aspects of crack propagation in brittle materials: Multi-million atom molecular dynamics simulations. *Annu. Rev. Matter. Res.*, 32:377–400, 2002.
- [31] C. L. Rountree, S. Prades, D. Bonamy, E. Bouchaud, R. Kalia, and C. Guillot. A unified study of crack propagation in amorphous silica: Using experiments and simulations. *J. Alloy. Comp.*, 434–435:60–63, 2007.
- [32] C. H. Scholz. *The Mechanics of Earthquakes and Faulting*. Cambridge University Press, 2nd edition, 2002.
- [33] D. van der Spoel, E. Lindahl, B. Hess, G. Groenhof, A. E. Mark, and H. J. Berendsen. Gromacs: fast, flexible, and free. *J. Comput. Chem.*, 26(16):1701–1718, 2005.

- [34] P. Vashishta, M. E. Bachlechner, T. Campbell, R. K. Kalia, H. Kikuchi, S. Kodiyalam, A. Nakano, S. Ogata, F. Shimojo, and P. Walsh. Multimillion atom simulation of nanostructured materials on parallel computers. *Prog. Theor. Phys. Supplement*, 138:135–170, 2000.
- [35] J. Vignollet, S. May, R. de Borst, and C. V. Verhoosel. Phase-field models for brittle and cohesive fracture. *Meccanica*, 49:2587–2601, 2014.
- [36] S. Xiao, S. A. Edwards, and F. Gräter. A new transferable forcefield for simulating the mechanics of CaCO_3 crystals. *J. Phys. Chem. C*, 115:20067–20075, 2011.
- [37] S. P. Patil. Doctoral dissertation: Multiscale modeling of spider dragline silk. RWTH Aachen University, 2015.

Bernd Markert, Institute of General Mechanics, RWTH Aachen University, Templergraben 64, 52062 Aachen, Germany

Sandeep P. Patil, Institute of General Mechanics, RWTH Aachen University, Templergraben 64, 52062 Aachen, Germany

Fractional Lattice Dynamics: Nonlocal constitutive behavior generated by power law matrix functions and their fractional continuum limit kernels

T.M. Michelitsch, B.A. Collet, A.P. Riascos, A.F. Nowakowski,
F.C.G.A. Nicolleau
michel@lmm.jussieu.fr

Abstract

We introduce positive elastic potentials in the harmonic approximation leading by Hamilton's variational principle to fractional Laplacian matrices having the forms of power law matrix functions of the simple local Born von Karman Laplacian. The fractional Laplacian matrices are well defined on periodic and infinite lattices in $n = 1, 2, 3, ..$ dimensions. The present approach generalizes the central symmetric second difference operator (Born von Karman Laplacian) to its fractional central symmetric counterpart (Fractional Laplacian matrix).

For non-integer powers of the Born von Karman Laplacian, the fractional Laplacian matrix is nondiagonal with nonzero matrix elements everywhere, corresponding to nonlocal behavior: For large lattices the matrix elements far from the diagonal expose power law asymptotics leading to continuum limit kernels of Riesz fractional derivative type. We present explicit results for the fractional Laplacian matrix in 1D for finite periodic and infinite linear chains and their Riesz fractional derivative continuum limit kernels. The approach recovers for $\alpha = 2$ the well known classical Born von Karman linear chain (1D lattice) with local next neighbor springs leading in the well known continuum limit of classic local standard elasticity, and for other integer powers to gradient elasticity. We also present a generalization of the fractional Laplacian matrix to n-dimensional cubic periodic (nD tori) and infinite lattices. For the infinite nD lattice we deduce a convenient integral representation. We demonstrate that our fractional lattice approach is a powerful tool to generate physically admissible nonlocal lattice material models and their continuum representations.

1 Introduction

Fractional calculus has turned out to be a powerful analytical tool in various disciplines: It has been recognized that especially in more recently emerging fields

dealing with complex, chaotic, turbulent, critical, fractal and anomalous transport phenomena, problems can appropriately be described by equations which involve fractional operators. A broad overview on applications of the fractional approach can be found in the review articles of Metzler and Klafter [5, 6].

There exist various definitions (Riemann, Liouville, Caputo, Grünwald-Letnikov, Marchaud, Weyl, Riesz, Feller, and others) for fractional derivatives and integrals, e.g. [3, 5, 15, 16, 17] among many others. This diversity of definitions is due to the fact that fractional operators take different kernel representations in different function spaces which is a consequence of the nonlocal character of fractional kernels. The present paper is organized as follows. In the first part of the paper we deduce from “fractional harmonic lattice potentials” on the cyclically closed linear chain a discrete fractional Laplacian matrix. We do so by applying our recent approach to generate nonlocal lattice models by matrix functions where the generator operator is the discrete centered Born von Karman Laplacian [9]. First we obtain the discrete fractional Laplacian in explicit form for the infinite chain for particle numbers $N \rightarrow \infty$, being in accordance with the fractional centered difference models of Ortiguiera [14] and Zoia et al. [19]. Utilizing the discrete infinite chain fractional Laplacian matrix we construct an explicit representation for the *fractional Laplacian matrix on the N -periodic finite 1D lattice* where the particle number N can be arbitrary not necessarily large. Then we analyse continuum limits of the discrete fractional model: The infinite space continuum limit of the fractional Laplacian matrix yields the well known infinite space kernel of the standard fractional Laplacian. The periodic string continuum limit yields an explicit representation for the kernel of the fractional Laplacian (Riesz fractional derivative) which fulfills periodic boundary conditions and is defined on the finite L -periodic string.

In the second part of the paper we suggest an extension of the fractional approach on nD periodic and infinite lattices. We deduce an integral representation for fractional Laplacian on the infinite nD lattice and proof that as asymptotic representation the well known Riesz fractional derivative of the nD infinite space is emerging. More detailed derivations of some of the results of the present paper can be found in recent articles [7, 8]. All these results are fully equivalent and can also be deduced by employing the more general approach of Riascos and Mateos for fractional diffusion problems on networks [12, 13], and see also the references therein.

2 Fractional Laplacian matrix on the finite periodic 1D lattice

We consider a periodic, cyclically closed linear chain (1D periodic lattice or ring) with equidistant lattice points $p = 0, \dots, N - 1$ consisting of N identical particles having all the same mass μ . Each mass point p has equilibrium position at $0 \leq x_p = ph < L = Nh$ ($p = 0, \dots, N - 1$) where L denotes the length of the chain and h the interparticle distance (lattice constant). Further we impose periodicity (cyclic closure of the chain). For convenience of our demonstration we introduce the unitary shift operator D defined by $Du_p = u_{p+1}$ and its adjoint $D^\dagger = D^{-1}$ with $D^\dagger u_p = u_{p-1}$. We employ periodic boundary conditions (cyclic closure of the chain) $u_p = u_{p+sN}$

($s \in \mathbf{Z}$) and equivalently, cyclic index convention $p \rightarrow p \bmod(N) \in \{0, 1, \dots, N-1\}$. Any elastic potential in the *harmonic approximation* defined on the 1D periodic lattice can be written in the representation [9]

$$V_f = \frac{\mu}{2} \sum_{p=0}^{N-1} u_p^* f(2\hat{1} - D - D^\dagger) u_p = -\frac{1}{2} \sum_{p=0}^{N-1} \sum_{q=0}^{N-1} u_q^* \Delta_f(|p-q|) u_p, \quad (1)$$

where $\Delta_f(|p-q|) = -\mu f_{|p-q|}$ indicates the (negative-semidefinite) Laplacian $N \times N$ -matrix, $\hat{1}$ the identity matrix, and f we refer to as the characteristic function: Physically admissible, elastically stable and translational invariant positive elastic potentials require for the 1D periodic lattice (cyclic ring) that the characteristic function f which is defined as a scalar function to have the following properties $0 < f(\lambda) < \infty$ for $0 < \lambda \leq 4$ (elastic stability) and $f(\lambda = 0) = 0$ (translational invariance, zero elastic energy for uniform translations of the lattice). For the approach to be developed we propose the characteristic function to assume power law form

$$f^{(\alpha)}(\lambda) = \Omega_\alpha^2 \lambda^{\frac{\alpha}{2}}, \quad \alpha > 0, \quad (2)$$

which fulfills for $\alpha > 0$ and $\Omega_\alpha^2 > 0$ the above required good properties for the characteristic function. Ω_α denotes a dimensional constant of physical dimension sec^{-1} . Note that $2\hat{1} - D - D^\dagger$ is the central symmetric second difference operator which is defined by $(2\hat{1} - D - D^\dagger)u_p = 2u_p - u_{p+1} - u_{p-1}$. The matrix function $f(2\hat{1} - D - D^\dagger)$ is in general a self-adjoint (symmetric) positive semidefinite $N \times N$ -matrix function of the simple $N \times N$ generator matrix $[2\hat{1} - D - D^\dagger]_{pq} = 2\delta_{pq} - \delta_{p+1,q} - \delta_{p-1,q}$. It can be easily seen that $f(2\hat{1} - D - D^\dagger)$ has Töplitz structure, i.e. its additional symmetry consists in the form $f_{pq} = f_{qp} = f_{|p-q|}$, $p, q = 0, \dots, N-1$ giving the fractional generalization of the Born von Karman centered difference operator. The fractional elastic potential has then with (1) the representation

$$V_\alpha = \frac{\mu \Omega_\alpha^2}{2} \sum_{p=0}^{N-1} u_p^* (2 - D - D^\dagger)^{\frac{\alpha}{2}} u_p = \frac{\mu}{2} \sum_{p=0}^{N-1} \sum_{q=0}^{N-1} u_q^* f_{|p-q|}^{(\alpha)} u_p, \quad (3)$$

with the matrix elements $f_{|p-q|}^{(\alpha)} = \Omega_\alpha^2 [(2\hat{1} - D - D^\dagger)^{\frac{\alpha}{2}}]_{|p-q|}$ of the *fractional characteristic matrix function*. In full analogy to the negative semidefinite continuous Laplacian (second derivative operator) we define here the fractional Laplacian matrix as the negative semidefinite matrix defined through Hamilton's variational principle¹

$$\Delta_\alpha u_p = -\frac{\partial}{\partial u_p} V_\alpha, \quad \Delta_\alpha = -\mu \Omega_\alpha^2 (2 - D - D^\dagger)^{\frac{\alpha}{2}}. \quad (4)$$

It turns out that the fractional Laplacian matrix for non-integer $\frac{\alpha}{2}$ has nonzero matrix elements everywhere with power law asymptotics $\sim |p-q|^{-\alpha-1}$ for $|p-q| \gg 1$ sufficiently large corresponding to nonlocal constitutive behavior. For the finite 1D

¹The sign convention differs in many references, so e.g. in [12, 13] the fractional Laplacian matrix is defined positive semidefinite corresponding to the definition of the characteristic fractional operator $(2\hat{1} - D - D^\dagger)^{\frac{\alpha}{2}}$.

periodic lattice the matrix elements of the fractional Laplacian matrix (4) will be evaluated explicitly which we shall do in the subsequent paragraph.

Infinite 1D lattice

This can be done using its spectral representation which assumes in the limiting case of an infinite lattice ($N \rightarrow \infty$), see e.g. [7, 8, 12]

$$f_{|p-q|}^{(\alpha)} = \Omega_\alpha^2 (2 - D - D^\dagger)_{|p-q|}^{\frac{\alpha}{2}}, \quad p, q \in \mathbf{Z}_0, \quad (5)$$

$$f_{|p|}^{(\alpha)} = \frac{\Omega_\alpha^2}{2\pi} \int_{-\pi}^{\pi} e^{i\kappa p} \left(4 \sin^2 \frac{\kappa}{2}\right)^{\frac{\alpha}{2}} d\kappa.$$

This expression can be obtained in explicit form [7, 8, 19]

$$f^{(\alpha)}(|p|) = \Omega_\alpha^2 \frac{\alpha!}{\frac{\alpha}{2}!(\frac{\alpha}{2} + |p|)!} (-1)^p \prod_{s=0}^{|p|-1} \left(\frac{\alpha}{2} - s\right) = \Omega_\alpha^2 (-1)^p \frac{\alpha!}{(\frac{\alpha}{2} - p)!(\frac{\alpha}{2} + p)!}, \quad (6)$$

where we introduced the generalized factorial function $\beta! = \Gamma(\beta + 1)$. In view of (6) we observe that for noninteger $\frac{\alpha}{2}$ any matrix element $f^{(\alpha)}(|p-q|) \neq 0$ is non-vanishing indicating the nonlocality of the harmonic fractional interparticle interaction (4). For $\frac{\alpha}{2} = m \in \mathbf{N}$ the matrix elements (6) take the values of the standard binomial coefficients. (5)₂ can be read as the Fourier coefficients of the infinite Fourier series

$$\omega_\alpha^2(\kappa) = \Omega_\alpha^2 \left(4 \sin^2 \frac{\kappa}{2}\right)^{\frac{\alpha}{2}} = \Omega_\alpha^2 (2 - e^{i\kappa} - e^{-i\kappa})^{\frac{\alpha}{2}} = \sum_{p=-\infty}^{\infty} f_{|p|}^{(\alpha)} e^{ip\kappa}. \quad (7)$$

This relation indicates the fractional dispersion relation of the infinite lattice leading to the remarkable relation which holds *only* for complex numbers on the unit circle $z = e^{i\kappa}$, namely

$$\left(2 - z - \frac{1}{z}\right)^{\frac{\alpha}{2}} = \sum_{p=-\infty}^{\infty} (-1)^p \frac{\alpha!}{(\frac{\alpha}{2} - p)!(\frac{\alpha}{2} + p)!} z^p, \quad |z| = 1. \quad (8)$$

This Laurent series converges nowhere except on the unit circle $|z| = 1$. For instance the zero eigenvalue $\omega_\alpha^2(\kappa = 0) = 0$ which corresponds to translational invariance (zero elastic energy for uniform translations) is obtained by putting $z = 1$ in (8). For integer $\frac{\alpha}{2} = m \in \mathbf{N}$ (6) takes the form of the standard binomial coefficients and the series (7), (8) then take the representations of standard binomial series of $(2 - z - \frac{1}{z})^{\frac{\alpha}{2}} = (-1)^m (\sqrt{z} - \frac{1}{\sqrt{z}})^{2m}$ breaking at $|p| = m$ corresponding to zero values for the matrix elements for (6) for $|p| > m$. We further observe for noninteger $\frac{\alpha}{2} \notin \mathbf{N}$ the *power law asymptotics* for $|p| \gg 1$ which can be obtained by utilizing Stirling's asymptotic formula for the Γ -function [7, 8]

$$f_{|p| \gg 1}^{(\alpha)} \rightarrow -\Omega_\alpha^2 \frac{\alpha!}{\pi} \sin\left(\frac{\alpha\pi}{2}\right) p^{-\alpha-1}. \quad (9)$$

The asymptotic power law (scale free) characteristics of the fractional Laplacian matrix $\Delta_{pq} \sim |p - q|^{-\alpha-1}$ is the essential property which gives rise to many ‘anomalous phenomena’ such as in ‘fractional diffusion’ problems on networks such as the emergence of Lévy flights [12, 13] (and references therein). The fractional continuum limit kernels are discussed in the subsequent section. The expressions (5)-(9) hold for the infinite 1D lattice corresponding to $N \rightarrow \infty$. As everything in nature is limited we shall consider now the fractional Laplacian matrix for a finite periodic lattice where the particle number N is arbitrary and not necessarily large.

1D finite periodic lattice - ring

It is only a small step to construct the finite lattice Laplacian matrix in terms of infinite lattice Laplacian matrix. We can perform this step by the following consideration: Let $-\mu f_{|p-q|}^{(\infty)}$ the Laplacian matrix of the infinite lattice, and $\omega^2(\kappa)$ the continuous dispersion relation of the infinite lattice matrix $f_{|p-q|}$ obeying the eigenvalue relation

$$\sum_{q=-\infty}^{\infty} f_{|p-q|}^{(\infty)} e^{iq\kappa} = \omega^2(\kappa) e^{ip\kappa}, \quad 0 \leq \kappa < 2\pi. \quad (10)$$

This relation holds identically in the entire principal interval $0 \leq \kappa < 2\pi$ and is 2π -periodic in the κ -space. Let us now choose $\kappa = \kappa_\ell = \frac{2\pi}{N}\ell$ with $\ell = 0, \dots, N-1$ being the Bloch wave number of the *finite* periodic lattice of N lattice points where N is not necessarily large. Since the Bloch wave numbers of the chain are discrete points within the interval $0 \leq \kappa_\ell < 2\pi$, then relation (10) holds as well for these N κ -points, namely [7, 8]²

$$\sum_{p=-\infty}^{\infty} f_{|q|}^{(\infty)} e^{iq\kappa_\ell} = \omega^2(\kappa_\ell), \quad 0 \leq \kappa_\ell = \frac{2\pi}{N}\ell < 2\pi,$$

$$\sum_{p=0}^{N-1} \sum_{s=-\infty}^{\infty} f_{|p+sN|}^{(\infty)} e^{i(p+sN)\kappa_\ell} = \sum_{p=0}^{N-1} e^{ip\kappa_\ell} \sum_{s=-\infty}^{\infty} f_{|p+sN|}^{(\infty)} = \sum_{p=0}^{N-1} e^{ip\kappa_\ell} f_{|p|}^{finite} = \omega^2(\kappa_\ell).$$

In the second relation the N -periodicity of the finite lattice Bloch eigenvector $e^{i(p+sN)\kappa_\ell} = e^{ip\kappa_\ell}$ has been used. The last relation can be read as the eigenvalue relation for the N -periodic lattice matrix of Töplitz structure

$$f_{|p-q|}^{finite} = \sum_{s=-\infty}^{\infty} f_{|p-q+sN|}^{(\infty)} = f_{|p-q|}^{(\infty)} + \sum_{s=1}^{\infty} (f_{|p-q+sN|}^{(\infty)} + f_{|p-q-sN|}^{(\infty)}). \quad (11)$$

It follows that in the limiting case $N \rightarrow \infty$ the finite lattice matrix (11) recovers the infinite lattice matrix $f_{|p-q|}^{finite} \rightarrow f_{|p-q|}^{(\infty)}$. From (11) we read of for the fractional lattice Laplacian of the finite periodic 1D lattice

²where $p = 0$ in (10) has been put to zero.

$$\Delta_{\alpha,N}(|p|) = -\mu f_{|p|}^{(\alpha,finite)}, \quad 0 \leq p \leq N - 1 \tag{12}$$

with

$$f_{|p|}^{(\alpha,finite)} = \Omega_\alpha^2 \frac{(-1)^p \alpha!}{(\frac{\alpha}{2} - p)! (\frac{\alpha}{2} + p)!} + \Omega_\alpha^2 \sum_{s=1}^{\infty} (-1)^{p+Ns} \alpha! \left(\frac{1}{(\frac{\alpha}{2} - p - sN)! (\frac{\alpha}{2} + p + sN)!} + \frac{1}{(\frac{\alpha}{2} - p + sN)! (\frac{\alpha}{2} + p - sN)!} \right). \tag{13}$$

We observe N -periodicity of (13) and furthermore the necessary property that in the limit of infinite chain $N \rightarrow \infty$, (13) recovers the infinite lattice expression of eq. (6).

3 Fractional continuum limit kernels

In this section we investigate the interlink between the lattice fractional approach introduced above and continuum fractional derivatives. To this end we introduce the following hypotheses which are to be observed when performing continuum limits. Following [9] we require in the continuum limit that extensive physical quantities, i.e. quantities which scale with the length of the 1D system, such as the total mass $N\mu = M$ and the total elastic energy of the chain remain finite when its length L is kept finite³, i.e. neither vanish nor diverge. Let $L = Nh$ be the length of the chain and h the lattice constant (distance between two neighbor atoms or lattice points). We can define two kinds of continuum limits:

- (i) The *periodic string continuum limit* where the length of the chain $L = Nh$ is kept finite and $h \rightarrow 0$ (i.e. $N(h) = Lh^{-1} \rightarrow \infty$).
- (ii) The *infinite space continuum limit* where $h \rightarrow 0$, however, the length of the chain tends to infinity $N(h)h = L(h) \rightarrow \infty^4$. The kernels of the infinite space limit can be recovered from those of the periodic string limit by letting $L \rightarrow \infty$. From the finiteness of the total mass of the chain, it follows that the particle mass $\mu = \frac{M}{N} = \frac{M}{L}h = \rho_0 h$ scales as $\sim h$. Then by employing expression (3) for the fractional elastic potential, the total continuum limit elastic energy \tilde{V}_α can be defined by

$$\tilde{V}_\alpha = \lim_{h \rightarrow 0^+} V_\alpha = \frac{\mu \Omega_\alpha^2}{2} \sum_{p=0}^{N-1} u^*(x_p) \left(-4 \sinh^2 \frac{h}{2} \frac{d}{dx} \right)^{\frac{\alpha}{2}} u(x_p). \tag{14}$$

Putting $D = e^{h \frac{d}{dx}}$ ($ph = x_p \rightarrow x$) and accounting for $2 - D(h) - D(-h) = -4 \sinh^2 \frac{h}{2} \frac{d}{dx} \approx -h^2 \frac{d^2}{dx^2} + O(h^4)$ we get

$$\lim_{h \rightarrow 0} \left(-4 \sinh^2 \frac{h}{2} \frac{d}{dx} \right)^{\frac{\alpha}{2}} = h^\alpha \left(-\frac{d^2}{dx^2} \right)^{\frac{\alpha}{2}}. \tag{15}$$

³In the case of infinite string $L \rightarrow \infty$ we require the mass per unit length and elastic energy per unit length to remain finite.

⁴which can be realized for instance by choosing by $N(h) \sim h^{-\delta}$ where $\delta > 1$.

The formal relation (15) shows that the continuum limit kernels to be deduced in explicit forms have the interpretation of the *Fractional Laplacian* or also in the literature referred to as *Riesz Fractional Derivative*. To maintain finiteness of the elastic energy in the continuum limit $h \rightarrow 0$ the following scaling relations for the characteristic model constants, the mass μ and the frequency Ω_α are required [7, 8]

$$\Omega_\alpha^2(h) = A_\alpha h^{-\alpha}, \quad \mu(h) = \rho_0 h, \quad A_\alpha, \rho_0 > 0 \quad (16)$$

where ρ_0 denotes the mass density with dimension $g \times cm^{-1}$ and A_α denotes a positive dimensional constant of dimension $sec^{-2} \times cm^\alpha$, where the new constants ρ_0, A_α are independent of h . Note that the dimensional constant A_α is only defined up to a non-dimensional positive scaling factor as its absolute value does not matter due to the scale-freeness of the power law. We obtain then as continuum limit of the elastic energy by taking into account $\sum_{p=0}^{N-1} hG(x_p) \rightarrow \int_0^L G(x)dx$ and $h \rightarrow dx$, $x_p \rightarrow x$,

$$\begin{aligned} \tilde{V}_\alpha &= \lim_{h \rightarrow 0} \frac{\mu(h)}{2} \sum_{q=0}^{N-1} \sum_{p=0}^{N-1} u_q^* f_N^{(\alpha)}(|p-q|) u_p \\ \tilde{V}_\alpha &= \frac{\rho_0 A_\alpha}{2} \int_0^L u^*(x) \left(-\frac{d^2}{dx^2} \right)^{\frac{\alpha}{2}} u(x) dx =: -\frac{1}{2} \int_0^L \int_0^L u^*(x') \tilde{\Delta}_\alpha(|x-x'|) u(x) dx dx'. \end{aligned}$$

The continuum limit Laplacian kernel $\tilde{\Delta}_\alpha(|x-x'|)$ can then formally be represented by the distributional kernel representation in the spirit of generalized functions [2]

$$\tilde{\Delta}_{\alpha,L}(|x-x'|) = -\rho_0 A_\alpha \left(-\frac{d^2}{dx^2} \right)^{\frac{\alpha}{2}} \delta_L(x-x'). \quad (17)$$

The last relation contains the distributional representation of the fractional Laplacian and is obtained for the infinite space limit (ii) in explicit form as [7, 8]

$$\mathcal{K}_\infty^{(\alpha)}(x) = - \left(-\frac{d^2}{dx^2} \right)^{\frac{\alpha}{2}} \delta_L(x-x') = -\frac{\alpha!}{\pi} \lim_{\epsilon \rightarrow 0^+} \Re \frac{i^{\alpha+1}}{(x+i\epsilon)^{\alpha+1}}, \quad (18)$$

being defined ‘under the integral’ which yields for noninteger $\frac{\alpha}{2} \notin \mathbf{N}$ for $x \neq 0$ the well known Riesz fractional derivative kernel of the infinite space $\mathcal{K}_\infty^{(\alpha)}(x) = \frac{\alpha! \sin(\frac{\alpha\pi}{2})}{\pi} \frac{1}{|x|^{\alpha+1}}$ with a characteristic $|x|^{-\alpha-1}$ power law nonlocality reflecting the asymptotic power law behavior (9) of (6) for sufficiently large $|p| \gg 1$.

3.1 (i) Periodic string continuum limit

The continuum procedure of L -periodic string where L is kept finite is then obtained as [7, 8]⁵

⁵where $\Re(\dots)$ denotes the real part of a quantity (\dots)

$$\begin{aligned}
 -\left(-\frac{d^2}{dx^2}\right)^{\frac{\alpha}{2}} \delta_L(x) &= K_L^{(\alpha)}(|x|) = \frac{\alpha! \sin\left(\frac{\alpha\pi}{2}\right)}{\pi} \sum_{n=-\infty}^{\infty} \frac{1}{|x-nL|^{\alpha+1}}, \quad \xi = \frac{x}{L}, \\
 K_L^{(\alpha)}(|x|) &= \frac{\alpha! \sin\left(\frac{\alpha\pi}{2}\right)}{\pi L^{\alpha+1}} \left\{ -\frac{1}{|\xi|^{\alpha+1}} + \tilde{\zeta}(\alpha+1, \xi) + \tilde{\zeta}(\alpha+1, -\xi) \right\} \\
 K_L^{(\alpha)}(|x|) &= -\frac{\alpha!}{\pi} \lim_{\epsilon \rightarrow 0^+} \Re \left\{ \sum_{n=-\infty}^{\infty} \frac{i^{\alpha+1}}{(x-nL+i\epsilon)^{\alpha+1}} \right\} \\
 &= \frac{\alpha!}{\pi L^{\alpha+1}} \lim_{\epsilon \rightarrow 0^+} \Re \left\{ i^{\alpha+1} \left(\frac{1}{(\xi+i\epsilon)^{\alpha+1}} - \zeta(\alpha+1, \xi+i\epsilon) - \zeta(\alpha+1, -\xi+i\epsilon) \right) \right\}. \tag{19}
 \end{aligned}$$

This kernel can be conceived as the explicit representation of the fractional Laplacian (Riesz fractional derivative) on the L -periodic string. The last relation is the distributional representation and is expressed by standard Hurwitz ζ -functions denoted by $\zeta(\cdot)$. The two variants of ζ -functions which occur in above relation are defined by

$$\tilde{\zeta}(\beta, x) = \sum_{n=0}^{\infty} \frac{1}{|x+n|^\beta}, \quad \zeta(\beta, x) = \sum_{n=0}^{\infty} \frac{1}{(x+n)^\beta}, \quad \Re \beta > 1. \tag{20}$$

We see for $\alpha > 0$ and $x \neq 0$ that the series in (19) are absolutely convergent as good as the power function integral $\int_1^\infty \xi^{-\alpha-1} d\xi$. For integer powers $\frac{\alpha}{2} \in \mathbf{N}$ the distributional representations (19)_{3,4} take the (distributional) forms of the (negative-semidefinite) 1D integer power Laplacian operators, namely

$$\begin{aligned}
 K_L^{(\alpha=2m)}(|x|) &= (-1)^{m+1} \frac{d^{2m}}{dx^{2m}} \sum_{n=-\infty}^{\infty} \lim_{\epsilon \rightarrow 0^+} \frac{1}{\pi} \frac{\epsilon}{((x-nL)^2 + \epsilon^2)}, \quad \frac{\alpha}{2} = m \in \mathbf{N}_0, \\
 &= (-1)^{m+1} \frac{d^{2m}}{dx^{2m}} \sum_{n=-\infty}^{\infty} \delta_\infty(x-nL) = -\left(-\frac{d^2}{dx^2}\right)^{\frac{\alpha}{2}=m} \delta_L(x), \tag{21}
 \end{aligned}$$

where $\delta_\infty(\cdot)$ and δ_L indicate the Dirac's δ -functions of the infinite and the L -periodic string, respectively. We further observe in full correspondence to the discrete fractional Laplacian matrix, the necessary property that in the limit of an infinite string $\lim_{L \rightarrow \infty} K_L^{(\alpha)}(|x|) = \mathcal{K}_\infty^{(\alpha)}(x)$ (19) recovers the expression of the standard 1D infinite space fractional Laplacian kernel (18) known from the literature (see for a further discussion [7, 8] and references therein).

4 Fractional Laplacian matrix on cubic lattices: towards fractional lattice dynamics

In this section we deduce the nD counterpart of the fractional Laplacian matrix introduced above. With that approach the fundamentals of ‘*fractional lattice dynamics*’ can be deduced as a generalization of conventional lattice dynamics.

In this section our goal is to generalize the above 1D lattice approach to cubic periodic lattices in $n = 1, 2, 3, \dots$ dimensions of the physical space where the 1D lattice case is contained. We assume the lattice contains $N = N_1 \dots \times N_n$ lattice points, each covered by identical atoms with mass μ . Each mass point is characterized by $\vec{p} = (p_1, p_2, \dots, p_n)$ ($p_j = 0, \dots, N_j - 1$) and $n = 1, 2, 3, \dots$ denotes the dimension of the physical space embedding the lattice. In order to define the lattice fractional Laplacian matrix, it is sufficient to consider a *scalar* generalized displacement field $u_{\vec{p}}$ (one field degree of freedom) associated to each mass point \vec{p} only. The physical nature of this scalar field can be any scalar field, such as for instance a one degree of freedom displacement field, an electric potential or, in a stochastic context a probability density function (pdf) or in a fractional quantum mechanics context a Schrödinger wave function. This demonstrates the interdisciplinary character of the present fractional lattice approach.

The fractional Laplacian matrix for general networks was only recently and to our knowledge for the first time introduced by Riascos and Mateos [12, 13] in the framework of fractional diffusion analysis on networks which include nD periodic lattices (nD tori) as special cases being subject of the present analysis. For cubic nD lattices the fractional Laplacian matrix can be written as [7, 8, 12, 13]

$$\Delta_{\alpha,n} = -\mu\Omega_{\alpha,n}^2 L_n^{\frac{\alpha}{2}}, \quad L_n^{\frac{\alpha}{2}} = (2n\hat{1} - A_n)^{\frac{\alpha}{2}}, \quad \alpha > 0, \quad (22)$$

where $\hat{1}$ denotes the identity matrix, n indicates the dimension of the physical space and $2n$ indicates the connectivity, i.e. the number of next neighbors of a lattice point in the nD cubic lattice. In (22) we introduced the adjacency matrix A_n which has for the cubic lattice with next neighbor connections the form

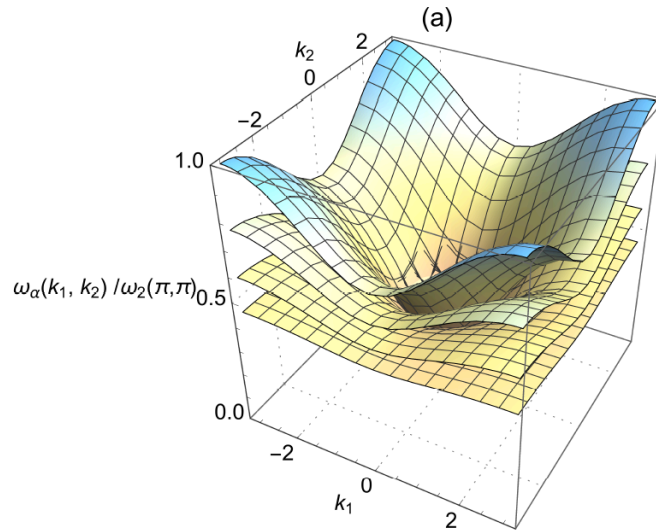
$$A_n = \sum_{j=1}^n (D_j + D_j^\dagger), \quad (23)$$

where then D_j and $D_j^\dagger = D_j^{-1}$ denote the next neighbor shift operators in the $j = 1, \dots, n$ -directions defined by $D_j u_{p_1, \dots, p_j, \dots, p_n} = \vec{u}_{p_1, \dots, p_j+1, \dots, p_n}$ and $D_j^\dagger \vec{u}_{p_1, \dots, p_j, \dots, p_n} = u_{p_1, \dots, p_j-1, \dots, p_n}$, i.e. D_j shifts the field associated to lattice point $\vec{p} = (\dots, p_j, \dots)$ to the field associated with the adjacent lattice point in the positive j -direction (\dots, p_{j+1}, \dots) , and the inverse (adjoint) shift operator $D_j^\dagger = D_j^{-1}$ to the adjacent lattice point in the negative j -direction (\dots, p_{j-1}, \dots) . All matrices introduced in (22) and (23) are defined on the nD lattice being $N \times N$ matrices ($N = N_1 \times \dots \times N_n$). As in the case of 1D lattice the so defined fractional Laplacian matrix (22) describes for non-integer powers $\frac{\alpha}{2}, \notin \mathbf{N}$ nonlocal elastic interactions, whereas they are generated by the ‘local’ next

neighbor Born von Karman Laplacian which is in our definition up to a negative dimension factor $-\mu\Omega_2$ equal to L_n . We therefore refer to L_n as ‘generator matrix’. We emphasize that the sign convention of what we call ‘(fractional) Laplacian matrix’ varies in the literature (e.g. by denoting the positive semidefinite matrix $L_n^{\frac{\alpha}{2}}$ as ‘fractional Laplacian matrix’, this convention is chosen, e.g. in [12, 13]). We have chosen to refer to as ‘fractional Laplacian matrix’ the negative-semidefinite matrix $-\mu\Omega_\alpha^2 L_n^{\frac{\alpha}{2}}$ to be in accordance with the negative definiteness of continuum limit fractional Laplacian (21) containing as a special case $\frac{\alpha}{2} = 1$ the negative semidefinite conventional Laplacian $\frac{d^2}{dx^2}\delta_L(x-x')$. For a discussion of some general properties of the fractional Laplacian (22) well defined on general networks including nD lattices, we refer to [12, 13]. In the periodic and infinite lattice the shift operators are unitary. Assuming N_j -periodicity in each direction j , the fractional Laplacian matrix is defined by the spectral properties of the L_n -matrix, namely by

$$[L_n^{\frac{\alpha}{2}}]_{(\vec{p}-\vec{q})} = \frac{1}{N} \sum_{\vec{\ell}} e^{i\vec{\kappa}_{\vec{\ell}}(\vec{p}-\vec{q})} \lambda_{\vec{\ell}}^{\frac{\alpha}{2}}, \quad \lambda_{\vec{\ell}} = \left(2n - 2 \sum_{j=1}^n \cos(\kappa_{\ell_j}) \right), \quad \alpha > 0, \quad (24)$$

where we denoted $\sum_{\vec{\ell}}(\dots) = \sum_{\ell_1=0}^{N_1-1}(\dots) \dots \sum_{\ell_n=0}^{N_n-1}(\dots)$ and $\vec{\kappa}_{\vec{\ell}} = (\kappa_{\ell_1}, \dots, \kappa_{\ell_n})$ denotes the Bloch wave vectors of the Brillouin zone where their components can take the values $\kappa_{\ell_j} = \frac{2\pi}{N_j} \ell_j$ ($\ell_j = 0, \dots, N_j - 1$). It can be seen that (24) has Töplitz structure depending only on $|p_1 - q_1|, \dots, |p_j - q_j|, \dots, |p_n - q_n|$. For the infinite lattice when all $N_j \rightarrow \infty$ in (24), the summation over the reciprocal lattice points assumes asymptotically the form of an integral $\frac{1}{N} \sum_{\vec{\ell}} g(\vec{\kappa}_{\vec{\ell}}) \sim \frac{1}{(2\pi)^n} \int_{-\pi}^{\pi} \dots \int_{-\pi}^{\pi} d\kappa_1 \dots d\kappa_n g(\vec{\kappa})$, where the integration intervals $[-\pi, \pi]$ can be chosen instead of $[0, 2\pi]$ for 2π -periodic functions $g(\kappa_j) = g(\kappa_j + 2\pi)$.



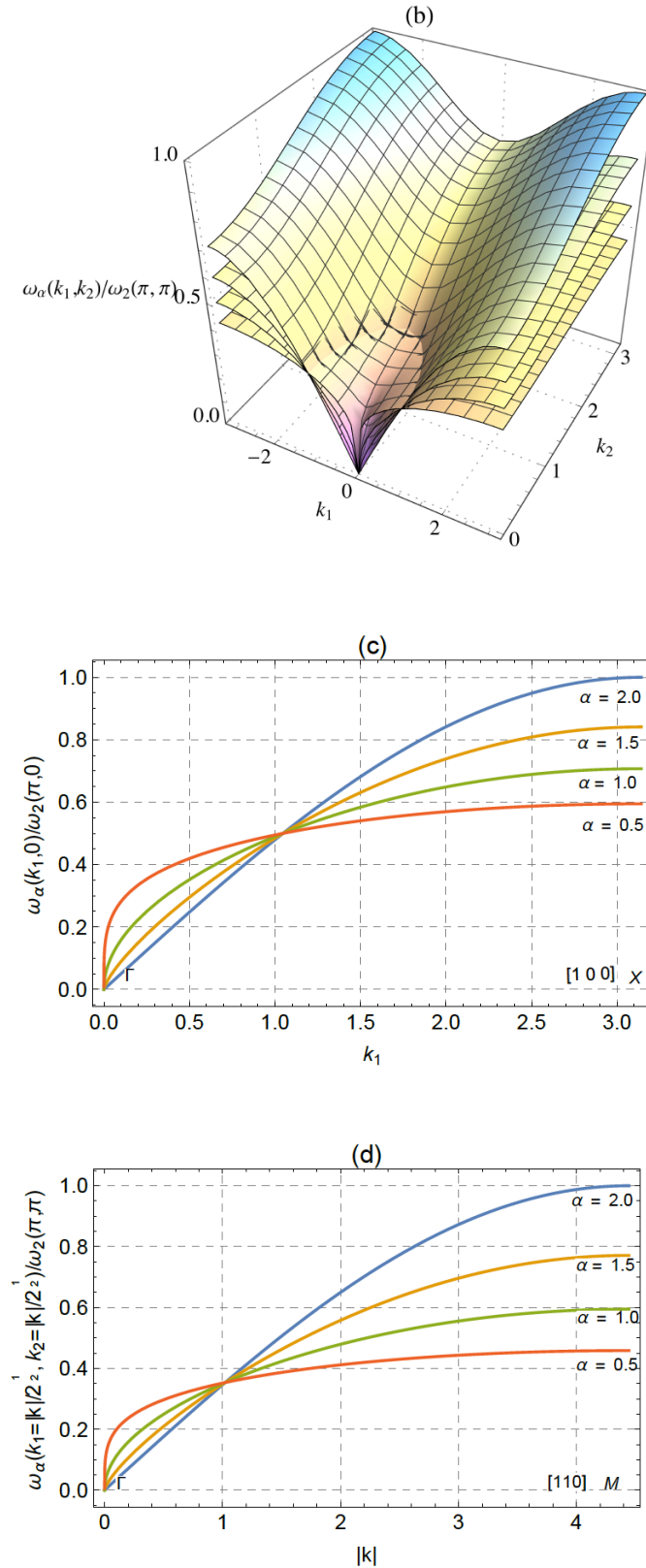


Fig.1 (a-b) Show the dispersion surfaces $\omega_\alpha(\kappa_1, \kappa_2)/\omega_2(\pi, \pi) = \lambda^{\frac{\alpha}{4}}(\kappa_1, \kappa_2)/2^{\frac{3}{2}} = 2^{\frac{\alpha-3}{2}}(\sin^2(\kappa_1/2) + \sin^2(\kappa_2/2))^{\frac{\alpha}{4}}$ for the 2D cubic lattice ($n = 2$) of (24) for four values of α , while (c-d) illustrate cross-sections of these dispersion sheets with the planes (0 1 0) and (1 1 0), respectively.

For α fixed, the circular frequency is given by $\omega_\alpha(\kappa_1, \kappa_2) = \lambda^{\frac{\alpha}{4}}$. The linear frequency spectra (a, b, d) , for $n = 2$, are normalized by the maximum frequency $\omega_{\alpha=2}(\pi, \pi) = \lambda^{\frac{1}{2}}(\pi, \pi) = 2^{\frac{3}{2}}$ obtained for a wave vector located in (001) plane. It will be noted that the sheets cut at dimensionless frequency $\omega_\alpha(\kappa_1, \kappa_2)/\omega_{\alpha=2}(\pi, \pi) \approx 0.351$ and the dispersion relations of the classical next neighbor Born von Karman lattice are recovered (indicated by $\omega_\alpha(\kappa_1, \kappa_2)/\omega_{\alpha=2}(\pi, \pi) \rightarrow 1$ for $\alpha = 2$ and $\kappa_{1,2} \rightarrow \pi$, $\omega_\alpha(\kappa_1, 0)/\omega_{\alpha=2}(\pi, 0) \rightarrow 1$ for $\alpha = 2$ and $\kappa_1 \rightarrow \pi$). When the value of α decreases, one observes in agreement with another work [7], namely a decrease of the maximum dimensionless frequency in end of the first Brillouin zone.

The goal is now to deduce a more convenient integral representation of (24). To this end we utilize the following observation: Let in the following \mathcal{L} be a positive semidefinite⁶ matrix and $\alpha > 0$ like (22) with the spectral representation

$$\mathcal{L} = \sum_{\vec{\ell}} \lambda_{\vec{\ell}} |\vec{\ell}\rangle \langle \vec{\ell}|, \quad \mathcal{L}_{pq} = \langle p | \mathcal{L} q \rangle, \quad (25)$$

where we have to put for the periodic nD lattice of (24) the Bloch-eigenvectors $\langle \vec{p} | \vec{\ell} \rangle = N^{-\frac{1}{2}} e^{i\vec{\kappa}_{\vec{\ell}} \cdot \vec{p}}$. Then it will be useful to define the matrix Dirac δ -function by

$$\delta(\mathcal{L} - \tau \hat{1}) = \sum_{\vec{\ell}} |\vec{\ell}\rangle \langle \vec{\ell}| \delta(\tau - \lambda_{\vec{\ell}}), \quad (26)$$

where τ is a scalar parameter and $\hat{1}$ the identity matrix and $\delta(\tau - \lambda_{\vec{\ell}})$ the conventional scalar Dirac δ -function. Then with the matrix δ -function defined in (26) we can write

$$\mathcal{L}^{\frac{\alpha}{2}} = \int_{-\infty}^{\infty} \delta(\mathcal{L} - \tau \hat{1}) |\tau|^{\frac{\alpha}{2}} d\tau \quad (27)$$

and by utilizing $\delta(\tau - \lambda_{\vec{\ell}}) = \frac{1}{(2\pi)} \int_{-\infty}^{\infty} e^{ik(\tau - \lambda_{\vec{\ell}})} dk$ together with the kernel $-\mathcal{D}_{\frac{\alpha}{2}}$ of the 1D fractional Laplacian (Riesz fractional derivative) of order $\frac{\alpha}{2}$ in its distributional form [11]

$$\mathcal{D}_{\frac{\alpha}{2}}(k - \xi) = \left(-\frac{d^2}{dk^2} \right)^{\frac{\alpha}{4}} \delta(k - \xi) =: \frac{1}{(2\pi)} \int_{-\infty}^{\infty} e^{i(k-\xi)\tau} |\tau|^{\frac{\alpha}{2}} d\tau = \quad (28)$$

$$\lim_{\epsilon \rightarrow 0^+} \frac{1}{\pi} \Re \int_0^{\infty} e^{-\tau(\epsilon - i(k-\xi))} |\tau|^{\frac{\alpha}{2}} d\tau = \lim_{\epsilon \rightarrow 0^+} \Re \frac{\Gamma(\frac{\alpha}{2} + 1)}{\pi(\epsilon - i(k - \xi))^{\frac{\alpha}{2}}}.$$

Then we can write for the matrix power function (27) the representation

$$\mathcal{L}^{\frac{\alpha}{2}} = \int_{-\infty}^{\infty} e^{ik\mathcal{L}} \mathcal{D}_{\frac{\alpha}{2}}(k) dk, \quad (29)$$

where the exponential $e^{ik\mathcal{L}}$ of the matrix $\mathcal{L} = L_n$ can be determined more easily for the generator $L_n = \sum_{j=1}^n L_j$ ($L_j = 2 - D_j - D_j^\dagger$) being the sum of the 1D generator

⁶i.e. all eigenvalues λ_{ℓ} of this matrix are non-negative.

matrices of the N_j -periodic 1D lattices and having therefore the eigenvalues $\lambda(\ell_j) = 2 - 2 \cos \kappa_{\ell_j}$ and as a consequence having a Cartesian product space spanned by the periodic Bloch eigenvectors $\frac{e^{i\vec{\kappa}_{\vec{\ell}} \vec{p}}}{\sqrt{N}} = \prod_{j=1}^n \frac{e^{ip_j \kappa_{\ell_j}}}{\sqrt{N_j}}$. The matrix elements of the spectral representation of the exponential of L_n can hence be written as

$$[e^{i\xi L_n}]_{\vec{p}-\vec{q}} = \sum_{\vec{\ell}} \frac{e^{i\vec{\kappa}_{\vec{\ell}}(\vec{p}-\vec{q})}}{N} e^{i\xi \lambda_{\vec{\ell}}} = \prod_{j=1}^n \sum_{\ell_j=1}^{N_j-1} \frac{e^{i(p_j-q_j)\kappa_{\ell_j}}}{N_j} e^{i2k(1-\cos \kappa_{\ell_j})}. \quad (30)$$

Infinite nD lattice

In the limiting case of an infinite nD lattice when all $N_j \rightarrow \infty$ we can write by using $\frac{1}{N} \sum_{\vec{\ell}} g(\vec{\kappa}_{\vec{\ell}}) \sim \frac{1}{(2\pi)^n} \int_{-\pi}^{\pi} \dots \int_{-\pi}^{\pi} d\kappa_1 \dots d\kappa_n g(\vec{\kappa})$ to arrive at

$$[e^{i\xi L_n}]_{\vec{p}-\vec{q}} = [e^{i\xi L_n}]_{|p_1-q_1|, \dots, |p_n-q_n|} = \prod_{j=1}^n \frac{1}{(2\pi)} \int_{-\pi}^{\pi} e^{i(p_j-q_j)\kappa} e^{i2\xi(1-\cos \kappa)} d\kappa. \quad (31)$$

Taking into account the definition of the modified Bessel functions of the first kind $I_p(z) = \frac{1}{\pi} \int_0^{\pi} e^{z \cos \varphi} \cos p\varphi d\varphi$ where $p = \mathbf{N}_0$ denotes non-negative integers [1], we can write the exponential matrix (31) in the form

$$[e^{i\xi L_n}]_{|p_1-q_1|, \dots, |p_n-q_n|} = e^{i2n\xi} \prod_{j=1}^n I_{|p_j-q_j|}(-2i\xi). \quad (32)$$

Applying now the matrix relation (27) and plugging in the exponential (32) yields an integral representation of the (negative semidefinite) fractional Laplacian matrix (22) in terms of a product of modified Bessel functions of the first kind, namely

$$\begin{aligned} [\Delta_{\alpha,n}]_{|p_1-q_1|, \dots, |p_n-q_n|} &= -\mu \Omega_{\alpha,n}^2 L_{|p_1-q_1|, \dots, |p_n-q_n|}^{\frac{\alpha}{2}} \\ &= -\mu \Omega_{\alpha,n}^2 \int_{-\infty}^{\infty} d\xi e^{i2n\xi} \mathcal{D}_{\frac{\alpha}{2}}(\xi) \prod_{j=1}^n I_{|p_j-q_j|}(-2i\xi), \end{aligned} \quad (33)$$

with $-\mathcal{D}_{\frac{\alpha}{2}}(\xi)$ indicating the Riesz fractional derivative kernel of (28).

Asymptotic behavior

Introducing the new vector valued integration variable $\vec{\xi} = \vec{\kappa} p$ ($\xi_j = p \kappa_j, \forall j = 1, \dots, n$) we can write for the infinite lattice integral of (24) by utilizing spherical polar coordinates $\vec{p} = p \vec{e}_{\vec{p}}$ ($\vec{e}_{\vec{p}} \cdot \vec{e}_{\vec{p}} = 1, p^2 = \sum_j^n p_j^2$)

$$L_n^{\frac{\alpha}{2}}(\mathbf{p}) = \frac{1}{(2\pi)^n} \int_{-\pi p}^{\pi p} \dots \int_{-\pi p}^{\pi p} \frac{d\xi_1 \dots d\xi_n}{p^n} \left(4 \sum_{j=1}^n \sin^2 \frac{\xi_j}{2p} \right)^{\frac{\alpha}{2}} \cos(\vec{\xi} \cdot \vec{e}_{\vec{p}}). \quad (34)$$

The dominating term for $p \gg 1$ becomes

$$L_n^{\frac{\alpha}{2}}(\mathbf{p}) \approx \frac{1}{p^{n+\alpha}} \frac{1}{(2\pi)^n} \int_{-\infty}^{\infty} \dots \int_{-\infty}^{\infty} d\xi_1 \dots d\xi_n \left(\sum_{j=1}^n \xi_j^2 \right)^{\frac{\alpha}{2}} \cos(\vec{\xi} \cdot \vec{e}_{\vec{p}}), \quad (35)$$

having the form

$$L_n^{\frac{\alpha}{2}}(\vec{p})_{p \gg 1} \approx -\frac{C_{n,\alpha}}{p^{n+\alpha}}, \quad (36)$$

where the positive normalization constant is obtained explicitly as $C_{n,\alpha} = \frac{2^{\alpha-1}\alpha\Gamma(\frac{\alpha+n}{2})}{\pi^{\frac{n}{2}}\Gamma(1-\frac{\alpha}{2})}$, e.g. [10, 11]. We can identify the asymptotic representation (35), (36) with the kernel of Riesz fractional derivative (fractional Laplacian) of the nD infinite space. For a more detailed discussion of properties we refer to [10, 11].

5 Conclusions

We have introduced a fractional lattice dynamics approach which defines exact expressions for fractional lattice Laplacian matrices on nD periodic and infinite lattices. These fractional Laplacian matrices have all ‘good’ properties of Laplacian matrices (translational invariance and negative semidefiniteness). The formulation of our approach is fully consistent with the fractional network approach of Riascos and Mateos [12, 13]. In the infinite space and periodic lattice continuum limits these fractional Laplacian matrices take the representations of the well known respective Riesz fractional derivative kernels, i.e. the convolutional kernels of the (continuous) fractional Laplacians. The approach allows to model ‘anomalous diffusion’ phenomena on lattices with fractional transport phenomena including asymptotic emergence of Lévy flights. In such a lattice diffusional model, the conventional Laplacian matrix is generalized by its fractional power law matrix function counterpart.

As a general framework, the present fractional lattice Laplacian appears to be fundamental in various physical contexts, especially as a point of departure for a newly emerging generalization of Lattice Dynamics to ‘*Fractional Lattice Dynamics*’.

Acknowledgements

Fruitful discussions with G.A. Maugin, A. Porubov are gratefully acknowledged.

References

- [1] Abramowitz and Stegun, Handbook of Mathematical Function, National Bureau of Standards: Applied Mathematics Series - 55, (1972), p. 376.
- [2] I.M. Gelfand, G.E. Shilov, Generalized Functions, Vol. I: Properties and Operations (New York: Academic), (1964).
- [3] R. Hilfer, Threefold Introduction to Fractional Derivatives, in: Anomalous Transport: Foundations and Applications, R. Klages et al. (eds.), Wiley-VCH, Weinheim, 2008, pp 17, ISBN: 978-3-527-40722-4.
- [4] N. Laskin, Fractional Schrödinger equation, Phys. Rev. E 66, 056108 (2002).

-
- [5] R. Metzler, J. Klafter, The random walk's guide to anomalous diffusion: A fractional dynamics approach. *Physics Reports* 339, pp. 1-77 (2000).
- [6] R. Metzler, J. Klafter, The restaurant at the end of the random walk: recent developments in the description of anomalous transport by fractional dynamics, *J. Phys. A: Math. Gen.* 37 R161-R208 (2004).
- [7] T.M. Michelitsch, B. Collet, A.F. Nowakowski, F.C.G.A. Nicolleau, Fractional Laplacian matrix on the finite periodic linear chain and its periodic Riesz fractional derivative continuum limit, *J. Phys. A: Math. Theor.* 48 295202 (2015). (arXiv:1412.5904).
- [8] T.M. Michelitsch, B. Collet, A.F. Nowakowski, F.C.G.A. Nicolleau, Lattice fractional Laplacian and its continuum limit kernel on the finite cyclic chain, *Chaos, Solitons & Fractals* 82, pp. 38-47 (2016). (arXiv:1511.01251).
- [9] T. Michelitsch, B. Collet, X. Wang, Nonlocal constitutive laws generated by matrix functions: Lattice dynamics models and their continuum limits, *International Journal of Engineering Science* 80, 106-123 (2014).
- [10] T.M. Michelitsch, G.A. Maugin, A.F. Nowakowski, F.C.G.A. Nicolleau, M. Rahman, The Fractional Laplacian as a limiting case of a self-similar spring model and applications to n-dimensional anomalous diffusion. *Fractional Calculus and Applied Analysis* vol. 16, no.4, 827-859 (2013).
- [11] T.M. Michelitsch; G.A. Maugin, S. Derogar, M. Rahman, A regularized representation of the fractional Laplacian in n dimensions and its relation to Weierstrass-Mandelbrot-type fractal functions, *IMA Journal of Applied Mathematics* 79, 753-777 (2014).
- [12] A.P. Riascos, J.L. Mateos, Fractional dynamics on networks: Emergence of anomalous diffusion and Lévy flights, *Phys. Rev. E* 90, 032809 (2014). (arxiv:1506.06167).
- [13] A.P. Riascos, J.L. Mateos, Fractional diffusion on circulant networks: emergence of a dynamical small world, *J. Stat. Mech.* (2015).
- [14] M.D. Ortiguera, Riesz Potential Operators and Inverses via Fractional Centered Derivatives, *International Journal of Mathematics and Mathematical Sciences*, no. 48391, 1-12 (2006).
- [15] S. Samko, A. Kilbas and O. Marichev, *Fractional Integrals and Derivatives: Theory and Applications*, Gordon and Breach, London (1993).
- [16] S. Samko, Fractional Weyl-Riesz Integrodifferentiation of Periodic Functions of Two Variables via the Periodization of the Riesz Kernel, *Applicable Analysis*, vol. 82, No 3, 269-299 (2003).
- [17] I. Podlubny, *Fractional Differential Equations*, Mathematics in Science and Engineering, vol 198, Academic Press California 1999.

- [18] M. Riesz, L'intégrale de Riemann-Liouville et le problème de Cauchy, *Acta Mathematica* 81, 1223 (1949), doi:10.1007/BF02395016, MR0030102, ISSN 0001-5962.
- [19] A. Zoia A, A. Rosso, M. Kardar, Fractional Laplacian in bounded domains, *Phys. Rev. E* 76, 021116 (2007).

Thomas M. Michelitsch, Bernard A. Collet

Sorbonne Universités, Université Pierre et Marie Curie (Paris 6), Institut Jean le Rond d'Alembert, CNRS UMR 7190, 4 place Jussieu, 75252 Paris cedex 05, France

Alejandro P. Riascos

Instituto de Física, Universidad Nacional Autónoma de México, Apartado Postal 20-364, 01000 México, D.F., México

Andrzej F. Nowakowski, Franck C.G.A. Nicolleau

Department of Mechanical Engineering, The University of Sheffield, Sir Frederick Mappin Building, Mappin Street, Sheffield S1 3JD, United Kingdom

Structural-mechanical AFM mapping of overstressed zones in stretched filled natural rubber

Ilya A. Morozov
ilya.morozov@gmail.com

Abstract

Surfaces of cracks in the stretched natural rubber filled with silica nanoparticles were studied. On the non-deformed material the notches were made and then the sample was stretched and fixed. As the result, the defects propagated deeper into the material and somehow stopped. The polymer matrix in the region of crack is in critical stress-strain state. The surface of such cracks was studied by atomic force microscope in nanomechanical mapping regime. It was found that the stiffness of the polymer in the crack is much higher than the stiffness of the material in the unloaded state. This is due to strain-induced crystallization and orientation of natural rubber. The formation of elastomer strands oriented orthogonal to the axis of the crack was observed. It was shown that the stiffness and structure of the polymer and oriented strands depend both on the filler fraction and the distance from the crack tip.

1 Introduction

Natural rubber (NR) and its vulcanizates are extensively used in rubber industry. Therefore, it is important to understand the mechanisms responsible for material failure and especially to prevent in-service failure of materials. The strain of a polymer in a static crack of the stretched material reaches its limiting value, and any increase of loading may lead to a further growth of the defect. Investigations the structural-mechanical properties of such regions on micro- and nano- levels provide insight into the processes involved into the resistance of NR vulcanizates to failure. Until recently, in situ studies of the microstructure of cracks and ruptures in rubber were performed by SEM under low vacuum conditions [1]. However, this procedure was not effective in achieving high resolution ($< 10\mu m$) necessary to observe changes taking place in the NR samples at the submicron scale. The unique advantage of NR is strain induced crystallization. Application of wide-angle X-ray diffraction (WAXD) has made it possible to evaluate the degree of crystallization of NR around a crack tip with spatial resolution of $100\mu m$ and more [2].

In the present study, we have used complementary high-resolution atomic force microscopy (AFM) allowing not only observation of the structure of cracks till the

scale of separate filler inclusions and oriented polymer fibrils, but also measurement of the stiffness of overstressed zones in the material being in a crystalline phase.

2 Materials and methods

In this work the natural rubber vulcanizates filled with silica oxide (mass fraction 0, 5, 30, and 50 wt. parts) Aerosil (nanoparticles 20nm in size) were used. For testing, thin-strip specimens were clamped in a miniature tensile device. Small-size notches were cut at the edges of the specimens, and after that they were stretched and fixed. To observe changes in the material in the crack, an AFM probe was placed in the "bottom" of the crack (Fig. 1).

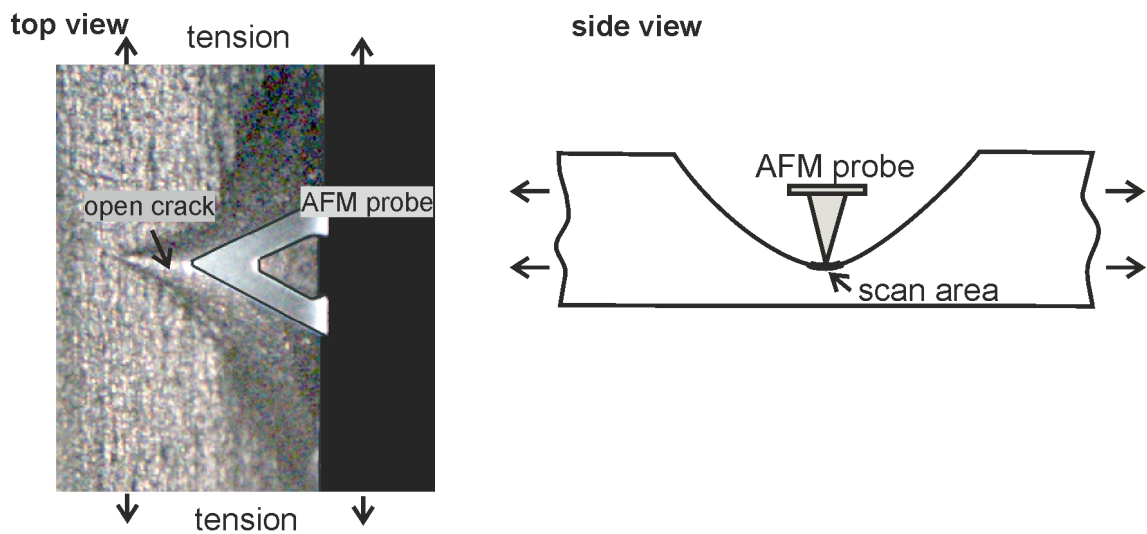


Figure 1: Illustration of AFM crack scanning

The structural-mechanical properties of surfaces were studied with an AFM Dimension Icon in PeakForce regime. Every point on the surface was subjected to nanoindentation, and, apart from a relief height, a force curve $F(z)$ - a relationship between the indentation force F applied by a cantilever to the specimen surface and its vertical displacement z was obtained. The high indentation rate allowed to get rid of undesirable inelastic interactions and to determine the high resolution mechanical characteristics of the material surface. The original algorithms based on the Maugis-Dugdale [3, 4] model of elastic interactions were used to fit the force curves. The result of this processing is the material stiffness at a given point.

According to the assumed properties of the material, AFM cantilevers of different stiffness calibrated by the method of free thermal oscillations were used. Figure 2 presents the examples of force curves obtained in PeakForce mode by scanning the NR surface areas with different stiffness (crystallization degree). The result of the Maugis-Dugdale approximation is shown in Fig.2b: markers - experimental data; lines - model fitting. The negative values of the indentation depth from Fig.2b correspond to the case when the material is entrained by the probe during its retrace.

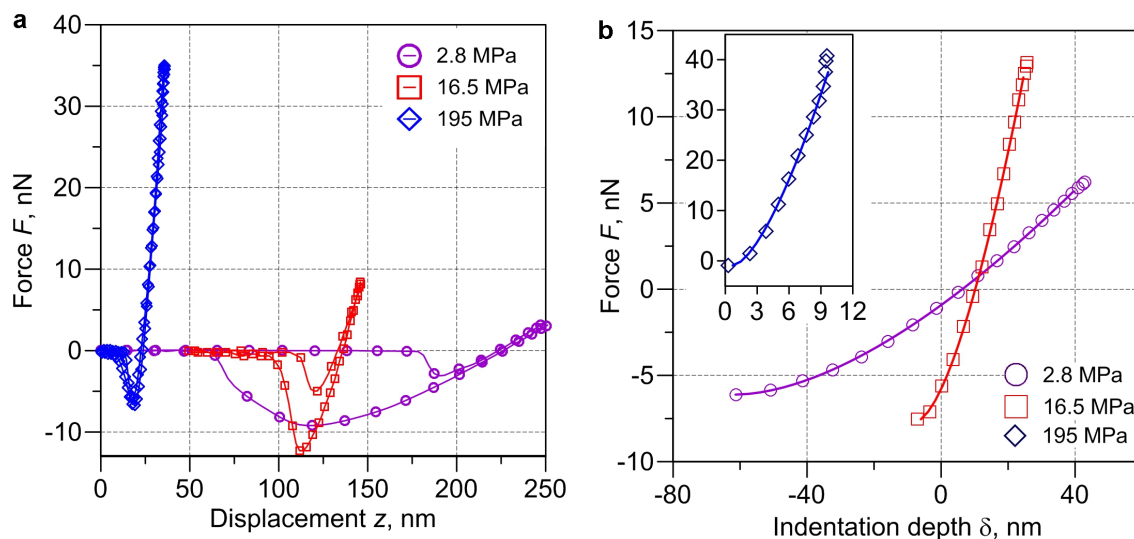


Figure 2: Force curves obtained for NR in different phases (a) and the corresponding identification depth (b)

3 Results

The surface relief and elastic modulus of NR in the area without defects are illustrated in Fig. 3.

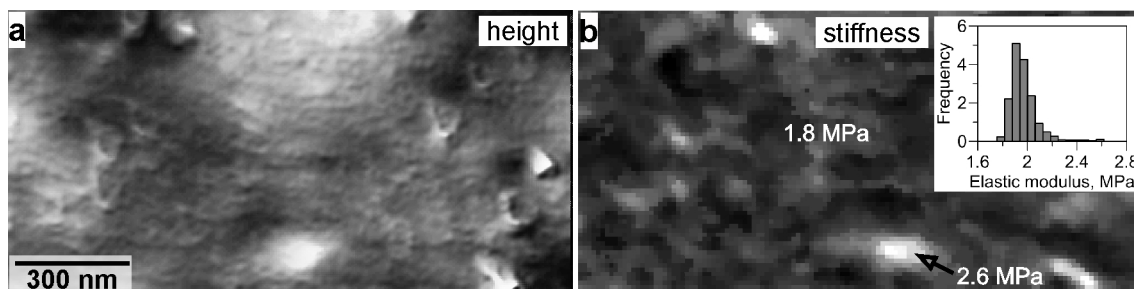


Figure 3: AFM-images of the NR surface height (a) and the map of the elastic modulus (b). Hereinafter the dark areas correspond to low values, while the light areas - to higher values

An inset in Fig.3b shows the distribution of the elastic modulus; its mean value is 2MPa , which is close to macroscopic measurements. Note that in the elastic modulus map there are relatively soft (1.8MPa) and more rigid regions (2.6MPa). Probably, this is associated with the local inhomogeneities of crosslinks.

The structural-mechanical properties of the material surface in a cross crack are dependent on a distance away from a sharp crack tip. Figure 4 presents the AFM-images obtained around the crack tip and in the vicinity of the crack opening in the stretched unfilled NR (schematic representation of scan positions are shown in the insets). Near the crack tip there are extended polymeric strands moving from the edges of the crack to its axis and exhibiting a bend towards the crack tip (indicated by $\Gamma\text{CAB}\Gamma\text{C}$ in Fig. 4a). Away from the tip or if the crack has a form of trench crossing the whole sample, the parallel polymer strands and local

longitudinal ruptures occur on the specimen surface.

Measurements have shown that the NR stiffness around the crack tip is 300 MPa, and in the crack opening - 600 MPa. The indentation depth is 9 nm and 5 nm, respectively. Such a high stiffness points to the fact that the material is in an oriented crystalline phase.

The stiffness of the material in a crack reaches its maximum values at a distance of $\pm 3 - 4 \mu\text{m}$ away from the rupture axis, and then it reduces sharply. Elastic modulus profiles along one of the crack cross-sections (dashed line) are given in Fig.4.

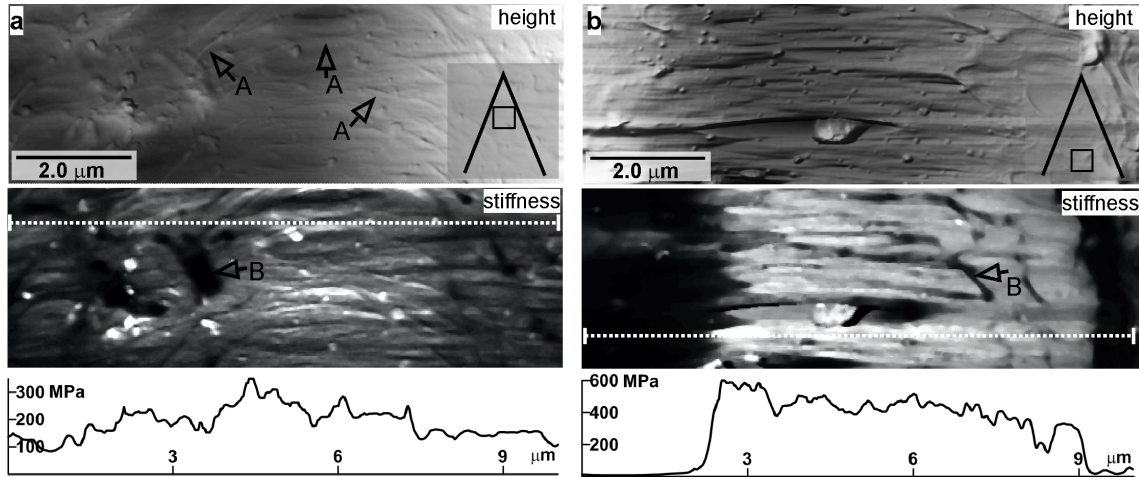


Figure 4: AFM-images of the relief and stiffness in cracks of the unfilled NR around the crack tip (a) and in opening (b). Explanations are provided in the text

The close-up views of strands at the rupture tip are given in Fig. 5b. Their cross-section size is 8...30 nm. The height of the visible part of the strand is 6...8 nm. Figure 5a shows a region at the crack tip that is free of strands (as in the center of Fig. 5b). The image is obtained using a sharp probe. It is seen that the structure of smooth regions in higher resolution is composed of a network of nanofibrils. The maximum visible transverse dimension of a fibril is 4 nm (validity is limited by the size of the probe tip). The height of the visible fibril part is 0.5...0.7 nm. If it is supposed that the fibril has a circular cross-section and rises half its size above the surface, then the true transverse dimension of these fibrils is 1.0...1.4 nm. Contrast in the probe-surface adhesion map is indicative of a difference between the mechanical properties of the polymer in fibrils and the surrounding material. Low adhesion (dark areas) corresponds to a more rigid material.

On the rupture surface there are also parts exhibiting stiffness (B in Fig. 4) less than that of the surrounding material. The stiffness of these structures (Fig.5c) is an order of magnitude lower than the stiffness of the surrounding material. They seem to be partially crystallized fragments of the polymer broken due to crack propagation.

An incorporation of filler into the polymer increases the number of strands in the crack. The rupture surface of NR with 5 wt. parts of filler is characterized by a larger number of strands (Fig.6). The cross-section dimensions of strands are 20...30 nm (Fig. 6a). The stiffness of the strand reaches 800 PĚPa, and the stiffness of the surrounding material is 200 PĚPa (Fig. 6b).

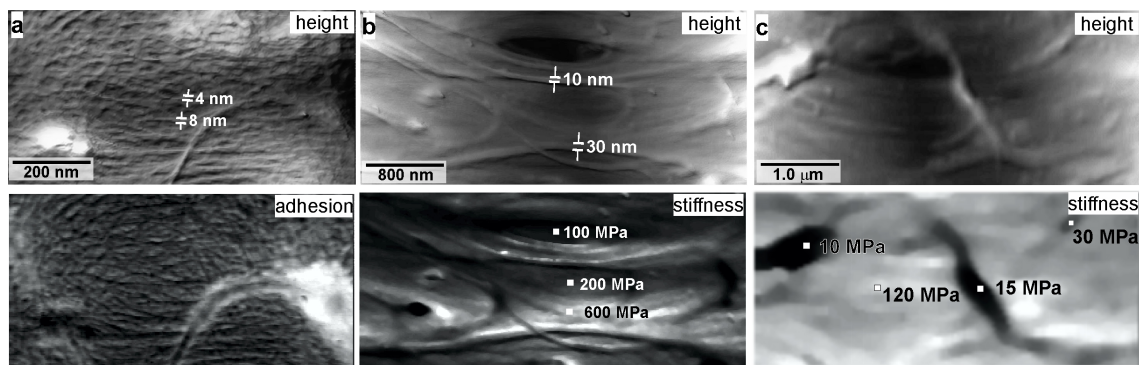


Figure 5: AFM-images of nanofibrills (a), stiff strands (b) and soft regions (c) on the unfilled NR crack surface

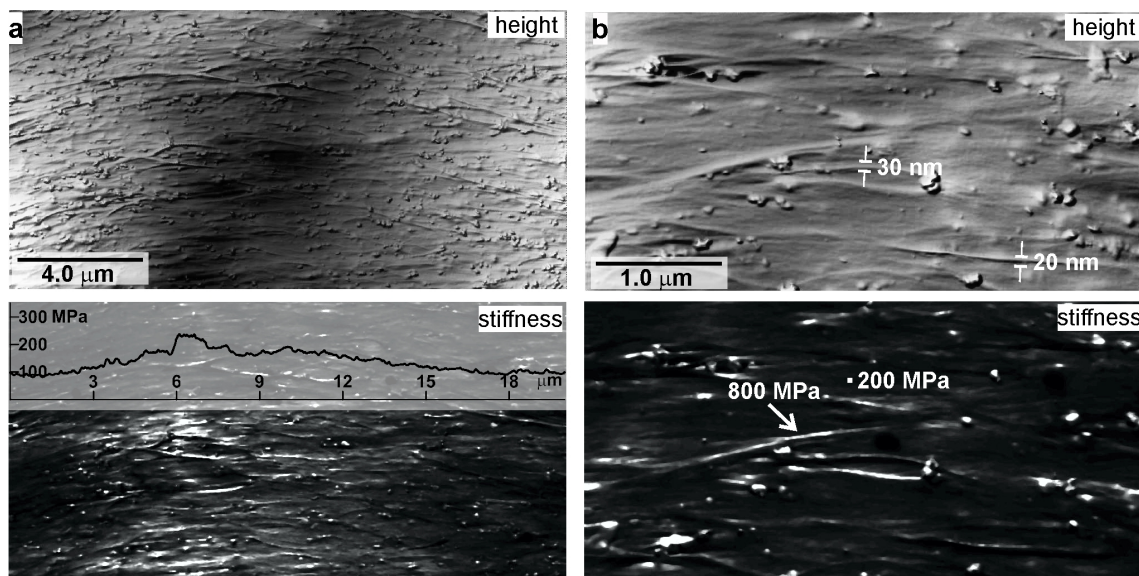


Figure 6: AFM-images of the height (a) and the stiffness (b) of the crack surface of NR with 5 wt. parts of filler

As the filler content increases, the number of strands increases as well and their length decreases. Figure 7a, b presents the images of cracks in NR with 30 and 50 wt. parts of filler. Filler distribution in the material is inhomogeneous, which causes the occurrence of regions with high and low concentration of inclusions. The highest stiffness (600...800 PĖPa) appears in the regions free of filler, where the polymer deformation is maximal. The strand sizes are comparable with the sizes of inclusions.

4 Conclusion

The surfaces of cross notches in the stretched natural rubber filled with silica oxide nanoparticles were investigated. Use of atomic force microscopy made it possible to study the structural-mechanical properties of the surface of these cracks. It has been found that the stiffness of the polymer in the crack (200BΓ3600 PĖPa) is many times

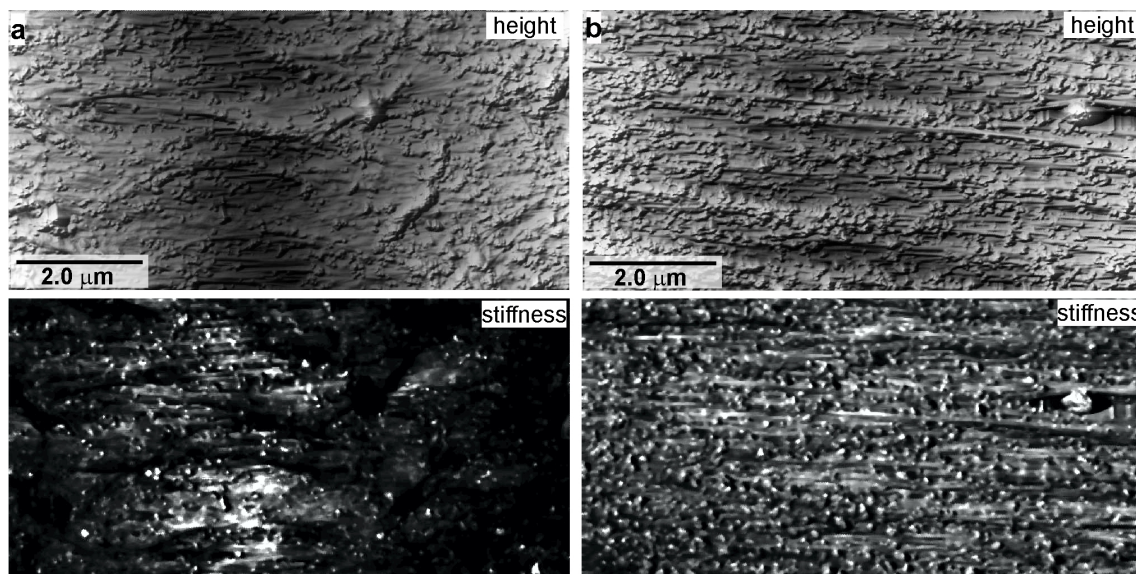


Figure 7: AFM-images of the height and stiffness of cracks in NR with 30 (a) and 50 (b) wt. parts of filler

as large as the stiffness of the material in an unloaded state ($2P$). The generation of the oriented elastomeric strands orthogonal to the rupture axis was observed. It is shown that the polymer stiffness, the structure and stiffness of strands are dependent on the filler concentration, as well as on the distance away from the crack tip.

Acknowledgements

This work was supported by RFBR grants 15-08-03881 and 14-01-96002.

References

- [1] Beurrot S., Huneau B., Verron E. In-situ SEM study of fatigue crack growth mechanism in carbon-black filled natural rubber // *Journal of applied polymer science*. 2010. V. 117. P. 1260-1269.
- [2] Bruning K., Schneider K., Roth S.V., Heinrich G. Strain-induced crystallization around a crack tip in natural rubber under dynamic load // *Polymer*. 2013. V. 54. P. 6200-6205.
- [3] Maugis D. Adhesion of Spheres: The JKR - DMT transition using a Dugdale model // *Journal of Colloid and Interface Science*. 1992. V. 150. P. 243-269.
- [4] Pietrement O., Troyon M. General equations describing elastic indentation depth and normal contact stiffness versus load // *Journal of Colloid and Interface Science*. 2000. V. 226. P. 166-171.

Ilya A. Morozov, Institute of Continuous Media Mechanics UB RAS, Perm, Russia

Chemoconvective structures driven by a neutralization reaction

Elena A. Mosheva, Alexey I. Mizev, Konstantin G. Kostarev
mosheva@icmm.ru

Abstract

The development of chemoconvective motion in the initial stationary and steadily stratified system of aqueous solutions of the reacting liquids is studied experimentally in the vertical Hele-Shaw cell under the neutralization reaction conditions. It was found that depending on the initial reactant concentration, there are two reaction modes (i) diffusive mode, in which the dominant mass transfer mechanism is diffusion and (ii) convective mode characterized by the formation of the intense convective motion and high rate of reaction. A physical model of the observed phenomenon and the dimensionless parameter, determining the type of the reaction regime have been proposed. Maps of reaction regimes for different “acid-base” pairs were built.

1 Introduction

In the last decades, considerable progress has been made in the area of chemohydrodynamics, which studies the heat/mass transfer processes, the mechanisms responsible for the onset of hydrodynamic instability and the structure and flow evolution in the system of reacting fluids. From the fundamental point of view these problems attract considerable attention as the examples of nonlinear systems, in which the spatial-temporal variations of physical properties of fluids described by the reaction-diffusion equations can give rise to hydrodynamic instability, affecting the intensity of the heat/mass transfer processes up to a change in the type of reaction.

The development of the reaction in miscible and immiscible fluids has quite different scenarios. In experimental studies [1, 2] the new effects produced by the interaction of the exothermic neutralization reaction with the liquid-liquid interface of the two-layer system, placed in the Hele-Shaw cell are described. It was shown that by changing reagents and their initial concentrations it is possible to obtain different types of convective structures — spontaneous spreading of convective finger-shaped structures [1], which is commonly observed in such systems and even the ideal periodic system of convective cells formed in the zone between the interface and the reaction front [2].

Essentially different situation is observed in the systems of miscible reacting fluids [3-5]. Because of the absence of the interface the only source of chemoconvective structures is the gravitational mechanisms of instability initiated by the formation

of local zones with unstable density stratification. The first reason for the occurrence of such zones is the reaction product, whose density can differ from that of the surrounding medium which can lead to the formation of the Rayleigh-Taylor (RT) instability. The second is the double diffusion (DD) instability caused by the difference in the diffusion rate between reactants and the reaction product. In both cases the development of instability can provoke the formation of irregular convective structures in the form of salt fingers travelling at both sides of the reaction front. However, our previous work [5] has revealed the existence of the structure, which is not common for miscible systems. It consists of *periodic* convective rolls localized within the stable transient zone between the reagent layers. The theoretical studies showed that the discovered type of instability (we called it concentration-dependent diffusion instability or CDD convection) can be classified as DD instability and its onset is the result of *concentration dependence* of the diffusion coefficient. Bibliographical retrieval has shown that although there has been a lot of relevant works in the literature, up to now no systematic investigation (neither experimental nor theoretical) of the stability problem has been undertaken for miscible reacting systems. The only exception is paper [4], in which an attempt has been made to develop a generalized approach to such systems. However, the correctness of their approach is doubtful. The objective of the present paper is to study experimentally the stability of a two-layer system of miscible reacting fluids in the context of the problem of neutralization reaction. Based on the results of experiments with several “acid-base” liquid systems carried out in a wide range of concentration we developed a unified approach to the description of such systems.

2 Experimental technique

The experiments were performed in a vertically oriented Hele-Shaw cell made by glass plates separated by an insert, which specified the inner dimensions of the cavity: 9.0 cm×2.4 cm×0.12 cm. The cell was filled with a two-layer system of miscible reacting fluids, which had steady density stratification. One of the layers was an aqueous solution of HNO₃ and the other was formed by an aqueous solution of LiOH, NaOH or KOH. The solution concentrations varied in the range of 1.0div 3.0 mol/l. The slots were cut in the walls of the cell along its midsection to fit in the sliding shutter separating the initial reagents. At the beginning of each experiment the cell was filled to half its volume with a denser fluid (depending on the reagent concentration this might be either an aqueous solution of the acid or one of the hydroxides), after which the shutter was slid into the place and the less dense solution was pored into the cuvette over the shutter. In order to start the reaction the shutter was slid out from the cell.

The Fizeau interferometer was used to visualize the refractive index distribution caused by changes in the concentration distribution of species and by heat generation due to reaction exothermicity. The maximum temperature increment recorded by a thermocouple probe near the reaction front was less than 1 K. Light-scattering particles were added to the solution to observe the patterns forming during the reaction. We also visualised the pH distribution by adding a small amount of the universal acid-base indicator to the solutions. All experiments were performed at

ambient temperature (23 ± 1)°C.

3 Results

The results of experiments showed that there are two basic regimens of the reaction evolution: diffusion and convection. In the first case after the withdrawal of the shutter the front of reaction becomes the site of the formation of a transient zone with a stable stratification, in which the reagent transport is accomplished solely by diffusion (Figure 1 a). With the passage of time, as the reaction proceeds further, the vertical dimension of the zone slowly increases. The characteristic time of the reaction process is comparable with the diffusion time evaluated throughout the height of the cuvette. In our experiments it ranged from a few hours up to several days, depending on the initial concentration of the reagents.

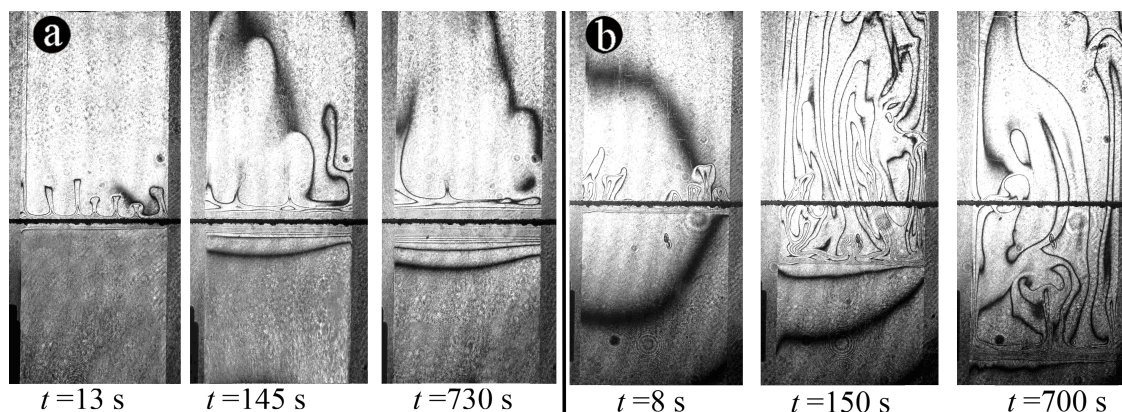


Figure 1: Time evolution of the reaction regimes. (a) Diffusive regime. The experiment is for HNO_3 ($C_a=1$ mol/l) and NaOH ($C_b=2$ mol/l); (b) Convective regime. The experiment is for HNO_3 ($C_a=1.5$ mol/l) and NaOH ($C_b=1.4$ mol/l)

In the case when the reaction proceeds in the convective regime, the withdrawal of the shutter leads to the formation of convective motion in the zone located above the reaction front. This motion develops in the form of rising plumes, which rapidly reach the upper boundary of the cell (Figure 1 b). As a result, an intensive fluid flow spreads throughout the upper layer. The reaction front moves downward rather quickly and reaches the lower boundary of the cell, after which the reaction ceases. The characteristic time of the reaction process ranged from 10 to 30 minutes depending on the initial reagent concentrations. It should be noted that all “acid-base” pairs used in our investigation followed the above mentioned reaction scenarios, no matter which of the reagents is present in the upper or lower layers.

The observed phenomena can be initiated by the following physical mechanisms. At the initial time, as soon as the reacting media come into contact, the diffusion of reagents into each other leads to the formation of a thin transient zone, which after completion of the reaction includes aqueous solutions of the reaction product and one of the reagents taken to excess. If the density of the transient zone is lower than the density of the upper layer, it rises due to the RT instability responsible for the generation of plumes observed in the experiment. This convective motion entrains

new portions of the upper reagent, which enter into the reaction forming another transient layer and the situation is repeated. Due to this fact, the upper layer becomes the zone of intensive convective motion, which continuously carries reagent in the reaction region and provides removal of the reaction product. If the density of the transient zone is higher than the density of the upper layer, the density stratification of the system becomes stable, which leads to the establishment of mechanical equilibrium in the system. As a result, the layers of the reagent solutions are found to be separated by a transient zone, which extends as the reaction goes further. Since in the absence of convective motion the transport of the reagents within the transient zone is accomplished by the diffusion processes, the rate of reaction turns to be a few orders of magnitude lower than in the convective regime.

To generalize the description of the evolution of the two-layer system we introduce a dimensionless parameter, representing the stability of the transient zone — $K_\rho = \rho_{dz}/\rho_u$, where ρ_{dz} is the transient zone density, ρ_u is the density of the upper layer of the reagent solution. The density of the transient zone can be calculated like $\rho_{dz} = \rho_s(C_s) + \rho_{res}(C_{res}) - \rho_0$, where ρ_s is the density of the solution of the resultant reaction product with the molar concentration C_s ; ρ_{res} is the density of the reagent solution with the molar concentration C_{res} , which was taken to excess and remains unreacted in the transient zone after completion of the reaction; ρ_0 is the density of the solvent (water in the examined case). The concentrations of the remaining reagent and the reaction product can be determined from the simple relations: $C_s = C_{min}/\delta_D$ and $C_{res} = (C_{max} - C_{min})/\delta_D$, where C_{min} and C_{max} are the maximal and minimal initial concentrations in the examined reagent pair, $\delta_D = D_{slow}/D_{fast} - 1$ is the parameter specified by the ratio of the diffusion coefficient D_{slow} of the “slower” reagent (slowly reacting substance) in the above pair to that of the “quicker” reagent (quickly reacting substance, D_{fast}). It is to be noted that the diffusion coefficients should be selected taking into account their dependence on the concentration.

The value of the obtained dimensionless parameter K_ρ specifies the system evolution. If $K_\rho < 1$, the reaction proceeds in the convective regime and in the opposite case when $K_\rho > 1$ it proceeds in the diffusive regime. The results of calculations were used to build the map of regimes of reaction evolution in the coordinates of initial reagent concentration. The map of reaction regimes for all used “acid-base” pairs are shown in Figure 2 a. The isopycnic line (depicted by a dashed line) divides the whole field of the map into two regions, in which the upper layer is generated by the solution of acid or base fluid of lower density. Coloured zones are zones, in which the reaction proceeds in the convective regime. For all other concentrations the reaction is governed by diffusion. The experiment results show good agreement with the results of computation, which supports the validity of the selected physical mechanism controlling the observed phenomenon and the adequacy of the dimensionless parameter. In Figure 2 b the same map is depicted in the $(C_a\beta_a, C_b\beta_b)$ parameter plane, where β_a and β_b are solutal expansion coefficients for acid and base, respectively. As it is evident from the figure, for the selected acid HNO_3 an increase in the ratio of the diffusion coefficients of the reagents ($D_{LiOH} < D_{NaOH} < D_{KOH}$) leads to the extension of the reagent concentration range, in which the reaction proceeds in the convective regime. Indeed, an increase in δ_D leads to a decrease in the con-

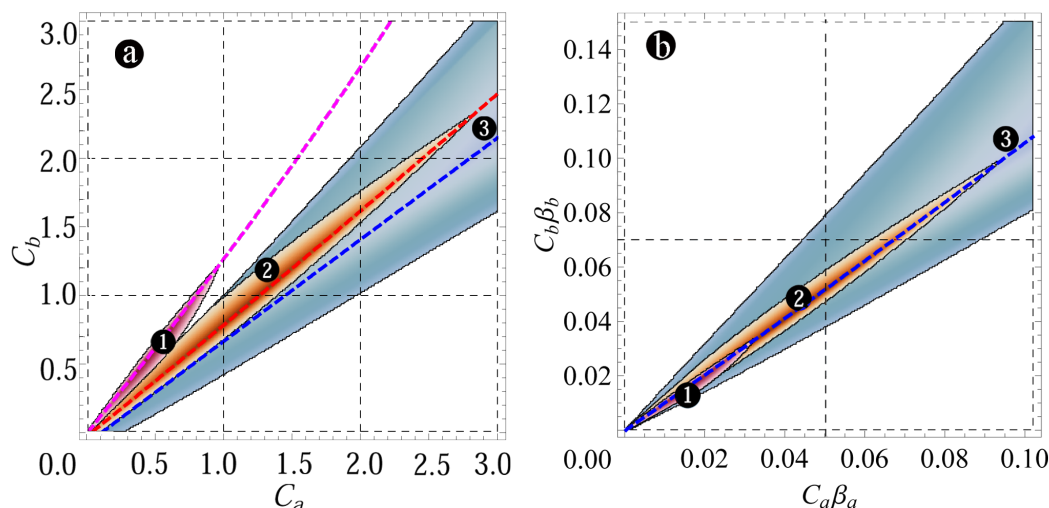


Figure 2: Maps of reaction regimes for the following systems of aqueous solutions: (1) $\text{HNO}_3\text{-LiOH}$, (2) $\text{HNO}_3\text{-NaOH}$, (3) $\text{HNO}_3\text{-KOH}$ in (a) $C_a - C_b$; (b) $C_a \beta_a - C_b \beta_b$. Colored regions are zones of the convective regime

concentrations of the reaction product and excess reactant in the transient zone after completion of the reaction and, consequently, to a decrease of the dimensionless parameter K_ρ . It should be noted that in a strict sense the zone of diffusive regime of the reaction evolution is not the region of mechanical equilibrium of the two-layer system. Inside this parameter region, the diffusion is just the prevailing mechanism of matter transfer in the vicinity of the reaction front, namely, inside the transient zone. However, in this case there is still a possibility for the development of convective motion due to the DD mechanism, but its intensity is generally low and has a rather weak effect on the mass transfer in the system. To substantiate this observation we investigated the propagation of the reaction front in different regimes of proceeding of the reaction. To our knowledge [6], in the case of purely diffusive mass transfer the propagation of the reaction front is governed by the following law: $x_f = C_f \sqrt{t}$, $C_f = \frac{C_a}{C_b} \sqrt{\frac{D_a}{D_b}} - 1$, where C_a and C_b are the concentrations, and D_a and D_b are the diffusion coefficients of the acid and base, respectively. It is seen that if $C_a = C_b$ and $D_a = D_b$, the position of the front does not vary with time. In other cases the front coordinate changes $\sim \sqrt{t}$. In this case, depending on the sign of the proportionality coefficient C_f , the front can move upward and downward. Figure 3 a, showing the map of regimes for the $\text{HNO}_3\text{-NaOH}$ pair, displays curves corresponding to $C_f = 0$, i.e., a change in the direction of the front propagation. Here also we indicate points, at which we measured the position of the reaction front as a function of time (Figure 3 b). Obtained dependencies for highlighted points are presented in Figure 3 b. It is seen that in the convective regime the reaction front propagates much quicker than in the diffusive regime, which is caused by the matter transport near the reaction front by the convective motion. In the range of parameters corresponding to the diffusive regime of reaction evolution the front moves as $x_f \propto t^{1/2}$. Crossing the curve C_f means that the reaction front reverses its direction. The above results show that in the region of diffusive regime of reaction

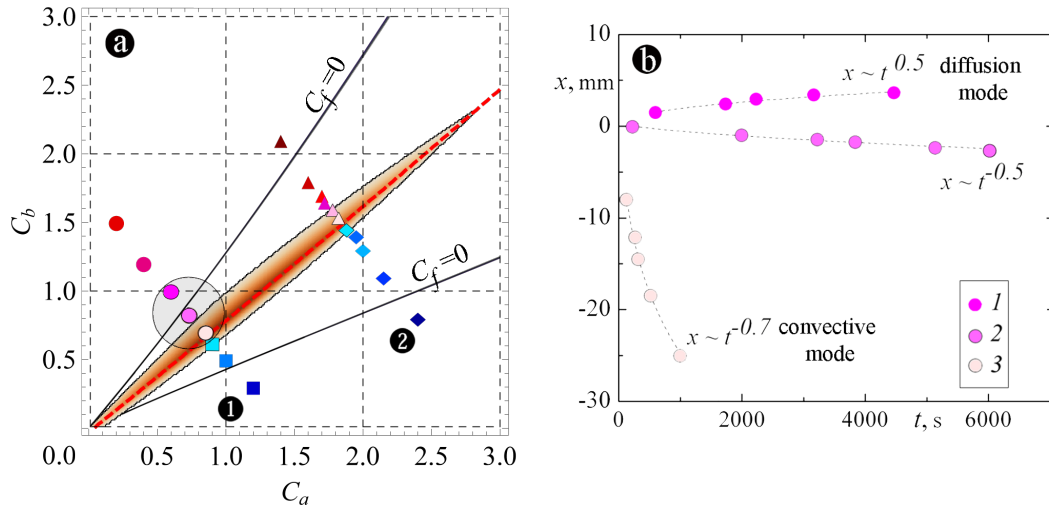


Figure 3: (a) The map of regimes for the $\text{HNO}_3\text{-NaOH}$ system with the indicated points for which experiments have been performed; (b) The position of the reaction front as a function of time for respective points in the (a)

evolution the transport of the reagents and reaction products is controlled by the diffusive mechanism, whereas weak movements of the fluid initiated by the double diffusion mechanism exert negligible effect on the mass transfer processes. Such a

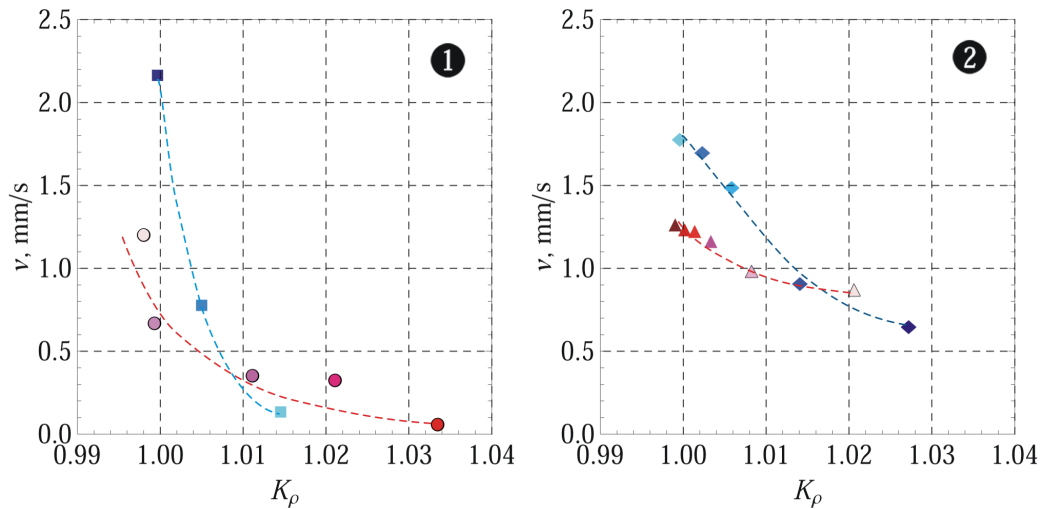


Figure 4: The velocity of plume rise at the initial instant of time as a function of dimensionless parameter K_ρ for experiments depicting in figure 3 a

conclusion can be drawn from the analysis of the plume rise velocity at the initial stage of the development of convective motion in the zone above the reaction front. The above parameter characterizes the intensity of arising convective motion. In figure 4 these dependences are plotted for reactions run at the parameters denoted in figure 3 a by symbols marked by numbers 1 and 2. It is seen that in crossing the boundary, corresponding to a change from the convective to diffusive regime, the intensity of the convective regime rapidly decreases up to zero values. In the range of parameters corresponding to a diffusive regime the experiment revealed a new

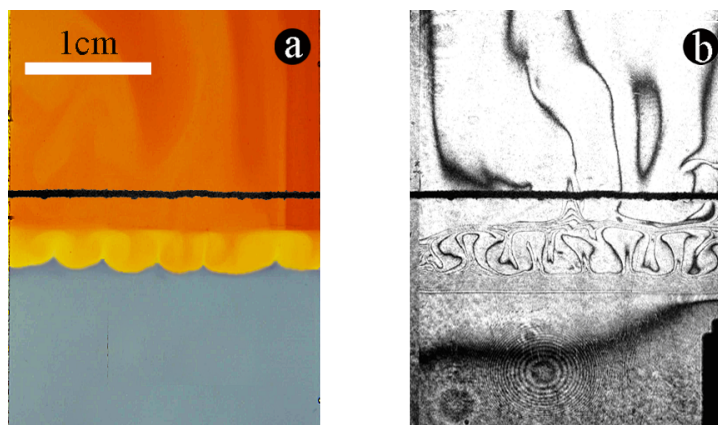


Figure 5: Localized convective structure. (a) pH distribution; (b) interferogram

type of instability, which can be qualified as another type of DD instability. The evolution of the system can be described as follows. The interaction of the reacting

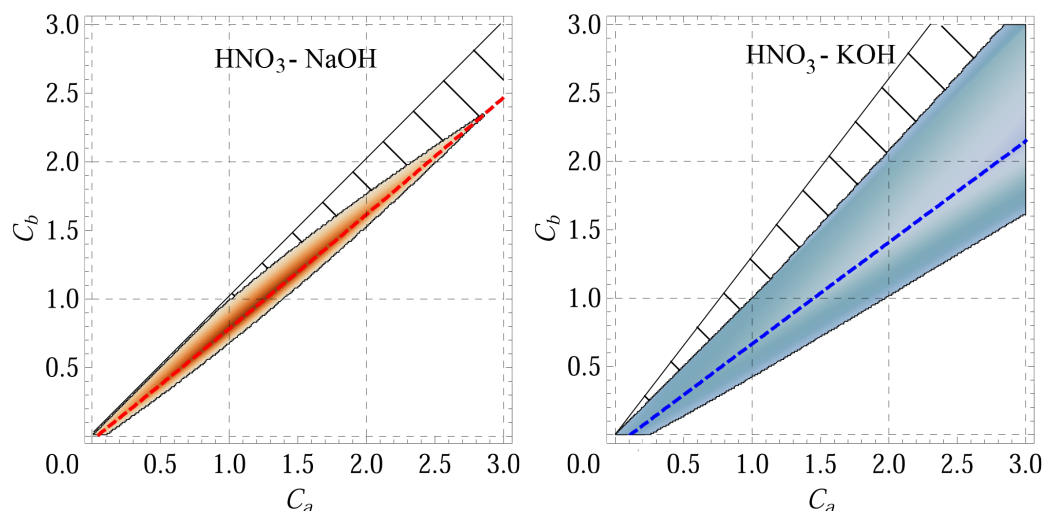


Figure 6: Maps of reaction regimes. CDD instability zones are dashed

layers immediately leads to the formation of a transient zone, inside which the reaction front is located. The transient zone remains immovable, whereas transport of the reagents and reaction products in the zone is accomplished by diffusion. As it has been mentioned above, the space above the transient zone is the region of the formation of a weak convective motion controlled by the DLC mechanism. A few minutes after the beginning of the experiment one can also observe the initiation of convective motion in the transient zone, yet in the form of a horizontal series of convective cells (Figure 5). The observed convective structure exists between two immovable sections of the transient zone, which is indicative of the formation of localized density “pocket” with unstable density stratification. The discovered structure exists for a few hours. With the lapse of time the size of the cells increases, while their number decreases. The cells remain in the transient zone, the vertical dimension of which also increases with time due to diffusion. The instability exists in a very narrow region on the map of reaction regimes. In figure 6, this is

dashed. It is seen that this type of instability is observed only at the one side from the isopycnic line (experiments where base is poured into the bottom layer). Such asymmetry along with the fact that the diffusion coefficient of acid is always higher than that of the base, also counts in favor of diffusion mechanism responsible for the initiation of CCD instability.

Acknowledgements

The reported study was supported by RFBR, research project No. 16-31-00251 mol_a and by Basic Research Program of UB RAS (No. 15-10-1-16).

References

- [1] Eckert K., Grahn A. Plume and finger regimes driven by an exothermic interfacial reaction // *Phys. Rev. Lett.* 1999. Vol. 82. No. 22. P. 4436-4439.
- [2] Eckert K., Acker M., Shi Y. Chemical pattern formation driven by a neutralization reaction. Mechanism and basic features // *Phys. Fluids.* 2004. Vol. 16. No. 2. P. 385-399.
- [3] Almarcha C., Trevelyan P.M.J., Grosfils P., and De Wit A. Chemically driven hydrodynamic instabilities // *Phys. Rev. Lett.* 2010. Vol. 104. No. 4. P. 044501(4).
- [4] Carballido-Landeira J., Trevelyan P.M.J., Almarcha C. and de Wit A. Mixed-mode instability of a miscible interface due to coupling between Rayleigh-Taylor and double-diffusive convective modes // *Phys. Fluids.* 2013. Vol. 25. No. 2. P. 024107(10).
- [5] Bratsun D., Kostarev K., Mizev A., Mosheva E. Concentration-dependent diffusion instability in reactive miscible fluids // *Phys. Rev. E.* 2015. Vol. 92. P. 011003.
- [6] Rongy L., Trevelyan P.M.J., de Wit A. Influence of buoyancy-driven convection on the dynamics of $A + B \rightarrow C$ reaction fronts in horizontal solution layers // *Chem. Eng. Sci.* 2010. Vol. 65. P. 2382-2391.

Elena A. Mosheva, Alexey I. Mizev, Konstantin G. Kotarev. Institute of Continuous Media Mechanics UB RAS, Academ. Koroleva str., 1, Perm, Russia, 614013

Assessing Deformation due to Self-Gravitation - Treachurous Pathways of Continuum Mechanics

Wolfgang H.Müller, Wolf Weiss, Elena N. Vilchevskaya
wolfgang.h.mueller@tu-berlin.de

Abstract

In an attempt of modeling the state of deformation in self-gravitating terrestrial bodies linear Hookean elasticity formulated in terms of linear strain measures is used initially. In this case the solutions for the stresses, the strains, and the displacements are unique and can be presented in closed form. The equations will be evaluated by using data for Mercury and Earth in order to show that the displacements can be enormous. This illustrates the limit of a geometrically linear theory.

In order to improve the situation we will then present an “extended model” and study the influence of linear terms of displacement gradients in the body force density, hence, we assume the body forces to adjust with the current configuration. This non-standard approach to linear elasticity serves as a bridge to a consistently performed large-deformation-analysis while keeping the advantage of a closed-form expression.

Next we choose a geometrically nonlinear version of Hooke’s law, the Saint-Venant-Kirchhoff constitutive equation written in terms of the current configuration. By doing that we should be able to handle large strains. However, even this relation creates problems, since it suffers from instability at very high compressive strains, *i.e.*, if the mass of the self-gravitating object becomes too large. There will be a limit mass beyond which stresses will go to infinity, similarly to the Chandrasekhar limit.

Finally we will turn to time-dependent modeling of deformation in terms of a deformation-wise linear viscoelastic model of the Kelvin-Voigt type. Surprisingly this model allows for a closed-form solution. As a new result it will turn out that in the early days of planet formation the so-called Love radius, which is the demarcation line between the completely compressive interior of a planet from a radial strain-wise tensile exterior, does not exist initially and requires time for its development.

1 Introduction

The purpose of this paper is quite a fundamental one: We wish to draw attention to the fact that modeling nature by using continuum theory can be based on treacherous assumptions. Whilst we may have some confidence in the applicability of the fundamental laws of classical physics, such as the conservation of mass, linear and

angular momentum, or energy, the use of constitutive relations requires special care and sound scepticism, even if they follow from principles of rational thermodynamics. As a matter of fact, many engineers of daily practice are not even aware of the fundamental difference between conservation laws and “material equations” as the latter are sometimes innocently called. They believe that they are “true laws of nature.” Surely, there might be limits to their applicability, if strains become too high or temperatures are too low (say), but very often this is attributed to numerical inaccuracy rather than a principal internal deficiency. This dilemma is nicely depicted in a recent textbook [7].

In our paper we will use self-gravitation in massive celestial bodies as a concrete example. We will concentrate on “solid bodies,” whatever a solid planet may be, since we all know that it will likely show an onion-like internal structure and some of the “onion skins” will be more on the liquid than on the solid side.

We will start on seemingly firm ground, so-to-speak: Linear Hookean elasticity formulated in terms of linear strain measures is the simplest way of modeling deformation in self-gravitating terrestrial bodies. In this case the solutions for the stresses, the strains, and the displacements are unique and can be presented in closed form, as was first shown by the great (linear) elastician A.E.H. Love around the beginning of last century [1]. We will, first, present the underlying theory in modern form. Second, solutions to the resulting equations will be obtained. Third, the limits of the equations will be illustrated by using physical data Mercury and Earth. This will show that under certain circumstances the displacements may be enormous. Consequently, the limits of linear strain theory will become evident.

As a special feature we will then leave the canonical pathway of linear elasticity, where it is conventionally assumed that the body forces are applied to the undeformed configuration [2]. In contrast to conventional (engineering) literature, we will present an extended model and study the influence of linear terms of displacement gradients in the body force density. In fact, this approach may serve as a bridge between linear elasticity at small strains and elasticity at large deformations. Moreover, it has the advantage of keeping its closed-form solution character.

In an attempt to remedy the problem of large deformations once and for all we will choose a geometrically nonlinear version of Hooke’s law in the current configuration. More precisely, the Cauchy stress will be related to the nonlinear deformation measure of the current configuration, the Euler-Almansi finite strain, which replaces the linear strain tensor of the ordinary Hooke’s law. This is known as the Saint-Venant-Kirchhoff constitutive equation in the literature [3], albeit stated in the current configuration. Using this type of stress-strain relation in context with self-gravitating objects was first suggested in the sixties of last century, see for example [4]. However, this approach has drawbacks: As we shall see, we will run into modeling and numerical problems again, if the mass of the self-gravitating object becomes too large. There will be a limit mass beyond which stresses will go to infinity, similarly to the case of the Chandrasekhar limit for the mass of white dwarf stars. However, this phenomenon is an artifact of the constitutive law we chose for the stress-strain relation: It can lead to a unique, two, three, or no solutions for the problem. In fact, today it is known (see [3], Section 4.3 and [5]) that this constitutive model suffers from material instability in large compressive deformation case.

Finally we will turn to time-dependent modeling of deformation. We will use a linear viscoelastic model of the Kelvin-Voigt type [6]. Surprisingly it allows for a closed-form solution for a solid as well as for a hollow sphere. As a new result it will turn out that in the early days of planet formation the so-called Love radius, which is the demarcation line between the completely compressive interior of a planet from a radially strain-wise tensile exterior, does not exist initially and requires time for its development. Interestingly the solution for the solid sphere will not lead to zero deformation in the limit of initial time. Rather it jumps abruptly to finite values varying linearly throughout the sphere. If the same limit is considered in the solution for the hollow sphere with a very small hole at the center one can see the reason for this behavior: The transition from zero to finite deformation is extremely fast. In other words: If gravitation is “switched on,” large amounts of mass will start moving and it is inapt to use the static form of the balance of momentum. Inertial forces should be taken into account. Hence, this time it is *not* a fault of the constitutive equation but an inappropriate simplification of the equations of motion, which creates a problem.

2 Linear Elasticity

We base our analysis on the static balance of momentum:

$$\nabla \cdot \boldsymbol{\sigma} = -\rho \mathbf{f}, \quad (1)$$

where ρ denotes the local current mass density, and $\boldsymbol{\sigma}$ the Cauchy stress tensor. The specific body force, \mathbf{f} , *i.e.*, the gravitational acceleration, is conservative and originates from self-gravity. Consequently, a gravitational potential $U^{\text{grav}}(\mathbf{x})$ exists, where \mathbf{x} denotes an arbitrary (current) position within the body, and we may write:

$$\mathbf{f}(\mathbf{x}) = -\nabla U^{\text{grav}}(\mathbf{x}). \quad (2)$$

The gravitational potential obeys Poisson’s equation:

$$\Delta U^{\text{grav}}(\mathbf{x}) = 4\pi G \rho(\mathbf{x}). \quad (3)$$

If we consider a perfectly spherical case, where we have only radial dependencies, we find from the last two relations that:

$$\rho(r) \mathbf{f}(r) = -G \frac{\rho(r) m(r)}{r^2} \mathbf{e}_r, \quad (4)$$

where \mathbf{e}_r is the radial unit vector, $m(r)$ denotes the total mass within a spherical region of radial extension r :

$$m(r) = 4\pi \int_{\tilde{r}=0}^{\tilde{r}=r} \rho(\tilde{r}) \tilde{r}^2 d\tilde{r}, \quad 0 \leq r \leq r_o, \quad (5)$$

and r_o stands for the current outer radius of the spherical body.

However, in linear elasticity it is customary to use the body force acting on the *undeformed* body. Consequently, if we pretend everything is initially homogeneous and use a constant mass density, ρ_0 , we obtain:

$$\rho(r)\mathbf{f}(r) \approx -G\frac{\rho_0 m(r)}{r^2} \mathbf{e}_r \approx -\frac{4\pi G\rho_0^2}{3}r \mathbf{e}_r. \quad (6)$$

For the stress tensor we assume Hooke's law for an isotropic body to hold:

$$\boldsymbol{\sigma} = \lambda \text{Tr}\boldsymbol{\epsilon} \mathbf{1} + 2\mu \boldsymbol{\epsilon}. \quad (7)$$

Moreover, in this context we use the *linear* strain tensor:

$$\boldsymbol{\epsilon} = \frac{1}{2}(\nabla\mathbf{u} + \nabla\mathbf{u}^\top). \quad (8)$$

\mathbf{u} refers to the displacement vector, *i.e.*, to $\mathbf{u} = \mathbf{x} - \mathbf{X}$, \mathbf{X} being the reference position of a material point of the sphere. λ and μ are Lamé's elastic constants.

If spherical coordinates are used and these relations are inserted into each other the following differential equation of second order for the dimensionless radial displacement, $u(x) := u_r(r)/r_o$, results:

$$u'' + 2\frac{u'}{x} - 2\frac{u}{x^2} = \frac{\alpha}{2}x, \quad (9)$$

where the dash refers to differentiation w.r.t. dimensionless position, $x := r/r_o$, and with a dimensionless factor, the gravity-stiffness constant:

$$\alpha = \frac{8\pi G\rho_0^2 r_o^2}{3(\lambda + 2\mu)}. \quad (10)$$

If regularity at $x = 0$ and a traction-free outer surface is prescribed, its solution reads (for further details see [8], $\nu = \frac{\lambda}{2(\lambda+\mu)}$ is Poisson's ratio):

$$u = -\frac{\alpha}{20} \left(\frac{3-\nu}{1+\nu} - x^2 \right) x. \quad (11)$$

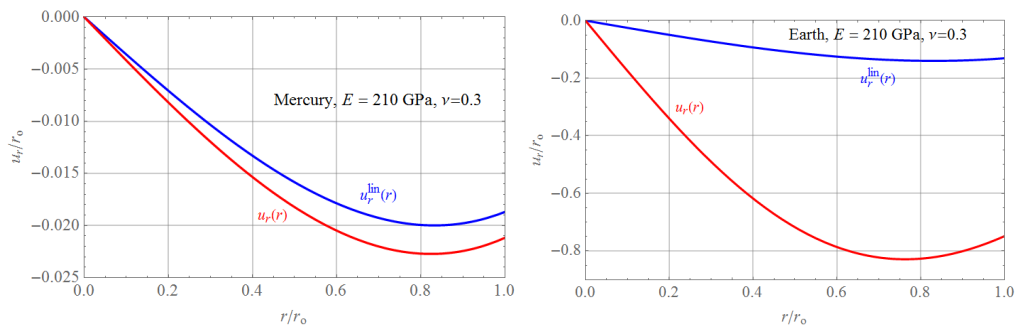


Figure 1: Radial displacement *vs.* normalized radius: Fully linear solution (blue) and “extended” solution (red); for data see text.

The blue curves in Fig.1 show plots of Eqn. (11) when data of Mercury (index M) and Earth (index E) are used for evaluation. Specifically we have values for

the average mass densities of $\rho_0^E = 5500 \frac{\text{kg}}{\text{m}^3}$ and $\rho_0^M = 5400 \frac{\text{kg}}{\text{m}^3}$ and (average) outer radii of $r_o^E = 6370 \text{ km}$ and $r_o^M = 2440 \text{ km}$, respectively. For the elastic data we assume in both cases the values of iron, *i.e.*, $E \equiv \frac{\mu(3\lambda+2\mu)}{\lambda+\mu} = 210 \text{ GPa}$ and $\nu = 0.3$. Consequently, the strains for Mercury are below 2% but the ones for Earth are huge and amount to a maximum of 14%. Hence one may question the validity of the use of linear elasticity in case of very large self-gravitating masses and turn to a non-linear formulation instead. Indeed, this has been done by the Indian school of Seth, who was one of the pioneers in large strain measures. We will explore this in the next section.

Note that, as it should be, the radial displacement is negative and that the curves show a minimum. The slope of the curves in Fig. 1 is proportional to radial strain. Hence the only positive (=tensile) radial strains can be found to the right of the minimum. The transition point between positive and negative strains, identifiable by locating the minimum of the displacement, is a.k.a. the *Love radius*:

$$r_{\text{Love}} = r_0 \sqrt{\frac{3 - \nu}{3(1 + \nu)}}. \quad (12)$$

The first edition of his monograph [1] makes it perfectly clear that Love was aiming at a failure criterion in context with this transition point, namely specifically at what is known today as *maximum principal strain theory*: Tensile strains might lead to damage. However, if one inserts real numbers into the expression for the corresponding strain (see [8], pp. 30) it turns out that the corresponding numbers are completely unrealistic. Nevertheless, so far no better model for studying damage due to severe self-gravitation has been developed. Consequently, it still has its merits, be it even just to remind us of the fact that a better model is needed.

Before turning to nonlinear theory we shall briefly depart from one of the crucial prerequisites of the linear theory of elasticity at small deformations: We shall no longer insist that the body force is applied to the undeformed configuration. In agreement with the principles of a consistently linearized theory we will now take *linear* terms of the displacement and its derivative on the right hand side of the momentum balance into account according to Eqns. (6)₁ and put:

$$\rho(\mathbf{x}) \approx \rho_0 [1 - \text{Tr} \boldsymbol{\epsilon}(\mathbf{x})]. \quad (13)$$

Hence it follows that:

$$\rho(r) \mathbf{f}(r) \approx -\frac{\lambda + 2\mu}{r_o} \frac{\alpha}{2} x \left(1 - u' - 5\frac{u}{x}\right) \mathbf{e}_r. \quad (14)$$

The equivalent to Eqn. (9) then reads:

$$u'' + \left(\frac{2}{x} + \frac{\alpha}{2}x\right) u' - \left(\frac{2}{x^2} - \frac{5\alpha}{2}\right) u = \frac{\alpha}{2}x. \quad (15)$$

It can be solved analytically:

$$u = \frac{1}{96\alpha} \frac{1}{x^2} \left[2x (6 + 5\alpha x^2 + 6A (2 - \alpha x^2)) - \right] \quad (16)$$

$$3(1 + 2A) \left(4 + 4\alpha x^2 - \alpha^2 x^4 \right) \exp \left(-\frac{\alpha x^2}{4} \right) \int_{\tau=0}^{\tau=x} \exp \left(\frac{\alpha \tau^2}{4} \right) d\tau \Bigg].$$

The remaining constant of integration, A , follows from the requirement of vanishing traction, *i.e.*, vanishing radial stress at the outside, r_o , of the sphere, $u'|_{x=1} + \frac{2\nu}{1-\nu} u|_{x=1} = 0$. The result is a very lengthy yet closed-form expression, which we decided not to present here.

Fig. 1 gives us a foretaste of what to expect if the gravitating mass becomes really large. Two curves are presented, the fully linear solution according to Eqn. (11) in blue and the “extended” solution based on Eqn. (16) in red. The equations were evaluated for Mercury and for Earth according to the data presented before. Although α is already equal to 0.347 in the case of Mercury (*i.e.*, it is *not* small but in the range of more than 30 percent) the difference between the two predictions for the normalized displacement are close together, and in the range of 2%. This is very different for Earth: Both predictions are far apart and we should expect normalized displacements up to 90%. We will get back to this issue in the next section.

3 Geometrically Nonlinear Elasticity

We start our discourse on nonlinear effects by mentioning that the original left hand side of the differential equation (15) consisted of three small quantities of first order, namely of u and its spatial derivatives. Consequently, its right hand side should also be small, *i.e.*, consist of first order terms comparable in magnitude to $u(x)$, $u'(x)$, and $u''(x)$. Hence, we must ask the question as to whether the factor α is “small” or not. Unfortunately the size of α is dictated by physics and not by mathematics. It cannot really be chosen freely and it is as large as required by the celestial object we wish to model. At the end of the last section we have seen that even for small gravitating objects like Mercury it is of the order of thirty percent, which cannot really be considered as small. We wish to improve upon the situation and use the most simple counterpart to Eqn. (7) by replacing ϵ with the Euler-Almansi finite strain tensor, e :

$$2e := 1 - \mathbf{F}^{-1\top} \cdot \mathbf{F}^{-1}, \quad \mathbf{F} := \nabla_{\mathbf{X}} \mathbf{x}(\mathbf{X}), \tag{17}$$

\mathbf{F} being the deformation gradient joining current and reference positions, \mathbf{x} and \mathbf{X} , respectively. The corresponding stress-strain relation could be called Saint-Venant-Kirchhoff law in the current configuration. It is physically linear but geometrically nonlinear and was originally suggested by Seth [9]:

$$\boldsymbol{\sigma} = \lambda \text{Tre } \mathbf{1} + 2\mu \mathbf{e} \tag{18}$$

A group of Indian scholars (see for example [4]) used it to study selfgravitation during the sixties. The corresponding differential equation for the normalized radial displacement reads (see [8], Section 3.1.3 for a proof):

$$\frac{d}{dx} \left[u' \left(1 - \frac{1}{2}u' \right) + \frac{2\nu}{1-\nu} \frac{u}{x} \left(1 - \frac{1}{2} \frac{u}{x} \right) \right] + \tag{19}$$

$$\frac{2(1-2\nu)}{1-\nu} \frac{1}{x} \left[u' \left(1 - \frac{1}{2}u' \right) - \frac{u}{x} \left(1 - \frac{1}{2}\frac{u}{x} \right) \right] = \frac{\alpha}{2} x(1-u') \left(1 - \frac{u}{x} \right)^5.$$

It must be solved numerically by taking into account vanishing displacement (or better “regularity”) at the center and vanishing radial stress at the outer surface. Various techniques are possible ranging from Runge-Kutta shooting methods, series expansions, up to finite differences and finite elements. Two results are shown in Fig. 2. For these plots the geometry and mass data for Mercury and Earth were chosen. There is a slight variation in the choice of Poisson’s ratio in the case of Earth compared to our study in Fig. 1.: If the original elastic data were used for Earth α increases up to 1.96. For this value a solution could no longer be obtained (see the discussion below). Hence, Poisson’s ratio was raised to 0.38, which is equivalent to $\alpha \approx 1.75$. The reason for the lack of solution becomes immediately apparent by looking at the plots: In the case of Mercury, there is already a slight discrepancy to the analytical solution, $u_r^{\text{anal}}(r)$, shown in Eqn. (7). The analytical solution (slightly) *underestimates* the displacement. This is not surprising since the radial strain, which is roughly given by u_r/r_o , is more than two percent, hence, probes the limits of a geometrically linear theory.

In the case of Earth the situation is much more dramatic. First, the difference between the analytical and the numerical solution is huge and, second, even the analytical solution already predicts strains of almost 10%, whereas the numerical solution amounts to 30% and more. Note that the curvature of $u_r(r)$ “on the left” becomes more and more pronounced when the α -values increase. For larger values of α , *i.e.*, for large values of reference density and small values of Young’s modulus and/or Poisson’s ratio, the $u_r(r)$ -curve will first decline very steeply and then show an essentially linear behavior with a moderate slope.

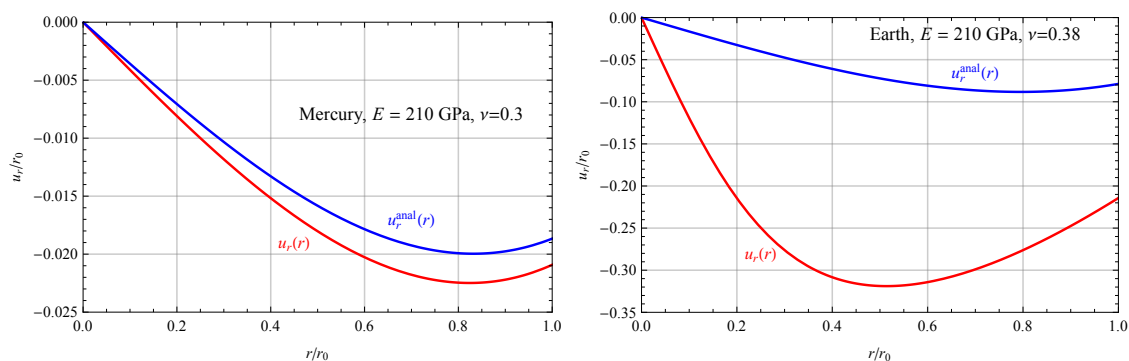


Figure 2: Radial displacement as a function of radial position.

We proceed to investigate this in more detail. The plots shown in Fig. 3 present a study of solutions to the nonlinear differential equation (19) in the following manner: For a given choice of Poisson’s ratio, ν , and gravity-stiffness-parameter, α , a numerical solution was found by using a shooting technique. To this end use was made of the boundary condition $u(0) = 0$ with $u(x) = x[1 - \beta(x)]$, where $\beta'(x=0) = 0$ and $\beta(0)$ was varied within a reasonable range. This allowed to calculate numerical values for the radial stresses σ_{rr} on the interval $x \in \{0, 1\}$ based on Eqn. (18) and, in particular, at the position $x = 1$, *i.e.*, at the right boundary, where it must vanish. Hence we have to insist on the condition that $\sigma_{rr}(x=1) \stackrel{!}{=} 0$ among all the values

found. During this procedure Poisson's ratio was kept constant, $\nu = 0.3$, while the value of α increased steadily.

The first inset where $\alpha = 0.35$ depicts the situation for Mercury. As we can see the nonlinear differential equation has only one well-defined solution, $\beta(x = 0) \approx 1.041$, and this would essentially lead to the displacement distribution shown in Fig. 2₁. If we increase α to 1 and to 1.3, the situation stays the same: There is only one solution. However, the curves become more and more non-monotonic. Finally at $\alpha \approx 1.3887$ a second solution appears and if we increase the parameter even a bit more, $\alpha = 1.39$, we even end up with three solutions. These disappear and only two solutions result again if $\alpha \approx 1.39618$. If we keep increasing the parameter, *i.e.*, we choose $\alpha \approx 1.3962$ and $\alpha \approx 1.4$, respectively, we find first only one and finally no solution at all. This is essentially what we observe in Fig. 2: There is an end to calculating a displacement distribution for large values of α . Does this mean that Earth might not show strains larger than 30 percent due to its huge self-gravity? Of course not! All of this is an artifact of the constitutive equation used to connect stresses and strains, even if nonlinear strain measures are used. It should be mentioned that the malfunction of the Saint-Venant-Kirchhoff model is well known and was put into context with Ball's notion of missing polyconvexity of the strain energy density function, [3], Section 4.3. As an example one may want to study the one-dimensional analogue to our selfgravitating sphere, the compression of a one-dimensional Saint-Venant-Kirchhoff beam [10].

This shows very clearly that the cure to the problem does not come by turning to non-linear deformation measures alone, as Love and the group of Seth may have thought. It is much more complex: We need to find a physically sound connection between stresses and strains *and* nonlinear strain measures.

Fig. 4₁ presents a study of the movement of various material points from the perspective of the reference configuration. Imagine a sphere of homogeneous mass density, ρ_0 , and outer radius, R_o , which is initially completely stress-free. In order to study its deformation after gravity has been "switched on," we first normalize distances and displacements in contrast to our previous line of reasoning by that outer radius, $\bar{x} = \frac{r}{R_o}$, $\bar{u} = \frac{u}{R_o}$ and then write in view of Eqn. (5) for the current mass of a radially-symmetric planet up to a position x_0 :

$$m(\bar{x}) = m_0 \bar{x}^3 \left(1 - \frac{\bar{u}}{\bar{x}}\right)^3, \quad m_0 = \frac{4\pi}{3} \rho_0 R_o^3. \quad (20)$$

Note that \bar{x} will always be smaller than one, which is in contrast to its counterpart, x . Eqn. (19) will now take the following form:

$$\begin{aligned} & \frac{d}{d\bar{x}} \left[\bar{u}' \left(1 - \frac{1}{2} \bar{u}'\right) + \frac{2\nu}{1-\nu} \frac{\bar{u}}{\bar{x}} \left(1 - \frac{1}{2} \frac{\bar{u}}{\bar{x}}\right) \right] + \\ & \frac{2(1-2\nu)}{1-\nu} \frac{1}{\bar{x}} \left[\bar{u}' \left(1 - \frac{1}{2} \bar{u}'\right) - \frac{\bar{u}}{\bar{x}} \left(1 - \frac{1}{2} \frac{\bar{u}}{\bar{x}}\right) \right] = \frac{\alpha_0}{2} \bar{x} (1 - \bar{u}') \left(1 - \frac{\bar{u}}{\bar{x}}\right)^5, \end{aligned} \quad (21)$$

where a counterpart to the original parameter α has been defined as follows:

$$\alpha_0 = \frac{3G}{2\pi} \frac{m_0^2}{R_o^4 (\lambda + 2\mu)}. \quad (22)$$

Moreover, we have to observe the following boundary conditions:

$$\bar{u}|_{\bar{x}=0} = 0, \quad (23)$$

$$\bar{u}'|_{\bar{x}=\bar{x}_o} \left(1 - \frac{1}{2}\bar{u}'|_{\bar{x}=\bar{x}_o}\right) + \frac{2\nu}{1-\nu}\bar{u}|_{\bar{x}=\bar{x}_o} \left(1 - \frac{1}{2}\bar{u}|_{\bar{x}=\bar{x}_o}\right) = 0.$$

Summarizing we may say that the determination of the (current) outer radius, $\bar{x}_o := \frac{r_o}{R_o}$, is now part of the problem. Due to the new normalization for the radius the outer surface of the sphere is no longer at $\bar{x} = 1$: The more massive the gravitating body, the smaller \bar{x}_o will become. Moreover, α_0 will be particularly large in case of very massive bodies of great resilience.

This is investigated in Fig. 4₁, where the “movement” of points originally at $0 \leq R/R_o \leq 1$, within a selfgravitating body, is depicted in form of blue trajectories in increments of 0.05, as a function of the mass-stiffness parameter α_0 for $\nu = 0.36$ up to the maximum value of $\alpha \approx 1.319$ (black line): The more gravitational mass, the higher the displacement. The red curve shows the displacement of the Love radius. Note that if nonlinearity is taken into account the location of the Love radius may change considerably when compared to the value from analytical solution of Eqn. (12): Fig. 4₂.

4 Viscoelasticity

We consider a linear viscoelastic material model at small strains of the Kelvin-Voigt type with no bulk viscosity, *i.e.*, stresses $\boldsymbol{\sigma}$, linear strains $\boldsymbol{\epsilon}$, and strain rates $\dot{\boldsymbol{\epsilon}}$ are connected by (η : shear viscosity):

$$\boldsymbol{\sigma} = \lambda \text{Tr}\boldsymbol{\epsilon} \mathbf{1} + 2\mu \boldsymbol{\epsilon} + 2\eta \left(\dot{\boldsymbol{\epsilon}} - \frac{1}{3} \text{Tr}\dot{\boldsymbol{\epsilon}} \mathbf{1} \right). \quad (24)$$

We assume perfectly spherical conditions. Then the ordinary differential equation (9) must be replaced by the following partial differential equation:

$$u'' + 2\frac{u'}{x} - 2\frac{u}{x^2} + \frac{4}{3} \left(\dot{u}'' + 2\frac{\dot{u}'}{x} - 2\frac{\dot{u}}{x^2} \right) = \frac{\alpha}{2}x, \quad (25)$$

where the dot now refers to differentiation w.r.t. dimensionless time, $\tau := \frac{\lambda+2\mu}{\eta}t$, and the dash means differentiation w.r.t. dimensionless position, x .

This equation can be solved in closed form, *e.g.*, by mapping it into Laplace space and finding the back transform. Details of the involved procedures are outlined in [8], Chapter 5. For a solid sphere one finds:

$$u(x, \tau = 0) = 0, \quad (26)$$

$$u(x, \tau > 0) = -\frac{\alpha}{20}x \left[\frac{3-\nu}{1+\nu} - x^2 \right] \left[1 - \exp\left(-\frac{3}{4}\tau\right) \right] - \frac{\alpha}{10} \frac{1-\nu}{1+\nu} x \exp\left(-\frac{3}{4}\tau\right),$$

and for a hollow sphere (r_i inner radius):

$$u(x, \tau) = \frac{\alpha}{20} \left[-x \left(3 - \nu + 2(1 - 2\nu)\xi^5 \right) + \frac{[3-\nu-(1+\nu)\xi^2]\xi^3}{x^2} \right] \times \quad (27)$$

Assessing Deformation due to Self-Gravitation - Treacherous Pathways of Continuum Mechanics

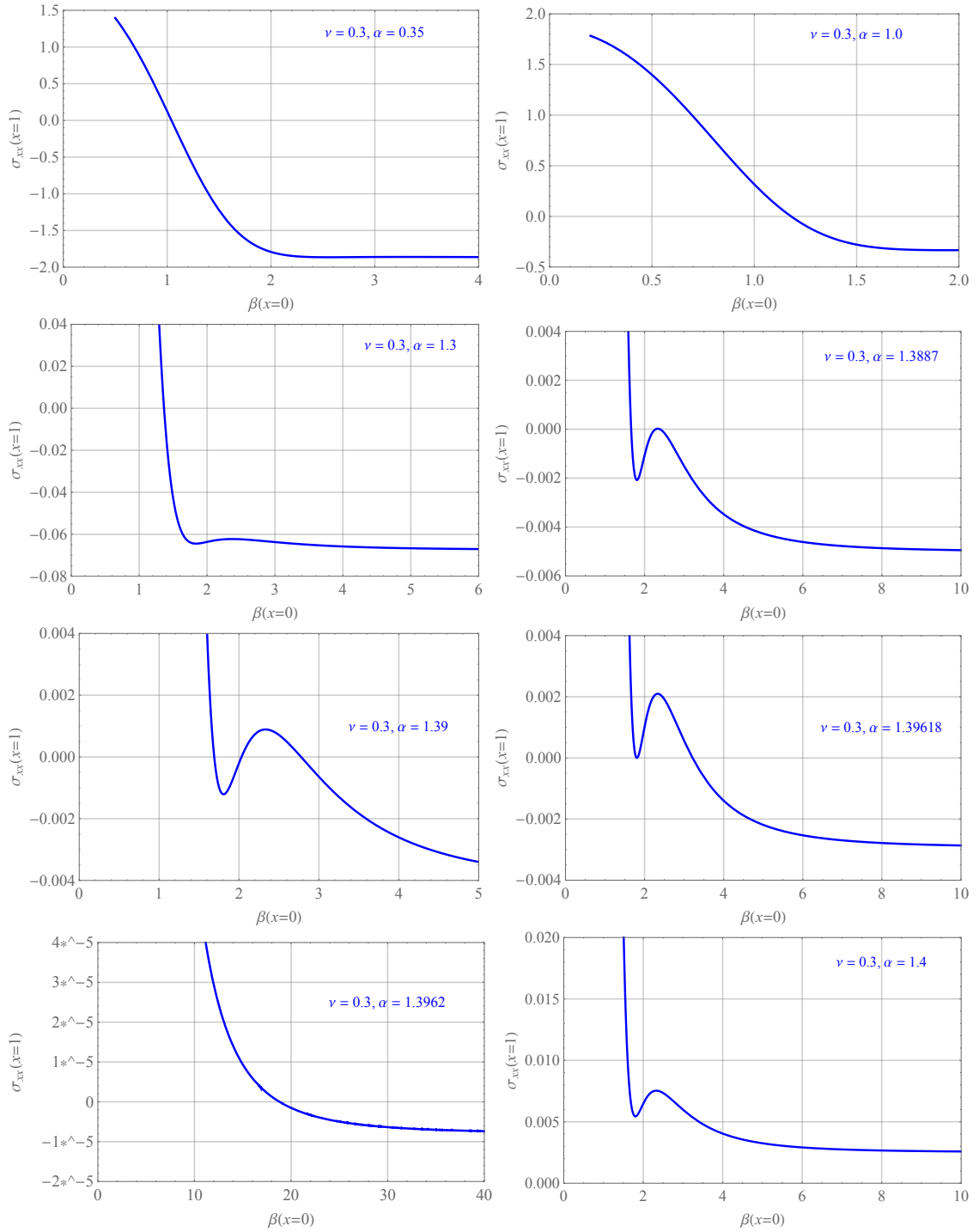


Figure 3: Behavior of the solution for increasing α -value (see text).

$$\left[\frac{1}{1+\nu+2(1-2\nu)\xi^3} - \frac{\exp\left(-\frac{3}{4}\tau\right)}{(1+\nu)(1-\xi^3)} + \frac{1-\nu}{1+\nu} \frac{3\xi^3 \exp\left[-\left(\frac{1-2\nu}{1-\nu} + \frac{1}{2\xi^3} \frac{1+\nu}{1-\nu}\right) \frac{\tau}{2}\right]}{(1-\xi^3)[1+\nu+2(1-2\nu)\xi^3]} \right] +$$

$$\frac{\alpha}{20} \frac{1-\nu}{1+\nu} \frac{1}{1-\xi^2} \left[-\left(2 + 3\xi^5\right) x + \frac{2\xi^3}{x^2} \right] \exp\left(-\frac{3}{4}\tau\right) \times$$

$$\left[1 - \exp\left(-\frac{1+\nu}{1-\nu} \frac{\tau}{4} \frac{1-\xi^3}{\xi^3}\right) \right] + \frac{\alpha}{20} x^3 \left[1 - \exp\left(-\frac{3}{4}\tau\right) \right], \quad \xi := \frac{r_i}{r_o} \leq x \leq 1.$$

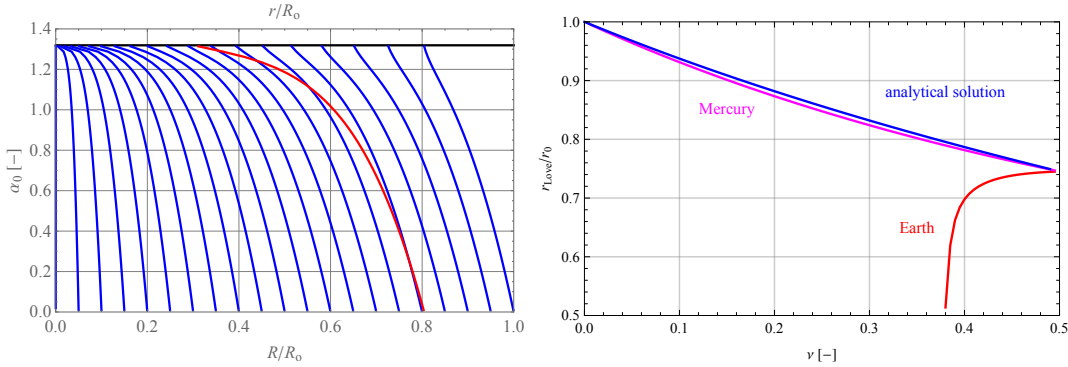


Figure 4: Studies of the nonlinear deformation due to self-gravitation (see text).

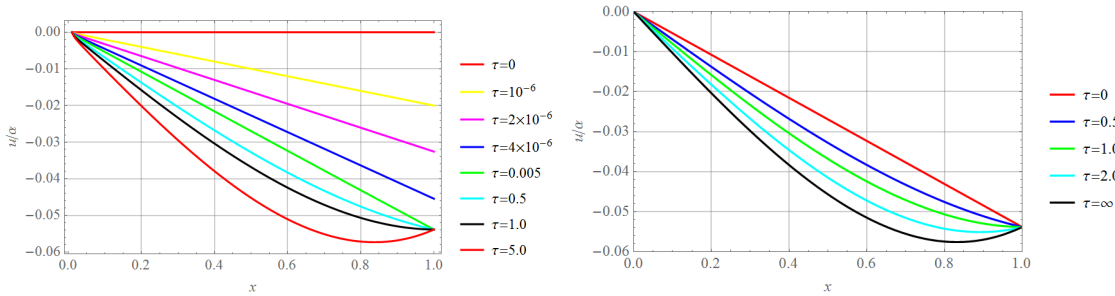


Figure 5: Temporal development of the displacement as a function of radial position for a hollow and a solid sphere (see text).

Note that special care has to be given to the case $\tau = 0$ in Eqn. (26)₂: If we consider the limit $\tau \rightarrow 0$ we find a non-vanishing initial displacement in contradiction to the requirement. This is not so for the more cumbersome looking Eqn. (27), where the limit leads to $u(x, \tau \rightarrow 0) = 0$. Fig. 5₁ depicts the temporal evolution of the displacement as a function of radial distance in dimensionless form as predicted by Eqn. (22) for the choice $\nu = 0.3$ for a hollow sphere with a very small hole, $\xi = 0.01$. In other words: This figure essentially represents the behavior of the solid sphere. Moreover, Fig. 5₂ depicts the temporal evolution of the displacement as predicted by Eqn. (21) for the solid sphere. Note that immediately after “gravity has been switched on” the dependence is nearly linear, in other words we observe a sudden jump, whereas the solution shown in Fig. 5₁ evolves continuously, but *fast* (observe the values for the dimensionless times).

However, this high speed gives us a clue of what is happening: Our quasistatic approximation from Eqn. (1) reaches its limits. There will be fast movements of mass if we “switch on gravity” and this would require us to solve the full balance of momentum with the inertia terms.

As far as the Love radius is concerned we may use Eqn. (26) to find the following analytical relation:

$$x_{\text{Love}} = \frac{1}{\sqrt{3}} \sqrt{\frac{3-\nu}{1+\nu} + \frac{1-\nu}{1+\nu} \frac{1}{\exp\left(\frac{3}{4}\tau\right) - 1}}. \quad (28)$$

For physical reasons the (normalized) Love radius must be smaller than one. Obviously it takes some time before this is the case. Before that time has passed the Love radius and the outer radius coincide. There is no tensile strain until then, *i.e.*, there is no damage possible.

5 Conclusions

We end this essay by a quote by Albert Einstein, which summarizes the predicament of modeling in physics quite concisely: “As far as the laws of mathematics refer to reality, they are not certain, and as far as they are certain, they do not refer to reality.”

References

- [1] Love, A.E.H., A treatise on the mathematical theory of elasticity. Volume 1. Cambridge University Press, 1892.
- [2] Kienzler, R., Schröder, R.: Einführung in die Höhere Festigkeitslehre. Springer, Dordrecht, Heidelberg, London, New York, 2009.
- [3] Ibrahimbegovic, A.: Nonlinear Solid Mechanics, Theoretical Formulations and Finite Element Solution Methods. Springer Dordrecht Heidelberg London New York, 2009.
- [4] Bose, S.C., Chattarji, P.P.: A note on the finite deformation in the interior of the Earth. Bull. Calcutta Math. Soc. 55(1), 11-18, 1963.
- [5] Bertram, A., Böhlke, T., Šilhavý, M.: On the rank 1 convexity of stored energy functions of physically linear stress-strain relations. Journal of Elasticity 86, 235-243, 2007.
- [6] Haupt, P.: Continuum mechanics and theory of materials. Springer-Verlag, Berlin, Heidelberg, New York, 2002.
- [7] Capaldi, Franco M.: Continuum mechanics: constitutive modeling of structural and biological materials. Cambridge University Press, 2012.

- [8] Müller, W. H., Weiss, W.: The State of Deformation in Earthlike Self-Gravitating Objects. Springer Singapore, 2016.
- [9] Seth, B. R.: Finite strain in elastic problems, Phil. Trans. R. Soc. Lond. A., **234**, pp. 231–264, 1935.
- [10] Polykonvexe Funktion: https://de.wikipedia.org/wiki/Polykonvexe_Funktion, Beispiel, 2016.

Wolfgang H. Müller and Wolf Weiss, Institute of Mechanics, Chair of Continuum Mechanics and Materials Theory, Technical University of Berlin, Einsteinufer 5, 10587 Berlin, Germany

Elena N. Vilchevskaya, Institute for Problems in Mechanical Engineering of the Russian Academy of Sciences, Bol'shoy pr. 61, V.O., 199178 St. Petersburg, Russia, and Peter the Great Saint-Petersburg Polytechnic University (POLYTEC), Politekhnikeskaja 29, 195251 St.-Petersburg, Russia

Molecular dynamics study of the relative sliding mechanisms in amorphous silica

Anton Yu. Nikonov, Andrey I. Dmitriev, Werner Österle
anickonoff@ispms.ru

Abstract

In the paper simulation of the treatment of two crystals with amorphous interlayer was carried out using the method of molecular dynamics. We studied a α -silica (quartz) sample with amorphous interlayer. The simulation result revealed several processes realized in the contact area as a result of shear loading. Depending on the temperature of the sample we observed deformation of an amorphous layer and formation of wear particles. It has been found that a necessary condition for the formation of wear particles is the presence of free volume in the interface. We compare the time dependencies of resistance forces for all samples. Results of simulation allows us to explain the low friction properties of silica tribofilm and also to say about silica amorphous layer as a solid lubricant.

1 Introduction

Carbon fibers and silica nanoparticles (SNPs) are widely used in all kinds of polymer matrix composites (PMCs) either reclusively or in combination. Compared to unfilled polymers, fiber-reinforced PMCs provide higher strength and wear resistance [1]. On the other hand, a number of interesting material properties were achieved by adding silica nano-particles (SNPs) to polymer materials [2]. Considering tribological properties, studies described in [3, 4] have shown that the application field of PMCs with micron-sized functional fillers can be extended by additionally incorporating a small fraction of inorganic nanoparticles. Especially SNPs are very effective in this respect, and it was shown that only 0.05 vol.% SNPs was enough to exert a measurable effect on friction evolution [5]. In the following, the composite containing micro- and nanofillers will be termed as hybrid composite whereas its counterpart without nanoparticles will be termed conventional composite.

The key for obtaining a better understanding of dry sliding properties of a tribological couple is a thorough investigation of the third body films, also termed tribofilms, forming at the tribological interface. The concept of a third body layer being responsible for load transfer and velocity accommodation between the first bodies of a tribological couple was first introduced by Godet [6]. Especially, antifriction and antiwear properties, i.e. a low coefficient of friction and wear rate, usually can be attributed to the formation of stable tribofilms [7]. During our own previous studies

we have shown that effective tribofilms, formed during automotive braking, consist of structural features on the nanometer scale [8]. Furthermore, we could simulate the sliding behavior of such films by nanoscale modeling. Since silica-based tribofilms are most crucial for providing wear protection and low friction, it was of great interest to simulate their sliding behavior. So the objective of this paper was to study the sliding behavior of silica tribofilm in order to understand the low friction properties of hybrid composites.

2 Materials

The raw materials used for preparation of the EP + 5% SiO₂ composite were: a standard diglycidil ether of bisphenol A (DBEBA) offered by DOW as DER331, a cycloaliphatic amine hardener HY 2954 from Huntsman and a colloidal silica masterbatch with a concentration of 40 mass% and a nominal particle diameter of 20 nm in DGBEBA offered as Nanopox F400 from Evonik. A thin slice was prepared from the EP + 5% SiO₂ composite by microtomy and investigated in a Scanning Transmission Electron Microscope (STEM) of type JEOL 2200FS.

3 Experimental Data

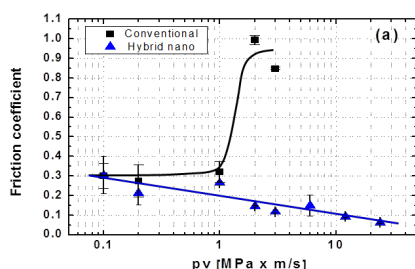


Figure 1: Friction coefficient as function of pv for composites with 5% silica nanoparticles (hybrid) and for the conventional composite without SNPs.

composite [4].

Striking differences were observed between the tribological performance of conventional and hybrid composites at certain stressing conditions, as shown in Fig. 1. Friction is almost the same at pv -values lower than 1 MPa m/s. Then a steep increase is observed for the conventional composite. It should be mentioned here that the beneficial effect of the SNPs is only observed in combination with the carbon fibers. Composites consisting solely of EP and SNP do not provide low friction at high pv , and furthermore, wear is not reduced to the same extent as for the hybrid

4 An overview of previous results

Details of modelling of tribofilm sliding behavior have been described in our recent paper [9]. The size of modelling elements was adjusted to 10 nm which is close to the size of the nanofiller of the polymer matrix composite (20 nm) and also is well suited for sliding simulations of 100 nm thick tribofilms, as demonstrated in previous studies [8, 10]. The method of Movable Cellular Automata (MCA) was used for sliding simulations [9]. It was expected that the results of these simulations may enable us to understand the very low friction coefficient observed for the hybrid

composite at $p v = 24$ MPa m/s. Unfortunately, this was not the case. Despite of a very well developed mechanically mixed layer and smooth sliding simulation the friction coefficient of tribofilms did not drop below 0.2 [10], whereas 0.06 was measured for the hybrid composite at $p v = 24$ MPa m/s.

The result shown in Fig. 2 is only one example of a comprehensive parameter study of the silica-graphite system. Briefly, the following trends were observed during this study: decreasing the graphite content to 6% increases the COF fluctuations significantly and the mean COF slightly. The same effect was observed for the structure with 10% graphite if the normal pressure was reduced from 130 to 70 MPa. On the other hand, an increase from 130 to 150 MPa made no difference. In order to find conditions of smooth sliding we identified the parameters given in Fig. 2 as an optimum for the silica film with 10% graphite inclusions.

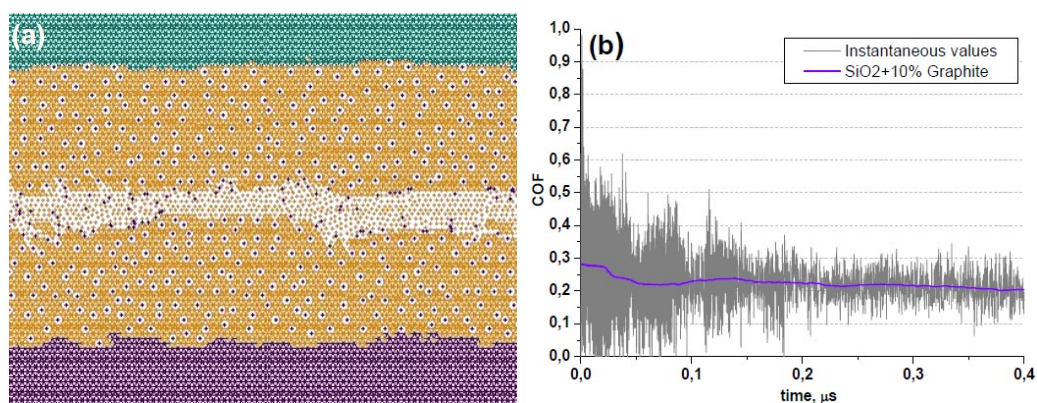


Figure 2: a) Structure formation and b) friction evolution during sliding simulation of a tribofilm consisting of 10% graphite (black) and 90% silica (orange) supported by carbon fiber (violet) and steel (green). External parameters: $p = 130$ MPa, $v = 10$ m/s.

A possible explanation of this very low friction coefficient could be assigned with silica transition to amorphous state. Another study even suggests amorphization of graphite being responsible for friction reduction [11]. Since we have found no means for considering such mechanisms in our model, the observed superlubricity effect could not be explained by the MCA method. Effort of finding explanation by Molecular Dynamics (MD) simulation was done in this work.

5 A model description

Since amorphous silicon oxide played a crucial role in the present study, we made an attempt to study its sliding behavior. The first step comprised of building a sample by linking SiO_4 tetrahedrons to form the appropriate crystal structure. Then an intermediate layer of this crystal sample was transformed to the amorphous state by virtual heating beyond the melting temperature and subsequent quenching. Next, the sliding behavior of the samples was studied while tangential and normal forces and a sliding velocity were applied to the rigid substrates comprising of crystalline SiO_2 .

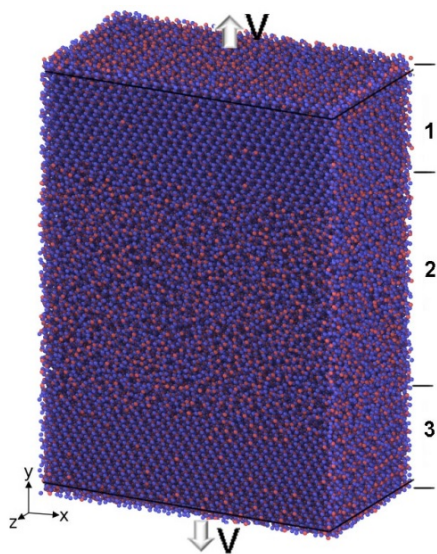


Figure 3: Initial structure of the modeled sample and a loaded scheme.

A modeled sample with two crystalline parts (on the top (block 1) and on the bottom (block 3)) and one amorphous centered layer with the initial thickness of about 8 nm (block 2) was designed as shown in Fig. 3. The total geometry of the sample was $14.3 \times 42.9 \times 8.58$ nm in $X \times Y \times Z$ axis respectively. Atoms located on top of the block 1 and on bottom of the block 3 within thickness of about 0.87 nm were subjected to external loading. Loading was applied through the constant velocity oriented along X axis and was equal to $V = 15$ m/s. Loading to top and bottom layer was applied in opposite direction, so totally the modeled sample was subjected to shear deformation with relative velocity of 30 m/s. Additionally a compression was applied to the loading layers through the constant force along Y direction. Taking into account the square of the loaded area this was equivalent to the loading with about 2 GPa on

top and on bottom layers.

The amorphous layer in the central part was created through instantly heating of the block 2 up to 6000 K and then quenching to the desired temperature. To study the behavior of silica sample the tree-body interatomic interaction suggested by Tersoff was used [12].

6 Results of simulation

As it was described above the sample was subjected simultaneously to sliding with the constant velocity and compression loading. The behavior of sample was investigated when quenched temperature was equal to 300 K (room temperature) and 1100 K (flash temperature easily reached during friction sliding with single contact).

6.1 Sliding at room temperature

According to the results of simulation the sliding behavior of silica sample at room temperature is very sensitive to the loading conditions and to the configuration of amorphous interlayer. By following we will try to systemize these features.

1. Sliding simulation of silica sample with amorphous layer under external compression.

The amorphous layer was created by heating and quenching as was described above. The thickness of that layer was about 20% of the whole sample size along Y direction. In case of shear loading applied simultaneously with compression the intensive deformation of the sample was observed without relative sliding of two blocks 1 and 3. Decreasing of loading pressure twice (from 4 GPa to 2 GPa) didn't change the behavior as shown in Fig. 4.

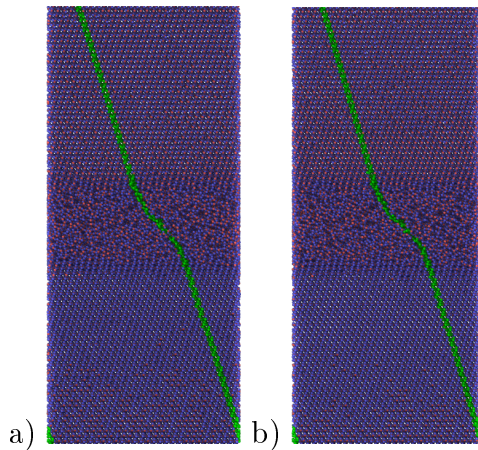


Figure 4: The resulting structure of the central fragment of the modeled sample after 0.5 ns with pressure (a) 4 GPa and (b) 2 GPa. The shear deformation corresponds to $\sim 34\%$.

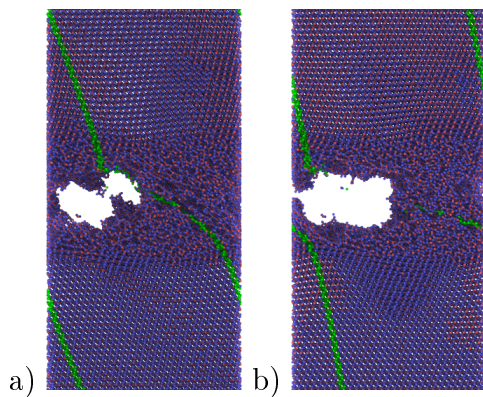


Figure 5: The resulting structure of the central fragment of the modeled sample after (a) 0.745 ns and (b) 0.750 ns without external pressure.

blocks through rolling of the formed lump of atoms. This sliding regime is characterized by very low resistance force.

3. Sliding simulation of silica sample under compression with pore inside amorphous layer.

Within the next step of our study we use the structure shown in the Fig. 5b as an initial structure for the sliding simulation under same loading condition as was used in case of tasks shown in Fig. 4a. This means that external pressure equivalent to 4 GPa was apply through loaded layers. In this case the pore still presents and relative sliding or two blocks is accompanied by rolling of atoms inside early formed lump. Fig. 6 shows the evolution of the modeled silica sample during relative sliding. Time dependencies of resistance forces (force acting on loaded atoms of block 1 in X direction) for the sample with pore inside the amorphous layer is shown in Fig. 7a.

Further shear loading until relative deformation of about 46% leads to total destruction of the silica sample. Probably this can be explained by relatively high compression and high initial density of amorphous interlayer.

2. Sliding simulation of silica sample with amorphous layer without external loading.

In order to check the previous assumption the sliding simulation of silica sample with amorphous interlayer without external pressure was implemented. The position of atoms in loaded layers along Y direction was fixed while X coordinates were linearly changed according to sliding velocity. This kind of loading provides discontinuity formation within amorphous layer after ~ 0.75 ns. This time corresponds to relative shear deformation of about 50%.

The analysis of structure gives us a certain explanation of this process. During shear deformation with fixed vertical positions of loaded atoms, both crystalline silica blocks (1 and 3) become intensively extended along the diagonal. As a result after reaching of a critical value the strength of amorphous layer is lower than tension forces and there is a separation of two blocks with discontinuity or pore formation inside the amorphous interlayer. Fig. 5 demonstrates the evolution of silica sample at two consistent moments of time corresponding to formation of inner pore inside block 2. Further shear loading leads to relative sliding of two

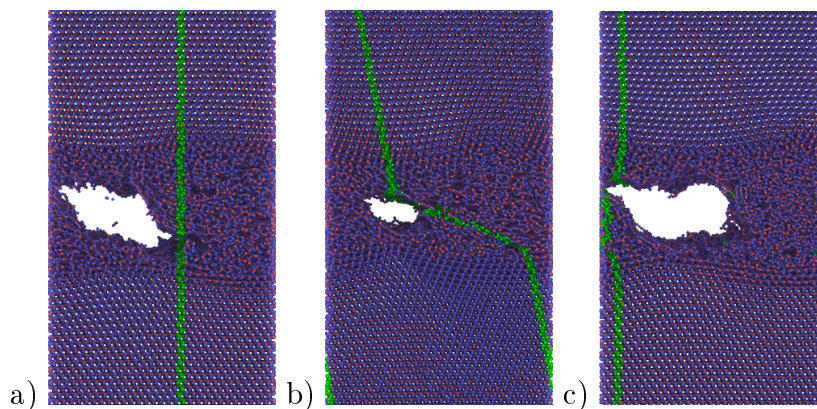


Figure 6: Evolution of the central fragment of the modeled silica sample. The structure at different moments of time: a) $t = 0$ ns, b) $t = 0.5$ ns and c) $t = 2.5$ ns.

According to Fig. 7a we can observe small stick-slip oscillations at the beginning of sliding connected with rolling of lamb of silica atoms. In spite of such oscillations the mean value of resistance force is very low. This result allows us to explain the low friction properties of silica tribofilm. Nevertheless, it is necessary to keep in mind that the sliding mechanisms of amorphous silica layer are very sensitive at room temperature to the loading conditions and layer structure.

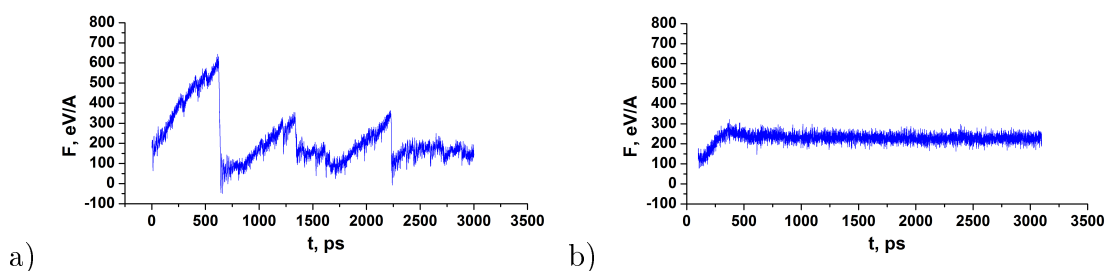


Figure 7: Time dependencies of resistance forces for the sample with pore inside amorphous interlayer at (a) 300 K and (b) 1100 K.

6.2 Effect of flash temperature

To study the features of silica sample sliding at elevated temperature the structure similar to one shown in Fig. 5 was taken as an initial structure for further shear deformation. The algorithm of the sample preparation was identical to the sample, shown in Fig. 6. First the dynamically equilibrium structure with amorphous interlayer in the central part of the silica sample was created by heating and quenching procedure of atoms from block 2. The next step includes deformation with constant velocity and fixed position of loaded atoms in vertical direction until micro-pore formation in the amorphous layer. Than simultaneously with shear deformation the compression with pressure equal to 4 GPa was applied. The evolution of the silica sample under combination of shear and normal loading at 1100 K is shown in Fig. 8. In comparison with similar sample behavior under room temperature here we can observe smooth sliding within amorphous interlayer.

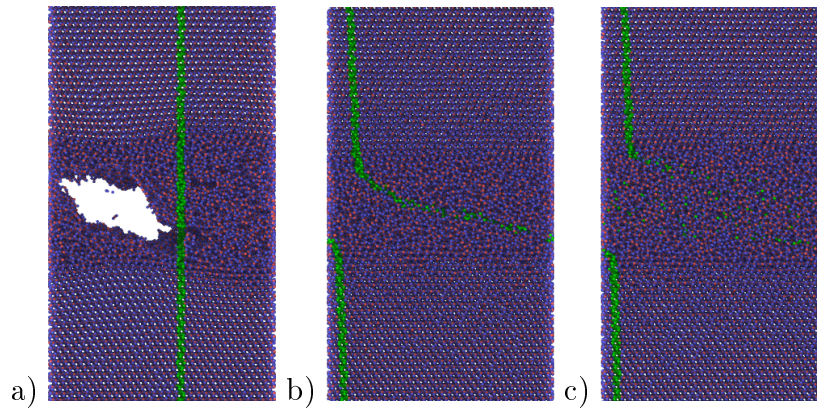


Figure 8: Evolution of the central fragment of the modeled silica sample. The structure at different moments of time: a) $t = 0$ ns, b) $t = 0.5$ ns and c) $t = 2.5$ ns.

Time dependence of resistance force is shown in Fig. 7b. The silica sample demonstrates low resistance force (about 250 eV/Å (4.0×10^{-7} N)). Thus not only amorphous carbon interlayer can represent solid lubricant with very low friction characteristics but amorphous silica layer as well.

7 Conclusion

As was described above the low COF of the silica-based tribofilm was partly confirmed by MCA modelling results, provided that an amount of 10 – 20 % soft inclusions was assumed. Furthermore, this result was verified by pin-on-disc tests with ball-milled powder blends, showing high friction (0.75) for pure silica, but a reduction to 0.2 for a blend of silica with 15% graphite and 10% Fe_2O_3 . Of course, we should not forget that modelling relies on many assumptions and simplifications and therefore cannot be considered as a reliable method for predicting tribological properties. We rather used modelling as an instrument for understanding what micro-mechanisms might be activated at sliding interfaces, and how variations of input parameters change the ongoing mechanisms. The stabilization of the wear rate up to the highest pv-values is attributed to the self-healing capability of the hybrid composite providing increasingly higher amounts of silica particles at more severe stressing conditions at the primary contact sites, the carbon fibers. As long as enough particles are available for cushioning the fibers and the films are thick enough to withstand complete removal before new layers are formed, the tribological system will function in the mild wear and low friction regime. It is very likely that the increase of carbon species with increasing pv will be responsible for the decrease of friction, although this could not be explained by MCA-modelling. MD-modelling of amorphous silica helps us to clear this point. Good correlation between tribological testing and modelling results indicates that sliding of thin surface films at asperity contacts can explain the observed antifriction and antiwear properties of the hybrid composite with hierarchical micro/nano-structure.

Acknowledgements

The results of MCA modelling were supported by RFBR grant no. 14-08-91330. MD results were obtained under RSF grant no. 14-19-00718.

References

- [1] S. Zhou, Q. Zhang, C. Wu, J. Huang. *Materials and Design* 44 (2013) 493-499
- [2] I. Ab Rahman, V. Padavettan. *J Nanomater* 2012. Doi:10.1155/2012/132424
- [3] K. Friedrich, Z. Zhang, A.K. Schlarb. *Composites Science and Technology* 65 (2005) 1411-1421
- [4] G. Zhang, R. Sebastian, T. Burkhart, K. Friedrich. *Wear* 292-293 (2012) 176-187
- [5] G. Zhang, I. Häusler, W. Österle, B. Wetzel, B. Jim. *Wear* 342-343 (2015) 181-188
- [6] M. Godet. *Wear* 1-3 (1984) 437-452
- [7] S. Jacobson, S. Hogmark. Tribofilms - on the crucial importance of tribologically induced surface modifications. In G.K. Niclas (ed.). *Recent Developments in Wear Prevention, Friction and Lubrication*. Kerala, India: Research Signpost; 2010, 197-225. ISBN:978-87-308-03777-7
- [8] W. Österle, A. Dmitriev. *SAE Int. J. Passeng. Cars - Mech. Syst.* 7(4) (2014), doi:10.4271/2014-01-2490
- [9] A.I. Dmitriev, W. Österle, B. Wetzel, G. Zhang. *Computational Materials Science* 110 (2015) 204-214
- [10] W. Österle, A.I. Dmitriev, H. Kloß. *Tribol. Lett.* 54 (2014) 257-262
- [11] P. Thomas, J.L. Mansot, A. Molza, F. Begarin, M. Dubois, K. Guerin. *Tribol.Lett.* 56 (2014) 259-271
- [12] J. Tersoff. *Phys.Rev.* B37 (1988) 6991

Nikonov A.Yu., Akademichesky 2/4, 634055, Tomsk, Russia

Dmitriev A.I., Akademichesky 2/4, 634055, Tomsk, Russia

Österle W., Unter der Eichen 87, Berlin, D-12200, Germany

Molecular dynamics study of the influence of the parameters of the crystallization process during selective laser sintering of alloy Ti-Nb

Anton Yu. Nikonov, Andrey I. Dmitriev, Yuriy P. Sharkeev
anickonoff@ispms.ru

Abstract

In the paper the study of the processes occurring at different stages of the process of laser sintering is performed using the method of computer simulation on the atomic scale. The initial configuration of the system is two spherical crystallites with properties of titanium and niobium, with the interface. Interatomic interaction was described by the embedded atom method. We analyzed the effect of cooling rate on the resulting crystal structure of the alloy Ti-Nb. We also investigated the dependence of the resistance forces to break of sintered particles on the heating time of the system and its rate of cooling. It is shown that the main parameter which determines the adhesive properties of sintered particles is the contact area obtained during sintering process. The simulation results can not only define the technological parameters of the process to provide the desired mechanical properties of the resulting products, but also are a necessary basis for calculations on large scale levels in order to study the behavior of implants in actual use.

1 Introduction

Currently, one of the dominant material for the production of bio-implants is titanium and titanium alloys. Along with the recognized advantages of titanium as the implant material (magnetic inertia, bio-compatibility, low density combined with high strength, high corrosion resistance and others.), titanium has a relatively high modulus of elasticity. It was found that from attractive high biomechanical compatibility point of view beta alloys of titanium-niobium, which may also have the effect of pseudoelasticity, bringing them closer in properties to the properties of cortical bone may be considered. [1, 2]. Metallurgical methods for producing such alloys are well known but they are complicated, laborious and expensive. This is caused, in particular, by a large difference between the melting points and densities of titanium and niobium. It should be noted that the titanium and niobium have a very significantly different in thermal properties (thermal conductivity, specific heat, coefficient of linear expansion). Manufacturing also requests complex multistep thermomechanical methods in order to generate alloys with homogeneous structure and

chemical composition. Furthermore, during such treatments the preform lost to half volume.

Recently use of the additive technology, in particular, methods of synthesis of layered laser solves the above problems and achieves the objectives of personalized medicine [3, 4]. Advantages of additive technology and selective laser sintering are especially the possibility of forming not only the volume of the product, but also the internal structure. When forming structure it is possible simultaneously to synthesize a new material (alloy), using as the starting powder mixture components in the desired proportions.

Obviously, the physical properties of samples are determined primarily by processing conditions and the properties of the starting powder. In turn, the problem of determining the optimal impact parameters on the starting powder to produce samples with desired mechanical properties requires a deep understanding of mechanisms that are taking place during laser sintering at different scale levels. A short time duration and high power laser beam makes particularly difficult to direct experimental study the effects of high-energy impact. One of the research directions allowing us to identify the main regularities of the formation of Ti-Nb alloy by layering laser synthesis, depending on the parameters and intensive modes of heating is the using of methods of numerical modeling. Thus using the numerical method of *ab initial* calculations described in [5] the optimal stoichiometry to obtain the desired elastic modulus for Ti-Nb alloy system was found. In the present paper, mathematical model of the process of low modulus β -Ti-Nb alloy system formation produced by laser sintering from titanium and niobium powders was developed. For this aim, the particle based method of atomic-scale - the method of molecular dynamics was used to simulate processes of alloy crystallization under different temperature gradients conditions. Varying the temperature gradients was determined by the original temperature conditions of the system and by changing the heat sink intensity given by the thermo-physical properties of the substrate. Future the adhesion properties between particles of obtained Ti-Nb alloy, determines by the duration of the high-energy laser exposure were estimated.

2 Results of calculation

2.1 Features of Ti-Nb alloy crystallization

To study the features of Ti-Nb alloy crystallization under different temperature gradient conditions on the scale of single atoms the method of molecular dynamics in the form of LAMMS software [6] was used. Interatomic interaction was described using an interatomic potential calculated in the framework of the embedded atom method [7, 8], which had earlier been verified in test problems on the calculation of elastic and energy characteristics. The simulated system consisted of two spherical crystallites, one of which was corresponded to the lattice of titanium, and the second one - niobium. The diameter of each sphere was 10 nm, which is 5 times less than the characteristic size of the powder particles used for laser synthesis. The total number of atoms exceeds 150000. The initial sample structure is shown in Fig. 1a. In order to study the effect of varying duration of a laser beam exposure the high-

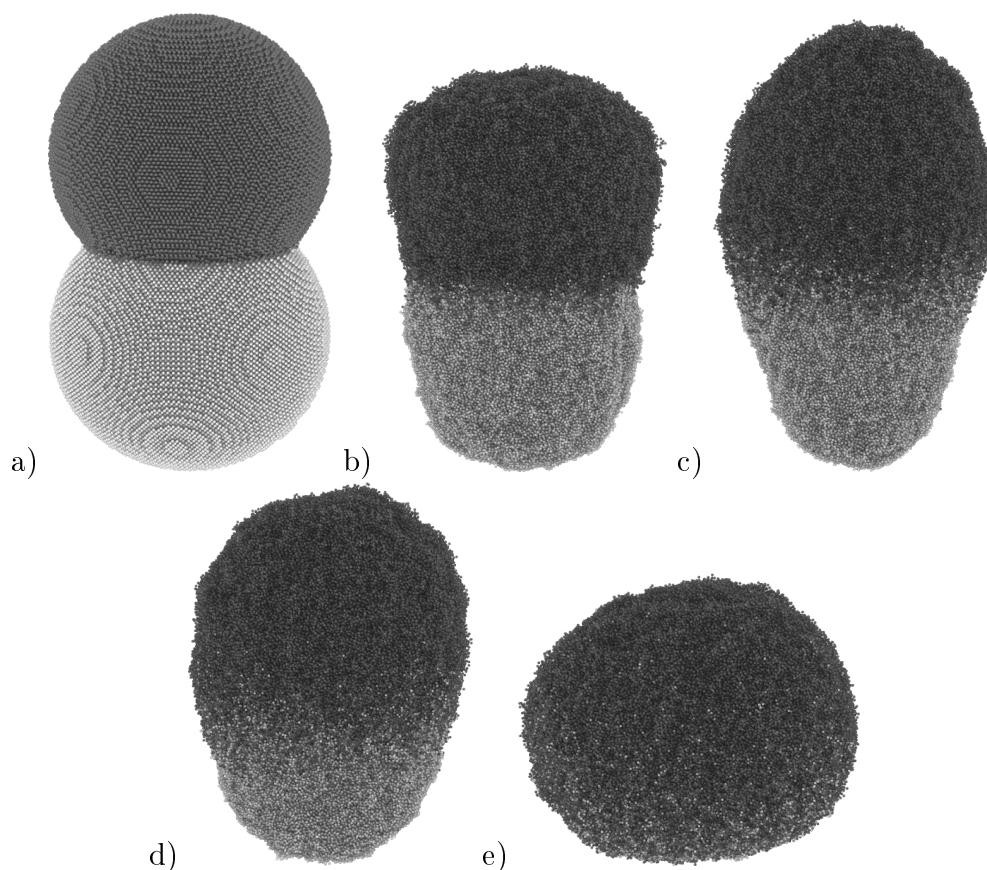


Figure 1: (a) The initial structure of the modeled particles of Ti (dark gray) and Nb (light gray) and structure corresponds to different moments of time of the high-speed heating process up to 6000 K: (b) 30 ps, (c) 70 ps, (d) 120 ps and (e) 220 ps.

speed warm-up of two particles up to temperature of 6000 K, 5000 K and 3000 K in various tasks was realized. Snapshots given on Figures 1b-d demonstrate the structure of the modeled system at different moments of time corresponding to the heating process. As a result of warm up stage the uniform melting for both metals within one particle was achieved as shown in Figure 1e.

The future solidification procedure during which a linearly decreasing of the system temperature from high value to ambient (300 K) one was carried out. The following cooling rates of the modeled ensemble of atoms were studied: 9.5, 5.7 and 3.1 K/ps. The corresponding time dependencies of the temperature changing for the modeled system during cooling stage are shown in Figure 2. Note that in order to achieve the cooling rate of 3.1 K/ps the resulting temperature of the system after heating stage was decreased to 5000 K. The resulting structure of the sample after cooling was analyzed using the algorithm which allows one to determine the local topology of interatomic structure corresponding to bcc, fcc and hcp crystal lattices. The influence of cooling rate on the ratio of atoms with bcc local topology of Ti-Nb alloy was studied.

The resulting structures for considered variants of cooling rates are shown in Figures 3a-c. Percentage of bcc atoms for the resultant state depends on the cooling rate and amounts to 11.2%, 56.2% and 87.7%, respectively. A further reduction of

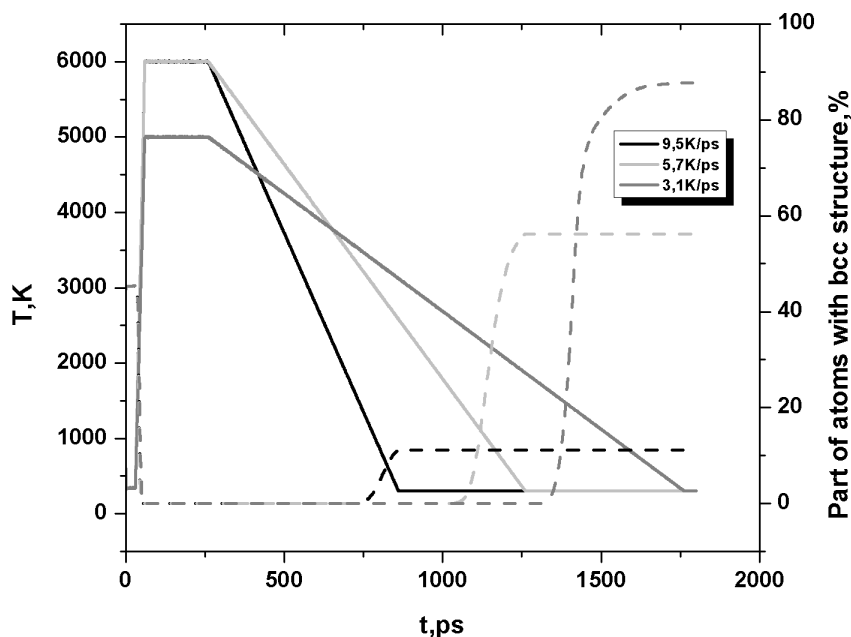


Figure 2: Time dependencies of the system temperature and parts of fcc atoms for three cooling rates.

the rate of the system cooling has not led to a noticeable change in the proportion of atoms with a bcc lattice in the resulting state. Thus, by trying of different cooling modes of the system we found that the cooling rate of 3.1 K/ps or less for two-component system is sufficient to ensure that to form the resulting polycrystalline structure of Ti-Nb beta-alloy. The remaining 12% corresponds to the surface atoms, and atoms located near the formed grain boundaries.

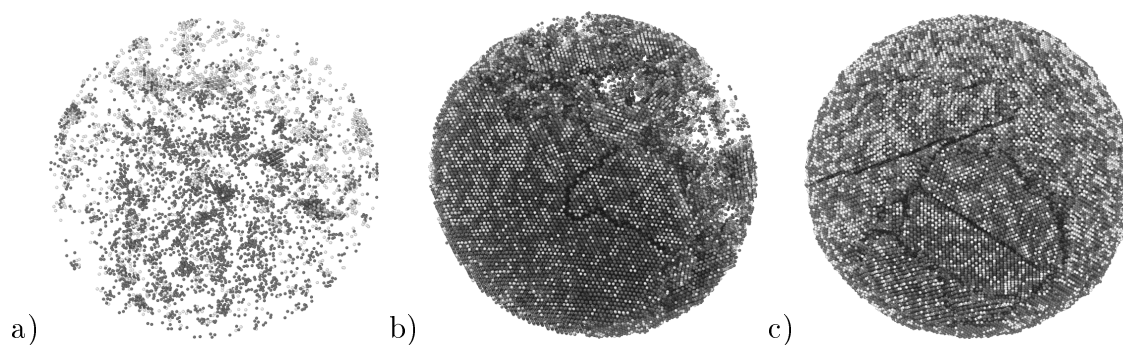


Figure 3: The final structure of the modeled sample after crystallization with different cooling rates: (a) 9.5 K/ps, (b) 5.7 K/ps and (c) 3.1 K/ps.

These results allow the use of mechanical and physical characteristics of the formed particles of the Ti-Nb alloy as the parameters needed to describe the interaction between particles for models of a mesoscopic scale. We can also note the qualitative agreement between results of simulation and existing experimental data on the effect of pre-heating the powder mixture and the use of the substrate during the preparation of beta-titanium-niobium alloy under selective laser sintering.

2.2 Adhesion properties of Ti-Nb particles

Next stage of research was devoted to study the influence of the alloy particle system heating duration and its cooling rate on the value of the resulting adhesive force. For this purpose two hemisphere-shaped particles with an internal structure corresponding to the structure of the β -alloy Ti-Nb system obtained by as a result of the crystallization process were simulated. Testing was carried out as follows. Initially hemisphere from their tops converged to a distance of about 1 nm. Obtained in this way configuration of the modeled system is shown in Figure 4a. The crystallographic orientation of the particles was chosen so that, in the area of convergence of the particles grain boundary was formed.

By the next stage of testing a local heating of both particles in the region of tops convergence by adding the kinetic energy to the surface atoms of the ratio of 1 eV/ps for the entire system was simulated. As a result melting of the hemispheres and their subsequent sintering were occurred. Depending on the duration of heating the sintering area has changed. The resulting structure, corresponding to the contact area of 8500 Å² is shown in Figure 4b. This configuration was obtained by heating the modeled system in the area of convergence of particles tops to \approx 3000 K within 50 ps, followed by cooling.

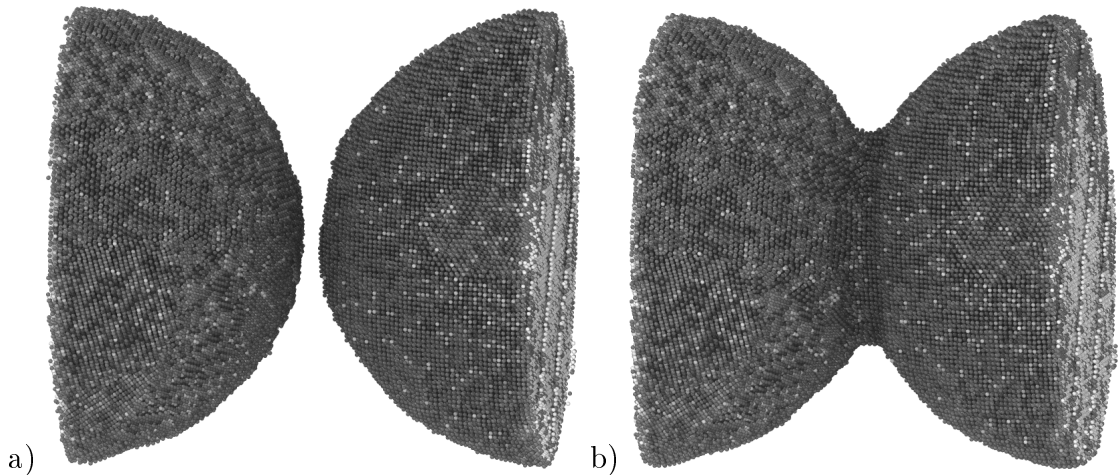


Figure 4: The structure of the modeled setup of Ti-Nb β -alloy at different stage: (a) before heating, (b) after heating.

To assess the adhesive force the configuration, not only with different values of the contact square, but with a different structure of resulting contact were created. The modifications in the structure were achieved by changing the cooling rate of the molten area. At low cooling rates the crystallization of the molten contact area with formation of a grain boundary was observed. At relatively high cooling rates the amorphization of a conjugated area was taking place. The final stage of adhesive forces estimation consists into modeling of rupture of the formed coupling. To this end, the movement with constant velocities of atoms located at the base of the hemispheres was modeled. Velocities were oriented in opposite directions along axis X. Figure 5 shows the dependence of the resistance force on the initial value of the square of molten area. It can be seen very well pronounced linear dependence

between forces and squares for all considered cases. In these particular cases features of structure of the molten area does not have a significant impact on the resulting dependence.

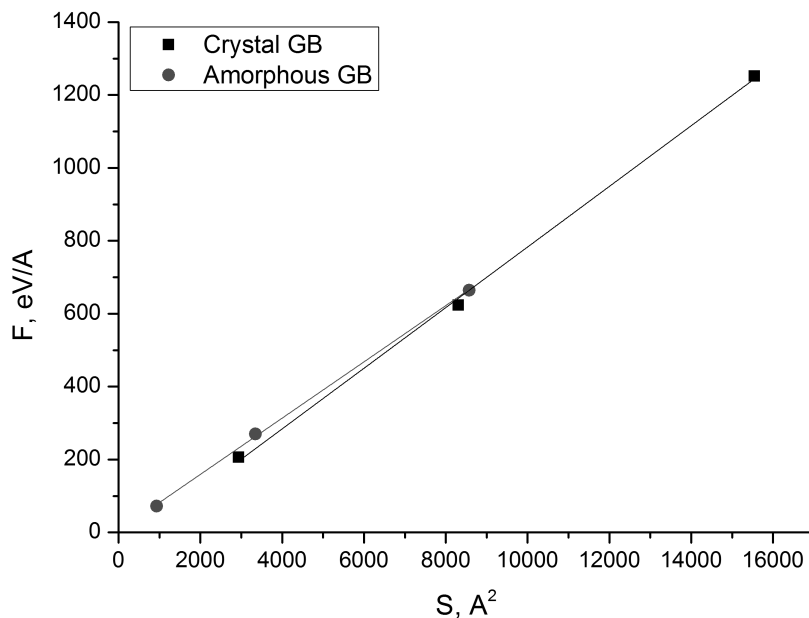


Figure 5: The dependence of adhesion strength on the square and the structure features of the molten area of two particles of Ti-Nb β -alloy.

Thus, the main factor determining the magnitude of the adhesive force is the square of the area involved in the contact between two particles. This parameter directly depends on the duration of thermal exposure. The cooling rate and the related structure of the molten area almost no effect on the resulting adhesion properties.

3 Conclusions

Computer simulation results of the melting process, followed by crystallization of a mixture of particles of titanium and niobium, for different values of the temperature gradient allowed to determine the conditions necessary to obtain a system with a maximum content of beta-crystal structure of the alloy Ti-Nb. It was found that the cooling rate of 3.1 K/ps or less for considered two-component system is sufficient to ensure that the resulting polycrystalline structure was beta alloy with a maximum content of the bcc lattice. At that variation of the temperature gradients determined by the initial system temperature and a different heat removal intensity defined by thermo-physical properties of the substrate. It should be noted that the obtained results qualitatively agree with experimental data on the effect of preheating the powder mixture and the use of substrate during the production of beta-alloy of titanium-niobium system by selective laser sintering [9, 10]. According to the simulation results it was shown that the main factor determining the value of the adhesion forces between the particles is the area of the region involved in the

contact between two particles. The rate of cooling and the structure of the obtained contact region almost no effect on the properties of the resulting adhesive. The obtained result will be used to specify the mechanical and physical characteristics of the formed powder particles of the alloy Ti-Nb in the description of the interaction between the particles in the model of a mesoscopic scale.

Acknowledgements

The research work was supported by the Russian Science Foundation, Grant No 15-19-00191.

References

- [1] Y. Bai, Y. Deng, Y. Zheng, Y. Li, R. Zhang, Y. Lv, Q. Zhao, S. Wei. *Mat. Sci. Eng. C* 59 (2016) 565
- [2] D. P. Andrade, L. M. R. Vasconcellos, I. C. S. Carvalho, E. L. S. Santos, R. F. Prado, D. R. Santos, C. A. A. Cairo, Y. R. Carvalho. *Mat. Sci. Eng. C* 56 (2015) 538-544
- [3] M. Fischer, D. Joguet, G. Robin, L. Peltier, P. Laheurte. *Mat. Sci. Eng. C* (2016) doi:10.1016/j.msec.2016.02.033
- [4] D. N. Silva, M. G. Oliveira, E. Meurer, M. I. Meurer, J. V. L. Silva, A. Santa-Bárbara. *J. Craniomaxillofac Surg* 36 (2008) 443-449
- [5] A. Yu. Nikonov, A. M. Zharmukhambetova, N. V. Skripnyak, A. V. Ponomareva, I. A. Abrikosov, S. A. Barannikova, A. I. Dmitriev. *AIP Conf. Proc.* 1683 (2015) 020165
- [6] S. J. Plimpton. *J. Comp. Phys.* 117 (1995) 1-19
- [7] M. S. Daw, M. I. Baskes. *Phys. Rev. B* 29 (1984) 6443
- [8] C. Jones, D. Farkas. *Comp. Mat. Sci.* 6 (1996) 231-239
- [9] M. A. Khimich, E. A. Parilov, Zh. G. Kovalevskaya, Yu. P. Sharkeev. *IOP Conf. Ser.: Mater. Sci. Eng.* 93 (2015) 012042
- [10] N. A. Saprykina, A. A. Saprykin, I. F. Borovikov, Y. P. ShPerkeev. *IOP Conf. Ser.: Mater. Sci. Eng.* 91 (2015) 012031

Nikonov A.Yu., Akademichesky 2/4, 634055, Tomsk, Russia
Dmitriev A.I., Akademichesky 2/4, 634055, Tomsk, Russia
Sharkeev Yu.P., Akademichesky 2/4, 634055, Tomsk, Russia

Effects of dispersion and structure molecules on time relaxation

Evelina V. Prozorova
e.prozorova@spbu.ru

Abstract

Here in the mechanics the influence of the angular momentum and the delay are investigated. Non-symmetric stress tensor is obtained. The delay process is counted, which is important in describing of the discrete space and for the relaxation of the complicated molecules. The analysis of the recording the Lagrangian function for the collective interaction of the particles are made with changing distance of the inertia center. Another definition of temperature is obtained for molecules with vibration and rotation and for mixture. This is making another value for pressure. The analysis is complemented by new results of computational experiments. The simplest interaction of two homogeneous flows that moving in the same direction at different speeds is investigated.

Keywords: angular momentum, conservation laws, nonsymmetrical stress tensor, Boltzmann equations, Chapman-Enskog method, conjugate problem the Navie-Stokes, the molecular dynamics method.

1 Introduction

In classical mechanics, the basic laws are the laws of conservation of mass, momentum and energy. The law of conservation of angular momentum is carried out indirectly on the basis of the law of the balance of power. The paper analyzes the provisions of the underlying mathematical models of continuum mechanics and the kinetic theory. We propose to include in the new model two types of effects: nonlocal effects and dispersion, i.e. we examine the impact of non-locality in time and space and the effect of the angular momentum on the processes occurring in the gas and liquid; we give a new interpretation of the conservation law of motion, which does not contain the arbitrary choice of the axis of rotation of the elementary volume. Each of the effects is considered separately. Angular momentum gives emergence of additional forces that can play the role of small perturbations affecting the stability of the structure. The resulting effects may affect in a critical and near a critical modes of aircraft, rockets, various devices, structures, as well as in some of the natural processes. The value of the additional force is determining by the gradient of physical quantities (density, velocity, momentum). The role of the delay observed

in experiments with shock waves in a rarefied gas, in lasers based on polyatomic gases, in chemical reactions. In some experiments with shock waves we can see the influence of the second viscosity [1]. In this work we give another definition of temperature for molecules with vibration and rotation and for mixture of molecules. This is making another value for pressure and temperature than in classic [2]. These new effects connect with nonlinear of definition the pressure and temperature. The influence of the angular momentum and the delay are investigated in the mechanics for: the interaction of many-particles, kinetic theory, the structural of molecules. Attention is drawn to the delay process, which is important in describing the discrete space. The analysis of the recording of the Lagrangian function [3,4] for the collective interaction of the particles with the change of the center of inertia of the moving particles and the effect influence angular momentum are made. Elementary volume can rotate around the axis of inertia or to be involved in the rotational movement. In both cases the flow density varies across the border on the value $\frac{d(\rho u)}{dr} \cdot (r' - r) + \dots$ by the rotation of the elementary volume [5-9]. For rarefied gas the second term (on space) in integral of collision of the Boltzmann equation is taken into account to calculate the self-diffusion and thermo-diffusion that was foretold by S.V. Vallander. It should be noted that for the kinetic theory (the Boltzmann equation) the law of conservation of angular momentum does not hold. Macroscopic parameters are determined in the equilibrium function of the Chapman-Enskog distribution in which used parameters of the Euler equations. Fromt this implies for the Chapman-Enskog distribution function formally we have values (density, linear moment and energy) with the first-order error. This fact was noted by Hilbert without further use and correction. The Boltzmann equation is invariant with respect to the choice of macro parameters. Therefore, the coincidence of the Navier-Stokes equations and the construction is of formal nature, order of approximation for the parameters in a locally equilibrium distribution function different. The Hilbert paradox was being solved. To solve this problem the iteration procedure was suggested. The new stress tensor is obtained for the molecules with their rotations and oscillations. Summary records of all effects lead to a cumbersome system of equations and therefore require the selection of main effects in a particular situation. Study is continued of the problem of Faulkner-Scan with a constant vortex at the outer edge of the boundary layer and with changing the vortex. The emergence of "banded" structures revealed under certain conditions of flow at the outer edge. We have results that small differ from classic results for the flows without vortex on the upper boundary.

2 The Lagrangian function

Here I would like to highlight some of the issues of theoretical mechanics. In the theoretical mechanics the Lagrangian form is considered [3,4]

$$L = \sum_i \frac{m_a v_i^2}{2} - U(r_1, r_2, \dots).$$

Here I would like to highlight some of the issues of theoretical mechanics. In the theoretical mechanics the Lagrangian form is considered [10,11]. Always implicitly

assumed that $U(r_1, r_2, \dots)$ – the full potential of the interaction of all particles, but in practice it is usually known interaction potentials of the two particles, and we use their sum. At equilibrium, or at small strains, but under nonequilibrium thermodynamic effects and perturbations lead to an uneven distribution of the physical parameters and the role of collective effects, that determined by the growing influence of the angular momentum. In addition, when these strains change position of the center of mass of elementary volume, that sign.

$$\frac{dL}{dt} = \sum_i \left[\frac{\partial L}{\partial q_i} \dot{q}_i + \frac{\partial L}{\partial \dot{q}_i} \ddot{q}_i \right] + \sum_i \left[\frac{\partial L}{\partial (q_i - a)} (\dot{q}_i - \dot{a}) + \frac{\partial L}{\partial (\dot{q}_i - \dot{a})} (\ddot{q}_i - \ddot{a}) \right],$$

$$a = \sum_i \frac{m_i r_i}{m_i}, \quad \text{for electrical interaction} \quad a = \sum_i \frac{e_i r_i}{e_i}.$$

In view of the time we are invited to consider force formula $F = F_0 + \nabla \left((R - a) \times \frac{\partial U}{\partial R} \right)$, R – the current radius. This formula is transformed with the permutability derivatives and directions of forces in the formula

$$F = F_0 + \nabla \left((R - a) \cdot \frac{\partial U}{\partial R} \right).$$

Usually, however, such as the Hamiltonian system of two interacting molecules after separation of the center of mass is represented as the sum of the Hamiltonians of isolated molecules $H_0 = H_A + H_B$ operator and their electrostatic interaction [10] $H = H_0 + V$

$$V = - \sum_{a=1}^{n_A} \sum_{j=1}^{N_B} \frac{Z_a}{r_{aj}} - \sum_{b=1}^{n_B} \sum_{j=1}^{N_A} \frac{Z_b}{r_{bj}} + \sum_{i=1}^{N_A} \sum_{j=1}^{N_B} \frac{1}{r_{ij}} + \sum_{a=1}^{n_A} \sum_{b=1}^{n_B} \frac{Z_a Z_b}{R_{ab}},$$

where the indices A, B numbered core indices i, j – the electrons of molecules A, B , respectively, the atomic units.

3 The kinetic theory

We can suggest the new formulation of some macrovalues (temperature, stress tensor, flow heat): in classic theory [11-15]

$$\frac{3}{2} kT = \frac{1}{n} \sum_k \int \frac{m_k (c^k)^2}{2} f_k d\xi_k, \quad (n = \sum_{k=1}^N n^k),$$

here k – number of components, T – temperature, $c^k = \xi_k - u$ (velocity of “ k ” components), “ q ” – heat flow, f – distribution function, one’s velocity of molecules, ξ_k velocity of molecules. Another definition is

$$\frac{3}{2} kT = \frac{\int (\sum_k \frac{n_k}{n} m_k) (\sum_k \frac{n_k}{n} c^k)^2 f d\xi}{2}.$$

Then we have one term is traditional and another is as the second viscosity. For stress tensor we can have $P_{ij} = \int (\sum_k \frac{n_k}{n} m_k c^k)_i (\sum_k \frac{n_k}{n} m_k c^k)_j f d\xi$.

For the flow of the heat

$$q = \frac{\int (\sum_k \frac{n_k}{n} c^k) (\sum_k \frac{n_k}{n} m_k) (\sum_k \frac{n_k}{n} c^k)^2 f d\xi}{2}$$

What we take in experiment?

$$f_\nu^{(0)} = n^\nu \left(\frac{m}{2\pi kT}\right)^{3/2} \exp\left(-\frac{m}{2kT}(c^\nu)^2\right) \text{ or for exclusive temperature}$$

$$f_\nu^{(0)} = n^\nu \left(\frac{m}{2\pi kT^\nu}\right)^{3/2} \exp\left(-\frac{m}{2kT^\nu}(c^\nu)^2\right).$$

For full temperature we can't conclude the right probability. The highest probability - transitions with a change in the quantum number by one $a_{\nu\mu}^{\nu+1,\mu} = a_\nu^{\nu+1}$. Deactivation process is

$a_\nu^{\nu-1} = a_{\nu-1}^\nu \exp\left(\frac{\Delta E^\nu}{kT}\right)$. In my opinion $a_\nu^{\nu-1} = a_{\nu-1}^\nu \exp\left(\frac{\Delta E^\nu}{kT^{\nu-1}}\right)$. For the internal energy remains the old equation, but with modified temperature value.

4 Interaction of two homogeneous flows

The simplest interaction is two homogeneous flows that moving in the same direction at different speeds. The classical formulation proposed in [16] (Fig. 1).

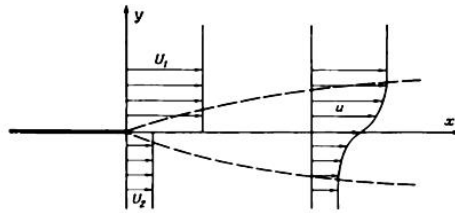


Figure 1: The overall picture of the interaction of two streams

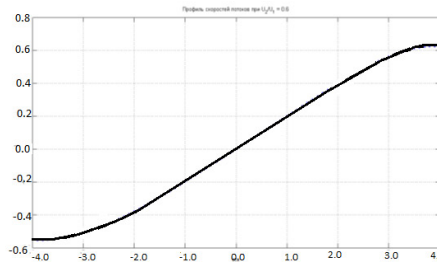


Figure 2: Stream interaction painting, $\frac{U_2}{U_1} = 0.6$

The problem is on the singularity. Two singularities dictate (the boundary conditions are set at infinity) a non-standard method of solution. Approximation boundary conditions at zero, and then the iterative process to satisfy the boundary conditions.

The problem was solved by student of fourth-year A. G. Garaev. The problem is on the singularity. Two singularities dictate (the boundary conditions are set at infinity) a non-standard method of solution. Approximation boundary conditions at zero, and then the iterative process to satisfy the boundary conditions. The problem was solved by student of fourth-year A. G. Garaev.

$$u \frac{\partial u}{\partial x} + v \frac{\partial u}{\partial y} = U_e \frac{\partial U_e}{\partial x} + \frac{\partial}{\partial y} \left(\mu \frac{\partial u}{\partial y} \right) + \frac{\partial}{\partial y} \left(\mu y \frac{\partial^2 u}{\partial y^2} \right), \quad \frac{\partial u}{\partial x} + \frac{\partial v}{\partial y} = 0,$$

u, v — velocity on x, y .

Once we have the dimensionless equations

$$\begin{aligned} -1/2\eta\Phi \frac{d\Phi}{d\eta} + V \frac{d\Phi}{d\eta} &= \mu \frac{d^2\Phi}{d\eta^2} + \frac{d}{d\eta} \left(\mu\eta \frac{d^2\Phi}{d\eta^2} \right), \\ -1/2\eta \frac{d\Phi}{d\eta} + \frac{dV}{d\eta} &= 0. \end{aligned}$$

In this way

$$\mu \frac{d}{d\eta} \left(\eta \frac{d^3\psi}{d\eta^3} \right) + \mu \frac{d^3\psi}{d\eta^3} + 2\Psi \frac{d^2\psi}{d\eta^2} = 0.$$

Here $\Psi^* = \sqrt{\mu/U_1} \Psi$, $y_1 = 1/2\sqrt{\mu/U_1} \eta$.

Then we have $2\eta\Psi'''' + 2\Psi''' + \Psi\Psi'' = 0$.

With boundary conditions

$$\Psi(0) = 0, \Psi'(0) = 1 - a, \Psi''(0+) = \Psi''(0-), \Psi(-\infty) = a.$$

The analytical solution has been found. Numerical results are presented in Fig. 2.

5 Conclusion

We propose the modified equations of continuum and Boltzmann equation in early works taking into account dispersion and delay, as well as the position of the center of inertia of the elementary volume. The possibility to describe discrete medium in the framework of continuum mechanics. Set the role of dispersion and delays in physical and chemical relaxation processes. The effect of angular momentum and, as a consequence, the nonsymmetrical of the stress tensor in the elementary volume was received. A model of the collective effects in the Lagrangian function was build. The results of the numerical solution of the modified problem of interaction of two parallel streams moving in the same direction are given.

References

- [1] Yury Nikitenko. On account of the feasibility of the bulk viscosity coefficient in aerodynamics problems. Seminar on fundamental problems of aerodynamics in a videoconference format. TSAGI. NOT. Zhukovsky, ITAM SB RAS, St. Petersburg Polytechnic State University, Moscow State University IMeh, High Temperatures, RAS, 02.02.2016.

-
- [2] M.N. Kogan. The dynamics of the rarefied gases. M.: Nauka, 1967. 440 p. (Russian).
- [3] L.D. Landau, EM Lifshitz. Mechanics. M.: Nauka, 1965. 204 p.
- [4] L.D. Landau, EM Lifshitz. Field theory. M.: Nauka, 1967. 400 p.
- [5] Evelina Prozorova. The role of dispersion effects and delay for continuum mechanics // Proceeding of 16th International Workshop on New Approaches to High-Tech: Nano-Design, Technology, Computer Simulations. NDTCS-2015, September 22-25, 2015, Grodno, Belarus. Pp. 136–138.
- [6] Evelina V. Prozorova. Influence of the Delay and Dispersion In mechanics. Journal of Modern Physics, 2014, 5, Pp. 1796–1805.
- [7] E.V. Prozorova. The influence of the dispersion of non-equilibrium continuum mechanics problems environment, Moscow State University Electronic Journal "Physical and chemical kinetics in gas dynamics". M.: MGU, 2012. T. 13.URL: <http://www.chemphys.edu.ru/pdf/2012-10-30-001.pdf> 30 p.
- [8] O. Galaev. E. Prozorova. Dispersion effects in the Falkner-Skan problem and in the kinetic theory. Proceeding of 13th International Conference on Heat Transfer, Thermal Engineering and Environment (HTE15), Salerno, Italy, June 27-29, 2015, pp. 69–76.
- [9] E.V. Prozorova, A. V. Shadrin. Influence of the nonequilibrium distribution function on dynamics of gas-surface scattering. Proceeding of the XL Summer School-Conference "Advanced Problems in Mechanics", XLI Summer School Advanced Problems in Mechanics (APM 2013) July Repino, St. Petersburg, Russia, pp. 462–472.
- [10] I.G. Kaplan. Introduction to the theory of intermolecular interactions. M.: Nauka. 1982. 312 p.
- [11] J.H. Ferziger, H.G. Kaper, Mathematical theory of transport processes in gases. Amsterdam-London, 1972.
- [12] J.O. Hirschfelder, C.F. Curtiss, R.B. Bird, The molecular theory of gases and liquids. New-York, 1954.
- [13] N.N. Bogolyubov. Problems of dynamical theory in statistical physics. M: Gostekhizdat. 1946, 146 p.
- [14] K.P. Gurov. The grounds of the kinetic theory. M.: Nauka, 1966. 350 p.
- [15] D.N. Zubarev. Nonequilibrium statistical thermodynamics. Nauka, 1971. 414 2012, St. Petersburg, Institute for problems in mechanical engineering. Pp. 300–304.

Evelina V. Prozorova, Mathematics & Mechanics Faculty, St. Peterburg State University, University av. 28, Peterhof, 198504, Russia.

Acoustic streaming in a rectangular cavity

Anna V. Pyatkova, Anna S. Semenova
 Vik040767@yandex.ru

Abstract

Acoustic streaming in a gas filled rectangular cavity subjected to the vibration effect is investigated numerically. Various vortices of acoustic streaming for small amplitude of vibration and three vibration frequencies are obtained. The cases of rectangular cavity and cylindrical cavity with similar problem formulation are compared. The differences between the two cases are shown. The nonlinear effects are quite small because of the small amplitude of vibration.

1 Introduction

Acoustic streaming is a directed time average mass transfer by steady vortices or time-independent circulations, which is often found in addition to the periodic motion in a compressible fluid driven by vibrating surface [1]. Features of acoustic processes need to be considered in the development of various thermoacoustic devices. In our time, acoustic streaming is widely investigated [2]–[9]. Hamilton et al. [2] obtained an approximate analytical solution for acoustic streaming for two-dimensional channels and for cylindrical tubes. This analytical solution does not account for the mean temperature variation, which may occur [3], [4]. Reyt et al. [6], [7] numerically and experimentally studied fast acoustic streaming in a cylindrical waveguide. Gubaidullin and Yakovenko [8] investigated the effects of heat exchange and nonlinearity on acoustic streaming in a cylindrical cavity. In this paper the amplitude of vibration was large and the frequencies of vibration were far from resonance. In [9] the features of acoustic streaming when heat exchange is taken into account are studied. The cylindrical cavity was taken. In this article, the results of [9] for isothermal boundary condition are compared with the case of rectangular cavity with similar problem formulation.

2 Problem formulation for rectangular cavity

A rectangular cavity of length L and width M with impermeable ends is considered (Figure 1). The cavity is filled with a perfect viscous gas (air). The gas in the cavity is initially in the state at rest and at constant temperature T_0 and constant pressure p_0 . The system is disturbed from the equilibrium by a vibration effect $A\cos(\omega t)$ with constant amplitude A and frequency ω . Constant temperature walls are taken.

The thermal conductivity, heat capacity, and viscosity are assumed constant. The upper half of the cavity is considered due to the symmetry.

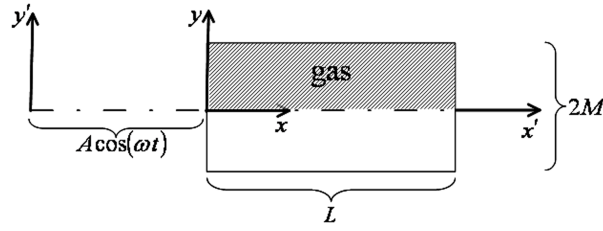


Figure 1: Schematic of the problem

The system of equations that describes the gas motion with respect to the vibrating cavity in the Cartesian coordinate system (X, Y) in dimensionless variables has the following form:

$$\frac{\partial \tilde{\rho}}{\partial \tau} + \frac{\partial \tilde{\rho}U}{\partial X} + \frac{\partial \tilde{\rho}V}{\partial Y} = 0, \quad (1)$$

$$\frac{\partial \tilde{\rho}U}{\partial \tau} + \frac{\partial \tilde{\rho}UV}{\partial X} + \frac{\partial \tilde{\rho}VU}{\partial Y} = -\frac{\partial P}{\partial X} + N\left(\frac{\partial^2 U}{\partial X^2} + \frac{\partial^2 U}{\partial Y^2}\right) + \frac{N}{3}\left(\frac{\partial^2 U}{\partial X^2} + \left(\frac{\partial^2 V}{\partial X \partial Y}\right)\right) + \tilde{\rho}\tilde{A}\Omega^2 \cos(\Omega\tau), \quad (2)$$

$$\frac{\partial \tilde{\rho}V}{\partial \tau} + \frac{\partial \tilde{\rho}UV}{\partial X} + \frac{\partial \tilde{\rho}VV}{\partial Y} = -\frac{\partial P}{\partial Y} + N\left(\frac{\partial^2 V}{\partial X^2} + \frac{\partial^2 V}{\partial Y^2}\right) + \frac{N}{3}\left(\frac{\partial^2 V}{\partial Y^2} + \left(\frac{\partial^2 U}{\partial X \partial Y}\right)\right), \quad (3)$$

$$\begin{aligned} \frac{\partial \tilde{\rho}\Theta}{\partial \tau} + \frac{\partial \tilde{\rho}U\Theta}{\partial X} + \frac{\partial \tilde{\rho}V\Theta}{\partial Y} &= \Gamma\gamma\frac{\partial}{\partial X}\left(\frac{\partial\Theta}{\partial X}\right) + \Gamma\gamma\frac{\partial}{\partial Y}\left(\frac{\partial\Theta}{\partial Y}\right) - \gamma(\gamma-1)P\left(\frac{\partial U}{\partial X} + \frac{\partial V}{\partial Y}\right) - \\ &- \frac{2}{3}\gamma(\gamma-1)N\left(\frac{\partial U}{\partial X} + \frac{\partial V}{\partial Y}\right)^2 + \gamma(\gamma-1)N\left(2\left(\frac{\partial U}{\partial X}\right)^2 + 2\left(\frac{\partial V}{\partial Y}\right)^2 + \left(\frac{\partial U}{\partial Y} + \frac{\partial V}{\partial X}\right)^2\right), \end{aligned} \quad (4)$$

$$P = \tilde{\rho}\left(\frac{\Theta+1}{\gamma}\right). \quad (5)$$

The initial and boundary conditions are as follows:

$$\tau = 0 : U = 0, V = 0, \Theta = 0, P = \frac{1}{\gamma}, \tilde{\rho} = 1, \quad (6)$$

$$1) X = 0 : U = 0, V = 0, \Theta = 0, \quad (7)$$

$$2) X = 1 : U = 0, V = 0, \Theta = 0, \quad (8)$$

$$3) Y = 0 : \frac{\partial U}{\partial y} = 0, V = 0, \frac{\partial \Theta}{\partial y} = 0, \quad (9)$$

$$4) Y = \tilde{M} : U = 0, V = 0, \Theta = 0. \quad (10)$$

The following dimensionless variables and parameters are introduced: $X = \frac{x}{L}$, $\tau = \frac{tc_0}{L}$, $U = \frac{u}{c_0}$, $Y = \frac{y}{L}$, $\tilde{\rho} = \frac{\rho}{\rho_0}$, $\Theta = \frac{T-T_0}{T_0}$, $V = \frac{v}{c_0}$, $P = \frac{p}{\gamma p_0}$, $\Omega = \frac{\omega L}{c_0}$, $\tilde{A} = \frac{A}{L}$, $\tilde{M} = \frac{M_0}{L}$, $N = \frac{\nu}{c_0 L}$ is the dimensionless kinematic viscosity, $\Gamma = \frac{\chi}{c_0 L}$ is the dimensionless thermal diffusivity, γ is the ratio of specific heats.

Here, t is time, x and r are the spatial coordinate, u and v are the axial and radial particle velocity components, respectively, ρ is density, $\rho_0 = \frac{p_0}{R_g T_0}$ is the initial density, $c_0 = \sqrt{\gamma R_g T_0}$ is the adiabatic speed of sound in the undisturbed medium, p is pressure, T is temperature, R_g is the gas constant, ν is the kinematic viscosity, and χ is the thermal diffusivity.

3 Problem formulation for cylindrical cavity

The geometry of the cylindrical cavity corresponds formally to the upper half of Figure 1, with the rectangular coordinates (x, y) replaced by the cylindrical coordinates (x, r) . Axial symmetry is assumed. The system of equations in the cylindrical coordinate system (X, R) in dimensionless variables has the following form:

$$\frac{\partial \tilde{\rho}}{\partial \tau} + \frac{\partial \tilde{\rho} U}{\partial X} + \frac{1}{R} \frac{\partial R \tilde{\rho} V}{\partial R} = 0, \quad (11)$$

$$\begin{aligned} \frac{\partial \tilde{\rho} U}{\partial \tau} + \frac{\partial \tilde{\rho} U U}{\partial X} + \frac{1}{R} \frac{\partial R \tilde{\rho} U V}{\partial R} = & -\frac{\partial P}{\partial X} + N \left(\frac{\partial^2 U}{\partial X^2} + \frac{1}{R} \frac{\partial}{\partial R} \left(R \frac{\partial U}{\partial R} \right) \right) + \frac{1}{3} N \left(\frac{\partial^2 U}{\partial X^2} + \right. \\ & \left. + \frac{1}{R} \frac{\partial}{\partial X} \left(\frac{\partial R V}{\partial R} \right) \right) + \tilde{\rho} \tilde{A} \Omega^2 \cos(\Omega \tau), \quad (12) \end{aligned}$$

$$\begin{aligned} \frac{\partial \tilde{\rho} V}{\partial \tau} + \frac{\partial \tilde{\rho} U V}{\partial X} + \frac{1}{R} \frac{\partial R \tilde{\rho} V V}{\partial R} = & -\frac{\partial P}{\partial R} + N \left(\frac{\partial^2 V}{\partial X^2} + \frac{1}{R} \frac{\partial}{\partial R} \left(R \frac{\partial V}{\partial R} \right) \right) + \frac{1}{3} N \left(\frac{1}{R} \frac{\partial}{\partial R} \left(R \frac{\partial V}{\partial R} \right) + \right. \\ & \left. + \frac{\partial}{\partial R} \left(\frac{\partial U}{\partial X} \right) \right) - \frac{4}{3} N \frac{V}{R^2}, \quad (13) \end{aligned}$$

$$\begin{aligned} \frac{\partial \tilde{\rho} \Theta}{\partial \tau} + \frac{\partial \tilde{\rho} U \Theta}{\partial X} + \frac{1}{R} \frac{\partial R \tilde{\rho} V \Theta}{\partial R} = & \gamma \Gamma \left(\frac{\partial^2 \Theta}{\partial X^2} + \frac{1}{R} \frac{\partial}{\partial R} \left(R \frac{\partial \Theta}{\partial R} \right) \right) - \gamma(\gamma-1) P \left(\frac{\partial U}{\partial X} + \frac{1}{R} \frac{\partial R V}{\partial R} \right) - \\ & - \frac{2}{3} \gamma(\gamma-1) N \left(\frac{\partial U}{\partial X} + \frac{1}{R} \frac{\partial R V}{\partial R} \right)^2 + \gamma(\gamma-1) N \left(\left(\frac{\partial U}{\partial R} + \frac{\partial V}{\partial X} \right)^2 + 2\gamma(\gamma-1) N \left(\left(\frac{\partial U}{\partial X} \right)^2 + \right. \right. \\ & \left. \left. + \left(\frac{\partial V}{\partial R} \right)^2 + \frac{V^2}{R^2} \right) \right), \quad (14) \end{aligned}$$

$$P = \frac{\tilde{\rho}(\Theta + 1)}{\gamma}. \quad (15)$$

The initial and boundary conditions are as follows:

$$\tau = 0 : U = 0, V = 0, \Theta = 0, P = \frac{1}{\gamma}, \tilde{\rho} = 1, \quad (16)$$

$$1) X = 0 : U = 0, V = 0, \Theta = 0, \quad (17)$$

$$2) X = 1 : U = 0, V = 0, \Theta = 0, \quad (18)$$

$$3) R = \tilde{M} : U = 0, V = 0, \Theta = 0, \quad (19)$$

Here, $R = \frac{r}{L}$. For comparison the results it is assumed that Y and R coordinates are the same.

4 Results and discussion

The problem was solved numerically using numerical method described in [9]. The following dimensionless gas parameters were used: $\gamma = 1.4$, $N = 8.6 \times 10^{-4}$, $\Gamma = 1.2 \times 10^{-5}$. The gas parameters correspond to the thermophysical properties of air at a temperature of 300 K. Width of the cavity was chosen as $\tilde{M} = 0.02$. The following range of vibration frequencies was used: $\Omega = 0.5, 1.5, 2.5$. Amplitude of vibration was chosen as $\tilde{A} = 0.01$. The computational grid had 1002×22 nodes. The time step was $\Delta\tau = 0.2 \Delta X$. For each calculation 500,000 timesteps are used. The CPU-time per 100 timesteps is 33 seconds on Intel(R) Core(TM) i3-2120 CPU @ 3.30GHz Processor.

The axial and radial streaming velocity components are given by [5]

$$U_{st} = \frac{\langle \tilde{\rho}U \rangle}{\langle \tilde{\rho} \rangle}, V_{st} = \frac{\langle \tilde{\rho}V \rangle}{\langle \tilde{\rho} \rangle} \quad (20)$$

Here, $\langle \rangle$ indicates the time-averaged quantities for the period $\tilde{T} = \frac{2\pi}{\Omega}$.

Figure 2 shows the streamlines of acoustic streaming for frequencies of vibration $\Omega = 0.5$ (a), 1.5 (b), and 2.5 (c) for rectangular cavity. It is visible that with the frequency of vibration $\Omega = 0.5$ two vortices are observed. The centers of these vortices are displaced to the cavity sidewalls. With the frequency of vibration $\Omega = 1.5$ near the central part of the top wall of the cavity two additional vortices appear. These vortices fill all upper part of the cavity at frequency of vibration $\Omega = 2.5$. These results are in a good agreement with the results of the article [9], where the formation of two additional vortices in the case of isothermal boundary conditions for cylindrical cavity is shown.

In Figure 3 streamlines of acoustic streaming for the case of cylindrical cavity considered in [9] are shown. It is visible that acoustic streaming in cases of rectangular cavity (Figure 2) and cylindrical cavity (Figure 3) qualitatively coincide, but there are some differences. At frequency $\Omega = 0.5$ the centers of vortices are more displaced to the top wall of the cavity in the case of cylindrical cavity. Two additional vortices which are formed at increase in vibration in the case of cylindrical cavity are larger than in the case of rectangular cavity. At frequency of vibration $\Omega = 2.5$ the boundary line of top and bottom vortices is closer to the top wall of the cavity in the case of rectangular cavity.

Let's carry out a comparison of change of the longitudinal acoustic streaming component along the cavity width (cavity radius) for the case of rectangular cavity and the case of cylindrical cavity (Figure 4). Some differences are visible. In general, we can conclude that acoustic streaming is more intensive in the case of cylindrical cavity (Figure 4 (a)) than in case of rectangular cavity (Figure 4 (b)).

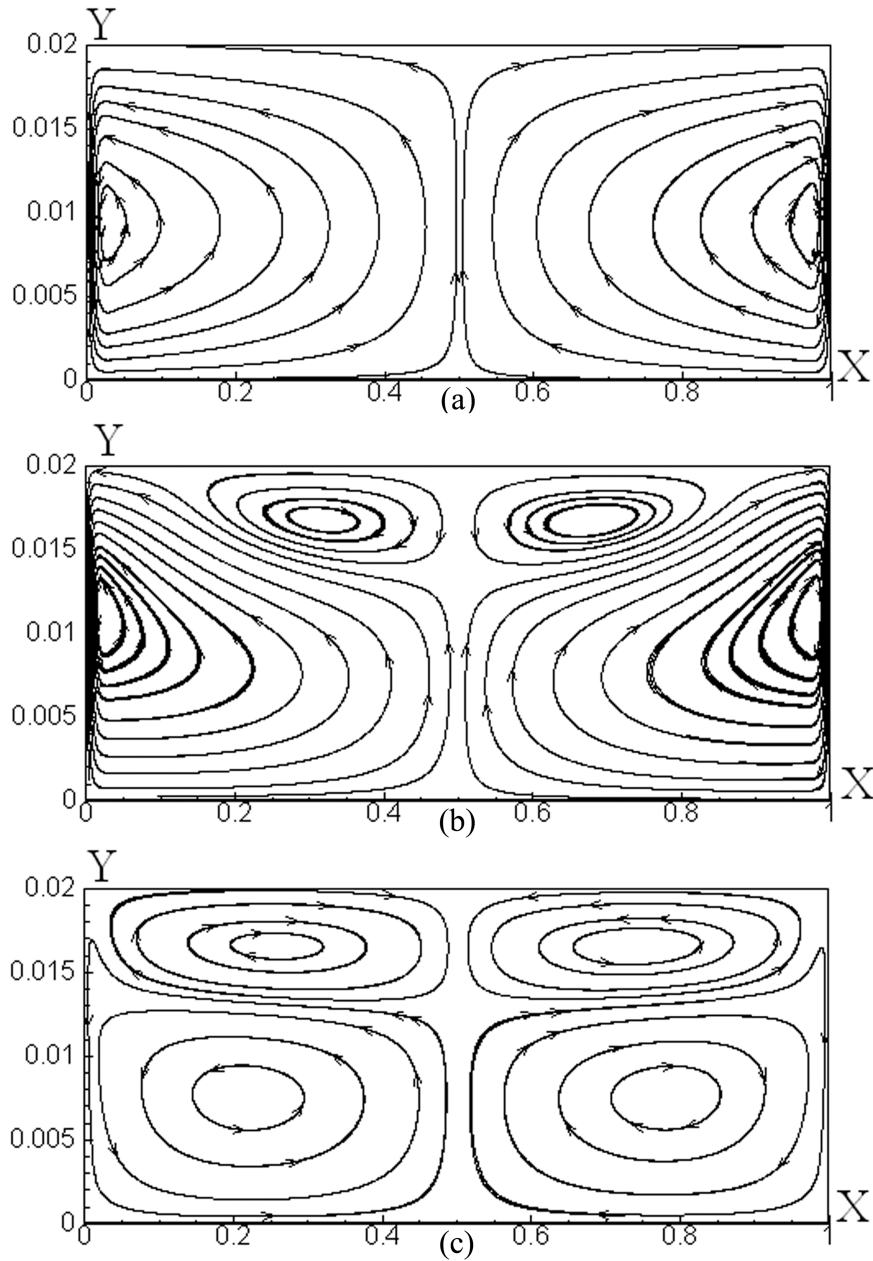


Figure 2: Streamlines of the streaming flow; (a) - $\Omega = 0.5$, (b) - $\Omega = 1.5$, (c) - $\Omega = 2.5$; rectangular cavity

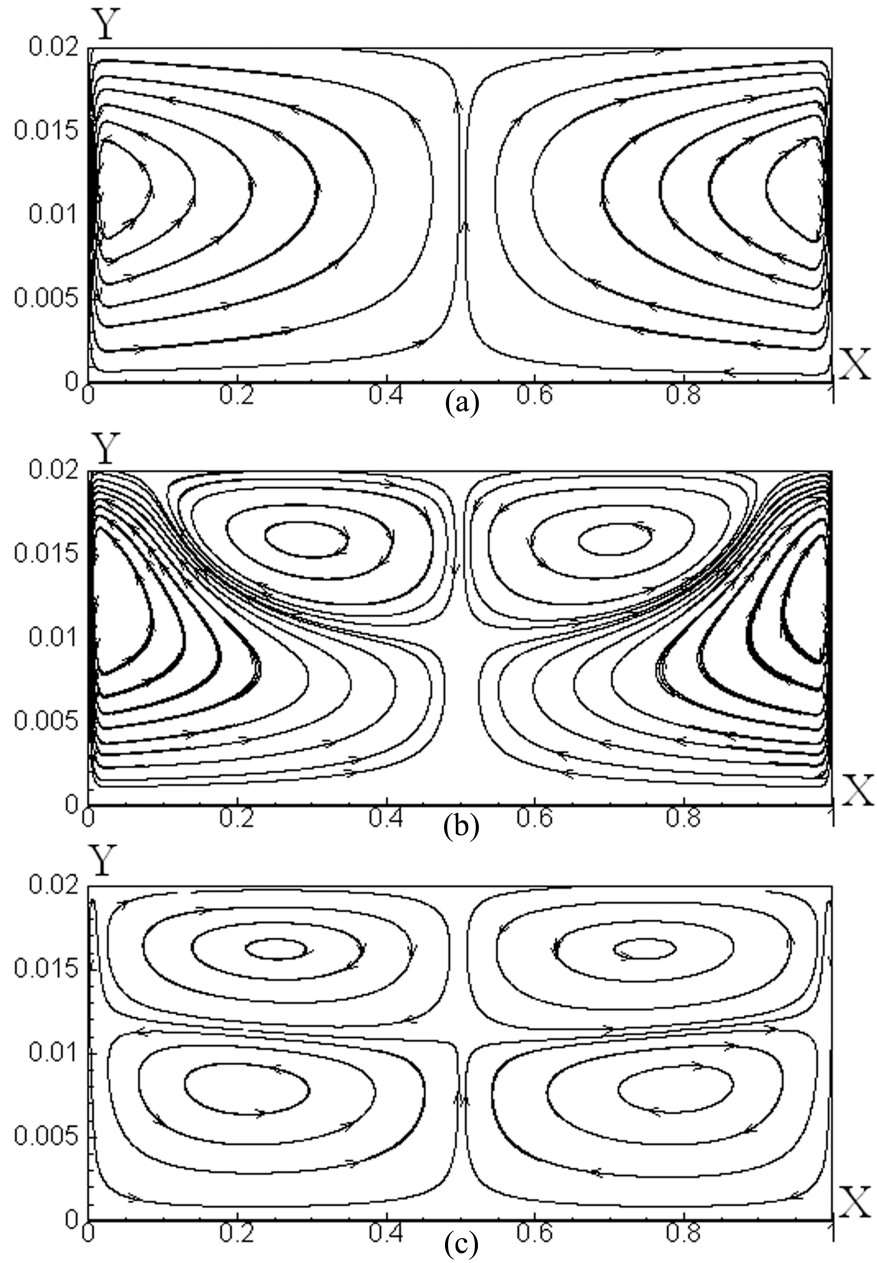


Figure 3: Streamlines of the streaming flow; (a) - $\Omega = 0.5$, (b) - $\Omega = 1.5$, (c) - $\Omega = 2.5$; cylindrical cavity

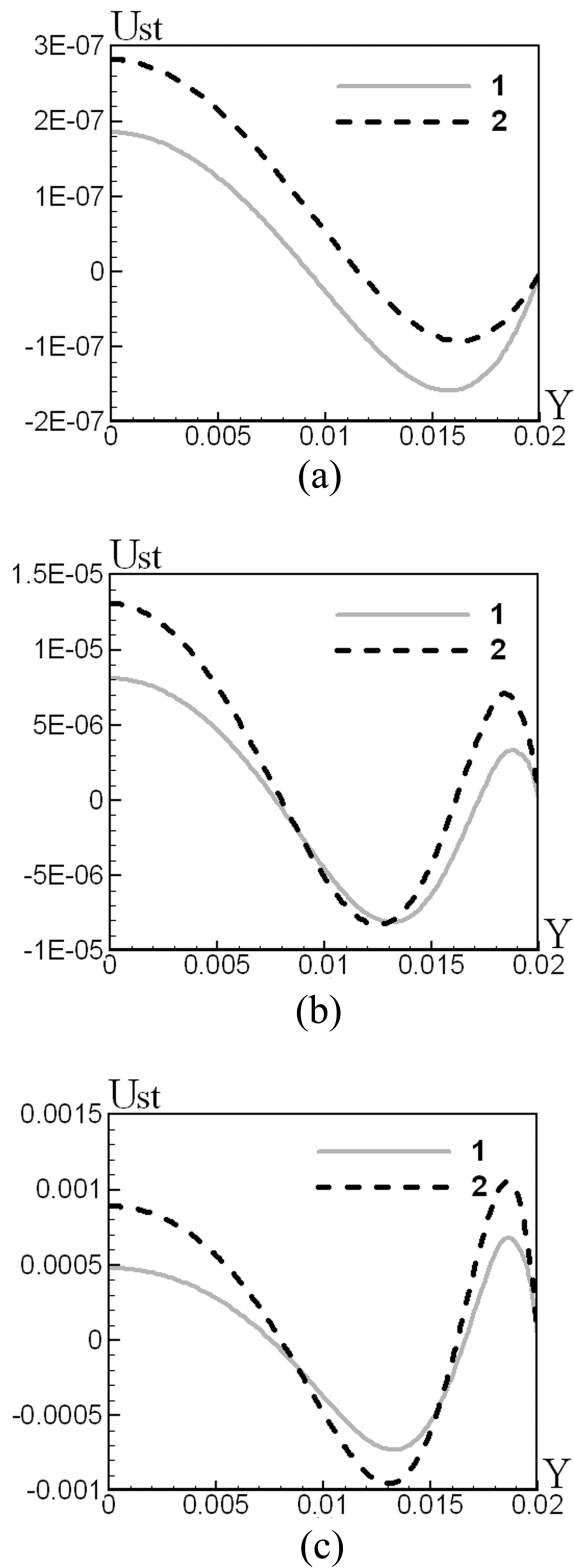


Figure 4: Variation of the streaming velocity along the Y coordinate; (a) - $\Omega = 0.5$, (b) - $\Omega = 1.5$, (c) - $\Omega = 2.5$; 1-rectangular cavity, 2- cylindrical cavity

5 Conclusions

Acoustic streaming in a rectangular cavity subjected to the vibration effect is investigated. Three frequencies of vibration $\Omega = 0.5, 1.5, 2.5$ are considered. In the case of frequency of vibration $\Omega = 0.5$ two vortices are observed. The centers of these vortices are displaced to the cavity sidewalls. At increase in frequency of vibration two additional vortices are formed near the central part of the top wall of the cavity. These vortices fill all upper part of the cavity with the frequency of vibration $\Omega = 2.5$. At the same time the centers of primary vortices are displaced from the cavity sidewalls to the cavity center.

After comparison of the results with the results of a similar problem in cylindrical statement it is possible to notice some differences. With the frequency $\Omega = 0.5$ the centers of vortices are more displaced to the top wall of the cavity in the case of cylindrical cavity. Two additional vortices which are formed at increase in vibration in the case of cylindrical cavity is larger than in the case of rectangular cavity. With the frequency of vibration $\Omega = 2.5$ the boundary line of top and bottom vortices is closer to the top wall of the cavity in the case of rectangular cavity. Also acoustic streaming is more intensive in the case of cylindrical cavity than in the case of rectangular cavity.

References

- [1] W.L. Nyborg. Acoustic streaming. Physical Acoustics, edited by W.P. Mason. Academic Press: New York, 1965. Vol. 2. Chap. 11. P. 265–331.
- [2] M.F. Hamilton, Y.A. Ilinskii, and E.A. Zabolotskaya. Thermal effects on acoustic streaming in standing waves // J. Acoust. Soc. Am. 2003. Vol. 114. P. 3092–3101.
- [3] A.A. Gubaidullin and A.V. Yakovenko. Numerical investigation of the perfect gas behavior in a vibrating cylindrical cavity with thermally insulated walls // Thermophys. Aeromech. 2014. Vol. 21. P. 589–599.
- [4] A.A. Gubaidullin and A.V. Yakovenko. Numerical investigation of the behavior of a perfect gas inside a vibrating cylindrical cavity under isothermal boundary conditions // High Temp. 2015. Vol. 53. No. 1. P. 73–79.
- [5] M.K. Aktas and T. Ozgumus. The effects of acoustic streaming on thermal convection in an enclosure with differentially heated horizontal walls // Int. J. Heat Mass Trans. 2010. Vol. 53. P. 5289–5297.
- [6] I. Reyt, V. Daru, H. Bailliet, S. Moreau, J.-C. Valie're, D. Baltean-Carle's, and C. Weisman. Fast acoustic streaming in standing waves: Generation of an additional outer streaming cell // J. Acoust. Soc. Am. 2013. Vol. 134. P. 1791–1801.
- [7] I. Reyt, H. Bailliet and J.-C. Valie're. Experimental investigation of acoustic streaming in a cylindrical wave guide up to high streaming Reynolds number // J. Acoust. Soc. Am. 2014. Vol. 135. P. 27–37.

REFERENCES

- [8] A.A. Gubaidullin and A.V. Yakovenko. Effects of heat exchange and nonlinearity on acoustic streaming in a vibrating cylindrical cavity // J. Acoust. Soc. Am. 2015 Vol. 137. No. 6. P. 3281–3287.
- [9] A.A. Gubaidullin and A.V. Pyatkova. Acoustic streaming with allowance for heat transfer // Acoustical Physics. 2016. Vol. 62. No. 3. P. 300–305.

Anna V. Pyatkova, Taymirskaya str. 74, Tyumen, Russia

Anna S. Semenova, Volodarskogo str. 6, Tyumen, Russia

Mathematical model of static deformation of micropolar elastic circular thin bar

Samvel H. Sargsyan, Meline V. Khachatryan
khachatryanmeline@mail.ru

Abstract

The boundary value problem of statics of plane stress state of micropolar theory of elasticity is considered in a thin circular area. Rather adequate hypotheses of general nature are formulated [1-3] and on the basis of these hypotheses applied (one-dimensional) model of micropolar elastic circular thin bar is constructed. Mechanic balance equation is obtained. It is confirmed that all energy theorems and Ritz, Bubnov-Galerkin, FEM variation methods are applicable for the constructed applied model of micropolar elastic circular thin bar and for solutions of corresponding boundary value problems of the applied model. One-dimensional variation functional is constructed and it is proved that all basic equations and natural boundary conditions of applied model of micropolar elastic circular thin bar will be obtained from the corresponding variation equation (as Euler equations).

1 Introduction

Papers [1-4] are devoted to the construction of applied theories of micropolar elastic thin plates and shells. Review of works in this direction has been implemented in the paper [5]. In the papers [6-9] general applied theory of micropolar elastic thin plates and shells is constructed on the basis of the hypotheses method, which are formulated adequately with the results of the asymptotic method of integration of three-dimensional boundary-value problem in thin domain [10]. In the paper [11] the applied theory of micropolar elastic thin straight bars is constructed in the same way.

In this paper, analogous hypotheses are formulated, on the basis of which general applied model of static deformation of micropolar elastic circular bar is constructed.

2 Problem statement.

A bar with a curved axis is considered (Fig. 1), which has a constant transverse cut with height $2h = r_2 - r_1$ and with width b so small that the problem of the bending of this bar can be viewed as plane (i.e. there is a plane stress state). The axis of

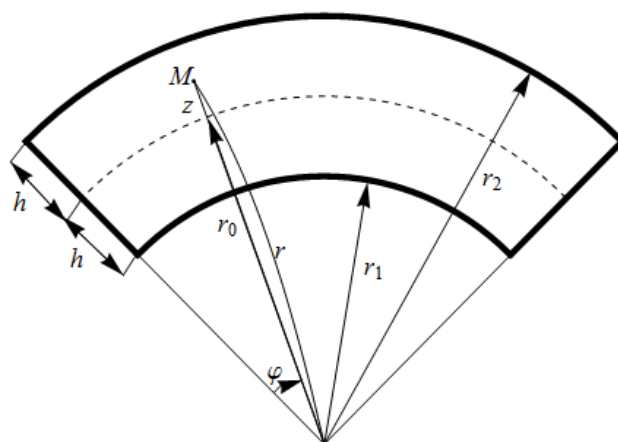


Fig. 1

the bar is the arc of a circle with radius r_0 ; the material of the bar is isotropic, micropolar-elastic.

Equations of the plane stress state of micropolar theory of elasticity are applicable in the middle plane of the bar, where the polar system of coordinates (r, φ) will be introduced: $r_1 \leq r \leq r_2$, $0 \leq \varphi \leq \varphi_1$ [12,13]:

Equilibrium equations

$$\begin{aligned} \frac{1}{r} \frac{\partial \sigma_{11}}{\partial \varphi} + \frac{\partial \sigma_{21}}{\partial r} + \frac{1}{r} (\sigma_{21} + \sigma_{12}) = 0, \quad \frac{\partial \sigma_{22}}{\partial r} + \frac{1}{r} (\sigma_{22} - \sigma_{11}) + \frac{1}{r} \frac{\partial \sigma_{12}}{\partial \varphi} = 0 \\ \frac{1}{r} \frac{\partial \mu_{13}}{\partial \varphi} + \frac{\partial \mu_{23}}{\partial r} + \frac{1}{r} \mu_{23} + \sigma_{12} - \sigma_{21} = 0 \end{aligned} \quad (1.1)$$

Elasticity relations

$$\begin{aligned} \gamma_{11} = \frac{1}{E} [\sigma_{11} - \nu \sigma_{22}], \quad \gamma_{22} = \frac{1}{E} [\sigma_{22} - \nu \sigma_{11}], \quad \gamma_{12} = \frac{\mu + \alpha}{4\mu\alpha} \sigma_{12} - \frac{\mu - \alpha}{4\mu\alpha} \sigma_{21} \\ \gamma_{21} = \frac{\mu + \alpha}{4\mu\alpha} \sigma_{21} - \frac{\mu - \alpha}{4\mu\alpha} \sigma_{12}, \quad \chi_{13} = \frac{1}{B} \mu_{13}, \quad \chi_{23} = \frac{1}{B} \mu_{23} \end{aligned} \quad (1.2)$$

Geometrical relations

$$\begin{aligned} \gamma_{11} = \frac{1}{r} \frac{\partial V_1}{\partial \varphi} + \frac{1}{r} V_2, \quad \gamma_{22} = \frac{\partial V_2}{\partial r}, \quad \gamma_{12} = \frac{1}{r} \frac{\partial V_2}{\partial \varphi} - \frac{1}{r} V_1 - \omega_3, \quad \gamma_{21} = \frac{\partial V_1}{\partial r} + \omega_3 \\ \chi_{13} = \frac{1}{r} \frac{\partial \omega_3}{\partial \varphi}, \quad \chi_{23} = \frac{\partial \omega_3}{\partial r} \end{aligned} \quad (1.3)$$

Here $\sigma_{11}, \sigma_{22}, \sigma_{12}, \sigma_{21}$ are power (normal) stresses; μ_{13}, μ_{23} are moment stresses; $\gamma_{11}, \gamma_{22}, \gamma_{12}, \gamma_{21}$ are deformations; χ_{13}, χ_{23} are bending-torsions; V_1, V_2 are displacements; ω_3 is free rotation; $E, \nu, \mu = \frac{E}{2(1+\nu)}, \alpha, B$ are elastic constants of the micropolar material.

It is assumed that on the front lines $r = r_1, r = r_2$ the external forces and moments are given:

$$\text{on } r = r_1, \quad \sigma_{21} = q_1^-; \quad \sigma_{22} = q_2^-; \quad \mu_{23} = m^-,$$

$$\text{on } r = r_2, \sigma_{21} = q_1^+; \sigma_{22} = q_2^+; \mu_{23} = m^+, \quad (1.4)$$

and one of the following variants of the boundary conditions can take place:

$$\begin{aligned} a) \text{ on } \varphi = 0, \sigma_{11} = \sigma'_{11}, \sigma_{12} = \sigma'_{12}, \mu_{13} = \mu'_{13}; \\ \text{on } \varphi = \varphi_1, \sigma_{11} = \sigma''_{11}, \sigma_{12} = \sigma''_{12}, \mu_{13} = \mu''_{13}; \end{aligned} \quad (1.5)$$

$$\begin{aligned} b) \text{ on } \varphi = 0, V_1 = V'_1, V_2 = V'_2, \omega_3 = \omega'_3; \\ \text{on } \varphi = \varphi_1, V_1 = V''_1, V_2 = V''_2, \omega_3 = \omega''_3; \end{aligned} \quad (1.6)$$

$$\begin{aligned} c) \text{ on } \varphi = 0, \sigma_{11} = \sigma'_{11}, V_2 = V'_2, \mu_{13} = \mu'_{13}; \\ \text{on } \varphi = \varphi_1, \sigma_{11} = \sigma''_{11}, V_2 = V''_2, \mu_{13} = \mu''_{13}; \end{aligned} \quad (1.7)$$

Further it is assumed that $2h \ll r$ and $2h \ll l$, where l is the length of the bar middle line (i.e. the bar is thin). The aim of the paper is the construction of the applied (one-dimensional) model of micropolar elastic circular thin bar. For this purpose the radius vector r of an arbitrary point of the domain is represented as follows: $r = r_0 + z$, where $-h \leq z \leq h$ ($r = r_0 - h$, $r = r_0 + h$), and on the basis of the fact that the bar is thin-walled, it will be assumed that

$$1 + \frac{h}{r_0} \doteq 1 \quad (1.8)$$

3 Hypotheses, displacements and rotation, deformations and bending-torsions, power and moment stresses.

Following assumptions (hypotheses) are formulated for the construction of the applied model of micropolar elastic circular thin bar [6-11]:

1. Hypothesis of the straight line is accepted as an initial kinematic hypothesis for displacements, i.e. Timoshenko's hypothesis. This means that the linear element, which is initially perpendicular to the middle plane of the circular bar before the deformation, remains straight and is rotated to a certain angle after the deformation, without changing its length and without remaining perpendicular to the deformed middle line. In addition, it is accepted that the free rotation ω_2 is a constant function along the coordinate z . As a result following linear law for displacements and free rotation will be obtained along the thickness of the middle plane of the circular bar:

$$V_1 = u(\varphi) + z\psi(\varphi), \quad V_2 = w(\varphi), \quad \omega_3 = \Omega_3(\varphi), \quad (2.1)$$

where $u(\varphi)$ and $w(\varphi)$ are displacements of points of the middle line in directions of its tangent and normal (i.e. $w(\varphi)$ is deflection of the bar); $\psi(\varphi)$ is the angle of rotation of initially normal element; $\Omega_3(\varphi)$ is the free rotation of this element points. As in the paper [6-11], the kinematic hypothesis (2.1) in general is called Timoshenko's generalized hypothesis in the case of micropolar thin bar (in this case, for the circular thin bar).

2. The hypothesis of the circular bar thin-wallness, where the approximate equality (1.8) is accepted, and as well as,

$$\frac{1}{r} = \frac{1}{r_0 + z} = \frac{1}{r_0(1 + \frac{z}{r_0})} \doteq \frac{1}{r_0}. \quad (2.2)$$

3. Assumptions about smallness of the normal stress σ_{22} , compared with the normal stress σ_{11} in the first equation of Hooke's law ((1.2)₁).

4. During the determination of the deformations, bending-torsions, force and moment stresses, it is accepted

$$\sigma_{21} = \sigma_{21}^0(\varphi). \quad (2.3)$$

After the determination of the mentioned quantities the formula for σ_{21} will be corrected in the following way. The second equilibrium equation from (1.1) ((1.1)₂) is integrated by z and during the determination of the constant of integration (functions from φ), it will be required that the integral from $-h$ to h of the obtained expression is equal to zero. After this specified integration the obtained final expression will be added to the formula (2.3).

In accordance with the accepted law (2.1) of distribution of displacements and rotation, substituting them into formulas (1.3), following expressions will be obtained for deformations and bending-torsions:

$$\begin{aligned} \gamma_{11} &= \left(\frac{1}{r_0} \frac{du}{d\varphi} + \frac{1}{r_0} w \right) + z \frac{1}{r_0} \frac{d\psi}{d\varphi}, \quad \gamma_{22} = 0, \quad \gamma_{12} = \frac{1}{r_0} \frac{dw}{d\varphi} - \frac{1}{r_0} u - \Omega_3, \\ \gamma_{21} &= \psi + \Omega_3, \quad \chi_{13} = \frac{1}{r_0} \frac{d\Omega_3}{d\varphi}, \quad \chi_{23} = 0 \end{aligned} \quad (2.4)$$

Following notations are accepted:

$$\begin{aligned} \Gamma_{11} &= \frac{1}{r_0} \frac{du}{d\varphi} + \frac{1}{r_0} w, \quad \Gamma_{12} = \frac{1}{r_0} \frac{dw}{d\varphi} - \frac{1}{r_0} u - \Omega_3, \quad \Gamma_{21} = \psi + \Omega_3 \\ K_{11} &= \frac{1}{r_0} \frac{d\psi}{d\varphi}, \quad k_{13} = \frac{1}{r_0} \frac{d\Omega_3}{d\varphi}, \end{aligned} \quad (2.5)$$

Then for deformations, bending-torsions will be obtained following formulas:

$$\gamma_{11} = \Gamma_{11} + zK_{11}, \quad \gamma_{22} = 0, \quad \gamma_{12} = \Gamma_{12}, \quad \gamma_{21} = \Gamma_{21}, \quad \chi_{13} = k_{13}, \quad \chi_{23} = 0. \quad (2.6)$$

Here Γ_{11} is the relative longitudinal deformation of the middle line; K_{11} is the change of middle line curvature (from the force stresses); Γ_{12}, Γ_{21} are shift deformations; k_{13} is the change of curvature of the middle line (from the moment stresses).

Using the hypothesis 3) and formula (2.6)₁, following expression will be obtained for the stress σ_{11} from the formula (1.2)₁:

$$\sigma_{11} = \sigma_{11}^0(\varphi) + z\sigma_{11}^1(\varphi), \quad (2.7)$$

where

$$\sigma_{11}^0(\varphi) = E\Gamma_{11}, \quad \sigma_{11}^1(\varphi) = EK_{11}. \quad (2.8)$$

The formulas (1.2)₃, (2.4)₃, (2.4)₄ will be used for determination of the power stress σ_{12} :

$$\sigma_{12} = (\mu + \alpha)\Gamma_{12} + (\mu - \alpha)\Gamma_{21}. \quad (2.9)$$

Taking into consideration formulas for σ_{11} ((2.7)), σ_{12} ((2.9)), the second equilibrium equation ((1.1)₂) is considered, which is integrated over r . Based on the thin-wallness of the domain and the boundary conditions from (1.4) for σ_{22} , we will finally obtain:

$$\sigma_{22} = \frac{1}{2}(q_2^+ + q_2^-) - \frac{h^2}{2} \frac{1}{r_0} \sigma_{11}^1 + z \left(\frac{1}{r_0} \sigma_{11}^0 - \frac{1}{r_0} \frac{d\sigma_{12}^0}{d\varphi} \right) + \frac{1}{r_0} \sigma_{11}^1 \frac{z^2}{2}. \quad (2.10)$$

On the basis of formulas (1.2)₅ and taking into account formulas from (2.6) for χ_{13} , following formula will be obtained for the moment stress μ_{13} :

$$\mu_{13} = Bk_{13}. \quad (2.11)$$

The expression for the moment stress μ_{23} will be obtained from the third equilibrium equation ((1.1)₃) by integrating it by r , taking into account formulas (2.11), (2.9) and (2.3):

$$\mu_{23} = \frac{1}{2}(m^+ + m^-) - z \left(\frac{1}{r_0} \frac{d\mu_{13}^0}{d\varphi} + \sigma_{12}^0 - \sigma_{21}^0 \right) \quad (2.12)$$

For determination of the force stress σ_{21} , the hypothesis 4) will be taken into account, then by using the first equilibrium equation ((1.1)₁), as well as the formula (2.3), it will be finally obtained:

$$\sigma_{21} = \sigma_{21}^0(\varphi) + \frac{1}{r_0} \frac{h^2}{6} \frac{d\sigma_{11}^1}{d\varphi} - z \left(\frac{1}{r_0} \frac{d\sigma_{11}^0}{d\varphi} + \frac{1}{r_0} \sigma_{12}^0 \right) - \frac{1}{r_0} \frac{z^2}{2} \frac{d\sigma_{11}^1}{d\varphi} \quad (2.13)$$

4 Forces and moments. Obtainance of the basic system of equations of micropolar elastic circular bar.

In order to bring two-dimensional problem of micropolar theory of elasticity to one-dimensional one, which has already been done for displacements and rotation, deformations and bending-torsions, force and moment stresses, following integral characteristics are introduced in the applied theory of micropolar elastic circular thin bar, which are statistically equivalent to the components of the force and moment stresses: efforts N , Q_1 , Q_2 and moments M_{11} , L_{13} , which are expressed by the following formulas:

$$\begin{aligned} N &= \int_{-h}^h \sigma_{11} dz, \quad Q_1 = \int_{-h}^h \sigma_{12} dz, \quad Q_2 = \int_{-h}^h \sigma_{21} dz, \\ M_{11} &= \int_{-h}^h \sigma_{11} z dz, \quad L_{13} = \int_{-h}^h \mu_{13} dz \end{aligned} \quad (3.1)$$

Now formulas for σ_{21} ((2.13)), σ_{22} ((2.10)) and μ_{23} ((2.12)) will be accepted as basic ones. Satisfying the boundary conditions (1.4) and considering the formula (3.1),

following system of equilibrium equations of the applied model of micropolar elastic circular bar will be obtained:

$$\begin{aligned} \frac{1}{r_0}N - \frac{1}{r_0} \frac{dQ_1}{d\varphi} &= q_2^+ - q_2^-, \quad \frac{1}{r_0}Q_1 + \frac{1}{r_0} \frac{dN}{d\varphi} = -(q_1^+ - q_1^-) \\ Q_2 - \frac{1}{r_0} \frac{dM_{11}}{d\varphi} &= h(q_1^+ + q_1^-), \quad Q_2 - Q_1 - \frac{1}{r_0} \frac{dL_{13}}{d\varphi} = m^+ - m^- \end{aligned} \quad (3.2)$$

Further, with the help of formulas for σ_{11} ((2.7)), σ_{12} ((2.9)), σ_{21} ((2.13)), μ_{13} ((2.11)) elasticity relations will be obtained for this model:

$$N = 2Eh\Gamma_{11}, \quad Q_1 = 2h(\mu + \alpha)\Gamma_{12} + 2h(\mu - \alpha)\Gamma_{21}, \quad Q_2 = 2h(\mu + \alpha)\Gamma_{21} + 2h(\mu - \alpha)\Gamma_{12}.$$

$$M_{11} = \frac{2Eh^3}{3}K_{11}, \quad L_{13} = 2Bhk_{13}. \quad (3.3)$$

Geometric equation (2.5) will be added to the equilibrium equations (3.2) and the elasticity relations (3.3):

$$\begin{aligned} \Gamma_{11} &= \frac{1}{r_0} \frac{du}{d\varphi} + \frac{1}{r_0}w, \quad \Gamma_{12} = \frac{1}{r_0} \frac{dw}{d\varphi} - \frac{1}{r_0}u - \Omega_3, \quad \Gamma_{21} = \psi + \Omega_3 \\ K_{11} &= \frac{1}{r_0} \frac{d\psi}{d\varphi}, \quad k_{13} = \frac{1}{r_0} \frac{d\Omega_3}{d\varphi}, \end{aligned} \quad (3.4)$$

The equilibrium equations (3.2), elasticity relations (3.3) and geometric relations (3.4) represent the system of basic equations of the applied model of micropolar elastic circular bar. The boundary conditions should be added to this system of equations:

I. Conditions of the power and moment load:

$$\begin{aligned} N|_{\varphi=0} &= N' = \int_{-h}^h \sigma'_{11} dz, \quad M_{11}|_{\varphi=0} = M' = \int_{-h}^h \sigma'_{11} z dz; \\ Q_1|_{\varphi=0} &= Q'_1 = \int_{-h}^h \sigma'_{12} dz, \quad L_{13}|_{\varphi=0} = L'_{13} = \int_{-h}^h \mu'_{13} dz; \\ N|_{\varphi=\varphi_1} &= N'' = \int_{-h}^h \sigma''_{11} dz, \quad M_{11}|_{\varphi=\varphi_1} = M'' = \int_{-h}^h \sigma''_{11} z dz; \\ Q_1|_{\varphi=\varphi_1} &= Q''_1 = \int_{-h}^h \sigma''_{12} dz, \quad L_{13}|_{\varphi=\varphi_1} = L''_{13} = \int_{-h}^h \mu''_{13} dz. \end{aligned} \quad (3.5)$$

In particular, from these conditions we will obtain conditions of free edges.

II. Conditions, when the displacements and rotation are set on the edge:

$$\begin{aligned} u|_{\varphi=0} &= u' = \frac{1}{2h} \int_{-h}^h V'_1 dz, \quad \psi|_{\varphi=0} = \psi' = \frac{3}{2h^3} \int_{-h}^h V'_1 z dz; \\ w|_{\varphi=0} &= w' = \frac{1}{2h} \int_{-h}^h V'_2 dz, \quad \Omega_3|_{\varphi=0} = \Omega'_3 = \frac{1}{2h} \int_{-h}^h \omega'_3 dz; \end{aligned}$$

$$\begin{aligned}
 u|_{\varphi=\varphi_1} = u'' &= \frac{1}{2h} \int_{-h}^h V_1'' dz, \quad \psi|_{\varphi=\varphi_1} = \psi'' = \frac{3}{2h^3} \int_{-h}^h V_1'' z dz; \\
 w|_{\varphi=\varphi_1} = w'' &= \frac{1}{2h} \int_{-h}^h V_2'' dz, \quad \Omega_3|_{\varphi=\varphi_1} = \Omega_3'' = \frac{1}{2h} \int_{-h}^h \omega_3'' dz.
 \end{aligned} \tag{3.6}$$

Particularly, conditions of full sealing edges will be obtained from the above mentioned conditions.

III. Hinged supported conditions:

$$\begin{aligned}
 N|_{\varphi=0} = N' &= \int_{-h}^h \sigma'_{11} dz, \quad M_{11}|_{\varphi=0} = M' = \int_{-h}^h \sigma'_{11} z dz; \\
 w|_{\varphi=0} = w' &= \frac{1}{2h} \int_{-h}^h V_2' dz, \quad L_{13}|_{\varphi=0} = L'_{13} = \int_{-h}^h \mu'_{13} dz; \\
 N|_{\varphi=\varphi_1} = N'' &= \int_{-h}^h \sigma''_{11} dz, \quad M_{11}|_{\varphi=\varphi_1} = M'' = \int_{-h}^h \sigma''_{11} z dz; \\
 w|_{\varphi=\varphi_1} = w'' &= \frac{1}{2h} \int_{-h}^h V_2'' dz, \quad L_{13}|_{\varphi=\varphi_1} = L''_{13} = \int_{-h}^h \mu''_{13} dz.
 \end{aligned} \tag{3.7}$$

Mathematical model of micropolar elastic circular thin bar is expressed by the system of equations (3.2)-(3.4) and boundary conditions (3.5) (or (3.6), or (3.7)).

The equation, expressing the law of conservation of mechanical energy in the case of deformation of micropolar circular bar, and corresponding general variation functional are also obtained. On the basis of the latter, finite element method will be developed in future for solving concrete boundary value problems of models (3.2)-(3.7).

It should be noted that if in the model (3.2) - (3.7) of micropolar elastic circular thin bar physical constant $\alpha(\alpha = 0)$ is equated to zero, then we will come to the model [14] of elastic circular thin bar in the classical formulation with consideration of transverse share deformations.

On the basis of the constructed applied model of micropolar elastic circular bar (3.2)-(3.7) some concrete problems of the applied character are considered. With the help of numerical analysis efficiency of micropolar material is established in comparison with classical in terms of stiffness and strength of the bar.

Acknowledgements

This work was supported by the RA MES State Committee of Science, in the frames of the research project No 15T-2C138.

References

- [1] Jilin, P. A., 1982. Basic equations of non-classical theories of elastic shells // Dynamics and Rigidity of Machines. No 386. pp. 29-42. (in Russian)

-
- [2] Palmov, V. A., 1986. The simplest consistent system of equations of theory of thin elastic shells of asymmetric elasticity // Journal of Mechanics of Deformable Bodies. Moscow: Publishing House "Science". pp. 106-112. (in Russian)
- [3] Altenbach, H., Eremeyev, V., 2009. On the linear theory of micropolar plates// Z. Angew. Math. Mech (ZAMM). V. 89. No 4. pp. 242-256.
- [4] Eremeyev, V. A., Zubov, L. M., 2008. Mechanics of elastic shells. M.: Science. p. 280. (in Russian)
- [5] Altenbach, J., Altenbach, H. and Eremeyev, V.A., 2010. On generalized Cosserat-tape theories of plates and shells: a short review and bibliography. Archive of Applied Mechanics, 80(1), pp.73-92.
- [6] Sargsyan, S. H., 2012. Mathematical model of micropolar elastic thin plates and their strength and stiffness characteristics// Journal of Applied Mechanics and Technical Physics. Vol. 53. No 2. pp. 275-282.
- [7] Sargsyan, S. H., 2011. Mathematical models of micropolar elastic thin shells// Advanced Structured Materials. Shell-like Structures. Non-classical Theories and Applications. Springer. Vol. 15. pp. 91-100.
- [8] Sargsyan, S. H., 2011. The general dynamic theory of micropolar elastic thin shells// Doklady Physics, Vol. 56. No 1. pp. 39-42.
- [9] Sargsyan, S. H., 2014. Energy balance equation, energetic theorems and variation equation for the general theory of micropolar elastic isotropic thin shells// International Journal of Mechanics. Vol. 8. pp. 93-100.
- [10] Sargsyan, S. H., 2015. Asymptotically confirmed hypotheses method for the construction of micropolar and classical theories of elastic thin shells // Advances in Pure Mathematics. No 5. pp. 629-642.
- [11] Sargsyan, S. H., 2012. Effective manifestations of characteristics of strength and rigidity of micropolar elastic thin bars// Journal of Materials Science and Engineering. Vol.2. No 1. pp. 98-108.
- [12] Morozov, N. F., 1984. Mathematical issues in theory of cracks. M.: Science. p. 256. (in Russian)
- [13] Nowacki, W., 1986. Theory of asymmetric elasticity. Pergamon Press. Oxford. New York. Toronto. Sydney. Paris. Frankfurt. p. 383.
- [14] Sargsyan, S.H., Khachatryan, M.V.,2016. Mathematical model of elastic plane curve beam (circular) with consideration of shear deformations on the basis of the classical theory of elasticity//Doklady NAS Armenia. V.116. No 1. pp. 34-42 (in Russian)

Samvel H. Sargsyan, Gyumri State Pedagogical Institute, Armenia

Meline V. Khachatryan, Gyumri State Pedagogical Institute, Armenia

Cases of integrability corresponding to the motion of a pendulum in the three-dimensional space

Maxim V. Shamolin
shamolin@rambler.ru, shamolin@imec.msu.ru

Abstract

In this activity, we systematize some results on the study of the equations of spatial motion of dynamically symmetric fixed rigid bodies–pendulums located in a nonconservative force fields. The form of these equations is taken from the dynamics of real fixed rigid bodies placed in a homogeneous flow of a medium. In parallel, we study the problem of a spatial motion of a free rigid body also located in a similar force fields. Herewith, this free rigid body is influenced by a nonconservative tracing force; under action of this force, either the magnitude of the velocity of some characteristic point of the body remains constant, which means that the system possesses a nonintegrable servo constraint, or the center of mass of the body moves rectilinearly and uniformly; this means that there exists a nonconservative couple of forces in the system.

1 Introduction

Earlier (see [1, 2]), the author already proved the complete integrability of the equations of a plane-parallel motion of a fixed rigid body–pendulum in a homogeneous flow of a medium under the jet flow conditions when the system of dynamical equations possesses a first integral, which is a transcendental (in the sense of the theory of functions of a complex variable, i.e., it has essential singularities) function of quasi-velocities. In [1, 2, 3], the planar problem was generalized to the spatial (three-dimensional) case, where the system of dynamical equations has a complete set of transcendental first integrals. It was assumed that the interaction of the homogeneous medium flow with the fixed body (the spherical pendulum) is concentrated on a part of the body surface that has the form of a planar (two-dimensional) disk. In this activity, the results relate to the case where all interaction of the homogeneous flow of a medium with the fixed body is concentrated on that part of the surface of the body, which has the form of a two-dimensional disk, and the action of the force is concentrated in a direction perpendicular to this disk. These results are systematized and are presented in invariant form.

2 Model assumptions

Let consider the homogeneous plane circle disk \mathcal{D} (with the center in the point D), the plane of which perpendicular to the holder OD . The disk is rigidly fixed perpendicular to the tool holder OD located on the spherical hinge O , and it flows about homogeneous fluid flow (Fig. 1). In this case, the body is a physical (spherical) pendulum. The medium flow moves from infinity with constant velocity $\mathbf{v} = \mathbf{v}_\infty \neq \mathbf{0}$. Assume that the holder does not create a resistance.

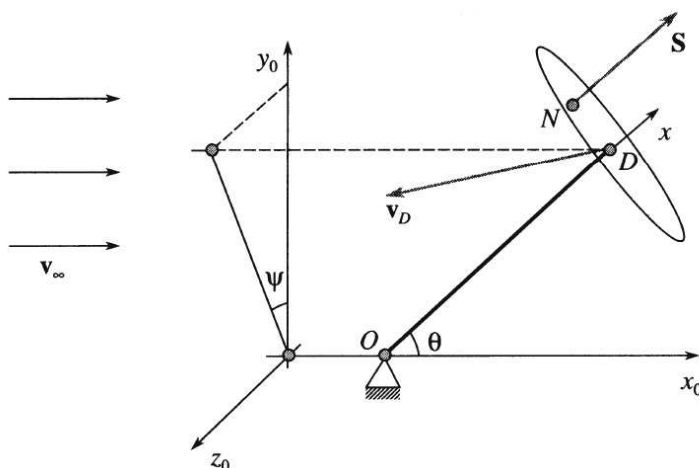


Figure 1: Fixed pendulum on a spherical hinge in the stream running medium

We suppose that the total force \mathbf{S} of medium flow interaction is parallel to the holder, and point N of application of this force is determined by at least the angle of attack α , which is made by the velocity vector \mathbf{v}_D of the point D with respect to the flow and the holder OD (Fig. 1); the total force is also determined by the angle β_1 , which is made in the plane of the disk \mathcal{D} (thus, (ν, α, β_1) are the spherical coordinates of the tip of the vector \mathbf{v}_D), and also the reduced angular velocity $\omega \cong l\Omega/v_D$, $v_D = |\mathbf{v}_D|$ (l is the length of the holder, Ω is the angular velocity of the pendulum). Such conditions arise when one uses the model of streamline flow around spatial bodies. Therefore, the force \mathbf{S} is directed along the normal to the disk to its side, which is opposite to the direction of the velocity \mathbf{v}_D , and passes through a certain point N of the disk such that the velocity vector \mathbf{v}_D and the force of the interaction \mathbf{S} lie in the plane ODN .

The vector $\mathbf{e} = \mathbf{OD}/l$ determines the orientation of the holder. Then $\mathbf{S} = s(\alpha)v_D^2\mathbf{e}$, $s(\alpha) = s_1(\alpha)\text{sign} \cos \alpha$, and the resistance coefficient $s_1 \geq 0$ depends only on the angle of attack α . By the axe-symmetry properties of the body–pendulum with respect to the point D , the function $s(\alpha)$ is even.

Let $Dx_1x_2x_3 = Dxyz$ be the coordinate system rigidly attached to the body, here-with, the axis $Dx = Dx_1$ has a direction vector \mathbf{e} , and the axes $Dx_2 = Dy$ and $Dx_3 = Dz$ lie in the plane of the disk \mathcal{D} (Fig. 1). In the same figure it is shown the angles $\theta = \xi$, $\psi = \eta_1$, i.e., the angles determining the pendulum position on the sphere. In this case, the angle θ is made by the holder and the direction of the over-running medium flow (the axis x_0); and the angle ψ is made by the projection

of the holder to the immovable plane y_0z_0 (which perpendicular to the over-running medium flow) and the axis y_0 (Fig. 1). Obviously, the angles $(\theta, \psi) = (\xi, \eta_1)$ are the spherical coordinates of the point D .

The space of positions of this spherical (physical) pendulum is the two-dimensional sphere

$$\mathbf{S}^2\{(\xi, \eta_1) \in \mathbf{R}^2 : 0 \leq \xi \leq \pi, \eta_1 \bmod 2\pi\}, \quad (1)$$

and its phase space is the tangent bundle of the two-dimensional sphere

$$T_*\mathbf{S}^2\{(\dot{\xi}, \dot{\eta}_1; \xi, \eta_1) \in \mathbf{R}^4 : 0 \leq \xi \leq \pi, \eta_1 \bmod 2\pi\}. \quad (2)$$

To the angular velocity, we put in correspondence $\Omega = \Omega_1\mathbf{e}_1 + \Omega_2\mathbf{e}_2 + \Omega_3\mathbf{e}_3$ ($\mathbf{e}_1, \mathbf{e}_2, \mathbf{e}_3$ the unit vectors of the coordinate system $Dx_1x_2x_3$) the skew-symmetric matrix

$$\tilde{\Omega} = \begin{pmatrix} 0 & -\Omega_3 & \Omega_2 \\ \Omega_3 & 0 & -\Omega_1 \\ -\Omega_2 & \Omega_1 & 0 \end{pmatrix}, \quad \tilde{\Omega} \in \mathfrak{so}(3). \quad (3)$$

The distance from the center D of the disk to the center of pressure (the point N , Fig. 1) has the form $|\mathbf{r}_N| = r_N = DN(\alpha, \beta_1, l\Omega/v_D)$, where $\mathbf{r}_N = \{0, x_{2N}, x_{3N}\} = \{0, y_N, z_N\}$ in system $Dx_1x_2x_3 = Dxyz$ (we omit the wave over Ω).

3 Set of dynamical equations in Lie algebra $\mathfrak{so}(3)$

If $\text{diag}\{I_1, I_2, I_2\}$ is the tensor of inertia of the body-pendulum in the coordinate system $Dx_1x_2x_3$ then the general equation of its motion has the following form:

$$\begin{aligned} I_1\dot{\Omega}_1 &= 0, \\ I_2\dot{\Omega}_2 + (I_1 - I_2)\Omega_1\Omega_3 &= -z_N \left(\alpha, \beta_1, \frac{\Omega}{v_D} \right) s(\alpha)v_D^2, \\ I_2\dot{\Omega}_3 + (I_2 - I_1)\Omega_1\Omega_2 &= y_N \left(\alpha, \beta_1, \frac{\Omega}{v_D} \right) s(\alpha)v_D^2, \end{aligned} \quad (4)$$

since the moment of the medium interaction force is determined by the following auxiliary matrix:

$$\begin{pmatrix} 0 & x_{2N} & x_{3N} \\ -s(\alpha)v_D^2 & 0 & 0 \end{pmatrix},$$

where $\{-s(\alpha)v_D^2, 0, 0\}$ is the decomposition of the medium interaction force \mathbf{S} in the coordinate system $Dx_1x_2x_3$.

Since the dimension of the Lie algebra $\mathfrak{so}(3)$ is equal to 3, the system of equations (4) is a group of dynamical equations on $\mathfrak{so}(3)$, and, simply speaking, the motion equations.

We see, that in the right-hand side of Eq. (4), first of all, it includes the angles α, β_1 , therefore, this system of equations is not closed. In order to obtain a complete system of equations of motion of the pendulum, it is necessary to attach several sets of kinematic equations to the dynamic equation on the Lie algebra $\mathfrak{so}(3)$.

3.1 Cyclic first integral

We immediately note that the system (4), by the existing dynamic symmetry

$$I_2 = I_3, \quad (5)$$

possesses the cyclic first integral

$$\Omega_1 \equiv \Omega_1^0 = \text{const.} \quad (6)$$

In this case, further, we consider the dynamics of our system at zero level:

$$\Omega_1^0 = 0. \quad (7)$$

Under conditions (5)–(7), the system (4) has the form of unclosed system of two equations:

$$I_2 \dot{\Omega}_2 = -z_N \left(\alpha, \beta_1, \frac{\Omega}{v_D} \right) s(\alpha) v_D^2, \quad I_2 \dot{\Omega}_3 = y_N \left(\alpha, \beta_1, \frac{\Omega}{v_D} \right) s(\alpha) v_D^2. \quad (8)$$

4 First set of kinematic equations

In order to obtain a complete system of equations of motion, it needs the set of kinematic equations which relate the velocities of the point D (i.e., the formal center of the disk D) and the over-running medium flow:

$$\mathbf{v}_D = v_D \cdot \mathbf{i}_v(\alpha, \beta_1) = \tilde{\Omega} \begin{pmatrix} l \\ 0 \\ 0 \end{pmatrix} + (-v_\infty) \mathbf{i}_v(-\xi, \eta_1), \quad (9)$$

$$\mathbf{i}_v(\alpha, \beta_1) = \begin{pmatrix} \cos \alpha \\ \sin \alpha \cos \beta_1 \\ \sin \alpha \sin \beta_1 \end{pmatrix}. \quad (10)$$

The equation (9) expresses the theorem of addition of velocities in projections on the related coordinate system $Dx_1x_2x_3$.

Indeed, the left-hand side of Eq. (9) is the velocity of the point D of the pendulum with respect to the flow in the projections on the related with the pendulum coordinate system $Dx_1x_2x_3$. Herewith, the vector $\mathbf{i}_v(\alpha, \beta_1)$ is the unit vector along the axis of the vector \mathbf{v}_D . The vector $\mathbf{i}_v(\alpha, \beta_1)$ has the spherical coordinates $(1, \alpha, \beta_1)$, which determines the decomposition (10).

The right-hand side of the Eq. (9) is the sum of the velocities of the point D when you rotate the pendulum (the first term), and the motion of the flow (the second term). In this case, in the first term, we have the coordinates of the vector $\mathbf{OD} = \{l, 0, 0\}$ in the coordinate system $Dx_1x_2x_3$.

We explain the second term of the right-hand side of Eq. (9) in more detail. We have in it the coordinates of the vector $(-\mathbf{v}_\infty) = \{-v_\infty, 0, 0\}$ in the immovable space. In order to describe it in the projections on the related coordinate system $Dx_1x_2x_3$, we need to make a (reverse) rotation of the pendulum at the angle $(-\xi)$ that is algebraically equivalent to multiplying the value $(-v_\infty)$ on the vector $\mathbf{i}_v(-\xi, \eta_1)$.

Thus, the first set of kinematic equations (9) has the following form in our case:

$$\begin{aligned} v_D \cos \alpha &= -v_\infty \cos \xi, \\ v_D \sin \alpha \cos \beta_1 &= l\Omega_3 + v_\infty \sin \xi \cos \eta_1, \\ v_D \sin \alpha \sin \beta_1 &= -l\Omega_2 + v_\infty \sin \xi \sin \eta_1. \end{aligned} \quad (11)$$

5 Second set of kinematic equations

We also need a set of kinematic equations which relate the angular velocity tensor $\tilde{\Omega}$ and coordinates $\xi, \eta_1, \dot{\xi}, \dot{\eta}_1$ of the phase space (2) of pendulum studied, i.e., the tangent bundle $T_*\mathbf{S}^2\{\xi, \eta_1; \dot{\xi}, \dot{\eta}_1\}$.

We draw the reasoning style allowing arbitrary dimension. The desired equations are obtained from the following two sets of relations. Since the motion of the body takes place in a Euclidean space $\mathbf{E}^n, n = 3$ formally, at the beginning, we express the tuple consisting of a phase variables Ω_2, Ω_3 , through new variable z_1, z_2 (from the tuple z). For this, we draw the following turn by the angle η_1 :

$$\begin{aligned} \begin{pmatrix} \Omega_2 \\ \Omega_3 \end{pmatrix} &= T_{1,2}(\eta_1) \begin{pmatrix} z_1 \\ z_2 \end{pmatrix}, \\ T_{1,2}(\eta_1) &= \begin{pmatrix} \cos \eta_1 & -\sin \eta_1 \\ \sin \eta_1 & \cos \eta_1 \end{pmatrix}. \end{aligned} \quad (12)$$

In other words, the relations

$$\begin{pmatrix} z_1 \\ z_2 \end{pmatrix} = T_{1,2}(-\eta_1) \begin{pmatrix} \Omega_2 \\ \Omega_3 \end{pmatrix} \quad (13)$$

hold, i.e.,

$$z_1 = \Omega_2 \cos \eta_1 + \Omega_3 \sin \eta_1, \quad z_2 = -\Omega_2 \sin \eta_1 + \Omega_3 \cos \eta_1. \quad (14)$$

Then we substitute the following relationship instead of the variable z :

$$z_2 = \dot{\xi}, \quad z_1 = -\dot{\eta}_1 \frac{\sin \xi}{\cos \xi}. \quad (15)$$

Thus, two sets of Eqs. (12) and (15) give the second set of kinematic equations:

$$\Omega_2 = -\dot{\xi} \sin \eta_1 - \dot{\eta}_1 \frac{\sin \xi}{\cos \xi} \cos \eta_1, \quad \Omega_3 = \dot{\xi} \cos \eta_1 - \dot{\eta}_1 \frac{\sin \xi}{\cos \xi} \sin \eta_1. \quad (16)$$

We see that three sets of the relations (8), (11), and (16) form the closed system of equations.

These three sets of equations include the following functions:

$$y_N \left(\alpha, \beta_1, \frac{\Omega}{v_D} \right), \quad z_N \left(\alpha, \beta_1, \frac{\Omega}{v_D} \right), \quad s(\alpha). \quad (17)$$

In this case, the function s is considered to be dependent only on α , and the functions y_N, z_N may depend on, along with the angles α, β_1 , generally speaking, the reduced angular velocity $\omega \cong l\Omega/v_D$.

6 Problem on free body motion under assumption of tracing force

Parallel to the present problem of the motion of the fixed body, we study the spatial motion of the free axially symmetric rigid body with the frontal plane butt-end (the circle disk \mathcal{D}) in the resistance force fields under the quasi-stationarity conditions with the same model of medium interaction.

If (v, α, β_1) are the spherical coordinates of the velocity vector of the center D of disk \mathcal{D} lying on the axis of symmetry of a body, $\Omega = \{\Omega_1, \Omega_2, \Omega_3\}$ are the projections of its angular velocity on the axes of the coordinate system $Dx_1x_2x_3$ related to the body (in this case, the axis of symmetry CD coincides with the axis $Dx_1 = Dx$, C is the center of mass), and the axes $Dx_2 = Dy$ and $Dx_3 = Dz$ lie in the hyperplane of the disk; $I_1, I_2, I_3 = I_2, m$ are characteristics of inertia and mass, then the dynamical part of the equations of motion in which the tangent forces of the interaction of the body with the medium are absent, has the form

$$\begin{aligned} \dot{v} \cos \alpha - \dot{\alpha} v \sin \alpha + \Omega_2 v \sin \alpha \sin \beta_1 - \Omega_3 v \sin \alpha \cos \beta_1 + \sigma(\Omega_2^2 + \Omega_3^2) &= \frac{F_x}{m}, \\ \dot{v} \sin \alpha \cos \beta_1 + \dot{\alpha} v \cos \alpha \cos \beta_1 - \dot{\beta}_1 v \sin \alpha \sin \beta_1 + \Omega_3 v \cos \alpha - \\ - \Omega_1 v \sin \alpha \sin \beta_1 - \sigma \Omega_1 \Omega_2 - \sigma \dot{\Omega}_3 &= 0, \\ \dot{v} \sin \alpha \sin \beta_1 + \dot{\alpha} v \cos \alpha \sin \beta_1 + \dot{\beta}_1 v \sin \alpha \cos \beta_1 + \Omega_1 v \sin \alpha \cos \beta_1 - \\ - \Omega_2 v \cos \alpha - \sigma \Omega_1 \Omega_3 + \sigma \dot{\Omega}_2 &= 0, \\ I_1 \dot{\Omega}_1 &= 0, \\ I_2 \dot{\Omega}_2 + (I_1 - I_2) \Omega_1 \Omega_3 &= -z_N \left(\alpha, \beta_1, \frac{\Omega}{v} \right) s(\alpha) v^2, \\ I_2 \dot{\Omega}_3 + (I_2 - I_1) \Omega_1 \Omega_2 &= y_N \left(\alpha, \beta_1, \frac{\Omega}{v} \right) s(\alpha) v^2, \end{aligned} \quad (18)$$

$F_x = -S$, $S = s(\alpha)v^2$, $\sigma = CD$, in this case

$$\left(0, y_N \left(\alpha, \beta_1, \frac{\Omega}{v} \right), z_N \left(\alpha, \beta_1, \frac{\Omega}{v} \right) \right)$$

are the coordinates of the point N of application of the force \mathbf{S} in the coordinate system $Dx_1x_2x_3 = Dxyz$ related to the body.

The first part of three equations of the system (18) describe the motion of the center of a mass in the three-dimensional Euclidean space \mathbf{E}^3 in the projections on the coordinate system $Dx_1x_2x_3$. And the second part of three equation of the system (18) is obtained from the theorem on the change of the angular moment of a rigid body in the König axis.

Thus, the direct product $\mathbf{R}^1 \times \mathbf{S}^2 \times \text{so}(3)$ of the three-dimensional manifold and the Lie algebra $\text{so}(3)$ is the phase space of sixth-order system (18) of the dynamical equations. Herewith, since the medium influence force dos not depend on the position of the body in a plane, the system (18) of the dynamical equations *is separated from the system of kinematic equations* and may be studied independently.

6.1 Cyclic first integral

We immediately note that the system (18), by the existing dynamic symmetry

$$I_2 = I_3, \tag{19}$$

possesses the cyclic first integral

$$\Omega_1 \equiv \Omega_1^0 = \text{const.} \tag{20}$$

In this case, further, we consider the dynamics of our system at zero level:

$$\Omega_1^0 = 0. \tag{21}$$

6.2 Nonintegrable constraint

If we consider *a more general problem* on the motion of a body under the action of a certain tracing force \mathbf{T} passing through the center of mass and providing the fulfillment of the equality

$$v \equiv \text{const}, \tag{22}$$

during the motion, then F_x in system (18) must be replaced by

$$T - s(\alpha)v^2. \tag{23}$$

As a result of an appropriate choice of the magnitude T of the tracing force, we can achieve the fulfillment of Eq. (22) during the motion. Indeed, if we formally express the value T by virtue of system (18), we obtain (for $\cos \alpha \neq 0$):

$$T = T_v(\alpha, \beta_1, \Omega) = m\sigma(\Omega_2^2 + \Omega_3^2) + s(\alpha)v^2 \left[1 - \frac{m\sigma \sin \alpha}{I_2 \cos \alpha} \left[z_N \left(\alpha, \beta_1, \frac{\Omega}{v} \right) \sin \beta_1 + y_N \left(\alpha, \beta_1, \frac{\Omega}{v} \right) \cos \beta_1 \right] \right]. \tag{24}$$

This procedure can be viewed from two standpoints. First, a transformation of the system has occurred at the presence of the tracing (control) force in the system which provides the corresponding class of motions (22). Second, we can consider this procedure as a procedure that allows one to reduce the order of the system. Indeed, system (18) generates an independent fourth-order system of the following form:

$$\begin{aligned} \dot{\alpha}v \cos \alpha \cos \beta_1 - \dot{\beta}_1 v \sin \alpha \sin \beta_1 + \Omega_3 v \cos \alpha - \sigma \dot{\Omega}_3 &= 0, \\ \dot{\alpha}v \cos \alpha \sin \beta_1 + \dot{\beta}_1 v \sin \alpha \cos \beta_1 - \Omega_2 v \cos \alpha + \sigma \dot{\Omega}_2 &= 0, \\ I_2 \dot{\Omega}_2 &= -z_N \left(\alpha, \beta_1, \frac{\Omega}{v} \right) s(\alpha)v^2, \\ I_2 \dot{\Omega}_3 &= y_N \left(\alpha, \beta_1, \frac{\Omega}{v} \right) s(\alpha)v^2, \end{aligned} \tag{25}$$

where the parameter v is supplemented by the constant parameters specified above.

The system (25) is equivalent to the system

$$\begin{aligned}
 \dot{\alpha} v \cos \alpha + v \cos \alpha [\Omega_3 \cos \beta_1 - \Omega_2 \sin \beta_1] + \sigma [-\dot{\Omega}_3 \cos \beta_1 + \dot{\Omega}_2 \sin \beta_1] &= 0, \\
 \dot{\beta}_1 v \sin \alpha - v \cos \alpha [\Omega_2 \cos \beta_1 + \Omega_3 \sin \beta_1] + \sigma [\dot{\Omega}_2 \cos \beta_1 + \dot{\Omega}_3 \sin \beta_1] &= 0, \\
 \dot{\Omega}_2 &= -\frac{v^2}{I_2} z_N \left(\alpha, \beta_1, \frac{\Omega}{v} \right) s(\alpha), \\
 \dot{\Omega}_3 &= \frac{v^2}{I_2} y_N \left(\alpha, \beta_1, \frac{\Omega}{v} \right) s(\alpha).
 \end{aligned} \tag{26}$$

We introduce new quasi-velocities in our system:

$$\begin{aligned}
 \begin{pmatrix} \Omega_2 \\ \Omega_3 \end{pmatrix} &= T_{1,2}(\beta_1) \begin{pmatrix} z_1 \\ z_2 \end{pmatrix}, \\
 T_{1,2}(\beta_1) &= \begin{pmatrix} \cos \beta_1 & -\sin \beta_1 \\ \sin \beta_1 & \cos \beta_1 \end{pmatrix}.
 \end{aligned} \tag{27}$$

In other words, the following relations

$$\begin{pmatrix} z_1 \\ z_2 \end{pmatrix} = T_{1,2}(-\beta_1) \begin{pmatrix} \Omega_2 \\ \Omega_3 \end{pmatrix} \tag{28}$$

hold, i.e.,

$$z_1 = \Omega_2 \cos \beta_1 + \Omega_3 \sin \beta_1, \quad z_2 = -\Omega_2 \sin \beta_1 + \Omega_3 \cos \beta_1. \tag{29}$$

We can see from (26) that the system cannot be solved uniquely with respect to $\dot{\alpha}$, $\dot{\beta}_1$ on the manifold

$$O = \left\{ (\alpha, \beta_1, \Omega_2, \Omega_3) \in \mathbf{R}^4 : \alpha = \frac{\pi}{2}k, k \in \mathbf{Z} \right\}. \tag{30}$$

Thus, formally speaking, the uniqueness theorem is violated on manifold (30). Moreover, the indefiniteness occurs for even k because of the degeneration of the spherical coordinates (v, α, β_1) , and an obvious violation of the uniqueness theorem for odd k occurs since the first equation of (26) is degenerate for this case.

This implies that system (25) outside of the manifold (30) (and only outside it) is equivalent to the following system:

$$\begin{aligned}
 \dot{\alpha} &= -z_2 + \frac{\sigma v s(\alpha)}{I_2 \cos \alpha} \left[z_N \left(\alpha, \beta_1, \frac{\Omega}{v} \right) \sin \beta_1 + y_N \left(\alpha, \beta_1, \frac{\Omega}{v} \right) \cos \beta_1 \right], \\
 \dot{z}_2 &= \frac{v^2}{I_2} s(\alpha) \left[z_N \left(\alpha, \beta_1, \frac{\Omega}{v} \right) \sin \beta_1 + y_N \left(\alpha, \beta_1, \frac{\Omega}{v} \right) \cos \beta_1 \right] - \\
 &- z_1^2 \frac{\cos \alpha}{\sin \alpha} - \frac{\sigma v s(\alpha)}{I_2 \sin \alpha} z_1 \left[z_N \left(\alpha, \beta_1, \frac{\Omega}{v} \right) \cos \beta_1 - y_N \left(\alpha, \beta_1, \frac{\Omega}{v} \right) \sin \beta_1 \right], \\
 \dot{z}_1 &= z_1 z_2 \frac{\cos \alpha}{\sin \alpha} + \left[-\frac{v^2}{I_2} s(\alpha) + \frac{\sigma v s(\alpha)}{I_2 \sin \alpha} z_2 \right] \times \\
 &\times \left[z_N \left(\alpha, \beta_1, \frac{\Omega}{v} \right) \cos \beta_1 - y_N \left(\alpha, \beta_1, \frac{\Omega}{v} \right) \sin \beta_1 \right], \\
 \dot{\beta}_1 &= z_1 \frac{\cos \alpha}{\sin \alpha} + \frac{\sigma v s(\alpha)}{I_2 \sin \alpha} \left[z_N \left(\alpha, \beta_1, \frac{\Omega}{v} \right) \cos \beta_1 - y_N \left(\alpha, \beta_1, \frac{\Omega}{v} \right) \sin \beta_1 \right].
 \end{aligned} \tag{31}$$

6.3 Constant velocity of the center of mass

If we consider *a more general problem* on the motion of a body under the action of a certain tracing force \mathbf{T} passing through the center of mass and providing the fulfillment of the equality

$$\mathbf{V}_C \equiv \text{const} \quad (32)$$

during the motion (\mathbf{V}_C is the velocity of the center of mass), then F_x in system (18) must be replaced by zero since the nonconservative couple of the forces acts on the body: $T - s(\alpha)v^2 \equiv 0$.

Obviously, we must choose the value of the tracing force T as follows:

$$T = T_v(\alpha, \beta_1, \Omega) = s(\alpha)v^2, \quad \mathbf{T} \equiv -\mathbf{S}. \quad (33)$$

The choice (33) of the magnitude of the tracing force T is a particular case of the possibility of separation of an independent fourth-order subsystem after a certain transformation of the system (18).

Indeed, let the following condition hold for T :

$$T = T_v(\alpha, \beta_1, \Omega) = \sum_{i,j=0, i \leq j}^3 \tau_{i,j} \left(\alpha, \beta_1, \frac{\Omega}{v} \right) \Omega_i \Omega_j = T_1 \left(\alpha, \beta_1, \frac{\Omega}{v} \right) v^2, \quad \Omega_0 = v. \quad (34)$$

At the beginning, we introduce new quasi-velocities (27)–(29).

We rewrite the system (18) for the cases (19)–(21) in the form

$$\begin{aligned} & \dot{v} + \sigma(z_1^2 + z_2^2) \cos \alpha - \\ & - \sigma \frac{v^2}{I_2} s(\alpha) \sin \alpha \left[y_N \left(\alpha, \beta_1, \frac{\Omega}{v} \right) \cos \beta_1 + z_N \left(\alpha, \beta_1, \frac{\Omega}{v} \right) \sin \beta_1 \right] = \\ & = \frac{T_1 \left(\alpha, \beta_1, \frac{\Omega}{v} \right) v^2 - s(\alpha)v^2}{m} \cos \alpha, \\ & \dot{\alpha} v + z_2 v - \sigma(z_1^2 + z_2^2) \sin \alpha - \\ & - \sigma \frac{v^2}{I_2} s(\alpha) \cos \alpha \left[y_N \left(\alpha, \beta_1, \frac{\Omega}{v} \right) \cos \beta_1 + z_N \left(\alpha, \beta_1, \frac{\Omega}{v} \right) \sin \beta_1 \right] = \\ & = \frac{s(\alpha)v^2 - T_1 \left(\alpha, \beta_1, \frac{\Omega}{v} \right) v^2}{m} \sin \alpha, \\ & \dot{\Omega}_3 = \frac{v^2}{I_2} y_N \left(\alpha, \beta_1, \frac{\Omega}{v} \right) s(\alpha), \\ & \dot{\Omega}_2 = -\frac{v^2}{I_2} z_N \left(\alpha, \beta_1, \frac{\Omega}{v} \right) s(\alpha), \\ & \dot{\beta}_1 \sin \alpha - z_1 \cos \alpha - \\ & - \frac{\sigma v}{I_2} s(\alpha) \left[z_N \left(\alpha, \beta_1, \frac{\Omega}{v} \right) \cos \beta_1 - y_N \left(\alpha, \beta_1, \frac{\Omega}{v} \right) \sin \beta_1 \right] = 0. \end{aligned} \quad (35)$$

If we introduce the new dimensionless phase variables and the differentiation by the formulas $z_k = n_1 v Z_k$, $k = 1, 2$, $\langle \cdot \rangle = n_1 v \langle' \rangle$, $n_1 > 0$, $n_1 = \text{const}$, system (35) has the following form:

$$v' = v \Psi(\alpha, \beta_1, Z_1, Z_2), \quad (36)$$

$$\begin{aligned} \alpha' = & -Z_2 + \sigma n_1 (Z_1^2 + Z_2^2) \sin \alpha + \\ & + \frac{\sigma}{I_2 n_1} s(\alpha) \cos \alpha [y_N(\alpha, \beta_1, n_1 Z) \cos \beta_1 + z_N(\alpha, \beta_1, n_1 Z) \sin \beta_1] - \\ & - \frac{T_1(\alpha, \beta_1, n_1 Z) - s(\alpha)}{m n_1} \sin \alpha, \end{aligned} \quad (37)$$

$$\begin{aligned} Z_2' = & \frac{s(\alpha)}{I_2 n_1^2} [1 - \sigma n_1 Z_2 \sin \alpha] [y_N(\alpha, \beta_1, n_1 Z) \cos \beta_1 + z_N(\alpha, \beta_1, n_1 Z) \sin \beta_1] - \\ & - \frac{\sigma}{I_2 n_1} Z_1 \frac{s(\alpha)}{\sin \alpha} [z_N(\alpha, \beta_1, n_1 Z) \cos \beta_1 - y_N(\alpha, \beta_1, n_1 Z) \sin \beta_1] - \\ & - Z_1^2 \frac{\cos \alpha}{\sin \alpha} + \sigma n_1 Z_2 (Z_1^2 + Z_2^2) \cos \alpha - Z_2 \frac{T_1(\alpha, \beta_1, n_1 Z) - s(\alpha)}{m n_1} \cos \alpha, \end{aligned} \quad (38)$$

$$\begin{aligned} Z_1' = & \frac{1}{I_2 n_1^2} \frac{s(\alpha)}{\sin \alpha} [\sigma n_1 Z_2 \sin \alpha - 1] [z_N(\alpha, \beta_1, n_1 Z) \cos \beta_1 - y_N(\alpha, \beta_1, n_1 Z) \sin \beta_1] - \\ & - \frac{\sigma}{I_2 n_1} Z_1 s(\alpha) \sin \alpha [z_N(\alpha, \beta_1, n_1 Z) \sin \beta_1 + y_N(\alpha, \beta_1, n_1 Z) \cos \beta_1] + \\ & + Z_1 Z_2 \frac{\cos \alpha}{\sin \alpha} + \sigma n_1 Z_1 (Z_1^2 + Z_2^2) \cos \alpha - Z_1 \frac{T_1(\alpha, \beta_1, n_1 Z) - s(\alpha)}{m n_1} \cos \alpha, \end{aligned} \quad (39)$$

$$\beta_1' = Z_1 \frac{\cos \alpha}{\sin \alpha} + \frac{\sigma}{I_2 n_1} \frac{s(\alpha)}{\sin \alpha} [z_N(\alpha, \beta_1, n_1 Z) \cos \beta_1 - y_N(\alpha, \beta_1, n_1 Z) \sin \beta_1], \quad (40)$$

$$\begin{aligned} \Psi(\alpha, \beta_1, Z_1, Z_2) = & -\sigma n_1 (Z_1^2 + Z_2^2) \cos \alpha + \\ & + \frac{\sigma}{I_2 n_1} s(\alpha) \sin \alpha [y_N(\alpha, \beta_1, n_1 Z) \cos \beta_1 + z_N(\alpha, \beta_1, n_1 Z) \sin \beta_1] + \\ & + \frac{T_1(\alpha, \beta_1, n_1 Z) - s(\alpha)}{m n_1} \cos \alpha. \end{aligned}$$

We see that the independent fourth-order subsystem (37)–(40) can be substituted into the fifth-order system (36)–(40) and can be considered separately on its own four-dimensional phase space.

7 Case where the moment of nonconservative forces is independent of the angular velocity

We take the function \mathbf{r}_N as follows (the disk \mathcal{D} is given by the equation $x_{1N} \equiv 0$):

$$\mathbf{r}_N = R(\alpha) \mathbf{i}_N, \quad (41)$$

where $\mathbf{i}_N = \mathbf{i}_v(\pi/2, \beta_1)$ (see (10)).

Thus, the equalities $x_{2N} = R(\alpha) \cos \beta_1$, $x_{3N} = R(\alpha) \sin \beta_1$ hold and show that for the considered system, the moment of the nonconservative forces is independent of the angular velocity (it depends only on the angles α, β_1).

And so, for the construction of the force field, we use the pair of dynamical functions $R(\alpha), s(\alpha)$; the information about them is of a qualitative nature. Similarly to the choice of the Chaplygin analytical functions, we take the dynamical functions s and R as follows:

$$R(\alpha) = A \sin \alpha, \quad s(\alpha) = B \cos \alpha, \quad A, B > 0. \quad (42)$$

Theorem 7.1. *The simultaneous equations (4), (11), (16), under conditions (5)–(7), (41), (42) can be reduced to the dynamical system on the tangent bundle (2) of the two-dimensional sphere (1).*

Indeed, if we introduce the dimensionless parameter and the differentiation by the formulas $b_* = ln_0, n_0^2 = AB/I_2, \langle \cdot \rangle = n_0 v_\infty \langle ' \rangle$, then the obtained equations have the following form:

$$\begin{aligned} \xi'' + b_* \xi' \cos \xi + \sin \xi \cos \xi - \eta_1'^2 \frac{\sin \xi}{\cos \xi} &= 0, \\ \eta_1'' + b_* \eta_1' \cos \xi + \xi' \eta_1' \frac{1 + \cos^2 \xi}{\cos \xi \sin \xi} &= 0, \quad b_* > 0. \end{aligned} \quad (43)$$

The phase pattern of the system (43) ($\xi \leftrightarrow \theta, \eta_1 \leftrightarrow \psi$) is shown in Fig. 2.

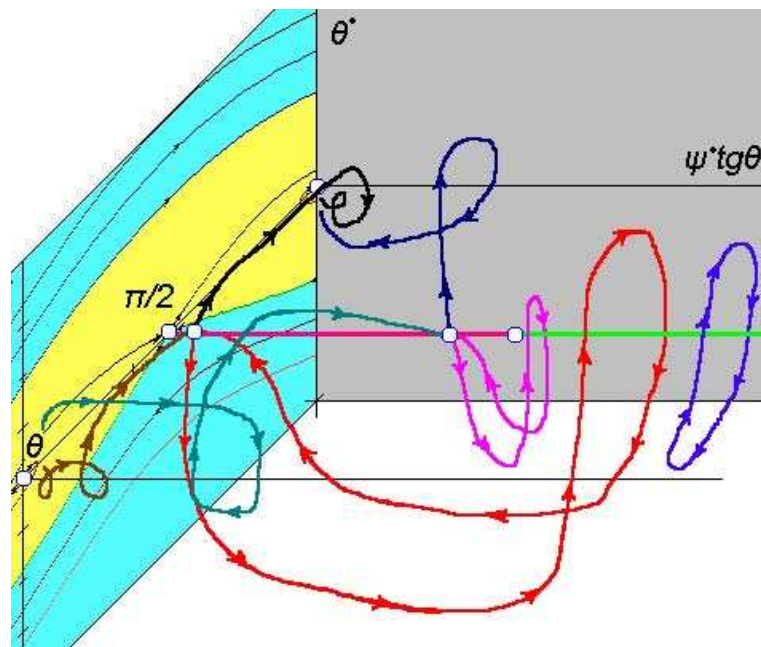


Figure 2: Phase pattern of the fixed pendulum on a spherical hinge situated in the medium flow

Theorem 7.2. *Three sets of relations (4), (11), (16) under conditions (5)–(7), (41), (42) possess three the first integrals (the complete set), which are the transcendental function (in the sense of complex analysis) and are expressed as a finite combination of elementary functions.*

We have the following topological and mechanical analogies in the sense explained above. (1) A motion of a fixed physical pendulum on a spherical hinge in a flowing medium (nonconservative force fields). (2) A spatial free motion of a rigid body in a nonconservative force field under a tracing force (in the presence of a nonintegrable constraint). (3) A spatial composite motion of a rigid body rotating about its center of mass, which moves rectilinearly and uniformly, in a nonconservative force field. On more general topological analogues, see also [4, 5, 6, 7, 8, 9].

Acknowledgements

This work was supported by the Russian Foundation for Basic Research, project no. 15-01-00848-a.

References

- [1] M. V. Shamolin, “Variety of Integrable Cases in Dynamics of Low- and Multi-Dimensional Rigid Bodies in Nonconservative Force Fields”, *Journal of Mathematical Sciences*, 204:4 (2015), 379–530.
- [2] M. V. Shamolin, “Dynamical Pendulum-Like Nonconservative Systems”, *Applied Non-Linear Dynamical Systems*, Springer Proceedings in Mathematics and Statistics, Vol. 93 (2014), 503–525.
- [3] M. V. Shamolin, “New Case of Integrability in the Dynamics of a Multidimensional Solid in a Nonconservative Field”, *Doklady Physics*, 58:11 (2013), 496–499.
- [4] M. V. Shamolin, “New case of integrability of dynamic equations on the tangent bundle of a 3-sphere”, *Russian Math. Surveys*, 68:5 (2013), 963–965.
- [5] M. V. Shamolin, “A New Case of Integrability in the Dynamics of a Multidimensional Solid in a Nonconservative Field under the Assumption of Linear Damping”, *Doklady Physics*, 59:8 (2014), 375–378.
- [6] M. V. Shamolin, “A Multidimensional Pendulum in a Nonconservative Force Field”, *Doklady Physics*, 60:1 (2015), 34–38.
- [7] M. V. Shamolin, “Classification of Integrable Cases in the Dynamics of a Four-Dimensional Rigid Body in a Nonconservative Field in the Presence of a Tracking Force”, *Journal of Mathematical Sciences*, 204:6 (2015), 808–870.
- [8] V. V. Trofimov, “Euler equations on Borel subalgebras of semisimple Lie algebras,” *Izv. Akad. Nauk SSSR, Ser. Mat.*, **43**, No. 3 (1979), 714–732.

REFERENCES

- [9] V. V. Trofimov, “Finite-dimensional representations of Lie algebras and completely integrable systems,” *Mat. Sb.*, **111**, No. 4 (1980), 610–621.

Maxim V. Shamolin, Lomonosov Moscow State University, Russian Federation

Features of simulation of the tire under conditions of movement of the car with acceleration

Alexander K. Sokolov, Alexander L. Svistkov, Lyudmila A. Komar,
Vladimir V. Shadrin and Viktor N. Terpugov
aleksandr_sokol@mail.ru

Abstract

The paper reports on a study of the influence of the Mullins softening effect on changes in the stress fields of a rotating car wheel under acceleration and braking conditions. In our opinion, this effect has received little attention in tire industry until recently. We have developed an algorithm to evaluate changes in the stress-strain of the wheel of the acceleration car taking into account the Mullins effect. With the algorithm proposed one can study the softening effect in different points of the tire during the turns of a wheel under acceleration conditions. The results of numerical simulations demonstrate that the softening effect should be taken into account even when developing a simplified model of a car wheel, in which the tire material is considered as isotropic, and the model tire has a simpler geometry than the real tire. It has been found that the deformation of the lateral surface of the tire calculated with the Mullins effect is significantly higher than the deformation obtained in calculations where this effect has been ignored. The degree of softening is evaluated in terms of the Ogden-Roxburgh model.

The purpose of this study is to investigate the influence of the Mullins effect [1-3] on changes in the stress-strain state in the moving wheel in such operating regimes as acceleration and braking. To our knowledge, the Russian tire industry has paid insufficient attention to this effect. It is ignored in many calculations, for instance, the rolling and head-on crash situations are described in [4-5] taking into account the complex structure of a tire, but ignoring the softening effect. Computer modeling of car tire softening is a complex mathematical problem. The material of a tire changes its properties during the first turn of the wheel, and these variations proceed differently at different points of this material. Accordingly, the pattern of strain distribution in the tire also changes. To obtain a stable solution allowing one to consider material softening accumulation in different parts of the tire, we have developed a special algorithm (Fig. 1).

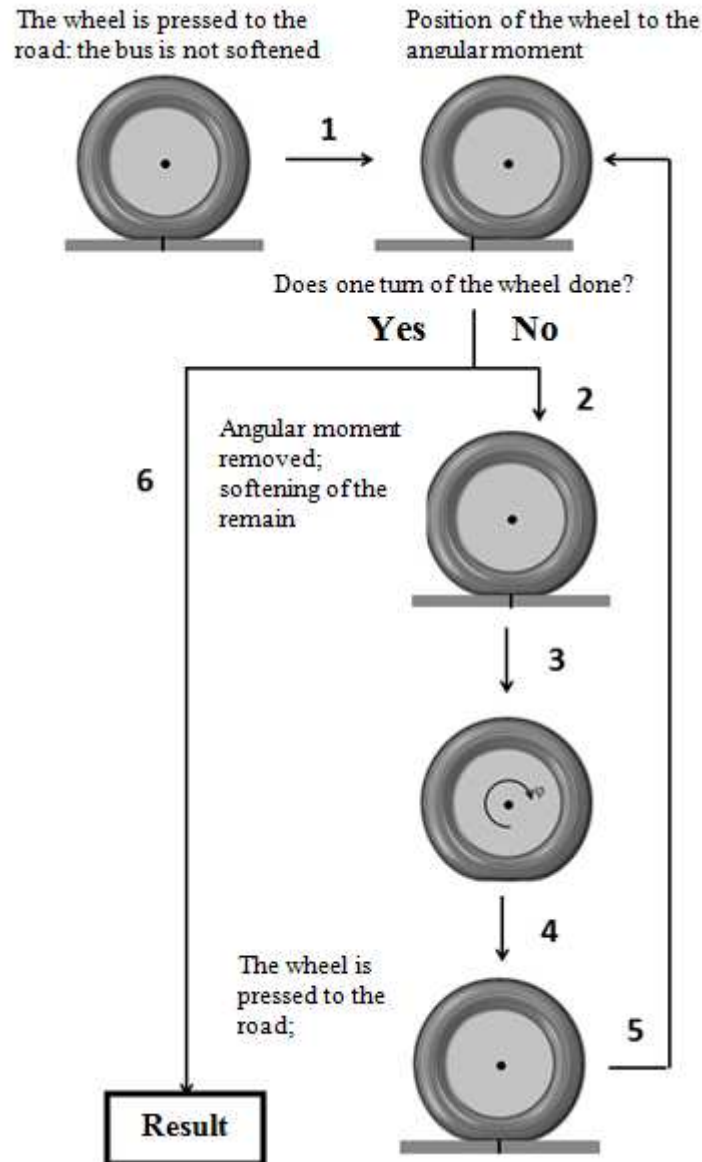


Figure 1: Algorithm for car tire loading

- 1 - road is shifted by the value l , which gives rise to an angular moment in the tire, the tire material softens.
 - 2 - wheel does not make a rotation, the road turns back to its initial state, the angular moment disappears.
 - 3 - road is removed, the wheel rotates to the angle ϕ ;
 - 4 - road is back to normal shape.
 - 5 - if the wheel does not make a full rotation, the road is again shifted by the value l , which gives rise to an angular moment in the tire, the tire material softens;
 - 6 - stress-strain state in the accelerated wheel tire is obtained in the calculation with consideration of the Mullins effect;
- In step 3, the wheel turning angle ϕ is found from the $\phi = \frac{2d}{l}$, where d is the external wheel diameter, l is the road shift
- This algorithm makes it possible to study the softening effect in different points of the tire during the first turn of a wheel under acceleration conditions.

The motion of the car wheel has been modeled for a 3D case. For the characteristics of the tire model, we have chosen a 1600 kg car, which accelerates from 0 to 100 kilometers per hour in 12 seconds. The value of force acting on the car is equal to 3700 H. A horizontal force of 1850 H is applied to the driving wheel. The tire pressure is assumed to be 0.17 MPa. The road is modeled as a rigid rectangular parallelepiped. The tire has the following geometrical characteristics: external diameter - 760 mm; track height - 180 mm; track width - 260 mm (Fig. 2).

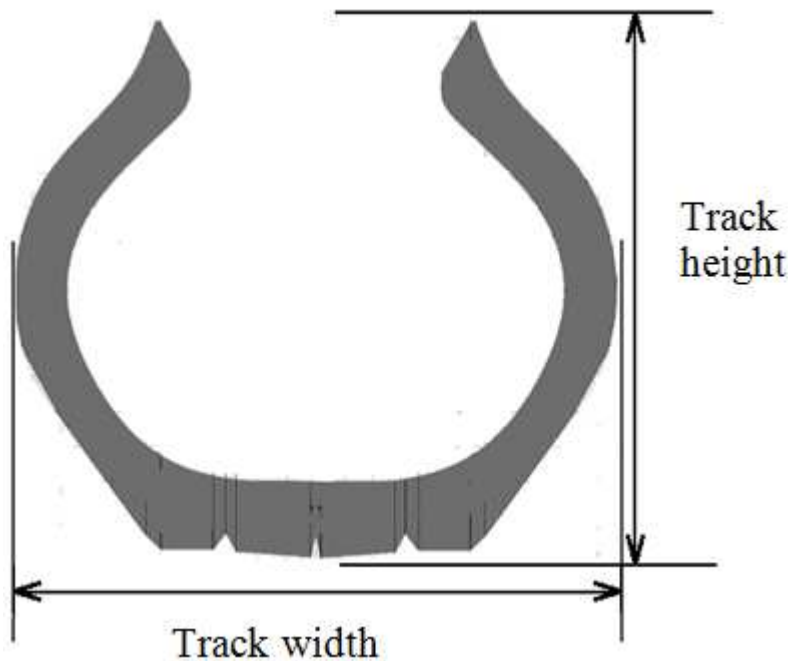


Figure 2: The geometrical characteristics of a car tire

Simulations indicate that the deformation of the lateral surface of the tire calculated with the Mullins effect is significantly higher than the deformation obtained in calculations, where this effect has been ignored (Fig. 3). The hyperelastic fourth-order Ogden model is applied to describe the mechanical properties of an elastomeric matrix of the tire. The degree of softening is evaluated in terms of the Ogden-Roxburgh model [6].

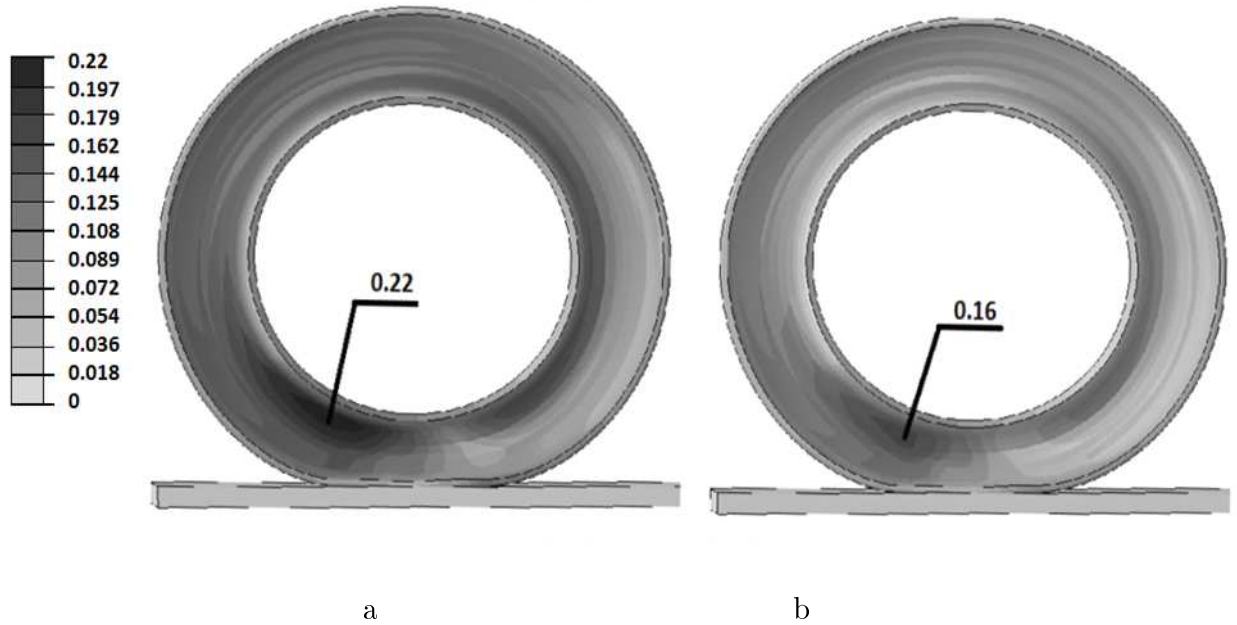


Figure 3: Distribution of the left stretch tensor fields found with (a) and without (b) taking into account the Mullins effect

Conclusions

We have developed an algorithm to evaluate changes in the stress-strain of the wheel of the moving car taking into account the Mullins effect. The results of modeling the behavior of an accelerated car wheel indicate that the distribution of deformations in the tire volume undergoes largest changes. Maximum equivalent Mises deformations have been observed on the tire lateral surface, which, in our opinion, may cause the formation of cracks in the tire. Changes in stress fields have been insignificant because of two opposite mechanisms: on the one hand, deformations increase and, on the other hand, the material softens. It has been found that the stress-strain state should be analyzed in each point of the car wheel diameter taking into account different degrees of the Mullins softening effect. Summing up, the softening effect modeling allows one to accurately predict the serviceable life of tires. In this study we focus on the significance of considering the Mullins effect, which enables the wheel model to be simplified significantly; the anisotropic and viscoelastic properties of an elastomeric matrix are neglected in the model. Our simulations also show that even such a simplified formulation of the problem makes it possible to reveal an essential difference in the stress-strain state obtained in calculations performed with and without consideration of the Mullins effect.

Acknowledgements

The study was supported by RFBR and Perm Ministry of Industry of Innovations and Science (grant 14-08-96013 r_urals_a), and the Complex Program UB RAS 15-10-1-18.

References

- [1] Mullins L., Tobin N.R. Stress softening in rubber vulcanizates. Part I. Use of a strain amplification factor to prescribe the elastic behavior of filler reinforced vulcanized rubber // *J. Appl. Polym. Sci.*, 1965. V. 9. P. 2993–3005.
- [2] Patrikeev G.A. Glava XXII. Tekhnologiya kauchuka i reziny. V kn. *Obshchaya khimicheskaya tekhnologiya* / pod red. S.I. Vol'fkovicha. – M.–L.: Gosudarstvennoe nauchno-tehnicheskoe izdatel'stvo khimicheskoi literatury, 1946. V. 2. P. 361–427.
- [3] Komar D.V., Svistkov A.L., Shadrin V.V. Modeling of hysteresis phenomena under loading rubbers / *Vysokomolek. soed.*, 2003. V. 4. P. 692–696.
- [4] Ryzhov S.A., Il'in K.A., Varjuhin A.N. Proektirovanie shin s ispol'zovaniem programmnoogo kompleksa ABAQUS [Designing tire using a ABAQUS] // *SAPR igrafika.*, 2006. V. 1. P. 77–81.
- [5] Vol'skaja N.S., Levenkov Ja.Ju., Rusanov O.A. Modelirovanie avtomobil'noj pnevmaticheskoy shiny, vzaimodejstvujushhej s tverdoj nerovnoj poverhnost'ju [Simulation tire interacting with the solid support] // *Nauka i Obrazovanie*, 2013. V. 1. P. 107–124.
- [6] Ogden R.W., Roxburgh D.G. A pseudo-elastic model for the Mullins effect in filled rubber // *Proceedings of the Royal Society of London*, 1999. V. 455. P. 2861–2877.

Alexander K. Sokolov, Institute of Continuous Media Mechanics UB RAS, Perm, Russia
Alexander L. Svistkov, Institute of Continuous Media Mechanics UB RAS, Perm, Russia,
State National Research University, Perm, Russia

Lyudmila A. Komar, Institute of Continuous Media Mechanics UB RAS, Perm, Russia
Vladimir V. Shadrin, Institute of Continuous Media Mechanics UB RAS, Perm, Russia,
Perm State National Research University, Perm, Russia
Viktor N. Terpugov, Perm State National Research University, Perm, Russia

On increasing efficiency of hydraulic fracture simulation by using dynamic approach of modified theory

A.D. Stepanov, A.M. Linkov
a.stepanov93@yandex.ru

Abstract

The work aims to make a further step in using the computational advantages of the modified theory for efficient simulation of hydraulic fracturing. The step is made by solving the KGD problem in frames of the dynamic approach in non-normalized coordinates with using hypersingular elasticity operator. It is shown that the obtained system of ODE may be efficiently integrated by employing accelerated Runge-Kutta or Adams methods. The approach developed provides acceptable accuracy for Newtonian and thinning fluids used in practice. We conclude that it may be extended to 3D problems.

1 Introduction

Numerical simulation is an important means to improve understanding and to control hydraulic fracturing (HF), which is widely used for many engineering purposes. They include oil, gas and heat recovery, CO₂ sequestration, waste disposal, excavation of hard rock, preconditioning in mines, etc. Despite numerous studies have been performed during the last four decades (see e. g. reviews in [1], [6], [16]), numerical simulation of truly 3D HF problems still remains "a formidable task" (see [2], p. 147). There is need to "dramatically speed up" simulators (see [1], p. 754). It is a challenge to radically improve HF simulation.

The recent findings [5, 6, 7, 10] suggest a means to meet the challenge. They are summarized in the modified formulation of the HF problem. The analytical and computational advantages of the modified formulation have been demonstrated by obtaining new analytical solutions and very accurate and computationally efficient numerical algorithms for 1D problems (e.g., [6], [8] - [10], [16]). These results confirm that drastic progress may be achieved in numerical simulation of 2D fractures in the 3D space.

Emphasize however that efficient techniques open by the modified formulation for *tracing* a moving fracture front, have not completely overcome the remaining difficulties caused by a) strong non-linearity of the problem, b) non-integrable singularity of the pressure gradient at points of the front, and c) the fact that, for a general 3D

problem, the dependence between the opening and net-pressure involves hypersingular operator. The cited 1D solutions have employed *ad hoc simplifications*, which being available in 1D cases, are unavailable in general 3D problems. Therefore, it is reasonable to re-visit the classical 1D problems for developing tools, which do not employ the *ad hoc* simplifications and may be extended to 3D problems.

The present work aims to make a step in this direction. To the date, except for the paper [5] considering the PKN [12], [13] model, the computational advantages of the modified theory have been confirmed by calculations only when the PKN and KGD [3],[4] problems were solved in coordinates *normalized* by the fracture length. This excluded singularity of the temporal derivative of the opening at the fracture tip. However, such beneficial normalizing is unavailable in 3D problems because, for them, the fracture front is composed of continuum of points. Thus, it is of value to solve the KGD problem in frames of the modified theory in *global* coordinates without using the normalizing. Furthermore, having in mind extensions to 3D problems, it is reasonable to employ *hypersingular* operator, which expresses the pressure via the opening, rather than its *weakly singular* inversion. The inversion, although beneficial when there is an analytical expression for the inverse operator (e.g. [8], [16]), is not available in an analytical form in general.

Summarizing, the objective of the paper is to develop methods, based on the modified formulation, which provide accurate, computationally efficient and stable solution of the KGD problem with two features, which suggest extensions to 3D problems:

- (i) the solution is found in the global rather than normalized coordinates,
- (ii) the solution is obtained by using the direct (hypersingular) rather than inverse (weakly singular) elasticity operator.

The second feature also opens the possibility to employ the *dynamic* approach in time stepping as an alternative to the schemes of the Crank-Nicolson type, which, strictly speaking, require ε -regularization. Below to demonstrate the extended options, we employ the dynamic approach. It consists of complementing the system of ODE, obtained after spatial discretization, with the speed equation, in which its r. h. s. is evaluated by using the universal asymptotic umbrella [7]. We reach the goal by developing numerical schemes, which show high efficiency and which may be promptly extended to 3D problems. The accuracy control is performed by the comparison of the results obtained with the self-similar solution found to the accuracy of four correct significant digits, at least. We focus on the comparison of the key quantities, which are the opening at the inlet and the fracture length. The time range considered covers two decimal orders (in practice, it corresponds to the time growth from first minutes to first hours what is typical for HF treatments). It is also established that the methods developed are applicable for Newtonian, as well as for thinning fluids, used in practice.

2 Problem formulation

We consider the plane KGD problem of HF for the practically important case when the rheology of a fracturing fluid is prescribed by the power-type dependence:

$$\tau = M\dot{\gamma}^n, \tag{1}$$

where τ is the shear stress, $\dot{\gamma}$ is the shear strain rate, M is the consistency index, n is the fluid behavior index. For a Newtonian fluid, $n = 1$; for a perfectly plastic fluid, $n = 0$; for thinning fluids, $0 < n < 1$.

We use the modified formulation of the problem. In contrast with the conventional formulation, it employs the particle velocity v instead of the flux, the speed equation (SE) instead of the global mass balance and the universal asymptotic umbrella to prescribe the r. h. s. of the SE.

The equations for a *fluid* include the *continuity equation*:

$$\frac{\partial w}{\partial t} = -\frac{\partial (wv)}{\partial x} - q_l, \tag{2}$$

and the Poiseuille-type *movement equation*:

$$v = \left[\frac{w^{n+1}}{\mu'} \left(-\frac{\partial p}{\partial x} \right) \right]^{1/n}, \tag{3}$$

where w is the fracture opening, p is the net-pressure, q_l is the term accounting for fluid leak-off into formation, $\mu' = \theta M$, $\theta = 2 \left[\frac{2(2n+1)}{n} \right]^{1/n}$.

We neglect a small lag and consider the physically consistent case when singularity, if it is generated by the leak-off term at the front, is not too strong to distort predominantly in-plane flow within the fracture. Then, as shown in [7], the SE has the form following from the Reynolds transport theorem. Specifically, in the considered case of a power-law fluid, the particle velocity v tends to the propagation speed v_* at the fracture tip $x = x_*$, so that the *speed equation* is:

$$\frac{dx_*}{dt} = v_* = \lim_{x \rightarrow x_*} \left(-\frac{w^{n+1}}{\mu'} \frac{\partial p}{\partial x} \right)^{1/n}. \tag{4}$$

The opening w is not prescribed in advance. For *elastic rocks*, it is defined by the equation of the elasticity theory, connecting the opening and net-pressure. Except for the particular cases of straight and penny-shaped factures, when there exists weakly singular analytical inversion, the explicit form of the equation contains hypersingular integral with density equal to the opening. The net-pressure is proportional (with known factor) to the integral. In the considered 1D problem, taking into account that the problem is symmetric about the origin ($w(-x) = w(x)$, $p(x) = p(-x)$), the *elasticity equation* is:

$$p(x, t) = -\frac{E'}{4\pi} \int_0^{x_*} \left[\frac{1}{(\xi - x)^2} + \frac{1}{(\xi + x)^2} \right] w(\xi, t) d\xi, \quad 0 \leq x \leq x_*, \tag{5}$$

where $E' = \frac{E}{1-\nu^2}$, E is Young's modulus, ν is Poisson's ratio. The density $w(x, t)$ is assumed to belong to the class of functions equal to zero at the fracture tip:

$$w(x_*, t) = 0. \tag{6}$$

The possibility of the fracture propagation is defined by the *fracture criterion* of linear fracture mechanics

$$K_I = K_{IC}, \tag{7}$$

where K_I is the stress intensity factor (SIF), K_{IC} is its critical value. Then equations of the elasticity theory yield for the opening near the tip $x = x_*$:

$$w(x, t) = \sqrt{\frac{32}{\pi} \frac{K_{IC}}{E'}} \sqrt{x_* - x} + O((x_* - x)^\alpha), \tag{8}$$

where $1 \geq \alpha > 1/2$. The exact asymptotic behavior of the opening, pressure and their spatial derivatives near the fracture front is completely defined by the propagation speed [7]. We focus on the viscosity dominated regime, when the major resistance to the fracture propagation is caused by the fluid viscosity μ' rather than fracture toughness K_{IC} . This regime is typical for HF propagation (see, e. g. [14]). For it, fracture toughness may be neglected ($K_{IC} = 0$). Then the first term on the r. h. s. of (8) vanishes and asymptotic dependence of the opening on the propagation speed becomes [7]:

$$w = A_\mu(\alpha) v_*^{1-\alpha} [(x_* - x)^\alpha], \tag{9}$$

where $\alpha = 2/(n + 2)$, $A_\mu(\alpha) = [(1 - \alpha) B(\alpha)]^{-\frac{\alpha}{2}}$, $B(\alpha) = \frac{\alpha}{4} \cot[\pi(1 - \alpha)]$. In view of the asymptotic umbrella (9), the SE (4) becomes

$$\frac{dx_*}{dt} = v_* = [A_\mu(\alpha)]^{-\frac{1}{1-\alpha}} \lim_{x \rightarrow x_*} \left[\frac{w(x)}{(x_* - x)^\alpha} \right]^{\frac{1}{1-\alpha}}. \tag{10}$$

The *boundary conditions* (BC) for the partial differential equations (2) and (3) are as follows. One of them is the condition of zero opening at the front (6). It is satisfied automatically by using the opening in the mentioned class of functions. In particular, accounting for the asymptotics (9) automatically meets the condition of zero opening at the front. The second BC is the condition of the prescribed influx $Q = 2q_0$ at the inlet ($x = 0$). In terms of the particle velocity it is:

$$w(0) v(0+) = q_0. \tag{11}$$

Using the limit $v(0+)$ of the velocity from right accounts for the fact that the velocity is discontinuous at the source point ($v(0+) = -v(0-)$). Consequently, the influx Q_0 is equally distributed between the left and right parts of the fracture, so that $q_0 = Q/2$.

The *initial conditions* (IC) assign the opening $w_0(x)$ and the fracture length x_{*0} at an initial moment t_0 of time:

$$\begin{aligned} w(x, t_0) &= w_0(x) & |x| &\leq x_*(0), \\ x_*(0) &= x_{*0}. \end{aligned} \tag{12}$$

We need to solve equations (2), (3), (5) in the class of functions $w(x, t)$ with the asymptotics (9), under the BC (11), the IC (12) and with the propagation speed dx_*/dt defined by (10).

3 Scaling

We introduce the normalizing opening w_n

$$w_n = \left(t_s \frac{E'}{\mu'} \right)^{\frac{1}{n+2}} \tag{13}$$

to exclude the elasticity E' and viscosity μ' constants from the movement and elasticity equations. The constant t_s in (13) denotes a time-scaling factor, which may be chosen for convenience. Specifically, when the shear strain rate in (1) is measured in the usual unit $1/s$, then taking $t_s = 60^n$ actually transforms the viscosity to time units of minutes. Then the particle velocity, leak-off term, the propagation speed, the influx in the source and the initial time may be specified with time measured in minutes. This is more convenient than tracing a HF propagation with time measured in seconds. In particular, with $t_s = 60^n$, the initial time $t_0 = 1$ corresponds to 1 minute. Accordingly, hundred-fold greater time $t = 100$ corresponds to 100 minutes what has the usual order of HF treatment time. Therefore, in further calculations we may consider the problem when the time changes in the range from first to hundreds units.

The normalized variables are:

$$\begin{aligned} w' &= \frac{w}{w_n} & p' &= \frac{p}{w_n E'} \\ q'_l &= \frac{q_l}{w_n} & w'_0 &= \frac{w_0}{w_n} \\ q'_0 &= \frac{q_0}{w_n}. \end{aligned} \tag{14}$$

In terms of the normalized quantities (14), marked by the primes, the system of equations (2), (3), (5), the SE (10), boundary conditions (6), (11) and initial conditions (12) keep their form with the only difference: now the constants E' and μ' are set unit. From now on to simplify notation, we write the normalized variables omitting primes.

4 Numerical solution by using dynamic approach

In this paper, we employ the pressure explicitly defined via the opening by hyper-singular operator. This suffices applicability of the *dynamic approach* [7], [9], [10].

It consists of reducing the problem to a complete system of ordinary differential equations (ODE) in time.

The complete system is obtained as follows. We start with an interval of the length L , exceeding, for certainty and convenience two-fold, the initial fracture half-length x_{*0} . On the interval, we spatially discretize the r. h. s. of equations (2), (3), (5) by using finite differences for PDE (2) and (3) and appropriate quadrature rules for the hypersingular integral in (5). An approximation of the opening and velocity involves a *fixed number* $M + 1$ values $w_i = w(x_i, t), v_i = v(x_i, t)$ at $M + 1$ points x_i with zero values of the opening and velocity at points *ahead* of the fracture front ($x \geq x_*$). Therefore, the r. h. s. of discretized continuity equation is actually set zero at nodal points ahead of the front. The hypersingular integral (5) provides the nodal values p_i of the pressure *behind* the front expressed via $M + 1$ values of the opening. Then substitution of the found p_i into discretized movement equation (3) gives the nodal values v_i of the particle velocity *behind* the front expressed via w_i . Thus the discretized r. h. s. of continuity equation (2) becomes expressed via the nodal values w_i of the opening. Equating it to the l. h. s. of (2), represented by the time derivatives $\partial w_i / \partial t$, at M nodal points yields M ODE in M unknowns w_i . (There is no sense to include the last $M + 1$ -th point, where the opening and its temporal derivative are always zero, because the interval is doubled when the front reaches this point). Still, the obtained system of ODE is not complete because it contains the unknown half-length $x_*(t)$, which enters through the elasticity equation. The SE gives the needed additional equation. Indeed, the time derivative dx_*/dt is defined via the opening by the SE (10). Hence, by adding the SE to the ODE, obtained from the continuity equation, we arrive at a complete system of $M + 1$ ODE with $M + 1$ unknowns: M nodal openings w_i plus the fracture half-length x_* .

We follow this line by using the same finite differences for spatial derivatives and quadrature rules for hypersingular integral as those used in [9]. However, in contrast with [9], we employ non-normalized spatial coordinates to make possible an extension to 3D problems. It is easy to show that in non-normalized coordinates, the temporal derivative of the opening is singular as $O((x_* - x)^{\alpha-1})$ at the fracture front. As noted in Introduction, this may unfavorably influence the accuracy of numerical results.

As mentioned, we start with an interval of the length L two-fold greater than the initial fracture half-length: $L = 2x_{*0}$. Later on, when the current fracture front $x_*(t)$ reaches end point $x = L$, the length L is doubled and the problem becomes similar to that at the start of calculations.

We use a standard mesh with $M + 1$ nodes on the interval L . The first node is always placed at the origin ($x = 0$). Next nodes are located successively at distances $\Delta x = L/M$ one from another: $x_i = x_{i-1} + \Delta x$ ($i = 2, \dots, M + 1$). The intermediate points are $x_{i-1/2} = x_i - \Delta x/2$, ($i = 2, \dots, M + 1$) and, equivalently, $x_{i+1/2} = x_i + \Delta x/2$ ($i = 1, \dots, M$). The position of the front $x = x_*$ is known on each current time step. It serves to find the number i_* of the node, which being ahead of the front is closest to it. Since the openings and velocities are zero at nodes ahead of the front, we set $w_i = 0, v_i = 0$ for $i = i_*, \dots, M + 1$. The last node with non-zero opening has the number $i_* - 1$.

The nodal values of the pressure behind the front are found by using piece-wise

constant approximation of the opening in the hypersingular integral (5):

$$-\frac{4\pi}{E'}p_i = \sum_{j=1}^{M+1} A_{ij}w_j \quad i = 1, \dots, i_* - 1, \quad (15)$$

where $A_{ij} = \frac{1}{\tau_j - x_i} - \frac{1}{\tau_{j+1} - x_i} + \frac{1}{\tau_j + x_i} - \frac{1}{\tau_{j+1} + x_i}$, with $\tau_1 = 0, \tau_2 = \Delta x/2, \tau_M = x_{M+1} - \Delta x/2, \tau_{M+1} = x_{M+1}$, and $\tau_j = x_{j-1/2}$ for $j = 2, \dots, M - 1$; to avoid dividing by zero, the first collocation point x_1 is taken slightly moved from the origin as $x_1 = 0.0000001\Delta x$. Note that the influence coefficients A_{ij} are inversely proportional to Δx . Hence, they may be evaluated by scaling the coefficients of a standard square matrix A_0 of order $M + 1$, calculated in advance for a particular value of Δx , say, $\Delta x_u = 1/M$. This corresponds to the unit interval of integration. Then for a current $\Delta x = L/M$, the coefficients of A_{ij} are obtained simply by dividing coefficients of the matrix A_0 by L .

The velocities behind the front are evaluated as follows. At the first node, the velocity is:

$$v_1 = (w_1^{n+1} \frac{p_1 - p_2}{\Delta x})^{1/n}.$$

At the point $i_* - 1$ closest to the front, the velocity is calculated by using its known asymptotic behavior:

$$v_{i_*-1} = v_*[1 + a_v(1 - x_{i_*-1}/x_*)],$$

where $a_v = -n/[(n+1)(n+4)]$, and the propagation speed $v_* = dx_*/dt$ is found by using the asymptotic umbrella (10) as

$$\frac{dx_*}{dt} = [A_\mu(\alpha)]^{-\frac{1}{1-\alpha}} \left[\frac{w_{i_*-1}}{(x_* - x_{i_*-1})^\alpha} \right]^{\frac{1}{1-\alpha}}. \quad (16)$$

At other points on the fracture ($i = 2, \dots, i_* - 2$), the velocity is found by using the finite difference equation suggested in [9] to account for strong singularity of the pressure near the front:

$$v_i = \left[w_i^{n+1} \frac{p_{i-1} - p_{i+1}}{\Delta f(x_{i-1}, x_i, x_{i+1})} \right]^{\frac{1}{n}}, \quad (17)$$

where $\Delta f = \frac{(x_* - x_i)^{\alpha(n+1)}}{\alpha(n+1)-1} \left[\frac{1}{(x_* - x_{i+1})^{\alpha(n+1)-1}} - \frac{1}{(x_* - x_{i-1})^{\alpha(n+1)-1}} \right]$. Thus, the openings and velocities become known at each node of the fixed mesh. They are used in finite differences representing the r. h. s. of continuity equation (2). At the first node, continuity equation is written by taking into account the BC (10) of prescribed influx Q . For certainty, the latter may be set unit ($Q = 1$), consequently, $q_0 = 1/2Q = 1/2$. Continuity equation for the first node yields the ODE:

$$\frac{dw_1}{dt} = \frac{3q_0 - (4w_2v_2 - w_3v_3)}{2\Delta x}. \quad (18)$$

At following nodes up to that with the number i_* , the ODE are

$$\frac{dw_i}{dt} = \frac{-w_{i+1}v_{i+1} + w_{i-1}v_{i-1}}{2\Delta x}. \quad (19)$$

For nodes with numbers exceeding i_* , the nodal openings and velocities are zero; consequently, the r. h. s. of continuity equation are zero, as well, and the ODE are:

$$\frac{dw_i}{dt} = 0. \quad (20)$$

The complete dynamic system is obtained by adding the SE (16) to the M ODE (18)-(20), generated by continuity equation. The resulting system of ODE (18)-(20), (16) is solved under the discretized IC (11):

$$\begin{aligned} w_i(t_0) &= w_{i0} & i &= 1, \dots, M \\ x_* &= x_{*0}. \end{aligned}$$

Herein w_{i0} and x_{*0} are known numbers; for nodes ahead of x_{*0} , the initial openings are set zero: $w_{i0} = 0$ when $x_i > x_{*0}$.

The complete system of ODE may be solved by standard methods like those by Euler, Runge-Kutta, Adams, etc. The coordinate x_* of the propagating front grows with increasing time. When it reaches the prescribed length L , the latter is doubled. Thus the interval again becomes equal to the doubled x_* . We keep the same number $M + 1$ of nodes for the doubled interval. Then the mesh size Δx is also doubled. If taking M even ($M = 2N$), odd nodes of the previous mesh become current nodes of the new mesh. The openings at these nodes are known; the current fracture half-length x_* is also known. Hence, we have the same system as that at the beginning of integration for previous L , with known initial values of nodal openings, with known half-length, and with doubled Δx . Since the mesh size Δx is increased, the time step may be also increased without loss of stability of an explicit scheme of integration.

5 Numerical results

We implemented the approach described by using two methods of time stepping: Runge-Kutta (R-K) of fourth order (without and with acceleration) and Adams. This tended to distinguish that method which provides stable accurate results with minimal time expense. A proper choice may serve for extending the approach to 3D HF problems.

We set $Q_0 = 1$ ($q_0 = 1/2$) and used various number of nodes: $M + 1 = 21, 41, 61$ and 81. In accordance with Sec. 3, the time range considered was from the initial time $t_0 = 1$ to the final time $t_{fin} = 100$ of conditional time units. The range covers the usual time of a HF treatment. When using the R-K method, the time step Δt was chosen small enough to guarantee stability. Since the stability condition involves the ratio $\Delta t/\Delta x^2$, the time step could be increased with growing mesh size Δx . Calculations by the R-K method were performed either with a fixed time step (without acceleration), or with time step doubled when the mesh size was doubled (with acceleration). To further decrease the time expense, we employed the Adams

inexplicit predictor-corrector method with iterations at a time step. The accuracy of the calculations was checked by comparison with the self-similar bench-mark solution, obtained to the accuracy of four significant digits, at least. To make the comparison applicable at any time step, the initial conditions (12) at $t_0 = 1$ were assigned as those corresponding to the self-similar solution at this instant. The typical numerical results obtained for a Newtonian fluid ($n = 1$) are illustrated by Figure 1.

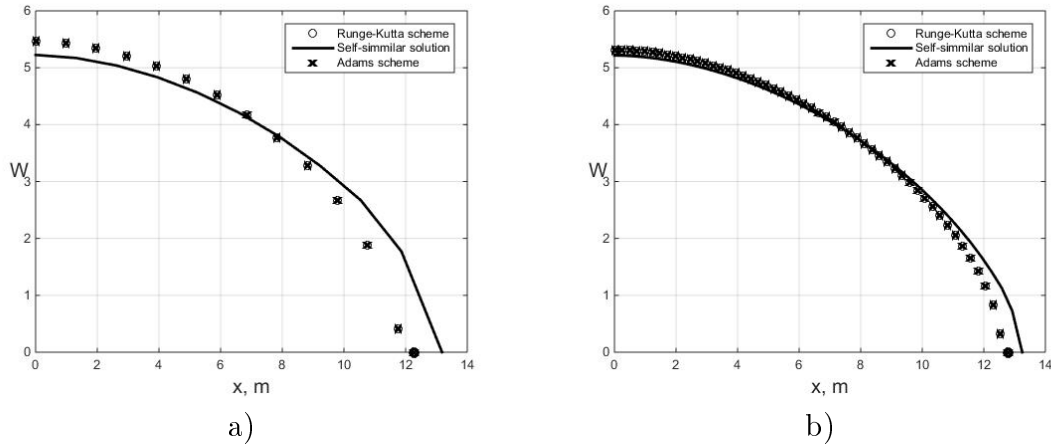


Figure 1: Computational results at time $t_{fin} = 100$ for a) $M + 1 = 21$ and b) $M + 1 = 81$

It presents distributions of the opening along the fracture half-length at the final time $t_{fin} = 100$ for $M + 1 = 21$ (Figure 1a) and $M + 1 = 81$ (Figure 1b) nodes. The last points at the x -axis correspond to the final half-length x_* . For comparison, the bench-mark self-similar solution is shown by the solid lines. It appears that for a quite coarse mesh with merely 21 nodes at the interval of the length $2x_*$, the error of the opening at the source is 3.7%, and the error of the half-length is 6.9%. For $M + 1 = 41$ nodes, the errors become 2.0% and 4.9%, respectively. For $M + 1 = 81$ nodes, they are 1.4% and 3.0%. As could be expected, these errors are greater than those reported in the paper [9], where the same meshes were used in the normalized coordinates. Then the error of the final half-length x_* did not exceed 0.94% even for $N + 1 = 21$ nodes. The growth of errors is explained by the fact that for non-normalized coordinates, the temporal derivative $\partial w / \partial t$ is singular as $O((x_* - x)^{\alpha-1})$ at the front, while in normalized coordinates it is non-singular being equal to zero ($\partial w / \partial t = 0$) at the front. Surely, the error may be decreased by more accurate integration of the elasticity equation and by direct accounting for the singularity discussed.

From Figure 1, it can be also seen that there is no significant differences in the accuracy of integration by the R-K and Adams methods. Hence, we may turn to the comparison of their computational efficiency. The calculations by the R-K method without acceleration with $M + 1 = 41$ nodes required 1 hour to cover the range from $t_0 = 1$ to $t_{fin} = 100$ at a conventional laptop in the Matlab environment. Using acceleration drastically decreased this time; it became 10 minutes. Employing the Adams scheme additionally decreased the time to 5 minutes. Calculations with

using FORTRAN required two-fold less time when employing arithmetics of double precision. Therefore, in the problem considered, the accelerated R-K method is acceptable, while the Adams method appears superior over it.

The approach developed has been tested for thinning fluids ($0 < n < 1$), as well. We could see that, similar to using the normalized coordinates [9], the accuracy notably decreased when the behavior index n approached zero. The reason is clear from equations (3) and (4). They contain the degree $1/n$, which tends to infinity when n goes to zero. This tremendously magnifies even small errors in the base of the exponent. Therefore for small n , the computational algorithm should be modified. It can be done by raising (3) and (4) to the degree n and expanding into Taylor's series in n . We do not employ this option, because in practice the behaviour index is not close to zero. Normally it exceeds the value 0.5 [11], for which the approach in the form described in the previous section provides results with acceptable accuracy. Specifically, for $n = 0.5$, when using the mesh with $M + 1 = 41$ nodes, the errors of the opening at the source and of the half-length are 3.9% and 2.6%, respectively.

6 Conclusion

Summarizing, we conclude that the approach developed is efficient when solving the HF problem in global coordinates with using direct (hypersingular) elasticity operator. In the time range typical for HF treatments, integration of the obtained system of ODE may be efficiently performed by employing accelerated R-K or Adams methods; the latter looks superior over the former. It is shown that the approach provides acceptable accuracy for Newtonian and thinning fluids used in practice. The results imply that it may be successfully extended to 3D problems of hydraulic fracturing.

Acknowledgement

The authors highly appreciate the support of the Russian Scientific Fund (Grant # 15-11-00017)

References

- [1] J. Adachi, E. Siebrits, A. Pierce, J. Desroches. Computer simulation of hydraulic fractures. *Int. J. Rock Mech. Mining Sci.*, 44, No 5 (2007) 739.
- [2] E. Detournay, A. Peirce. On the moving boundary conditions for a hydraulic fracture. *Int. J. Eng. Sci.*, 84 (2014) 147.
- [3] J. Geertsma, F. de Klerk. A rapid method of predicting width and extent of hydraulically induced fractures. *J. Pet. Tech.*, 21 (1969) 1571.
- [4] S. A. Khristianovich, V. P. Zheltov. Formation of vertical fractures by means of highly viscous fluid. *Proc. 4-th World Petroleum Congr. Rome (1955)* 579.

-
- [5] A. M. Linkov. Speed equation and its application for solving ill-posed problems of hydraulic fracturing. *Doklady Physics*, 56 (2011) 436.
- [6] A. M. Linkov. On efficient simulation of hydraulic fracturing in terms of particle velocity. *Int. J. Eng. Sci.*, 52 (2012) 77.
- [7] A. M. Linkov. The particle velocity, speed equation and universal asymptotics for the efficient modelling of hydraulic fractures. *J. Appl. Math. Mech.*, 79 (2015) 54.
- [8] A. M. Linkov. Solution of axisymmetric hydraulic fracture problem for thinning fluids. *J. Appl. Math. Mech.*, 80 (2016) 208.
- [9] A. M. Linkov. Solution of plane hydraulic fracture problem by Runge-Kutta method under arbitrary initial conditions. *Russian Mining Science*, 2 (2016). In print.
- [10] G. Mishuris, M. Wrobel, A. Linkov. On modeling hydraulic fracture in proper variables: Stiffness, accuracy, sensitivity. *Int. J. Eng. Sci.*, 61 (2012) 10.
- [11] C. Montgomery. Key-Note lecture: Fracturing fluids. Proc. Int. Conf. HF-2013 "Effective and Sustainable Hydraulic Fracturing ", Brisbane, Australia, 20–22 May 2013, A. P. Bungler et al. (eds), Croatia, InTech (2013) 3.
- [12] R. P. Nordgren. Propagation of a vertical hydraulic fracture. *Soc. Pet. Eng. J.*, 12 (1972) 306.
- [13] T. K. Perkins , L. R. Kern. Widths of hydraulic fractures. *J. Pet. Tech.*, 13, No 9 (1961) 937.
- [14] A. A. Savitski, E. Detournay. Propagation of a penny-shaped fluid-driven fracture in an impermeable rock: asymptotic solutions. *Int. J. Solids Structures*, 39 (2002) 6311.
- [15] D. A. Spence, P. W. Sharp. Self-similar solutions for elastohydrodynamic cavity flow. *Proc. Roy. Soc. London, Ser. A.*, 400, No 819 (1985) 289.
- [16] M. Wrobel, G. Mishuris. Hydraulic fracture revisited: Particle velocity based simulation. *Int. J. Eng. Sci.*, 94 (2015) 23.
- A. D. Stepanov, Institute of Problems of Mechanical Engineering RAS, 61, Bol'shoy pr. V.O., St. Petersburg, 199178, Russia*
- A. M. Linkov, Institute of Problems of Mechanical Engineering RAS, 61, Bol'shoy pr. V.O., St. Petersburg, 199178, Russia*

A Neural Network Model to Investigate the Effect of Frequency and Time on Loading Induced Osteogenesis

Abhishek Kumar Tiwari, Navin Kumar
ktabhishek@iitrpr.ac.in, nkumar@iitrpr.ac.in

Abstract

Cyclic and low magnitude mechanical loading is considered beneficial in prevention and the reversal of bone loss. It is believed that loading on bone induces normal strain which inhibits resorption and promotes osteogenesis (i.e., new bone formation) at the sites of elevated normal strain magnitude. Thus, computer models of bone adaptation have assumed normal strain as a stimulus and successfully predicted the locations of osteogenesis; however, these models fall short in fitting the quantity of newly formed bone. Such limitation may be due to non-incorporation of loading parameters such frequency, cycles and time etc. which considerably influence the amount of new bone formation. Nevertheless, a relationship between loading parameters and a remodeling parameter such as mineral apposition rate (MAR) to quantify the amount of newly formed bone, is needed. Accordingly, this study presents a back-propagation neural network model to identify the relationship between loading parameters and MAR. The model establishes an empirical relationship to estimate MAR as a function of loading parameters. The model's predictions closely fits several in-vivo experimental data. The model can be further utilized to define MAR derived remodeling rate coefficients in computer model. These findings may improve the capability of bone adaptation models to predict qualitative and quantitative new bone distribution; and thus will be ultimately useful in design and development of bio-mechanical interventions to prevent or cure bone loss.

1 Introduction

Long bones are usually subjected to various mechanical loads such as gravity, ground reaction force and muscle contraction forces in daily routine. In-vivo studies have reported that these physiological loads are essential to maintain the weight bearing capacity of bone since bone/muscle disuse in case of bedridden patients, physically challenged individuals and microgravity in astronauts result into significant bone loss and thus increases bone fracture risks[1, 2]. Prevention or treatment of such bone loss is a serious concern for clinicians. Recent research efforts have shown

that low-amplitude and cyclic loading on bone may be effective in the recovery from bone loss as it stimulates the osteogenesis (i.e., new bone formation) at the location of elevated normal strain [3, 4, 5]. Computer models of bone adaptation have considered normal strain as a stimulus and successfully predicted the locations of new bone formation for in-vivo experiments [6, 7, 8]. However, these studies have modeled osteogenesis for specific in-vivo experiment and accordingly tuned the model with specific remodeling parameter to fit the amount of new bone formation. Thus, the same model may fail to precisely predict the amount of new bone formation for other experimental studies. It is important to note that loading parameters such as frequency, loading cycle and time significantly influence the amount of new bone formation and remodeling parameters. For example, Hsieh and Turner have shown that an increase in loading frequency may enhance the new bone thickness [9]; whereas, Cullen *et al.* had shown that the amount of newly formed bone increases with increase in number of loading cycles/time [10]. This aspect has been overlooked in most of the computational models. It indicates that models parameter such remodeling rate coefficient must be selected based on loading parameters to improve the efficacy of computational prediction. However, there is no unifying principle to relate bone remodeling parameters such as MAR with loading parameters. In recent years, neural network models have emerged as an efficient tool for establishing an unseen relationship among the given set of parameters [11, 12]. Accordingly, this preliminary study proposes a neural network approach to identify an empirical relationship between loading parameters, e.g., normal strain, frequency and cycles, and MAR. The model opts for a back propagation algorithm. The model captures the characteristics from available experimental data in the literature and provides an equation to estimate MAR as a function of loading parameters. The model has been trained and tested by several in-vivo experimental data. The model's prediction of MAR closely fits several in-vivo experimental results. The results clearly indicate the importance of loading parameters in bone remodeling estimation. These finding may be useful for the development of efficient and universal approaches/models to predict loading induced osteogenesis, which can be further extended to design of bio-mechanical therapies for the prevention and cure of bone loss.

2 Method

2.1 Experimental Data Collection

In the present study, we attempt to model the relationship between loading parameters and a remodeling parameter, i.e., MAR using a neural network modeling approach. There are several in-vivo experimental studies readily available in the literature where rodent long bones especially tibia or ulna of rat/mice were loaded in cantilever bending [13], axial compression[14], four point [15] and three point bending [16] and MAR were reported in response to loading. However, different loading cases have led to different new bone formation even when the strain distribution were similar. This may be mainly because of differences in other loading parameters such as frequency and cycles etc. Hence, loading parameters such as frequency, cycles, time along with strain and corresponding MAR have been collected from 70

in-vivo studies. 108 experimental data sets have been prepared out of these studies and these data-sets were further used as inputs to the model. We have listed few of these in-vivo studies [17, 18, 19, 20, 21, 22, 10, 9]

2.2 Network Model

A back propagation neural network model with a single hidden layer with four nodes has been used to relate MAR with loading parameters (Fig. 1). Three loading parameters, i.e., normal strain, frequency and loading cycles have been incorporated as inputs to the model whereas corresponding MAR has been considered as an output. Hence, the model has four nodes in hidden layer and one node in output layer. These layers have been connected through synaptic weights. A sigmoid function has been used as an activation function for the hidden and the output layers. MATLAB (Mathworks Inc. Boston) was used to build the neural networks model. The model has been trained with few experimental data sets to capture the characteristics of experimental data. The error (sum of squared errors (SSE)) between model output and the target updates synaptic weights through a feedback algorithm during training. Finally, the model has been tested to check the accuracy of the model. In this study, we have supplied 25%, 50% and 75% of experimental data as training inputs and remaining 75%, 50% and 25% has been tested to check the efficacy of the model. A step-wise learning rate has been used for training the data.

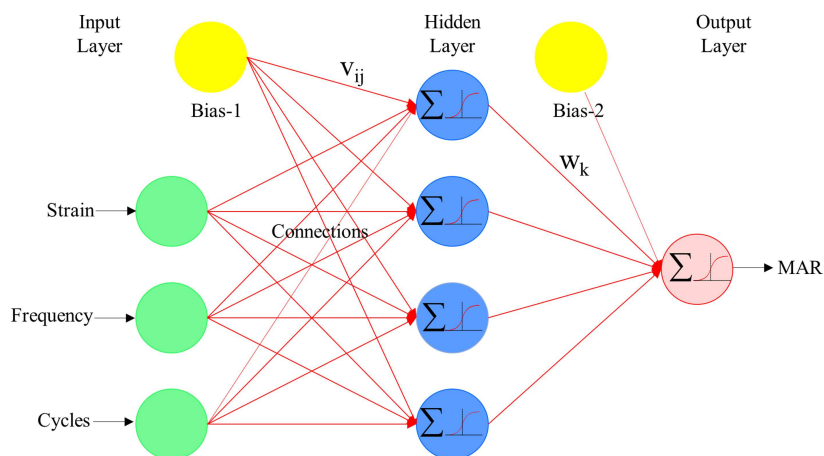


Figure 1: The neural network model to predict MAR

3 Results

3.1 Training Results

The network has been trained in three different batches of 25%, 50% and 75% of experimental data sets. The training performance of the network for these data sets can be noticed from Figs. 2, 3 and 4. The error decreases with an increase in iterations or epochs. The network minimizes the error for all training data sets using multiple learning rates. The training performance was found satisfactory for all batches as the error between the network and the targeted outputs was minimal. These training results establishes an empirical equation to estimate MAR as a function of strain (ϵ), loading frequency(f) and cycles (c), which is as follows:

$$MAR = \frac{1}{1 + e^{-\sum_{j=1}^4 Z_j w_{jk}}} \quad (1)$$

where

$$Z_j = \frac{1}{1 + e^{-\sum_{i=1}^3 x_i v_{ij}}} \quad (2)$$

x_i are the inputs, i.e., ϵ , f and c to the model. w_{jk} and v_{ij} are constants obtained from training of experimental data. The constants obtained from training of 50% data sets are given bellow:

$$v_{ij} = \begin{bmatrix} -1.29 & -4.59 & 1.79 \\ 0.82 & 0.85 & 0.36 \\ -2.62 & 5.26 & -10.95 \\ -0.25 & -1.16 & 3.09 \end{bmatrix}$$

and

$$w_{jk} = \begin{bmatrix} -0.48 \\ -8.72 \\ -7.00 \\ 5.89 \end{bmatrix}$$

3.2 Testing Results

The model has been tested to predict MAR for remaining 75%, 50% and 25% of experimental data-sets after training. It can be observed from Fig. 2 that the error between predicted output and experimental data is high (SSE = 0.40) when 75% of experimental data has been tested and only 25% was sent for training. The model's prediction improved when 50% and 75% of data were sent for training and correspondingly 50% and 25% of experimental data have been tested (Figs. 3 and 4). It is interesting to note that the model more closely (SSE = 0.05) predicts MAR for 50% of experimental data which include most of the in-vivo loading cases such as axial loading, cantilever bending and four point bending (Fig. 2). Moreover, the same model closely predicts MAR for a broader range of frequencies (i.e., 1, 2, 5, 10 and 30 Hz) and loading cycles (i.e., 90-1200) which can be noticed from Fig. 2.

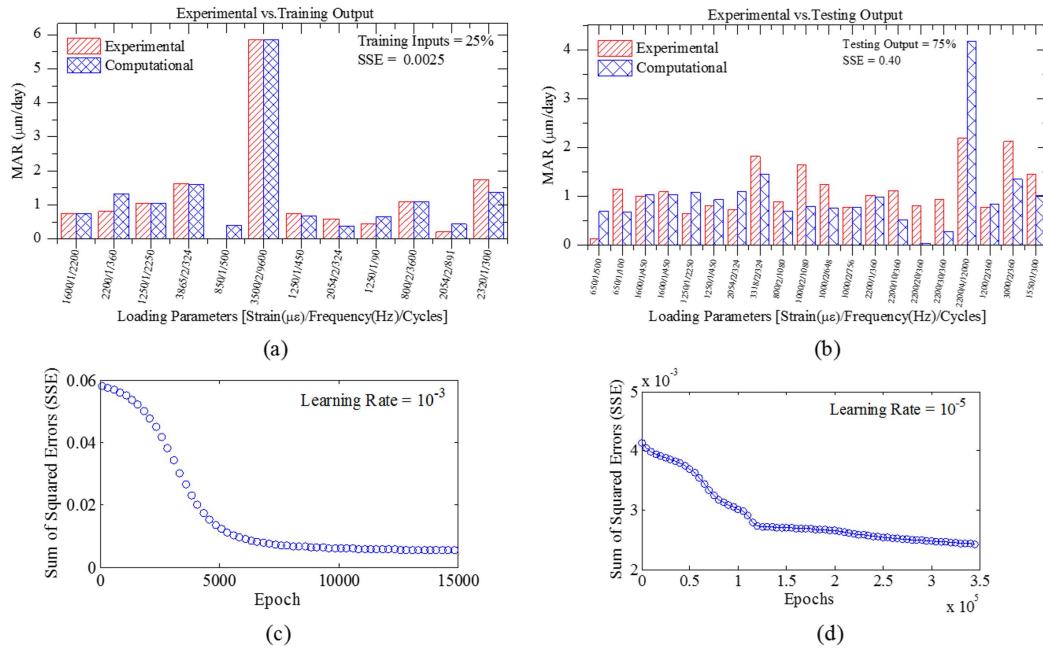


Figure 2: (a) Training and (b) testing outputs vs. experimental data; (c and d) SSE vs. epochs/iterations showing network training performance for 25% data sets.

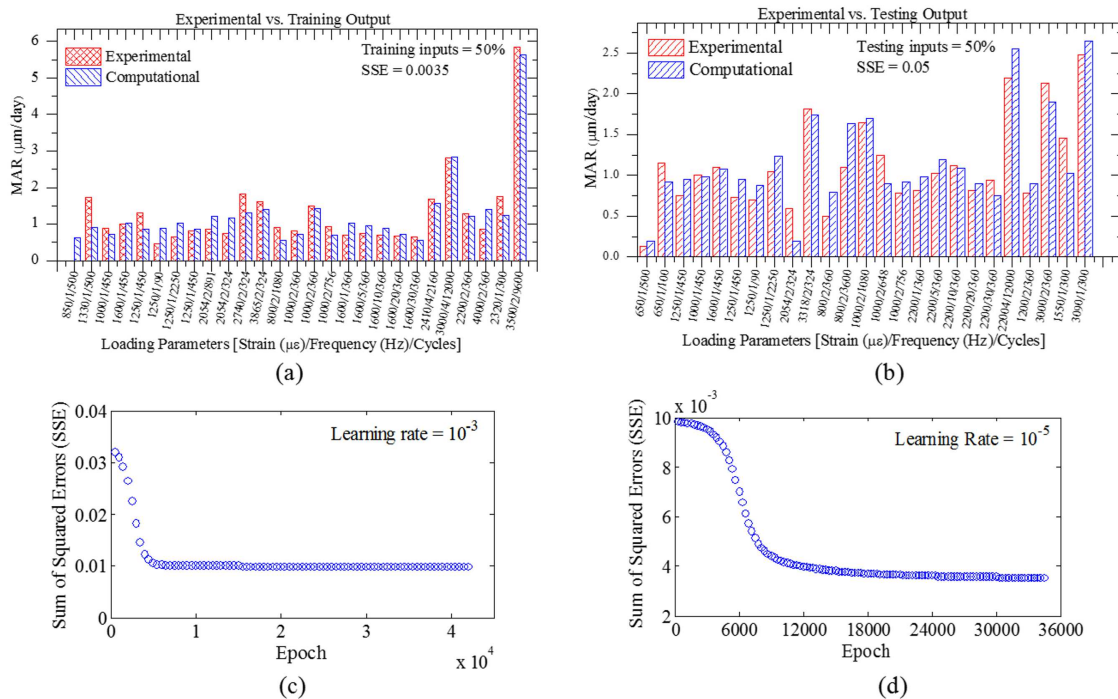


Figure 3: (a) Training and (b) testing outputs vs. experimental data; (c and d) SSE vs. epochs/iterations showing network training performance for 50% data sets.

A Neural Network Model to Investigate the Effect of Frequency and Time on Loading Induced Osteogenesis

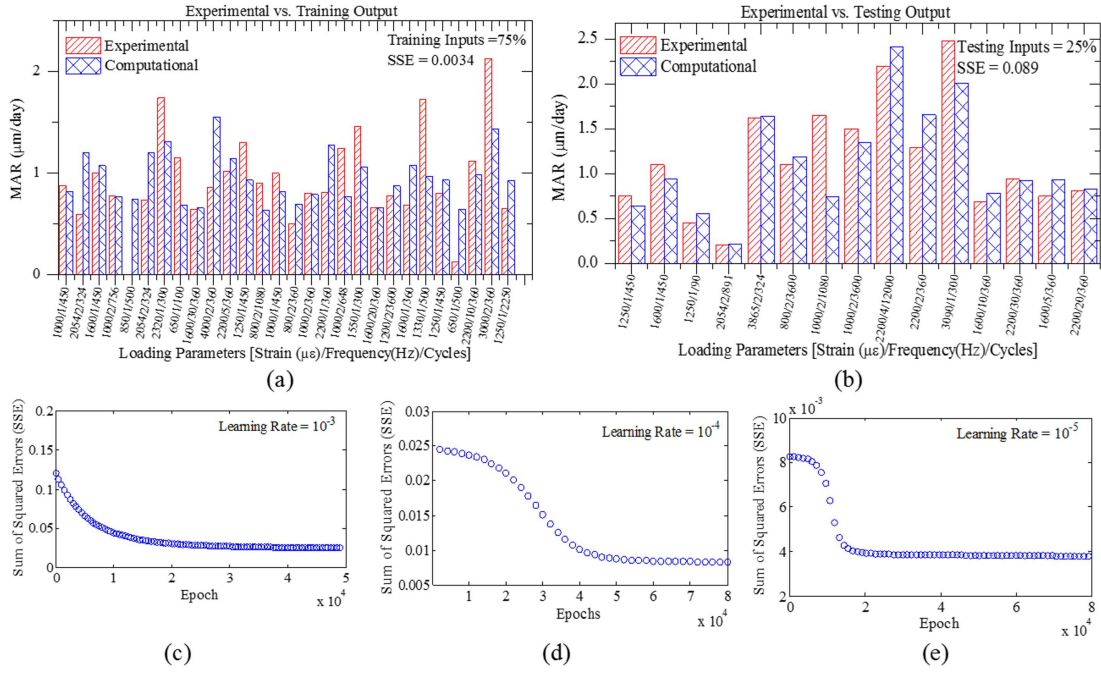


Figure 4: (a) Training and (b) testing outputs vs. experimental data; (c, d and e) SSE vs. epochs/iterations showing network training performance for 75% data sets.

4 Discussion

This study fills the gap between computational prediction and in-vivo experimental results. Available computational models in the literature predict the location of new bone formation, however, failed in predicting the amount of new bone formation as loading parameters change with experiments. Most of the models tuned the remodeling rate parameters to make prediction more close to the in-vivo results. This study may be useful for existing computer models in selection of a suitable remodeling rate constants according to experimental loading condition. The present model in combination with stimulus based models may be useful in the development of a robust computational model to fit all the available experimental data in the literature; thus, the same model can be extended in future to accurately predict the new bone formation for any other in-vivo study. The model can also be useful in understanding the role of frequency and loading cycles. For example, the model captures the characteristic from experimental data that the MAR increase with loading frequency and cycles which can be noticed from the results as well. This is one of the advantage of our model. However, one of the limitations of the model that it captures only a limited number of experimental data. Hence, incorporation of more data will surely improve the accuracy. In addition, the age of the animals and rest insertion time between cycles will be incorporated in future as these parameters also governs the osteogenesis. Collectively, this model provides an insight that a model based on all experimental result can be useful in understanding the loading induced osteogenesis which will surely improve the bio-mechanical intervention to treat or prevent bone loss.

Acknowledgements

The authors acknowledge IIT Ropar for the fellowship and Department of Science and Technology(Sanction order no. SB/S3/MMER/046/2013) Government of India for computational facilities. We also acknowledge to Mr. Ajay Goyal, PhD student with Department of Mechanical Engineering, IIT Ropar for his inputs in programming the model.

References

- [1] Harri Siev hnen. Immobilization and Bone Structure in Humans. Arch. of Biochem. and Biophys., 2010, vol. 503(1), p. 146-152.
- [2] R. Y. Lau and X. Guo. A Review on Current Osteoporosis Research: With Special Focus on Disuse Bone Loss. J. Osteoporos., 2011, vol. 2011, p. 1-6
- [3] R. A. Hillam and T. M. Skerry. Inhibition of Bone Resorption and Stimulation of Formation by Mechanical Loading of the Modeling Rat Ulna In-Vivo. J. Bone Miner. Res.,1995, vol. 10(5), p. 683 - 689.
- [4] L. C. Shackelford. Resistance Exercise As A Countermeasure to Disuse-Induced Bone Loss. J. Appl. Physiol., 2004, vol. 97(1), p. 119 - 129.
- [5] C. T. Rubin and L. E. Lanyon. Regulation of Bone Mass by Mechanical Strain Magnitude. Calcif. Tissue Int., 1985, vol. 37(4), p. 411 - 417.
- [6] N. Chennimalai Kumar, J. A. Dantzig, I. M. Jasiuk, A. G. Robling, and C. H. Turner. Numerical Modeling of Long Bone Adaptation Due to Mechanical Loading: Correlation with Experiments. Ann. Biomed. Eng., 2010, vol. 38 (3), pp. 594 - 604.
- [7] C. S. Florio and K. A. Narh. Effect of Modeling Method on Prediction of Cortical Bone Strength Adaptation Under Various Loading Conditions. Meccanica, 2013, vol. 48(2), p. 393 - 413.
- [8] P. Fridez, A. Terrier, L. Rakotomanana, and P.F. Leyvraz. Three dimensional Model of Bone External Adaptation. Computer Methods in Biomechanics and Biomedical Engineering, 1996, vol. 1, p. 189 - 196.
- [9] Yeou Fang Hseih and Charles H. Turner. Effects of Loading Frequency on Mechanically Induced Bone Formation. J. Bone Miner. Res., vol. 16(5), p. 918 - 924
- [10] D. M. Cullen , R. T. Smith, and M. P. Akhter. Bone-Loading Response Varies with Strain Magnitude and Cycle Number. Journal of Applied Physiology, 2001, vol 91(5), 1971 - 1976.

-
- [11] L. Y. Mi, M. Basu, S. P. Fritton, and S. C. Cowin. Analysis of Avian Bone Response to Mechanical Loading, Part Two: Development of a Computational Connected Cellular Network to Study Bone Intercellular Communication. *Biomech. Model. Mechanobiol.*, 2005, vol. 4(2-3), pp. 132 - 146.
- [12] Ridha Hambli, Houda Katerchi, and Claude-Laurent Benhamou. Multiscale Methodology for Bone Remodelling Simulation Using Coupled Finite Element and Neural Network Computation. *Biomechanics and Modeling in Mechanobiology*, 2011, vol. 10(1), p. 133 - 145.
- [13] Sundar Srinivasan et al. Low-Magnitude Mechanical Loading Becomes Osteogenic When Rest Is Inserted Between Each Load Cycle. *J. Bone Miner. Res.*, vol. 17(9), p. 1613 - 1620
- [14] Toshihiro Sugiyama, Joanna S. Price, and Lance E. Lanyon. Functional Adaptation to Mechanical Loading in Both Cortical and Cancellous Bone is Controlled Locally and is Confined to the Loaded Bones. *Bone*, 2010, 46(2), p. 314 - 321.
- [15] M. R. Forwood, and C. H. Turner. Skeletal Adaptations to Mechanical Usage: Results from Tibial Loading Studies in Rats. *Bone* 1995, vol. 17(4), p. S197 - S205
- [16] H. N. Matsumoto, Y. Koyama, and K. Takakuda. Effect of Mechanical Loading Timeline on Periosteal Bone Formation. *J. Biomech. Sci. Eng.*, 2008, vol. 3(2), p. 176 - 187.
- [17] E. A. Pedersen et al. Bone Response to In-Vivo Mechanical Loading in C3HHeJ mice. *Calcified tissue international*, 1999, vol. 65(1), p. 41 - 46.
- [18] Sundar Srinivasan, et al. (2003). Enabling Bone Formation in the Aged Skeleton via Rest-inserted Mechanical Loading. *Bone*(2003), vol. 33(6), p. 946-955.
- [19] M. Jeremy, and Ronald F. Zernicke. Rest Insertion Combined with High-Frequency Loading Enhances Osteogenesis. *Journal of Applied Physiology*, (2004), vol. 96(5), p. 1788 - 1793
- [20] Alexander G. Robling, David B. Burr, and Charles H. Turner. Recovery Periods Restore Mechanosensitivity to Dynamically Loaded Bone. *Journal of Exp Biol.*, 2001, vol. 204(19), p. 3389-3399
- [21] Matthew J. Silva, and Michael D. Brodt. Mechanical Stimulation of Bone Formation is Normal in the SAMP6 Mouse. *Calcified tissue international*, 2008, vol. 82(6), p. 489-497.
- [22] Kurt D. Hankenson et al., Increased Marrow-Derived Osteoprogenitor Cells and Endosteal Bone Formation in Mice Lacking Thrombospondin 2. *J. Bone Miner. Res.*, 2000, vol. 15(5), p. 851-862.

Abhishek Kumar Tiwari, Biomechanical Creativity and Innovation Lab, Indian Institute of Technology Ropar, Nangal Road, Roopnagar Punjab, 140001, India.

REFERENCES

Dr. Navin Kumar, Room No. 222, Department of Mechanical Engineering, Indian Institute of Technology Ropar, Nangal Road, Roopnagar Punjab, 140001, India.

Formation and propagation of methane seepage wave in stressed coal

Valery N. Zakcharov, Olga N. Malinnikova, Vitaly A. Trofimov
olga_malinnikova@mail.ru

Abstract

The numerical simulation of filtration streams of gas in a coal layer with allowance for of character of distribution of stresses in a boundary part of a layer is conducted. The numerical algorithm of problem solving about mass transfer of methane to openings in gas content coal seams is developed and realized on the computer. The model of gas seepage in a coal bed has revealed features of the process based on the dependence of coal permeability on effective stresses and adsorbed gas amount. A seepage wave forms in this case; the wave travels in an originally impermeable coal bed, generates permeability zone in it and provides outflow of gas through exposures to mined-out area.

1 Introduction

Underground coal mining is usually faced with the challenging tasks concerned with gas flow analysis. The relevance of such studies grows as mining goes to deeper levels. Large volumes of gas, especially methane, emitting from coal beds into mined-out areas create difficult and, sometimes, hazardous operation conditions in mines.

Among all characteristics of methane mass-transfer in a porous medium of coal, a special place belongs to permeability coefficient connecting gas seepage rate and pressure gradient. Many researchers attempted to determine permeability of coal specimens under varied confining pressure in a laboratory with a purpose of using the results to judge on coal bed permeability and on the permeability variation with rock pressure. Such tests are of interest for qualitative descriptions of mechanisms of change in permeability versus rock pressure. Quantitative estimation of coal bed permeability in the influence zone of rock pressure relaxation needs ad hoc approaches to determining in situ real-time permeability of coal beds. The theoretical basis of the methods to determine apparent permeability of coal beyond influence zones of underground excavations was given in [1], with the exemplified procedure of corresponding tests to be carried out in mines.

The already available findings of theoretical and experimental research have laid foundation for modern understanding of methane mass-transfer in coal beds saturated with gas. Advancement in numerical methods to solve boundary value problems in terms of partial derivatives and the high-performance computers enable

new-level formulation of basic problems on gas seepage in coal beds and allow new mechanisms to be determined with regard to kinetics of methane desorption from coal [2], [3], [4].

It has been shown in [2] that gas-bearing coal beds in a virgin rock mass are impermeable. Permeability zones appear when alteration of the intact state results in opening of fractures in coal beds. Fractures grow with gas outflow. When this happens, pressure in a sealed hole drilled in a coal bed and in a permeability zone around this hole is lower than the natural gas pressure in intact coal.

The key influence on initiation of permeability zones in coal beds is mining-induced alteration of coal bed stress. Stress relaxation and shearing cause joints oriented mainly along the major principal stress, spacing of joints grows, and thus a system of seepage channels connecting pores appears in coal. The zone with such system of channels is gas-permeable. The zone is confined by a certain level of stresses that comparatively fast abate with distance from a mine opening.

Another factor related with initiation and expansion of gas-permeable zone in coal is shrink (volume reduction) of coal substance when adsorbed gas releases. Joints, initially tightly crowded, deform, and spacing grows between them (cleats). When cleats are sufficiently wide, a system of seepage channels is formed as in the case of coal bed relaxation.

Based on the in situ observation data on gas pressure variation in coal beds and reasoning from the analysis of coal shrinkage and swelling in the course of adsorption-desorption, it is shown in [3] that gas flow in coal bed can be considered as a gas seepage wave with a jump in adsorbed gas value at the wave front coincident with the moving boundary of the permeability zone. A determinant in this case is a gas saturation limit Q^* , at which gaps sufficient for gas seepage (outflow) appear in gas-impermeable part of coal bed.

Inasmuch as Q^* is associated with widening of microcracks and gaps between joints, it is naturally dependent on stress state of coal, first of all, then on tectonic damage and gas content of coal, and on gas sorption-storage capacity and adsorption-deformation properties of coal. For this reason, because of considerable variability of damage and sorption properties within a coal bed section, either along the strike or down the dip, the values of Q^* at the boundaries of gas-permeable zones will differ. This is one of the main causes for different pressures in closely spaced holes within the same coal bed.

2 Gas seepage model

This section gives details of theoretical notions on formation of permeability in a coal bed under conditions of its natural occurrence.

A volume of coal bed with voids represented by fractures and pores that can be filled with gas is named active porosity and denoted by m apparently, in coal beds:

$$m = m(\sigma, Q). \quad (1)$$

where σ is a certain generalized stress related with fracture opening; Q is the adsorbed gas concentration, i.e. gas amount per unit volume of coal bed. It is noteworthy that these two parameters give a complete characteristic of state of a coal

bed as other characteristics are described in terms of these parameters. For natural rock pressure and natural gas saturation of coal, these parameters are denoted as σ^0 and Q^0 , respectively.

Flow of fluid and gas in porous media under effect of pressure difference is characterized by a seepage rate \vec{u} . The seepage rate is defined as the flow rate per unit area of porous medium oriented perpendicularly to the flow direction. As a rule, in permeability zones in coal beds, seepage is a slow flow and, thus, is assumable as inertialess. This fact enables connecting the seepage rate \vec{u} and the seepage flow pressure p in the form of the linear Darcy law:

$$\vec{u} = -\frac{k}{\mu} \text{grad}(p), \quad (2)$$

where k is permeability; μ is viscosity. The value k has the dimension of area and is only related with the geometry of a porous medium. Such geometrical parameters of permeability zones in coal beds are, for instance, representative sizes of open fractures and sizes of joints. These parameters, as the active porosity, depend on stresses and adsorbed gas concentration. Therefore, in coal beds, generally:

$$k = k(\sigma, Q). \quad (3)$$

The coal bed stresses σ , conditioned by the original stress state of rock mass, depend on occurrence depth of the coal bed and can be arbitrary and as like as not plenty high. On the other hand, adsorbed gas is limited in amount by the coal adsorption limit Q^0 . Accordingly, the state of coal in the coordinates (Q, σ) is described by an arbitrary point in a half-string $0 < Q < Q^0, \sigma > 0$.

The basic equation of gas seepage in permeability zone is given by:

$$\frac{\partial}{\partial x} \left(\frac{k}{\mu} p \frac{\partial p}{\partial x} \right) = \frac{\partial}{\partial t} (m\rho + Q), \quad (4)$$

where ρ is the gas density related with the pressure p by the linear equation of state:

$$\rho = \frac{p}{RT}.$$

It follows from (4):

$$\frac{\partial}{\partial x} \left(\frac{k}{\mu} p \frac{\partial p}{\partial x} \right) = \frac{m}{RT} \frac{\partial p}{\partial t} + \frac{\partial Q}{\partial t}. \quad (5)$$

In this case [5]:

$$\frac{\partial Q}{\partial t} = \delta \left[\frac{Q}{b(a-Q)} - p \right]. \quad (6)$$

The diffusive mass-transfer of gas in coal bed is as a rule a slow process; incidentally, desorption kinetics in permeability zone is neglected, i.e., the gas-dynamic state of coal bed is assumed equilibrium at any time, and the corresponding sorption

isotherm is used to connect p and Q . In this case, in (5), instead of (6), it is possible to use:

$$\frac{\partial Q}{\partial t} = \frac{ab}{(1+bp)^4} \frac{\partial p}{\partial t}. \quad (7)$$

This case will be discussed below with illustrated generation of a gas seepage wave in an originally impermeable coal bed.

Let the coordinate axis x be connected with the free surface of a semi-infinite coal bed and oriented in line of expansion of a permeability zone. The boundary of this zone is denoted as $\tilde{x}(t)$.

The initial distribution of coal bed gas pressure is assumed as the natural formation pressure p^0 , i.e.:

$$p = p_0, x > 0, t = 0.$$

At the free surface of a semi-infinite bed, it is possible to set pressure or a linear combination of pressure and its normal derivative to the free surface. Consequently, the respective boundary condition in a general form is given by:

$$\alpha_1 p + \alpha_2 \frac{\partial p}{\partial x} = f(t), x = 0, t > 0, \quad (8)$$

where α_1, α_2 are constants; $f(t)$ is a certain function.

In the permeability zone, the distributions of the gas pressure and adsorbed gas concentration, $p(x, t)$ and $Q(x, t)$, are continuous at any time t up to the boundary $\tilde{x}(t)$. At the boundary, the flow continuity condition should hold true:

$$\tilde{p} \frac{k}{\mu} \frac{\partial p}{\partial x} = \beta (Q^0 - \tilde{Q}) \frac{d\tilde{x}}{dt}, x = \tilde{x}(t), t > 0, \quad (9)$$

where

$$\tilde{p} = p(\tilde{x}, t), \tilde{Q} = Q(\tilde{x}, t), \quad (10)$$

β is a constant.

In the coordinates (σ, Q, k) the relation (3) describes a permeability surface schematically shown in Figure 1. The structural features of this surface and its application are comprehensively discussed in [6].

The equation (4) of gas seepage in coal bed is a quasi-linear equation of thermal conduction relative to the pressure p , where k and m depend on the wanted function p and can be discontinuous functions of the arguments x and t . The permeability k , in view of (3), depends on Q and, eventually, via the sorption isotherm, on the pressure p .

At the present day, the most efficient method to solve quasi-linear equations is the finite difference method. With this method, it is inexpedient to use explicit schemes inasmuch as the stability condition:

$$\tau \leq \frac{h^2}{2max\alpha(y)} \quad (11)$$

requires a very small time increment τ at sound selection of a coordinate increment h .

In connection with this, an implicit scheme is constructed within the accuracy $O(h^2 + \tau)$

$$(k_i^j p_i^j - k_{i+1}^j p_{i+1}^j) (p_{i+1}^{j+1} - p_i^{j+1}) - (k_{i-1}^j p_{i-1}^j - k_i^j p_i^j) (p_i^{j+1} - p_{i-1}^{j+1}) = \frac{2h^2}{\tau} E_i (p_i^{j+1} - p_i^j). \quad (12)$$

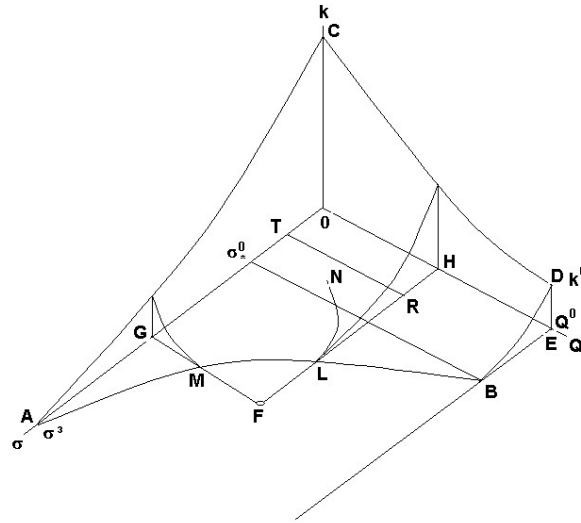


Figure 1: Permeability surface

Simple transformations modify the scheme to suite the double-sweep method:

$$A_i p_{i-1}^{j+1} - C_i p_i^{j+1} + D_i p_{i+1}^{j+1} = -F_i, 0 < i < N, \quad (13)$$

where

$$A_i = k_{i-1}^j p_{i-1}^j + k_i^j p_i^j,$$

$$D_i = k_i^j p_i^j + k_{i+1}^j p_{i+1}^j,$$

$$C_i = (k_{i-1}^j p_{i-1}^j + k_i^j p_i^j) + (k_i^j p_i^j + k_{i+1}^j p_{i+1}^j) + \frac{2h^2}{\tau} E_i,$$

$$F_i = \frac{2h^2}{\tau} E_i p_{ij}. \quad (14)$$

The boundary conditions in the general form may be given by:

$$y_0 = \kappa_1 y_1 + v_1, \quad (15)$$

$$y_N = \kappa_2 y_{N-1} + v_2 \quad (16)$$

It is of no particular difficulty to set boundary conditions at the free boundary of the computational domain. In the simplest case, a constant pressure is set (pressure in

open hole or in underground excavation - 1 atm), in other words, $\kappa_1 = 0, v_1 = p_{hole}$ should be accepted in (15).

At the moving boundary of the permeability zone, the flow continuity condition (9) should be set. Written in the form of (16), it reduces to:

$$y_{N+1} - y_N = v_2, \quad (17)$$

where

$$v_2 = \frac{RT\mu h}{kp_{bound}} M_{bound},$$

T is the absolute temperature of gas; R is the universal gas constant.

The flow M_{bound} , entering the permeability zone from the impermeable zone, is defined by the diffusive flow of gas from coal particles, M_{coal} :

$$M_{coal} = \beta(Q^0 - \tilde{Q}). \quad (18)$$

With the denotation of the difference scheme:

$$Q^0 \Rightarrow q_{N+1}, \tilde{Q} \Rightarrow q_N.$$

The parameter β is a free-varied value characterizing kinetics of gas desorption from coal.

This approach requires continuous positioning of the boundary $\tilde{x}(t)$, which seems inconvenient as the computational domain undergoes permanent variation and should include fractional cells. This inconvenience may be overcome in the framework of the shock-capturing method. The finite difference scheme should be conservative in this case, which means that the flow continuity condition is automatically satisfied at any point of the domain. The permeability k is assigned to be non-zero in accordance with (3) over the entire mesh and to be zero in the remaining part. With such formulation, the calculation, pursuant to (13), (14), embraces the whole mesh, without identifying the boundary $\tilde{x}(t)$, which is determined as a jump in the pressure (permeability, adsorbed gas amount, etc.).

The isotherm of methane adsorption by coal is given by the relation:

$$Q = \frac{abp}{1 + bp} \quad (19)$$

at the adsorption parameters $a = 15kg/m^3$, $b = 0.1atm^{-1}$. These values are within the real ranges of the adsorption characteristic of coal.

Furthermore, the permeability surface (3) is given by:

$$k = 10^{-18} \left[\frac{25(1 - \bar{\sigma})^2 - Q}{25(1 - \bar{\sigma})} \right]^{1.5}, Q \leq 15kg/m^3. \quad (20)$$

where $\bar{\sigma}$ is the stress referred to the minimum initial rock pressure when gas outflow is insufficient to induce permeability ($0 \leq \bar{\sigma} \leq 1$).

The gas-saturation limit Q^* is related with the stress set as $\bar{\sigma}$ as follows: $Q^* = 25(1 - \bar{\sigma})^2$

Obtained in such a manner, the surface, which is the boundary of the permeability zone in coal bed, has the form as in Figure 1 and is qualitatively described by the relation (20). A quantitative description of this surface in actual coal strongly needs experimentation, which calls for special equipment and proper procedures. There are almost no such data available at present time.

3 Results and discussion

The calculations of the parameters of gas flow in underground excavations within the developed approach trace the time variation in the state and dimension of the permeable zone in coal bed ($0 \leq x \leq \tilde{x}$); the left-hand boundary $x = 0$ of this zone is the excavation surface, and the right-hand boundary $x = \tilde{x}$ is the moving front of the permeable zone. Initially, at $t = 0$ an exposure is instantly created, i.e. the excavation wall is made, and gas outflow from coal starts in accordance with the laws (4)-(10).

The parameters that determine the coal bed state at the initial time are: $p = p_0 = 50 \text{ atm}$, $Q = Q_0 = 12.5 \text{ kg/m}^3$, $m = m_0 = 0.03$, and the initial stress $\bar{\sigma}(x)$ included in (20) ranges from 0 to 1. For another thing, it is assumed that at the initial time the rock mass adjoining the exposure undergoes partial stress relaxation. The consequent assumption says that in the stress relaxation zone, $\bar{\sigma}(x)$ linearly grows from zero value at the exposure ($x = 0$) up to a certain maximum at $x = 0.5 \text{ m}$. Beyond this zone ($x > 0.5$) m, rock mass is in the initial stress state.

The most significant parameter is the gas flow rate in a hole or in an excavation, and the time variation in the rate. This is nearly a single characteristic measurable directly in field conditions. By comparing with this parameter, it is possible, to a certain degree, to adjust problem input parameters which are impossible to determine experimentally.

Figures 2 and 3 show time dependences of gas emission rate and total gas outflow in mine in logarithmic coordinates for the selected values $\bar{\sigma} = 0.0, 0.1, 0.4, 0.5, 0.6, 0.7$.

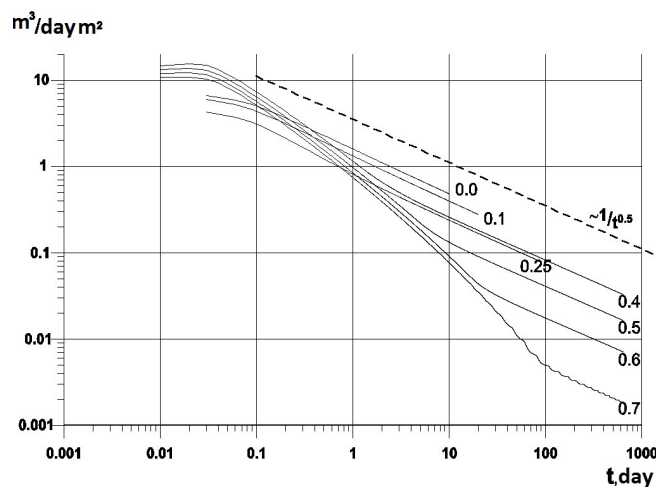


Figure 2: Gas emission rate

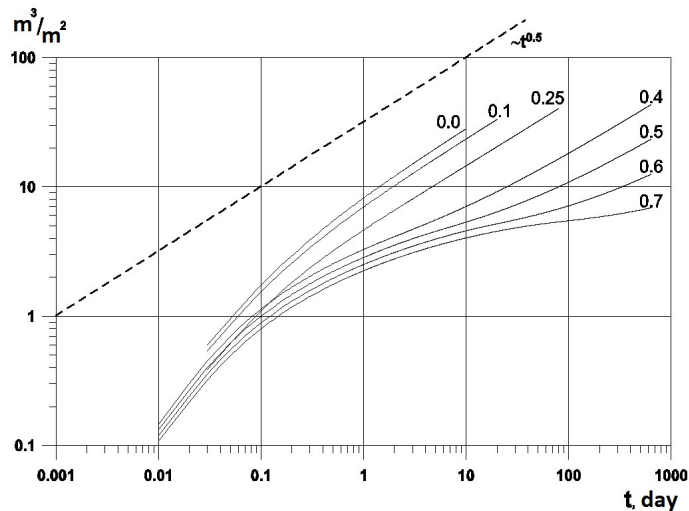


Figure 3: Total gas outflow in mine

A feature of this theory of seepage is the fact that gas seepage takes place only in a limited zone adjoining coal exposure. This zone continuously enlarges with time, which is illustrated in Figure 4 for various values of $\bar{\sigma}$. Figures 5 and 6 give plots

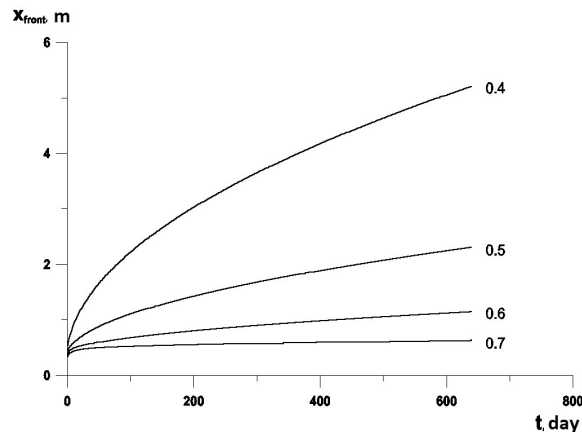


Figure 4: Gas seepage zone enlarge with time

of gas pressure and permeability distributions in the mentioned zone at different times at $\bar{\sigma} = 0.4$. There are two clear sub-zones within the permeability zone: in one sub-zone permeability is generated by stress relaxation of coal at the exposure ($0 < x < \sim 0.5m$), in the other sub-zone permeability is the consequence of gas desorption and outflow from coal.

These seepage calculations assume that stresses are independent of time; in other words, coal shrinkage due to gas outflow and the associated redistribution of stresses in overlying rock mass are neglected.

In case that initial stress is relatively low (in the case analysed, $< \sim 0.28$), coal bed, in line with (2), becomes permeable at any t irrespective of adsorbed gas amount Q . Otherwise (i.e. when $\bar{\sigma}(x) > 0.28$), stress relaxation induces permeability in a certain area where $Q < Q(\sigma)$. Outside this area coal bed remains impermeable and its state can only alter with the reduction in Q with time.

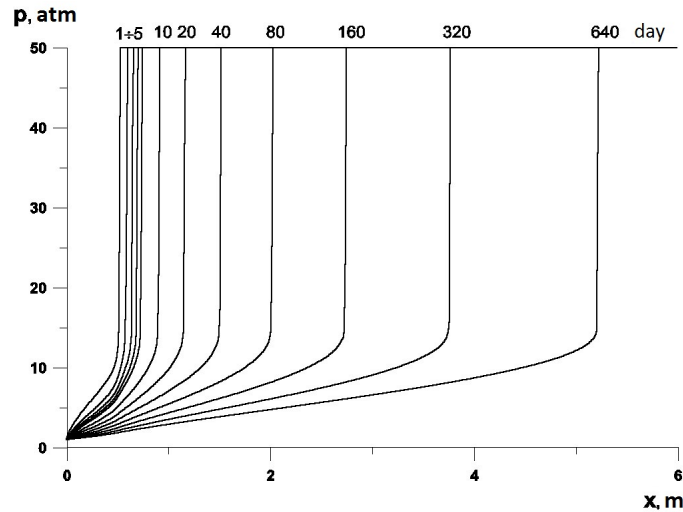


Figure 5: Gas pressure distribution at different times

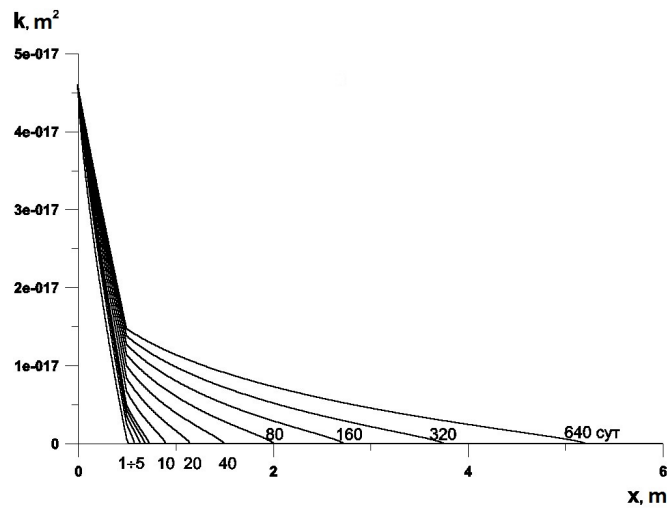


Figure 6: Permeability distribution at different times

4 Conclusions

The model of gas seepage in a coal bed has revealed features of the process based on the dependence of coal permeability on effective stresses and adsorbed gas amount (see Figure 1). A seepage wave forms in this case—it is clearly seen in Figure 5; the wave travels in an originally impermeable coal bed, generates permeability zone in it and provides outflow of gas through exposures to mined-out area.

The seepage wave travel to a great extent depends on effective compressive stresses. From the analysis of this dependence, it is concluded on the limitedness of dimension of the permeability zone and, as a consequence, on the finiteness of gas emission in mined-out area.

The accepted gas pressure in an underground excavation (at the left-hand boundary of the computational domain) is 1 atm. In line with the sorption isotherm (19), this pressure fits with adsorbed gas amount $Q = 1.36 \text{ kg/m}^3$, which, in its turn, on the strength of (20), agrees with the constraining stress $\bar{\sigma} = 0.766$. This means

that when calculations assume maximum stress as equal or higher than 0.766, the behaviour of gas seepage changes cardinally. In this case, the permeability zone extends until the stress at the zone front reaches the value 0.766. From then on, dimension of gas-drained area in coal bed remains unchanged and pressure here drops down to 1 atm. Supposing coal bed stress originally exceeds 0.766 (for the parameters accepted in the present calculations), seepage does not start at all, and slow diffusive escape of gas from coal takes place.

Acknowledgements

The study has been supported by the Russian Science Foundation, Project No. 16-17-00029 (V.N. Zakharov), and by the Russian Foundation for Basic Research, Project No. 15-05-07542).

References

- [1] Kuznetsov S.V., Krigman R.N. (1978) Natural permeability of coalbeds and the determination methods. Moscow: Nauka. (in Russian)
- [2] Kuznetsov S.V., Trofimov V.A. (1998) Analysis of gas pressure measurements in coal seams in connection with the manifestation of permeability around holes and mine workings, *Journal of Mining Science*, vol. 34, no. 2, pp. 113-118.
- [3] Kuznetsov S.V., Trofimov V.A. (1999) Gas-permeable zones in coal seams and the nature and mechanism by which they form, *Journal of Mining Science*, vol. 35, no. 1, pp. 19-25.
- [4] Kuznetsov S.V., Trofimov V.A. (1999) Basic problem of the theory of gas filtration in coal seams, *Journal of Mining Science*, vol. 35, no. 5, pp. 455-460.
- [5] Kuznetsov S.V., Trofimov V.A. (2009) Gasdynamics in a coal seam. Part I: Mathematical description of the desorption kinetics, *Journal of Mining Science*, vol. 45, no. 1, pp. 1-8.
- [6] Zakharov V.N., Malinnikova O.N., Trofimov V.A., Filippov Yu.A. (2016) Relationship of coal bed permeability, gas content and effective stress, *Journal of Mining Science*, vol. 52, no. 2 (in print).

*Valery N. Zakcharov, Krukovsky tup.,4, Moscow, Russia
Olga N. Malinnikova, Krukovsky tup.,4, Moscow, Russia
Vitaly A. Trofimov, Krukovsky tup.,4, Moscow, Russia*

Scattering of flexural–gravitational waves by a periodic array of obstacles in an elastic plate floating on a thin fluid layer

M.G. Zhuchkova
m.zhuchkova@list.ru

Abstract

Low-frequency time-harmonic flexural-gravitational waves of a small amplitude in a floating elastic plate are considered. Straight-line obstacles in the plate are periodically spaced in the horizontal coordinate with an equal separation. Propagation of flexural-gravitational waves through the plate is analytically studied under a thin fluid layer approximation. We are concerned with stopping and passing frequency bands, of which the boundaries are found.

1 Introduction

In [1] under a shallow-water approximation transmission of flexural-gravitational waves through a periodic floating elastic plate was investigated. The plate simulated an ice cover of ocean shelf with two kinds of straight-line obstacles: areas of broken ice and ice hummocks. The paper [2] was devoted to scattering of flexural-gravitational waves by periodically spaced arrays of straight-line narrow cracks in ice sheets modelled by a periodic elastic plate floating on water of finite depth. In [3] wave propagation in periodic plates and cylindrical shells composed by alternating segments of different elastic materials was considered.

A mathematically similar problem of transmission of waves along a periodically weighted strings and beams was studied in [4]. It was pointed out that two oncoming decaying waves can transfer energy. An elastically supported string with point-wise defects and waves in it were considered in [5]. Flexural waves in an elastic beam with periodic system of weights were explored in [6].

Note that the study and development of periodic models such as strings, rods, mass-springs, beams, plates, shells have increasing attention due to a wealth of different engineering applications, e.g., vibration protection, noise isolation, railway track dynamics simulation etc.

In our previous work [7] we investigated transmission of flexural-gravitational waves through multiple straight-line obstacles in a floating elastic plate. In the case of equidistant obstacles complete transmission of an incident wave was obtained at certain frequencies. The plot of energy transmission coefficient against the separation between the obstacles is featured by consecutive peaks reaching 1 in limited

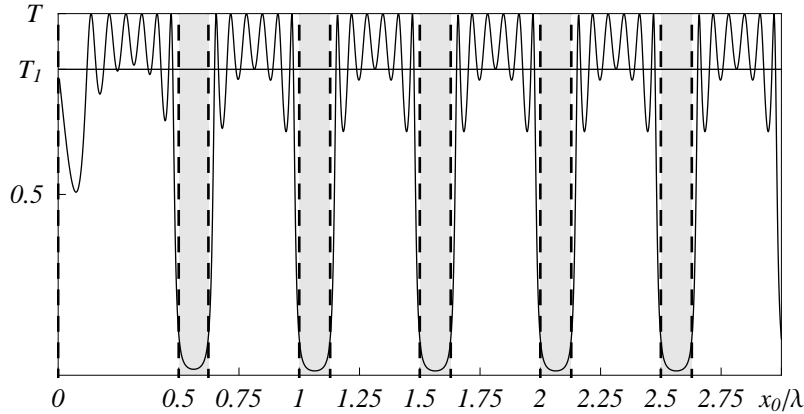


Figure 1: Energy transmission coefficient T of an incident flexural-gravitational wave against the fractional separation x_0/λ between the movable clamps. $N = 7$. A thin fluid layer approximation. The horizontal line displays energy transmission coefficient T_1 in a case of one movable clamp. Hereafter, we use the values of parameters taken from the work [8]. In particular, the plate density $\rho = 917 \text{ kg/m}^3$, the Young's module $E = 4.2 \cdot 10^9 \text{ N/m}^2$, the Poisson ratio $\nu = 0.3$, the thickness of the plate $h = 1.6 \text{ m}$, the thickness of the fluid layer $h_1 = 50 \text{ m}$, the density of the fluid $\rho_1 = 1000 \text{ kg/m}^3$. Wave frequency is $\omega = 1.2 \text{ s}^{-1}$, wave length is $\lambda = 139.4 \text{ m}$. Vertical dashed lines show the boundaries of the stopping bands. The stopping bands are shaded.

intervals (Fig. 1). The number of the consecutive peaks is equal to $N - 1$, where N is the number of obstacles. As the number of obstacles increases, the peaks fill in these intervals. Intervals with the peaks alternated with another intervals inside which the energy transmission coefficient is closed to zero. We suggested in [7] that in the case of a periodic array of obstacles passing and stopping bands would occur. The present paper is devoted to this case and organized as follows. We begin with the study of flexural-gravitational waves in an elastic periodically supported plate floating on a thin fluid layer. After that, we consider flexural waves in an elastic periodically supported beam and compare obtained results with each other.

2 An elastic periodically supported floating plate

A thin elastic plate floats on the surface of an ideal incompressible fluid of the thickness h_1 and the density ρ_1 . A periodic array of movable clamps at lines $x_n = x_0 n$ ($n \in \mathbb{Z}$) divides the plate into infinite number of identical strips of the width x_0 . Configuration of the model is shown in Fig. 2. We deal with time-harmonic flexural-gravitational waves of a small amplitude propagating at a low frequency ω . Time-dependent factor $e^{-i\omega\tau}$ is omitted everywhere. The fluid layer is thin in comparison to all wave lengths.

The velocity potential $\Phi(x, z)$ is developed as a series in $z + h_1$

$$\Phi(x, z) = \alpha_0(x) + \alpha_1(x)(z + h_1) + \alpha_2(x)(z + h_1)^2 + \dots, \quad -h_1 < z < 0. \quad (1)$$

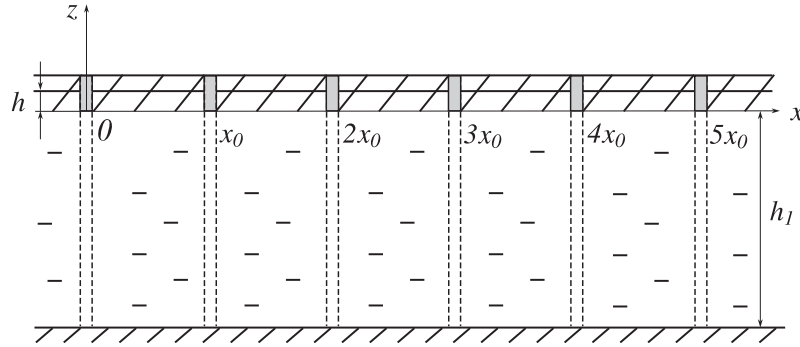


Figure 2: Cross-section of a periodic elastic plate floating on a thin fluid layer.

From the Laplace equation $\Delta\Phi(x, z) = 0$, where $\Delta = \frac{\partial^2}{\partial x^2} + \frac{\partial^2}{\partial z^2}$, we derive

$$\alpha_{2k}(x) = \frac{(-1)^k}{(2k)!} \frac{\partial^{2k}\alpha_0(x)}{\partial x^{2k}}, \quad \alpha_{2k+1}(x) = \frac{(-1)^k}{(2k+1)!} \frac{\partial^{2k}\alpha_1(x)}{\partial x^{2k}}, \quad k = 1, 2, \dots \quad (2)$$

In particular, we have

$$\alpha_2(x) = -\alpha_0''(x)/2. \quad (3)$$

From the boundary condition $\frac{\partial\Phi(x, -h_1)}{\partial z} = 0$ on the rigid bottom $z = -h_1$ we obtain

$$\alpha_1(x) = 0. \quad (4)$$

With account of the terms of the first order of smallness inclusively, in view of (4), we have

$$\Phi(x, 0) = \alpha_0(x). \quad (5)$$

From the kinematic boundary condition $\frac{\partial\Phi(x, 0)}{\partial z} = -i\omega\zeta(x)$ at the interface $z = 0$, in view of (3), we get

$$\zeta(x) = -\frac{i}{\omega}\alpha_0''(x)h_1, \quad (6)$$

where $\zeta(x)$ is the elevation of the plate. The dynamic boundary condition

$$D\zeta''''(x) + (\rho_1g - \rho h\omega^2)\zeta(x) - i\omega\rho_1\Phi(x, 0) = 0, \quad x \neq x_n$$

at the interface $z = 0$ gives

$$D\frac{d^6\alpha_0(x)}{dx^6} + (\rho_1g - \rho h\omega^2)\frac{d^2\alpha_0(x)}{dx^2} + \frac{\rho_1\omega^2}{h_1}\alpha_0(x) = 0, \quad x \neq x_n, \quad (7)$$

where D is the flexural rigidity, ρ is the density, h is the thickness of the plate. Thus, under a thin fluid layer approximation we will employ the equation (7) instead of the Laplace equation and the boundary conditions at $z = 0$ and $z = -h_1$. The matching conditions are imposed at $x = x_0n$ ($n \in \mathbb{Z}$).

$$\begin{aligned} \lim_{x \rightarrow x_n^+} \alpha_0(x) &= \lim_{x \rightarrow x_n^-} \alpha_0(x), \quad \lim_{x \rightarrow x_n^+} \alpha_0'(x) = \lim_{x \rightarrow x_n^-} \alpha_0'(x), \quad \lim_{x \rightarrow x_n^+} \zeta(x) = \lim_{x \rightarrow x_n^-} \zeta(x), \\ \lim_{x \rightarrow x_n} \zeta'(x) &= 0, \quad \lim_{x \rightarrow x_n^+} \zeta'''(x) = \lim_{x \rightarrow x_n^-} \zeta'''(x). \end{aligned} \quad (8)$$

Let us consider the equation (7) on the interval $(0, 2x_0)$. According to the theorem of Floquet [9], the general solution of the problem takes the form

$$\alpha_0(x) = \begin{cases} \sum_{n=0}^2 (C_n^+ e^{i\lambda_n x} + C_n^- e^{-i\lambda_n x}), & x \in (0, x_0), \\ \sum_{n=0}^2 (C_n^+ e^{i\lambda_n(x-x_0)} + C_n^- e^{-i\lambda_n(x-x_0)}) e^{i\varphi}, & x \in (x_0, 2x_0), \end{cases} \quad (9)$$

where $\lambda_0, \lambda_1, \lambda_2$ are the roots of the dispersion equation

$$D\lambda^6 + (\rho_1 g - \rho h \omega^2) \lambda^2 - \frac{\rho_1 \omega^2}{h_1} = 0. \quad (10)$$

λ_0 is the positive root, λ_1 and λ_2 are two complex roots located in the upper half plane ($\lambda_2 = -\overline{\lambda_1}$). Satisfying the matching conditions at $x = x_0$ leads to an inhomogeneous linear system of equations $Pu = v$, with a matrix P equals to

$$P = \begin{pmatrix} 1 & 1 & 1 & 0 & 0 & 0 \\ 0 & 0 & 0 & \lambda_0 & \lambda_1 & \lambda_2 \\ -\lambda_0^2 & -\lambda_1^2 & -\lambda_2^2 & 0 & 0 & 0 \\ 0 & 0 & 0 & -i\lambda_0^3 & -i\lambda_1^3 & -i\lambda_2^3 \\ \lambda_0^4 & \lambda_1^4 & \lambda_2^4 & 0 & 0 & 0 \\ 0 & 0 & 0 & i\lambda_0^5 & i\lambda_1^5 & i\lambda_2^5 \end{pmatrix}. \quad (11)$$

Variables u are introduced by the formulae

$$\begin{aligned} u_n &= C_n^+ (e^{i\varphi} - e^{i\lambda_n x_0}) + C_n^- (e^{i\varphi} - e^{-i\lambda_n x_0}), \\ u_{n+3} &= C_n^+ (e^{i\varphi} - e^{i\lambda_n x_0}) - C_n^- (e^{i\varphi} - e^{-i\lambda_n x_0}), \quad n = 0, 1, 2. \end{aligned}$$

A column-vector v is determined by $v = \frac{i\omega}{H} (0, 0, 0, 0, \frac{B}{D}, 0)^t$. The first and second equations of the system describe continuity of $\alpha_0(x)$ and its first derivative $\alpha_0'(x)$ at $x = x_0$. The third, fourth and sixth equations show continuity of the elevation $\zeta(x)$ and its first $\zeta'(x)$ and third $\zeta'''(x)$ derivatives at $x = x_0$, respectively. According to the fifth equation, the jump of the second derivative $\zeta''(x)$ is non-zero. The quantity B represents the bending moment at $x = x_0$. Solution of the system is

$$\begin{aligned} u_0 &= \frac{i\omega B}{HD(\lambda_0^2 - \lambda_1^2)(\lambda_0^2 - \lambda_2^2)}, & u_1 &= \frac{i\omega B}{HD(\lambda_1^2 - \lambda_0^2)(\lambda_1^2 - \lambda_2^2)}, \\ u_2 &= \frac{i\omega B}{HD(\lambda_2^2 - \lambda_0^2)(\lambda_2^2 - \lambda_1^2)}, & u_3 &= u_4 = u_5 = 0. \end{aligned} \quad (12)$$

Coefficients $C_0^\pm, C_1^\pm, C_2^\pm$ are calculated by

$$\begin{aligned} C_0^\pm &= \frac{i\omega B v_0^\pm}{2DH(\lambda_0^2 - \lambda_1^2)(\lambda_0^2 - \lambda_2^2)}, & C_1^\pm &= \frac{i\omega B v_1^\pm}{2DH(\lambda_1^2 - \lambda_0^2)(\lambda_1^2 - \lambda_2^2)}, \\ & & C_2^\pm &= \frac{i\omega B v_2^\pm}{2DH(\lambda_2^2 - \lambda_0^2)(\lambda_2^2 - \lambda_1^2)}, \end{aligned} \quad (13)$$

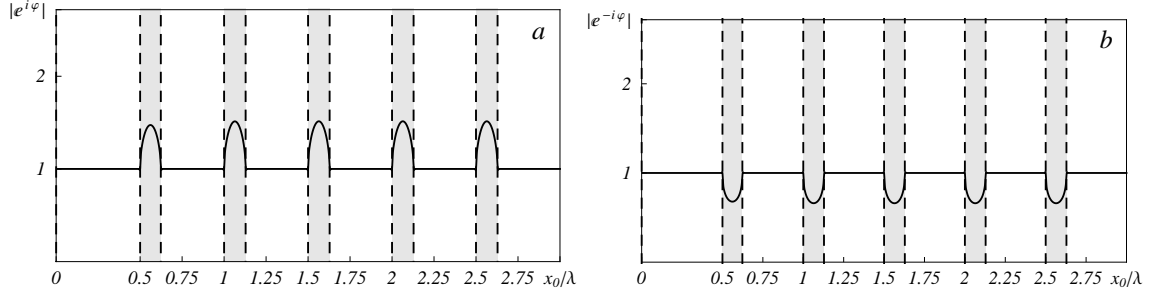


Figure 3: Moduli $|e^{i\varphi}|$ and $|e^{-i\varphi}|$ against the fractional separation x_0/λ between the movable clamps. Wave frequency is $\omega = 1.2 \text{ s}^{-1}$, wave length is $\lambda = 139.4 \text{ m}$. Vertical dashed lines show the boundaries of the stopping bands. The stopping bands are shaded

with $v_n^\pm = 1/(e^{i\varphi} - e^{\pm i\lambda_n x_0})$, $n = 0, 1, 2$. We set $\zeta'(x)$ equal to zero at $x = x_0$ and derive a simple algebraic equation

$$\frac{v_0^+ - v_0^-}{(\lambda_0^2 - \lambda_1^2)(\lambda_0^2 - \lambda_2^2)} \lambda_0^3 + \frac{v_1^+ - v_1^-}{(\lambda_1^2 - \lambda_0^2)(\lambda_1^2 - \lambda_2^2)} \lambda_1^3 + \frac{v_2^+ - v_2^-}{(\lambda_2^2 - \lambda_0^2)(\lambda_2^2 - \lambda_1^2)} \lambda_2^3 = 0. \quad (14)$$

Let us consider the cases a) $|e^{i\varphi}| = 1$ and b) $|e^{i\varphi}| \neq 1$ separately. In the case a) the solution $\alpha_0(x)$ undergoes a change in phase φ across two neighboring cells of the width x_0 and represents a wave propagating without attenuation throughout the periodic array of the movable clamps. The phase velocity of the wave is directed to the side of increasing or decreasing of coordinate x . The frequency is said to lie in a passing band. Under condition b) relation $\alpha_0(x + x_0) = e^{i\varphi}\alpha_0(x)$ indicates that amplitude of the wave process exponentially grows or decays when passing from one cell to another. The frequency is said to lie in a stopping band.

It can be shown straightforwardly that the boundaries of passing and stopping bands satisfy the equations

$$\begin{cases} \lambda_0^3(\lambda_1^2 - \lambda_2^2) \operatorname{ctg} \frac{\lambda_0 x_0}{2} + \lambda_1^3(\lambda_2^2 - \lambda_0^2) \operatorname{ctg} \frac{\lambda_1 x_0}{2} + \lambda_2^3(\lambda_0^2 - \lambda_1^2) \operatorname{ctg} \frac{\lambda_2 x_0}{2} = 0, \\ \lambda_0^3(\lambda_1^2 - \lambda_2^2) \operatorname{tg} \frac{\lambda_0 x_0}{2} + \lambda_1^3(\lambda_2^2 - \lambda_0^2) \operatorname{tg} \frac{\lambda_1 x_0}{2} + \lambda_2^3(\lambda_0^2 - \lambda_1^2) \operatorname{tg} \frac{\lambda_2 x_0}{2} = 0, \\ \sin(\lambda_0 x_0) = 0. \end{cases} \quad (15)$$

If $e^{i\varphi}$ is a solution of the equation (14) then so is $e^{-i\varphi}$. It means that waves have no preference in the direction in which they propagate. Dependencies of $|e^{\pm i\varphi}|$ from the fractional separation x_0/λ between the movable clamps are shown in Fig. 3.

3 An elastic periodically supported beam

We also concern with an infinitely long elastic beam with a periodic array of movable clamps at the points $x_n = x_0 n$, $n \in \mathbb{Z}$. The wave motion of the beam is governed by the equation

$$D\zeta''''(x) - \rho h \omega^2 \zeta(x) = 0, x \neq x_n, \quad (16)$$

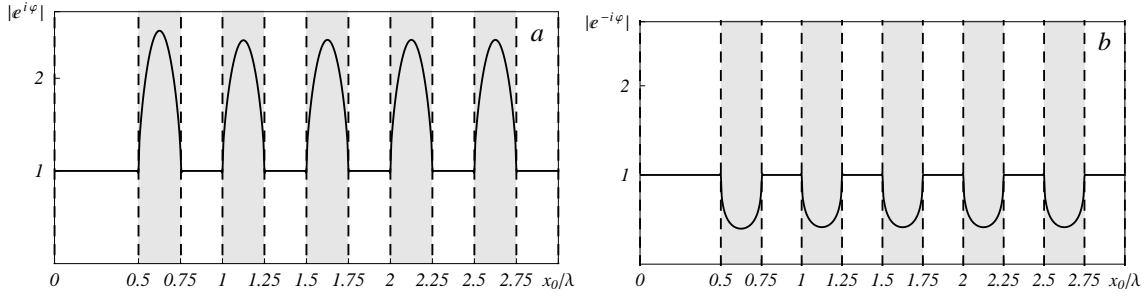


Figure 4: Moduli $|e^{i\varphi}|$ and $|e^{-i\varphi}|$ against the fractional separation x_0/λ between the movable clamps. Wave frequency is $\omega = 1.2 \text{ s}^{-1}$, wave length is $\lambda = 184.6 \text{ m}$. Vertical dashed lines show the boundaries of the stopping bands. The stopping bands are shaded.

where $\zeta(x)$ is the elevation of the beam, D is the flexural rigidity, ρ is the density, h is the thickness, ω is a wave angular frequency. The elevation $\zeta(x)$ must satisfy the matching conditions at the points $x = x_n$

$$\lim_{x \rightarrow x_n^+} \zeta(x) = \lim_{x \rightarrow x_n^-} \zeta(x), \quad \lim_{x \rightarrow x_n^+} \zeta'''(x) = \lim_{x \rightarrow x_n^-} \zeta'''(x), \quad \lim_{x \rightarrow x_n} \zeta'(x) = 0. \quad (17)$$

The periodicity of the configuration allows us to consider the equation (16) on the interval $(0, 2x_0)$ and in accordance with the Floquet theorem write the general solution in the form

$$\zeta(x) = \begin{cases} C_1 e^{ikx} + C_2 e^{-ikx} + \alpha e^{-kx} + \beta e^{kx}, & x \in (0, x_0), \\ (C_1 e^{ik(x-x_0)} + C_2 e^{-ik(x-x_0)} + \alpha e^{-k(x-x_0)} + \beta e^{k(x-x_0)}) e^{i\varphi}, & x \in (x_0, 2x_0), \end{cases} \quad (18)$$

where k is the arithmetical root of the equation $Dk^4 - \rho h \omega^2 = 0$. Unknown coefficients C_1 , C_2 , α and β must satisfy the inhomogeneous linear system of equations

$$\begin{cases} C_1(e^{i\varphi} - e^{ikx_0}) + C_2(e^{i\varphi} - e^{-ikx_0}) + \alpha(e^{i\varphi} - e^{-kx_0}) + \beta(e^{i\varphi} - e^{kx_0}) = 0, \\ C_1(e^{i\varphi} - e^{ikx_0}) - C_2(e^{i\varphi} - e^{-ikx_0}) + i\alpha(e^{i\varphi} - e^{-kx_0}) - i\beta(e^{i\varphi} - e^{kx_0}) = 0, \\ C_1(e^{i\varphi} - e^{ikx_0}) + C_2(e^{i\varphi} - e^{-ikx_0}) - \alpha(e^{i\varphi} - e^{-kx_0}) - \beta(e^{i\varphi} - e^{kx_0}) = \frac{B}{D}, \\ C_1(e^{i\varphi} - e^{ikx_0}) - C_2(e^{i\varphi} - e^{-ikx_0}) - i\alpha(e^{i\varphi} - e^{-kx_0}) + i\beta(e^{i\varphi} - e^{kx_0}) = 0 \end{cases} \quad (19)$$

to which we arrive from the matching conditions (17). The solution of the system is

$$\begin{aligned} C_1 &= \frac{B}{4D(e^{i\varphi} - e^{ikx_0})}, & C_2 &= \frac{B}{4D(e^{i\varphi} - e^{-ikx_0})}, \\ \alpha &= -\frac{B}{4D(e^{i\varphi} - e^{-kx_0})}, & \beta &= -\frac{B}{4D(e^{i\varphi} - e^{kx_0})}. \end{aligned} \quad (20)$$

The derivative $\zeta'(x)$ must be equated to zero at $x = x_0$ to find the characteristic equation with respect to the unknown factor $e^{i\varphi}$

$$\frac{e^{ikx_0}}{e^{i\varphi} - e^{ikx_0}} - \frac{e^{-ikx_0}}{e^{i\varphi} - e^{-ikx_0}} - i \frac{e^{-kx_0}}{e^{i\varphi} - e^{-kx_0}} + i \frac{e^{kx_0}}{e^{i\varphi} - e^{kx_0}} = 0. \quad (21)$$

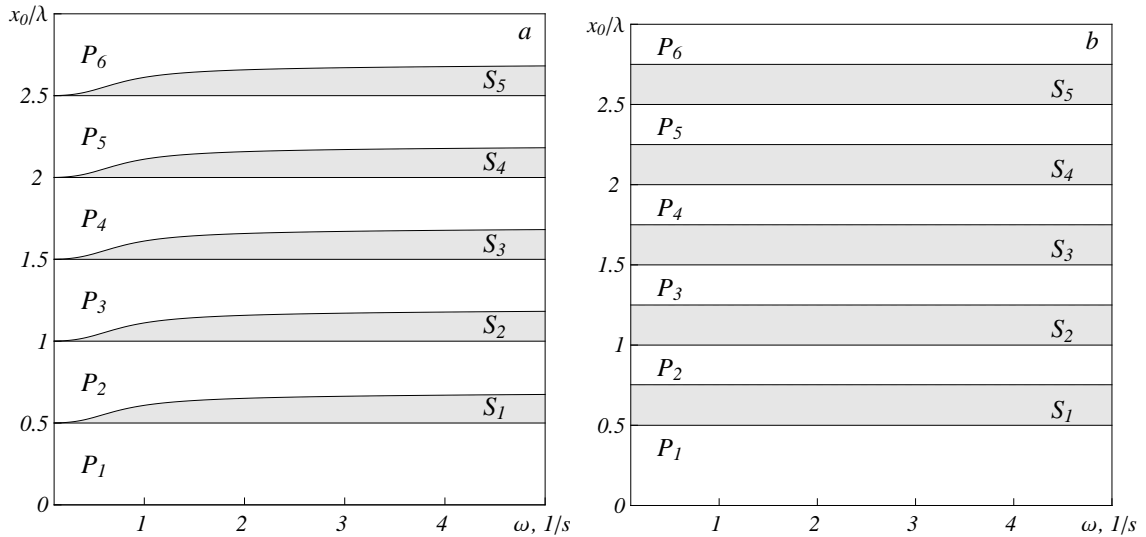


Figure 5: Passing and stopping bands in relation to the angular frequency ω and the fractional separation x_0/λ between the movable clamps. Stopping bands are shaded. λ is a wave length. a) An elastic periodic floating plate. b) An elastic periodic beam.

The boundaries of passing and stopping bands are described by equations

$$\operatorname{tg} \frac{kx_0}{2} \pm \operatorname{th} \frac{kx_0}{2} = 0, \quad \sin(kx_0) = 0. \tag{22}$$

Fig. 4 shows $|e^{\pm i\varphi}|$ versus the fractional separation x_0/λ between the movable clamps. Fig. 5 demonstrates the passing and stopping bands in relation to the frequency ω and the fractional separation x_0/λ between the movable clamps. The left subplot shows the curves obtained in the case of a floating elastic plate, the right subplot – in the case of an elastic beam. It is seen that the presence of a fluid layer markedly affects on the propagation of flexural waves. Stopping bands are narrowed. At very low frequencies they vanish. On the other hand, passing bands are broaden. Apparently this result has the following physical explanation. A fluid layer represents an additional channel of energy transfer, which facilitates the transmission of waves. Another feature is that the width of the first passing band is larger then others and is equal to a half-wave length.

4 Conclusion

Calculations performed by formulae (15) show that the maxima of energy transmission coefficient in a case of a finite number of movable clamps are reached within passing bands, and the minima – within stopping bands (Fig. 1). Since the maxima of transmission of an incident wave are accompanied by considerable internal efforts that are developed in all movable clamps and also by great amplitudes of the plate elevation, the knowledge of the boundaries and location of stopping and passing bands is of practical value.

References

- [1] Marchenko, A. V., 1996, Swell wave propagation in an inhomogeneous ice sheet, *Fluid Dynamics*. Vol. **31**, no. 5, pp. 761–767.
- [2] Porter, R., Evans D. V., 2006, Scattering of flexural waves by multiple narrow cracks in ice sheets floating on water, *Wave Motion*. Vol. **43**, issue 5, pp. 425–443.
- [3] Sorokin, S.V., Ershova, O. A., 2004, Plane wave propagation and frequency band gaps in periodic plates and cylindrical shells with and without heavy fluid loading, *Journal of Sound and Vibrations*. Vol. **278**, issue 3, pp. 501–526.
- [4] Kouzov, D. P., 1990, One-variable generalized functions and their applications in mechanics. Textbook. *Leningrad Shipbuilding Institute Publishers*, Leningrad, pp. 84
- [5] Glushkov, E., Glushkova, N., Wauer, J., 2011, Wave propagation in an elastically supported string with point-wise defects: gap-band and pass-band effects, *Z. Angew. Math. Mech.*. Vol. **91**, issue 1, pp. 4–22.
- [6] Filippenko, G. V., 2015, The bending waves in the beam with periodically located point masses, *Computational continuum mechanics*. Vol. **8**, no. 2, pp. 153–163.
- [7] Zhuchkova, M. G., Kouzov, D. P., 2014, The transmission of a flexural-gravitational wave through several straight obstacles in a floating plate, *J. Appl. Math. Mech.* Vol. **78**, no 4, pp. 359–366.
- [8] Brocklehurst, P., Korobkin, A. A., Parau, E. I., 2010, Interaction of hydro-elastic waves with a vertical wall, *J. Eng. Math.*. Vol. **68**, pp. 215–231, doi: 10.1007/s10665-010-9386-8.
- [9] Leon Brillouin. Wave Propagation in Periodic Structures, Electric Filters and Crystal Lattices. (International series in Pure and Applied Physics), New York and London, 1946.

M. G. Zhuchkova, V.O., Bolshoj pr., 61, St. Petersburg, 199178, Russia